Natural Resources Canada | Ressources naturelles Canada

GEOLOGICAL SURVEY OF CANADA
OPEN FILE 7852

Targeted Geoscience Initiative 4: Contributions to the Understanding of Precambrian Lode Gold Deposits and Implications for Exploration

B. Dubé and P. Mercier-Langevin
(Editors)

2015

Canada

GEOLOGICAL SURVEY OF CANADA
OPEN FILE 7852

Targeted Geoscience Initiative 4: Contributions to the Understanding of Precambrian Lode Gold Deposits and Implications for Exploration

B. Dubé and P. Mercier-Langevin

Geological Survey of Canada, Québec, Quebec

2015

doi:10.4095/296624

This publication is available for free download through GEOSCAN (http://geoscan.nrcan.gc.ca/)

Recommended citation

Dubé, B. and Mercier-Langevin, P. (ed.), 2015. Targeted Geoscience Initiative 4: Contributions to the Understanding of Precambrian Lode Gold Deposits and Implications for Exploration; Geological Survey of Canada, Open File 7852, 297 p. doi:10.4095/296624

Publications in this series have not been edited; they are released as submitted by the author.

Contribution to the Geological Survey of Canada's Targeted Geoscience Initiative 4 (TGI-4) Program (2010-2015)

TABLE OF CONTENTS

Appendix

GEOLOGICAL SURVEY OF CANADA
OPEN FILE 7852

Targeted Geoscience Initiative 4: Contributions to the Understanding of Precambrian Lode Gold Deposits and Implications for Exploration

Precambrian lode gold deposits — a summary of TGI-4 contributions to the understanding of lode gold deposits, with an emphasis on implications for exploration

Benoît Dubé[1], Patrick Mercier-Langevin[1], Sébastien Castonguay[1], Vicki J. McNicoll[2], Wouter Bleeker[2], Christopher J.M. Lawley[2], Stéphane De Souza[1], Simon E. Jackson[2], Céline Dupuis[1], Jian-Feng Gao[2], Valérie Bécu[1], Pierre Pilote[3], Jean Goutier[4], Gary P. Beakhouse[5], David Yergeau[6], William Oswald[6], Vivien Janvier[6], Arnaud Fontaine[6], Mireille Pelletier[6], Anne-Marie Beauchamp[6], Michel Malo[6], Laura R. Katz[7], Daniel J. Kontak[7], Zsuzsanna Tóth[7], Bruno Lafrance[7], Blandine Gourcerol[7], Phillip C. Thurston[7], Robert A. Creaser[8], Randolph J. Enkin[9], Najib El Goumi[9], Eric C. Grunsky[2], David A. Schneider[10], Colter J. Kelly[10], and Kathleen Lauzière[1]

[1]Geological Survey of Canada, Québec, Quebec
[2]Geological Survey of Canada, Ottawa, Ontario
[3]Ministère de l'Énergie et des Ressources naturelles, Montréal, Quebec
[4]Ministère de l'Énergie et des Ressources naturelles, Rouyn-Noranda, Quebec
[5]Ontario Geological Survey, Sudbury, Ontario
[6]Institut national de la recherche scientifique – Centre Eau Terre Environnement, Québec, Quebec
[7]Laurentian University, Sudbury, Ontario
[8]University of Alberta, Edmonton, Alberta
[9]Geological Survey of Canada, Sidney, British Columbia
[10]University of Ottawa, Ottawa, Ontario

2015

This publication is available for free download through GEOSCAN (http://geoscan.nrcan.gc.ca/)

Recommended citation

Dubé, B., Mercier-Langevin, P., Castonguay, S., McNicoll, V.J., Bleeker, W., Lawley, C.J.M., De Souza, S., Jackson, S.E., Dupuis, C., Gao, J.-F., Bécu, V., Pilote, P., Goutier, J., Beakhouse, G.P., Yergeau, D., Oswald, W., Janvier, V., Fontaine, A., Pelletier, M., Beauchamp, A.-M., Katz, L.R., Kontak, D.J., Tóth, Z., Lafrance, B., Gourcerol, B., Thurston, P.C., Creaser, R.A., Enkin, R.J., El Goumi, N., Grunsky, E.C., Schneider, D.A., Kelly, C.J., and Lauzière, K., 2015. Precambrian lode gold deposits — a summary of TGI-4 contributions to the understanding of lode gold deposits, with an emphasis on implications for exploration, *In:* Targeted Geoscience Initiative 4: Contributions to the Understanding of Precambrian Lode Gold Deposits and Implications for Exploration, (ed.) B. Dubé and P. Mercier-Langevin; Geological Survey of Canada, Open File 7852, p. 1–24.

Publications in this series have not been edited; they are released as submitted by the author.

Contribution to the Geological Survey of Canada's Targeted Geoscience Initiative 4 (TGI-4) Program (2010–2015)

TABLE OF CONTENTS

Precambrian lode gold deposits — a summary of TGI-4 contributions to the understanding of lode gold deposits, with an emphasis on implications for exploration

Benoît Dubé[1]*, Patrick Mercier-Langevin[1]†, Sébastien Castonguay[1], Vicki J. McNicoll[2], Wouter Bleeker[2], Christopher J.M. Lawley[2], Stéphane De Souza[1], Simon E. Jackson[2], Céline Dupuis[1], Jian-Feng Gao[2], Valérie Bécu[1], Pierre Pilote[3], Jean Goutier[4], Gary P. Beakhouse[5], David Yergeau[6], William Oswald[6], Vivien Janvier[6], Arnaud Fontaine[6], Mireille Pelletier[6], Anne-Marie Beauchamp[6], Michel Malo[6], Laura R. Katz[7], Daniel J. Kontak[7], Zsuzsanna Tóth[7], Bruno Lafrance[7], Blandine Gourcerol[7], Phillip C. Thurston[7], Robert A. Creaser[8], Randolph J. Enkin[9], Najib El Goumi[9], Eric C. Grunsky[2], David A. Schneider[10], Colter J. Kelly[10], and Kathleen Lauzière[1]

[1]Geological Survey of Canada, 490 rue de la Couronne, Québec, Quebec G1K 9A9
[2]Geological Survey of Canada, 601 Booth Street, Ottawa, Ontario K1A 0E9
[3]Ministère de l'Énergie et des Ressources naturelles, 201 avenue du Président-Kennedy, Montréal, Quebec H2X 3Y7
[4]Ministère de l'Énergie et des Ressources naturelles, 70 avenue Québec, Rouyn-Noranda, Quebec J9X 6R1
[5]Ontario Geological Survey, 933 Ramsey Lake Road, Sudbury, Ontario P3E 6B5
[6]Institut National de la Recherche Scientifique, Centre Eau-Terre-Environnement, 490 rue de la Couronne, Québec, Quebec G1K 9A9
[7]Mineral Exploration Research Centre, Laurentian University, 933 Ramsey Lake Road, Sudbury, Ontario P3E 6B5
[8]University of Alberta, 126 Earth Sciences Building, Edmonton, Alberta T6G 2R3
[9]Geological Survey of Canada, P.O. Box 6000, Sidney, British Columbia V8L 4B2
[10]Department of Earth Sciences, University of Ottawa, Ottawa, Ontario K1N 6N5
*Corresponding author's e-mail: bdube@nrcan.gc.ca
†Corresponding author's e-mail: pmercier@nrcan.gc.ca

ABSTRACT

The TGI-4 Lode Gold project, which comprises numerous site-specific and thematic research activities, covers the entire spectrum of crustal settings for lode gold deposits, from orogenic banded iron formation-hosted and greenstone-hosted quartz carbonate vein-type gold deposits formed deep in the crust (>5 km), to intrusion-related deposits that are formed at shallower crustal levels (~2–5 km), and to deposits formed at or near the seafloor. Herein we synthesize a number of important project contributions that have significant implications for on-going mineral exploration for hidden deposits. Among the key findings is a newly established link between major faults, their early evolution, syntectonic magmatism and synorogenic sedimentary basin evolution, and gold metallogenesis in various greenstone belts. The revised model incorporates a phase of tectonic extension—a distinct feature recognized in gold-rich settings worldwide—that is applicable to mineral exploration targeting across the Canadian Shield. Importantly, the simultaneous multidisciplinary study of a number of large banded iron formation-hosted gold deposits and districts allows for the development of a unifying genetic model for such deposits that integrates critical structural, stratigraphic, hydrothermal, and metamorphic elements. Several key features that are common to all of the studied deposits, but elements specific to dominantly banded iron formation-hosted gold deposits or to deposits that are only partly hosted in banded iron formation, were also established. The Lode Gold project also bridges a major knowledge gap by characterizing a spectrum of "unusual" or "atypical" gold deposits in the Superior Province. The new and revised models incorporate synvolcanic as well as pre-deformation and synorogenic synmagmatic or intrusion-related gold deposits that represent a large part of the newly discovered resources in the Canadian Shield in both "brownfield" and "greenfield" exploration environments.

Dubé, B., Mercier-Langevin, P., Castonguay, S., McNicoll, V.J., Bleeker, W., Lawley, C.J.M., De Souza, S., Jackson, S.E., Dupuis, C., Gao, J.-F., Bécu, V., Pilote, P., Goutier, J., Beakhouse, G.P., Yergeau, D., Oswald, W., Janvier, V., Fontaine, A., Pelletier, M., Beauchamp, A.-M., Katz, L.R., Kontak, D.J., Tóth, Z., Lafrance, B., Gourcerol, B., Thurston, P.C., Creaser, R.A., Enkin, R.J., El Goumi, N., Grunsky, E.C., Schneider, D.A., Kelly, C.J., and Lauzière, K., 2015. Precambrian lode gold deposits — a summary of TGI-4 contributions to the understanding of lode gold deposits, with an emphasis on implications for exploration, *In:* Targeted Geoscience Initiative 4: Contributions to the Understanding of Precambrian Lode Gold Deposits and Implications for Exploration, (ed.) B. Dubé and P. Mercier-Langevin; Geological Survey of Canada, Open File 7852, p. 1–24.

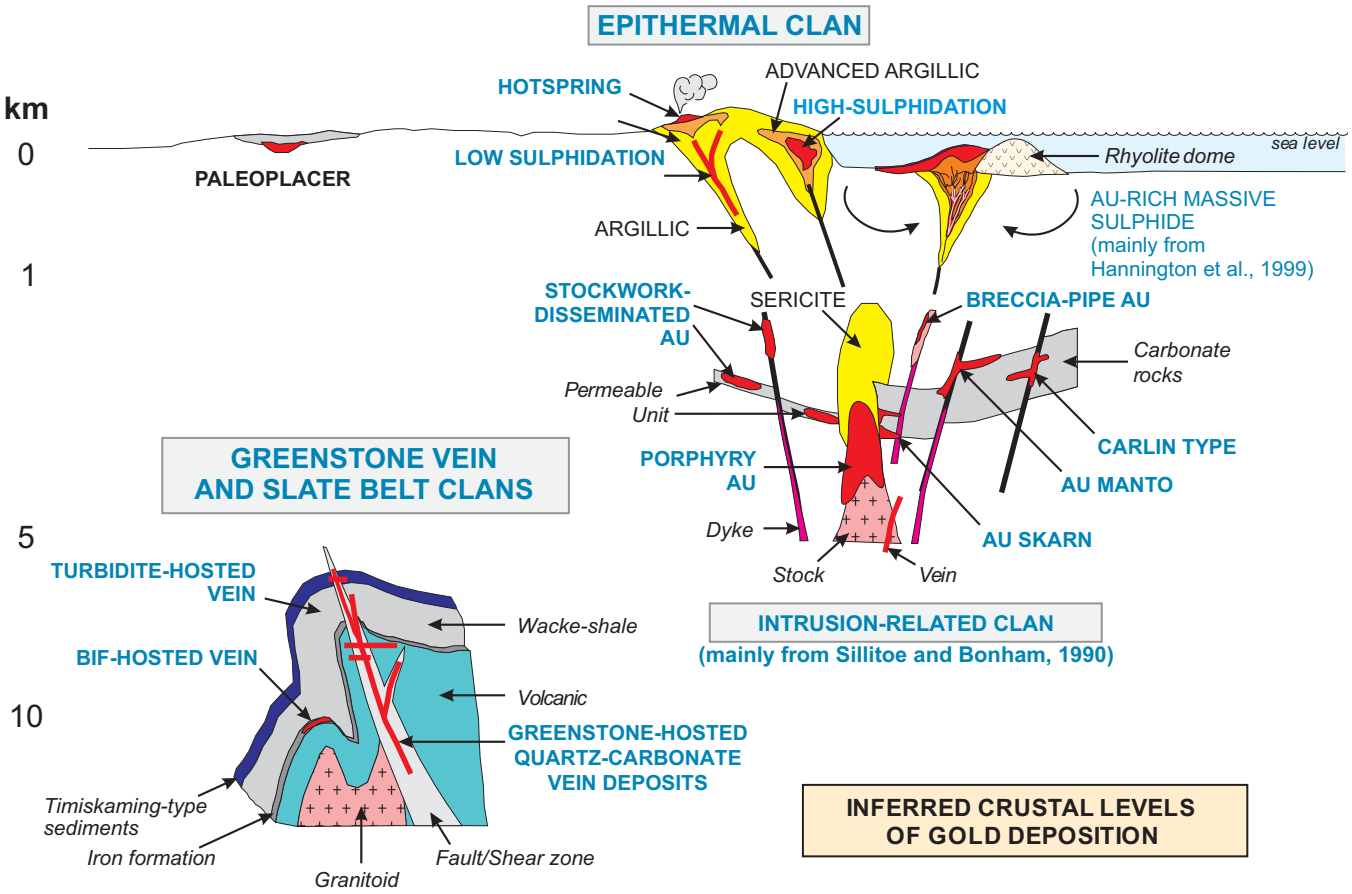

Figure 1. Schematic crustal section showing the inferred levels of gold deposition for the different types of lode gold deposits and their inferred clan (modified from Poulsen et al., 2000 and from Dubé and Gosselin, 2007).

INTRODUCTION

Gold is a major commodity that drives the Canadian mineral production and exploration industries (Mining Association of Canada, 2014). Over 90% of the historical gold production in Canada originates from Precambrian terranes, with as much as 85% coming from the Superior Province (based on 2009 figures; B. Dubé and V. Bécu, unpub. data). Despite a preponderance of Archean greenstone-hosted orogenic quartz-carbonate vein-type gold deposits, other types or styles of Precambrian gold deposit significantly contribute to the overall Canadian gold production, including BIF-hosted gold, intrusion-related, stockwork-disseminated gold (sediment- and volcanic-hosted), and gold-rich and auriferous volcanogenic massive sulphide (VMS) deposits (Fig. 1). Recent major discoveries in Canada (e.g. Côté Gold, Rainy River, Borden and Westwood; Fig. 2) illustrate that some deposit types and favourable geological settings are relatively poorly understood and/or underexplored, providing great scientific and exploration challenges that must be addressed prior to improving exploration models and guides. Most lode gold deposits, irrespective of deposit type, occur in deformed and metamorphosed terranes and are distributed along major structures, such as the Larder Lake-Cadillac or the Porcupine-Destor fault zones in the Southern Abitibi (Fig. 3; Miller and Knight, 1915; Groves, 1993; Hodgson, 1993; Kerrich and Cassidy, 1994; Groves et al., 1998; Kerrich et al., 2000; Goldfarb et al., 2005; Robert et al., 2005; Dubé and Gosselin, 2007). However, the key geological parameters controlling the fertility of such crustal-scale fault zones and the distribution and preservation of adjacent large gold deposits represent major knowledge gaps in lode gold systems that require further investigation (Robert et al. 2005; Dubé and Gosselin, 2007; Dubé et al., 2011).

MAIN RESEARCH THEMES

To develop a new generation of geological and exploration models based on modern, multi-parameter documentation of lode gold deposits, three main research themes were prioritized: 1) BIF-hosted gold deposits, 2) intrusion-related and stockwork-disseminated gold deposits, and 3) crustal-scale fault zones fertility. There are commonalities among these three research themes, and there are some linkages with other TGI-4 projects, including precious metal-rich VMS deposits. Methodology development is another common aspect of most of the research activities undertaken under the

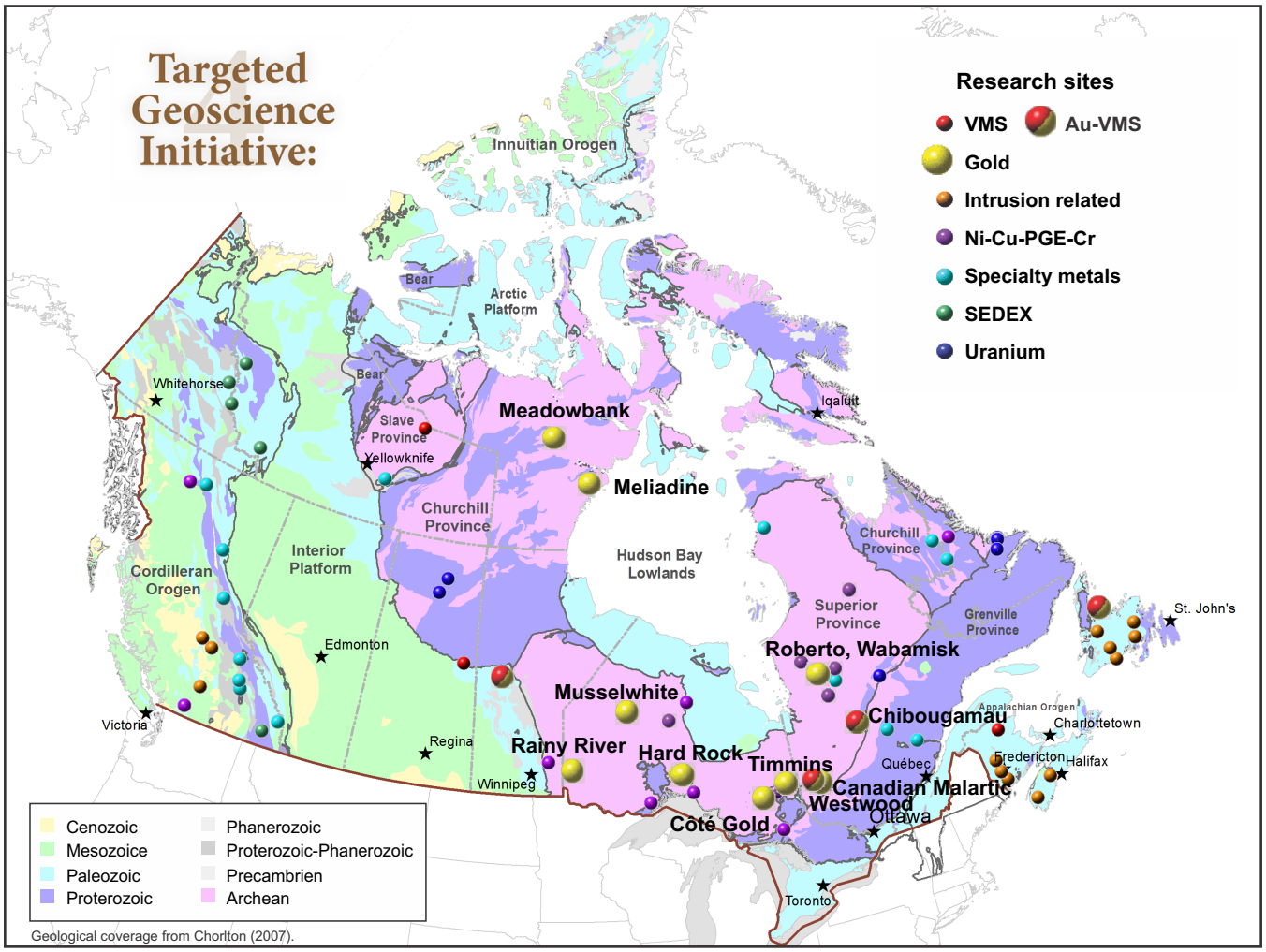

Figure 2. Location map of the TGI-4 Lode Gold project research activities. Geology from Chorlton (2007).

Lode Gold project. Selected key findings from each research theme are highlighted below.

Banded Iron Formation-Hosted Gold Deposits

Globally, BIF-hosted gold deposits significantly contribute to the gold endowment of Precambrian terranes, partly due to giant, high-grade deposits (e.g. Homestake Mine, South Dakota; 40 Moz: Caddey et al., 1991). These deposits represent a prime exploration target in northern Canada. Although various origins (syngenetic versus epigenetic: Fripp, 1976; Phillips et al., 1984) and classifications were proposed in the past for BIF-hosted gold deposits (e.g. stratiform syngenetic versus non-stratiform epigenetic deposits: Kerswill, 1993), the selected case studies differentiate two distinct groups of BIF-hosted gold deposits in Canada: 1) large deposits in which the ore is mainly hosted in Algoma-type (Gross, 1995) BIF (i.e. Musselwhite Mine, Ontario, and Meadowbank Mine, Nunavut; Fig. 4), and 2) deposits where only part of the mineralization is hosted in BIF. In the latter, the mineralized zones, which generally consist of orogenic greenstone-hosted quartz±carbonate vein gold, tend to cluster along a major fault zone (e.g. Meliadine district, Nunavut, and Geraldton district, Ontario; Figs. 1, 4). The simultaneous study of these four selected sites facilitated the description and comparison of the various geological setting, tectonic evolution, and primary and hydrothermal signature of BIF-hosted gold deposits. Each of the selected sites also represent different time periods (e.g. Archean versus Paleoproterozoic), and metamorphic grade (e.g. greenschist versus amphibolite facies) that together define a set of common and specific processes and exploration criteria for a variety of settings favourable for BIF-hosted gold deposits. (Fig. 2; Tóth et al., 2013a,b, 2014, 2015; Gourcerol et al., 2014, 2015a,b; Oswald et al., 2014, 2015a,b; Kelly and Schneider, 2015; Lawley et al., 2015; Janvier et al., 2015a,b). Some key aspects of BIF-hosted gold deposits are summarized in Figure 4.

Geological and Structural Settings

Favourable geological settings for BIF-hosted gold deposits are variable and range from BIF-rich

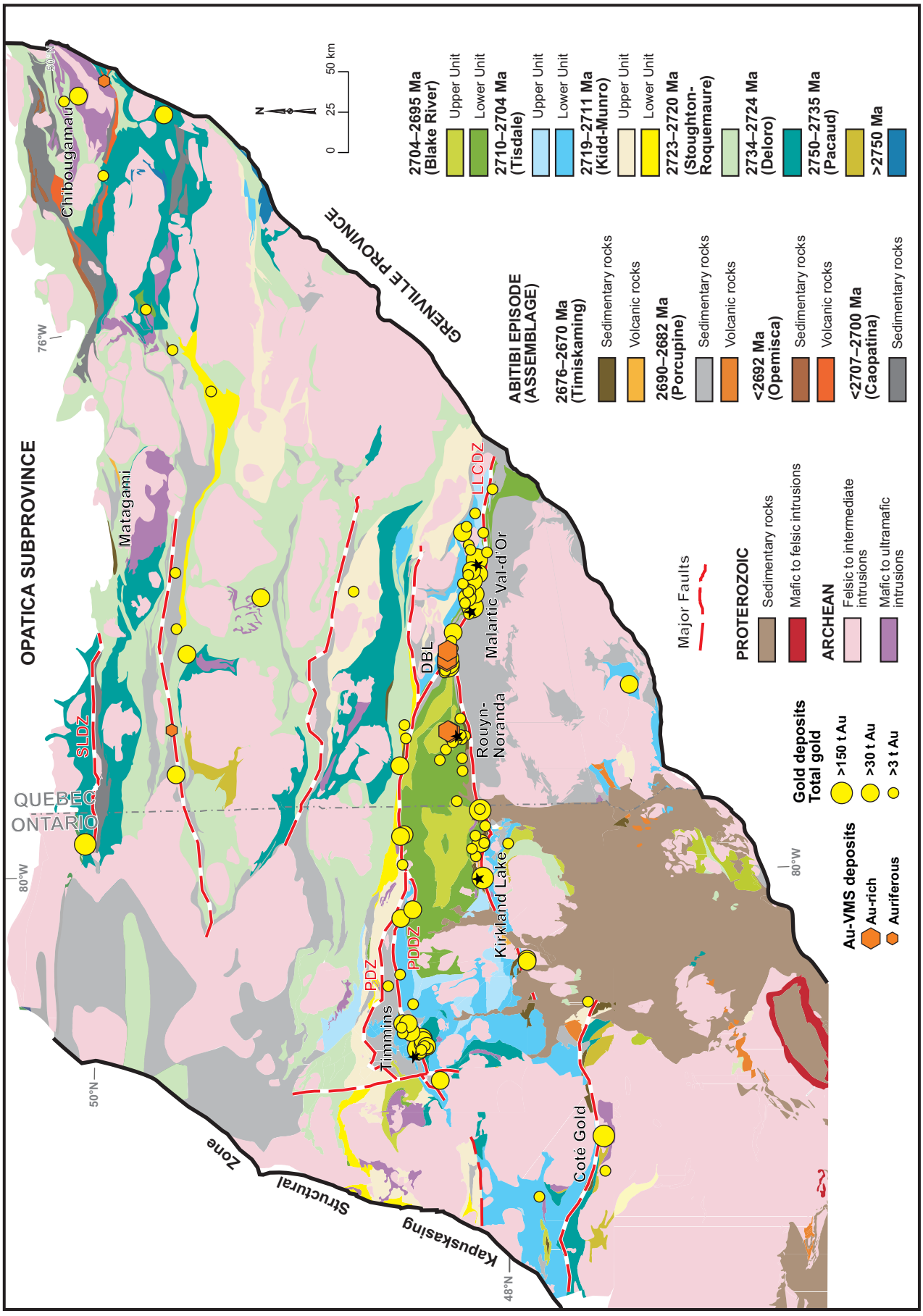

Figure 3. Simplified geological map of the Abitibi Subprovince with location of major gold deposits. From Ayer et al. (2010). Data for major gold and gold-rich VMS deposits modified from Gosselin and Dubé (2005) and Mercier-Langevin et al. (2011).

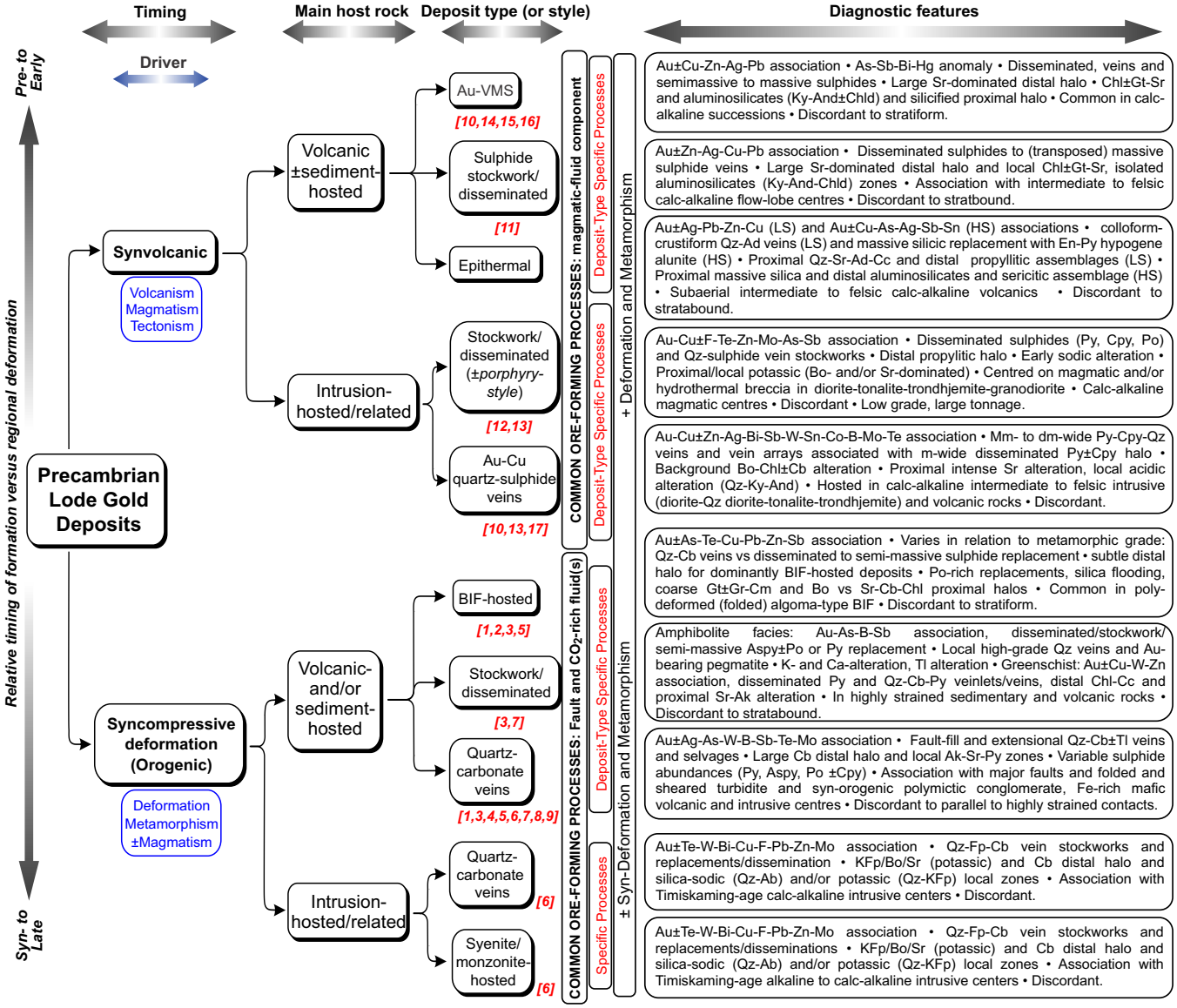

Figure 4. Graphic summary of the many different possible settings and main characteristics of lode gold deposits, with an emphasis on Precambrian lode gold deposits, more particularly on those studied as part of the TGI-4 Lode Gold project. The numbers in brackets refer to the deposits studied through the project. 1 = Musselwhite (Ontario), 2 = Meadowbank (Nunavut), 3 = Vault (Nunavut), 4 = Meliadine (Nunavut), 5 = Geraldton (Ontario), 6 = Canadian Malartic (Quebec), 7 = Roberto (Quebec), 8 = Wabamisk (Quebec), 9 = Timmins (Ontario), 10 = Westwood (Quebec), 11 = Rainy River (Ontario), 12 = Côté Gold (Ontario), 13 = Doyon (Quebec), 14 = Bousquet 2-Dumagami (Quebec), 15 = Lemoine (Quebec), 16 = Lalor (Manitoba), 17 = Chester (Ontario). Modified and adapted from Poulsen et al. (2000) and Mercier-Langevin (2014, unpublished). Abbreviations: Ab = albite, Ad = adularia, Ak = ankerite, And = andalusite, Aspy = arsenopyrite, Bo = biotite, Cb = carbonate, Cc = calcite, Chl = chlorite, Chld = chloritoid, Cm = cummingtonite, Cpy = chalcopyrite, En = enargite, Fp = feldspar, Gr = grunerite, Gt = garnet, HS = High-Sulphidation, KFp = potassium feldspar, Ky = kyanite, LS = Low-Sulphidation, Po = pyrrhotite, Py = pyrite, Qz = quartz, Tl = tourmaline. Modified from Poulsen et al. (2000).

volcano-sedimentary basins (e.g. Meadowbank and Musselwhite) to lithotectonic settings that are relatively BIF-poor (e.g. Meliadine and Geraldton). Both geological settings are prospective for large BIF-hosted gold deposits. Banded iron formations are volumetrically and laterally much more important in deposits dominantly hosted in BIF horizons, whereas these rocks are not as abundant in districts where deposits are only partly hosted in BIF units. The BIF units can be tens of metres thick and extend for thousands of metres as at Meadowbank and Musselwhite, or the ore-hosting BIF units can generally be much thinner and discontinuous at deposit to district scales as at Meliadine and Geraldton. Similarly, ultramafic flows form an integral part of the host stratigraphy in some dominantly BIF-hosted gold deposits (e.g. Meadowbank and Musselwhite), and appear sparse to minor in districts where BIFs represent a minor host. In such cases, a good understanding of the stratigraphy and of the structures controlling its geometry becomes essential for

developing more effective exploration strategies. For example, at Musselwhite, reappraisal of stratigraphic and polyphase structural relationships, supported by U-Pb geochronology, indicates that the mine stratigraphy is inverted, i.e., part of the overturned limb of a kilometre-scale refolded F_1 syncline (McNicoll et al., 2013; Oswald et al., 2015a,b). The previously underestimated regional F_1 folding event, which is strongly overprinted by the dominant D_2 deformation associated with the main mineralizing event at Musselwhite, has influenced the distribution and geometry of the BIF units hosting the bulk of the gold (Oswald et al., 2014, 2015a,b) and provides new key information for exploration models at local and regional scales.

The complex stratigraphic and polyphase structural settings of the Meadowbank deposit represent a good scientific challenge. The region comprises four major BIF units, with only the Central BIF hosting significant gold mineralization (Janvier et al., 2015a,b) in what are otherwise largely similar BIFs (Gourcerol et al., 2015a). Targeted geochronology suggests that the deposit is located along the boundary between two distinct Archean assemblages (ca. 2717 Ma and ca. 2711 Ma) that are possibly separated by long-lived fault(s) and splays. The presence of this major structure affecting the Central BIF points to a large-scale structural-control on BIF-hosted gold at the Meadowbank deposit and may explain why only this BIF is mineralized with gold and not in BIF units that are located away from that structure (Janvier et al., 2015a,b). It suggests that such first-order fault zones control the formation and distribution of other auriferous mineralized zones in the area.

The structural setting at Meadowbank is complicated by Paleoproterozoic tectonometamorphic events superimposed on Archean rocks and fabrics, as described elsewhere in the western Churchill Province (e.g. Sherlock et al., 2004; Carpenter et al. 2005; Pehrsson et al., 2013; Lawley et al., 2015). Previous research in the Meadowbank area (e.g. Armitage et al., 1996; Sherlock et al., 2001a,b, 2004; Hrabi et al., 2003) has indicated that gold was introduced during the second phase of regional Proterozoic deformation at ca. 1.85–1.83 Ga. Based on detailed mapping, structural analysis, and Re-Os geochronology, Janvier et al. (2015a,b) suggest that gold mineralization occurred earlier, possibly prior to, or at least very early during the second phase of regional Proterozoic deformation. Similarly, the Vault deposit, located approximately 8 km north of Meadowbank, is characterized by finely disseminated pyrite mineralization hosted in a major D_2 shear zone that separates two distinct Archean volcaniclastic rock packages (Dupuis et al., 2014) and that is parallel to the Proterozoic Third Portage thrust (Hrabi et al., 2003). Although entirely shear-zone hosted, the ore at Vault is spatially associated with a swarm of Archean (V. McNicoll et al., unpub. data) felsic dykes and sills. Auriferous pyrite at this deposit records a complex growth history that suggests an early, pre-main deformation mineralization (Dupuis et al., 2014), perhaps suggesting a pre- (Archean ?) or early-thrusting hydrothermal activity.

A similar complex and protracted hydrothermal and deformation history is suggested for the Meliadine district south of Meadowbank, which is located at the boundary between the Hearne and the Chesterfield block of the Western Churchill Province (Lawley et al., 2015) (Fig. 2). Detailed surface and underground mapping reveal a very complex structural setting with several strain increments and polyphased folding. The ore zones are associated with high-strain zones or second-order fault zones, such as the Lower Fault located a few hundred metres north of the first-order Pyke Fault (Carpenter and Duke, 2004; Carpenter et al., 2005; Lawley et al., 2014, 2015). The latter also parallels a particularly favourable lithostratigraphic setting that comprises structurally thickened BIF intervals structurally imbricated with turbidite and mafic volcanic rock packages. Geochronology (zircon and xenotime U-Pb and arsenopyrite Re-Os dating) suggest that gold at the Meliadine district was introduced during an early hydrothermal event(s) (ca. 2.27 and/or 1.90 Ga) that predates gold remobilization, coupled with arsenopyrite recrystallization, during the latest stage of the Trans-Hudson orogeny at 1.86–1.85 Ga (Carpenter et al., 2005; Lawley et al., 2015).

Establishing the exact timing of gold mineralization and metamorphism in BIF-hosted gold deposits represents a significant challenge. Kelly and Schneider (2015) used secondary ion mass spectrometry (SIMS) U-Pb depth profiles on unpolished detrital zircon from the Musselwhite deposit area to better constrain the age of hydrothermal activity and metamorphism in the mine area. Hydrothermal zircon rim ages range from 2788 to 2703 Ma, which is up to 250 million years younger than igneous zircon cores and possibly represents the age of a gold-bearing episode in the Musselwhite deposit area.

Primary Composition, Hydrothermal Alteration, and Metamorphic Assemblages

The primary chert composition of auriferous BIF intervals does not appear to exert a major control on gold mineralization, based on LA-ICP-MS analysis at Meadowbank, Musselwhite and Meliadine (Gourcerol et al., 2014, 2015a,b). However, ongoing systematic in situ geochemical analysis of chert samples collected outward from the gold zones at all three deposits is expected to provide more data that will help define the primary depositional setting of the ore-associated BIF

as well as the hydrothermal footprint of the deposits in the chert chemistry (Gourcerol et al., 2015b).

The extent and intensity of hydrothermal alteration in the studied BIF-hosted gold deposits depend on several aspects: 1) the setting of the deposit, i.e., dominantly BIF-hosted (Musselwhite and Meadowbank) versus partly BIF-hosted (Meliadine and Geraldton), 2) fluid chemistry and the composition of the host rock and their capacity to react with the fluid (e.g. chert-magnetite versus garnet-grunerite facies), 3) the metamorphic grade, and 4) the state of preservation of the original distribution and geometry of the hydrothermal system.

Gold deposits that are dominantly BIF-hosted are associated with a rather subtle mineralogical hydrothermal footprint (e.g. local chlorite alteration) compared with gold deposits that are only partly hosted in minor BIF units (e.g. large Fe-carbonate alteration halo). This may in part be due to variations in metamorphism grade and host rock types (e.g. poorly reactive chert), but nevertheless represents a fundamental difference between the two styles of deposits that must be taken into account when for exploring for BIF-hosted gold deposits.

In deposits that are only partly BIF-hosted and have undergone greenschist-facies metamorphic conditions, gold is quartz±carbonate±tourmaline vein-hosted and also occurs within hydrothermally altered and sulphidized vein selvages containing variable amounts of disseminated arsenian pyrite and/or arsenopyrite (Lawley et al., 2015; Tóth et al., 2015). Discontinuous auriferous BIF-hosted sulphide-rich replacements (pyrite, arsenopyrite, pyrrhotite) of magnetite bands typify high-strain zones, and/or transposed quartz-sulphide stockworks in magnetite and chert bands (Tóth et al., 2013a,b, 2014, 2015; Janvier et al., 2015a,b; Lawley et al., 2015). Key sulphide mineral assemblages within BIF, even in minor amounts, represent a potential guide to gold ore (Boyle, 1979; Phillips et al., 1984; Kerswill, 1993; Bierlein et al., 1998, 2000). Silicification occurs as quartz (± carbonate) replacement (flooding) within BIF and mafic volcanic host rocks. The latter is characteristic of high-grade ore at Meliadine (Lawley et al., 2015) and Meadowbank (Janvier et al., 2015a,b). In mafic/ultramafic rocks, a strong and extensive carbonate (ankerite-calcite) alteration is associated with various proportions of sericite and sulphides (arsenopyrite-pyrite-pyrrhotite-galena-chalcopyrite: Lawley et al., 2015; Tóth et al., 2015). The partial to semi-massive sulphide replacement of magnetite in BIF units is associated with sericite-carbonate and/or chlorite replacement surrounding quartz-carbonate±chlorite veins. Local pervasive chlorite alteration or chlorite «clots» represent a good visual indicator to mineralization and occur within auriferous quartz (±ankerite) veins and mineralized BIF intervals (Janvier et al., 2015a; Lawley et al., 2015). Hydrothermal chlorite is generally Fe-rich compared to hydrothermal chlorite and, where present, occurs with gold within quartz-carbonate veins and hydrothermally altered BIF (Lawley et al., 2015). In greywacke, mudstone, or intermediate to mafic volcaniclastic rocks, gold is associated with pyrite and arsenopyrite in sericite-carbonate (ankerite, dolomite, or calcite) and sericite±chlorite alteration selvages around the quartz-carbonate±tourmaline± pyrite±pyrrhotite veinlets and is characterized by K_2O gains and associated Na_2O losses. Such potassic alteration is expressed as hydrothermal sericite or biotite and is recognized as an important exploration vector at Meliadine and Geraldton (Lawley et al., 2015; Tóth et al., 2015).

At amphibolite grade, and especially in deposits that are dominantly hosted in thick Algoma-type BIF units, the hydrothermal alteration assemblages are commonly more difficult to visually distinguish from regional metamorphism due to syn-peak metamorphism hydrothermal mineral assemblages that are largely similar to regional metamorphism-related paragenesis, which hampers the development of vectors towards mineralization. In such cases, the use of pathfinder elements becomes critical for recognizing alteration haloes (e.g. Lawley et al., 2015). At amphibolite grade, the ore zones are dominated by stratabound pyrrhotite-rich (±pyrite) replacements and are locally associated with silica flooding of the BIF in the high-grade ore zones. Part of the ore is also hosted in discordant syntectonic grey quartz-pyrrhotite±pyrite veins that cut chert-magnetite BIF (Oswald et al., 2014, 2015). Volcanic and volcaniclastic rocks occurring proximal to the ore zones can display a biotite (±carbonate) alteration. The high-grade pyrrhotite-rich ore zones are associated with Fe-carbonate, Ca-amphibole, and Ca-Fe clinopyroxene (hedenbergite) minerals and display a metasomatic⁄ metamorphic layering delineated by abundant coarse-grained almandine garnet porphyroblasts, intergrown with fine- to medium-grained grunerite-cummingtonite and biotite (e.g. Musselwhite and Meadowbank Goose zone: Janvier et al., 2015a,b; Oswald et al., 2015). Several of the ore-associated minerals may also be part of the regional metamorphic paragenesis; a careful characterization is instrumental to distinguish and map the hydrothermal footprint of the deposit. Silicate minerals such as garnet, grunerite, ferro-tschermakite, and biotite are found in both regional metamorphic and ore-related mineral assemblages. The differentiation between proximal and distal alteration assemblages relative to gold mineralization with regional metamorphism resides partly in mineral textures, composition, and abundance. For example, the distal, least altered garnet-grunerite facies at

Musselwhite contains anhedral to subhedral almandine garnet whereas typical ore has abundant and coarse, subhedral to euhedral, fractured red calium-rich almandine garnet with associated pyrrhotite (Moran, 2008; Kolb, 2011; Oswald et al., 2014, 2015a,b). Pathfinder elements common to the investigated deposits are Au, S, Te, As, Cu, and Sb. For example, anomalous pathfinder element concentrations and domains of hydrothermally altered rocks can be traced from 10s to 100s of metres beyond high-grade lodes at Meliadine (Lawley et al., 2015). Critically, this multivariate hydrothermal footprint (e.g. S and As) can be mapped in real time utilizing a conditional probability-based approach and portable X-Ray Fluorescence (pXRF) spectrometry (Lawley et al., 2015).

Discussions and Implications for Exploration — Banded Iron Formation-Hosted Gold

The results from our study at Meliadine and Meadowbank indicate that gold is not solely Trans-Hudson in age (1.9–1.8 Ga) but may be associated with earlier tectonic events. New age determinations also suggest that the Proterozoic gold metallotect model as defined by Miller et al. (1994) in fact represents the end-product of successive auriferous hydrothermal events and/or younger gold remobilization. A good understanding of this complex Archean to Paleoproterozoic tectonic and metallogenic history is fundamental to define efficient exploration models in northern Canada. It also has implications for assessing the prospectivity of other reworked Precambrian cratonic margins, which represent prospective settings for world-class orogenic gold deposits (Lawley et al., 2015).

Our work indicates or confirms that BIF-hosted gold zones are the product of several structurally and stratigraphically controlled phases of gold mineralization (or remobilization) associated with various generations of Archean to Proterozoic deformation zones. Ore zones are concentrated along thickened fold hinges and strongly attenuated limbs of shallow-plunging folds (syn- and/or post-ore) as well as second- and third-order deformation zones (Oswald, 2014, 2015; Tóth et al., 2014, 2015; Lawley et al., 2015). The location of the ore zones is also strongly influenced by competency contrasts between sheared ultramafic/mafic volcanic rocks versus BIF, or BIF versus siliciclastic rocks. The layer anisotropy of the host BIFs induces significant structural complexities pre- and post-gold deposition; understanding these complexities is critical to optimize exploration models and mine development (e.g. Janvier et al., 2015a,b; Oswald et al., 2015; Tóth et al., 2015). The capacity of the rocks to buffer the gold-bearing hydrothermal fluid (chemical trap) is also fundamental in the process; in some cases, the ore is almost entirely (>80%) hosted within a specific competent and highly reactive silicate BIF facies (e.g. Musselwhite), and indicating that BIF-hosted gold deposits are not the sole product of ductile deformation (Oswald et al., 2015). The broader lithotectonic setting of BIF-hosted deposits is perhaps the area with the greatest potential for improving regional-scale targeting. Understanding the volcano-sedimentary basin increases the chance of finding the most favourable host units within a rock sequence that has recorded polyphase deformation.

Intrusion-Related and Stockwork-Disseminated Gold Deposits

Diverse styles of gold deposits are commonly spatially associated with, and/or hosted in intrusive rocks, including porphyry Cu-Au, syenite-associated disseminated gold, and reduced Au-Bi-Te-W intrusion-related deposits as well as stockwork-disseminated gold (e.g. Sillitoe, 1991; Thompson et al., 1999; Rowins, 2000; Robert, 2001; Goldfarb et al., 2005; Hart et al., 2007). In the Abitibi greenstone belt, several multi-million ounce Archean gold deposits, including Canadian Malartic, Kirkland Lake, Camflo, Young Davidson, Doyon, Westwood, and the McIntyre Cu-Au-Mo zone at Hollinger-McIntyre, are spatially associated with intrusions. A genetic link with intrusions is inferred for some of these deposits and indicates that there is a potential for finding such large intrusion-related deposits in greenstone terranes (Robert, 2001; Robert et al., 2007; Mercier-Langevin et al., 2012b, and references therein; Helt et al., 2014). This hypothesis is supported by examples located elsewhere in the Superior Province (e.g. the ~2 Moz Au-Cu Troilus deposit in the Frotet-Evans belt, and the ~7 Moz Au(-Cu) Côté Gold deposit in the Swayze belt: Figs. 2, 3). The Superior Province, due to its exceptional gold endowment, constitutes a prime laboratory to develop geological models and exploration criteria for such intrusion-related and stockwork-disseminated deposits. As the genesis of these «atypical» deposits remains controversial, the processes responsible for their formation are still highly debated (e.g. Pyke and Middleton, 1971; Davies and Lutha, 1978; Mason and Melnyk, 1986; Pilote et al., 1995; Brisbin, 2000; Robert, 2001; Groves et al., 2003; Goldfarb et al., 2005; Beaudoin and Raskevicius, 2014; Helt et al., 2014). During the course of the project, the key characteristics, and geological and hydrothermal footprints of some of the best examples of such gold deposits in the Superior Province were investigated, highlighting parameters responsible for their formation and distribution (e.g. Fig. 4). In the context of this report, the term stockwork-disseminated is essentially descriptive and does not infer a genetic process.

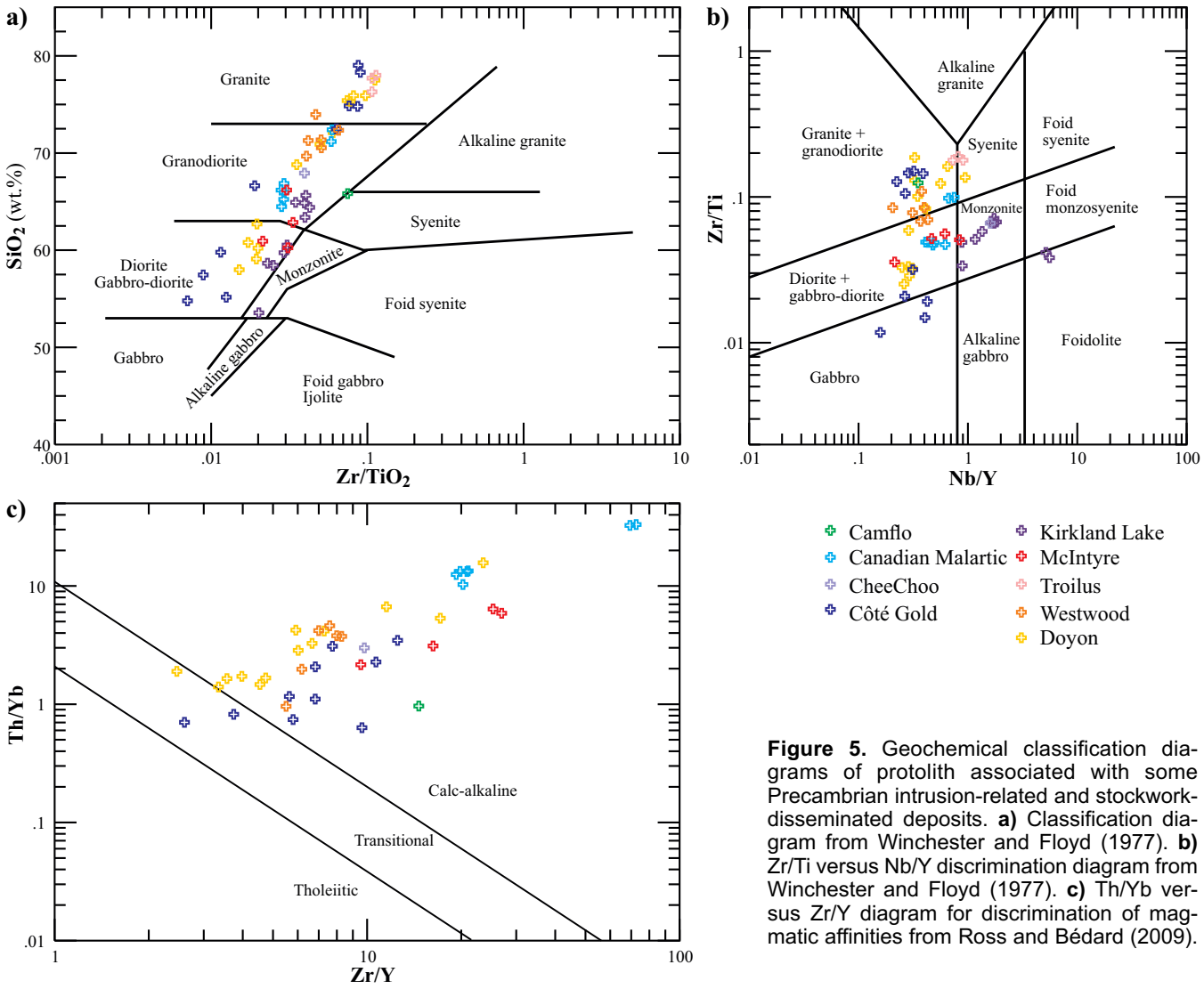

Figure 5. Geochemical classification diagrams of protolith associated with some Precambrian intrusion-related and stockwork-disseminated deposits. **a)** Classification diagram from Winchester and Floyd (1977). **b)** Zr/Ti versus Nb/Y discrimination diagram from Winchester and Floyd (1977). **c)** Th/Yb versus Zr/Y diagram for discrimination of magmatic affinities from Ross and Bédard (2009).

Relative and Absolute Timing of Ore-Forming Events versus Geological and Structural Settings

Most of the intrusion-related and stockwork-disseminated gold deposits investigated through the Lode Gold project (Fig. 2) are located near or within a major fault zone and its splays, which constitute favourable, but transient pathways to the upper crust for magma and/or gold-bearing fluids. The ore-associated intrusions can be located on either side of these fault zones, as illustrated by the Canadian Malartic and Camflo deposits, which are associated with ca. 2678–2677 Ma quartz monzodiorite to granodiorite (Canadian Malartic: De Souza et al., 2015) and with 2680 ± 4 Ma quartz monzonite (Camflo: Jemielita et al., 1990) but are located south and north of the Larder Lake – Cadillac fault zone, respectively (Fig. 3, Trudel and Sauvé, 1992; Pilote, 2013). Some of the intrusion-related gold deposits, which generally consist of stockwork- and disseminated-style mineralized zones, are entirely or partly hosted in clastic sedimentary rocks and/or volcanic rocks, whereas others are mainly confined to the associated intrusion or intrusive complex. The distribution and perhaps the composition of these intrusions are potentially linked to early stage extension along the main faults (e.g. Bleeker, 2012, 2015) and/or associated to flexures in major fault zone orientation, allowing the magma and ore-bearing fluids to invade the dilation zones and to form magmatic centres (e.g. Malartic area).

There is a large spectrum of ages of Archean intrusion-related and stockwork-disseminated gold systems in the Superior Province, and most are associated with diverse magmatic suites that include gabbro, diorite, granodiorite, monzodiorite, monzonite, syenite, tonalite, trondhjemite, granite, lamprophyre/albitite dykes and lithium, cesium, and tantalum (LCT) pegmatite dykes (Fig. 5a,b, Table 1). One recurring characteristic is the calc-alkaline to transitional subalkaline affinity of these ore-associated intrusions (Figs. 4, 5c). However, the diversity of the host intrusion's age

Table 1. Spectrum of ages and composition of selected deposits interpreted as Archean intrusion-related and/or stockwork-disseminated Au and Au-Cu deposits and prospects.

Deposit	Interpreted age(s) of Au (U-Pb host intrusion and/or Re-Os)	Associated Intrusion(s)	Selected References
Troilus	ca. 2782 Ma (U-Pb)	diorite and felsic dykes	Boily, 1995; Pilote et al., 1995; Dion et al., 1998; Rowins, 2011
Côté Gold	ca. 2740 Ma (U-Pb and Re-Os)	low-Al tonalite-diorite complex	Katz et al., 2015
Chibougamau Cu-Au	ca. 2714 Ma (U-Pb)	tonalite	Pilote et al., 1995, 1997; Dion et al.,1998; Leclerc et al., 2012
Doyon	ca. 2698 Ma (U-Pb)	diorite to trondhjemite	Galley and Lafrance, 2014; McNicoll et al., 2014
Young-Davidson	ca. 2680–2672 Ma (U-Pb)	syenite	Martin, 2012; Zhang et al., 2014
Kirkland Lake	ca. 2675 Ma (Re-Os)	alkalic intrusive	Ispolatov et al., 2008
Canadian Malartic	2678–2664 Ma (U-Pb and Re-Os)	granodiorite to quartz monzodiorite	De Souza et al., 2015
Camflo	ca. 2680 Ma (U-Pb)	monzonite	Jemielita et al. 1990
Cu-Au-Mo McIntyre	≤2689 ± 1 Ma (U-Pb); ca. 2672 Ma (Re-Os)	quartz-feldspar porphyry	Corfu et al., 1989; Bateman et al., 2004, 2005
CheeChoo	ca. 2612 Ma (U-Pb)	tonalite to granodiorite	Fontaine et al., 2015

and composition, and disparate gold events across the Superior Province highlights that conditions favourable for gold are not unique. Alternatively, deposits assigned to the intrusion-related group are commonly diverse and may include deposits of unrelated types, which partially explains the variability of ore deposits settings and styles (e.g. Sillitoe, 2000).

Superimposed tectonometamorphic events can significantly modify the original ore deposit characteristics, mask genetic relationships between intrusions and gold, and cause significant remobilization of the ore (e.g. Mercier-Langevin et al., 2012a,b). Moreover, geochronology and crosscutting relationships reveal that some deposits are the product of multiple auriferous hydrothermal and remobilization events. For example, the sediment-hosted stockwork-disseminated Canadian Malartic and Roberto deposits are the product of multi-phased auriferous events and/or remobilization (Ravenelle et al., 2010; De Souza et al., 2015; Fontaine et al., 2015). The Canadian Malartic deposit is hosted in clastic sedimentary rocks and quartz monzodiorite to granodiorite dykes and stocks, but the actual geometry and distribution of the ore zones are controlled by younger brittle-ductile structures associated with the main regional deformation event (De Souza et al., 2015). In some cases, the intrusion-related mineralization becomes part of a much larger ore system, as illustrated by the McIntyre Cu-Au-Mo zone (2689–2672 Ma: Mason and Melnik, 1986; Corfu et al., 1989; Brisbin, 1997; Bateman et al., 2004, 2005) that is overprinted by the ≤2673 Ma giant Hollinger-McIntyre greenstone-hosted orogenic quartz-carbonate vein system (Dubé and Gosselin, 2007; Bateman et al., 2008). Therefore, a good understanding of the relative timing of the intrusive, tectonic, and ore-forming event(s) combined with high-precision geochronology become essential to understand the causative role of the host intrusion(s) (i.e. active or passive) and the superposition of events in the formation of the deposits. Both factors are critical for effective mineral exploration in such complex geological environments. In very broad terms, pre-main compressive deformation intrusions seems to play an active role in the deposits genesis, whereas early- to syn-main compression intrusions, which may partly play an active role, seem to also act as passive hosts (Fig. 4) as the ore is often preferentially associated to structural features as discussed below.

Distribution and Diversity of Deposit Styles

Mineralization at some intrusion-related deposits is hosted in sedimentary and volcaniclastic rocks and ore distribution is controlled, at least in part, by folds, faults, and associated vein networks or stockworks (e.g. Canadian Malartic and Roberto). Elsewhere, such as at the Côté Gold Au(-Cu) deposit, the ore zones are centred on a multiphase magmatic-hydrothermal breccia, including a mineralized Au-Cu±Mo±Ag hydrothermal breccia that intrudes tonalitic (transitional to calc-alkaline) and dioritic (tholeiitic) phases of the Chester Intrusive Complex (CIC) (Katz et al., 2015 and references therein). The magmatic-hydrothermal breccia is itself overprinted by several ore-related hydrothermal alteration types (biotite, sericite, silica-sodic). The overlapping Re-Os age of syn-gold molybdenite with U-Pb zircon ages for the CIC highlight the spatio-temporal link between magmatism and gold-bearing hydrothermal events (Kontak et al., 2013; Katz et al.,

2015). As such, the Côté Gold deposit shares some analogies with Phanerozoic porphyry Cu-Au systems (Katz et al., 2015). At Westwood, intrusion-associated gold-sulphide veins and gold-rich VMS-type mineralization are considered to represent various components of an Archean auriferous synvolcanic magmatic-hydrothermal system (Yergeau et al., 2015 and references therein) and is reminiscent, at least in terms of geometry, of telescoped porphyry-epithermal systems (Yergeau, 2015; Yergeau et al., 2015). The quartz-carbonate-chalcopyrite veins of the former Chester 1, 2, 3 gold deposits, which are located in the immediate vicinity of the Côté Gold deposit, are also interpreted as pre-main deformation vein systems (Smith et al., 2014). The composition and relative timing of formation of the Chester veins are analogous to the intrusion-related Doyon and Westwood Zone 2 Extension high-grade quartz-pyrite-chalcopyrite vein systems.

Some stockwork-disseminated deposits are not readily associated with intrusions and represent synvolcanic gold in the seafloor/subseafloor environment. For example, at the Rainy River deposit, ca. 2717 Ma calc-alkaline dacite and rhyodacite host disseminated pyrite-sphalerite-chalcopyrite mineralized bodies and minor quartz-sulphide-tourmaline-carbonate veinlets and stockworks that are transposed in the main foliation (Pelletier et al., 2015). The setting and ore-style at the Rainy River deposit suggest that it may represent a subseafloor analogue to Archean gold-rich VMS systems (e.g. LaRonde Penna, Westwood, and Bousquet 1 deposits; Mercier-Langevin et al., 2015; Pelletier et al., 2015).

Hydrothermal Alteration, Mineral Assemblages, and Metallic Signature

To help develop geological and exploration models, hydrothermal vectors and fertility indicators have been defined. At Canadian Malartic and Coté Gold, these include a distal biotite or biotite-calcite dark-colour assemblages (disseminations and veins), which constitute the largest footprint and earliest alteration, and a proximal fracture-controlled, light colour to red-pink pervasive silica-sodic (quartz-albite) and/or potassic (quartz-microcline) alteration with sericite-carbonate±phlogopite, rutile, and pyrite replacement assemblage (De Souza et al., 2015; Katz et al., 2015). Traces of chalcopyrite are present in both the distal and proximal zones at Côté Gold. At present, biotite (Mg#, F, and Ti content) offers the best potential for mineral chemistry vectoring (De Souza et al., 2015; Katz et al., 2015). The whole-rock geochemistry of intrusive and sedimentary rocks reveals progressive distal to proximal gains in K_2O, Na_2O, CO_2, and S towards mineralization (De Souza et al., 2015; Katz et al., 2015). Furthermore, at Canadian Malartic, the ore (i.e. ≥0.3 ppm Au) is associated with the most strongly carbonatized rocks. Irrespective of the rock type, molar ratios (CO_2/CaO and CO_2/(CaO+MgO)) appear to represent a better proxy to estimate the intensity and style of carbonate alteration (e.g. molCO_2/molCaO >0.8) than the raw, whole-rock CO_2 content in wt% (De Souza et al., 2015).

At the Westwood deposit, manganiferous (Mn-garnet) and potassic (sericite and biotite) alteration haloes combined with sodium depletion are good indicators of modified seawater circulation in the volcanic edifice and VMS potential, whereas, barium and potassium enrichment (white micas) are associated with intrusion-related ore zones at the same deposit (Yergeau, 2015; Yergeau et al., 2015). Quartz-sericite and quartz-biotite-garnet schist with anomalous Zn, Cu, Au, and Ag values represent the distal footprint of deformed and metamorphosed gold-rich polymetallic VMS deposits in the Doyon-Bousquet-LaRonde district (Dubé et al., 2007, 2014; Yergeau et al., 2015). At Rainy River, the ore zones are directly associated with a diffuse potassic, sericite-dominated alteration. Manganiferous garnet, chloritoid, and kyanite also occur, at least locally, proximal to ore zones (Pelletier et al., 2015). At the metamorphosed Roberto deposit, the gold-bearing hydrothermal system shows distal calcic metasomatism that increases in intensity toward the ore zone, where it forms auriferous quartz±actinolite±diopside±biotite±arsenopyrite±pyrrhotite stockworks and veinlets. Quartz±actinolite±diopside±biotite±arsenopyrite±pyrrhotite vein stockworks and quartz-dravite-arsenopyrite veinlets contained within microcline, phlogopite, dravite, and arsenopyrite-pyrrhotite replacement zones comprise the bulk of the ore at the Roberto zone (Ravenelle et al., 2010; Ravenelle, 2013; Fontaine et al., 2015 and references therein).

A common feature to some of the studied deposits is the presence of gold-bearing pegmatite in the deposit's vicinity. At Roberto, a series of 2620–2603 Ma LCT pegmatite locally carries gold (Ravenelle et al., 2010; Fontaine et al., 2015) and as such could share analogies with the mineralized pegmatite at Canadian Malartic (Derry, 1939) and with the auriferous pegmatite that host some of the mineralized zones at the metamorphosed Borden gold deposit (e.g. Probes Mines Ltd, 2014). Both Roberto and Borden are metamorphosed deposits partly hosted in high-grade metamorphic rocks and share similar styles of mineralization, including a preferential association with deposit-scale fold hinges and the occurrence of late, locally auriferous pegmatite.

The metallic signature of the studied deposits is variable with a Au-Cu-F-Te-Zn ± Mo association at Côté Gold (Katz et al., 2015), a Au-Te-W-Bi-Ag ±Pb-Mo association at Canadian Malartic (De Souza et al.,

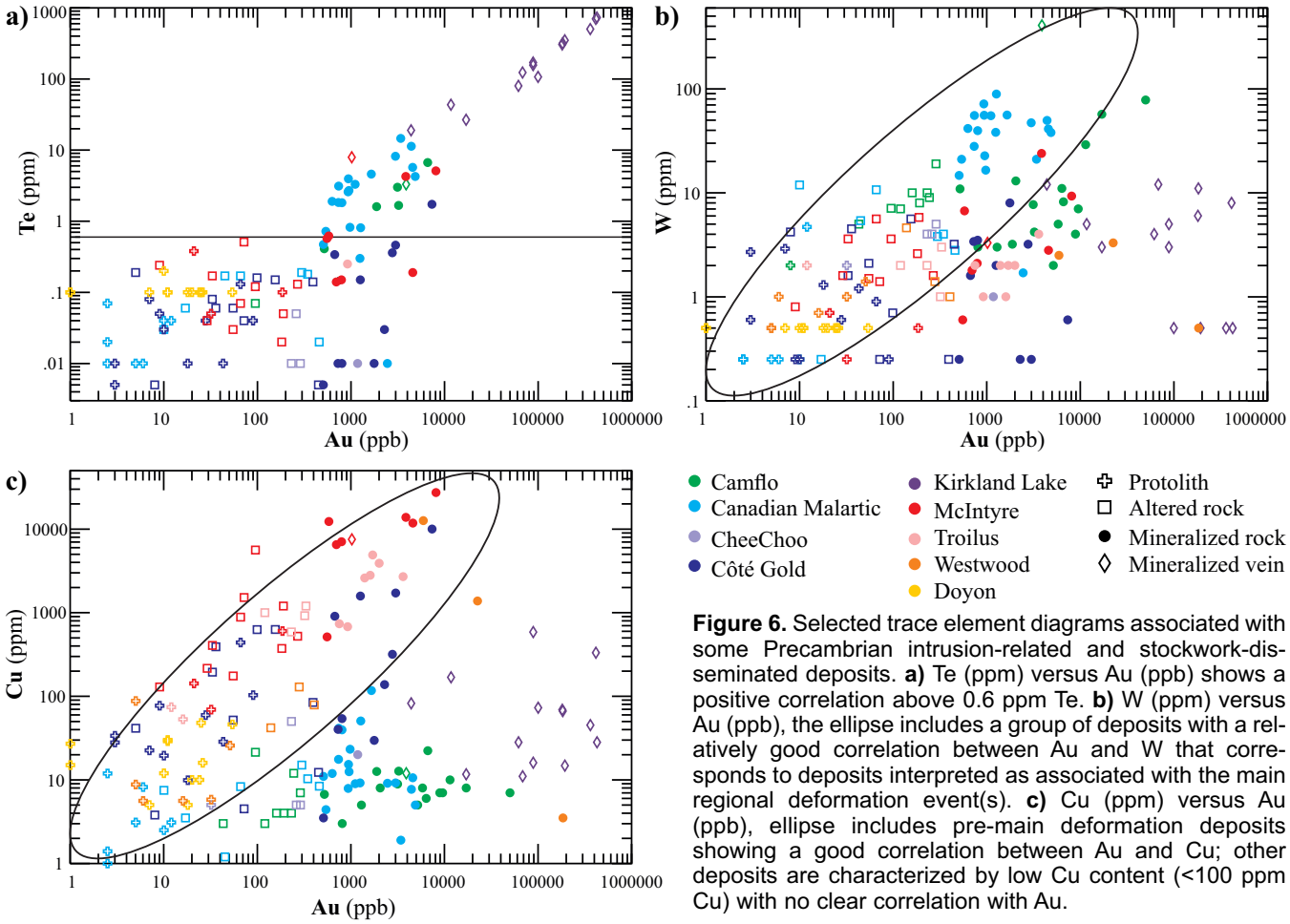

Figure 6. Selected trace element diagrams associated with some Precambrian intrusion-related and stockwork-disseminated deposits. **a)** Te (ppm) versus Au (ppb) shows a positive correlation above 0.6 ppm Te. **b)** W (ppm) versus Au (ppb), the ellipse includes a group of deposits with a relatively good correlation between Au and W that corresponds to deposits interpreted as associated with the main regional deformation event(s). **c)** Cu (ppm) versus Au (ppb), ellipse includes pre-main deformation deposits showing a good correlation between Au and Cu; other deposits are characterized by low Cu content (<100 ppm Cu) with no clear correlation with Au.

2015), and a Au-Cu-Zn-Ag-Pb association at Westwood (Yergeau, 2015; Yergeau et al., 2015). Among the studied deposit, there is an overall good correlation between Au and Te (>0.6 ppm Te), as shown in Figure 6a. There is an overall weak correlation between Au and W, although two trends or groups of deposits can be distinguished in Figure 6b: one with a relatively good Au-W correlation that corresponds to deposits that are associated with the main regional deformation event, and one with a very poor Au-W correlation that corresponds to deposits interpreted to have been formed prior to the main regional deformation. Similarly, two trends can be distinguished in the Au versus Cu diagram (Fig. 6c): one with a good correlation between Au and Cu (e.g. pre-main deformation deposits: Côté Gold, Westwood, Troilus, McIntyre) and a low-Cu (<100 ppm Cu) trend with no clear Au correlation (e.g. syn- to late-main deformation deposits: Camflo, Canadian Malartic, Kirkland Lake).

Pyrite is the most common sulphide in the studied deposits, with the exception of the Roberto deposit, and LA-ICPMS element and textural mapping systematically reveals several generations of pyrite, including inclusion-poor and inclusion-rich pre-, syn-, and post-ore pyrite (Dupuis et al., 2014; Pelletier et al., 2014, 2015; Gao et al., 2015; Yergeau, 2015), suggesting a very complex interplay between primary (synsedimentary and synvolcanic) processes and precipitation-dissolution episodes related to hydrothermal activity, deformation, and metamorphic recrystallization. Despite complex relationships, in most of the deposits that were studied, gold is largely concentrated in the inclusion-rich pyrite, together with Ag, Sb, Te, Pb, Bi, Zn, Cu, and Pb (Gao et al., 2015; Pelletier et al., 2015; Yergeau, 2015). Details about paragenesis and trace-metal distribution and associations in pyrite are presented in the site-specific studies and will be further investigated as ongoing research (e.g. thesis projects) progresses.

Discussions and Implications for Exploration – Intrusion-Related Gold Deposits

The Côté Gold and Canadian Malartic deposits represent two distinct end-members of intrusion-related and stockwork-disseminated deposits investigated in detail over the course of this project. While Coté Gold is a ca. 2740 Ma synvolcanic magmatic-hydrothermal system, Canadian Malartic represents a 2678–2664 Ma syndeformation system in which early tectonic (ca. 2678 Ma)

subalkaline porphyritic quartz monzodiorite and granodiorite intrusions have potentially contributed part of the metals to the system (De Souza et al., 2015). Despite distinct settings and origins, both deposits are associated with stockwork and disseminated-style mineralization (Fig. 4). Each deposit is also enveloped by distal potassic alteration haloes (biotite or biotite-calcite, sericite) that are anomalous in gold and proximal silica-sodic or silica-potassic alteration assemblages characterized by the presence of minor amounts of molybdenite. The presence of Cu and magmatic-hydrothermal breccia, which commonly characterize Cu-Au porphyry systems, are notable at the Côté Gold deposit but absent at Canadian Malartic. In the case of the Canadian Malartic deposit, combined potassic (biotite-sericite) and carbonate (calcite) alteration zones are coincident with brittle-ductile faults, high-strain zones, and fold hinges. These hydrothermally altered deformation-corridors represent interesting sub-kilometre exploration targets in the vicinity of the Larder Lake-Cadillac fault zone. As such, Canadian Malartic shares analogies with a group of structurally controlled stockwork, disseminated, and replacement sediment-hosted intrusion-related deposits (e.g. Sillitoe, 1991; Robert et al., 2007).

The results of the ongoing Côté Gold deposit study define a new and significant early stage gold metallogenic event in the Swayze greenstone belt at ca. 2740 Ma (Katz et al., 2015), significantly older than the gold-rich VMS deposits (ca. 2728 Ma and 2700 Ma), the syenite-associated gold deposits (ca. 2678 Ma), and the greenstone-hosted quartz-carbonate vein deposit (2670–2660 Ma) of the southern Superior Province. Together with deposits such as the ca. 2790–2780 Ma reduced porphyry-style Troilus gold deposit in the Frotet-Evans belt in Northwestern Quebec (Boily, 1995; Pilote et al., 1995, 1997; Dion et al., 1998; Rowins, 2011), Côté Gold provides a guide for future exploration associated with early stage composite, subvolcanic, low-Al trondhjemite-tonalite-diorite (TTD) and/or trondhjemite-tonalite-granodiorite (TTG)-intrusions in the Superior Province (Katz et al., 2015).

Unequivocal examples of typical porphyry Au or Cu-Au deposits and Au deposits genetically related to intrusions in Archean greenstone belts in Canada remain contentious (Sinclair, 2007). Attributes and processes driving their formation, including specific age and/or composition of the fertile magmatic source, fluid transport, and stratigraphic and structural traps are still debated (e.g. Sinclair, 1982; Mason and Melnyk, 1986; Fraser, 1993; Robert, 1994; Sinclair et al., 1994; Pilote et al., 1995; Brisbin, 2000; Goodman et al., 2005; Rowins, 2011; Beaudoin and Raskevicius, 2014; Helt et al., 2014; De Souza et al., 2015). However, several Archean deposits clearly share analogies with porphyry systems, including Troilus (Boily, 1995; Dion, 1998; Sinclair, 2007; Rowins, 2011 and references therein), the McIntyre Cu-Au-Ag-Mo mineralized zones at Hollinger-McIntyre (Griffis, 1962; Burrows and Spooner, 1986; Melnik-Proud, 1992, Brisbin, 2000; Bateman et al., 2008), and the porphyry-type mineralization in the Doré Lake complex (Robert, 1994; Sinclair et al., 1994; Pilote et al., 1995, 1997). Although the geometry of these ore zones and particularly their relationship to hydrothermal alteration facies and the geometry of the intrusive complex still need to be established in greater detail in many of these ancient systems, and in the absence of key data, such as pressure-temperature estimates and details on terrane-arc context at the inferred timing of the ore-forming events, we can nonetheless mention that exploration models based on Phanerozoic-type examples need to be adapted. These adapted models must take into consideration possibly slightly different genetic conditions in Precambrian settings (e.g. Mercier-Langevin et al., 2012b and references therein), as well as the common post-ore tectonometamorphic reworking of the original characteristics, as well as superposition of gold-bearing systems, which appear to be a common feature of such deposits in ancient deformed and metamorphosed terranes (Poulsen et al., 2000; Mercier-Langevin et al., 2012a,b and references therein).

Fingerprinting Fertile Fault Systems as Vectors to Large Gold Deposits

The geological parameters controlling the fertility of major fault zones and the formation, distribution, and preservation of diverse types of large gold deposits (greenstone-hosted orogenic quartz-carbonate veins, syenite-associated disseminated gold, gold-rich VMS, etc.; Fig. 3) along such structures was identified as a major knowledge gap in lode gold systems (Robert et al., 2005; Dubé and Gosselin, 2007; Dubé et al., 2011). The Timmins gold district is the largest Archean gold district in the world and represents by far the main source of gold in Canada (>68 Moz Au) for the last century, hosting the largest Canadian gold deposit ever found (Hollinger-McIntyre; >36 Moz Au: Gosselin and Dubé, 2005; Dubé and Gosselin, 2007). The Timmins district, due to its unique endowment, exposure, and complexity, represents a prime area to gather essential knowledge on several key topics: 1) the structural evolution and kinematics of large-scale gold-bearing fault zones that control the distribution of large gold deposits, including the nature and significance of pre-ore, early stage deformation; and 2) the tectonic and metallogenic significance of Timiskaming-type sedimentary basins and their spatial and/or genetic relationship with large fault zones, subvolcanic intrusions, and large gold deposits (Dubé et al., 2011). Although, the

focus was on Timmins for the Faults Fertility research theme, most deposits or areas investigated as part of the Lode Gold project have also contributed to this theme because of their location near major deformation zones and/or metamorphic fronts (e.g. Beauchamp et al., 2015; De Souza et al., 2015, Fontaine et al., 2015; Lafrance, 2015; Lawley et al., 2015; Tóth et al., 2015).

Deposits Distribution

Irrespective of ore type or style, most large Precambrian gold systems are distributed along major, first-order fault zones and their splays (e.g. Miller and Knight, 1915; Hodgson, 1993; Kerrich and Cassidy, 1994; Groves et al., 1998; Goldfarb et al., 2005; Robert et al., 2005; Dubé and Gosselin, 2007) or metamorphic fronts that demarcate the fault zones and characterize some boundaries between subprovinces (Gauthier et al., 2007). However, gold is preferentially associated with second- and third-order compressional reverse-oblique to oblique, brittle-ductile, high-angle shear zones that are commonly located within 5 km of the first-order fault (Robert, 1990). The various sites investigated in the Superior and Churchill provinces during the course of the project all support this historical exploration criterion. These structural corridors represent the pathways towards higher crustal levels for hydrothermal fluids and/or magma of diverse compositions, precious and base metal contents and origins. The fault zones are also responsible for the juxtaposition and preservation of deposits formed at different times and at different crustal depths (Poulsen et al., 2000; Dubé and Gosselin, 2007). For example, the ca. 2698 Ma synvolcanic Westwood deposit and the ca. 2678–2664 Ma Canadian Malartic deposit are located next to the Larder Lake-Cadillac fault zone, but were formed at different times and at different crustal levels. As part of the project, a gold fertility model has been developed for the two main fertile fault zones («breaks») of the Abitibi greenstone belt (Porcupine-Destor and Larder Lake-Cadillac) incorporating a critical phase of extension and coeval alkaline magmatism (Bleeker, 2012, 2015, Lafrance, 2015). According to this model, the main "breaks" were initiated as deep-seated, listric, synorogenic extensional faults that were coeval with a flare-up in «alkaline» magmatism and were then reactivated as thick-skinned thrusts that buried the synorogenic clastic rocks (Timiskaming basins) in their immediate structural footwall; thus explaining the preservation of gold deposits mainly on one side (footwall) of the long-lived structures (Bleeker, 2012, 2015). This model helps explain a long-standing empirical link between unconformities, major faults and major gold deposits (Miller and Knight, 1915; Poulsen et al., 1992; Hodgson, 1993; Cameron, 1993; Robert, 2001; Dubé et al., 2003, 2004; Robert et al., 2005; Dubé and Gosselin, 2007).

Deposit Characteristics versus Orogenic Pressure-Temperature-Time Path

Gold deposits are characterized by their geological setting, style(s) and types of mineralization, and also on the timing of mineralization relative to the orogenic pressure-temperature-time path. Several of the studied deposits are coeval with the main compressive phase of deformation (orogenic gold) and are all variably deformed and metamorphosed (prograde and retrograde paths). Other deposits are synvolcanic and were strongly overprinted and modified during younger deformation and metamorphic events (e.g. Westwood and Rainy River). Several deposits are syndeformational, but have recorded younger deformation and metamorphic events that may have remobilized gold (e.g. Roberto, Meadowbank, Meliadine, and Hard Rock). Many gold systems are the result of superimposed gold-bearing mineralizing events (e.g. Hollinger-McIntyre, Hard Rock, and Roberto), contributing to their complex geological and hydrothermal footprints. Moreover, evidence for gold remobilization is common and in some cases may control the geometry of high-grade gold ore zones (e.g. Meliadine, Westwood, Musselwhite, Hard Rock, and Bousquet 2-Dumagami).

Exploration Implications

The occurrence of alkaline magmatism concomitant with fault-bounded, clastic «Timiskaming-type» basins is a diagnostic criterion for recognizing potentially fertile major faults (e.g. Bleeker, 2012, 2015). The presence of «Timiskaming-type» conglomerate not only provides an indication for the potential presence of a major fault, it also indicates a favourable level of erosion and thus signals the potential for preservation of large gold deposits hosted lower in the stratigraphy by more competent and reactive rocks (e.g. Tisdale Formation, Timmins; Balmer basalt, Red Lake: Poulsen et al., 1992; Robert, 2001; Dubé et al., 2003, 2004; Robert et al., 2005; Bleeker, 2012 and references therein). This is illustrated by the occurrence of such a panel of synorogenic clastic rocks in the Penhorwood area of the northern Swayze greenstone belt, 80 km west of Timmins (Bleeker et al., 2014). This panel suggests that a major fault, most likely the western extension of the highly fertile Porcupine-Destor fault zone, is probably nearby and buried these clastic rocks in its structural footwall during the late thick-skinned thrusting phase (Bleeker et al., 2014). The presence of highly deformed and metamorphosed Timiskaming-age polymictic conglomerate, proximal to, or hosting, gold mineralization at the recent major Borden gold discovery (Probe Minerals, 165 km southwest of Timmins in

high-grade metamorphic rocks of the Kapuskasing structural zone), strongly supports the link between such synorogenic clastic sedimentary rocks, major fault zones, and large gold deposits. It opens significant new exploration ground for potential large gold deposits (Atkinson, 2014). Such a potential has been earlier emphasized by the correlation of major Archean gold-bearing fault zones across the Kapuskasing uplift by Leclair et al. (1993). Using a combination of high-strained rocks, linear belts of Timiskaming-type conglomerate, and calc-alkaline to alkaline igneous rocks, Leclair et al. (1993) extended the Porcupine-Destor and Larder Lake-Cadillac fault zones by hundreds of kilometres east and west of the Kapuskasing structural zone (Fig. 3), with both major tectonic and exploration implications. The newly discovered occurrence of Timiskaming-age polymictic conglomerate immediately to the north of the Larder Lake-Cadillac fault zone in the Malartic area adds new key information on the structural history of the Larder Lake-Cadillac fault zone and its potential fertility in an area where there are several Timiskaming-age intrusions and significant gold deposits (e.g. Camflo, Canadian Malartic: Pilote et al., 2014). The presence of the Canadian Malartic deposit immediately south of the Larder Lake-Cadillac fault zone, the Barnat (Sansfaçon and Hubert, 1990) and Lapa (Simard et al., 2013) deposits within the fault zone, and the Camflo deposit ~7 km north of the fault zone highlight that significant gold deposits can be formed (and preserved) within the footwall and hanging-wall successions of such major fault zones. The preservation potential of these deposits depends, in part, on the amplitude of the throw of the reverse faulting and the level of erosion (e.g. Bleeker et al., 2012, 2015).

In the Musselwhite deposit area, the presence of a newly discovered polymictic conglomerate in the upper stratigraphic sequence of the mine may indicate the presence of a major structure and provide guidelines for exploration throughout the North Caribou greenstone belt, especially if combined with tightly folded silicate-rich BIF horizons (Oswald et al., 2014, 2015a,b). The past-producing gold mines in the Geraldton area were all located in the southern sedimentary assemblage, including polymictic conglomerate, and mostly within the kilometre-wide Tombill-Bankfield deformation zone (Tóth et al., 2013). A similar setting may also characterize the Meadowbank area with the presence of Archean, polymictic basal-type conglomerate. These conglomerate units structurally overly the Meadowbank host succession, although the primary geometry of these relict sedimentary basins is unknown due to a major Paleoproterozoic overprint (Janvier et al., 2015a,b).

Early massive iron-carbonate veins pre-main-stage gold mineralization are present at the Hard Rock deposit in the Beardmore-Geraldton gold district (Tóth et al., 2015), as well as in numerous deposits in Timmins including Dome, Paymaster, and at the Campbell-Red Lake deposit in Red Lake (Dubé et al., 2003, 2004). These veins may represent a key hydrothermal event in the formation of large gold deposits and illustrate the protracted nature of hydrothermal activity and more particularly large-scale CO_2 metasomatism.

Technology Development

The Lode Gold project was also the opportunity to contribute to the development of advanced analytical and material characterization methodologies, either as specific research activities or as components to field-based and site-specific studies. These include in situ geophysical measurements and their correlation with mineralogy and geochemistry (Canadian Malartic Mine: El Goumi et al., 2015), the classification of ore samples based on whole-rock geochemistry (OSNACA project: Grunsky et al., 2015), pXRF spectrometry (e.g. Lawley et al., 2015), and the systematic use of LA-ICP-MS geochemistry in all site-specific research activities and a thematic fertility fingerprinting project (Gao et al., 2015).

In direct collaboration with the Canada Mining Innovation Council's footprint project at the Canadian Malartic Mine (Linnen et al., 2014), variability of rock physical properties was measured in the open-pit area to relate lithology and alteration assemblages to physical properties. The objective of this collaborative research was to better constrain geophysical surveys on this type of ore deposit and help define and detect the footprint of the deposit. The results indicate that no single geophysical technique can provide a particularly useful measure of the presence of hydrothermal alteration or gold content (El Goumi et al., 2015). However, a combination of decreasing density and magnetic susceptibility with increasing chargeability coincides with changes in the alteration assemblages (e.g. carbonate saturation index), gold concentration, and proximity to ore, especially in the sedimentary rocks that host ≥70% of the ore. A petrophysical proxy has been established as representative of this gradual hydrothermal mineralization process by assessing composite petrophysical properties (density, magnetic susceptibility, and chargeability) and quantifying their principal component analysis. Such proxy could potentially improve the geophysical approach in exploration for such low-grade bulk-tonnage deposits (El Goumi et al., 2015).

The OSNACA (Ore Samples Normalized to Average Crustal Abundance) international project is a new approach jointly developed by the mineral exploration industry, the Centre for Exploration Targeting,

University of Western Australia, and the TGI-4 Lode Gold project to characterize and classify representative ore samples from a wide spectrum of lode gold deposit types based on whole-rock geochemistry (Grunsky et al., 2015). The developed classification scheme, based on a statistical analysis of chemical concentrations, consists of a log-centred-ratio transformation of a suite of 24 ore-associated trace elements, which helps discriminate ore deposit types according to specific trace-element correlations. This can therefore become an extra tool to assess exploration potential in both greenfield and brownfield areas by providing another way of recognizing well known ore types at an early stage.

CONCLUSIONS

The integration of many site studies (Canadian Malartic, Coté Gold, Geraldton, Meadowbank, Meliadine, Musselwhite, Rainy River, Roberto, Timmins, Vault, Wabamisk, Westwood), thematic research, and the interaction with other TGI-4 projects (e.g. VMS) has broadened the knowledge base for a large spectrum of Precambrian gold deposit types and their footprints at various metamorphic grades, leading to a more targeted approach in greenfield terranes (e.g. Rainy River, Wabamisk, and Roberto deposits) while stimulating a reappraisal of models in mature (brownfield) districts at depth. The classic Abitibi «orogenic» quartz-carbonate vein exploration model used in Archean terranes for decades is being revised, as there is clearly a much broader spectrum of gold deposit types/styles, including "syngenetic/synmagmatic" and metamorphosed gold deposits that are distinct from the orogenic model (e.g. Poulsen et al., 2000; Goldfarb et al., 2005, Robert et al., 2005; Ravenelle et al., 2010), as well illustrated here. Such a reappraisal has an impact on exploration models in deformed and metamorphosed Precambrian and younger terranes in Canada.

Collectively, the TGI-4 Lode Gold project provides a wealth of new data and descriptions of selected key deposits or districts and new greenfield discoveries (e.g. Wabamisk), as well as ideas and concepts that will be applicable to exploration and that broadly contribute to our general understanding of the geological and metallogenic evolution of Archean cratons and Paleoproterozoic belts that represent major sources of metals worldwide, including most of the gold production in Canada. The unique gold endowment, or heritage of the southern Abitibi greenstone belt, in addition to specific ore-forming processes, must also be taken into account when trying to understand key ore-forming processes in uniquely endowed areas such as the southern Superior Province (e.g. Sillitoe, 2008). The huge amount of gold present in districts such as Timmins and Doyon-Bousquet-LaRonde may be related to specific, fundamental geological characteristics in terms of favourable source-rock environments, gold reservoirs, and/or early gold enrichment (i.e. provinciality concept: Hodgson, 1993; Hutchinson, 1993; Sillitoe, 2000; Gray and Hutchinson, 2001; Dubé and Gosselin, 2007; Sillitoe, 2008; Mercier-Langevin et al., 2012b) as summarized on Figure 7. Enriched gold "reservoirs" could have been tapped at different times during the evolution of the greenstone belt to form various types of gold deposits (e.g. Au-rich VMS, syenite associated Au, orogenic quartz-carbonate Au veins, etc). In such a model, the major fault zones that had access to these gold-enriched reservoirs through time acted as conduits to auriferous hydrothermal fluids and are associated with the development large deposits and districts. Advances in our understanding of key deposits and ore systems in the southern Abitibi belt, which was largely generated through the Targeted Geoscientific Initiative, puts us into a good position to tackle a major remaining knowledge gap that is the reason why there is so much gold in such a small part of Earth's crust.

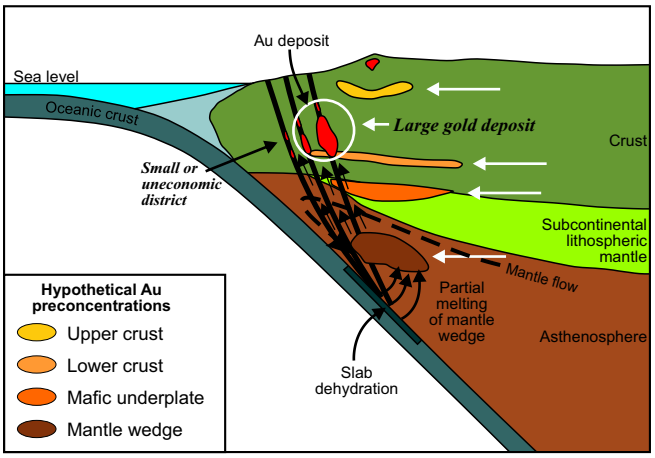

Figure 7. Schematic section of a convergent margin showing hypothetical sites of gold preconcentration(s) in the lower crust and upper mantle that may constitute a common source of gold for magmatic-hydrothermal and orogenic deposits. Modified from Sillitoe (2008).

Finally, but not the least, the Lode Gold project has also considerably contributed to the training of highly qualified personnel for the mineral industry and research institutions by supporting two visiting fellows, eight doctoral projects, five master's projects, and four undergraduate honours' theses. These talented young research scientists have directly interacted with the industry and academia, and gained academic and hands-on experience to be part of the new generation of young economic geologists.

ACKNOWLEDGEMENTS

This project was conducted in collaboration with the Ministère de l'Énergie et des Ressources naturelles du Québec, the Ontario Geological Survey, and the

Canada Mining and Innovation Council (CMIC) footprints project, which are all gratefully acknowledged for their participation and scientific contributions. We express our sincerest thanks to numerous colleagues from the federal and provincial surveys, academia, and the numerous mining and exploration companies involved, for strongly contributing and sharing their knowledge of Precambrian gold deposits and belts, and for access to the study sites, datasets, and support. This project could not have been conducted without the strong contribution by a group of young talented and motivated visiting fellows, graduate, and undergraduate students. We also acknowledge the TGI-4 management team for their full support, especially M. Villeneuve, S. Paradis, and D. Richardson TGI-4 management and Lode Gold project managers. We also want to warmly acknowledge Elizabeth Ambrose for her excellent work; her editing skills definitely made the Lode Gold synthesis Open File a much better product.

REFERENCES

Armitage, A.E., James, R.S., and Goff, S.P., 1996. Gold mineralization in Archean banded iron formation, Third Portage Lake area, Northwest Territories, Canada; Exploration and Mining Geology, v. 5, p. 1–15.

Atkinson, B., 2014. Kapuskasing structural zone: A budding new exploration frontier; The Ontario Prospector, v. 18, p. 6–10.

Ayer, J., Goutier, J., Thurston, P., Dubé, B., and Kamber, B., 2010. Abitibi-Wawa Subprovince tectonic and metallogenic evolution, *In:* Yilgarn-Superior Workshop – Abstracts; Fifth International Archean Symposium, Geological Survey of Western Australia, Perth, Australia, September 10, 2010, Record 2010/20, p. 7–11.

Bateman, R., Ayer, J.A., Barr, E., Dubé, B., and Hamilton, M.A., 2004. Gold subproject 1. Protracted structural evolution of the Timmins-Porcupine gold camp and the Porcupine-Destor shear zone; Ontario Geological Survey, Miscellaneous Paper, p. 41-1 to 41-10.

Bateman, R., Ayer, J.A. Dubé, B., and Hamilton, M.A., 2005. The Timmins-Porcupine gold camp, northern Ontario: the anatomy of an Archean greenstone belt and its gold mineralization: Discover Abitibi Initiative; Ontario Geological Survey, Open File Report 6158, 90 p.

Bateman, R., Ayer, J.A., and Dubé, B., 2008. The Timmins-Porcupine gold camp, Ontario: Anatomy of an Archean greenstone belt and ontogeny of gold mineralization; Economic Geology, v. 103, p. 1285–1308.

Beauchamp, A.-M., Dubé, B., Malo, M., McNicoll, V.J., Archer, P., Lavoie, J., and Chartrand, F., 2015. Geology, mineralization and alteration of the turbidite-hosted Mustang Au showing, Lower Eastmain greenstone belt, Superior Province, Quebec, *In:* Targeted Geoscience Initiative 4: Contributions to the Understanding of Precambrian Lode Gold Deposits and Implications for Exploration, (ed.) B. Dubé and P. Mercier-Langevin; Geological Survey of Canada, Open File 7852, p. 227–243.

Beaudoin, G. and Raskevicius, T., 2014. Constraints on the genesis of the Archean oxidized, intrusion-related Canadian Malartic gold deposit, Quebec, Canada: A discussion; Economic Geology, v. 109, p. 2067–2068.

Bierlein, F.P., Arne, D.C., McKnight, S., Lu, J., Reeves, S., Besanko, J., Marek, J., and Cooke, D., 2000. Wall-rock petrology and geochemistry in alteration halos associated with mesothermal gold mineralization, central Victoria, Australia; Economic Geology, v. 95, p. 283–312.

Bierlein, F.P., Fuller, T., Stuwe, K., Arne, D.C., and Keays, R.R., 1998. Wallrock alteration associated with turbidite-hosted gold deposits—examples from Central Victoria, Australia; Ore Geology Reviews, v. 13, p. 345–380.

Bleeker, W., 2012. Targeted Geoscience Initiative (TGI-4) Lode Gold Deposits in Ancient Deformed and Metamorphosed Terranes: The role of extension in the formation of Timiskaming basins and large gold deposits, Abitibi greenstone belt—A discussion, *In:* Summary of field work and other activities 2011; Ontario Geological Survey, Open File Report 6280, p. 47-1 to 47-12.

Bleeker, W., 2015. Syn-orogenic gold mineralization in granite-greenstone terranes: the deep connection between extension, major faults, syn-orogenic clastic basins, magmatism, thrust inversion and long-term preservation, *In:* Targeted Geoscience Initiative 4: Contributions to the Understanding of Precambrian Lode Gold Deposits and Implications for Exploration, (ed.) B. Dubé and P. Mercier-Langevin; Geological Survey of Canada, Open File 7852, p. 25–47.

Bleeker, W., Atkinson, B.T., and Stalker, M., 2014. A "new" occurrence of Timiskaming sedimentary rocks in the northern Swayze greenstone belt, Abitibi Subprovince—with implications for the western continuation of Porcupine–Destor fault zone and nearby gold mineralization, *In:* Summary of Field Work and Other Activities 2014; Ontario Geological Survey, Open File Report 6300, p. 43-1 to 43-10.

Boily, B., 1995. Porphyry-type mineralization in the Troïlus-Frotet Greenstone belt—The Lac Troïlus Cu-Au deposit, *In:* Metallogeny and Geologic Evolution of the Chibougamau Area— from Porphyry Cu-Au-Mo to Mesothermal Lode Gold Deposits, (ed.) P. Pilote; Geological Survey of Canada, Open File 3143, p. 123–130.

Boyle, R.W., 1979. The geochemistry of gold and its deposits (together with a chapter on geochemical prospecting for the element); Geological Survey of Canada, Bulletin 280, 584 p.

Brisbin, D.I., 1997. Geological setting of gold deposits in the Porcupine gold camp, Timmins, Ontario; Ph.D. thesis, Queen's University, Kingston, Ontario, 523 p.

Brisbin, D.I., 2000. World-class intrusion-related Archean vein gold deposits of the Porcupine gold camp, Timmins, Ontario, *In:* Symposium Proceedings; Geology and Ore Deposits 2000: The Great Basin and Beyond, Geological Society of Nevada, May 15-18, 2000, p. 19–35.

Burrows, D.R. and Spooner, E.T.C., 1986. The McIntyre Cu-Au deposit, Timmins, Ontario, Canada, *In:* Proceedings Volume, (ed.) A.J. MacDonald; Gold '86, International Symposium on the Geology of Gold Deposits, Toronto, Ontario, p. 23–39.

Caddey, S.W., Bachman, R.L., Campbell, T.J., Reid, R.R., and Otto, R.P., 1991. The Homestake gold mine, an Early Proterozoic iron-formation-hosted gold deposit, Lawrence County, South Dakota; United States Geological Survey, Bulletin 1857-J, 67 p.

Cameron, E.M., 1993. Precambrian gold: Perspective from top to bottom of shear zones; The Canadian Mineralogist, v. 31, p. 917– 944.

Carpenter, R.L. and Duke, N.A., 2004. Geological setting of the West Meliadine gold deposits, Western Churchill Province, Nunavut, Canada; Exploration and Mining Geology, v. 13, p. 49–65.

Carpenter, R.L., Duke, N.A., Sandeman, H.A., and Stern, R., 2005. Relative and absolute timing of gold mineralization along the Meliadine trend, Nunavut, Canada: Evidence for

Paleoproterozoic gold hosted in an Archean greenstone Belt; Economic Geology, v. 100, p. 567–576.

Chorlton, L.B., 2007. Generalized geology of the world: Bedrock domains and major faults in GIS format; Geological Survey of Canada, Open File 5529, 1 CD-ROM.

Corfu, F., Krogh, T.E., Kwok, Y.Y., and Jensen, L.S., 1989. U-Pb zircon geochronology in the southwestern Abitibi greenstone belt, Superior province; Canadian Journal of Earth Sciences, v. 26, p. 1747–1763.

Davies, J.F. and Lutha, L.E., 1978. An Archean "porphyry-type" disseminated copper deposit, Timmins, Ontario; Economic Geology, v. 73, p. 383–396.

Derry, D.R., 1939. The geology of the Canadian Malartic gold mine, N. Québec; Economic Geology, v. 34, p. 495–523.

De Souza, S., Dubé, B., McNicoll, V.J., Dupuis, C., Mercier-Langevin, P., Creaser, R.A., and Kjarsgaard, I.M., 2015. Geology, hydrothermal alteration, and genesis of the world-class Canadian Malartic stockwork-disseminated Archean gold deposit, Abitibi, Quebec, *In:* Targeted Geoscience Initiative 4: Contributions to the Understanding of Precambrian Lode Gold Deposits and Implications for Exploration, (ed.) B. Dubé and P. Mercier-Langevin; Geological Survey of Canada, Open File 7852, p. 113–123.

Dion, C., Pilote, P., David, J., and Cater, D., 1998. Géologie et âge de la minéralisation Au-Cu à la mine Troilus, ceinture de Froter Evans, Québec, Dans : Résumés; Association géologique du Canada – Association minéralogique du Canada réunion annuelle conjointe, Montréal, Québec, Mai 2014, v. 23, p. 46.

Dubé, B. and Gosselin, P., 2007. Greenstone-hosted quartz-carbonate vein deposits, *In:* Mineral Deposits of Canada: A Synthesis of Major Deposit Types, District Metallogeny, the Evolution of Geological Provinces, and Exploration Methods, (ed.) W.D. Goodfellow; Geological Association of Canada, Mineral Deposits Division, Special Publication, No. 5, p. 49–73.

Dubé, B., Williamson, K., and Malo, M., 2003. Gold mineralization within the Red Lake Mine trend:example from the Cochenour-Willans Mine area, Red Lake Ontario with some new key information from the Red Lake Mine and potential analogy with the Timmins camp; Geological Survey of Canada, Current Research 2003-C21, 15 p.

Dubé, B., Williamson, K., McNicoll, V., Malo, M., Skulski, T., Twomey, T., and Sanborn-Barrie., M.J., 2004. Timing of gold mineralization in the Red Lake gold camp, northwestern Ontario, Canada: new constraints from U-Pb geochronology at the Goldcorp high-grade zone, Red Lake mine and at the Madsen mine; Economic Geology, v. 99, p. 1611–1642.

Dubé, B., Mercier-Langevin, P., Hannington, M., Lafrance, B., Gosselin, G., and Gosselin, P., 2007. The LaRonde Penna world-class Au-rich volcanogenic massive sulfide deposit, Abitibi, Québec: mineralogy and geochemistry of alteration and implications for genesis and exploration; Economic Geology, v. 102, p. 633–666.

Dubé, B., Mercier-Langevin, P., Castonguay, S., McNicoll, V., Pehrsson, S.J., Bleeker, W., Schetselaar, E.M., and Jackson, S., 2011. Targeted Geoscience Initiative 4. Lode gold deposits in ancient, deformed and metamorphosed terranes – footprints and exploration implications: a preliminary overview of themes, objectives and targeted areas, *In:* Summary of field work and other activities 2011; Ontario Geological Survey, Open File Report 6270, p. 38-1 to 38-10.

Dupuis, C., Mercier-Langevin, P., McNicoll, V., Janvier, V., Dubé, B., Castonguay, S., de Chavigny, B., Pehrsson, S., and Côté-Mantha, O., 2014. The Vault gold deposit, Meadowbank area, Nunavut: Preliminary results on the nature and timing of mineralization, *In:* Abstracts; Geological Association of Canada – Mineralogical Association of Canada Joint Annual Meeting, Fredericton, New Brunswick, May 2014, v. 37, p. 81.

El Goumi, N., De Souza, S., Enkin, R.J., and Dubé, B., 2015. Petrophysical signature of gold mineralization and alteration assemblages at the Canadian Malartic deposit, Quebec, Canada, *In:* Targeted Geoscience Initiative 4: Contributions to the Understanding of Precambrian Lode Gold Deposits and Implications for Exploration, (ed.) B. Dubé and P. Mercier-Langevin; Geological Survey of Canada, Open File 7852, p. 127–138.

Fontaine, A., Dubé, B., Malo, M., McNicoll, V.J., Brisson, T., Doucet, D., and Goutier J., 2015. Geology of the metamorphosed Roberto gold deposit (Éléonore Mine), Baie-James region, Québec: diversity of mineralization styles in a polyphase tectono-metamorphic setting, *In:* Targeted Geoscience Initiative 4: Contributions to the Understanding of Precambrian Lode Gold Deposits and Implications for Exploration, (ed.) B. Dubé and P. Mercier-Langevin; Geological Survey of Canada, Open File 7852, p. 209–225.

Fraser, R.J., 1993. The Lac Troilus gold-copper deposit, northwestern Quebec: a possible Archean porphyry system; Economic Geology, v. 88, p. 1685–1699.

Fripp, R.E.P., 1976. Stratabound gold deposits in Archean banded iron-formation, Rhodesia; Economic Geology, v. 71, p. 58–75.

Galley, A.G. and Lafrance, B., 2014. Setting and evolution of the Archean synvolcanic Mooshla Intrusive Complex, Doyon-Bousquet-LaRonde mining camp, Abitibi greenstone belt: emplacement history, petrogenesis, and implications for Au metallogenesis; Economic Geology, v. 109, p. 205–229.

Gao, J.-F., Jackson, S.E., Dubé, B., Kontak, D.J., and De Souza, S., 2015. Genesis of the Canadian Malartic, Côté Gold, and Musselwhite gold deposits: Insights from LA-ICP-MS element mapping of pyrite, *In:* Targeted Geoscience Initiative 4: Contributions to the Understanding of Precambrian Lode Gold Deposits and Implications for Exploration, (ed.) B. Dubé and P. Mercier-Langevin; Geological Survey of Canada, Open File 7852, p. 157–175.

Gauthier, M., Trepanier, S. and Gardoll, S., 2007. Metamorphic gradient: A regional-scale area selection criterion for gold in the northeastern Superior province, eastern Canadian Shield; Society of Economic Geologist Newsletter, v. 69, p. 10–15.

Goldfarb, R.J., Baker, T., Dubé, B., Groves, D.I., Hart, C.J.R., and Gosselin, P., 2005. Distribution, character, and genesis of gold deposits in metamorphic terranes, *In:* Economic Geology 100th Anniversary Volume, (ed.) J.W. Hedenquist, J.F.H. Thompson, R.J. Goldfarb, and J.P. Richards; Society of Economic Geologists, Littleton, Colorado, p. 407–450.

Goodman, S., Williams-Jones, A.E., and Carles, P., 2005. Structural controls on the Archean Troilus gold-copper deposit, Quebec, Canada; Economic Geology, v. 100, p. 577–582.

Gourcerol, B., Thurston, P.C., Kontak, D.J., and Côté-Mantha, O., 2014. Interpretations and implications of preliminary LA ICP-MS analysis of chert for the origin of geochemical signatures in banded iron formations (BIFs) from the Meadowbank gold deposit, western Churchill province, Nunavut; Geological Survey of Canada, Current Research 2014-1, 26 p.

Gourcerol, B., Thurston, P.C., Kontak, D.J., Côté-Mantha, O., and Biczok, J., 2015a. Depositional setting of Algoma-type banded iron formation from the Meadowbank, Meliadine, and Musselwhite gold deposits, *In:* Targeted Geoscience Initiative 4: Contributions to the Understanding of Precambrian Lode Gold Deposits and Implications for Exploration, (ed.) B. Dubé and P. Mercier-Langevin; Geological Survey of Canada, Open File 7852, p. 55–68.

Gourcerol, B., Thurston, P.C., Kontak, D.J., Côté-Mantha, O., and Biczok, J., 2015b. Distinguishing primary and mineralization-

related signatures of chert from the banded iron formation-type gold deposits at Musselwhite, Ontario and Meadowbank, Nunavut; Geological Survey of Canada, Current Research 2015-1, 21 p.

Gosselin, P. and Dubé, B., 2005. Gold deposits of Canada: distribution, geological parameters and gold content; Geological Survey of Canada, Open File 4896, 105 p., 1 CD-ROM.

Gray, M.D. and Hutchinson, R.W., 2001. New evidence for multiple periods of gold emplacement in the Porcupine mining district, Timmins area, Ontario, Canada; Economic Geology, v. 96, p. 453–475.

Griffis, A.T., 1962. A geological study of the McIntyre Mine; Canadian Institute of Mining and Metallurgy, Transactions, v. 65, p. 47–54.

Gross, G.A., 1995. Stratiform iron: Lake Superior-type iron-formation, Algoma-type iron-formation, Ironstone, *In:* Geology of Canadian Mineral Deposit Types, (ed.) O.R. Eckstrand, W.D. Sinclair, and R.I. Thorpe; Geological Survey of Canada, Geology of Canada Series no. 8, p. 41–80.

Groves, D.J., 1993. The crustal continuum model for late Archean lode-gold deposits of the Yilgarn Block, Western Australia; Mineralium Deposita, v. 28, p. 366–374.

Groves, D.J., Goldfarb, R.J., Gebre-Mariam, M., Hagemann, S.G., and Robert, F., 1998. Orogenic gold deposits: A proposed classification in the context of their crustal distribution and relationships to other gold deposit types; Ore Geology Reviews, v. 13, p. 7–27.

Groves, D.I., Goldfarb, R.J., Robert, F., and Hart, C.J.R., 2003. Gold deposits in metamorphic belts: Overview of current understanding, outstanding problems, future research, and exploration significance; Economic Geology, v. 98, p. 1–29.

Grunsky, E.C., Dubé, B., Hagemann, S., and Brauhart, C.W., 2015. A Global Database of Gold Deposits: Quantification of Multi-element Ore Signatures, *In:* Targeted Geoscience Initiative 4: Contributions to the Understanding of Precambrian Lode Gold Deposits and Implications for Exploration, (ed.) B. Dubé and P. Mercier-Langevin; Geological Survey of Canada, Open File 7852, p. 271–286.

Hannington, M.D., Poulsen, K.H., Thompson, J.F.H., and Sillitoe, R., 1999. Volcanogenic gold in the massive sulfide environment, *In:* Volcanic-Associated Sulfide Deposits: Processes and Examples in Modern and Ancient Settings; Society of Economic Geologists, Reviews in Economic Geology, v. 8, p. 325–356.

Hart, C.J.R., 2007. Reduced intrusion-related gold systems, , *In:* Mineral Deposits of Canada: A Synthesis of Major Deposit Types, District Metallogeny, the Evolution of Geological Provinces, and Exploration Methods, (ed.) W.D. Goodfellow; Geological Association of Canada, Mineral Deposits Division, Special Publication, No. 5, p. 95–112.

Helt, K.M., Williams-Jones, A.E., Clark, J.R., Wing, B., and Wares, R.P., 2014. Constraints on the genesis of the Archean oxidized, intrusion-related Canadian Malartic gold deposit, Québec, Canada; Economic Geology, v. 109, p. 713–735.

Hodgson, C.J., 1993. Mesothermal lode-gold deposits, *In:* Mineral Deposit Modelling, (ed.) R.V. Kirkham, W.D. Sinclair., R.I. Thorpe, and J.M. Duke; Geological Association of Canada, Special Paper 40, p. 635–678.

Hrabi, R.B., Barclay, W.A., Fleming, D., and Alexander, R.B., 2003. Structural evolution of the Woodburn Lake Group in the area of the Meadowbank gold deposit, Nunavut; Geological Survey of Canada, Current Research 2003-C27, 10 p.

Hutchinson, R.W., 1993. A multi-stage, multi-process genetic hypothesis for greenstone-hosted gold lodes; Ore Geology Reviews, v. 8, p. 349–382.

Ispolatov, V., Lafrance, B., Dubé, B., Creaser, R., and Hamilton, M., 2008. Geology and structural setting of gold mineralization in the Kirkland Lake-larder lake gold belt, Ontario; Economic Geology, v. 103, p. 1309–1340.

Jemielita, R.A., Davis, D.W., and Krogh, T.E., 1990. U-Pb evidence for Abitibi gold mineralization postdating greenstone magmatism and metamorphism; Nature, v. 346, p. 831–834.

Janvier, V., Castonguay, S., Mercier-Langevin, P., Dubé, B., McNicoll, V., Pehrsson, S., Malo, M., De Chavigny, B., and Côté-Mantha, O., 2015a. Preliminary results of geology of the Portage deposit, Meadowbank gold mine, Churchill Province, Nunavut, Canada; Geological Survey of Canada, Current Research 2015-2, 18 p. doi:10.4095/295532

Janvier, V., Castonguay, S., Mercier-Langevin, P., Dubé, B., Malo, M., McNicoll, V.J., Creaser, R.A., de Chavigny, B., and Pehrsson, S.J., 2015b. Geology of the banded iron formation-hosted Meadowbank gold deposit, Churchill Province, Nunavut, *In:* Targeted Geoscience Initiative 4: Contributions to the Understanding of Precambrian Lode Gold Deposits and Implications for Exploration, (ed.) B. Dubé and P. Mercier-Langevin; Geological Survey of Canada, Open File 7852, p. 255–269.

Katz, L.R., Kontak, D.J., Dubé, B., and McNicoll, V.J., 2015. The Archean Côté gold intrusion-related Au (-Cu) deposit, Ontario, Canada: A large-tonnage, low-grade deposit centred on a magmatic-hydrothermal breccia, *In:* Targeted Geoscience Initiative 4: Contributions to the Understanding of Precambrian Lode Gold Deposits and Implications for Exploration, (ed.) B. Dubé and P. Mercier-Langevin; Geological Survey of Canada, Open File 7852, p. 139–155.

Kelly, C.J. and Schneider, D.A., 2015. Insights into the timing of mineralization and metamorphism in the North Caribou Greenstone Belt, Western Superior Province, *In:* Targeted Geoscience Initiative 4: Contributions to the Understanding of Precambrian Lode Gold Deposits and Implications for Exploration, (ed.) B. Dubé and P. Mercier-Langevin; Geological Survey of Canada, Open File 7852, p. 245–253.

Kerrich, R. and Cassidy, K.F., 1994. Temporal relationships of lode gold mineralization to accretion, magmatism, metamorphism and deformation – Archean to present: A review; Ore Geology Reviews, v. 9, p. 263–310.

Kerrich, R., Goldfarb, R., Groves, D., and Garwin, S., 2000. The geodynamic of world-class gold deposits: characteristics, space-time distribution and origins, *In:* Gold in 2000, (ed.) S.G. Hagemann and P.E. Brown; Society of Economic Geologists, Reviews in Economic Geology, v. 13, p. 501–551.

Kerswill, J.A., 1993. Models for iron-formation-hosted gold deposits, *In:* Mineral Deposit Modelling, (ed.) R.V. Kirkham, W.D. Sinclair, R.I. Thorpe, and J.M. Duke; Geological Survey of Canada, Special Paper 40, p. 171–199.

Kolb, M., 2011. A microstructural study of Musselwhite Mine and Hammond Reef shear-zone-hosted gold deposits; M.Sc. thesis, Lakehead University, Thunder Bay, Ontario, 204 p.

Kontak, D.J., Creaser, R.A., and Hamilton, M., 2013. Geological and geochemical studies of the Côté Lake Au(-Cu) deposit Area, Chester Township, Northern Ontario, *In:* Results from the Shining Tree, Chester Township and Matachewan Gold Projects and the Northern Cobalt Embayment Polymetallic Vein Project, (ed.) J.A. Ayer, D.J. Kontak, R.L. Linnen, and S. Lin; Ontario Geological Survey, Miscellaneous Release Data 294. http://www.geologyontario.mndmf.gov.on.ca/gosportal/gos

Lafrance, B., 2015. Structural and lithological controls on gold mineralization at the Cheminis mine: Implications for the formation of gold deposits along the Cadillac – Larder Lake deformation zone, Ontario, *In:* Targeted Geoscience Initiative 4: Contributions to the Understanding of Precambrian Lode Gold

Deposits and Implications for Exploration, (ed.) B. Dubé and P. Mercier-Langevin; Geological Survey of Canada, Open File 7852, p. 49–54.

Lawley, C.J.M., Creaser, R.A., McNicoll, V., Dubé, B., Mercier-Langevin, P., Pehrsson, S., and Vaillancourt, D., 2014. Re-Os arsenopyrite and U-Pb detrital zircon geochronology at the Meliadine gold district, Nunavut: implications for the geologic setting and age of the Tiriganiaq deposit; Geological Survey of Canada, Open File 7510, 19 p. doi: 10.4095/293939

Lawley, C.J.M., Dubé, B., Mercier-Langevin, P., McNicoll, V.J., Creaser, R.A., Pehrsson, S.J., Castonguay, S., Blais, J.-C., Simard, M., Davis, W.J., and Jackson, S.E., 2015. Setting, age, and hydrothermal footprint of the emerging Meliadine gold district, Nunavut, *In:* Targeted Geoscience Initiative 4: Contributions to the Understanding of Precambrian Lode Gold Deposits and Implications for Exploration, (ed.) B. Dubé and P. Mercier-Langevin; Geological Survey of Canada, Open File 7852, p. 99–111.

Leclair, A.D., Ernst, R.E., and Hattori, K., 1993. Crustal-scale auriferous shear zones in the central Superior province, Canada; Geology, v. 21, p. 399–402.

Leclerc, F., Harris, L.B., Bédard, J.H., Van Breemen, O., and Goulet, N., 2012. Structural and stratigraphic controls on magmatic, volcanogenic, and shear zone-hosted mineralization in the Chapais-Chibougamau mining camp, northeastern Abitibi, Canada; Economic Geology, v. 107, p. 963–989.

Linnen, R., Perrouty, S., Piercey, S.J., Crocker, M., and Wares, R., 2014. Canadian Malartic footprint: New insight from portable XRF data, *In:* Abstracts; Geological Association of Canada – Mineralogical Association of Canada Joint Annual Meeting, Fredericton, New Brunswick, May 2014, v. 37, p. 165–166.

Martin, R., 2012. Syenite-hosted gold mineralization and hydrothermal alteration at the Young-Davidson deposit, Matachewan, Ontario; M.Sc. thesis, University of Waterloo, Waterloo, Ontario, 172 p.

Mason, R. and Melnik, N., 1986. The anatomy of an Archean gold system - the McIntyre-Hollinger complex at Timmins, Ontario, Canada, *In:* Proceedings Volume, (ed.) A.J. MacDonald; Gold '86, International Symposium on the Geology of Gold Deposits, Toronto, Ontario, p. 40–55.

McNicoll, V., Dubé, B., Biczok, J., Castonguay, S., Oswald, W., Mercier-Langevin, P., Skulski, T., and Malo, M., 2013. The Musselwhite gold deposit, North Caribou greenstone belt, Ontario: new high-precision U-Pb ages and their impact on the geological and structural setting of the deposit. *In:* Abstracts; Geological Association of Canada – Mineralogical Association of Canada Joint Annual Meeting, Winnipeg, Manitoba, May 2013, v. 36, p. 142.

McNicoll, V., Goutier, J., Dubé, B., Mercier-Langevin, P., Ross, P.-S., Dion, C., Monecke, T., Legault, M., Percival, J., and Gibson, H., 2014. New U-Pb geochronology from the Blake River Group, Abitibi Subprovince, Québec: implications for geological interpretations and base metal exploration; Economic Geology, v. 109, p. 27–59.

Melnik-Proud, N., 1992. The geology and ore controls in and around the McIntyre Mine at Timmins, Ontario, Canada; Ph.D. thesis, Queen's University, Kingston, Ontario, 353 p.

Mercier-Langevin, P., Hannington, M., Dubé, B., McNicoll, V., Goutier, J., and Monecke, T. 2011. Geodynamic influences on the genesis of Archean world-class gold-rich VMS deposits: examples from the Blake River Group, Abitibi greenstone belt, Canada, *In:* Proceedings; 11th Biennal SGA meeting, Antofagasta, Chile, September 2011, p. 85–87.

Mercier-Langevin, P., Daigneault, R., Goutier, J., Dion, C., and Archer, P., 2012a. Geology of the Archean intrusion-hosted La-Grande-Sud Au-Cu prospect, La Grande Subprovince, James Bay Region, Québec; Economic Geology, v. 107, p. 935–962.

Mercier-Langevin, P., Houlé, M.G., Dubé, B., Monecke, T., Hannington, M.D., Gibson, H.L., and Goutier, J., 2012b. A special issue on Archean magmatism, volcanism, and ore deposits: Part 1. Komatiite-associated Ni-Cu-(PGE) sulfide and greenstone-hosted Au deposits–Preface; Economic Geology, v. 107, p. 745−753.

Mercier-Langevin, P., Hannington, M.D., Dubé, B., Piercey, S.J., Peter, J.M., and Pehrsson, S.J., 2015. Precious metal enrichment processes in volcanogenic massive sulphide deposits – A summary of key features, with an emphasis on TGI-4 research contributions, *In:* Targeted Geoscience Initiative 4: Contributions to the Understanding of Volcanogenic Massive Sulphide Deposit Genesis and Exploration Methods Development, (ed.) J.M. Peter and P. Mercier-Langevin; Geological Survey of Canada, Open File 7853, p. 117–130.

Miller, W.G. and Knight, C.W., 1915. Metallogenic epochs in the Pre-Cambrian of Ontario, Part 1; Ontario Bureau of Mines, v. 24, p. 242–248.

Miller, A.R., Balog, M.J., Barham, B.A., and Reading, K.L., 1994. Geology of the Early Proterozoic gold metallotect, Hurwitz Group in the Cullaton-Griffin lakes area, central Churchill structural province, Northwest Territories, *In:* Current Research 1994-C; Geological Survey of Canada, p. 135–146.

Mining association of Canada, 2014. Facts and Figures of the Canadian Mining industry, 112 p. http://mining.ca/documents/facts-and-figures-2014.

Moran, P., 2008. Lithogeochemistry of the sedimentary stratigraphy and metasomatic alteration in the Musselwhite gold deposit. North Caribou Lake metavolcanic-metasedimentary belt, Superior Province, Canada: implications for deposition and mineralization; M.Sc. thesis, Lakehead University, Thunder Bay, Ontario, 351 p.

Oswald, W, Castonguay, S., Dubé, B., Mercier-Langevin, P., Malo, M., Biczok, J., McNicoll, V., 2014. Targeted Geoscience Initiative 4. Lode gold deposits in ancient deformed and metamorphosed terranes: detailed mapping of key stripped outcrops in the Musselwhite Mine area, Northwestern Ontario, and implications for the geological and structural setting of the gold mineralization, *In:* Summary of Field Work and Other Activities 2014; Ontario Geological Survey, Open File Report 6300, p. 42-1 to 42-15.

Oswald, W., Castonguay, S., Dubé, B., McNicoll, V.J., Biczok, J., Malo, M., and Mercier-Langevin, P., 2015a. Geological setting of the world-class Musselwhite gold Mine, Superior Province, northwestern Ontario, and implications for exploration, *In:* Targeted Geoscience Initiative 4: Contributions to the Understanding of Precambrian Lode Gold Deposits and Implications for Exploration, (ed.) B. Dubé and P. Mercier-Langevin; Geological Survey of Canada, Open File 7852, p. 69–84.

Oswald, W., Castonguay, S., Dubé, B., McNicoll, V.J., Biczok, J., Malo, M., and Mercier-Langevin, P., 2015b. New insights on the geological and structural settings of the Musselwhite banded iron formation-hosted gold deposit, North Caribou greenstone belt, Superior Province, Ontario; Geological Survey of Canada, Current Research 2015-3, 19 p.

Pehrsson, S.J., Berman, R.G., and Davis, W.J., 2013. Paleoproterozoic orogenesis during Nuna aggregation: A case study of reworking of the Rae craton, Woodburn Lake, Nunavut; Precambrian Research, v. 232, p. 167–188.

Pelletier, M., Mercier-Langevin, P., Crick, D., Tolman, J., Beakhouse, G.P., and Dubé, B., 2014. Targeted Geoscience Initiative 4. Lode gold deposits in ancient deformed and metamorphosed terranes: Preliminary observations on the nature

and distribution of the deformed and metamorphosed hydrothermal alteration associated with the Archean Rainy River gold deposit, northwestern Ontario, *In:* Summary of Field Work and Other Activities 2014; Ontario Geological Survey, Open File Report 6300, p. 41-1 to 41-10.

Pelletier, M., Mercier-Langevin, P., Dubé, B., Crick, D., Tolmen, J., McNicoll, V.J., Jackson, S.E., and Beakhouse, G.P., 2015. The Rainy River "atypical" Archean Au deposit, western Wabigoon Subprovince, Ontario, *In:* Targeted Geoscience Initiative 4: Contributions to the Understanding of Precambrian Lode Gold Deposits and Implications for Exploration, (ed.) B. Dubé and P. Mercier-Langevin; Geological Survey of Canada, Open File 7852, p. 193–207.

Phillips, G.N., Groves, D.I., and Martyn, J.E., 1984. An epigenetic orogin for Archean banded iron-formation-hosted gold deposits; Economic Geology. v. 79, p. 162–171.

Pilote, P., Robert, F., Sinclair, W.D., Kirkham, R.V., and Daigneault, R., 1995. Porphyry-type mineralization in the Doré Lake Complex: Clark Lake and Merrill Island areas, *In:* Metallogenic Evolution and Geology of the Chibougamau Area - from Porphyry Cu-Au-Mo to Mesothermal Lode Gold Deposits, (ed.) P. Pilote; Precambrian '95 Field Trip Guidebook, Geological Survey of Canada, Open File 3143, p. 65–86.

Pilote, P., Dion, C, Joanisse, A., David, J., Machado, N., Kirkham, R., and Robert, F., 1997. Géochronologie des minéralisations d'affiliation magmatique de l'Abitibi, secteurs Chibougamau et de Troilus-Frotet: Implications geotectoniques; Ministère des Ressources naturelles du Québec, DV 97-03, 47 p.

Pilote, P., 2013. Géologie – Malartic; Ministère des Ressources naturelles du Québec, CG-32D01D-2013-01.

Pilote, P., Lacoste, P., Moorhead, J., Daigneault, R., McNicoll, V., and David, J., 2014. Géologie de la région de Malartic, *In:* Abstracts of Oral Presentations and Posters; Québec Mines 2014, Ministère de l'Énergie et des Ressources naturelles du Québec, Québec, November 17-20, 2014, DV 2014-04, p. 27.

Probes Mines limites, 2014. Mineral Resource Estimate update Borden Gold project, project No. V1393 – N143-101 Technical report, June 10, 2014, 179 p.

Poulsen, K.H., Card, K.D., and Franklin, J.M., 1992. Archean tectonic and metallogenic evolution of the Superior Province of the Canadian Shield; Precambrian Research, v. 58, p. 25–54.

Poulsen K.H., Robert, F., and Dubé, B., 2000. Geological classification of Canadian gold deposits; Geological Survey of Canada, Bulletin 540, 106 p.

Pyke, D.R. and Middleton, R.S., 1971. Distribution and characteristics of the sulphide ores of the Timmins area; Canadian Institute Mining Metallurgy Transactions, v. 74, p. 157–168.

Ravenelle J.-F., Dubé B., Malo M, McNicoll V., Nadeau L., and Simoneau J., 2010. Insights on the geology of the world-class Roberto gold deposit, Eléonore property, James Bay area, Québec; Geological Survey of Canada, Current Research 2010-1, 26 p.

Ravenelle J.-F., 2013. Amphibolite Facies Gold Mineralization: An example from the Roberto deposit, Eleonore property, James Bay, Quebec; Ph.D. thesis, Institut national de la recherche scientifique, Centre Eau Terre Environnement, Québec, Quebec, 283 p.

Robert, F., 1990. Structural setting and control of gold-quartz veins of the Val d'Or area, southeastern Abitibi subprovince, *In:* Gold and Base-Metal Mineralization in the Abitibi Subprovince, Canada, with Emphasis on the Quebec Segment; Geology Department (Key Centre) & University Extension, The University of Western Australia, Publication No. 24, p. 167–210.

Robert, F., 1994. Timing relationships between Cu-Au mineralization, dykes, and shear zones in the Chibougamau camp, northwestern Abitibi subprovince, Quebec, *In:* Current Research 1994-C; Geological Survey of Canada, p. 287−294.

Robert, F., 2001. Syenite-associated disseminated gold deposits in the Abitibi greenstone belt, Canada; Mineralium Deposita, v. 36, p. 503–516.

Robert, F., Brommecker, R., Bourne, B.T., Dobak, P.J., McEwans, C.J., Rowe, R.R., and Zhou, X., 2007. Models and exploration methods for major gold deposit types, *In:* Proceedings of Exploration 07, (ed.) B. Milkereit; Fifth Decennial International Conference on Mineral Exploration, Toronto, September 9-12, 2007, p. 691–711.

Robert, F., Poulsen, K.H., Cassidy, K.F., and Hodgson, C.J., 2005. Gold metallogeny of the Superior and Yilgarn cratons, *In:* Economic Geology 100th Anniversary Volume, (ed.) J.W. Hedenquist, J.F.H. Thompson, R.J. Goldfarb, and J.P. Richards; Society of Economic Geologists, Littleton, Colorado, p. 1001−1033.

Ross, P.-S. and Bédard, J.H., 2009. Magmatic affinity of modern and ancient subalkaline volcanic rocks determined from trace-element discriminant diagrams; Canadian Journal of Earth Sciences, v. 46, p. 823−839.

Rowins, S.M., 2000. Reduced porphyry copper-gold deposits: A new variation on an old theme; Geology, v. 28, p. 491−494.

Rowins, S.M., 2011. The Troilus Au-Cu deposit: A deformed Archean porphyry of the reduced variety, *In:* Program with Abstracts; Geological Association of Canada-Mineralogical Association of Canada-Society of Economic Geologists-Society for Geology Applied to Mineral Deposits (GAC-MAC-SEG-SGA) joint meeting, Ottawa, May 25-27, 2011, v. 34, p. 189−190.

Sansfaçon, R. and Hubert, C., 1990. The Malartic gold district, Abitibi greenstone belt, Québec: geological setting, structure and timing of gold emplacement at Malartic Gold Fields, Barnat, East-Malartic, Canadian Malartic and Sladen mines, In: The Northwestern Quebec Polymetallic Belt, (ed.) M. Rive, P., P. Vertaelst, Y. Gagnon, J.M. Lulin, G. Riverin, and A. Simard; Canadian Institute of Mining and Metallurgy, Special Volume 43, p. 221−235.

Sherlock, R. L., Alexander, R. B., March, R., Kellner, J., and Barclay, W. A., 2001a. Geological setting of the Meadowbank iron-formation-hosted gold deposits, Nunavut; Geological Survey of Canada, Current Research 2001-C11, 10 p.

Sherlock, R., Alexander, B., March, R., and Kellner, J., 2001b. Geology of the Meadowbank iron formation-hosted gold deposits; Geological Survey of Canada, Open File 3149, 1 sheet.

Sherlock, R., Pehrsson, S.J., Logan, A.V., Hrabi, R.B., and Davis, W.J., 2004. Geological setting of the Meadowbank gold deposits, Woodburn Lake Group, Nunavut; Exploration and Mining Geology, v. 13, p. 67–107.

Sillitoe, R.H., 1991. Intrusion-related gold deposits, *In:* Gold Metallogeny and Exploration, (ed.) R.P. Foster; Blackie and Sons, Glasgow, United Kingdom, p. 165–209.

Sillitoe, R.H., 2000. Enigmatic origins of giant ore deposits, *In:* Symposium Proceedings; Geology and Ore Deposits 2000: The Great Basin and Beyond, Geological Society of Nevada, May 15-18, 2000, p. 1-18.

Sillitoe, R.H., 2008. Major gold deposits and belts of the North and South American Cordillera: Distribution, tectonomagmatic settings, and metallogenic considerations; Economic Geology, v. 103, p. 663−687.

Sillitoe R.H. and Bonham H.F., 1990. Sediment-hosted gold deposits: Distal products of magmatic-hydrothermal systems; Geology, v. 18, p. 157–161

Simard, M., Gaboury, D., Daigneault, R., and Mercier-Langevin, P., 2013. Multistage gold mineralization at the Lapa mine, Abitibi Subprovince: insights into auriferous hydrothermal and meta-

somatic processes in the Cadillac-Larder Lake fault zone; Mineralium Deposita, v. 48, p. 883–905.

Sinclair, W.D., 1982. Gold deposits of the Matachewan Area, Ontario, *In:* Geology of Canadian Gold Deposits, (ed.) R.W. Hodder and W. Petruk; Canadian Institute of Mining and Metallurgy, Special Volume 24, p. 83–93.

Sinclair, W.D., 2007. Porphyry deposits, *In:* Mineral Deposits of Canada: A Synthesis of Major Deposit Types, District Metallogeny, the Evolution of Geological Provinces, and Exploration Methods, (ed.) W.D. Goodfellow; Geological Association of Canada, Mineral Deposits Division, Special Publication, No. 5, p. 223−243.

Sinclair, W.D., Pilote, P., Kirkham, R.V., Robert, F., and Daigneault, R., 1994. A preliminary report of porphyry Cu-Mo-Au and shear zone-hosted Cu-Au deposits in the Chibougamau area, Quebec, *In:* Current Research 1994-C; Geological Survey of Canada, p. 303–309.

Smith, J., Lafrance, B. and Kontak, D., 2014. A comparative study of the deformation history of auriferous quartz veins in the Archean Côté Gold deposit and the structural evolution of the spatially-related Ridout Deformation Zone, Swayze Greenstone Belt, northern Ontario, *In:* Abstracts; Geological Association of Canada – Mineralogical Association of Canada Joint Annual Meeting, Fredericton, New Brunswick, May 2014, v. 37, p. 257−258.

Thompson, J.F.H., Sillitoe, R.H., Baker, T., Lang, J.R., and Mortensen, J.K., 1999. Intrusion-related gold deposits associated with tungsten-tin provinces; Mineralium Deposita, v. 34, p. 323−334.

Tóth, Z., Lafrance, B., Dubé, B., Mercier-Langevin, P., and McNicoll, V.J., 2013a. Targeted Geoscience Initiative 4. Lode gold deposits in ancient deformed and metamorphosed terranes: geological mapping and structural re-appraisal of the banded iron formation-hosted gold mineralization in the Geraldton area, Ontario; Ontario Geological Survey, *In:* Summary of Field Work and Other Activities 2013; Ontario Geological Survey, Open File 6290, p. 58-1 to 58-14.

Tóth, Z., Lafrance, B., Dubé, B., Mercier-Langevin, P., and McNicoll, V., 2013b. Geological setting of banded iron formation-hosted gold mineralization in the Geraldton area, Northern Ontario: preliminary results; Geological Survey of Canada, Open File 7370, 54 p. doi:10.4095/292558

Tóth, Z., Lafrance, B., Dubé, B., Mercier-Langevin, P., and McNicoll, V.J., 2014. Targeted Geoscience Initiative 4. Lode gold deposits in ancient deformed and metamorphosed terranes: relative chronology between hydrothermal activity, gold mineralization and deformation events in the Geraldton area, Northwestern Ontario, *In:* Summary of Field Work and Other Activities 2014; Ontario Geological Survey, Open File 6300, p. 40-1 to 40-10.

Tóth, Z., Lafrance, B., Dubé, B., McNicoll, V.J., Mercier-langevin, P., and Creaser, R.A., 2015. Banded Iron formation-hosted gold mineralization in the Geraldton area, Northwestern Ontario: structural setting, mineralogical characteristics and geochronology, *In:* Targeted Geoscience Initiative 4: Contributions to the Understanding of Precambrian Lode Gold Deposits and Implications for Exploration, (ed.) B. Dubé and P. Mercier-Langevin; Geological Survey of Canada, Open File 7852, p. 85–97.

Trudel, P. and Sauvé, P., 1992. Synthèse des caractéristiques géologiques des gisements d'Or du district de Malartic; Ministère des Ressources naturelles du Québec, MM89-04, 113 p.

Winchester, J.A, and Floyd, P.A., 1977. Geochemical discrimination of different magma series and their differentiation products using immobile elements; Chemical Geology, v. 20, p. 325−343.

Yergeau, D., 2015. Géologie du gisement synvolcanique aurifère atypique Westwood, Abitibi, Québec; Thèse de doctorat Université du Québec, Institut National de la Recherche Scientifique Centre Eau Terre Environnement, Québec, Québec, 841 p.

Yergeau, D., Mercier-Langevin, P., Dubé, B., Malo, M., McNicoll, V.J., Jackson, S.E., Savoie, A., and La Rochelle, F., 2015. The Archean Westwood Au deposit, southern Abitibi: telescoped Au-rich VMS and intrusion-related Au systems, *In:* Targeted Geoscience Initiative 4: Contributions to the Understanding of Precambrian Lode Gold Deposits and Implications for Exploration, (ed.) B. Dubé and P. Mercier-Langevin; Geological Survey of Canada, Open File 7852, p. 177–191.

Zhang, J., Linnen, R., Lin, S., Davis, D.W., and Martin, R., 2014. Paleoproterozoic hydrothermal reactivation in a Neoarchean orogenic lode-gold deposit of the southern Abitibi Subprovince: U-Pb monazite geochronological evidence from the Young-Davidson mine, Ontario; Precambrian Research, v. 249, p. 263–272.

GEOLOGICAL SURVEY OF CANADA
OPEN FILE 7852

Targeted Geoscience Initiative 4: Contributions to the Understanding of Precambrian Lode Gold Deposits and Implications for Exploration

Synorogenic gold mineralization in granite-greenstone terranes: the deep connection between extension, major faults, synorogenic clastic basins, magmatism, thrust inversion, and long-term preservation

Wouter Bleeker

Geological Survey of Canada, Ottawa, Ontario

2015

Recommended citation

Bleeker, W., 2015. Synorogenic gold mineralization in granite-greenstone terranes: the deep connection between extension, major faults, synorogenic clastic basins, magmatism, thrust inversion, and long-term preservation, *In:* Targeted Geoscience Initiative 4: Contributions to the Understanding of Precambrian Lode Gold Deposits and Implications for Exploration, (ed.) B. Dubé and P. Mercier-Langevin; Geological Survey of Canada, Open File 7852, p. 25–47.

Publications in this series have not been edited; they are released as submitted by the author.

Contribution to the Geological Survey of Canada's Targeted Geoscience Initiative 4 (TGI-4) Program (2010–2015)

TABLE OF CONTENTS

Synorogenic gold mineralization in granite-greenstone terranes: the deep connection between extension, major faults, synorogenic clastic basins, magmatism, thrust inversion, and long-term preservation

Wouter Bleeker

Geological Survey of Canada, 601 Booth Street, Ottawa, Ontario K1A 0E8
Corresponding author's e-mail: wbleeker@nrcan.gc.ca

ABSTRACT

Structurally controlled "lode gold" systems within or in proximity to major fault zones (colloquially known as "breaks") represent a dominant deposit type in Canada, particularly in the Archean cratons of the Canadian Shield. This paper describes some of the critical characteristics of these deposits, specifically their relationship to the major faults and the complicated kinematic history of these faults, and to the panels of synorogenic clastic (±volcanic) rocks that occur along these faults. The synthesis that emerges is mainly based on the Timmins area, Canada's most prolific gold camp, but critical elements apply equally to and have been ground-truthed in other gold camps, i.e., Kirkland Lake, the Abitibi more generally, the Rice Lake belt, Yellowknife, and the Agnew camp of the Yilgarn craton. In all of these areas, the key faults cut early fold-and-thrust structures and were likely initiated as crustal-scale, synorogenic extensional faults in association with a flare-up in synorogenic, typically more alkaline magmatism. Extension, the associated mantle-derived magmatism, and the resulting thermal pulse into the lower crust were likely the ultimate drivers of the gold mineralizing events. Synorogenic extension also minimized post-orogenic uplift, thus playing an important indirect role in preservation of the upper crustal depositional environments. Following synorogenic extension and the initiation of the magmatic and hydrothermal processes that produced the gold systems, the crustal-scale faults were invariably inverted as thick-skinned thrusts, burying synorogenic basin remnants and gold deposits in their structural footwall, while deposits were removed or largely eroded from the structural hanging wall of these thrusts. This thrust inversion thus plays a critical role in the preservation of the gold endowment and explains the fundamental asymmetry across most of these camps. Gold mineralization appears to have peaked during the thrust-inversion stage and subsequent shortening, but had waned prior to final strike-slip overprinting of the fault zones. The integrated model provides a coherent guide for identifying and analyzing similar settings in more remote settings of northern Canada.

INTRODUCTION

The majority of gold produced in Canada has come from Archean cratons embedded within the Canadian Shield, principally the Superior and Slave cratons. Within these Archean cratons[1] economic gold mineralization is known to occur in several different settings (e.g. Poulsen et al., 2000):

1. Volcanogenic base metal mineralization with above average gold tenor (e.g. the Doyon-Bousquet-LaRonde camp: Mercier-Langevin et al., 2007).
2. Disseminated gold and gold-bearing veins within and around high-level intermediate to felsic plutons (e.g. Coté Gold: Katz et al., 2015).
3. Gold associated with metamorphism and sulphide replacement of iron formations (e.g. Lupin, Meadowbank, and Musselwhite: Lothka and Nesbitt, 1989).
4. Structurally controlled vein systems within or in proximity to major fault zones (e.g. Hollinger, Dome, Pamour, Giant Yellowknife: Hodgson, 1993).
5. Paleoplacer deposits (e.g. some basal conglomerate beds within the Huronian Supergroup, of earliest Proterozoic age: Roscoe and Minter, 1993).

Paleoplacer deposits (type 5 above), resulting from uplift, erosion, and epiclastic concentration of vein-hosted free gold (type 4), are rare in Canada but worldwide form perhaps the single largest known gold resource, the Witwatersrand gold-bearing conglomerate of South Africa (Frimmel et al., 2005). Together, the five types of gold deposits represent, in essence, the

Bleeker, W., 2015. Synorogenic gold mineralization in granite-greenstone terranes: the deep connection between extension, major faults, synorogenic clastic basins, magmatism, thrust inversion, and long-term preservation, *In:* Targeted Geoscience Initiative 4: Contributions to the Understanding of Precambrian Lode Gold Deposits and Implications for Exploration, (ed.) B. Dubé and P. Mercier-Langevin; Geological Survey of Canada, Open File 7852, p. 24–47.

complete orogenic cycle from initial juvenile crust formation, to partial melting and formation of evolved felsic magmas, to metamorphism and polyphase deformation and faulting of heterogeneous crust, and finally to uplift and erosive reworking of that crust. Gold concentration thus occurs in different settings and as a consequence of a number of different processes. Nevertheless, structurally controlled vein systems within or proximal to major faults zones ("lode gold deposits"[2]) represent a dominant deposit type in Canada, both in number of deposits and in historic production (e.g. Hodgson, 1993). They include the major deposits in classical mining camps such as Val-d'Or, Kirkland Lake, Timmins, Red Lake, and Yellowknife. It is this deposit type that is being illuminated in this study. It will be shown that the majority of these deposits are the result of a complex but largely predictable sequence of processes:

- Volcano-sedimentary deposition, possibly on the edge of thinned, somewhat older crust.
- Significant early deformation and imbrication.
- Uplift and onset of synorogenic extension.
- Initiation of the major faults, as crustal-scale extensional faults.
- A coeval flare-up of extension-related alkaline magmatism.
- Heating of the lower crust and transport of fluids and magmas up the main faults.
- Formation and deepening of synorogenic clastic basins (±volcanic rocks).
- A tectonic switch back to regional shortening.
- Inversion of main extensional faults into thick-skinned thrust.
- Rapid filling and deformation of synorogenic clastic basins.
- Burial of synorogenic clastic basin remnants, and gold deposits, in the footwalls of the major inverted faults.
- Long-term preservation of gold deposits (contingent on sufficient tectonic burial).
- Slow but significant post-orogenic uplift (~10–15 km), exposing gold deposits at the present surface or bringing them to within minable depth (i.e. within ~1–3 km of the present surface).

The list above represents a "process chain" of essential processes, i.e., one is missing and economic gold deposits either failed to form or are no longer preserved. Although this general concept has been recognized before to various extents (e.g. Poulsen et al., 1992; Cameron, 1993; Hodgson, 1993), the synthesis presented here argues more explicitly for many of the critical steps, particularly the role of synorogenic extension in initiating the key faults; extension-related magmatism as a likely gold transport mechanism and a critical determinant of overall gold endowment; and thrust inversion of the main faults as essential to tectonic burial and successful preservation. Conversely, it downplays the role of some other factors that have long been thought to be important, for instance the presence of ultramafic rocks (komatiite). The model presented (see also Bleeker, 2012) is the first coherent attempt to explicitly recognize the role of synorogenic extension in an area such as the Abitibi greenstone belt in a way that is consistent with field evidence and first-order structural and stratigraphic constraints. It also brings the model for large Archean lode gold deposits closer, in terms process understanding, to models for major gold mineralization in younger tectonic environments. Finally, the model makes strong predictions for how to search for this class of deposits in less explored parts of the Canadian Shield.

STRUCTURALLY CONTROLLED VEIN SYSTEMS WITHIN OR IN PROXIMITY TO MAJOR FAULT ZONES

Gold deposits hosted by structurally controlled quartz±carbonate vein systems and their alteration envelopes, known as lode gold deposits, show a wide variation in size and styles and occur throughout the geological record (Goldfarb et al., 2001). They are particularly prolific in Archean granite-greenstone terranes, at least those that are not too deeply eroded. As the quartz veins that host much of the gold represent structural damage to the host rocks, these deposits are invariably associated with deformation of the host terranes, and commonly specific phases of deformation (e.g. Groves, 1993; Hodgson, 1993; Kerrich and Cassidy, 1994; Groves et al., 1998; Kerrich et al., 2000). Some of the smaller deposits can be scattered throughout a deformed host terrane, and represent local dilations in fold hinges or along minor faults. Hence, not all deposits of this type are necessarily associated with major fault corridors. However, in many terranes, a century of exploration, geological mapping, and mine production has shown a distinct clustering of deposits

[1]Long stabilized, ancient, heterogeneous crustal fragments composed of various granitoid rocks and deformed remnants of volcanic and sedimentary rocks, i.e., "granite-greenstone terrains", and locally deeper exhumed plutonic infrastructure, i.e., "gneiss terrains".

[2]Lode: an old English miner's term for a mineralized vein, vein system, or zone "leading"' them through unmineralized waste rocks, i.e., "a lead".

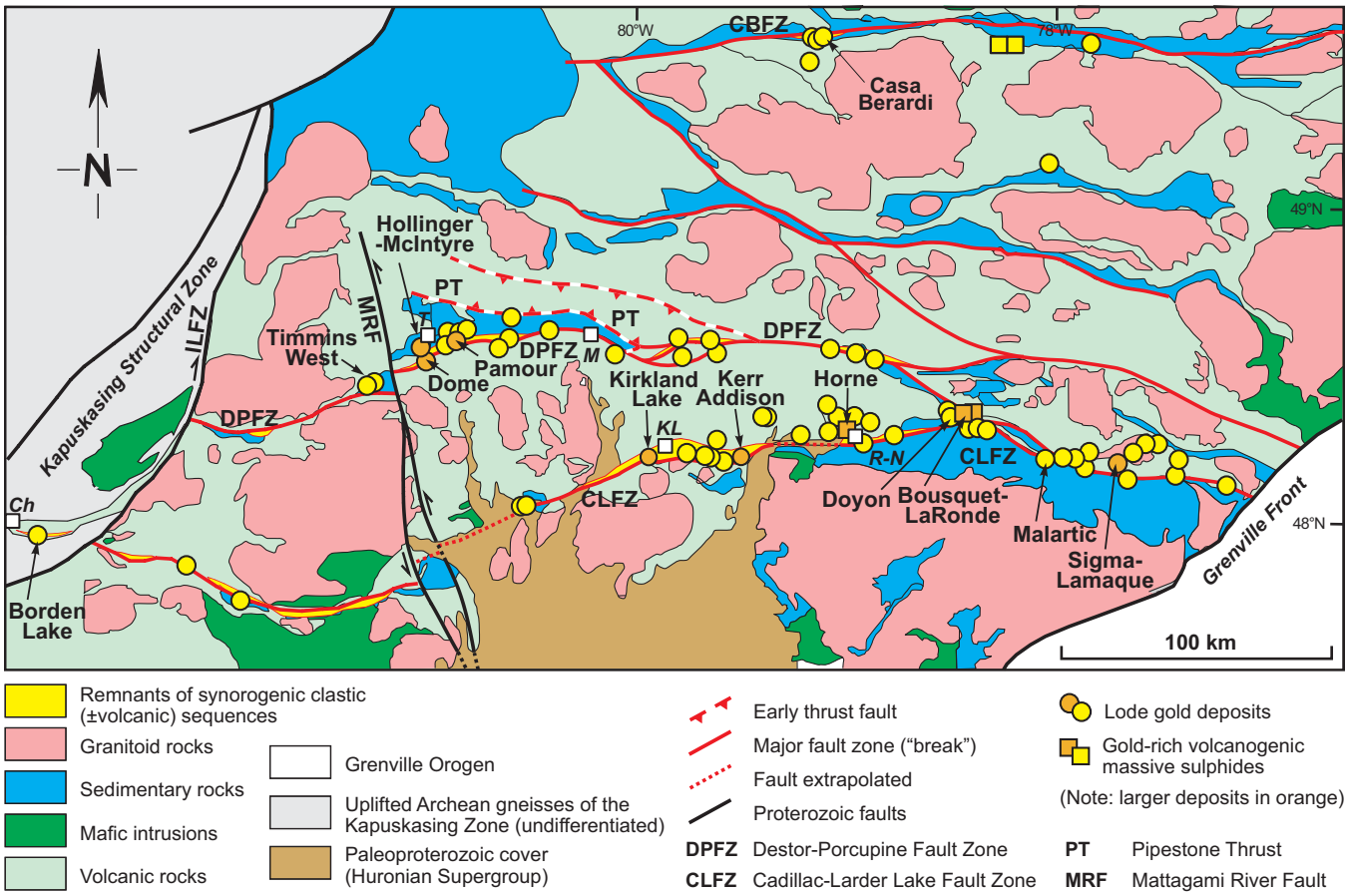

Figure 1. Simplified geological map of the central and southern Abitibi greenstone belt, highlighting the major faults and the distribution of gold deposits (modified after Poulsen et al., 2000; and Dubé and Gosselin, 2007). Abbreviations: CLFZ, Cadillac-Larder Lake Fault Zone; CBFZ, Casa Berardi Fault Zone; DPFZ, Destor-Porcupine Fault Zone; ILFZ, the Ivanhoe Lake Fault Zone; MRF, the Paleoproterozoic Matagami River Fault; and PT, the Pipestone Thrust. Towns: Ch, Chapleau; KL, Kirkland Lake; M, Matheson; R-N, Rouyn-Noranda; T, Timmins. Specifically note the two major fault zones, DPFZ and CLFZ, and the strong spatial association with gold deposits, as well as with thin panels of synorogenic clastic rocks (in yellow).

along structural corridors that are the locus of one or several major faults or fault strands (Fig. 1, Hodgson, 1993; Robert et al., 2005, and references therein). It is this important subclass of lode gold deposits, and their spatial and genetic association with the major fault corridors, that is the specific focus of this paper.

MAJOR FAULT CORRIDORS: THE "BREAKS"

Early mappers named the dominant fault traces "breaks", explicitly recognizing that they represent major discontinuities in map patterns (e.g. Knight, 1924; Gunning, 1937; Gunning and Ambrose, 1939). In the Abitibi greenstone belt of northern Ontario and Quebec, the importance and longevity of these "breaks" is demonstrated by the simple observation that few Archean rock units, not even late granites, are seen to crosscut these faults—i.e., there are few obvious "stitching plutons". In the Abitibi belt, the first rock unit to cut across the "breaks" are approximately north-trending Paleoproterozoic Matachewan diabase dykes, the oldest pulse of which has been dated at 2479 ± 4 Ma (Bleeker et al., 2012). In the southern Abitibi greenstone belt, two major "breaks" are recognized (Fig. 1): the Destor-Porcupine Fault Zone (DPFZ), and the Cadillac-Larder Lake Fault Zone (CLFZ). A third major fault zone and possibly others occur farther north and south (e.g. Casa-Berardi Fault Zone, CBFZ, see Fig. 1). Analogous structures are known elsewhere in the Superior craton and in the granite-greenstone terranes of other cratons, in each case associated with significant gold mineralization, e.g., the Yellowknife River Fault Zone of the southern Slave craton (e.g. Bleeker and Hall, 2007), or the Ida Fault Zone and its along-strike equivalents of the eastern Yilgarn craton (e.g. Duuring et al., 2012; Mole et al., 2013).

The kinematic history of these major faults is typically complex, as will be discussed later. Late transpressional deformation has deformed and steepened the faults such that, in their present attitude, they are steep to subvertical. Their map traces are typically 100s of km long and may be somewhat arcuate (Fig. 1). In

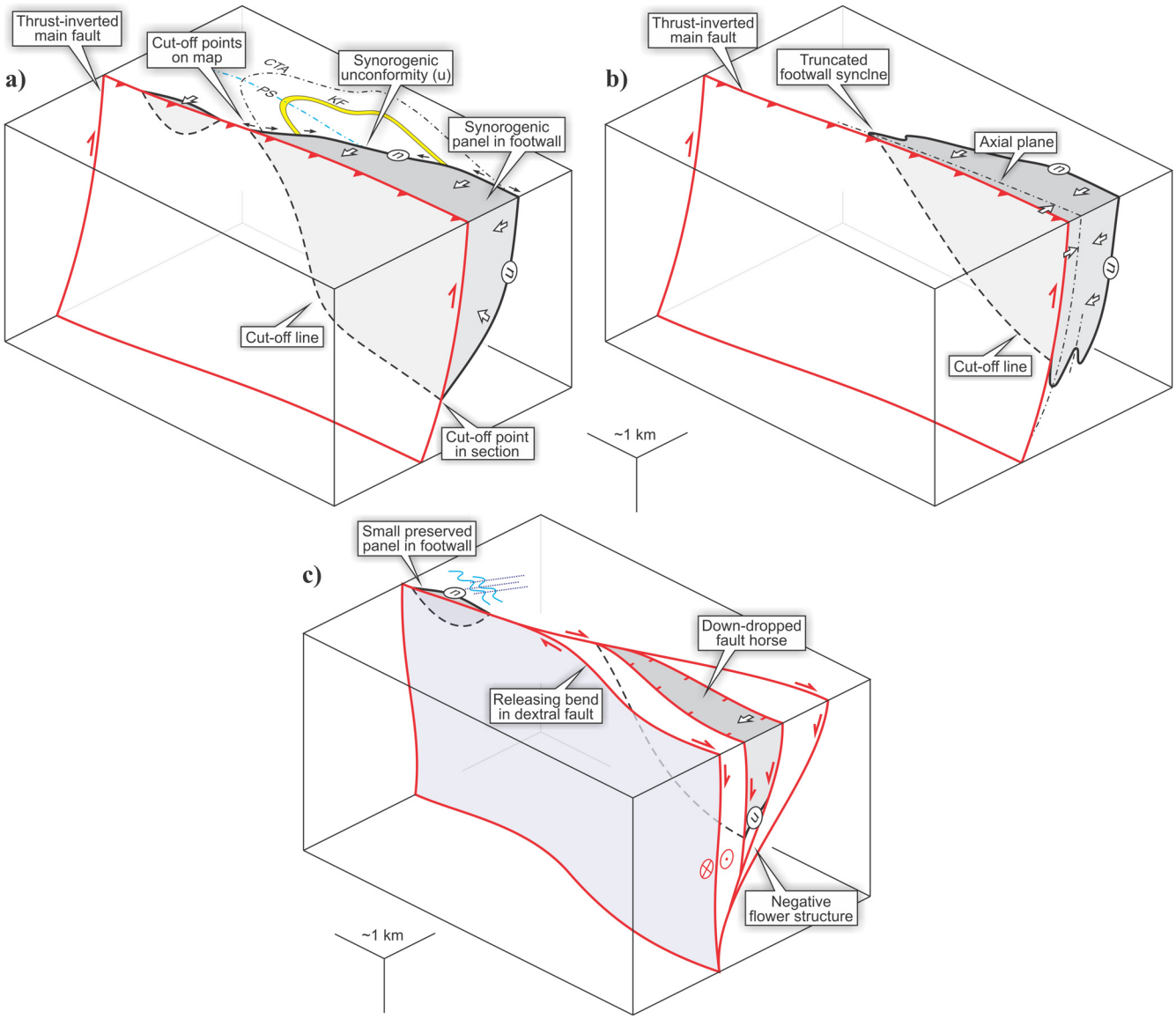

Figure 2. Typical setting of preserved panels of synorogenic clastic rocks in the footwall of a thrust-inverted main fault, either as **(a)** a truncated asymmetric panel younging one-way into the main fault, as modeled on the Timmins area, or as **(b)** a truncated asymmetric footwall syncline with minor preservation of a sheared overturned limb. The main fault is shown in red; bold white arrows show the younging direction in the clastic panel; and the bold black line is the synorogenic unconformity (u) at the base of the clastic panel. This unconformity truncates earlier structures in the stratigraphic footwall. In Timmins, these are: axial planes of early, tight to isoclinal folds (e.g. CTA, Central Tisdale Anticline); and the younger, east-plunging Porcupine Syncline (PS), both limbs of which are also truncated; shown in yellow is the ca. 2688 Ma Krist Fragmental unit (KF). Small black arrows are the facing directions projected onto the base of the synorogenic unconformity, demonstrating that two phases of folding (both the CTA and then the PS) predate the synorogenic unconformity surface (Bleeker, 1995). Note also that the down-dip extent of the synorogenic panel is determined by the "cut-off line" with the fault plane. This intersection line can be irregular, as shown in (a). Where the present erosion level reaches below this cut-off line, much of the diagnostic information on the age and kinematics of the fault is lost. **(c)** Down-dropped fault-bounded panel of synorogenic clastic rocks (grey) in a "negative flower structure", during late-stage strike-slip movement on the major fault system. This is a potential mechanism how strike-slip may have contributed to preservation.

some cases the main fault traces have been so distorted by late deformation that they may not be easily recognized as the key faults (e.g. the Rice Lake belt).

In addition to their association with gold mineralization (e.g. Hodgson, 1993), another first-order attribute of these major fault corridors is the occurrence of panels of synorogenic clastic rocks (Figs. 1, 2), as first recognized by Knight (1924). A typical occurrence of such clastic rocks consists of steeply dipping, polymict conglomerate and crossbedded sandstone (Fig. 3). At their stratigraphic base, the clastic rocks unconformably overlie previously deformed greenstone rocks (e.g. Burrows, 1924; Hurst, 1939; Wilson, 1962), whereas towards their stratigraphic top they young into the

major fault zone. Where the overall structure is not too complex, it can be shown that the synorogenic clastic rocks occur in the structural footwall of the main faults, either as asymmetric truncated panels (Fig. 2a) or as asymmetric, truncated, footwall synclines (Fig. 2b). In other words, the synorogenic clastic rocks have been tectonically buried below the main faults, and these faults must have acted as thrusts during this phase of their evolution. These observations are consistent enough that they cannot be explained as local artefacts of complicated strike-slip deformation (cf. Cameron, 1993). However, it is not uncommon that late deformation has steepened the faults to vertical, or even led to local overturning of the entire geometry, such that a panel of synorogenic clastic rocks, which originally was buried below a main fault, now occupies what appears to be the structural hanging wall of this fault. Some of these typical complexities are illustrated in Figure 4, which is modeled on the structural set-up in Timmins (Bleeker, 1999). An example of highly deformed conglomerate adjacent to the main fault trace of the DPFZ in Timmins, showing dip-slip kinematic indicators, is shown in Figure 5.

THE SPATIAL ASSOCIATION BETWEEN LODE GOLD DEPOSITS AND MAJOR FAULT CORRIDORS: IS IT REAL AND WHAT DOES IT MEAN?

An important question is whether the apparent strong spatial association between lode gold deposits and major fault corridors (Fig. 1) is real? This question may seem naive but is far from trivial. A cycle of gold discovery, additional exploration nearby, drilling and more discoveries may lead to a spatial pattern that is biased simply as a function of where money was spent to drill exploration holes. If the apparent spatial association is real, it puts strong constraints on any model that aims to explain this class of gold deposits. If, on the other hand, the spatial distribution merely reflects where money was spent on drilling, it will falsely inform a possible model. So this question is important.

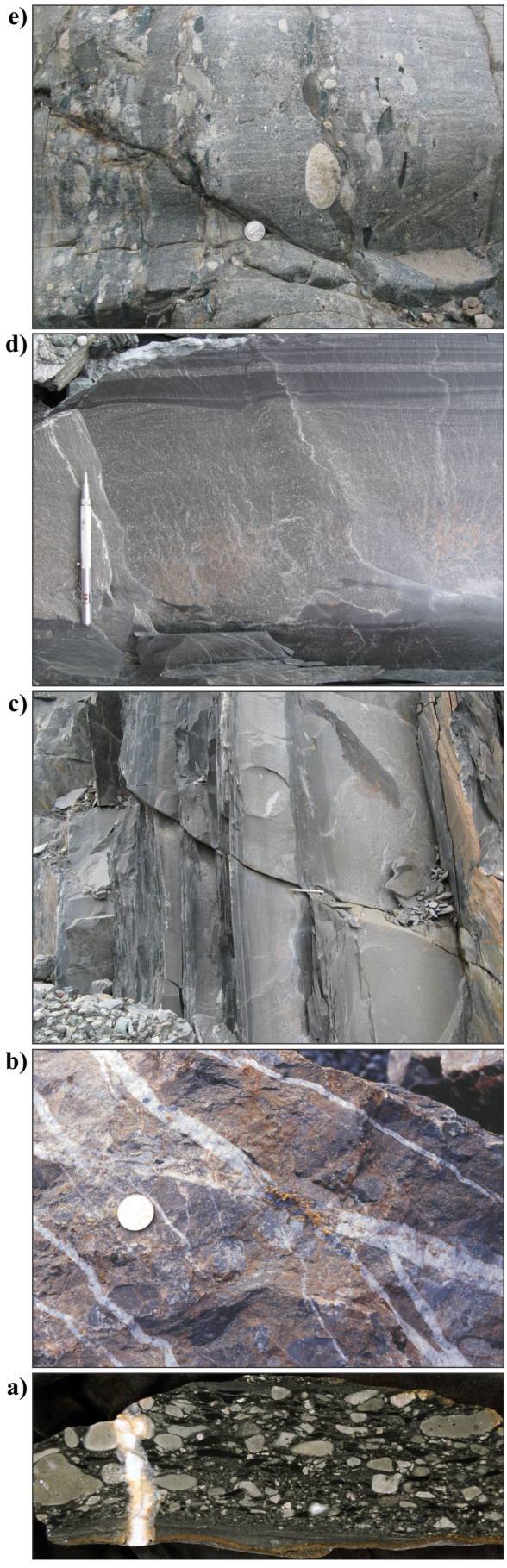

Figure 3. Representative photographs of synorogenic clastic rocks from the Timmins area. Photographs are in stratigraphic order from bottom (a) to top (e). **a)** Oligomict basal conglomerate of the synorogenic sequence in Timmins, Pamour Mine; sample is dominated by angular to subrounded mafic volcanic clasts, representing erosion and moderate transport of metavolcanic rocks from the uplifted volcanic footwall. **b)** Polymict conglomerate (the "Pamour Conglomerate") cut by intersecting quartz veins carrying gold (in the centre of the picture, with minor sphalerite). **c)** Steeply dipping turbiditic greywacke that is representative of the middle part of the sequence in Timmins. **d)** Close-up of graded greywacke-siltstone beds; note load casts at the base of the graded bed and ripple laminations near the top of the sand layer. **e)** Polymict conglomerate and pebbly sandstones, representative of the upper part of the sequence. Note the rounded plutonic clast (near the centre), which contains a pre-depositional deformation fabric.

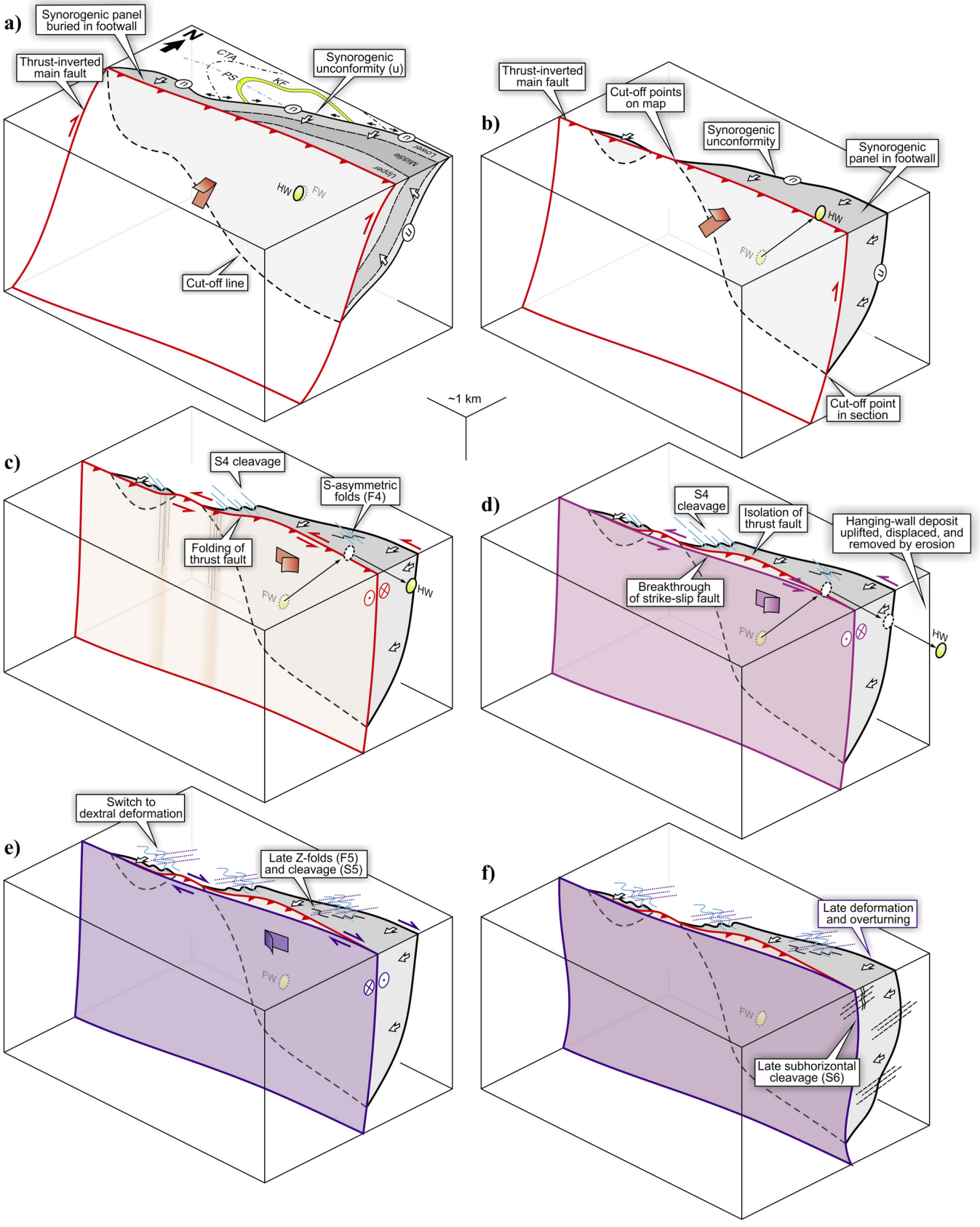
a)
Synorogenic panel buried in footwall
Thrust-inverted main fault
Synorogenic unconformity (u)
CTA
PS
KF
Lower
Middle
Upper
HW
FW
Cut-off line
b)
Thrust-inverted main fault
Cut-off points on map
Synorogenic unconformity
Synorogenic panel in footwall
HW
FW
Cut-off point in section
~1 km
c)
S4 cleavage
S-asymmetric folds (F4)
Folding of thrust fault
FW
HW
d)
S4 cleavage
Isolation of thrust fault
Hanging-wall deposit uplifted, displaced, and removed by erosion
Breakthrough of strike-slip fault
FW
HW
e)
Switch to dextral deformation
Late Z-folds (F5) and cleavage (S5)
FW
f)
Late deformation and overturning
FW
Late subhorizontal cleavage (S6)

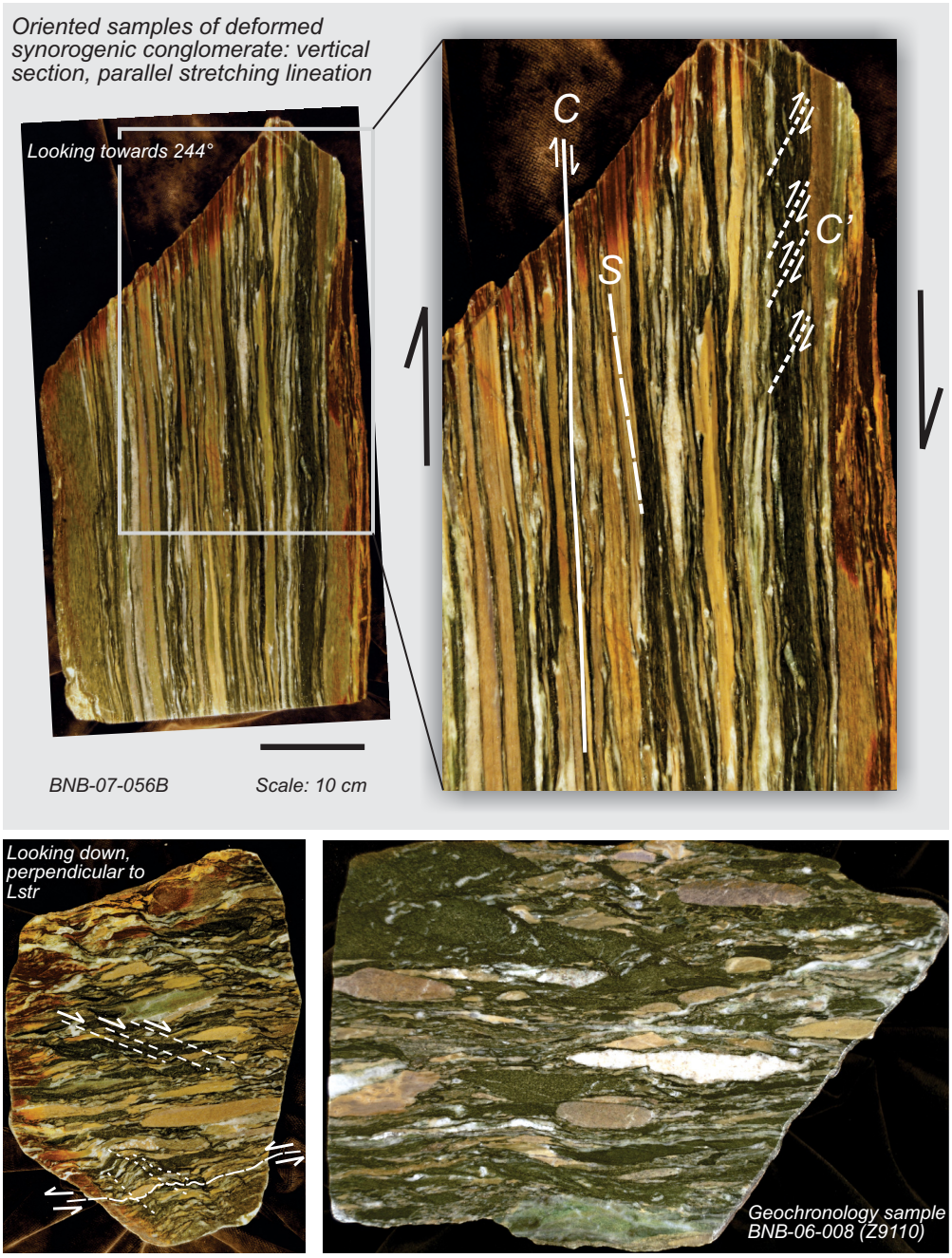

Figure 5. Cross-sectional view of highly deformed conglomerate at the stratigraphic top of the synorogenic conglomerate panel in Timmins (Buffalo-Ankerite open pit), immediately north of the steepened thrust fault. View is towards the west-southwest (244°), in a vertical section parallel to the steeply plunging stretching lineation. Kinematic indicators (low-angle C-S relationships, and late shear bands, C') indicate that the conglomerate moved down relative to the older volcanic rocks to the south of the fault. The initial thrust geometry has been severely steepened and is in fact slightly overturned. In a strict sense, therefore, the deformed conglomerate, which initially was buried in the footwall of the thrust fault, now appears to sit in the structural hanging wall of the fault, confusing the overall interpretation. Lower pictures show subhorizontal sections, perpendicular to the stretching lineation (Lstr), with two generations of strike-slip related minor structures. The picture on the right is from the conglomerate from which synorogenic detrital zircons were extracted that were dated at ca. 2675 Ma (Bleeker and van Breemen, 2011).

Figure 4 (opposite page). Illustration of the complex geometric and kinematic history of the main fault(s), modeled on the Timmins area. The six block diagrams (a to f) are ordered in time, starting with the ca. 2665 Ma thrust inversion of the main fault and burial of the synorogenic clastic sequence below the main fault plane. **a)** Thick-skinned thrust-inversion phase, details as in Figure 2. **b)** Continued thrust burial, possibly oblique, and steepening of fault plane due to north-south shortening. This figure shows a slightly deeper cut through the structure than (a). **c)** Transition to sinistral strike slip, and folding (S-asymmetry) of the steepened thrust plane (red shading). S_4 cleavage development in association with the transpressional deformation. **d)** Break-through of a new, more planar strike-slip fault (purple shading), isolating the older and folded thrust fault to the north. In Timmins, the older thrust fault is the Dome Fault, whereas the new strike-slip fault is the main DPFZ trace. **e)** Late reversal to dextral strike slip and formation of late Z-asymmetric folds and a ubiquitous northeast-trending crenulation cleavage (S_5). **f)** Further deformation of the fault geometry, with local overturning and formation of a subhorizontal crenulation cleavage (S_6). Note that due to this late deformation, the synorogenic clastic rocks now sit in the apparent hanging wall of the steeply north-dipping fault. Figures track the position of a gold deposit (yellow ovals) that forms along the fault during thrust inversion. Whereas the footwall portion (FW) of this deposit is preserved, the hanging-wall portion (HW) is uplifted (b), laterally displaced (c and d), and ultimately eroded.

In the Timmins area, the first discovery of gold at surface was made over a century ago (Doherty, 1986; Barnes, 1991) and since then numerous deposits have been found (Table 1), some highly profitable whereas others had marginal economics and were abandoned. The entire area has been intensely prospected, for tens of kilometres away from the main faults. Tens of thousands of test holes have been drilled, and numerous test shafts have been sunk. Hence, for the wider Timmins area, there has been enough random testing away from the faults that the pattern that has emerged is likely to reflect underlying processes. The same can probably be said for much of the southern Abitibi and probably also the Eastern Goldfields of the Yilgarn craton. Elsewhere the picture may be less mature or "saturated". It is thus concluded that for highly endowed belts, such as the southern Abitibi, the main faults must play a key role in any comprehensive model for the gold mineralization.

Another important observation serves to amplify this conclusion. To the north of Timmins, ~20 km north of the trace of the DPFZ, there occurs another major fault—the Pipestone fault (Fig. 1). This fault has often been portrayed as a splay fault of the DPFZ and for this reason, and for its relative proximity to Timmins, has seen equally intense prospecting and exploration. Yet no major correlation with productive gold deposits has emerged, although there are some minor deposits in the area. The reason for this distinct difference in gold endowment of the two fault zones is that they have radically different origins. The Pipestone fault, renamed the Pipestone Thrust by Bleeker and van Breemen (2011), represents an early high-level thrust fault that was subsequently folded, whereas the DPFZ was initiated somewhat later as a deep-reaching crustal-scale extensional fault, which was then inverted as a thick-skinned thrust. Although the folded Pipestone Thrust (see structural cross-section in Bleeker and van Breemen, 2011) may have seen some reactivation at critical times, it lacks the extensional history and the associated gold endowment. These important differences, despite both faults having seen a century of prospecting and drilling, underscore that the spatial pattern of Figure 1 is sufficiently saturated to be meaningful.

As part of this discussion on the reality of the spatial distribution, it is useful to introduce yet one other key observation, one which is not immediately apparent from Figure 1 because of scale. If one tabulates all the gold deposits and their production along the DPFZ, at least for that portion that occurs in Ontario, and one classifies the deposits as being situated north, within (or ambiguous), or south of the principal fault trace(s), it turns out that >>95% of all gold produced has come from one side of the fault—i.e., the north side (Table 1). For the Porcupine camp proper, essentially ~25–30 km along the DPFZ on either side of Timmins, this statistic is >99% (Bleeker, 1995). In other words, not only is the overall spatial association with the major fault zone robust, but essentially all historic and on-going gold production has come from one side (north side), or from within, the fault zone. Combining this key observation with knowledge of the initial fault geometry leads to the conclusion that essentially all gold production has come from the structural footwall of the main fault(s), i.e., from the side that also preserves the tectonically buried panels of synorogenic clastic rocks (Fig. 4).

At the time that the gold-bearing quart±carbonate veins were emplaced, there is no obvious reasons why hydrothermal fluids, or the fluid-assisted opening of veins, would be able to differentiate between footwall and hanging wall of a major fault zone and fluid conduit. The robust observation above, that essentially all gold was produced from the footwall, therefore must mean that (1) veins emplaced in the hanging wall were preferentially uplifted and eroded; and (2) thrust displacement on the principal faults must have outlasted the peak of gold mineralization. This in turn must lead to a third conclusion: (3) the transition to late-stage strike-slip dominated movement, on a steepened fault trace, largely post-dated gold emplacement. In other words, the major strike-slip displacement and transpressional deformation that is easily demonstrated on the faults (in the case of the DPFZ and CLFZ: first sinistral and then dextral; Bleeker, 1995, 1999) is late and of little bearing on a detailed genetic model for the mineralization. Strike-slip deformation is important, however, in redistributing remaining mineralization on either side of the faults by possibly tens of kilometres. In other words, the uplifted and partly eroded roots of a major mineralized gold system, if still partially preserved on the hanging-wall side of a major fault, may be displaced ~10 to 100 km laterally relative to the main part of the deposit that is preserved in the footwall. Understanding and quantifying the late strike-slip history on the faults is thus important for exploration and for finding possible complements of known deposits, but it is less important in terms of understanding the genetic aspects of the lode gold hydrothermal systems.

SYNOROGENIC BASINS AND THEIR ROLE

The typical setting of a preserved panel of synorogenic clastic rocks was introduced in Figures 1, 2, and 4. A reconstructed and generalized stratigraphy of these preserved panels is shown in Figure 6, largely based on observations in Timmins, but augmented by critical aspects from other localities in the Abitibi greenstone belt, particularly the Kirkland Lake area (Thomson,

Table 1. Gold production, to the end of 2013, in the vicinity of the Destor-Porcupine Fault Zone; modified after Bleeker et al. (2014).

Mine	Township	Years of Production	Tons Milled	Production (ounces gold)	Grade[1] (oz/ton)	Position relative to the DPFZ[2]
Aljo	Beatty	1940	2333	42	0.02	N
American Eagle	Munro	1911	60	40	0.67	N
Ankerite/March	**Deloro**	**1926–1935**	**317 769**	**61 039**	**0.19**	**N**
Aquarius	**Macklem**	**1984, 1988–1989**	**139 634**	**27 117**	**0.19**	**S**
Argyll	Beatty	1918	12 455	851	0.07	N
Aunor (Pamour #3)	**Deloro**	**1940–1984**	**8 482 174**	**2 502 214**	**0.30**	**N**
Banner	**Whitney**	**1927–1928, 1933, 1935**	**315**	**670**	**0.13**	**N**
Bell Creek	**Hoyle**	**1987–1991, 1992–1994, 2011-2013**	**576 017 609 670**	**112 739 74 825**	**0.20 0.13**	**N**
Black Fox (Glimmer)	Hislop	1997–2001, 2009–2013	5 020 823	561 645	0.11	Within
Blue Quartz	Beatty	1923, 26, 28, 34	500	81	0.16	N
Bonetal	**Whitney**	**1941–1951**	**352 254**	**51 510**	**0.15**	**N**
Bonwhit	**Whitney**	**1951–1954**	**200 555**	**67 940**	**0.34**	**N**
Broulan Porcupine	**Whitney**	**1939–1953**	**1 146 059**	**243 757**	**0.21**	**N**
Broulan Reef Mine	**Whitney**	**1915–1965**	**2 144 507**	**498 932**	**0.23**	**N**
Buffalo Ankerite	**Deloro**	**1926–1953, 1978**	**4 993 929**	**957 292**	**0.19**	**N**
Buffonta	Garrison	1981, 91–92	117 013	12 139	0.10	S
Canadian Arrow	Hislop	1974–76, 1980–83	303 449	19 140	0.06	S
Canamax Matheson Project	Holloway	1988	38 675	5391	0.14	Within
Centre Hill	Munro	1967–70	327 007	422	0.001	N
Cincinnati	**Deloro**	**1914, 1922–1924**	**3200**	**736**	**0.23**	**N**
Clavos	**Stock**	**2005–2007**	**188 743**	**24 609**	**0.13**	**N**
Concordia	**Deloro**	**1935**	**230**	**16**	**0.07**	**S**
Coniarum/Carium	**Tisdale**	**1913–1918, 1928–1961**	**4 464 006**	**1 109 574**	**0.25**	**N**
Croesus	Munro	1915–18, 23, 31–36	5333	14 859	2.79	N
Crown	**Tisdale**	**1913–1921**	**226 180**	**138 330**	**0.61**	**N**
Davidson–Tisdale	**Tisdale**	**1918–1920, 1988**	**53 221**	**9739**	**0.18**	**N**
Delnite (open pit)	**Deloro**	**1937–1964 1987–1988**	**3 847 364 56 067**	**920 404 3602**	**0.24 0.06**	**N**
DeSantis	**Ogden**	**1933, 1939–1942, 1961–1964**	**196 928**	**35 842**	**0.18**	**N**
Dome	**Tisdale**	**1910–2013**	**114 624 858**	**16 361 420**	**0.14**	**N**
Faymar	**Deloro**	**1940–1942**	**119 181**	**21 851**	**0.18**	**S**
Fuller (Vedron)	**Tisdale**	**1940–1944**	**44 028**	**6566**	**0.15**	**N**
Gillies Lake	**Tisdale**	**1921–1931, 1935–1937**	**54 502**	**15 278**	**0.28**	**N**
Goldhawk (open pit)	**Cody**	**1947 1980**	**636 40 000**	**53 3967**	**0.08 0.10**	**S**
Goldpost	Hislop	1989	9403	2913	0.31	S
Gold Pyramid	Guibord	1911	175	36	0.21	N
Hallnor (Pamour #2)	**Whitney**	**1938–1968, 1981**	**4 226 419**	**1 645 892**	**0.39**	**N**
Hislop (Hislop East)	Hislop	1990–91, 1993–95, 1999–2007, 2010–13	1 992 346	124 373	0.062	?
Hollinger–Schumacher	**Tisdale**	**1915–1918**	**112 124**	**27 182**	**0.24**	**N**

Table 1 continued.

Mine	Township	Years of Production	Tons Milled	Production (ounces gold)	Grade[1] (oz/ton)	Position relative to the DPFZ[2]
Hollinger	**Tisdale**	**1910–1968**	**65 778 234**	**19 327 691**	**0.29**	**N**
Pamour Timmins Property		**1976–1988**	**2 615 866**	**182 058**	**0.07**	
Holloway	Holloway	1993, 95, 96–2006, 2011–13	6 091 733	946 384	0.16	Within
Holloway-Holt	Holloway	2007–2010	601 778	89 703	0.15	Within
Holt	Holloway	1988–2004, 2011–13	9 191 442	1 409 473	0.15	Within
Hoyle–Falconbridge	**Whitney**	**1941–1944, 1946–1949**	**725 494**	**71 843**	**0.10**	**N**
Hoyle Pond	**Hoyle**	**1985–2013**	**9 215 939**	**3 233 793**	**0.35**	**N**
Hugh–Pam	**Whitney**	**1926, 1948–1965**	**636 751**	**119 604**	**0.19**	**N**
Marlhill	**Hoyle**	**1989–1991**	**156 800**	**30 924**	**0.20**	**N**
McIntyre Pamour	**Tisdale**	**1912–1988**	**37 634 691**	**10 751 941**	**0.29**	**N**
Schum.		**1988–1989**	**2 549 189**	**18 260**	**0.01**	
(ERG tailings recovery)						
McLaren	**Deloro**	**1933–1937**	**876**	**201**	**0.23**	**N**
Moneta	**Tisdale**	**1938–1943**	**314 829**	**149 250**	**0.47**	**N**
Naybob (Kenilworth)	**Ogden**	**1932–1964**	**304 100**	**50 731**	**0.17**	**N**
Newfield	Garrison	1996	55 000	9680	0.18	Within
Nighthawk	**Macklem**	**1995–1999**	**1 479 607**	**175 803**	**0.12**	**S**
Owl Creek	**Hoyle**	**1981–1989**	**1 984 400**	**236 880**	**0.12**	**N**
Pamour # 1 (incl. pits 3, 4	**Whitney**	**1936–1999**	**45 795 863**	**4 078 525**	**0.09**	**N**
and 7 and Hoyle)		**2005–2011**	**17 750 312**	**698 771**	**0.04**	
Pamour (other sources)	**Whitney**	**1936–1999**	**7 416 634**	**676 645**	**0.09**	**N**
Paymaster	**Deloro**	**1915–1919, 1922–1966**	**5 607 402**	**1 192 206**	**0.21**	**N**
Porcupine Lake (Hunter)	**Whitney**	**1937–1940, 1944**	**10 821**	**1369**	**0.13**	**S**
Porcupine Peninsular	**Cody**	**1924–1927, 1940, 1947**	**99 688**	**27 354**	**0.27**	**S**
Preston	**Tisdale**	**1938–1968**	**6 284 405**	**1 539 355**	**0.24**	**N**
Preston NY	**Tisdale**	**1933**	**2800**	**153**	**0.05**	**N**
Preston/Porcupine Pet	**Deloro**	**1914–1915**	**1000**	**314**	**0.31**	**N**
Preston/Porphyry Hill	**Deloro**	**1913–1915**	**46**	**312**	**6.78**	**N**
Ross	Hislop	1936–1989	6 714 482	995 832	0.15	S
Stock	**Stock**	**1989–1994, 2000**	**821 304**	**129 856**	**0.16**	**Within**
Taylor	**Taylor**	**2007**	**19 259**	**2043**	**0.11**	**Within**
Timmins West	**Bristol**	**2009–2013**	**2 108 651**	**308 298**	**0.15**	**N**
Tisdale Ankerite	**Tisdale**	**1952**	**14 655**	**2236**	**0.15**	**N**
Tommy Burns/Arcadia	**Shaw**	**1917**	**21**	**14**	**0.66**	**S**
Triple Lake	McArthur	1932	155	121	0.78	N
Vipond	**Tisdale**	**1911–1941**	**1 565 218**	**414 367**	**0.26**	**N**
White-Guyatt	Munro	1911	50	10	0.20	N
		Total	**388 599 637**	**72 537 028**	**0.19**	

[1]Grade: ounces of gold per ton; all tonnages have been converted to imperial units using a conversion factor of 1.1023113.
[2]Position relative to the Destor-Porcupine Fault Zone (DPFZ): N, north of fault; S, south of fault; Within, within fault zone; ?, ambiguous position or unknown.

Deposits shown in bold font are within the Porcupine Camp proper, where 99.6% of the ounces produced have come from north of or within the DPFZ. Including deposits further east (i.e. east of Matheson), ~95% of all gold produced has come from north of or within the DPFZ.

Deposits shown in red occur along the Nighthawk Lake Fault trend, a poorly understood fault trend south of the main DPFZ, and likely a splay thereof.

For the Faymar deposit (shown in blue, Deloro Twp and south of the DPFZ) there is some uncertainty of the true provenance of the quoted production.

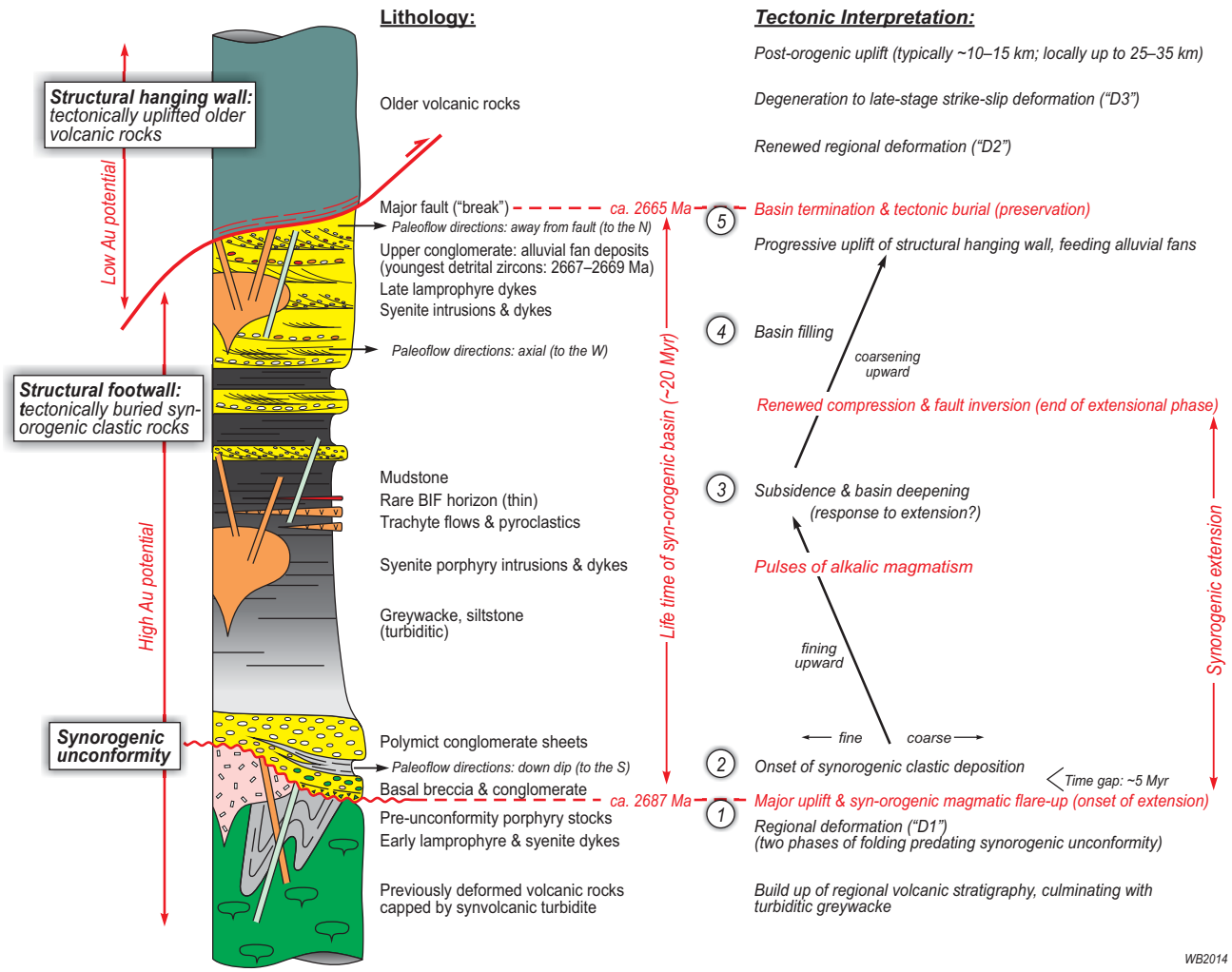

Figure 6. Stratigraphic reconstruction of the preserved panels of synorogenic clastic (± volcanic-plutonic) rocks below the main thrust-inverted faults, synthesized from both the Timmins and Kirkland Lake areas. Stratigraphic column and main lithologies are shown on the left, and tectonic interpretation is given on the right. The overall evolution or "life time" of the synorogenic basin remnants can be divided into five phases, with a total duration of approximately 20 Myr (see text for discussion). The basin remnants overlie a synorogenic unconformity at their base, and young up into a thrust-inverted main fault at their stratigraphic top. The synorogenic processes started with uplift, significant erosion, and the onset of alkaline magmatism. This phase is only recorded by early alkaline intrusions that predate the unconformity surface. The depositional record started significantly later, probably when extension-driven subsidence took over. The basin remnants then recorded a cycle of deepening, and then shallowing and basin filling, the latter indicating the onset of thrust inversion. Final thrust inversion terminates the basin and places deeper volcanic footwall rocks on top of the tectonically buried basin remnant. Gold deposits were largely uplifted and eroded from the hanging-wall side of the system, explaining the overall asymmetry in gold distribution (in Timmins >99% of gold produced from the footwall environment).

1950).[3] In the Abitibi, the total "life time" of the synorogenic basins is about 20 million years, from ca. 2686 Ma to ca. 2665 Ma. Their evolution was initiated immediately following intense folding and imbrication of the underlying greenstones, deformation that culminated at about 2688–2687 Ma ("D1" deformation phase). In more detail, the evolution of the synorogenic basin(s) can be divided into five distinct phases (see Fig. 6):

1. Following "D1" deformation: uplift and a flare-up of synorogenic alkaline magmatism.
2. Subsidence and initial deposition (and preservation) of basal clastic rocks.
3. On-going extension: basin deepening and episodic synorogenic magmatism (and volcanism).
4. Switch to renewed shortening, leading to fault inversion and basin filling.
5. Basin termination and tectonic burial.

[3]In the Abitibi greenstone belt, the synorogenic conglomerates have long been referred to as "Timiskaming conglomerates", in reference to a type locality west of Lake Temiskaming. In the present paper, these rocks are described in terms of more general processes and hence preference is given to the adjective "synorogenic" rather than a locality (and time) specific term.

Phase 1: Uplift and Flare-Up of Alkaline Magmatism (ca. 2687–2685 Ma)

The first major deformation of the volcanic stratigraphy resulted in two responses: 1) major uplift and emergence of deformed and imbricated greenstones and overlying turbidites; and 2) a switch to and sudden flare-up of alkaline magmatism. These processes are also seen in modern mountain belts following major orogenic phases. The uplift and ensuing subaerial erosion created an unconformity surface that cuts through the early fold structures. The earliest clastic deposits that overlie this unconformity surface were probably ephemeral and were removed by additional uplift and erosion. The depositional record, therefore, did not start until about 5 million years later (see Phase 2 below). The flare-up of alkaline magmatism is expressed as early lamprophyre and syenite dykes and high-level stocks, the earliest of which have been dated at 2687–2686 Ma (Frarey and Krogh, 1986; Barrie, 1990). In Wawa, along strike to the west of Timmins, ultramafic lamprophyre produced vent-facies rocks and brought mantle xenoliths and diamonds to the surface (Stachel et al., 2006; Wyman et al., 2006). South of Timmins, a major pluton of quartz syenite to alkali granite, dated at 2686 Ma (Frarey and Krogh, 1986) intrudes across early folds (Fig. 7a). Although verification of this age is in progress, the aggregate of existing ages indicates without much doubt that the transition to synorogenic processes had occurred by 2687–2686 Ma. As pre-folding rocks are known to be as young as 2690–2688 Ma (e.g. Corfu et al., 1989; Corfu, 1993; Ayer et al., 2003), this leaves a remarkable short time span (~1 million years) for the intense folding of the volcanic stratigraphy.

Phase 2: First Deposition and Preservation of Basal Clastic Rocks (ca. 2680 Ma)

Following uplift and erosional down-cutting of the synorogenic (angular) unconformity surface, the depositional record started at ca. 2680 Ma, typically with local lenses of regolithic breccia or oligomict angular conglomerate, followed by polymict conglomerate (Fig. 3a,b). In Timmins, these basal conglomerate units are only on the order of 10–20 m thick, giving way quickly to fine-grained, thinly bedded siltstones. This must reflect basin widening (e.g. from a river to a larger basin or delta), a receding shoreline, and possibly basin deepening.

Phase 3: Ongoing Extension, Basin Deepening, and Episodic Magmatism (ca. 2680–2672 Ma)

The middle part of the synorogenic sequence is dominated by greywackes and mudstones with turbiditic layering (Fig. 3c,d). Evidently, these sedimentary rocks were deposited in a more extensive and deepening basin, below wave base (~100 m, dependent on the size of the basin and wave amplitude). This stratigraphic signal is interpreted in terms of relatively rapid deepening in response to ongoing extension. This interpretation may also explain the ongoing alkaline magmatism, which in the Kirkland Lake area produced trachyte lava and pyroclastic rocks (e.g. Mueller et al., 1994). Farther east, near Larder Lake, a thin laminated iron formation is deposited at this stage of basin evolution, intercalated in dark green siltstone and intruded by synorogenic mafic dykes. In Timmins, this middle part of the sequence culminates in several metres of black mudstone.

Phase 4: Switch to Renewed Shortening, Leading to Fault Inversion and Basin Filling (ca. 2672–2669 Ma)

Following the deposition of siltstones and mudstones in the middle part of the sequence, a coarsening-upward trend is observed with a return of pebbly sandstone and polymict conglomerates (Fig. 3e), and also well developed crossbedded sandstones (e.g. the Three Nations Formation in Timmins). This coarsening-upward trend is interpreted as the end of extension and a switch to renewed compression, which led to rapid filling of the basin with coarser polymict and quartz-rich detritus. It seems likely that the major faults were being inverted as thrusts, leading to uplift of a mountain front to the south of Timmins (and also to the south of Kirkland Lake). In Timmins, paleocurrents in these upper sandstone and conglomerate units are unidirectional, from east to west, and suggest axial transport in front of the rising mountain front. In Kirkland Lake, spectacular polymict conglomerates and crossbedded sandstones at the top of the section, interpreted as alluvial fan deposits, show paleocurrents up the dip from south to north, away from the main fault trace of the CLFZ that lies to the south (i.e. transverse). Both in Timmins and in Kirkland Lake, the youngest detrital zircons that make it into these uppermost clastic rocks are 2669 Ma (e.g. Ayer et al., 2005; Bleeker and van Breemen, 2011; see also Krogh, 1993).

Phase 5: Basin Termination and Tectonic Burial (shortly after 2669 Ma)

The uppermost alluvial fan deposits are overlain, structurally, by the main fault planes, the DPFZ in Timmins and the CLFZ in Kirkland Lake, respectively. This relationship, now steep and “on end”, is interpreted as inverted faults having overridden the synorogenic basin remnants, from south to north, and thus terminating their depositional history. The exact timing of this basin termination is not known in detail but the excellent agreement of youngest detrital zircon ages, at ca. 2669–2667 Ma, from several basin remnants across the

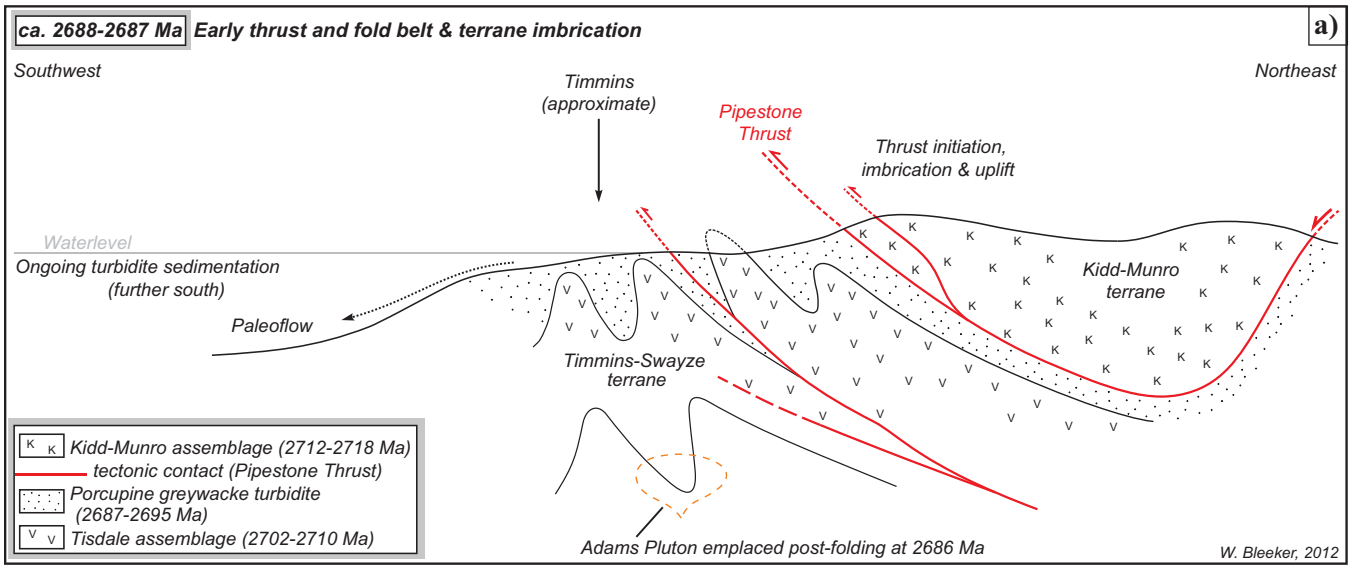

Figure 7 (above and on the following pages). Six time-sequential structural-stratigraphic sections across the southern Abitibi belt and the main fault planes, illustrating the inception of the main faults as synorogenic extensional faults, and their subsequent inversion as thick-skinned thrust faults. Only critical elements are shown, and details are not to scale. Overall view is towards the west (modified from Bleeker, 2012). Abbreviations: Au, gold; CLFZ, Cadillac-Larder Lake Fault Zone; DPFZ, the Destor-Porcupine Fault Zone; u, the synorogenic unconformity at the base of the clastic panels. **a)** Simplified section showing the early fold-thrust belt architecture affecting the south-central Abitibi greenstone belt, Timmins area, at ca. 2688–2687 Ma, just prior to the flare-up of alkaline magmatism. Porcupine Group greywacke turbidites are being fold- and thrust-imbricated with older volcanic rocks. Major thrust slices, such as the Kidd-Munro terrane, are emplaced on top of the structural pile. Overall vergence of these early folds is towards the west (southwest). There is no indication at this stage that the major "breaks", such as the DPFZ, were present. Timing is constrained by the 2686 Ma Adams pluton south of Timmins (shown in dashed outline) cutting across tightly folded stratigraphy deeper in the section.

Abitibi, suggests that it occurred shortly thereafter. Alternatively, no plutonic zircons younger than ca. 2669 Ma were available to provide a monitor of even younger depositional ages and a later timing of basin termination. The faults that terminated the synorogenic basins, and tectonically buried small basin remnants in their structural footwall, must have acted as major thrusts at this stage of their evolution. They emplaced deeper, older, and previously deformed volcanic rocks on top of the uppermost alluvial fan conglomerates.

The key faults were probably moderately steep, thick-skinned thrusts that were inverted from earlier extensional faults. These characteristics make them ideal deep-reaching fluid conduits for the advection of gold-bearing hydrothermal fluids. The thick-skinned thrust inversion had two important, and linked, consequences: 1) major thrust movement deeply buried the synorogenic basin remnants in their footwall, preserving them against substantial post-orogenic erosion; and 2) at the same time, substantial uplift of the hanging wall brought deeper rocks, and gold deposits, to the surface and exposed them to erosion. It is this footwall (preservation) versus hanging-wall (uplift and erosion) asymmetry that explains the distribution of gold deposits in Timmins (and Kirkland Lake) with >99% of all the gold having been produced from the northern footwall side of the principle fault systems.

SYNTHESIS: AN INTEGRATED MODEL

Here the main elements of an integrated model are outlined that explains essentially all the key observations. This is done most easily by means of a time sequence (from old to young) of six schematic sections (Fig. 7a-f). This sequence starts at ca. 2688 Ma (Fig. 7a) with the onset of major deformation in the volcanic stratigraphy and immediately overlying Porcupine Group turbiditic greywackes (Bleeker and Parrish, 1996). There is no indication, either from the distribution of stratigraphic rock units and facies, or from structures, that the principal faults (DPFZ and CLFZ) were present at this time. The sequential sections then illustrate the onset of extension and the inception of the main faults (Fig. 7b); uplift and somewhat later formation of the synorogenic clastic basin(s); a subsequent switch back to regional shortening and inversion of the main faults as thick-skinned thrusts (Fig. 7c); tectonic burial of synorogenic basin remnants below the faults (Fig. 7d,e); and final degeneration of the fault system to late-stage strike slip (Fig. 7f).

In some of the later structural sections, the distribution of gold deposits (yellow stars in Fig. 7) and the overall envelope to gold mineralization (bold yellow outline in Fig. 7) are shown. The envelope to gold mineralization is simply a function of two key parameters: 1) vertical: gold deposition is concentrated in the near-

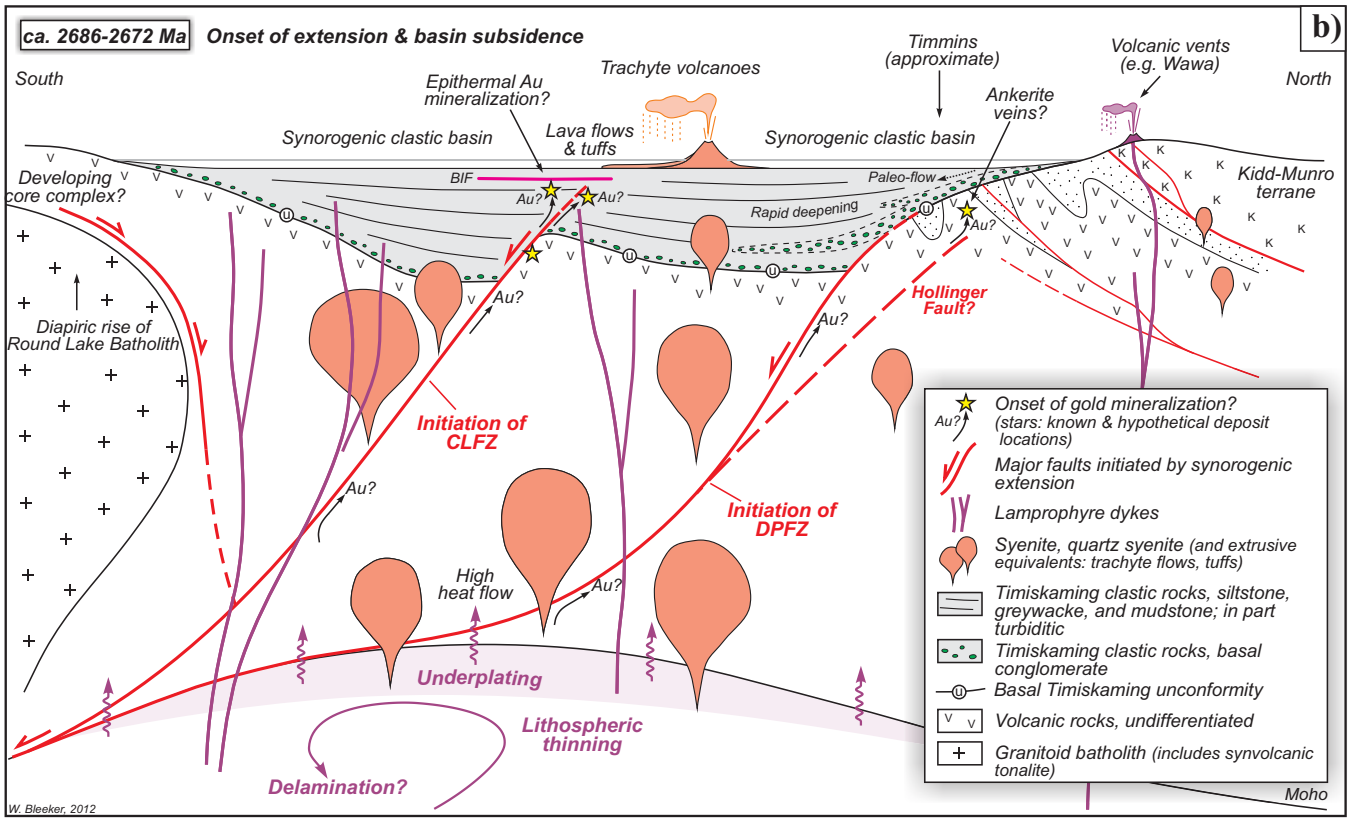

Figure 7 continued. b) Formation of synorogenic clastic basins at ca. 2680 Ma. Rapid deepening of these basins, as well as the sudden flare-up of alkaline magmatism, suggests a link with extension and upper mantle processes (delamination?). The major "breaks", i.e., the DPFZ in the north and the CLFZ further south, were likely initiated at this time as crustal-scale extensional faults, listric to the south. Numerous syenitic plutons were emplaced and lithospheric thinning increased the heat flow into the lower crust. During this extensional deformation, composite granitoid batholiths, such as the Round Lake batholith, rose diapirically, their ascent aided by additional extensional shear zones.

surface environment where pressure and temperature gradients were highest, and low confining pressures allowed the dilation and opening up of veins systems; and 2) horizontal: because the faults acted as principal conduits for hydrothermal fluids from deep reservoirs, gold mineralization peaks in proximity to the fault traces. The resulting envelope is fundamentally asymmetric because the fault system is asymmetric; and this asymmetry increased during thrust inversion, with uplift of the structural hanging walls. In the final section, now also incorporating the complications imposed by significant strike-slip, the distribution of gold deposits (yellow stars in Fig. 7f) is projected as accurately as possible and reflects the statistic that >99% of gold has been produced from within or north of the principal faults, i.e., from the structural footwalls.

The schematic sections also highlight the distribution of synorogenic magmatic rocks, both syenite suite intrusions (and minor extrusives) and lamprophyre dykes, with an origin that was likely tied to extension and perturbations of the mantle lithosphere (delamination?). Prolific syenite suite magmatism likely played a critical role, at some level, in overall gold transport from the upper mantle and deep crust; although final fluids likely represented mixtures of both magmatic fluids and metamorphic fluids (see also Cameron, 1993). At the camp scale, overall gold endowment probably scales with the intensity (or volume) of synorogenic magmatism.

DISCUSSION

Why is Extension so Important?

It is useful to return to this question, because the answer is complicated. Empirically, as well as from an understanding of younger gold deposits, there is often a direct or indirect connection with synorogenic alkaline magmatism (e.g. Richards, 1995). Furthermore, the switch to more alkaline synorogenic magmatism represents a change in overall tectonic regime, from steady-state subduction or accretion to a regime of extension. The onset of extension is often linked to perturbations of the mantle lithosphere, and it is these perturbations that are fuelling the alkaline magmatic flare-up (Fig. 7b). Although far from a perfect analogue for Archean lode gold deposits, the very large Carlin gold province of the western USA (Cline et al., 2005) is important in this respect. This province has a long tectonic pre-history of 1–2 billion years, but gold miner-

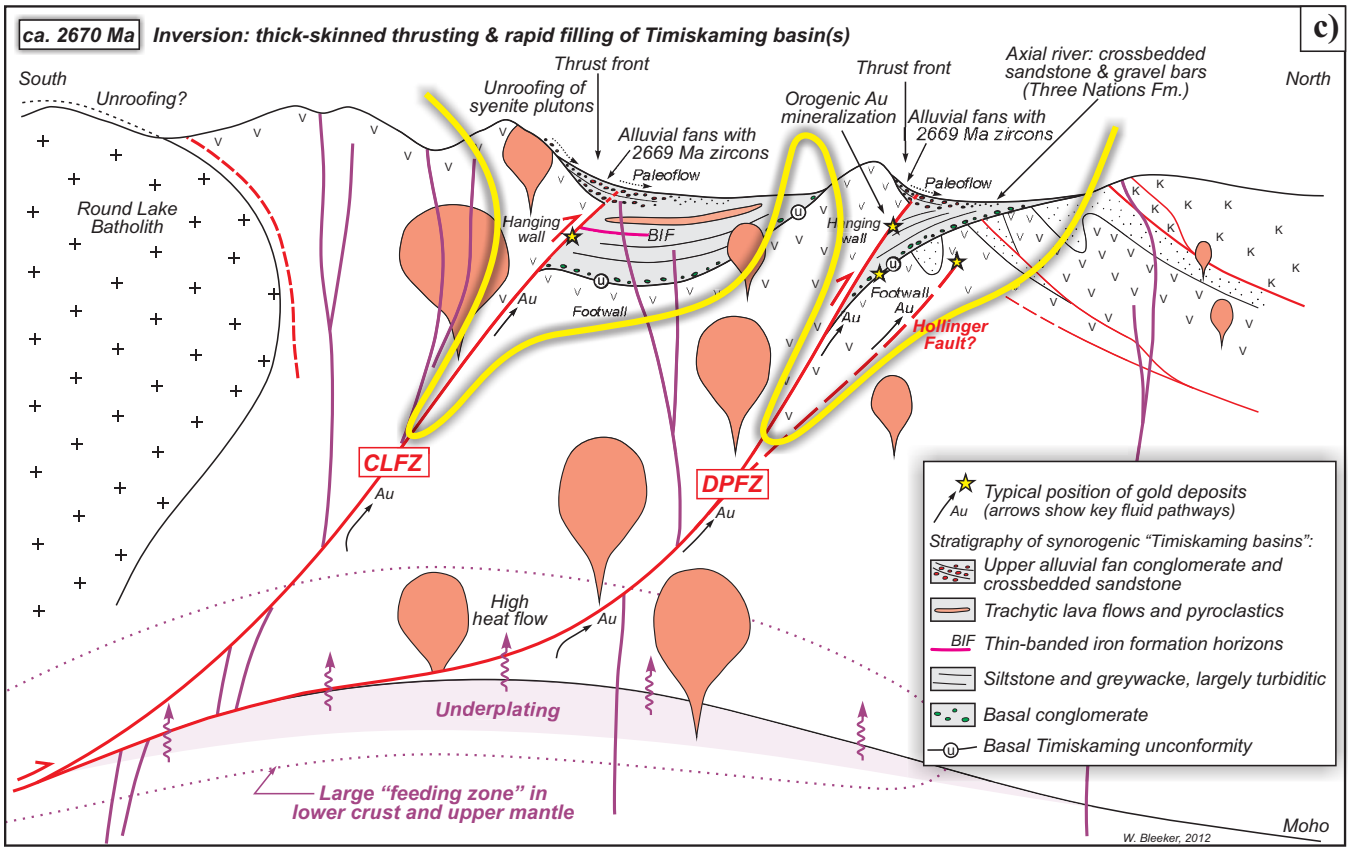

Figure 7 continued. c) Transition from extension to renewed north-south shortening at ca. 2670 Ma, with the major breaks being inverted as thick-skinned thrusts, overriding and burying remnants of the synorogenic clastic basin in their footwalls. Rising mountain fronts were flanking the basin remnants on their south side, shedding alluvial fans to the north. Conglomerate and crossbedded fluvial sandstone filled the basin. This stage is dated by precise ages (2669 Ma) on detrital zircons that were captured in the uppermost alluvial fan conglomerates. Yellow stars show the position of gold deposits forming along the faults, which acted as the principal fluid conduits. The bold yellow envelope outlines the favourable ground for gold mineralization, its asymmetry being a function of the intrinsic asymmetry of the fault system. Gold deposits formed near the synorogenic surface and in proximity to the inverted extensional faults.

alization only initiated in the Paleocene when extension and coeval magmatism overprinted the broad active margin of western North America (e.g. Cline et al., 2005). Extension is also critical because it creates or reactivates relatively simple, deep-reaching faults that provide ideal conduits for advection of gold-bearing hydrothermal fluids from large fluid-generation zones in the deep crust or even upper mantle (e.g. Bierlein et al., 2006). Furthermore, extension leads to thinning of the crust and lithosphere, rapidly increasing the geothermal gradient. This leads to fluid generation in the lower crust. Finally, extension has a subtle but critical link to final preservation. As gold deposition is strongly concentrated in the upper crust (at synorogenic time; Fig. 7b,c), potential deposits are sensitive to the degree of post-orogenic uplift. A scenario of multiple phases of crustal shortening will only thicken the crust and lead to substantial post-orogenic uplift, and thus erosion of the mineralized upper crust. Synorogenic extension counter-balances orogenic thickening and minimizes post-orogenic uplift, thus leading to preservation of the gold depositional sites in the shallow crust.

Thrust Inversion—Why is it Important?

The answer to this question is straightforward and revolves largely around preservation. As gold deposition is strongly skewed towards the upper crust (at synorogenic time), this upper crustal section needs to be preserved. Tectonic burial, with thick-skinned thrust burial of upper crustal sections in the footwall below the main faults, is a very efficient process. The synorogenic clastic rocks can be thought of as a proxy for the surface at synorogenic time (e.g. Fig. 7c). Their presence indicates successful burial of the mineralized upper crustal section and thus long-term preservation. The synorogenic conglomerate and the underlying unconformity, long recognized empirically as being important (e.g. Hodgson, 1993; Robert, 2001), do not play any more significant, deeper, process role; they simply indicate (1) preservation of the optimum crustal level; (2) proximity to a major fault that achieved this

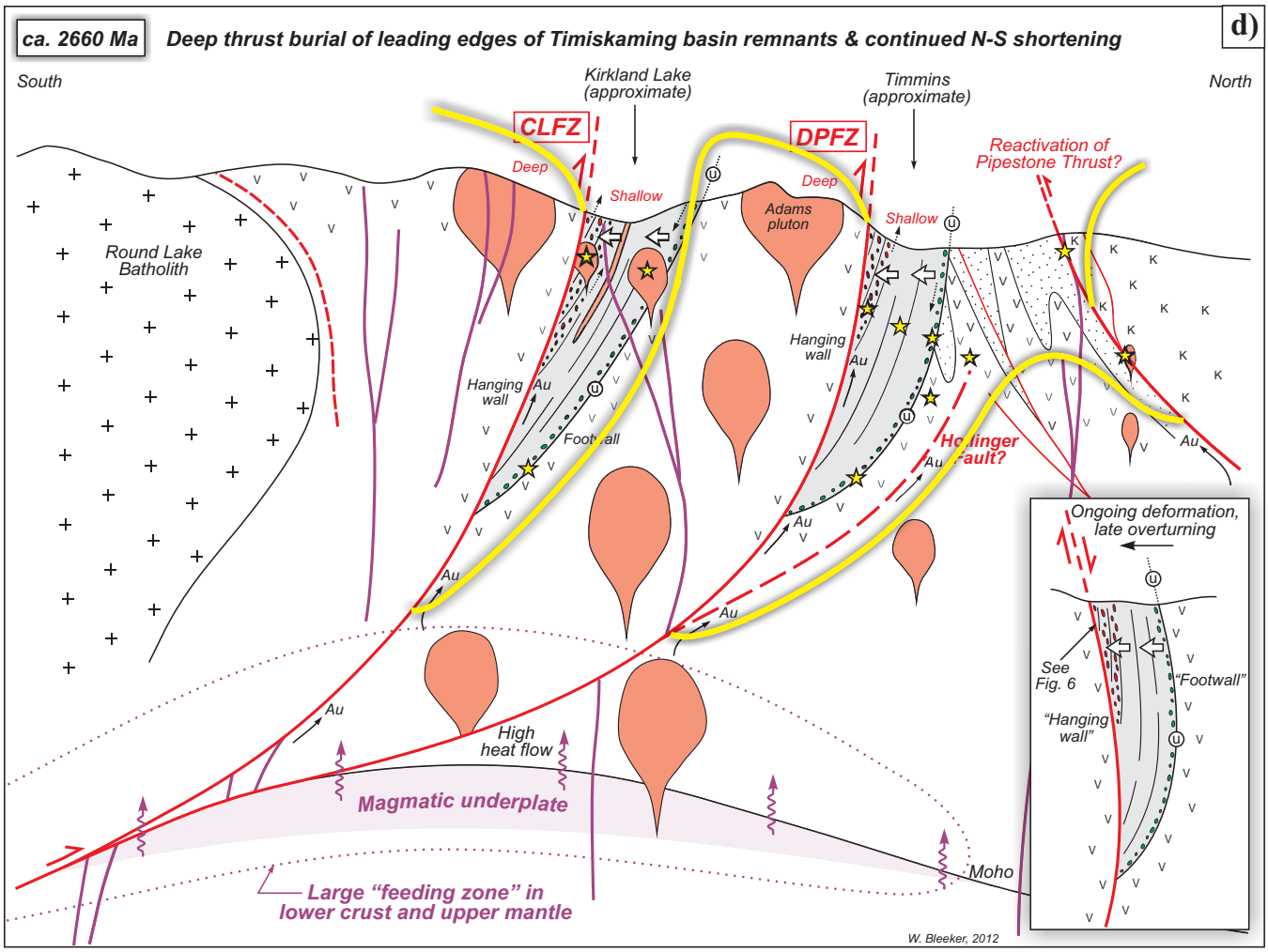

Figure 7 continued. d) Deep burial and steepening of the basin remnants underneath the thick-skinned thrusts. Deeper exhumation of the southern structural hanging walls is indicated by generally deeper tectono-stratigraphy and larger plutons being exposed south of the faults. Substantial thrust motion has now also offset the mineralization envelope (see bold yellow lines), increasing the asymmetry across the faults system. Continued north-south shortening steepened all structures to near vertical, and likely also reactivated other discontinuities (e.g. the earlier Pipestone Thrust). Locally the basin remnants and bounding structures were overturned, leading to confusing kinematics (see inset; see also Figs. 4 and 5). Approximate positions of gold deposits are again indicated by yellow stars. Note their strong asymmetry with respect to the main faults. Bold arrows (white) indicate the overall younging direction in the fundamentally asymmetric panels of synorogenic clastic rocks captured below the faults (i.e. structural footwall).

preservation—i.e., a major fault with significant late-stage thrust motion, and likely an inverted extensional fault; and (3) the overall asymmetry of the fault system—i.e., preserved footwall versus uplifted hanging wall (Fig. 7c,d,e).

Diapirism?

Late-stage diapirism and rapid sinking of intervening greenstone keels between composite granitoid domes is another process that could achieve efficient tectonic burial and thus long-term preservation of upper crustal synorogenic environments (Bleeker, 2002a,b; Lin et al., 2013). Indeed some gold deposits may owe their fluid generation and subsequent preservation to this process. In general, however, the diapir model would predict that synorogenic clastic sections young away from rising diapirs, whereas in the Abitibi greenstone belt, where diapirs are present (e.g. Round Lake batholith, Fig. 7), the opposite is observed. Also, diapiric granitoid domes are lacking in many localities along the laterally extensive principal fault traces. Thrust inversion and associated tectonic burial is therefore the more general mechanism.

When Did Gold Mineralization Peak and the Relevance of Strike Slip?

Although many gold camps show a diversity of deposits, and likely some variation in the timing of gold emplacement, simple crosscutting relationships often argue for a relatively late emplacement of the gold vein systems, from the time of first emplacement of synorogenic plutons hosting disseminated mineral-

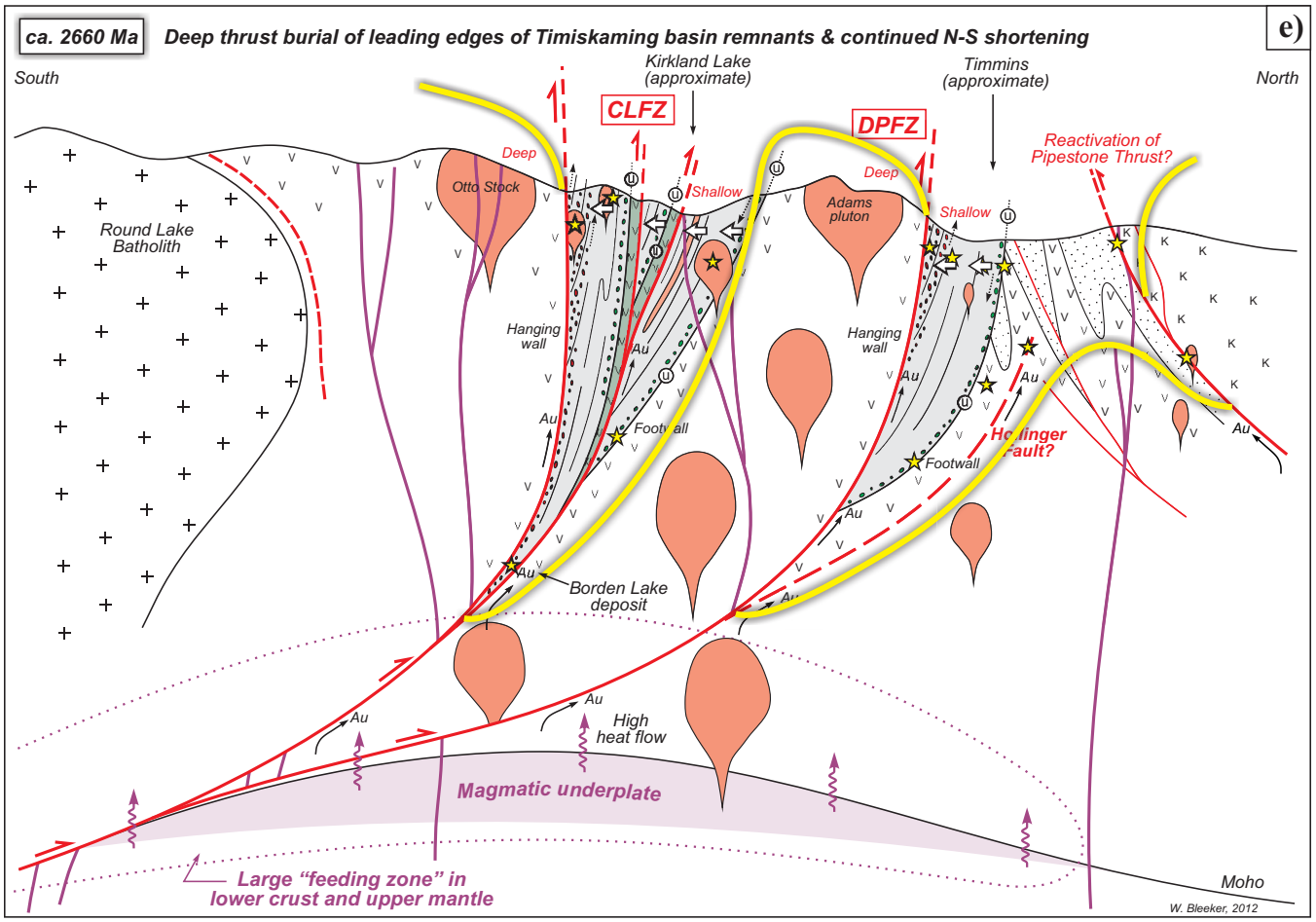

Figure 7 continued. e) This section shows an important variant on the previous section, now incorporating one or more duplex structures within the thrust architecture of the overall synorogenic basin panel below one of the faults (CLFZ). Duplex structures, or stacked thrust slices, are a common consequence of thrust faulting. Slivers of footwall volcanic rocks (highlighted in green) have been incorporated in these thrust slices, creating the observed interleaving of altered mafic-ultramafic volcanic rocks (e.g. Piché Group in Quebec) and synorogenic clastic rocks along some of the faults. Note also the deep tectonic burial of the leading edge of the synorogenic basin panel (and associated gold deposit) below the southern fault. This is essentially the position of the newly discovered Borden Lake gold deposit in the deeply exhumed Kapuskasing Zone near Chapleau (see Fig. 1).

ization to late sub-horizontal veins systems that must post-date much of the steepening of the synorogenic clastic sequences. At the scale of the Abitibi greenstone belt, however, the critical statistic that >95% of all gold comes from one side of the fault systems must mean that most of the gold was emplaced prior to the cessation of the thrust inversion and well prior to the final transition to strike-slip dominated fault motion.

Hydrothermal fluids coming up along a steep fault conduit do not differentiate between footwall and hanging wall, and gold distribution would likely occur on either side. If the fault zone is mainly one of strike slip, gold mineralization would merely be translated sideways and there is no mechanism to favour preservation largely on one side of the fault systems. In fact, strike-slip faulting does not have any preservational aspect and does not explain the systematic deep burial of the synorogenic clastic rocks.

Given that the historical production figures are so strongly skewed (>95% from footwall or within faults), most if not all the gold must have been emplaced either during the extensional phase or during the subsequent thrust-inversion phase, with very little additional gold emplacement during the strike-slip phase. Late-stage strike-slip fault offsets just rearranged the remaining gold endowment laterally—thus complicating the overall picture—but cannot have contributed to overall gold endowment. One exception may involve the formation of "negative flower structures" along some of the major faults, dropping down fault slices during late strike-slip movement, and thus possibly contributing to preservation of higher structural levels (Fig. 2c).

Delayed Gold Mineralization Relative to Extensional Drivers?

Although the detailed timing of gold-bearing quartz vein systems is incompletely known, even in places like Timmins, it seems likely that most of the vein sys-

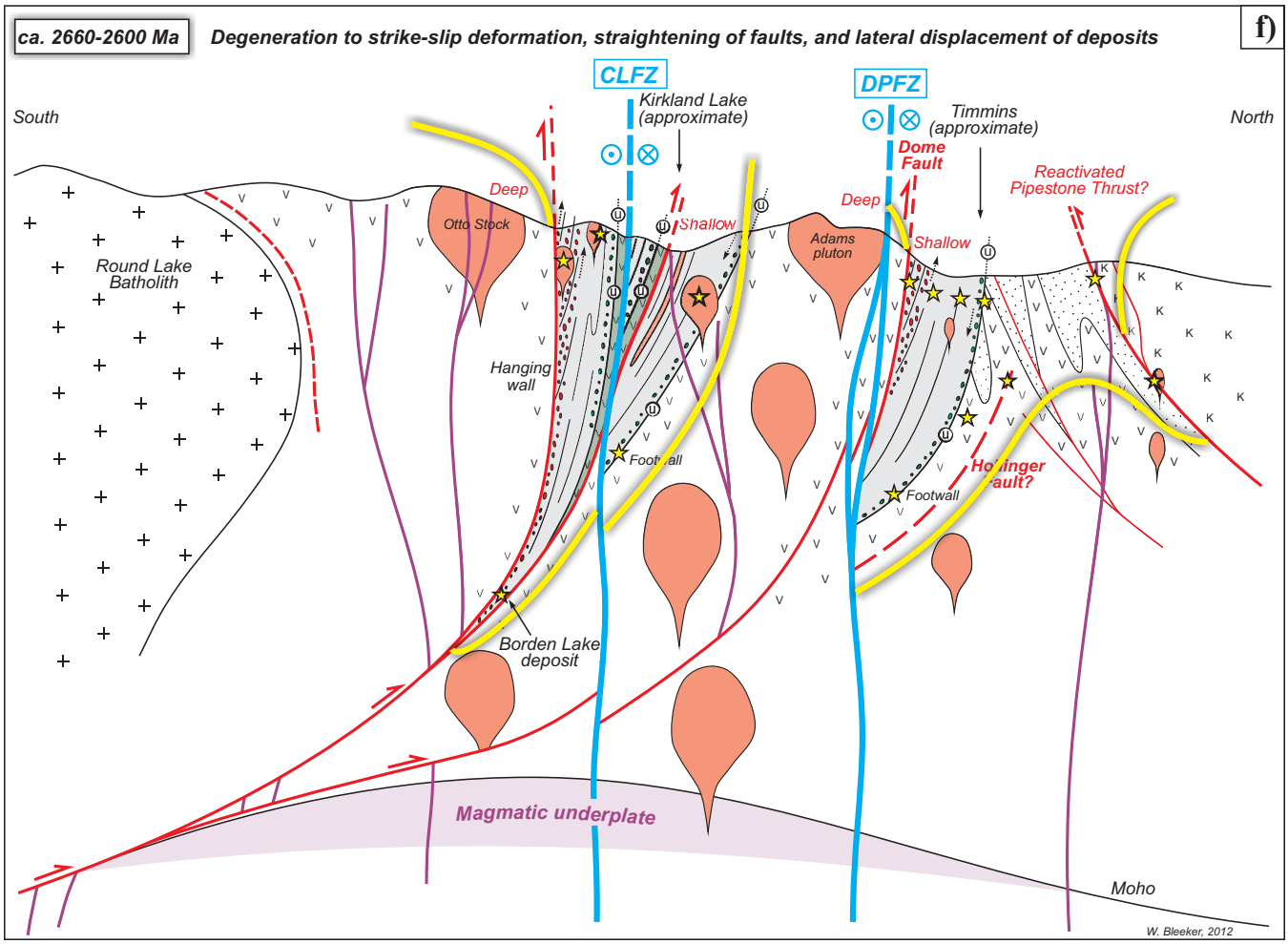

Figure 7 continued. f) Degeneration of the fault systems to strike-slip fault zones. Major strike-slip fault planes (in blue), now typically mapped as "the breaks", broke through to minimize local asperities. Locally the fault planes may follow and overprint the earlier steepened thrust structures, but elsewhere they deviate from and isolate the main thrust faults in separate slices, such as the Dome Fault in the Dome Mine, Timmins. Hence, in some cases the fault trace referred to as "the break" is actually not the most important fault of the system. Staying with the example of the Dome Mine near Timmins (illustrated above), it is the Dome Fault (red) that is the key structure and it is mineralized. In contrast, the DPFZ (in blue) broke through later, further to the south, and is a barren strike-slip fault zone. Both in Timmins and Kirkland Lake there is evidence for early sinistral strike-slip, followed by a latest phase of dextral strike-slip deformation (not shown here, but see Fig. 4e). Net offsets, determined by matching pairs of the most likely piercing points on either side of the principal faults, indicate large sinistral net displacements (e.g. ~10–100 km).

tems came in during the thrust-inversion phase given the ubiquitous observation of shear veins with reverse kinematics (e.g. Colvine et al., 1988). Yet, the overall engine driving the gold mineralization—i.e., extension, faulting, extension-related magmatism, and the ensuing thermal pulse—was initiated earlier. Why this apparent delay of approximately 10 to 15 million years? The most likely answer to this important question is that thermal processes, particularly at somewhat larger distance scales, have a time delay due to the slow thermal conductivity (or diffusivity rather) of silicate rocks. Thermal effects of the extension-related magmatism and initial thinning of the lithosphere may only have reached their maximum at a time when the tectonic regime had already switched back to compression. So, while significant volumes of fluid were still being generated deep in the crust, the main faults were already being reactivated as thick-skinned thrusts. Hence the observed time delay. Nevertheless, there likely were some early high-level epithermal deposits, or late-stage magmatic deposits in syenite suite plutons, that formed during the peak of extension (Fig. 7b). The delicately banded ankerite veins of the Dome Mine, i.e., the "Kurtz veins" with colloform growth forms indicating open-space filling (e.g. Rogers, 1982), were likely part of an early, synextensional mineralizing phase. Being emplaced early during the extensional phase, the veins experienced the initial uplift and were partially eroded into the synorogenic debris of the basin. Clasts of ankerite veins have been reported from the overlying

conglomerate at the Dome Mine (Dubé and Gosselin, 2007).

CONCLUSIONS

A comprehensive model has been developed that explains the intricate relationships between major faults, remnants of synorogenic basins, the distribution of major gold deposits, and the fundamental asymmetry in this distribution relative to the fault traces. In detail, the model is based on extensive observations in the classic Timmins and Kirkland Lake gold camps, Ontario, but it has been tested in other areas such as the Yellowknife belt, Northwest Territories, and the Agnew-Wiluna belt, Western Australia. The model explicitly recognizes the role of synorogenic extension in an area such as the Abitibi greenstone belt in a way that is consistent with field evidence and first-order structural and stratigraphic constraints.

Synorogenic extension initiated the major faults, and was intimately linked to upper mantle processes, a flare-up in alkaline magmatism, increased heat flow into the lower crust, and synorogenic basin development. Synorogenic extension also helps to minimize post-orogenic uplift, thus contributing to preservation of upper crustal environments where gold mineralization is concentrated. Later inversion of the deep-reaching extensional faults, as thick-skinned thrusts, tectonically buried and preserved the upper crustal sections, including gold deposits and synorogenic basin remnants, in the structural footwall of the principal faults. Significant uplift of the hanging walls of these faults removed synorogenic rocks and gold deposits from that side of the faults. This explains the fundamental asymmetry in the distribution of gold deposits, with >99% of the gold having been produced from the footwall side in an area such as Timmins. Similarly, in Yellowknife and the Agnew camp, all gold production has come from the footwall side. Preservation of this marked asymmetry across the principal fault traces must mean that gold mineralization likely was initiated during extension and then peaked before the end of the thrust inversion phase. Late-stage strike-slip, although important in all these areas, has no mechanism to explain this asymmetry in gold distribution. It merely complicated the overall picture by having redistributed remaining mineralization laterally.

Extension, mantle-related magmatism, increased heat flow, and the formation of major faults as crustal-scale fluid conduits, probably represent the overall engine that drove the gold mineralization events. At the belt scale, gold endowment probably scales with the volume of synorogenic (alkaline) magmatism (see also Spooner, 1991). As many of the vein systems were emplaced during thrust inversion, the apparent delay between peak extension and peak gold mineralization (~10–15 Myr) was likely caused by the slow thermal diffusion in the lower crust.

How can these new insights be used to more effectively explore more remote parts of the Canadian Shield? A straightforward approach would assess all the conglomerates and major faults across the north against the model describe herein. Where the occurrence of demonstrable synorogenic conglomerates "intersects" (in a Venn diagram sense) with major faults: what is the local asymmetry of the system? What is the footwall versus hanging wall? Next, the granitoid rocks in promising areas would need to be re-evaluated. Are there any mantle-derived synorogenic plutons (e.g. syenite, monzonite, quartz-monzonite)? Are there any coeval lamprophyre dyke swarms? And what is the overall degree of post-orogenic uplift? Areas that pass all these test should then be reassessed in terms of the gold content in surficial materials (stream and lake sediments, and till). With a more complete understanding of these systems, advanced exploration will be able to focus on the most productive part of the systems, i.e., the structural footwalls.

ACKNOWLEDGEMENTS

Observations and ideas presented in this paper have been assembled over many years, with much of the funding provided by the Geological Survey of Canada through its TGI-3 Abitibi and TGI-4 Lode Gold projects. Support from several mining companies in the Abitibi is acknowledged. Access to their properties, and drill core, as well as in-depth discussions with their geological staff, has been critical in elucidating the full complexity of the fault systems. I would like to acknowledge numerous discussions with colleagues at the GSC and OGS, particularly Benoît Dubé (GSC). Thanks also to Brian Atkinson, long-time Resident Geologist of the Ontario Geological Survey in Timmins. Brian's enthusiasm and readiness to co-lead yet another field trip in the Timmins area will be sorely missed now he has retired. Patrick Mercier-Langevin and Valérie Bécu contributed comments and corrections to this paper on a short time frame. Elizabeth Ambrose handled the final editing and lay-out of the manuscript.

REFERENCES

Ayer, J.A., Barr, E., Bleeker, W., Creaser, R.A., Hall, G., Ketchum, J.W.F., Powers, D., Salier, B., Still, A., and Trowell, N.F., 2003. Discover Abitibi. New geochronological results from the Timmins area: implications for the timing of late-tectonic stratigraphy, magmatism and gold mineralization, *In:* Summary of Field Work and Other Activities 2003; Ontario Geological Survey, Open File Report 6120, p. 33-1 to 33-11.

Ayer, J.A., Thurston, P.C., Bateman, R., Dubé, B., Gibson, H.L., Hamilton, M.A., Hathway, B., Hocker, S.M., Houlé, M.G., Hudac, G., Ispolatov, V.O., Lafrance, B., Lesher, C.M., MacDonald, P.J., Péloquin, A.S., Piercey, S.J., Reed, L.E., and

Thompson, P.H., 2005. Overview of results of the Greenstone Architecture Project: Discover Abitibi Initiative; Ontario Geological Survey, Open File Report 6154, 146 p.

Barnes, M., 1991. Timmins—The Porcupine Country; The Boston Mills Press, Erin, Ontario, 144 p.

Barrie, C.T., 1990. U–Pb garnet and titanite age for the Bristol Township lamprophyre suite, western Abitibi Subprovince, Canada; Canadian Journal of Earth Sciences, v. 27, p. 1451–1456.

Bierlein, F.P., Groves, D.I., Goldfarb, R.J., and Dubé, B., 2006. Lithospheric controls on the formation of provinces hosting giant orogenic gold deposits; Mineralium Deposita, v. 40, p. 874–886.

Bleeker, W., 1995. Day 1: Surface geology of the Porcupine camp, *In:* Tectonics and metallogeny of Archean crust in the Abitibi–Kapuskasing–Wawa region, field trip guidebook; Geological Survey of Canada, Open File 3141, p. 13–37.

Bleeker, W., 1999. Structure, stratigraphy, and primary setting of the Kidd Creek volcanogenic massive sulphide deposit: a semi-quantitative reconstruction, *In:* The Giant Kidd Creek Volcanogenic Massive Sulfide Deposit, western Abitibi Subprovince, Canada, (ed.) M.D. Hannington and C.T. Barrie; Society of Economic Geologist, Economic Geology Monograph 10, p. 71–121.

Bleeker, W., 2002a. Archaean tectonics: a review, with illustrations from the Slave craton, *In:* The Early Earth: Physical, Chemical and Biological Development, (ed.) C.M.R. Fowler, C.J. Ebinger, and C.J. Hawkesworth; Geological Society of London, Special Publication No. 199, p. 151–181.

Bleeker, W., 2002b. "Timiskaming-type" conglomerate-sandstone sequences: indicators of the buoyant ascent and unroofing of composite Archean granitoid-gneiss domes, *In:* Abstracts; Geological Association of Canada-Mineralogical Association of Canada, joint annual meeting, Saskatoon, May 27-29, 2002, v. 27, p. 11.

Bleeker, W., 2012. Targeted Geoscience Initiative (TGI-4) Lode Gold Deposits in Ancient Deformed and Metamorphosed Terranes: The role of extension in the formation of Timiskaming basins and large gold deposits, Abitibi greenstone belt—A discussion, *In:* Summary of Field Work and Other Activities, 2012; Ontario Geological Survey, Open File Report 6280, p. 47-1 to 47-12.

Bleeker, W. and Hall, B., 2007. The Slave Craton: geology and metallogenic evolution, *In:* Mineral Deposits of Canada: A Synthesis of Major Deposit Types, District Metallogeny, the Evolution of Geological Provinces, and Exploration Methods, (ed.) W.D. Goodfellow; Geological Association of Canada, Mineral Deposits Division, Special Publication No. 5, p. 849–879.

Bleeker, W. and Parrish, R.R., 1996. Stratigraphy and U–Pb zircon geochronology of Kidd Creek: implications for the formation of giant volcanogenic massive sulphide deposits and the tectonic history of the Abitibi greenstone belt; Canadian Journal of Earth Sciences, v. 33, p. 1213–1231.

Bleeker, W. and van Breemen, O., 2011. New geochronological, stratigraphic, and structural observations on the Kidd–Munro assemblage and the terrane architecture of the south-central Abitibi greenstone belt, Superior Craton, Canada, Chapter 2 *In:* Results from the Targeted Geoscience Initiative III, Kidd–Munro Project; Ontario Geological Survey, Open File Report 6258, 142 p.

Bleeker, W., Hamilton, M.A., Ernst, R.E., and Söderlund, U., 2012. Resolving the age structure of the Matachewan event: Magmatic pulses at c. 2445–2452 Ma, 2458–2461 Ma, and 2475–2480 Ma, Reports A96, A97, and A98, *In:* Reconstruction of Supercontinents back to 2.7 Ga using the Large Igneous Province (LIP) Record: With Implications for Mineral Deposit Targeting, Hydrocarbon Exploration, and Earth System Evolution, (comp.) R.E. Ernst, W. Bleeker, and the LIPs reconstruction project team; Year 3 Confidential Summary for Project Sponsors, internal 2013 report.

Bleeker, W., Atkinson, B.T., and Stalker, M., 2014. A "New" Occurrence of Timiskaming Sedimentary Rocks in the Northern Swayze Greenstone Belt, Abitibi Subprovince—With Implications for the Western Continuation of the Porcupine-Destor Fault Zone and Nearby Gold Mineralization, *In:* Summary of Field Work and Other Activities 2014; Ontario Geological Survey, Open File Report 6300, p.43-1 to 43-10.

Burrows, A.G., 1924. The Porcupine gold area; Thirty-Third Annual Report of the Ontario Department of Mines, v. 33, pt. 2, 112 p. and accompanying map.

Cameron, E.M., 1993. Precambrian gold: Perspective from top to bottom of shear zones; The Canadian Mineralogist, v. 31, p. 917–944.

Cline, J.S., Hofstra, A.H., Muntean, J.L., Tosdal, R.M., and Hickey, K.A., 2005. Carlin-type gold deposits in Nevada: critical geologic characteristics and viable models, *In:* 100th Anniversary Volume, (ed.) J.W. Hedenquist, J.F.H. Thompson, R.J. Goldfarb, and J.P. Richards; Society of Economic Geologists, p. 451–484.

Colvine, A.C., Fyon, J.A., Heather, K.B., Marmont, S., Smith, P.M., and Troop D.G., 1988. Archaean lode gold deposits in Ontario; Ontario Geological Survey, Miscellaneous Paper 139, 136 p.

Corfu, F., 1993. The evolution of the southern Abitibi greenstone belt in light of precise U-Pb geochronology; Economic Geology, v. 88, p. 1323–1340.

Corfu, F., Krogh, T.E., Kwok, Y.Y., and Jensen, L.S., 1989. U-Pb zircon geochronology in the southwestern Abitibi greenstone belt, Superior Province; Canadian Journal of Earth Sciences, v. 26, p. 1747–1763.

Doherty, K., 1986. History of the Timmins area, *In:* Gold '86 Excursion Guidebook, (ed.) J. Pirie and M.J. Downes, Toronto, p. 3–5.

Dubé, B. and Gosselin, P., 2007. Greenstone-hosted quartz-carbonate vein deposits, *In:* A synthesis of Major Deposit Types, District Metallogeny, the Evolution of Geological Provinces, and Exploration Methods, (ed.) W.D. Goodfellow; Geological Association of Canada, Mineral Deposits Division, Special Publication No. 5, p. 49–73.

Duuring, P., Bleeker, W., Beresford, S.W., Fiorentini, M.L., and Rosengren, N.M., 2012. Structural evolution of the Agnew-Wiluna greenstone belt, Eastern Yilgarn Craton and implications for komatiite-hosted Ni sulfide exploration; Australian Journal of Earth Sciences, v. 59, p. 765–791.

Frarey, M.J. and Krogh, T.E., 1986. U-Pb zircon ages of late internal plutons of the Abitibi and eastern Wawa subprovinces, Ontario and Quebec; Geological Survey of Canada, Paper 86-1A, p. 43–48.

Frimmel, H.E., Groves, D.I., Kirk, J., Ruiz, J., Chesley, J., and Minter, W.E.L., 2005. The formation and preservation of the Witwatersrand Goldfields, the world's largest gold province, *In:* 100th Anniversary Volume, (ed.) J.W. Hedenquist, J.F.H. Thompson, R.J. Goldfarb, and J.P. Richards; Society of Economic Geologists, Littleton, Colorado, p. 769–797.

Goldfarb, R.J., Groves, D.I., and Gardoll, S., 2001. Orogenic gold and geologic time: A global synthesis; Ore Geology Reviews, v. 18, p. 1–75.

Groves, D.J., 1993. The crustal continuum model for late Archean lode-gold deposits of the Yilgarn Block, Western Australia; Mineralium Deposita, v. 28, p. 366–374.

Groves, D.J., Goldfarb, R.J., Gebre-Mariam, M., Hagemann, S.G., and Robert, F., 1998. Orogenic gold deposits: A proposed classification in the context of their crustal distribution and rela-

tionships to other gold deposit types; Ore Geology Reviews, v. 13, p. 7–27.

Gunning, H.C., 1937. Cadillac area, Quebec; Geological Survey of Canada, Memoir 206, 80 p.

Gunning, H.C. and Ambrose, J.W., 1939. The Timiskaming-Keewatin problem in the Rouyn-Harricanaw region, northwestern Quebec; Transactions of the Royal Society of Canada, Section IV, p. 19–49.

Hodgson, C.J., 1993. Mesothermal lode-gold deposits, *In:* Mineral Deposit Modelling, (ed.) R.V. Kirkham, W.D. Sinclair., R.I. Thorpe, and J.M. Duke; Geological Association of Canada, Special Paper 40, p. 635–678.

Hurst, M.E., 1939. Porcupine area, District of Cochrane, Ontario; Ontario Department of Mines, Annual Report Map 47a, scale 1:24 000.

Katz, L.R., Kontak, D.J., Dubé, B., and McNicoll, V.J., 2015. The Archean Côté Gold intrusion-related Au(-Cu) deposit, Ontario: a large tonnage, low-grade deposit centred on a magmatic-hydrothermal breccia, *In:* Targeted Geoscience Initiative 4: Contributions to the Understanding of Precambrian Lode Gold Deposits and Implications for Exploration, (ed.) B. Dubé and P. Mercier-Langevin; Geological Survey of Canada, Open File 7852, p. 139–155.

Kerrich, R. and Cassidy, K.F., 1994. Temporal relationships of lode gold mineralization to accretion, magmatism, metamorphism and deformation – Archean to present: A review; Ore Geology Reviews, v. 9, p. 263–310.

Kerrich, R., Goldfarb, R., Groves, D., and Garwin, S., 2000. The geodynamic of world-class gold deposits: characteristics, space-time distribution and origins, *In:* Gold in 2000, (ed.) S.G. Hagemann, and P.E. Brown; Society of Economic Geologists, Reviews in Economic Geology, v. 13, p. 501–551.

Knight, C.W., 1924. Lightning River gold area; Thirty-third Annual Report of the Ontario Department of Mines, v. 33, part 3, p. 41–49.

Krogh, T.E., 1993. High precision U-Pb ages for granulite metamorphism and deformation in the Archean Kapuskasing structural zone, Ontario: implications for structure and development of the lower crust; Earth and Planetary Science Letters, v. 119, p. 1–18.

Lin, S., Parks, J., Heaman, L.M., Simonetti, A., and Corkery, M.T., 2013. Diapirism and sagduction as a mechanism for deposition and burial of "Timiskaming-type" sedimentary sequences, Superior Province: Evidence from detrital zircon geochronology and implications for the Borden Lake conglomerate in the exposed middle to lower crust in the Kapuskasing uplift; Precambrian Research, v. 238, p. 148–157.

Lhotka, P.G. and Nesbitt, B.E., 1989. Geology of unmineralized and gold-bearing iron formation, Contwoyto Lake-Point Lake region, Northwest Territories, Canada; Canadian Journal of Earth Sciences, v. 26, p. 46–64.

Mercier-Langevin, P., Dubé, B., Hannington, M.D., Davis, D.W., Lafrance, B., and Gosselin, G., 2007. The LaRonde Penna Au-rich volcanogenic massive sulfide deposit, Abitibi Greenstone Belt, Quebec: Part I. geology and geochronology; Economic Geology, v. 102, p. 585–609.

Mole, D.R., Fiorentini, M.L., Cassidy, K.F., Kirkland, C.L., Thebaud, N., McCuaig, T.C., Doublier, M.P., Duuring, P., Romano, S.S., Maas, R., Belousova, E.A., Barnes, S.J., and Miller, J., 2013. Crustal evolution, intra-cratonic architecture and the metallogeny of an Archaean craton, *In:* Ore Deposits in an Evolving Earth, (ed.) G.R.T. Jenkins, P.A.J. Lusty, I. McDonald, M.P. Smith, A.J. Boyce, and J.J. Wilkinson; Geological Society of London, Special Publication 393, p. 23–80. doi:10.1144/SP393.8

Mueller, W., Donaldson, J.A., and Doucet, P., 1994. Volcanism and tectono-plutonic influences on sedimentation in the Archean Kirkland Lake Basin, Abitibi greenstone belt, Canada; Precambrian Research, v. 68, p. 201–230.

Poulsen, K.H., Card, K.D., and Franklin, J.M., 1992. Archean tectonic and metallogenic evolution of the Superior Province of the Canadian Shield; Precambrian Research, v. 58, p. 25–54.

Poulsen, K.H., Robert, F., and Dubé, B., 2000. Geological classification of Canadian gold deposits; Geological Survey of Canada, Bulletin 540, 106 p.

Richards, J.P., 1995. Alkalic-type epithermal gold deposits—A review, *In:* Magmas, Fluids, and Ore Deposits, (ed.) J.F.H. Thompson; Mineralogical Association of Canada, Short Course Series 23, p. 367–400.

Robert, F., 2001. Syenite-associated disseminated gold deposits in the Abitibi greenstone belt, Canada; Mineralium Deposita, v. 36, p. 503–516.

Robert, F., Poulsen, K.H., Cassidy, K.F., and Hodgson, C.J., 2005. Gold metallogeny of the Superior and Yilgarn cratons, *In:* 100th Anniversary Volume, (ed.) J.W. Hedenquist, J.F.H. Thompson, R.J. Goldfarb, and J.P. Richards; Society of Economic Geologists, Littleton, Colorado, p. 1001–1033.

Rogers, D.S., 1982. The geology and ore deposits of the No. 8 shaft area, Dome mine, *In:* Geology of Canadian Gold Deposits, (ed.) R.W. Hodder and W. Petruk; Canadian Institute of Mining and Metallurgy, Special Volume 24, p. 161–168.

Roscoe, S.M. and Minter, W.E.L., 1993. Pyritic paleoplacer gold and uranium deposits. *In:* Mineral Deposit Modeling, (ed.) R.V. Kirkham, W.D. Sinclair, R.I. Thorpe, and J.M. Duke; Geological Association of Canada, Special Paper 40, p. 103–124.

Spooner, E.T.C., 1991. The magmatic model for the origin of Archean Au quartz vein ore systems: Assessment of the evidence, *In:* Brazil Gold '91: The Economics, Geology, Geochemistry and Genesis of Gold Deposits, (ed.) E.A. Ladeira; Brookfield; Rotterdam, p. 313–318.

Stachel, T., Banas, A., Muehlenbachs, K., Kurszlaukis, S., and Walker, E.C., 2006. Archean diamonds from Wawa (Canada): samples from deep cratonic roots predating cratonization of the Superior Province; Contributions to Mineralogy and petrology, v. 151, p. 737–750.

Thomson, J.E., 1950. Geology of Teck Township and the Kenogami Lake area, Kirkland Lake gold belt; Ontario Department of Mines, Annual Report v. 57, p. 1–53.

Wilson, M.E., 1962. Rouyn-Beauchastel map areas; Geological Survey of Canada, Memoir 315, 140 p.

Wyman, D.A., Ayer, J.A., Conceição, R.V., and Sage, R.P., 2006. Mantle processes in an Archean orogen: evidence from 2.67 Ga diamond-bearing lamprophyres and xenoliths; Lithos, v. 89, p. 300–328.

GEOLOGICAL SURVEY OF CANADA
OPEN FILE 7852

Targeted Geoscience Initiative 4: Contributions to the Understanding of Precambrian Lode Gold Deposits and Implications for Exploration

Structural and lithological controls on gold mineralization at the Cheminis mine: Implications for the formation of gold deposits along the Larder Lake - Cadillac deformation zone, Ontario

Bruno Lafrance

Laurentian University, Sudbury, Ontario

2015

This publication is available for free download through GEOSCAN (http://geoscan.nrcan.gc.ca/)

Recommended citation

Lafrance, B., 2015. Structural and lithological controls on gold mineralization at the Cheminis mine: Implications for the formation of gold deposits along the Larder Lake - Cadillac deformation zone, Ontario, *In:* Targeted Geoscience Initiative 4: Contributions to the Understanding of Precambrian Lode Gold Deposits and Implications for Exploration, (ed.) B. Dubé and P. Mercier-Langevin; Geological Survey of Canada, Open File 7852, p. 49–54.

Publications in this series have not been edited; they are released as submitted by the author.

Contribution to the Geological Survey of Canada's Targeted Geoscience Initiative 4 (TGI-4) Program (2010–2015)

TABLE OF CONTENTS

Structural and lithological controls on gold mineralization at the Cheminis mine: Implications for the formation of gold deposits along the Larder Lake - Cadillac deformation zone, Ontario

Bruno Lafrance

Mineral Exploration Research Centre, Department of Earth Sciences, Goodman School of Mines,
Laurentian University, Sudbury, Ontario P3E 2C6
Author's e-mail: blafrance@laurentian.ca

ABSTRACT

The Larder Lake-Cadillac deformation zone (LLCDZ) is a major deformation zone within the southern Abitibi subprovince of the Archean Superior Province. It hosts several gold deposits, including the Cheminis and the giant Kerr Addison – Chesterville deposits in Ontario. The two deposits occur along a strongly deformed band of Fe-rich tholeiitic basalt and komatiite of the Larder Lake Group (ca. 2705 Ma), bounded on both sides by younger, less deformed, Timiskaming turbidite (2680–2670 Ma). Gold was emplaced during D_2 closure of an extensional Timiskaming basin, following the formation of early F_1 folds. D_2 deformation was a progressive compressive deformation event that began with regional F_2 folding and the formation of a regional S_2 cleavage, and ended with the localization of the deformation along the band of older volcanic rocks, the formation of the LLCDZ, and the introduction of gold during south-side-up reverse-slip faulting along the LLCDZ. The presence of weakly deformed syenite dykes suggests a minor magmatic contribution to the gold-bearing hydrothermal fluids. Thus, gold was deposited as hydrothermal fluids flowed upward along the LLCDZ during D_2 south-side-up shearing.

INTRODUCTION

The Larder Lake - Cadillac deformation zone (LLCDZ) can be traced from Val D'Or, Quebec, to Matachewan, Ontario, in the southern Abitibi subprovince of the Archean Superior Province. The deformation zone generally follows the contact between sedimentary and alkaline volcanic rocks of the Timiskaming Group (2680–2670 Ma: Ayer et al., 2005) to the north and older volcanic rocks of the Larder Lake Group (ca. 2705 Ma: Corfu et al., 1989) to the south (Fig. 1). East of Larder Lake, it leaves this contact and is localized along a 100–350 m wide band of ultramafic rocks and Fe-rich tholeiitic basalt of the Larder Lake Group, between two panels of Timiskaming turbidite. The giant Kerr Addison – Chesterville deposit and the smaller satellite Cheminis deposit occur within this band of deformed volcanic rocks. The objectives of the study are to determine the relative chronology and the structural and lithological controls on gold mineralization at the Cheminis mine and highlight implications for the formation of lode gold deposits along the LLCDZ.

RESULTS

The earliest deformation feature in the Timiskaming rocks in the Cheminis mine area is the presence of F_1 folds. These folds, which lack an axial plane cleavage, are refolded by regional F_2 folds with a sericitic and chloritic, axial planar, S_2 cleavage, which strikes east to east-northeast and dips steeply (75–85°) to the south or north. S_2 cleavage becomes more pronounced in the band of Larder Lake volcanic rocks, where it is associated with a strong, steeply plunging, mineral stretching lineation and asymmetrical internal structures (S-C fabrics, asymmetrical strain shadows), suggesting south-side-up movement along S_2 (Ispolatov et al., 2005, 2008). This band of localized shearing and intense deformation represents the LLCDZ. During later dextral trans-current reactivation of the LLCDZ, S_2 cleavage is overprinted by asymmetrical, Z-shaped F_3 folds with an axial planar S_3 slaty/crenulation cleavage.

Gold in the LLCDZ is associated with disseminated pyrite in altered Fe-rich tholeiitic basalt ("flow ore") and with quartz carbonate veins in highly altered fuchsite-carbonate ultramafic schist ("green-carbonate ore") and turbidite (Thompson, 1941; Kishida and Kerrich, 1987; Smith et al., 1993). Fe-rich tholeiitic basalt underwent extensive ankerite alteration (up to 65% of the rock) and sericitization, resulting in sericite largely replacing metamorphic chlorite. Pyrite occurs as small disseminated grains (<1 mm) parallel to S_2

Lafrance, B., 2015. Structural and lithological controls on gold mineralization at the Cheminis mine: Implications for the formation of gold deposits along the Larder Lake - Cadillac deformation zone, Ontario, *In:* Targeted Geoscience Initiative 4: Contributions to the Understanding of Precambrian Lode Gold Deposits and Implications for Exploration, (ed.) B. Dubé and P. Mercier-Langevin; Geological Survey of Canada, Open File 7852, p. 49–54.

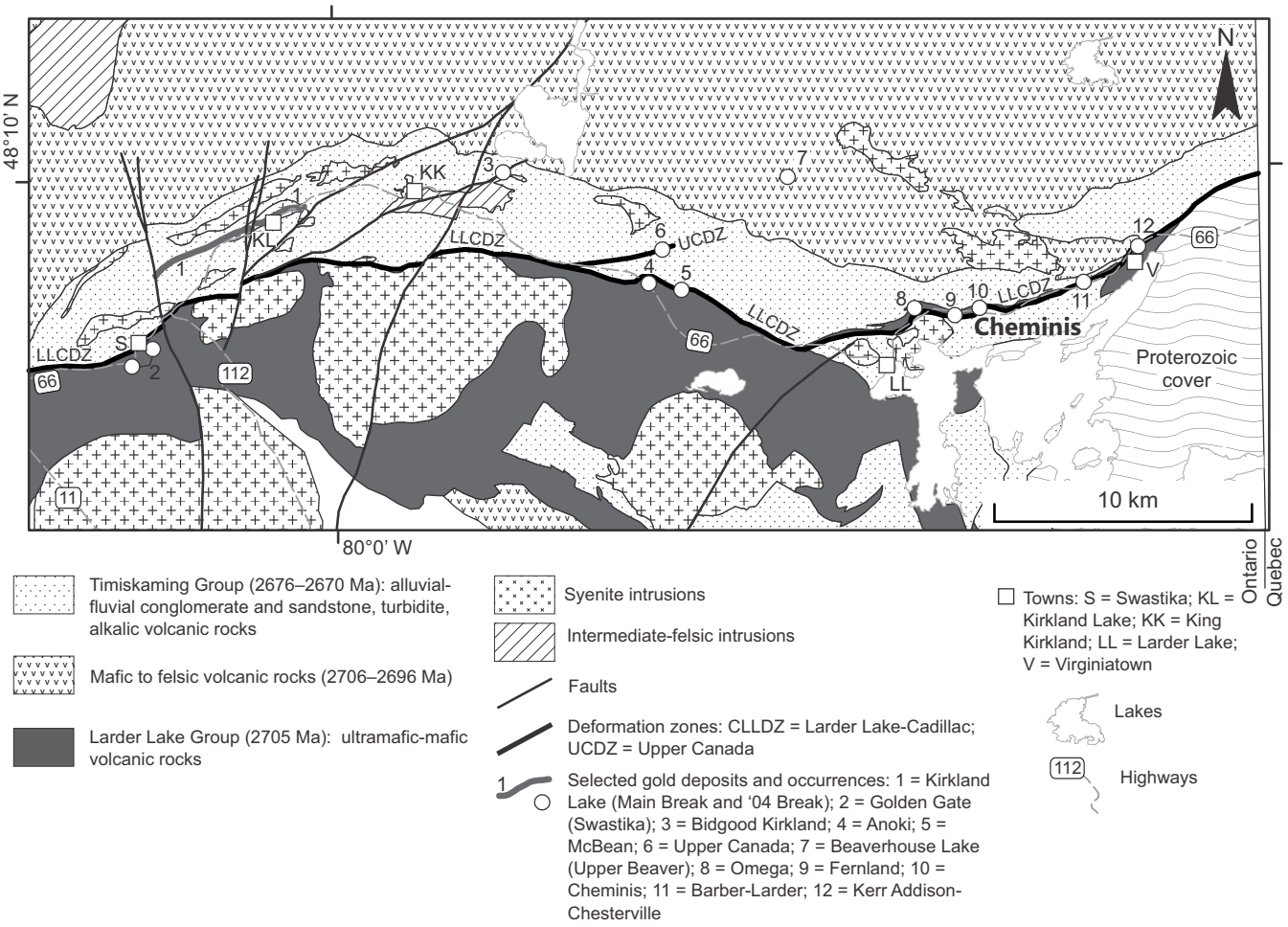

Figure 1. Simplified geological map of the Larder Lake-Cadillac deformation zone from Kirkland Lake to the Ontario – Québec provincial border, showing the location of the Cheminis mine. Modified after Ispolatov et al. (2008).

and as large cubes (up to ≤5 mm) that are surrounded by and truncate S_2 cleavage (Fig. 2a). Strain shadows around pyrite cubes are filled with ankerite, quartz and sericite (Fig. 2b), which also occur as inclusions within the pyrite cubes. Gold grains are present as inclusions within pyrite and along grain boundaries of both disseminated and cube pyrite. Green fuchsitic-carbonate ultramafic schist consists of fuchsite, ferroan dolomite, magnesite, and quartz, replacing all primary and/or metamorphic minerals. Gold is associated with grey quartz-carbonate veins that are boudinaged, folded, and transposed parallel to S_2 cleavage. Syenite dykes are parallel to S_2 in fuchsite-carbonate ultramafic schist, and they are weakly foliated parallel to S_2. Turbidite-hosted mineralization consists of an alteration halo of ankerite, sericite, arsenopyrite and pyrite surrounding fibrous quartz-carbonate veins.

DISCUSSION

The relative chronology of gold mineralization and structural evolution of the LLCDZ can be interpreted from microstructural relationships. In fuchsite-carbonate ultramafic schist, quartz-carbonate veins associated with gold mineralization are folded and transposed parallel to S_2 cleavage, suggesting that mineralization was deposited either before or early during D_2 deformation. In Fe-rich tholeiitic basalt, S_2 cleavage is either truncated by pyrite grains or wraps around pyrite grains that have strain shadows infilled with hydrothermal alteration minerals. These textural relationships and the association of the gold with pyrite suggests that the gold mineralization was emplaced during D_2 deformation.

Syenite dykes are surrounded by rocks with a strong S_2 foliation but are only weakly foliated parallel to S_2. This suggests that the dykes were emplaced either prior to or late during D_2 deformation, as deformation along the LLCDZ became localized in the surrounding weaker ultramafic rocks. The dykes have a similar trace element geochemistry as intramineral albitite dykes at the Kerr-Addison mine (Smith et al., 1993). The latter dykes are interpreted to have been emplaced late during the development of the main foliation along the LLCDZ (Smith et al. 1993). Thus, magmatic fluids may have contributed to the hydrothermal system at Cheminis, as Smith et al. (1993) suggest at Kerr Addison. However, as only three syenite dykes have

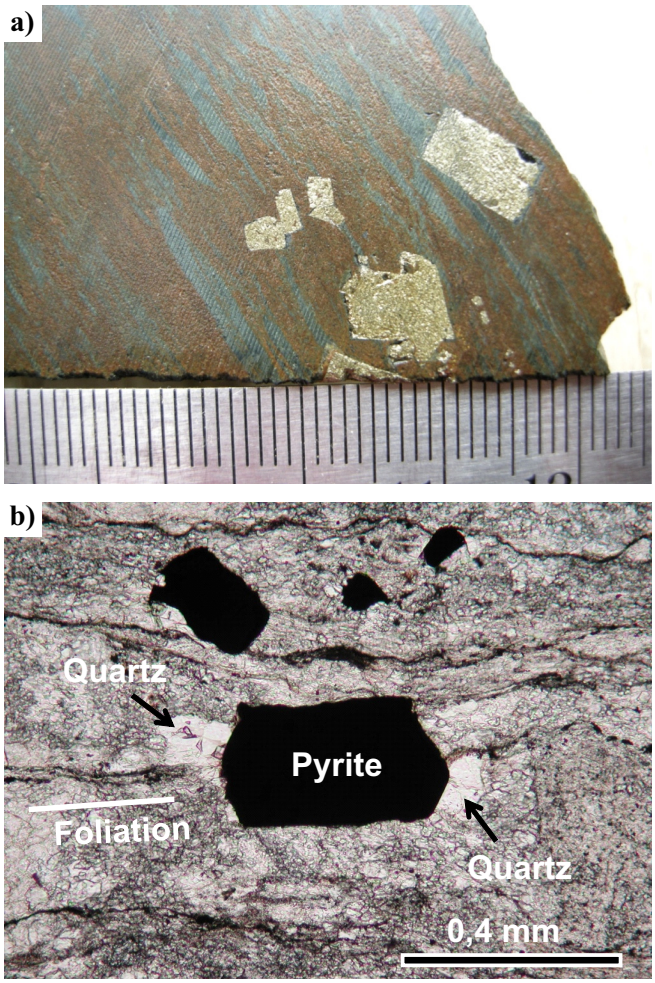

Figure 2. a) Drill core showing a coarse-grained pyrite cube overgrowing S2 foliation in an altered Fe-rich tholeiitic basalt. **b)** Photomicrograph of altered Fe-rich tholeiitic basalt showing a pyrite cube truncating S2 and surrounded by strain shadows filled with quartz. Natural light.

been mapped at Cheminis, this contribution could only have been a minor component of the hydrothermal fluid system.

The migration of hydrothermal fluids and alkaline magmas could have begun before D_2 deformation along an early syn-depositional normal fault that constrains the Timiskaming basin to the south (Dimroth et al., 1982; Cameron, 1993; Mueller et al., 1994; Bleeker, 2012). During the closure and shortening of the Timiskaming basin, the fault was reactivated forming the reverse, south-side-up LLCDZ during D_2 deformation (Bleeker, 2012). The main phase of gold mineralization was emplaced during this contractional D_2 event, as hydrothermal fluids flowed upward along the structure (Card et al., 1989; Hodgson and Hamilton, 1989; Cameron, 1993).

IMPLICATIONS FOR EXPLORATION

The LLCDZ remains an excellent target for new gold discoveries. Within the LLCDZ, detailed mapping of the intensity of ankerite and sericite alteration is warranted, as both are directly associated with gold mineralization (Poulsen et al., 2000; Robert et al., 2005; Dubé and Gosselin, 2007). Slivers of Fe-rich tholeiitic basalt enclosed by more ductile ultramafic schist are favourable targets because the more ductile ultramafic schist was likely less permeable and could have focused or restricted the flow of hydrothermal fluids into the more competent Fe-rich tholeiitic basalt (Ispolatov et al., 2008). Zones with a strong foliation, stretching lineation, and asymmetrical shear sense indicators are also worthy of further study as they represent zones of more intense shear and permeability, which may have acted as channels for the migration of hydrothermal fluids.

ACKNOWLEDGEMENTS

Don Lavigne, François Viens, and Jeff Cormier are thanked for providing access to the Cheminis mine site. The work benefited from stimulating discussions with Vladimir Ispolatov, Benoît Dubé, and John Ayer. Benoît Dubé is thanked for his review. Funding was provided from a NSERC Discovery grant to B. Lafrance.

REFERENCES

Ayer, J.A., Thurston, P.C., Bateman, R., Dubé, B., Gibson, H.L., Hamilton, M.A., Hathway, B., Hocker, S.M., Houlé, M.G., Hudak, G., Ispolatov, V.O., Lafrance, B., Lesher, C.M., MacDonald, P.J., Péloquin, A.S., Piercey, S.J., Reed, L.E., and Thompson, P.H., 2005. Overview of results from the greenstone architecture project: Discovery Abitibi initiative; Ontario Geological Survey Open File Report 6154, 146 p.

Cameron, E.I, 1993. Precambrian gold: perspectives from the top and bottom of shear zones; The Canadian Mineralogist, v. 31, p. 917–944.

Card, K.D., Poulsen, K.H., and Robert, F., 1989. The Archean Superior Province of the Canadian Shield and its lode gold deposits, *In:* The Geology of Gold Deposits: the Perspective in 1988, (ed.) R.R. Keays, W.R.H. Ramsay, and D.I. Groves; Society of Economic Geologists, Monograph 6, p. 19–36.

Corfu, F., Krogh, T.E., Kwok, Y.Y., and Jensen, L.S., 1989. U-Pb zircon geochronology in the southwestern Abitibi greenstone belt, Superior Province; Canadian Journal of Earth Sciences, v. 26, p. 1747–1763.

Dimroth, E., Imreh, L., Rocheleau, M., and Goulet, N., 1982. Evolution of the south-central part of the Archean Abitibi belt, Quebec. Part I: Stratigraphy and paleogeographic model; Canadian Journal of Earth Sciences, v. 19, p. 1729–1758.

Dubé, B. and Gosseli, P., 2007. Greenstone-hosted quartz-carbonate vein deposits, *In:* Mineral Deposits of Canada: A Synthesis of Major Deposit Types, District Metallogeny, the Evolution of Geological Provinces, and Exploration Methods, (ed) W.D. Goodfellow; Geological Association of Canada, Mineral Deposits Division, Special Publication No. 5, p. 49–73.

Hodgson, C.J. and Hamilton, J.V., 1989. Gold mineralization in the Abitibi greenstone belt: end-stage results of Archean collisional tectonics? *In:* The Geology of Gold Deposits: the Perspective in 1988, (ed.) R.R. Keays, W.R.H. Ramsay, and D.I. Groves; Society of Economic Geologists, p. 86–100.

Ispolatov, V., Lafrance, B., Dubé, B., Hamilton, M., and Creaser, R., 2005. Geology, structure, and gold mineralization, Kirkland Lake and Larder Lake areas (Gauthier and Teck townships): Discovery Abitibi initiative; Ontario Geological Survey, Open File Report 6159, 170 p.

Ispolatov, V., Lafrance, B., Dubé, B., Creaser, R., and Hamilton, M., 2008. Geologic and structural setting of gold mineralization in the Kirkland Lake-Larder Lake gold belt, Ontario: Economic Geology, v. 103, p. 1309–1340.

Kishida, A. and Kerrich, R., 1987. Hydrothermal alteration zoning and gold concentration at the Kerr-Addison Archean lode gold deposit, Kirkland Lake, Ontario; Economic Geology, v. 82, p. 649–690.

Mueller, W., Donaldson, J.A., and Doucet, P., 1994. Volcanic and tectono-plutonic influences on sedimentation in the Archean Kirkland Basin, Abitibi greenstone belt, Canada; Precambrian Research, v. 68, p. 201–230.

Poulsen, K.H., Robert, F., and Dubé, B., 2000. Geological Classification of Canadian Gold Deposits; Geological Survey of Canada, Bulletin 540, 106 p.

Robert, F., Poulsen, K.H., Cassidy, K.F., and Hodgson, C.J., 2005. Gold metallogeny of the Yilgarn and Superior cratons, *In:* Economic Geology One Hundredth Anniversary Volume, (ed.) R.J. Goldfarb, and J.P. Richards; Society of Economic Geologists, Littleton, Colorado, p. 1001–1033.

Smith, J.P., Spooner, E.T.C., Broughton, D.W., and Ploeger, F.R., 1993. Archean Au-Ag-(W) quartz vein/disseminated mineralisation within the Larder Lake – Cadillac Break, Kerr Addison – Chesterville system, North East Ontario, Canada; Ontario Geological Survey, Open File Report 5831, 309 p.

Thompson, J.E., 1941. Geology of McGarry and McVittie townships, Larder Lake area; Ontario Department of Mines, Annual Report 50, Part VII, 99 p.

GEOLOGICAL SURVEY OF CANADA
OPEN FILE 7852

Targeted Geoscience Initiative 4: Contributions to the Understanding of Precambrian Lode Gold Deposits and Implications for Exploration

Depositional setting of Algoma-type banded iron formation from the Meadowbank, Meliadine, and Musselwhite gold deposits

Blandine Gourcerol[1], Phillip C. Thurston[1], Daniel J. Kontak[1], Olivier Côté-Mantha[2], and John Biczok[3]

[1]Laurentian University, Sudbury, Ontario
[2]Agnico Eagle Mines Ltd., Val d'Or, Quebec
[3]Goldcorp Canada Ltd., Thunder Bay, Ontario

2015

Recommended citation

Gourcerol, B., Thurston, P.C., Kontak, D.J., Côté-Mantha, O., and Biczok, J., 2015. Depositional setting of Algoma-type banded iron formation from the Meadowbank, Meliadine, and Musselwhite gold deposits, *In:* Targeted Geoscience Initiative 4: Contributions to the Understanding of Precambrian Lode Gold Deposits and Implications for Exploration, (ed.) B. Dubé and P. Mercier-Langevin; Geological Survey of Canada, Open File 7852, p. 55–68.

Publications in this series have not been edited; they are released as submitted by the author.

Contribution to the Geological Survey of Canada's Targeted Geoscience Initiative 4 (TGI-4) Program (2010–2015)

TABLE OF CONTENTS

Depositional setting of Algoma-type banded iron formation from the Meadowbank, Meliadine, and Musselwhite gold deposits

Blandine Gourcerol[1]*, Phillip C. Thurston[1], Daniel J. Kontak[1],
Olivier Côté-Mantha[2], and John Biczok[3]

[1]Mineral Exploration Research Centre, Laurentian University, Sudbury, Ontario, P3E 2C6
[2]Agnico Eagle Mines Ltd. – Division Exploration, 765 Chemin de la mine Goldex, Val-d'Or, Quebec, J9P 4N9
[3]Goldcorp Canada Ltd., Musselwhite Mine, P.O. Box 7500, Thunder Bay, Ontario, P7B 6S8
*Corresponding author's e-mail: gourcerol.blandine@gmail.com

ABSTRACT

Algoma-type banded iron formations (BIFs) are chemical sedimentary rocks in Archean greenstone belts that comprise alternating layers of iron-rich minerals and chert and are generally interstratified with bimodal submarine volcanic rocks. However, the geological setting for Algoma-type BIF deposition remains equivocal due to the overprinting effects of post-depositional deformation and metamorphism, and the absence of modern analogues for comparative studies. Recent studies suggest the abundance of rare earth elements and yttrium (REE+Y) in chert bands may reflect the primary BIF geochemical signature and therefore may constrain geological settings favourable for BIF deposition.

In this study, the results of LA-ICP-MS analysis of chert at three BIF-hosted gold deposits are presented to assess whether epigenetic gold mineralization is preferentially developed within a particular geochemical type of BIF. Three deposits were studied: 1) the Meadowbank deposit (Churchill Province); 2) the Meliadine gold district (Churchill Province); and 3) the Musselwhite deposit (Superior Province). The results of this study, which explores REE and yttrium as tracers of depositional processes for Algoma-type BIF, suggest that chert bands record either (1) interaction of seawater with Fe-oxyhydroxides, as suggested by heavy REE enrichment coupled with La and Y enrichment; (2) high-temperature (>250ºC) hydrothermal fluids, as suggested by positive Eu excursions; and/or (3) hydrogeneous contamination, which is suggested by relatively consistent REE concentrations and a chondritic Y/Ho ratio. Moreover, the pH conditions of the water column at the time of BIF deposition are evaluated using Ce/Ce* as a pH proxy, with acidic conditions associated with positive Ce/Ce* anomalies. This data set does not suggest there is a chemical preference of the studied BIF for epigenetic gold mineralization.

INTRODUCTION

Algoma-type banded iron formation (BIF) is thinly bedded, chemical sedimentary rocks comprising alternating layers of iron-rich minerals and chert. These rocks are typically intercalated with Eoarchean to late Paleoproterozoic volcano-sedimentary sequences within greenstone belts (Goodwin, 1973; Bekker et al., 2010). Based on their sedimentary and geochemical features, a restricted basin under the influence of seawater and hydrothermal vent fluids is one potential BIF depositional setting (e.g. Bolhar et al., 2005; Ohmoto et al., 2006). In this model, the iron-rich minerals precipitated contemporaneously with hydrothermal vent fluids to form siderite and various iron oxyhydroxides. These primary minerals are diagenetically transformed to hematite, magnetite, iron silicates, and sulphides, which characterize the type BIF mineral assemblage. The interbedded chert horizons are considered to reflect (1) periods of hydrothermal quiescence; (2) a temporary decrease in the contribution of the hydrothermal fluid (Bolhar et al., 2005; Thurston et al., 2011); (3) hydrothermal precipitates from vent fluids (Allwood et al., 2010; Thurston et al., 2011); and/or (4) the products of secondary replacement (Hanor and Duchac, 1990).

In this study, we explore the chert geochemistry at three BIF-hosted gold deposits (the ~4 Moz Au Meadowbank deposit, hosted by the 2.71 Ga Woodburn Lake greenstone belt; the ≥2.8 Moz Au Meliadine district, hosted by the 2.6 Ga Ennadai-Rankin greenstone belt; and the ~6 Moz Au Musselwhite deposit, hosted by the 2.9–3 Ga North Caribou greenstone belt; Fig. 1). The BIFs at each of these deposits are either intercalated with mafic to ultramafic volcanic rocks or associated interflow sediments. These three gold deposits were selected to validate and refine the restricted-basin

Gourcerol, B., Thurston, P.C., Kontak, D.J., Côté-Mantha, O., and Biczok, J., 2015. Depositional setting of Algoma-type banded iron formation from the Meadowbank, Meliadine, and Musselwhite gold deposits, *In:* Targeted Geoscience Initiative 4: Contributions to the Understanding of Precambrian Lode Gold Deposits and Implications for Exploration, (ed.) B. Dubé and P. Mercier-Langevin; Geological Survey of Canada, Open File 7852, p. 55–68.

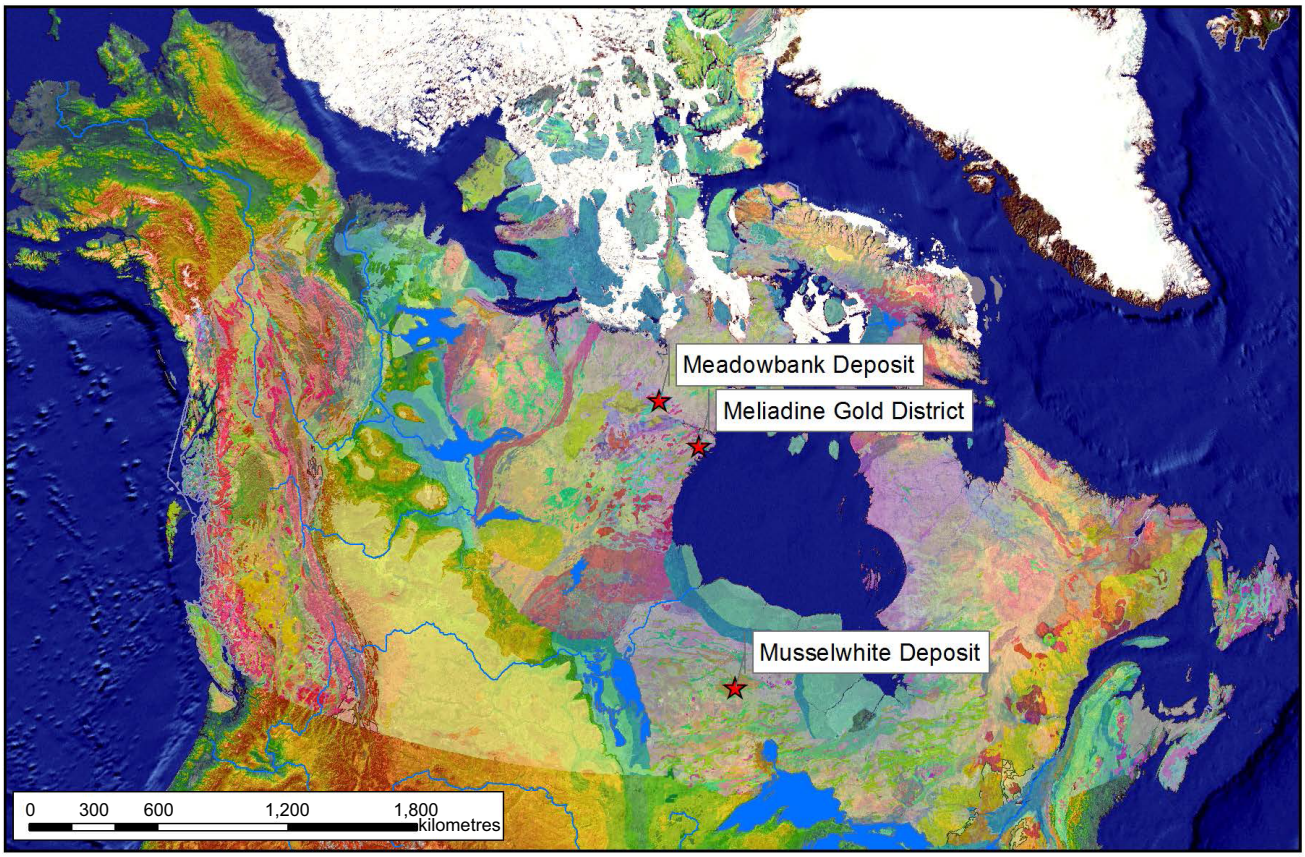

Figure 1. Localization of the three deposits investigated in this study. The Meadowbank deposit and the Meliadine gold district are within the Churchill Province, west of Hudson Bay; the Musselwhite deposit is within the Superior Province, south of Hudson Bay (after Wheeler et al., 1996).

model as a depositional setting for Algoma-type BIFs by using the geochemical signature of the chert bands as a proxy for the primary signature of ocean water chemistry and hydrothermal vent fluids. In detail, this hypothesis was tested by (1) defining the role of chemical reservoirs (i.e. seawater, hydrothermal fluids, and terrestrial detritus) in chert deposition; and (2) using redox-sensitive rare earth elements (REE) + Y to assess the oxygenation state of the water column during chert precipitation.

ANALYTICAL METHODS AND DATA TREATMENT

The BIF samples collected for the study included (1) 37 samples from drillcore and outcrops from the Meadowbank deposit (i.e. West IF, Central BIF, East BIF); (2) 40 samples in the Meliadine deposit area (i.e. Pump, F-Zone, and Discovery); and (3) 23 samples from the Musselwhite deposit (i.e. chert-magnetite (4B), garnet-grunerite-(chert) (4EA), garnetiferous amphibolite (4E), and garnet-biotite schist (4F) facies) (Fig. 1). Polished thin sections (100 µm thick) were examined, using both transmitted and reflected light microscopy, and selected material was studied in more detail using the scanning electron microscopy with X-ray microanalysis (SEM-EDS) to select the chert bands with minimal amounts of detrital mineral inclusions and other contaminants related to alteration, diagenesis, metamorphic, or ore-forming events.

The trace element and REE analyses of the chert were obtained using a Resonetics Resolution M-50 laser ablation instrument coupled to a Thermo X-Series II quadrupole inductively coupled plasma mass spectrometry (ICP-MS) at the Geochemical Fingerprinting Laboratory at Laurentian University, Sudbury, Ontario following the protocol of Kamber and Webb (2007). As chert bands have very low concentration of REE, spot analyses may be below the limit of detection for many elements. Thus, in order to circumvent this issue, line traverses using both 140 and 190 µm beam diameters with a repetition rate of 10 Hz and an energy density of 7 J/cm^2 were used to obtain data that is above the detection limit. However, the line traverse method increases the influence of any detrital contaminants, either as inclusions or minerals disseminated along the traverse line. Therefore, the Queensland alluvial shale composite (MUQ) was used to normalize the REE+Y values to attenuate the influence of potential terrigenous input. The MUQ composition represents a mixed bimodal felsic and mafic volcanic provenance (Kamber

Table 1. Estimated detection limits for elements and rare earth elements referred to in this study.

Element	Estimated LOD (ppm)	Element	Estimated LOD (ppm)	Element	Estimated LOD (ppm)
Li	0.011	Y	0.006	Pb	0.004
Be	0.086	Zr	0.010	Th	0.005
Si	43.522	Nb	0.007	U	0.003
Sc	0.025	Mo	0.035	Ho	0.004
Ti	0.072	Ag	0.005	Er	0.012
V	0.007	Cd	0.071	Tm	0.004
Cr	0.111	In	0.005	Yb	0.016
Mn	0.062	Sn	0.006	Lu	0.003
Fe	0.202	Er	0.012	Hf	0.011
Co	0.005	Tm	0.004	Ta	0.004
Ni	0.050	Yb	0.016	W	0.016
Cu	0.042	Lu	0.003	Au	0.015
Zn	0.021	Hf	0.011	Tl	0.002
Ga	0.007	Ta	0.004	Pb	0.004
As	0.028	W	0.016	Th	0.005
Rb	0.004	Au	0.015	U	0.003
Sr	0.005	Tl	0.002		

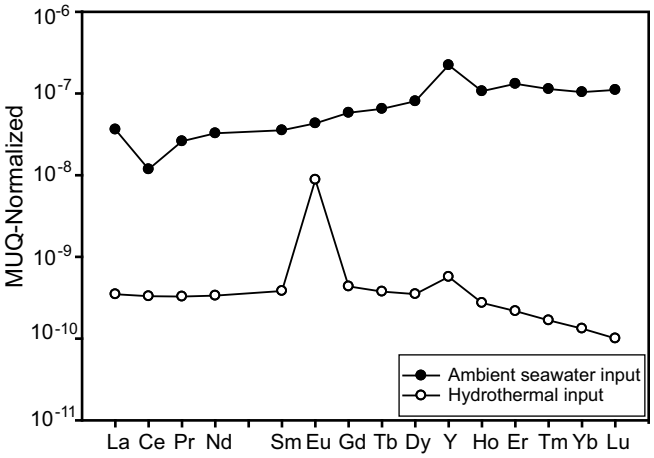

Figure 2. Upper crust MUQ-normalized REE patterns illustrating the chemical signatures of the two modern settings relevant to this study: ambient seawater and hydrothermal vent fluid (data from Bau and Dulski, 1996).

et al., 2005), which acts as a proxy for the expected average terrigenous input from a typical bimodal greenstone belt into the Archean ocean (e.g. Bolhar et al., 2005; Thurston et al., 2011).

The elemental concentrations reported in this study represent the integrated signal over the length of the traverse. The element list used for each analysis included the 14 REEs in addition to Li, Be, Si, Sc, Ti, V, Cr, Mn, Fe, Co, Ni, Cu, Zn, Ga, As, Rb, Sr, Zr, Nb, Mo, Ag, Cd, In, Sn, Sb, Cs, Ba, Hf, Ta, W, Tl, Pb, Th, and U. The NIST 612 glass standard was analysed at the beginning and at the end of each line traverse. The data interpretation presented below focuses on samples that yielded REE concentrations that are consistently above the analytical detection limits (Table 1).

RARE-EARTH AND YTTRIUM SYSTEMATICS

The presence and abundance of REE+Y in chert bands may represent a primary signature, which can be influenced by one or more processes: 1) precipitation from open marine seawater (e.g. Bau and Dulski, 1996); 2) precipitation from vent-sourced hydrothermal fluids (e.g. Danielson et al., 1992; Allwood et al., 2010); and 3) chemical inheritance due to replacement of primary BIF minerals (e.g. Hanor and Duchac, 1990). Chert geochemistry is also strongly dependent on the extent of terrigenous detritus (Alexander et al., 2008) and oceanographic processes (e.g. phosphate circulation and precipitation).

Several studies have shown that the REE+Y systematics of Archean seawater is analogous to the modern ocean (Fig. 2; e.g. Bau and Dulski, 1996; Lawrence and Kamber, 2006; Thurston et al., 2011). It follows, therefore, that the shale (i.e. MUQ) normalized REE+Y pattern from the Archean seawater will be characterized by (1) a depletion in light rare earth elements (LREE) relative to heavy rare earth elements (HREE); (2) a super-chondritic Y/Ho ratio (i.e. >27), yielding a positive Y/Y^*_{MUQ} anomaly, commonly between 40 and 90; and (3) a slightly positive La anomaly (La/La^*_{MUQ} between 1.15 and 1.3). Moreover, as the chemistry of Archean seawater was also influenced by volcanism, water-rock interaction (Veizer, 1988), and the contribution of high-temperature (>250ºC) hydrothermal fluids (Fig. 2; Bau and Dulski, 1996; Kamber et al., 2004), these processes are characterized by variable, but well developed positive Eu anomalies (Fig. 2; Kamber et al., 2004).

Metamorphism and ore-forming processes (i.e. epigenetic fluids) may remobilize REE+Y and consequently alter the primary signature of chert bands. Therefore, the REE+Y signature of seawater and hydrothermal vent fluids will not be detected in MUQ-normalized profiles, as this paper addresses, thus a careful selection of samples was done prior to analytical studies.

DISCUSSION

Rare Earth and Yttrium Systematic Characteristics

Meadowbank Area

Data for chert samples from the Central BIF, East BIF, and West IF within the Meadowbank area (Gourcerol et al., 2014) show relatively uniform REE+Y patterns that include a slight to moderate enrichment in HREE, relative to LREE and MREE (Nd/Yb_{MUQ} = 0.05–0.54), that are associated with slight to moderate positive La, Y, and Eu anomalies (La/La^*_{MUQ} = 0.89–4.65, Y/Y^*_{MUQ} = 0.88–1.96, Eu/Eu^*_{MUQ} = 1.25–5.12) and super-chondritic to chondritic Y/Ho values (Y/Ho = 24.2–53.72) (Fig. 3). These observations record the

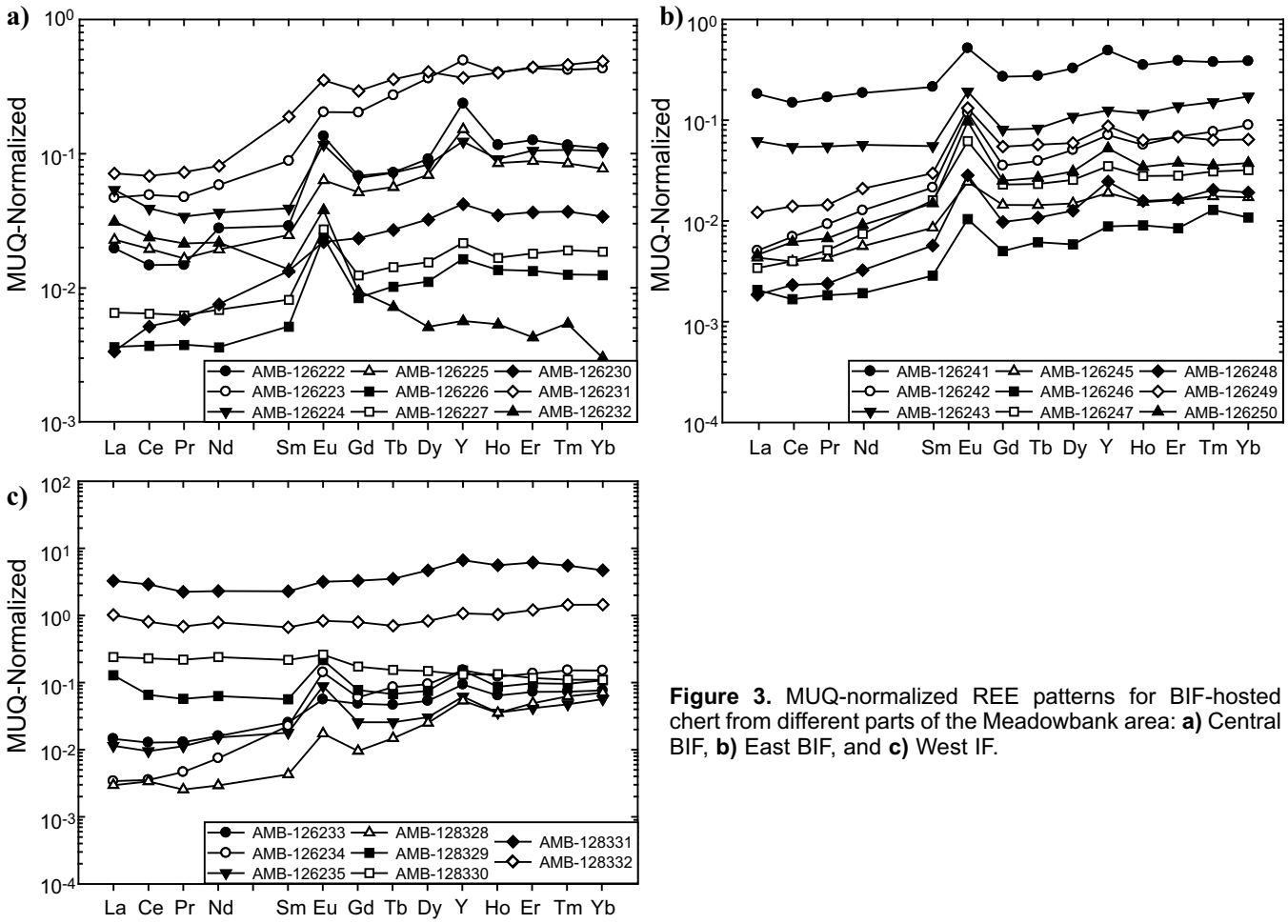

Figure 3. MUQ-normalized REE patterns for BIF-hosted chert from different parts of the Meadowbank area: **a)** Central BIF, **b)** East BIF, and **c)** West IF.

influence of ambient seawater and high-temperature (>250ºC) hydrothermal fluids during chert deposition. Some of the notable departures of the data from the expected pattern are discussed below and in this context we note that enrichments in particular elements serve as proxies for other influences: Sr for C and hence apatite, Ga for Al and thus detritus, and Zr for zircon (representing felsic ash), all of which are confirmed by petrographic study.

A group of samples from the East BIF (samples AMB-126241 and AMB-126243; Fig. 3b) and the West IF (samples AMB-128330, AMB-128331, and AMB-128332; Fig. 3c) show relatively flat REE patterns (Pr/Sm_{MUQ} = 0.79–1.03) associated with chondritic Y/Ho values (Y/Ho = 26.02–36.71). Enrichments in Sr (i.e. 27.9–55 ppm, Fig 3b; and 64.9–1090 ppm, Fig. 2c), Zr (i.e. 0.97–2.17 ppm, Fig. 3b; and 19.1–43.4 ppm, Fig. 3c), and variable amounts of Th (i.e. 1.055–4.2 ppm, Fig. 3c) and Ga (i.e. 16.04–27.8 ppm, Fig. 3c) relative to the bulk of samples is illustrated for most of samples from the West IF. Two samples from the Central BIF (samples AMB-126223 and AMB-126231; Fig. 3a) show depletion in LREE relative to HREE, but moderate to flat patterns for the MREE and HREE, which are associated with chondritic Y/Ho values (Y/Ho = 24.2–32.41) and enrichment in Zr (i.e. 104.9–183 ppm), Ga (i.e. 6.83–141.4 ppm), Sr (i.e. 20.4–95.2 ppm), and Th (i.e. 1.22–7.7 ppm). These numbers suggest variable amounts of detrital contamination during chert deposition. The presence of apatite in chert bands from different BIFs, as revealed in SEM images, could explain the elevated Sr values, as it is a proxy for Ca, and suggests, therefore, that the West IF chert chemistry is more affected by sulphate (apatite) deposition. Moreover, zircon and monazite were seen in SEM images of samples AMB-126223 and AMB-126231, which may account for the strong enrichment in Zr and anomalous HREE enrichment in chert from the Central BIF.

Meliadine Gold District

Data for chert samples from the Pump, F-Zone, and Discovery deposits within the Meliadine gold district yield variable REE+Y patterns (Fig. 4). Chert samples at Pump yield LREE-depleted patterns (Nd/Yb_{MUQ} = 0.06–0.75), sub-chondritic to chondritic Y/Ho values (Y/Ho = 11.44–32.53), variable La and Y concentrations (La/La^*_{MUQ} = 0.08–1.11, Y/Y^*_{MUQ} = 0.54–1.13), and positive Eu anomalies (Eu/Eu^*_{MUQ} = 2.17–6.13) (Fig. 4a). These results suggest that chert precipitated

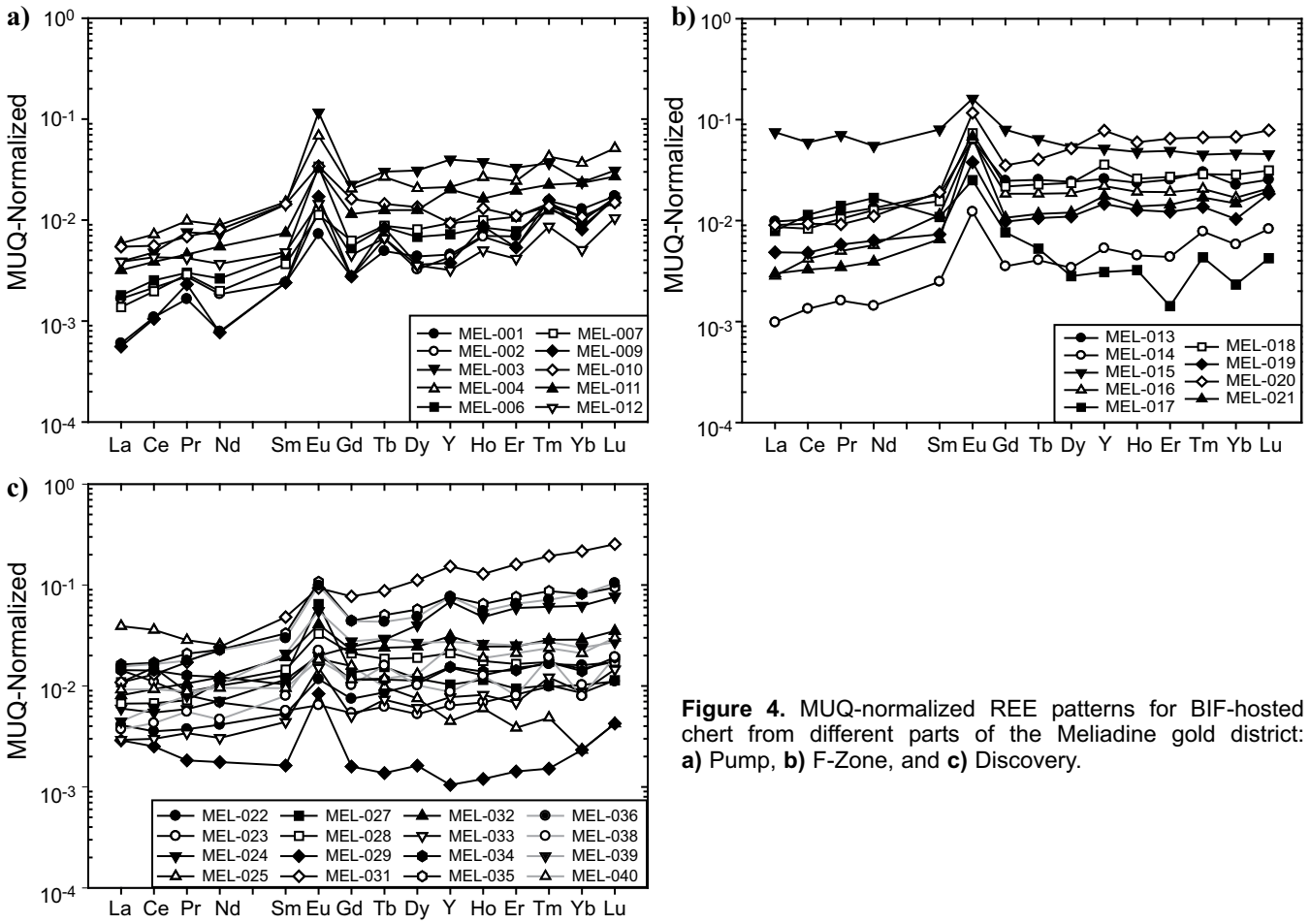

Figure 4. MUQ-normalized REE patterns for BIF-hosted chert from different parts of the Meliadine gold district: **a)** Pump, **b)** F-Zone, and **c)** Discovery.

from high-temperature (>250ºC) hydrothermal vent fluids. The Y/Ho ratios for most of the samples are lower than chondritic values (i.e. 27) and correspond with negative La and Y anomalies, which together represent compositions that are unlike that of modern ocean water.

All chert samples at F-Zone show LREE-depleted patterns (Nd/Yb_{MUQ} = 0.16–0.59). In detail, samples MEL015 and MEL017 yield slightly anomalous HREE-depleted concentrations (Nd/Yb_{MUQ} = 1.19–7.21) and slightly to strongly enriched La, Y, and Eu concentrations (La/La^*_{MUQ} = 1.00–1.43, Y/Y^*_{MUQ} = 1.05–1.35, Eu/Eu^*_{MUQ} = 2.12–8.14; Fig. 4b). These trace-element patterns are characteristic of high-temperature (>250ºC) hydrothermal vent fluids and/or seawater. In contrast, all samples yield chondritic Y/Ho values (Y/Ho = 25.25–36.34) and Sr enrichment (i.e. 6.5–30.6 ppm) that suggest detrital input and possible primary apatite grains.

Chert samples from the Discovery deposit are LREE-depleted (Nd/Yb_{MUQ} = 0.11–0.87) (N.B. except sample MEL-027: Nd/Yb_{MUQ} = 12.89) (Fig. 4c). Slight to moderate La, Y, and Eu enrichments (La/La^*_{MUQ} = 0.69–2.1, Y/Y^*_{MUQ} = 0.80–1.28, Eu/Eu^*_{MUQ} = 1.05–7.46) are also typical of most samples (N.B. except for sample MEL-038: La/La^*_{MUQ} = 0.47, Y/Y^*_{MUQ} = 0.85, Eu/Eu^*_{MUQ} = 2.13) (Fig. 4c). The Y/Ho ratios vary from sub-chondritic to chondritic (Y/Ho = 18.23–37.48). These chemical features are typical of an input of seawater and/or high-temperature (>250ºC) hydrothermal vent fluids during chert deposition. Most of the samples exhibit chondritic Y/Ho values associated with Sr enrichment (i.e. 0.3–177 ppm) and moderate Ga enrichment (i.e. 1.32–7.04 ppm). In contrast, samples MEL-038, MEL-039, and MEL-040 yield trace-element concentrations (± elevated Ca) that are consistent with detrital contamination. Sample MEL-038 yielded elevated Y/Ho ratios that correspond to depletion in La and Y concentrations, which was also reported for some chert samples from the Pump deposit.

Musselwhite Area

Data for chert samples from the chert-magnetite (4B facies; Fig. 5a), the garnetiferous amphibolite (4E facies; Fig. 5b), the garnet-grunerite-(chert) (4EA facies; Fig. 5c), and the garnet-biotite schist (4F facies; Fig. 5f) within the Musselwhite area were reported by Gourcerol et al. (2015). These samples exhibit rela-

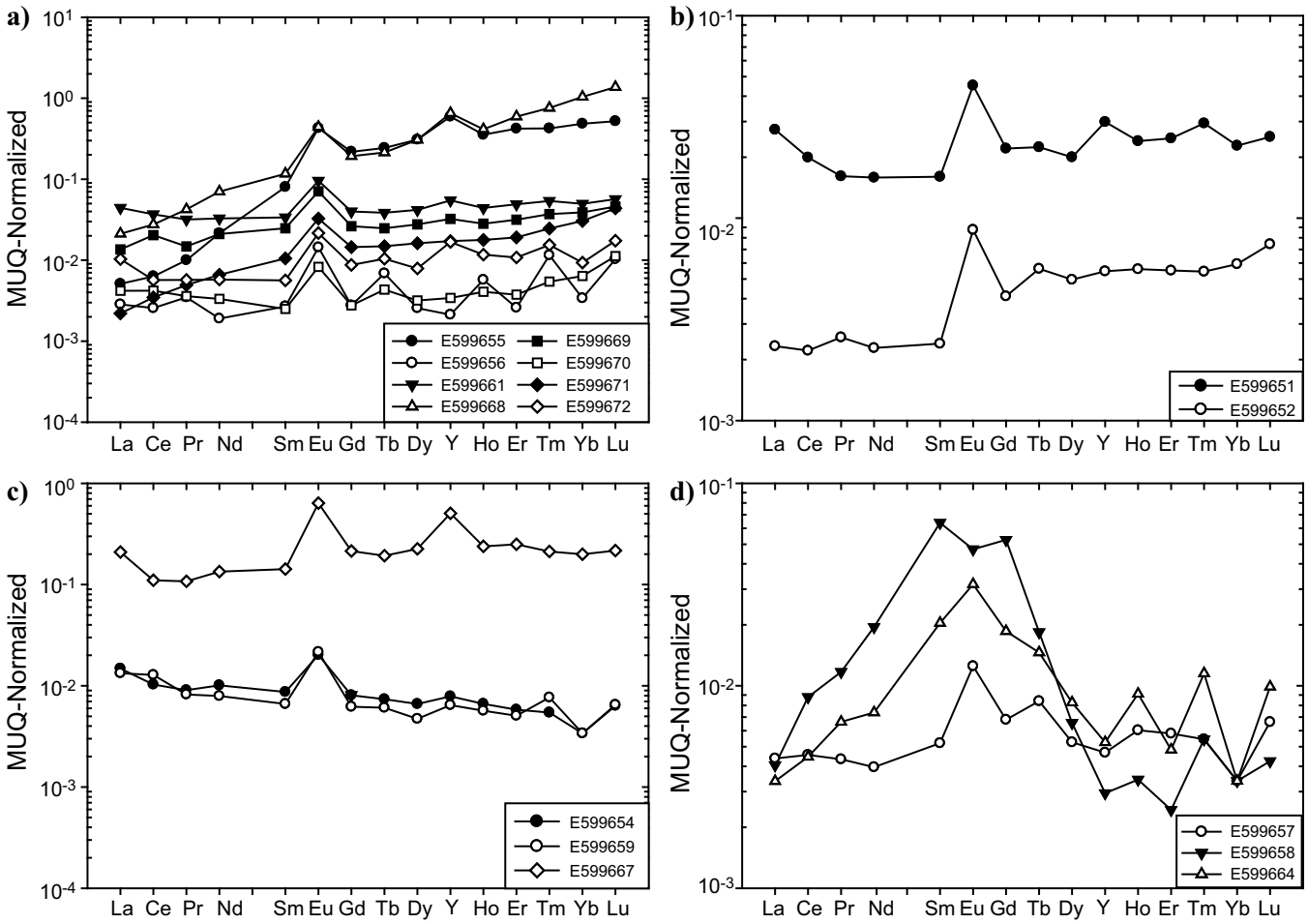

Figure 5. MUQ-normalized REE patterns for chert samples from BIFs in different parts of the Musselwhite area: **a)** unit 4B — oxide-dominant facies samples, **b)** unit 4E — garnetiferous amphibolite samples, **c)** unit 4EA — garnet-grunerite samples, excluding samples E599660, E599665, and E599666, and **d)** unit 4F — biotite-garnet schist samples.

tively uniform REE+Y patterns, except for the 4F facies (Fig. 5d). Most chert sampled from the 4B facies are HREE enriched (Nd/Yb_{MUQ} = 0.04–0.66), yield slight to moderate positive La, Y, and Eu anomalies (La/La^*_{MUQ} = 0.8–1.49, Y/Y^*_{MUQ} = 0.87–1.49, Eu/Eu^*_{MUQ} = 2.6–3.61), and chondritic Y/Ho values (Y/Ho = 22.13–44.01) (Fig. 5a). These concentrations may record seawater and/or high-temperature (>250ºC) hydrothermal vent fluids during chert deposition. Variable detrital input is also suspected based on the chondritic Y/Ho values. Sample E599656 differs from the majority of samples by its negative La and Y anomalies (La/La^*_{MUQ} = 0.21, Y/Y^*_{MUQ} = 0.51) and very low Y/Ho value (i.e. 9.79), which could reflect precipitation of chert under the influence of high-temperature (>250ºC) hydrothermal vent fluid with variable seawater input. It should be noted that samples E599655 and E599668 are Sr-enriched, (i.e. 848.8 ppm and 150.8 ppm, respectively), which may be due to the presence of carbonate minerals in the chert. The presence of carbonate in the LA-ICP-MS traverse is illustrated by stronger depletion in LREE relative to HREE.

The two samples from the 4E facies show LREE depletion (Nd/Yb_{MUQ} = 0.39–0.7), are slightly to moderately La, Y, and Eu enriched (La/La^*_{MUQ} = 0.7–1.66, Y/Y^*_{MUQ} = 0.98–1.23, Eu/Eu^*_{MUQ} = 2.43–2.6), and yield super-chondritic to chondritic Y/Ho values (Y/Ho = 25.71–32.8) (Fig. 5b). These seem to record seawater, high-temperature (>250ºC) hydrothermal fluid and/or a minor detrital input during chert deposition.

The chert samples from 4EA facies are characterized by relatively flat to slightly fractionated patterns with LREE enrichment (Nd/Yb_{MUQ}= 0.39–0.7), except for samples E599654 and E599659 that show depleted HREE patterns LREE (i.e. Nd/Yb_{MUQ} = 1.51–2.04) and are associated with positive Eu anomalies (Eu/Eu^*_{MUQ} = 2.34–3.97) (Fig. 5c). Considering the La and Y anomalies and Y/Ho values, two groups of samples are present: (1) samples E599654, E599659, and E599667 show positive La and Y anomalies (La/La^*_{MUQ} = 1.51–3.02, Y/Y^*_{MUQ} = 1.2–2.07) and super-chondritic Y/Ho ratios (Y/Ho = 29.86– 55.91; Fig. 5c); and (2) samples E599660, E599665, and E599666 show negative La and Y anomalies

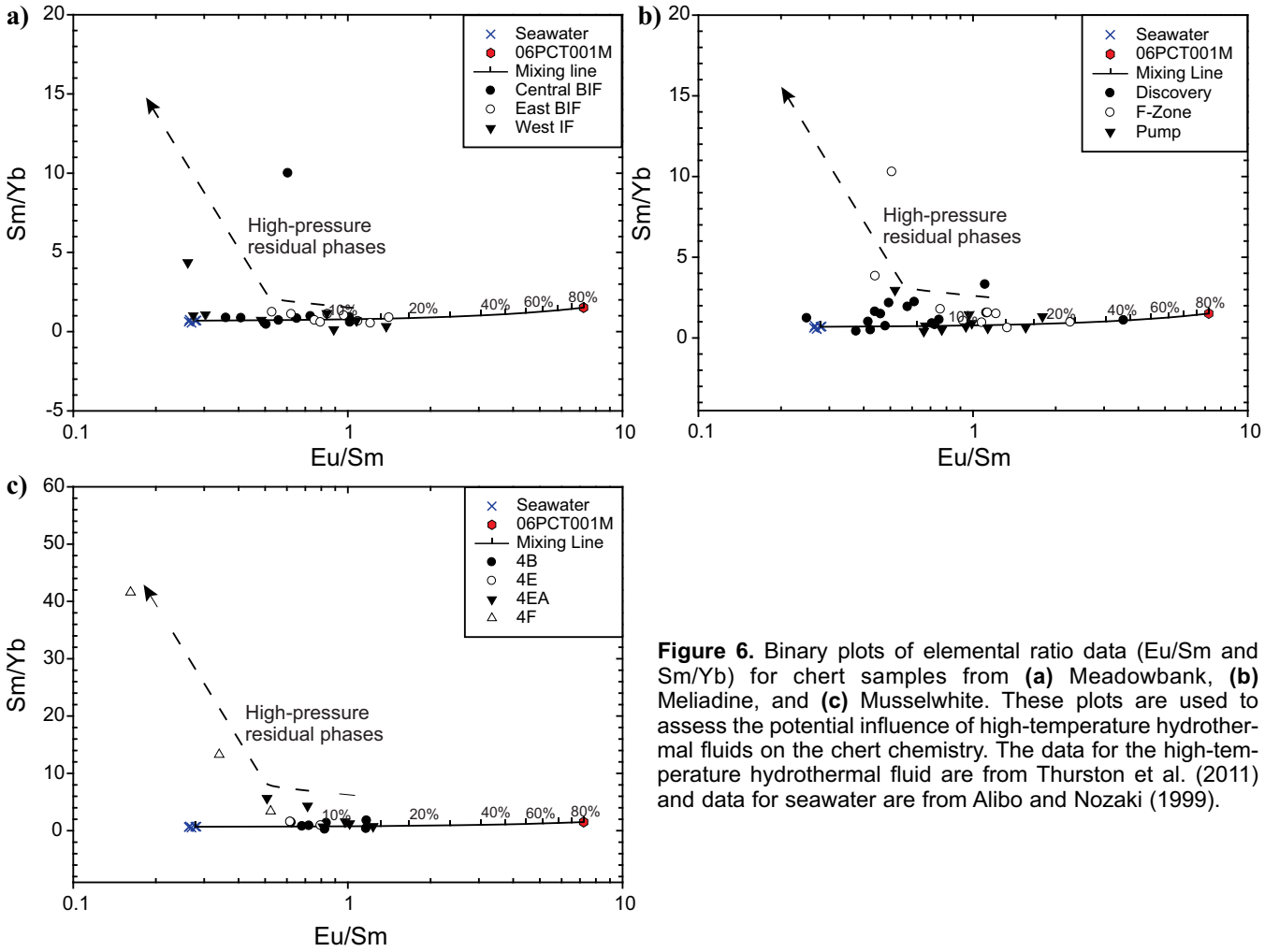

Figure 6. Binary plots of elemental ratio data (Eu/Sm and Sm/Yb) for chert samples from **(a)** Meadowbank, **(b)** Meliadine, and **(c)** Musselwhite. These plots are used to assess the potential influence of high-temperature hydrothermal fluids on the chert chemistry. The data for the high-temperature hydrothermal fluid are from Thurston et al. (2011) and data for seawater are from Alibo and Nozaki (1999).

(La/La^*_{MUQ} = 0.04–0.12, Y/Y^*_{MUQ} = 0.22–0.71) and very low Y/Ho ratios (Y/Ho = 4.11–16.52; Fig. 5c).

These results suggest that a seawater and/or high-temperature (>250ºC) hydrothermal vent-fluid component is recorded within chert bands for the first group of samples, whereas the second group likely precipitated from high-temperature (>250ºC) hydrothermal vent fluid with variable seawater influence, which is similar to the Meliadine samples.

The chert bands within the garnet-biotite schist (4F) facies are geochemically anomalous compared to chert at the other studied deposits. The former samples show variable, but elevated LREE and MREE enrichments (Pr/ Sm_{MUQ} = 0.18–0.83) and only moderately positive Eu anomalies (Eu/Eu^*_{MUQ} =1.08–1.94) are noted (Fig. 5d). This facies is distinguished from the others by its REE+Y signature and, furthermore, is similar to the argillite studied by Thurston et al. (2011), which documented only a weak hydrothermal-fluid influence.

Assessing the Influence of High-Temperature Hydrothermal Fluids

Most chert samples from Meadowbank, Meliadine, and Musselwhite show the influence of seawater and high-temperature (>250ºC) hydrothermal fluids. In this section, we calculate a binary mixing line between seawater and hydrothermal fluids in order to explore the relative importance of these fluids in chert deposition. The two end-members of this mixing line are represented in Figure 6: 1) seawater composition from the North Pacific (Alibo and Nozaki, 1999); and 2) an Archean hydrothermally precipitated chert sample (i.e. sample 06PCT001M; Thurston et al., 2011). Modern vent fluids were not used for mixing models due to geochemical differences between these fluids and Archean greenstone belt hydrothermal fluids (SiO_2-rich, Fe-poor, and highly alkaline fluids, which differ from the modern Fe-rich and acidic hydrothermal fluids; Shibuya et al., 2010).

Most of the samples in this study fall on the mixing line despite some samples exhibiting high Sm/Yb ratios (Fig. 6). The Sm/Yb ratio is particularly sensitive to high-pressure residual magmatic or metamorphic phases, such as amphibole and garnet, which may reflect the presence of some of these phases in chert bands derived from eroding source rocks during BIF formation.

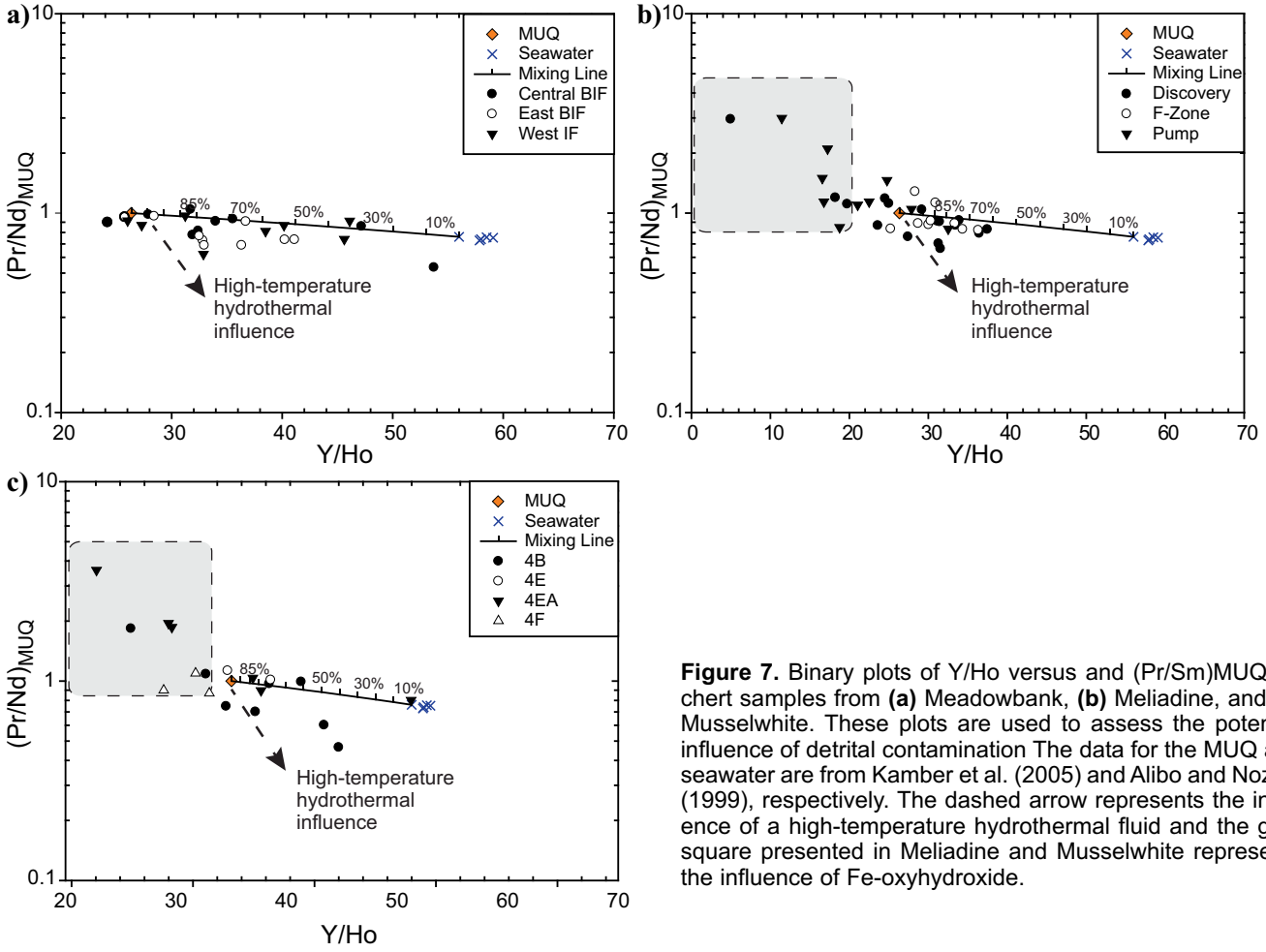

Figure 7. Binary plots of Y/Ho versus and (Pr/Sm)MUQ for chert samples from **(a)** Meadowbank, **(b)** Meliadine, and **(c)** Musselwhite. These plots are used to assess the potential influence of detrital contamination The data for the MUQ and seawater are from Kamber et al. (2005) and Alibo and Nozaki (1999), respectively. The dashed arrow represents the influence of a high-temperature hydrothermal fluid and the grey square presented in Meliadine and Musselwhite represents the influence of Fe-oxyhydroxide.

At Meadowbank, samples from the Central BIF suggest an input from the high-temperature fluid of 1–11%, versus 3–16% for the East BIF and 0–16% for the West IF (Fig. 6a). It is notable that samples from the southern part of the West IF show a very low hydrothermal-fluid input based on their flat REE patterns. At Meliadine, most samples record a moderate hydrothermal influence (2–3% for the Discovery zone, 4–28% for the F-Zone, 3–22% for the Pump zone) during chert precipitation (Fig. 6b). At Musselwhite, input from the high-temperature fluid was generally low during chert formation, at 0–15% for the 4B facies, 4–7% for the 4E facies, 2–11% for the 4EA facies, and 0–5% for the 4F facies (Fig. 6c). The 4F facies samples seem to record more restricted influence by hydrothermal fluids, which is consistent with a slightly positive Eu anomaly.

The data suggest that chert geochemistry records ambient seawater and hydrothermal vent fluids for the majority of samples at all three of the studied BIF-hosted gold deposits. However, a number of samples from Pump, Discovery (sample MEL-038), and Musselwhite (samples E599656, E599660, E599665, and E599666) yield very low Y/Ho ratios associated with negative La and Y anomalies, which may represent a detrital input.

Sources and Influence of Detrital Contamination

The REE data for most chert samples from Meadowbank, Meliadine, and Musselwhite reflect the influence of seawater and some detrital contamination, as illustrated by their flat REE patterns ($Pr/Sm_{MUQ} \approx 1$) and chondritic Y/Ho ratios (i.e. Y/Ho ≈ 27). We emphasize that samples were normalized to MUQ, which we expect is a reasonable proxy for detritus during BIF deposition in the greenstone belt environment. This detrital contamination is key to understanding the depositional setting for Algoma-type BIF and thus the validity of REE+Y systematics. Therefore, to estimate the influence of the detrital component, a mixing line was calculated using the seawater composition from the North Pacific referred to above (Alibo and Nozaki, 1999) and MUQ (Kamber et al., 2005) as the two end-members (Fig. 7). The MUQ composition represents a suitable estimate of the composition of the most probable detrital contamination of cherts in Archean greenstone belts due to its basalt-dominant bimodal provenance. Prior to discussing the data in Figure 7, we note that the reason for the bulk of the samples plotting below the mixing line is due to the influence of the

high-temperature hydrothermal vent fluids input (i.e. $Pr/Sm_{MUQ} = 0.73$).

For samples from Meadowbank (Fig. 7a), the detrital influence on the REE chert chemistry is estimated at 8–100% for the Central BIF, 50–100% for the East BIF, and 30–100% for the West IF. Thus, these data indicate the East and West IF seem to record the most detrital contamination, whereas the REE composition of East and Central BIF appear to extends towards seawater compositions, which is consistent with the previous plot (Fig. 6a). All the Meadowbank samples are located either on the mixing line or below it (Fig. 7a), suggesting that detritus contributed to the chert REE signature in addition to seawater and a high-temperature hydrothermal fluid.

Some of the Meliadine samples (Fig. 7b) are distinguished by their low Y/Ho ratios, in particular the data from the Pump zone and samples MEL-025 and MEL-038 from the Discovery zone. Considering only samples located on, or directly below the mixing line, the detrital influence during chert deposition is estimated at 60–100% for Discovery, 65–100% for the F-Zone, and 85–95% at Pump. All of the F-Zone samples and most samples from Discovery (except samples MEL-025 and MEL-038) are located either on or below the mixing line, which suggests a detrital component along with variable contributions from seawater and high-temperature hydrothermal fluids (Fig. 7b).

At Musselwhite, chert samples are distinguished by their low Y/Ho ratios, especially for units 4B, 4EA, and 4F (Fig. 7c), which is similar to what is seen in some of the Meliadine samples. A detrital influence of approximately 40–100%, 80–100%, and 0–85% is estimated for units 4B, 4E, and 4EA, respectively when considering only samples located on or directly below the mixing line. According to the data, unit 4EA seems to be less affected by detrital contamination than the other facies and unit 4B shows the strongest influence of hydrothermal fluids.

The estimated influence of a detrital component as indicated above cannot be considered quantitative; however, it still indicates that for those chert samples that suggest up to 100% of MUQ contamination, there is some chemical indications of seawater influence (positive La and Y anomalies). These data, therefore, suggest chert precipitation occurred in a seawater environment associated with high-temperature hydrothermal venting fluids and some detrital input. Importantly, these data illustrate that the influence of only trace amounts of clastic detritus in the chert bands may be enough to dominate the bulk REE content and signatures of the chert.

Though the anomalous sub-chondritic Y/Ho ratios for Meliadine and Musselwhite samples are inconsistent with a detrital contamination, the ratios could indicate particle scavenging in the water column at the time of chert deposition. Scavenging may have involved Fe-oxyhydroxide minerals and may explain slightly sub-chondritic ratios for the chert bands (rather than Mn-oxyhydroxide in an Archean context; e.g. Minami et al., 1998; Bau, 1999; Kawabe et al., 1999). According to Bau (1999), Fe-oxyhydroxide precipitates, which are introduced by hydrothermal discharge in seawater, display less positive or even negative La and Y anomalies associated with a M-type lanthanide tetrad effect (Masuda et al., 1987). As a result, the association between low Y/Ho ratios and negative La and Y anomalies appears to record Fe-oxyhydroxide within the chert bands.

Influence of Fe-Oxyhydroxide Precipitation and Information about pH Precipitation

As previously suggested, some of the Meliadine and Musselwhite samples may reflect co-precipitation of chert and Fe-oxyhydroxide minerals (i.e. low Y/Ho ratio associated with negative La and Y anomalies; Bau, 1999). These Fe-oxyhydroxides may have formed under the influence of a dynamic pH shift during the mixing of alkaline hydrothermal fluids with acidic to neutral Archean seawater, which can precipitate Fe^{3+} out of Fe^{2+}-rich seawater under anoxic conditions (Shibuya et al., 2010), and/or by biological oxidation of Fe^{2+} onto the seafloor by photoautotrophic bacteria (i.e. Kappler et al., 2005; Konhauser et al., 2005). In order to explore the potential role played by Fe-oxyhydroxide minerals on chert geochemistry, mixing lines were calculated using the Alibo and Nozaki (1999) seawater composition, Fe-oxyhydroxide precipitates, and graphitic mudstone from Meliadine (the KMG unit) as end-members (Fig. 8). Fe-oxyhydroxide precipitated under experimental conditions from acidic seawater (Bau, 1999) and Fe-oxyhydroxide precipitates under experimental conditions from alkaline solutions (Kawabe et al., 1999) were selected as end-members representing a range of seawater conditions. The KMG samples are graphitic mudstone representing carbon biomass, possibly reflecting biological oxidation of Fe^{2+}.

The Meadowbank samples represent interaction of acidic seawater with Fe-oxyhydroxides (Fig. 8a), which produced the observed positive La and Y anomalies.

At Meliadine, most samples are located in the seawater domain except for the samples from the Pump deposit and samples MEL-025 and MEL-028 from the Discovery zone, which are located in the Fe-oxyhydroxide domain and thus confirm their presence in chert bands (Fig. 8b). Samples located in the seawater

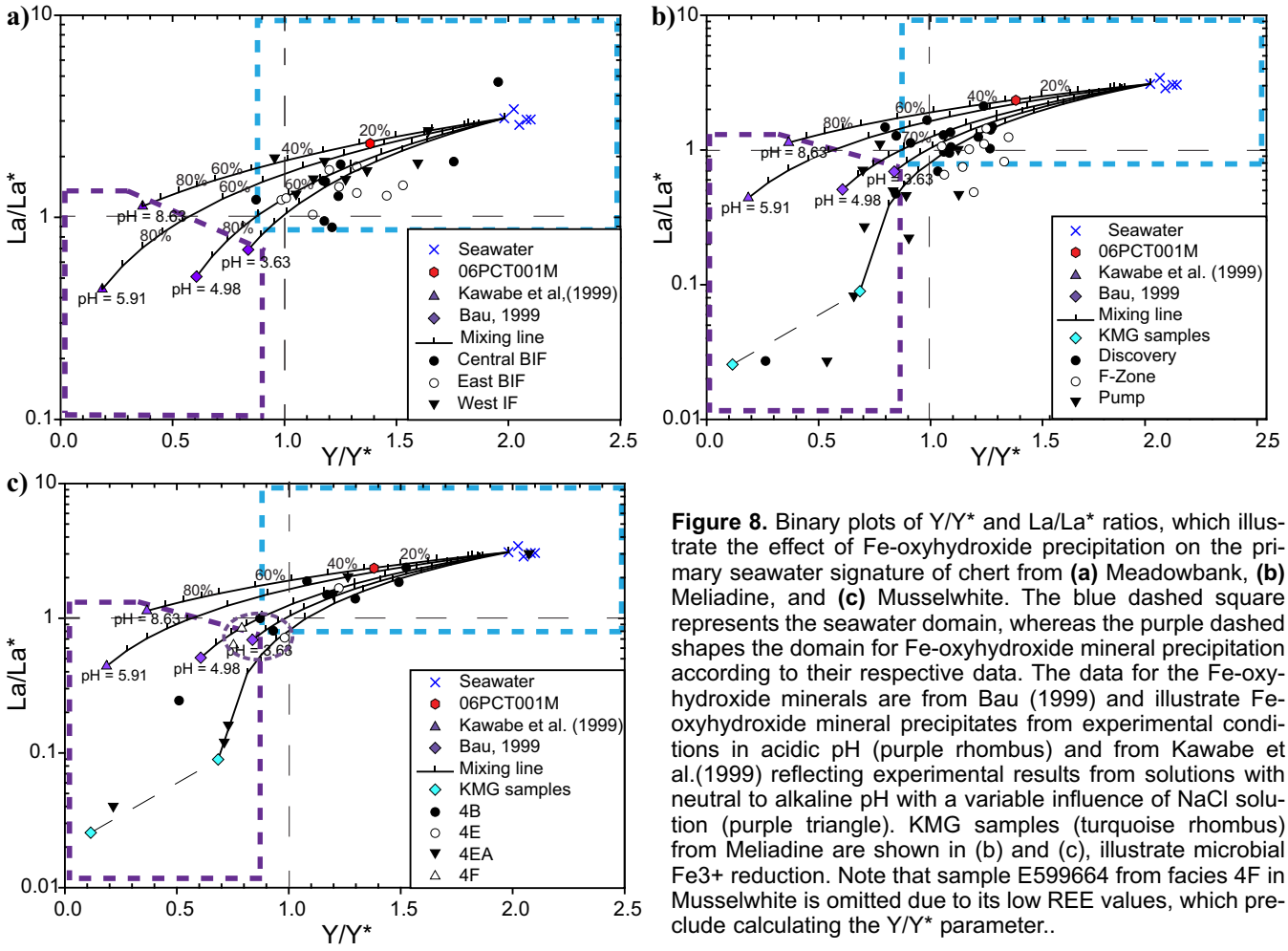

Figure 8. Binary plots of Y/Y* and La/La* ratios, which illustrate the effect of Fe-oxyhydroxide precipitation on the primary seawater signature of chert from **(a)** Meadowbank, **(b)** Meliadine, and **(c)** Musselwhite. The blue dashed square represents the seawater domain, whereas the purple dashed shapes the domain for Fe-oxyhydroxide mineral precipitation according to their respective data. The data for the Fe-oxyhydroxide minerals are from Bau (1999) and illustrate Fe-oxyhydroxide mineral precipitates from experimental conditions in acidic pH (purple rhombus) and from Kawabe et al.(1999) reflecting experimental results from solutions with neutral to alkaline pH with a variable influence of NaCl solution (purple triangle). KMG samples (turquoise rhombus) from Meliadine are shown in (b) and (c), illustrate microbial Fe3+ reduction. Note that sample E599664 from facies 4F in Musselwhite is omitted due to its low REE values, which preclude calculating the Y/Y* parameter..

domain suggest interaction of seawater and Fe-oxyhydroxide. In this deposit, two mechanisms for precipitation of Fe-oxyhydroxide are proposed: 1) influence of a dynamic pH shift between alkaline hydrothermal fluids and acidic-neutral seawater; and 2) biological oxidation of Fe^{2+}.

At Musselwhite, three groups are present. The first group reflects the interaction of seawater with Fe-oxyhydroxide and may reflect precipitation under variable pH conditions (Fig. 8c). The second group reflects precipitation of Fe-oxyhydroxide by biological oxidation (Fig. 8c). And finally, the third group could represent Fe-oxyhydroxide precipitation under acidic conditions (e.g. Bau, 1999) (Fig. 8c).

Given anoxic Archean seawater, the shale-normalized REE+Y patterns for Archean seawater will differ from modern seawater, which shows a well developed, negative Ce anomaly resulting from the oxidation of Ce^{+3} to Ce^{+4} (Planavsky et al., 2010). However, Bau (1999) experimented with the scavenging of dissolved REE+Y by precipitating Fe-oxyhydroxide at pH ranging from 3.6 to 6.2 and ambient oxygen content, and demonstrated that in the presence of Fe-oxyhydroxide, pH has a more important impact on Ce than oxygen. At pH ≤ 5, oxidative scavenging of Ce is favoured in the presence of Fe-oxyhydroxide and generates a positive Ce anomaly (Fig. 9), whereas at pH ≥ 5, the REE+Y systematics shows a negative Ce anomaly (Fig. 9).

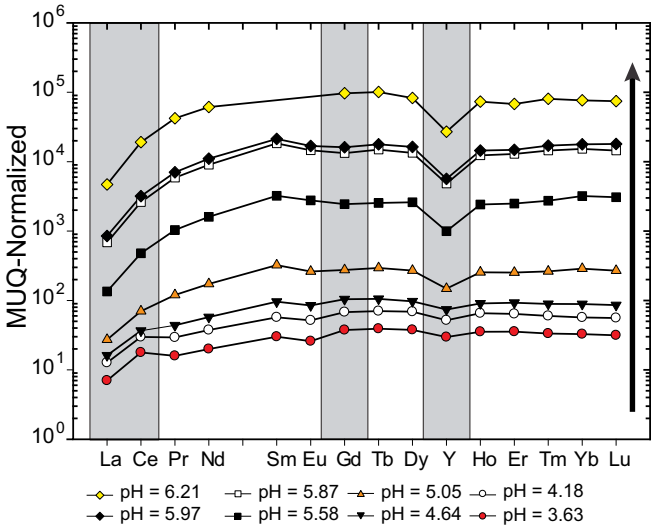

Figure 9. Plot of MUQ-normalized REE+Y patterns for experimentally produced Fe-oxyhydroxide precipitates at variable pH values (data from Bau, 1999).

Therefore, in theoretically acidic to neutral Archean seawater (e.g. Grotzinger and Kasting, 1993; Holland, 2003), the REE+Y systematics will display a weak negative Ce anomaly even in anoxic conditions.

Based on the previous statement, samples from the Pump zone, samples MEL-025, MEL-028 from the Discovery zone, and the second group of samples from Musselwhite, which may indicate interaction of Fe-oxyhydroxide from bacteria and seawater, show negative Ce anomalies that may reflect precipitation at a pH > 5, whereas most samples from the three deposits that are associated with positive Ce anomalies may reflect precipitation of Fe-oxyhydroxide at a pH < 5.

IMPLICATIONS FOR EXPLORATION

Based on the results and conclusions summarized herein, it does not appear that the primary depositional setting of the BIFs is a key ingredient for gold mineralization. This conclusion likely relates to the fact that the gold mineralization in each of these deposits occurs as part of an epigenetic event(s) during regional orogenesis; instead the dominant factor for such BIF-hosted gold deposits is the Fe-rich nature of the host, which is similar in all the BIF settings studied. However, our systematic sampling outward from the gold zones at all three deposits should provide a hydrothermal footprint in the chert chemistry, which will be defined in future stages of this project. These latter data can then be used to evaluate the influence of gold mineralizing fluids in Algoma-type BIFs.

FUTURE WORK

In the near future, the KMG samples will be analysed for their $\delta^{13}C$ signature, which will provide more insight into their nature of formation and origin. Furthermore, chert samples from the Beardmore-Geraldton gold deposit area and some additional samples from Musselwhite deposit will be analysed and interpreted in the same manner as the other samples above and a depositional setting will be defined. Moreover, a potential hydrothermal footprint at both the regional- and macroscopic-scale will also be defined where feasible (i.e. respectively at Beardmore-Geraldton and Meliadine).

ACKNOWLEDGEMENTS

The study is supported by both TGI-4 funding from Natural Resources Canada and funding through a Natural Sciences and Engineering Research Council Collaborative Research and Development agreement with participation by Agnico Eagle Mines Ltd. and Goldcorp. The authors also thank Drs. M. Leybourne, C. Lawley, and S. Pehrsson for discussions regarding the geochemistry and regional geological setting of the study areas, respectively. The LA-ICP-MS analyses were done in the Geochemical Fingerprinting Laboratory at Laurentian University with the capable assistance of Dr. J. Petrus. Finally, we sincerely acknowledge the contribution of Drs. B. Dubé, S. Castonguay, and P. Mercier-Langevin of the Geological Survey of Canada for their input and continued support.

REFERENCES

Alexander, B.W., Bau, M., Andersson, P., and Dulski, P., 2008. Continentally-derived solutes in shallow Archean sea water; rare earth element and Nd isotope evidence in iron formation from the 2.9 Ga Pongola Supergroup, South Africa; Geochimica et Cosmochimica Acta, v. 72, p. 378–394.

Alibo, D.S. and Nozaki, Y., 1999. Rare earth elements in seawater: particle association, shale-normalization, and Ce oxidation; Geochimica et Cosmochimica Acta, v. 63, p. 363–372.

Allwood, A.C., Kamber, B.S., Walter, M.R., Burch, I.W., and Kanik, I., 2010. Trace element record depositional history of an Early Archean stromatolitic carbonate platform; Chemical Geology, v. 270, p. 148–163.

Bau, M., 1999. Scavenging of dissolved yttrium and rare-earths by precipitating iron-oxyhydroxide: Experimental evidence for Ce oxidation, Y-Ho fractionation, and lanthanide tetrad effect; Geochimica et Cosmochimica Acta, v. 63, no. 1, p.67–77.

Bau, M. and Dulski, P., 1996. Distribution of Y and rare-earth elements in the Penge and Kuruman Iron Formations, Transvaal Supergroup, South Africa; Precambrian Research, v. 79, p. 37–55.

Bekker, A., Slack, J.F., Planavsky, N., Krapez, B., Hofmann, A., Konhauser, K.O., and Rouxel, J., 2010. Iron formation: the sedimentary product of a complex interplay among mantle, tectonic, oceanic and biospheric processes; Economic Geology, v. 105, p. 467–508.

Bolhar, R., Van Kranendonk, M.J., and Kamber, B.S., 2005. A trace element study of siderite-jasper banded iron formation in the 3.45 Ga Warrawoona Group, Pilbara craton-Formation from hydrothermal fluids and shallow seawater; Precambrian Research, v. 137, p. 93–114.

Danielson, A., Moeller, P., and Dulski, P., 1992. The europium anomalies in banded iron formations and the thermal history of the oceanic crust; Chemical Geology, v. 97, p. 89–100.

Goodwin, A.M., 1973. Archean iron-formations and tectonic basins of the Canadian Shield; Economic Geology, v. 68, p. 915–933.

Gourcerol, B., Thurston, P.C., Kontak, D.J., and Côté-Mantha, O., 2014. Interpretations and implications of preliminary LA ICP-MS analysis of chert for the origin of geochemical signatures in banded iron formations (BIFs) from the Meadowbank gold deposit, Western Churchill Province, Nunavut; Geological Survey of Canada, Current Research 2014-1, 26 p.

Gourcerol, B., Thurston, P.C., Kontak, D.J., Côté-Mantha, O., and Biczok, J., 2015. Distinguishing primary and mineralization-related signatures of chert from the banded iron formation-type gold deposits at Musselwhite, Ontario and Meadowbank, Nunavut; Geological Survey of Canada, Current Research 2015-1, 21 p.

Grotzinger, J.P. and Kasting, J.F., 1993. New constraints on Precambrian ocean composition; Journal of Geology, v. 101, p. 235–243.

Hanor, J.S. and Duchac, K.C., 1990. Isovolumetric silicification of early Archean komatiites; geochemical mass balances and constraints on origin; Journal of Geology, v. 98, p. 863–877.

Holland, H.D., 2003. The geologic history of seawater, *In:* Treatise on Geochemistry, (ed.) H.D. Holland and K.K. Turekian; Pergamon, Oxford, p. 583–625.

Kamber, B.S. and Webb, G.E., 2007. Transition metal abundances in microbial carbonate: a pilot study based on in situ LA-ICP-MS analysis; Geobiology, v. 5, p. 375–389.

Kamber, B.S., Bolhar, R., and Webb, G.E., 2004. Geochemistry of late Archean stromatolites from Zimbabwe: evidence for microbial life in restricted epicontinental seas; Precambrian Research, v. 132, p. 379–399.

Kamber, B.S., Greig, A., and Collerson, K.D., 2005. A new estimate for the composition of weathered young upper continental crust from alluvial sediments, Queensland, Australia; Geochimica et Cosmochimica Acta, v. 69, p. 1041–1058.

Kappler, A., Pasquero, C., Konhauser, K.O., and Newman D.K.,2005, Deposition of banded iron formations by anoxygenic phototrophic Fe(II)-oxidizing bacteria: Geology, v. 33, p. 865–868.

Kawabe, I., Ohta, A., Ishii, S., Tokumura, M., and Miyauchi, K., 1999. REE partitioning between Fe–Mn oxyhydroxide precipitates and weakly acid NaCl solutions: Convex tetrad effect and fractionation of Y and Sc from heavy lanthanides; Geochemical Journal, v. 33, p. 167–179.

Konhauser, O.K., Newman, D.K., and Kappler, A., 2005. The potential significance of microbial Fe(III) reduction during deposition of Precambrian banded iron formations; Geobiology, v. 3, p. 167–177.

Lawrence, M.G. and Kamber, B.S., 2006. The behavior of the rare earth elements during estuarine mixing- revisited; Marine Chemistry, v. 100, p.147–161.

Masuda, A., Kawakami, O., Dohmoto, Y., and Takenaka, T., 1987. Lanthanide tetrad effects in nature: two mutually opposite types, W and M; Geochemical Journal, v. 21, p. 119–124.

Minami, M., Masuda, A., Takahashi, K., Adachi, M., and Shimizu, H., 1998. Y-Ho fractionation and lanthanide tetrad effect observed in cherts; Geochemical Journal, v. 32, p. 405–419.

Ohmoto, H., Watanabe, Y., Yamaguchi, K.E., Naraoka, H., Haruna, M., Kakegawa, T., Hayashi, K., and Kato, Y., 2006. Chemical and biological evolution of early Earth: Constraints from banded iron formations; Geological Society of America Memoir, v. 198, p. 291−331.

Planavsky, N., Bekker, A., Rouxel, O.J., Kamber, B.S., Hofmann, A.W., Knudsen, A., and Lyons, T.W., 2010. Rare earth element and yttrium compositions of Archean and Paleoproterozoic Fe formations revisited: new perspectives on the significance and mechanisms of deposition; Geochimica et Cosmochimica Acta, v. 74, p. 6387–6405.

Shibuya, T., Komiya, T., Nakamura, K., Takai, K., and Maruyama, S., 2010. Highly alkaline, high-temperature hydrothermal fluids in the early Archean ocean; Precambrian Research, v. 182, p. 230–238.

Thurston, P.C., Kamber, B.S., and Whitehouse, M., 2011. Archean cherts in banded iron formation: Insight into Neoarchean ocean chemistry and depositional processes; Precambrian Research, v. 214-215, p. 227–257.

Veizer, J., 1988, The evolving exogenic cycle, *In:* Chemical Cycles in the Evolution of the Earth, (ed.) B.C. Gregor, R.M. Garrels, F.T. Mackenzie, and B.J. Maynard; Wiley-Interscience, New York, p. 175–218.

Wheeler, J.O., Hoffman, P.F., Card, K.D., Davidson, A., Sanford, B.V., Okulitch, A.V., and Roest, W.R., 1996. Geological map of Canada; Geological Survey of Canada, Map 1860A, CD-ROM.

GEOLOGICAL SURVEY OF CANADA
OPEN FILE 7582

Targeted Geoscience Initiative 4: Contributions to the Understanding of Precambrian Lode Gold Deposits and Implications for Exploration

Geological setting of the world-class Musselwhite gold mine, Superior Province, northwestern Ontario: implications for exploration

William Oswald[1], Sébastien Castonguay[2], Benoît Dubé[2], Vicki J. McNicoll[3], John Biczok[4], Michel Malo[1], and Patrick Mercier-Langevin[2]

[1]Institut national de la recherche scientifique – Centre Eau Terre Environnement, Québec, Quebec
[2]Geological Survey of Canada, Québec, Quebec
[3]Geological Survey of Canada, Ottawa, Ontario
[4]Goldcorp Inc., Thunder Bay, Ontario

2015

This publication is available for free download through GEOSCAN (http://geoscan.nrcan.gc.ca/)

Recommended citation

Oswald, W., Castonguay, S., Dubé, B., McNicoll, V.J., Biczok, J., Malo, M., and Mercier-Langevin, P., 2015. Geological setting of the world-class Musselwhite gold mine, Superior Province, northwestern Ontario: implications for exploration, *In:* Targeted Geoscience Initiative 4: Contributions to the Understanding of Precambrian Lode Gold Deposits and Implications for Exploration, (ed.) B. Dubé and P. Mercier-Langevin; Geological Survey of Canada, Open File 7582, p. 69–84.

Publications in this series have not been edited; they are released as submitted by the author.

Contribution to the Geological Survey of Canada's Targeted Geoscience Initiative 4 (TGI-4) Program (2010–2015)

TABLE OF CONTENTS

Geological setting of the world-class Musselwhite gold mine, Superior Province, northwestern Ontario: implications for exploration

William Oswald[1*], Sébastien Castonguay[2†], Benoît Dubé[2], Vicki J. McNicoll[3], John Biczok[4], Michel Malo[1], and Patrick Mercier-Langevin[2]

[1]Institut national de la recherche scientifique – Centre Eau Terre Environnement, 490 rue de la Couronne, Québec, Quebec G1K 9A9
[2]Geological Survey of Canada, 490 rue de la Couronne, Québec, Quebec G1K 9A9
[3]Geological Survey of Canada, 601 Booth Street, Ottawa, Ontario K1A 0E8
[4]Goldcorp Inc., Musselwhite Mine, Thunder Bay, Ontario P7B 6S8
*Corresponding author's e-mail: william.oswald@ete.inrs.ca
†Corresponding author's e-mail: sebastien.castonguay@RNCan-NRCan.gc.ca

ABSTRACT

The Musselwhite world-class Au deposit is hosted in polydeformed amphibolite-facies banded iron formation of the Opapimiskan-Markop metavolcanic assemblage, part of the Mesoarchean North Caribou greenstone belt (northwestern Superior Province). The deposit is located approximately 2 km west of the tectonic boundary with the gneissic Island Lake Domain. Major and trace element geochemical data show that the South Rim and Opapimiskan-Markop metavolcanic assemblages have variable magmatic affinities and diverse normalized rare earth element patterns. The bulk of the Au at Musselwhite is hosted in silicate-rich banded iron formation and occurs in association with stratabound pyrrhotite replacements and associated silica flooding, with local discordant quartz±pyrrhotite veins. The ore zones are associated with D_2 high-strain zones that are preferentially developed along hinges and strongly attenuated fold limbs of tight F_2 folds. The layered anisotropy induced by the presence of competent banded iron formation layers in mafic and ultramafic volcanic rocks has clearly influenced the rheological response to deformation at all scales, and hence played an important role in Au-bearing fluid flow and ore formation and distribution. A new U-Pb preliminary age of 2666 Ma on late-M_2 monazite provides a minimum age constraint for the regional D_2 metamorphic/deformation event to which most of the Au mineralization at Musselwhite is associated. Reappraisal of stratigraphic relationships, supported by U-Pb geochronology, indicates that the mine stratigraphy is inverted and is part of the overturned limb of a kilometre-scale F_1 syncline, which is in agreement with multiple occurrences of mesoscopic refolded F_1 folds. Previously unrecognized regional F_1 folding, which is strongly overprinted by the dominant D_2 deformation, has influenced the distribution and geometry of the banded iron formation, which hosts the bulk of the Au at Musselwhite, and provides new vectors for regional exploration. Future work will focus on additional documentation of mineral chemistry and microscopic textural relationships, as well as further analyses of lithogeochemical data in order to ultimately define key exploration vectors for iron formation-hosted Au deposits in other Precambrian terranes.

INTRODUCTION

The Goldcorp Musselwhite mine is located near Opapimiskan Lake, 475 km north of Thunder Bay, within the North Caribou greenstone belt, which is part of the North Caribou Terrane of the western Superior Province (Thurston et al., 1991; Fig. 1). Production started in 1997 and had reached over 4 Moz of gold with total proven and probable reserves of 1.85 Moz as of December 31, 2013 (www.goldcorp.com).

This research project at Musselwhite, a component of the Targeted Geoscience Initiative 4 (TGI-4) Lode Gold project of Natural Resources Canada, is conducted in collaboration with Goldcorp Inc., the Ontario Geological Survey and the University of Ottawa. It aims at understanding the structural, lithological, and geochemical controls on the formation and distribution of the banded iron formation-hosted Au mineralization. Another objective is to define the geochemical footprint of the hydrothermal system in order to develop improved geological and exploration models for similar deposit types in the North Caribou greenstone belt and elsewhere in Precambrian terranes (Dubé et al., 2011).

Oswald, W., Castonguay, S., Dubé, B., McNicoll, V.J., Biczok, J., Malo, M., and Mercier-Langevin, P., 2015. Geological setting of the world-class Musselwhite gold mine, Superior Province, northwestern Ontario: implications for exploration, *In:* Targeted Geoscience Initiative 4: Contributions to the Understanding of Precambrian Lode Gold Deposits and Implications for Exploration, (ed.) B. Dubé and P. Mercier-Langevin; Geological Survey of Canada, Open File 7582, p. 69–84.

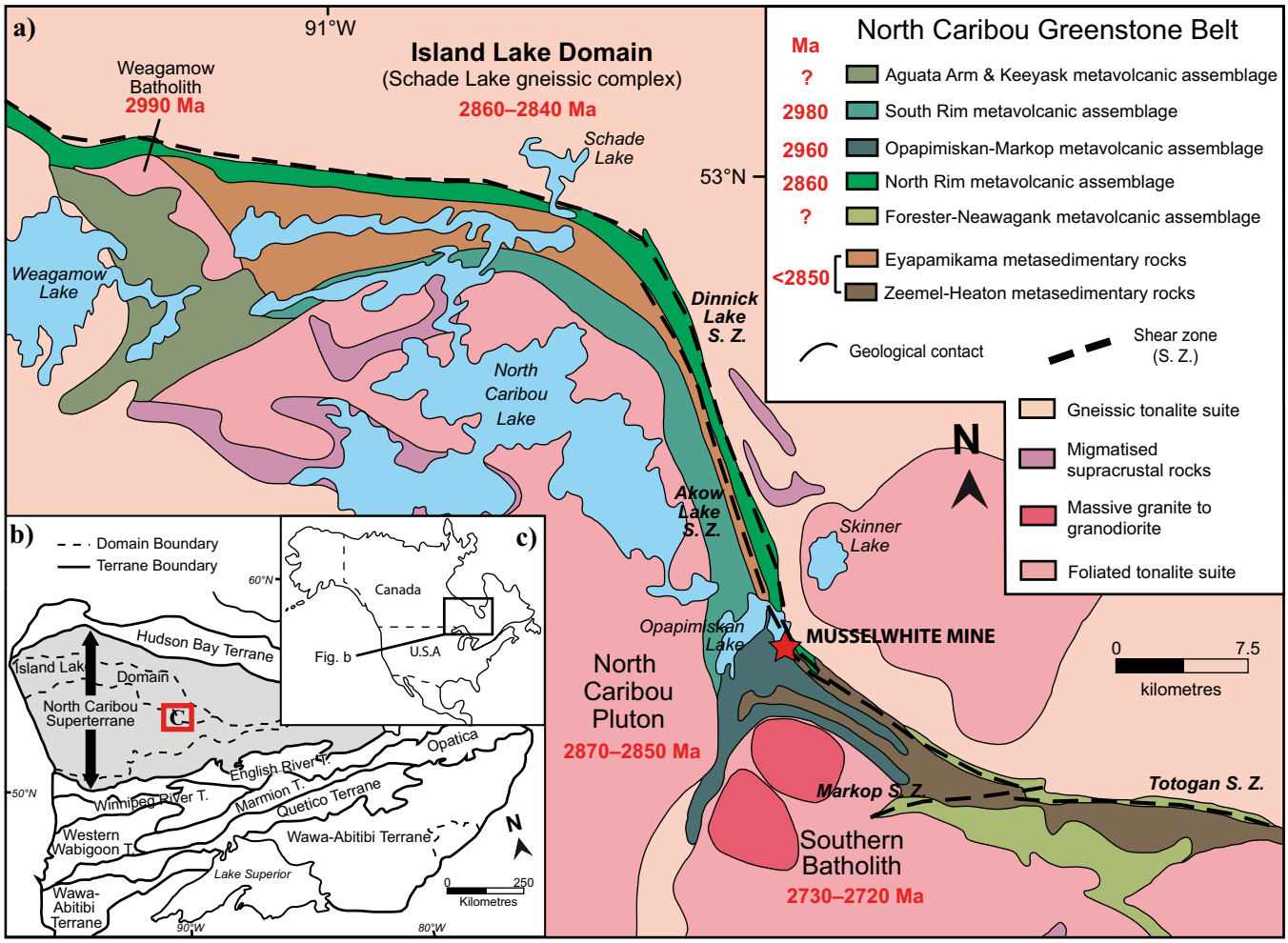

Figure 1. a) Simplified tectonostratigraphic map of the North Caribou greenstone belt and surrounding area (geology modified from McNicoll et al., 2013; geochronological data from Breaks, 2001; McNicoll et al., 2013; Van Lankvelt, 2013). **b and c)** Location of the study area and terranes of the western Superior Province (insets modified from Rayner and Stott, 2005; Stott et al., 2010).

This report presents a brief summary of the current status of the ongoing multidisciplinary research being conducted at Musselwhite. Our investigation of the distal and proximal settings of Au mineralization and of the relative and absolute chronology of events at Musselwhite comprises a major surface, underground, and drill-core mapping component, including sampling for petrographic and geochemical analyses. The study of the Musselwhite deposit (Oswald et al., 2014a,b), which builds on previous studies at deposit scale (e.g. Hall and Rigg, 1986; Couture, 1995; Isaac, 2008; Moran, 2008), also includes targeted geochronology across most of the Opapimiskan Lake area (McNicoll et al., 2013, submitted) to establish the age of the host-rock successions and the major structural and metamorphic episodes, to put our work into a regional context, and to address key questions that cannot be readily resolved at deposit scale. Other specific ongoing research activities at Musselwhite or its vicinity (e.g. Kalbfleisch, 2012; Van Lankvelt et al., 2013; Duff, 2014; Gourcerol et al., 2015) involve geochronology, structural mapping, metamorphic petrology, and lithogeochemistry, which will collectively contribute to a better understanding of the evolution of the North Caribou greenstone belt and its bounding structures and assemblages.

REGIONAL AND LOCAL GEOLOGICAL SETTING

The North Caribou greenstone belt is located south-southwest of the Island Lake domain (Fig. 1), in the central part of the North Caribou Terrane, which is considered the core of the western Superior Province (Percival et al., 2007). Regional-scale mapping programs and studies (Breaks et al., 1985; Piroshco et al., 1989; Breaks and Barlett, 1991; Breaks et al., 1991, 2001; Thurston et al., 1991) have defined various lithostratigraphic assemblages in the North Caribou greenstone belt (from northwest to southeast; Fig. 1a): the Agutua Arm metavolcanic assemblage; the

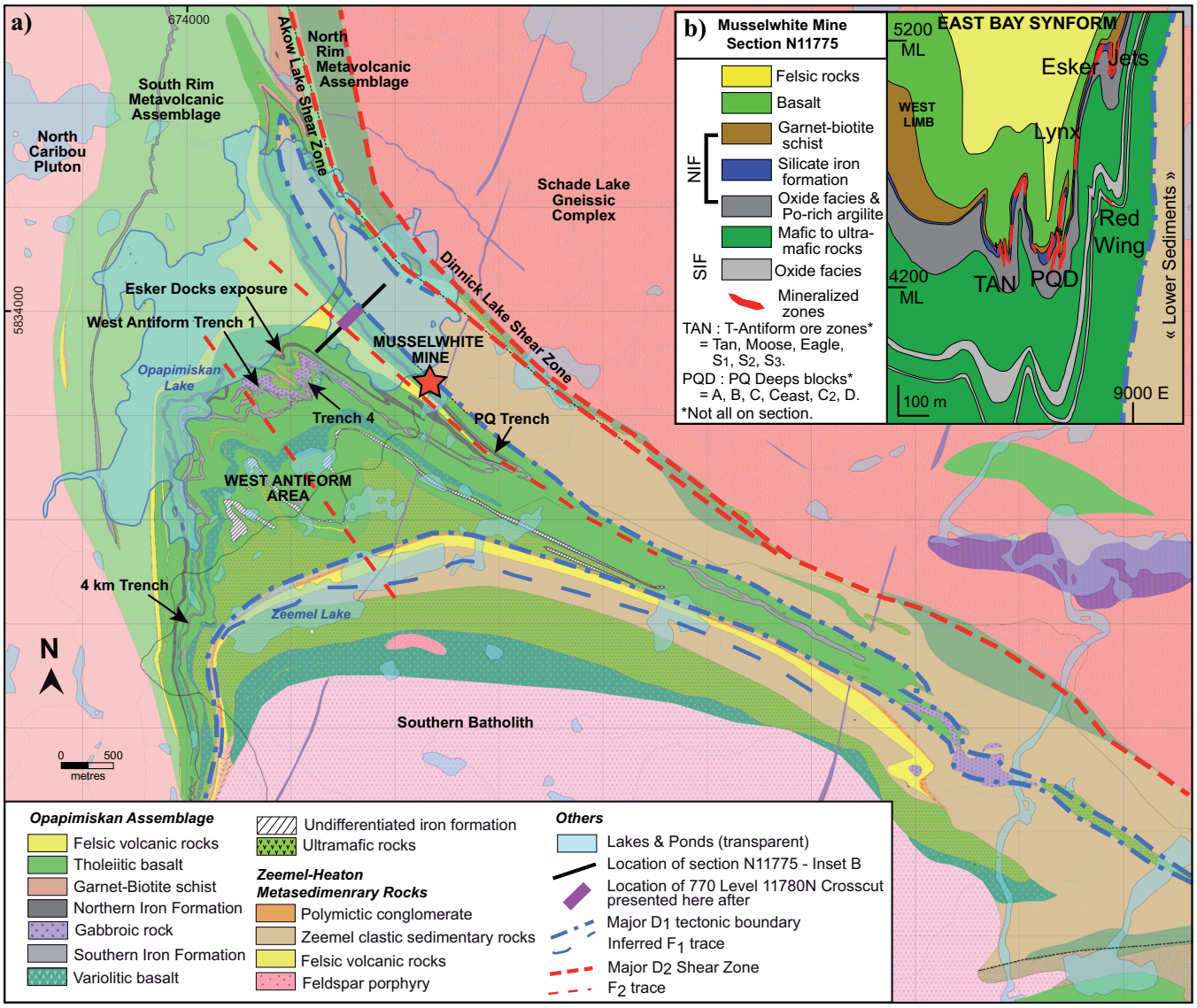

Figure 2. a) Geological map of the Opapimiskan Lake area and major structural features, with locations of the surface exposures that were selected for detailed mapping for this project (geology based on unpublished Goldcorp data). Universal Transverse Mercator (UTM) co-ordinates provided using North American Datum 1983 (NAD83) in Zone 15. **b)** Simplified geological section of the mine at N11775 mine grid, showing the locations of the main ore zones. Abbreviations: bt = biotite; gt = garnet; ML = mine level; NIF = Northern Iron Formation; po = pyrrhotite; SIF = Southern Iron Formation.

metasedimentary and metavolcanic rocks of the Keeyask metavolcanic assemblage; the metasedimentary rocks of the Eyapamikama assemblage; the North Rim metavolcanic assemblage; the South Rim metavolcanic assemblage; the Opapimiskan-Markop metavolcanic assemblage (OMA); the Zeemel-Heaton metasedimentary assemblage (ZHA); and the Forester-Neawagank metavolcanic assemblage. The greenstone belt is surrounded by the tonalite-trondhjemite-granodiorite (TTG)-type batholiths of the North Caribou pluton (NCP) and the Schade Lake gneissic complex (SLGC), both comprising several intrusive phases dated between 2.87 and 2.84 Ga, and by the smaller, composite, ca. 2730–2723 Ma Southern batholith (Fig. 1; Biczok et al., 2012).

The Musselwhite deposit host succession consists of the South Rim metavolcanic assemblage and the underlying OMA, which structurally overlies the ZHA (Fig. 2a). The whole succession is folded by a northwest-trending, F_2 synform-antiform pair (i.e. East Bay Synform and West Antiform). The OMA comprises two main iron formations, i.e., the Northern iron formation (NIF) and Southern iron formation (SIF), both intercalated with, from structural top to bottom, calc-alkaline, felsic to intermediate volcanic rocks, tholeiitic, mafic volcanic and subvolcanic rocks, and tholeiitic, komatiitic basalt and ultramafic volcanic rocks. The structurally uppermost iron formation sequence (NIF) hosts the bulk of the economic Au mineralization (Fig. 2b).

Three main phases of regional deformation have been documented (Breaks et al., 1985, 1991; Piroshco and Shields, 1985) The earliest event, D_1, consists of tight to isoclinal mesoscopic folds, associated with a penetrative S_1 foliation, which is commonly subparallel to bedding or layering (Breaks et al., 2001). D_2, the dominant regional phase of deformation, consists of open to isoclinal shallowly northwest-plunging folds, coupled with a steeply dipping axial-planar foliation (S_2), commonly obliterating D_1 fabrics. In the project area, rocks are affected by strong, eastward-increasing D_2 deformation that culminates in a major fault zone at the contact with the Schade Lake gneissic complex (Fig. 2a). D_3 deformation structures are heterogeneously developed and consist of asymmetric broad open or chevron folds, locally accompanied by a steep southwest-trending S_3 crenulation cleavage. Major, probably long-lived or reactivated fault or shear zones commonly mark lithostratigraphic boundaries in the greenstone belt and overprint contacts with surrounding batholiths (Figs. 1, 2; Breaks et al., 2001).

The regional metamorphic grade varies from middle to upper greenschist facies in the northern part of the belt, near Eyapamikama Lake (Breaks and Bartlett, 1991), to middle amphibolite facies around Opapimiskan Lake and further east (Breaks et al., 1985). According to Hall and Rigg (1986), peak regional metamorphism occurred during the later stages of D_2.

RESULTS

Methodology

Detailed geological and structural mapping was carried out using a high-resolution GPS (AshTech Promark 800) on a selection of five stripped exposures, which allowed for increased speed of data collection as well as overcoming the challenge of structural measurements on iron formations. This latter issue was resolved during underground mapping by measuring fabrics and structures with respect to the surveyed orientation of mine workings. Systematic logging and sampling of drill core has also been completed on a set of sections across the deposit to link geological and structural mapping information with petrographic data, mineral chemistry, and whole-rock lithogeochemistry.

Mine Stratigraphy

Geological mapping (Fig. 3; see also Oswald et al., 2014a,b), description of drill core, and lithogeochemical data have refined the stratigraphy of the deposit (Fig 4). Previously defined units of the Opapimiskan metavolcanic assemblage (Fig. 4a; Hollings and Kerrich, 1999) have been geochemically characterized. Volcanic rocks from the "Avol" are dominantly dacitic with a calc-alkaline affinity (Fig. 4b,c). The "Bvol" package comprises tholeiitic mafic rocks with three contrasting rare earth element (REE) signatures: one with light REE enrichment and two flat-profile groups with different REE enrichment relative to primitive mantle values (Fig. 4d). The "Basement Basalts" contain ultramafic rocks with a transitional to calc-alkaline affinity and light REE enrichment, intercalated with ultramafic rocks of tholeiitic affinity and flat normalized REE patterns, calc-alkaline intermediate rocks showing strong light REE enrichment, and tholeiitic to slightly calc-alkaline mafic rocks showing various degrees of light REE enrichment. Four samples of basalt and komatiitic basalt of the lowermost section of the OMA were collected close to the boundary with the ZHA (Fig. 2a); they have tholeiitic affinity and exhibit flat normalized REE patterns.

The NIF comprises garnet amphibolite and garnet-biotite schist (unit 4E and 4F, Fig. 4a), which, although not banded iron formation *sensu stricto*, contain over 15 wt% total Fe_2O_3 (Fig. 4d) and are thereby considered iron formation (James, 1954). Unit 4F includes a thin quartz-feldspar-biotite volcaniclastic interval (unit 6). These units structurally overlie the more typical banded iron formation, including a silicate (i.e. garnet-grunerite) facies (unit 4EA), a clastic chert-magnetite facies (unit 4Bc), a chert-magnetite facies (unit 4B), and a chert-grunerite facies (unit 4A). A sulphide-rich meta-argillite (unit 4H) forms the structural base of the NIF sequence (Fig. 4a). The Al_2O_3 content of samples is used in ternary projections (Fig. 4e) as a proxy for detrital input (Klein, 2005); the hydrothermal input is mainly defined by a positive Eu anomaly, whereas a weakly to strongly positive Y anomaly characterizes the seawater input (Fig. 4f). Following Moran (2008), REE+Y data was chondrite (C1)-normalized and was also normalized to the mudstone of Queensland (MUQ; Kamber et al., 2005; Fig. 4f) to minimize the detrital REE signature and to emphasize potential hydrothermal and seawater inputs (Baldwin, 2011).

The study of the chert component of the iron formations at Musselwhite and in other BIF-hosted deposits (e.g. Meadowbank Mine, and Meliadine district, Nunavut) by Gourcerol et al. (2014, 2015), which is complementary to our work, aims to establish if there is specific geochemical signature for BIF that contains Au mineralization and whether a hydrothermal footprint can be detected.

Structure

Complementing the work of Hall and Rigg (1986) 2 to 3 km west of the Musselwhite Mine, our surface and underground mapping has documented structures and fabrics related to the three phases of regional deformation and provides comprehensive insights about polyphase structural styles and geometric relationships

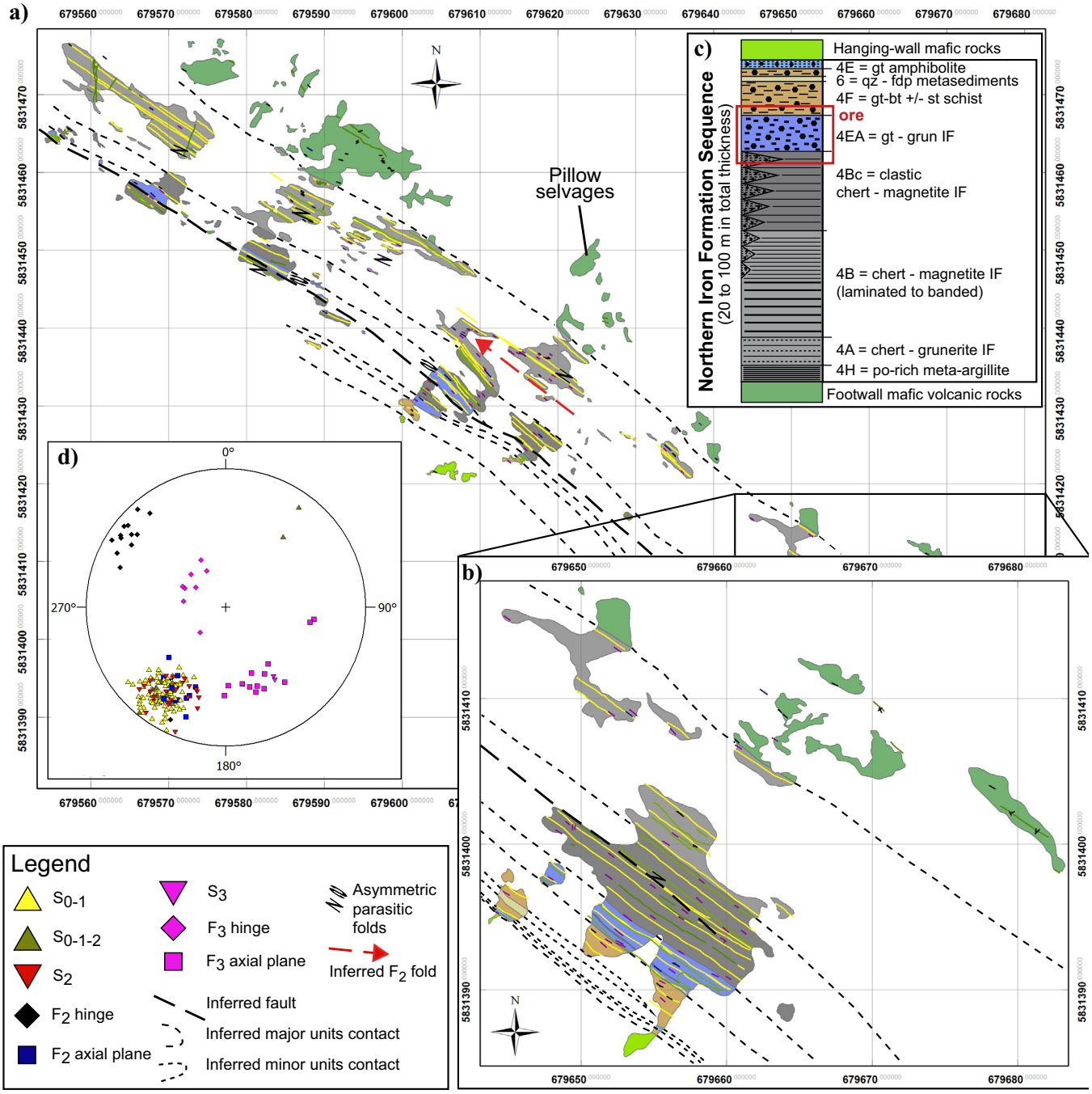

Figure 3. a) Geological map of the PQ Trench exposure (see Fig. 2 for location). **b)** Close-up view of the southern part of the exposure, UTM NAD83 Zone 15 coordinates. **c)** Schematic column of the facies of the Northern Iron Formation and adjacent volcanic rocks (based on unpublished Goldcorp data). Abbreviations: bt = biotite; fdp = feldspar; grun = grunerite; gt = garnet; IF = iron formation; po = pyrrhotite; qz = quartz; st = staurolite. **d)** Stereographic projection (lower hemisphere) of planar and linear structural data.

and their significance for gold mineralization (Oswald et al., 2014a,b,c). The West Antiform Trench 1, Esker Docks exposure, and Trench 4 are located in a domain of lower intensity D_2 deformation, which provides a favourable context to document earlier structures that include penetrative, northeast-southwest-trending, S_1 foliation (Fig. 5a), refolded F_1 folds (Fig. 5b), and locally, evidence of soft-sediment deformation. Shallowly northwest-plunging upright F_2 folds have deformed D_1 structures and produced type 3 F_1/ F_2 fold interference pattern in the West Antiform area. The expression of the axial-planar northwest-trending S_2 foliation is lithology-dependent (Fig. 5c). In a relatively low-intensity D_2 deformation domain, it is developed as a spaced cleavage in igneous rocks and as a more penetrative foliation in iron formation. In areas

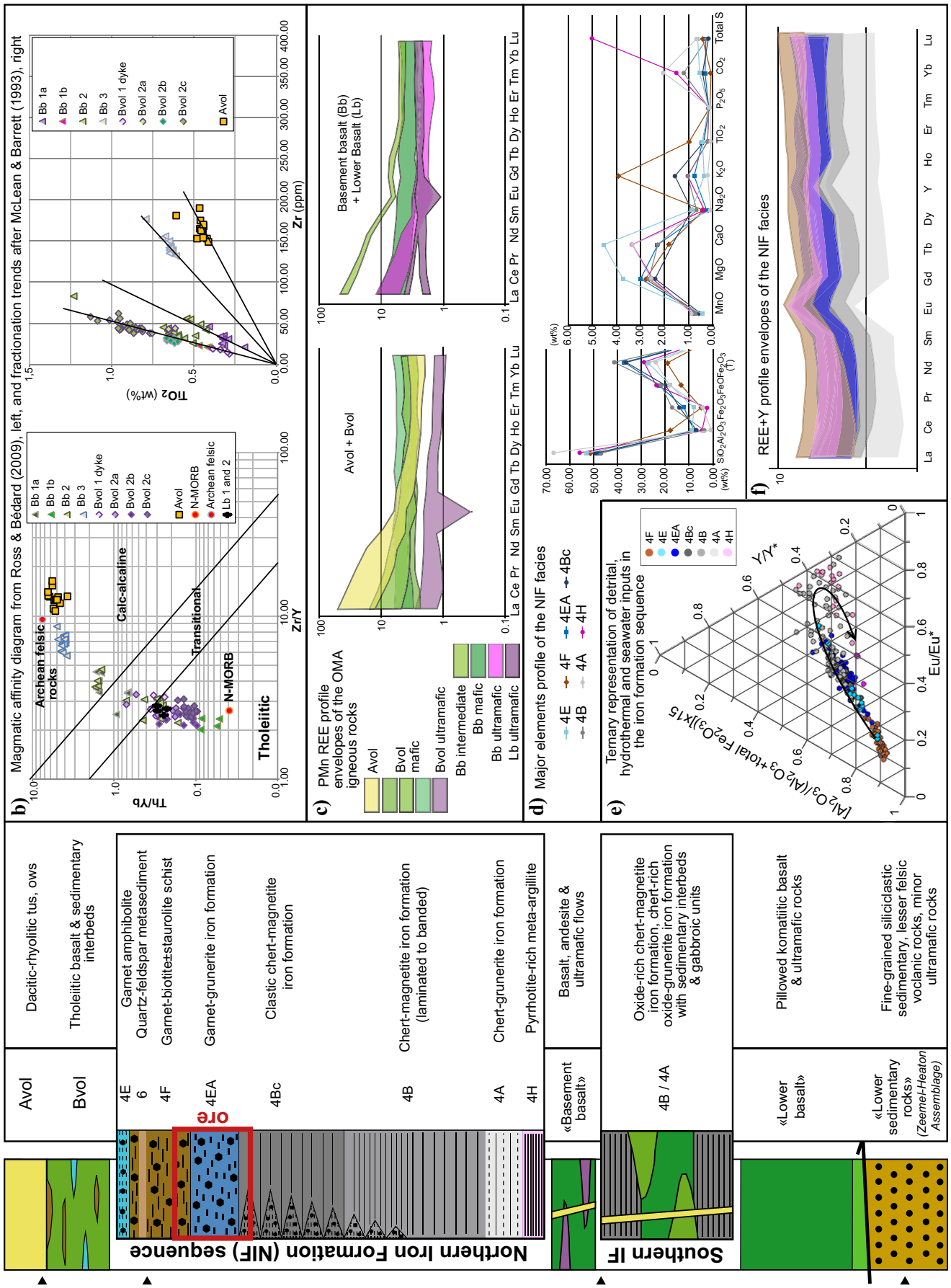
a)
2978,7 Ma
<2967 Ma
Felsic dyke: 2909,4 Ma
<2853 Ma
Avol
Bvol
Dacitic-rhyolitic tus, ows
Tholeiitic basalt & sedimentary interbeds
Garnet amphibolite
Quartz-feldspar metasediment
Garnet-biotite±staurolite schist
Garnet-grunerite iron formation
Clastic chert-magnetite iron formation
Chert-magnetite iron formation (laminated to banded)
Chert-grunerite iron formation
Pyrrhotite-rich meta-argillite
Basalt, andesite & ultramafic flows
Oxide-rich chert-magnetite iron formation, chert-rich oxide-grunerite iron formation with sedimentary interbeds & gabbroic units
Pillowed komatiitic basalt & ultramafic rocks
Fine-grained siliciclastic sedimentary, lesser felsic volcanic rocks, minor ultramafic rocks
4E
6
4F
4EA
4Bc
4B
4A
4H
ore
«Basement basalt»
4B / 4A
«Lower basalt»
«Lower sedimentary rocks» (Zeemel-Heaton Assemblage)
Northern Iron Formation (NIF) sequence
Southern IF
b)
Magmatic affinity diagram from Ross & Bédard (2009), left, and fractionation trends after McLean & Barrett (1993), right
Th/Yb
ZrY
Archean felsic rocks
Calc-alcaline
Transitional
N-MORB
Tholeiitic
Bb 1a
Bb 1b
Bb 2
Bb 3
Bvol 1 dyke
Bvol 2a
Bvol 2b
Bvol 2c
Avol
N-MORB
Archean felsic
Lb 1 and 2
TiO2 (wt%)
Zr (ppm)
c)
PMn REE profile envelopes of the OMA igneous rocks
Avol
Bvol mafic
Bvol ultramafic
Bb intermediate
Bb mafic
Bb ultramafic
Lb ultramafic
Avol + Bvol
Basement basalt (Bb) + Lower Basalt (Lb)
La Ce Pr Nd Sm Eu Gd Tb Dy Ho Er Tm Yb Lu
d)
Major elements profile of the NIF facies
4E
4F
4EA
4Bc
4B
4A
4H
(wt%)
MnO MgO CaO Na2O K2O TiO2 P2O5 CO2 Total S
SiO2-Al2O3-Fe2O3-FeO-Fe3O4 (T)
e)
Ternary representation of detrital, hydrothermal and seawater inputs in the iron formation sequence
[Al2O3/(Al2O3+total Fe2O3)]x15
Y/Y*
Eu/Eu*
f)
REE+Y profile envelopes of the NIF facies
La Ce Pr Nd Sm Eu Gd Tb Dy Y Ho Er Tm Yb Lu

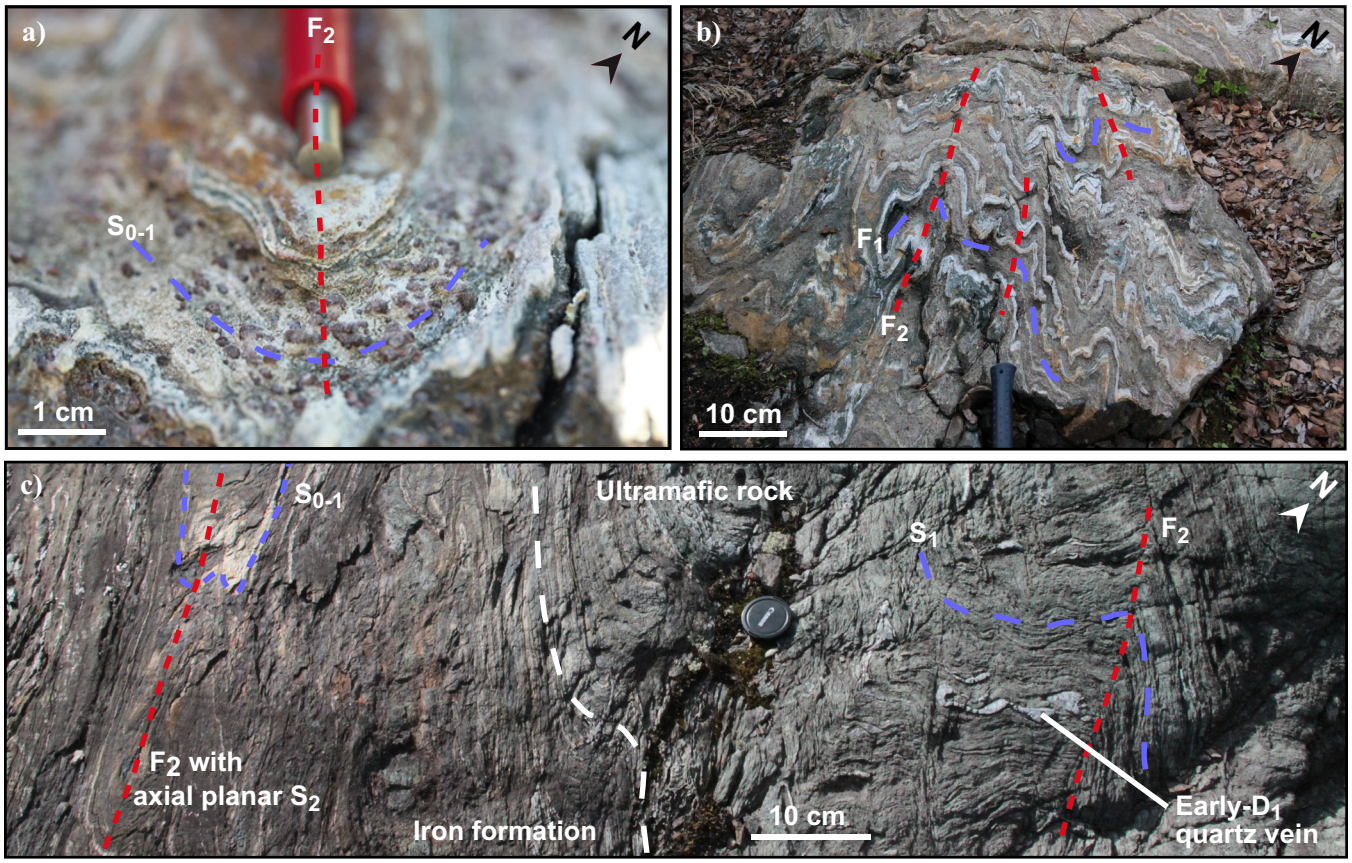

Figure 5. Photographs of representative structural features. **a)** Close-up view of the S_1 foliation in a garnet-biotite band along a F_2 fold hinge (Esker Docks exposure). **b)** F_1/F_2 fold interference pattern (type 3) in cherty garnet-biotite schist (Esker Docks exposure). **c)** Part of the West Antiform exposure illustrating the contrast in the development of the S_1 foliation in the chert-magnetite iron formation and the adjacent ultramafic rocks, overprinted by F_2 folds.

of strong D_2 overprint, S_2 is penetrative in all rock types and is associated with boudinaged beds in chert-magnetite iron formation. Strain features suggest that D_2 deformation in the mine area was dominated by flattening and minor shearing with dextral and east-side-up components of motion. D_3 deformation mostly consists of open or chevron-type folds. Two possibly conjugate sets of S_3 crenulation cleavage are oriented ENE-WSW and NNE-SSW. Field evidence reveals that S_3 cleavage is unevenly developed in the BIF units, and it is preferentially developed near and within high-strain zones in volcanic rocks.

Mineralization and Alteration

The crosscutting relationships of multiple vein generations are documented here. The earliest vein type includes barren, glassy, white to grey, quartz veins, which are thought to be early-D_1 (Fig. 5c). Three vein types are associated with D_2 structures: 1) grey, quartz-dominated, pyrrhotite- and carbonate-bearing, auriferous veins with a variably developed calc-silicate alteration halo; 2) milky white quartz-carbonate veins that can be auriferous or barren; and 3) barren, sugary-textured, calcite-dominated, quartz-carbonate late-D_2 veins. D_3-related veins, which are usually barren, white to greyish, and quartz-dominated, remobilized Au and sulphides locally where they cut pre-existing mineralized structures.

Characteristics of the mineralized zones have been documented by logging of drill core and underground mapping (Oswald et al., 2014a). As previously proposed for the West Antiform zone by Hall and Rigg

Figure 4 (opposite page). a) Detailed stratigraphic column of the mine sequence (geochronological data from McNicoll et al. (2013)). **b)** Left plot: magmatic affinity diagram from Ross and Bédard (2009) using Zr/Y versus Th/Yb, and right plot: fractionation trends after McLean and Barrett (1993) using Zr versus TiO_2 for the least altered drill-core samples. **c)** Rare earth element (REE) profile envelopes of igneous rocks samples from the mine sequence (normalized to primitive mantle from Sun and McDonough, 1989). **d)** Average values for major elements of the least altered drill-core samples of each Northern Iron Formation (NIF) facies. **e)** Ternary projection of NIF drill-core samples showing the relative importance of detrital input ($Al_2O_3/(A_2O_3$+total $Fe_2O_3)$x15), hydrothermal input (Eu anomaly), and seawater input (Y anomaly) for each facies. Black arrow shows the overall trend. **f)** Mudstone of Queensland (MUQ)-normalized REE+Y profile envelopes of the least altered drill-core samples of each NIF facies (normalized to MUQ from Kamber et al., 2005). See Figure 4e for colour legend.

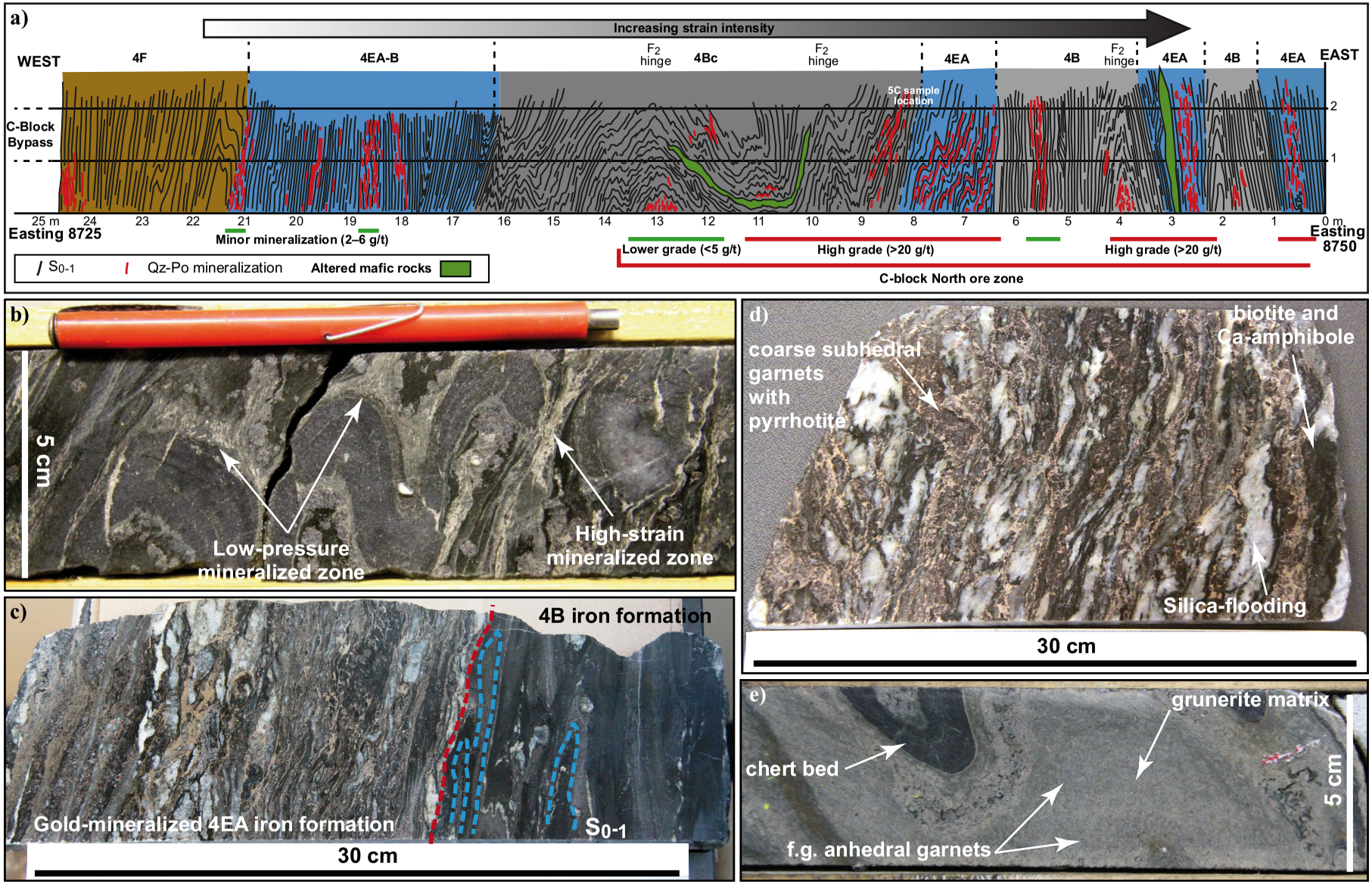

Figure 6. a) Geology of the northern wall of the 770 Level 11780N Crosscut (see Fig. 3a for colour legend). **b)** Photograph of drill core (sample MW-2011-107) showing the style and distribution of the mineralization, which is similar to those mapped on the 770 Level 11780N crosscut face. **c)** Photograph of a polished slab of ore sampled on the north-facing wall of the 770 Level 11780N Crosscut illustrating preferential pyrrhotite replacement in the garnet-grunerite unit to the left, compared to the essentially barren chert-magnetite unit to the right. **d)** Photograph of a polished slab of typical Musselwhite ore showing intense silica flooding and pyrrhotite replacement of the iron formation. **e)** Photograph of a drill-core sample of very weakly altered garnet-grunerite iron formation. Abbreviations: f.g. = fine grained; Po = pyrrhotite; Qz = quartz.

(1986), the mineralized zones at Musselwhite show close spatial relationship with the D_2 deformation-related high-strain zones and adjacent lower pressure areas, such as F_2 fold hinge zones, supporting the syn-D_2 timing of Au mineralization, in association with sulphides such as pyrrhotite. Two end-members of ore can be distinguished: quartz-flooded zones with over 50% quartz and zones of strong pyrrhotite replacement (up to 40% pyrrhotite).

The 11780N Crosscut on level 770 exposes one of the PQD ore zones (Figs. 2b, 6a), which represents typical high-grade ore in the 4EA facies and its relationships with D_2 structures. A D_2 strain gradient, similar to that mapped at kilometre-scale between the West Antiform area and the mine area, is documented at decametre-scale underground and in drill core, where Au mineralization mainly occurs in high-strain zones, but likewise in adjacent low-pressure areas, such as fold hinges (Fig. 6a,b). Lithological control on sulphide precipitation and associated Au deposition is also evidenced by the contrast in intensity of pyrrhotite replacement and/or quartz-flooding between the garnet-grunerite facies (unit 4EA) and the chert-magnetite facies (unit 4B) of the iron formation (Fig. 6c). Ore-grade mineralization in chert-magnetite iron formation only occurs in zones of high strain, intense transposition, and that contain numerous fault-fill laminated quartz-pyrrhotite veins.

Typical Au ore in the garnet-grunerite iron formation (Fig. 6d) mainly comprises smoky grey to black quartz veins and/or quartz flooding with pyrrhotite and iron carbonate. Pyrrhotite is the dominant sulphide associated with Au mineralization. Chalcopyrite is very rarely present in hand samples. Arsenopyrite is also only locally present, and does not correlate with elevated Au grades. In garnet-grunerite layers, pyrrhotite occurs as very fine-grained aggregates along foliation planes and in pressure shadows and filling fractures of coarse-grained dark red almandine porphyroblasts. Boudinaged chert bands, quartz veins, or quartz-flooded layers contain dark green, fine-grained amphibole, biotite, and local clinopyroxene, likely hedenbergite.

Silicate minerals, such as garnet, grunerite or ferrotschermakite, and biotite are found in both regional metamorphic and ore-related mineral assemblages. Documentation of the different mineral textural relationships is critical to understanding the series of event that occurred. In this regard, garnet is a particularly important phase, as it is present in many lithologies and in various textural contexts (Fig. 7a). Differences between proximal and distal Au mineralization are partly illustrated in garnet textures. For example, the distal, least altered 4EA facies (Fig. 6e) comprises anhedral to subhedral almandine garnet, whereas typical ore contains coarse-grained, subhedral to euhedral, red almandine garnets (Fig. 6d).

Geostatistical analysis of the lithogeochemical data (e.g. binary and ternary plots, principal component analysis (PCA), correlation coefficient calculations) shows that Au is associated with Ag, Se, Te, and Cu, in addition to total-sulfur and loss-on-ignition components (Fig. 7b,c). The weaker correlation of CaO and CO_2, compared to an average greenstone-hosted orogenic deposit (Dubé and Gosselin, 2007), may denote the overprint of Au-bearing structures by calcite-rich structures, which were documented in underground mapping and in drill-core analyses. As proposed by Davies et al. (1982), CO_2/CaO and CO_2/CaO+MgO molar ratios will be used to investigate the carbonate-alteration intensity, as these ratios take into account the availability of Ca and Mg in the altered rock protolith. The absence of As (as well as Sb, Bi, and Pb) in the trace metals associated with Au is noteworthy as it is usually abundant in orogenic Au deposits (Pitcairn et al., 2006; Dubé and Gosselin, 2007). The distinct, isolated signature of SiO_2 suggests that multiple parameters have influenced its distribution in the iron formation (primary chert, barren early quartz vein, Au-bearing silica-flooding, etc.).

DISCUSSION

Stratigraphy and Structure

Detailed surface mapping in the Musselwhite area reveals that early (D_1) deformation had a major influence on the geometry and regional distribution of prospective BIF horizons. Tight to isoclinal F_1 folds are refolded, and locally obliterated by D_2 folds and fabrics, which dominate the regional structural pattern. The presence of local metric to decametric F_1 folds suggests they occur at regional-scale. New U-Pb geochronology (Fig. 4; McNicoll et al., 2013) indicates that unit 6 and unit 4F of the Northern BIF are both <2967 Ma, and the structurally overlying felsic tuff (Avol unit) of the South Rim assemblage yielded an age of 2978.7 Ma. Coupled with regional geological data, this data confirms that the mine sequence is overturned and occurs along the northern overturned limb of a kilometre-scale F_1 fold, with an inferred axial plane located along Zeemel Lake (Fig. 2a). New U-Pb isotope dilution thermal ionization mass spectrometry (ID-TIMS) geochronology results have also uncovered a ca. 60 to 110 Ma age difference between the OMA (<2967 to >2909.4 Ma) and the adjacent ZHA (<2853 Ma) in the mine stratigraphic succession (Fig. 4; McNicoll et al., 2013, submitted). Drill-core descriptions show this major gap or boundary is marked by increased strain intensity and carbonate alteration. Regional mapping (Fig. 2) suggests that this sheared contact likely delineates an early, D_1 thrust fault, which

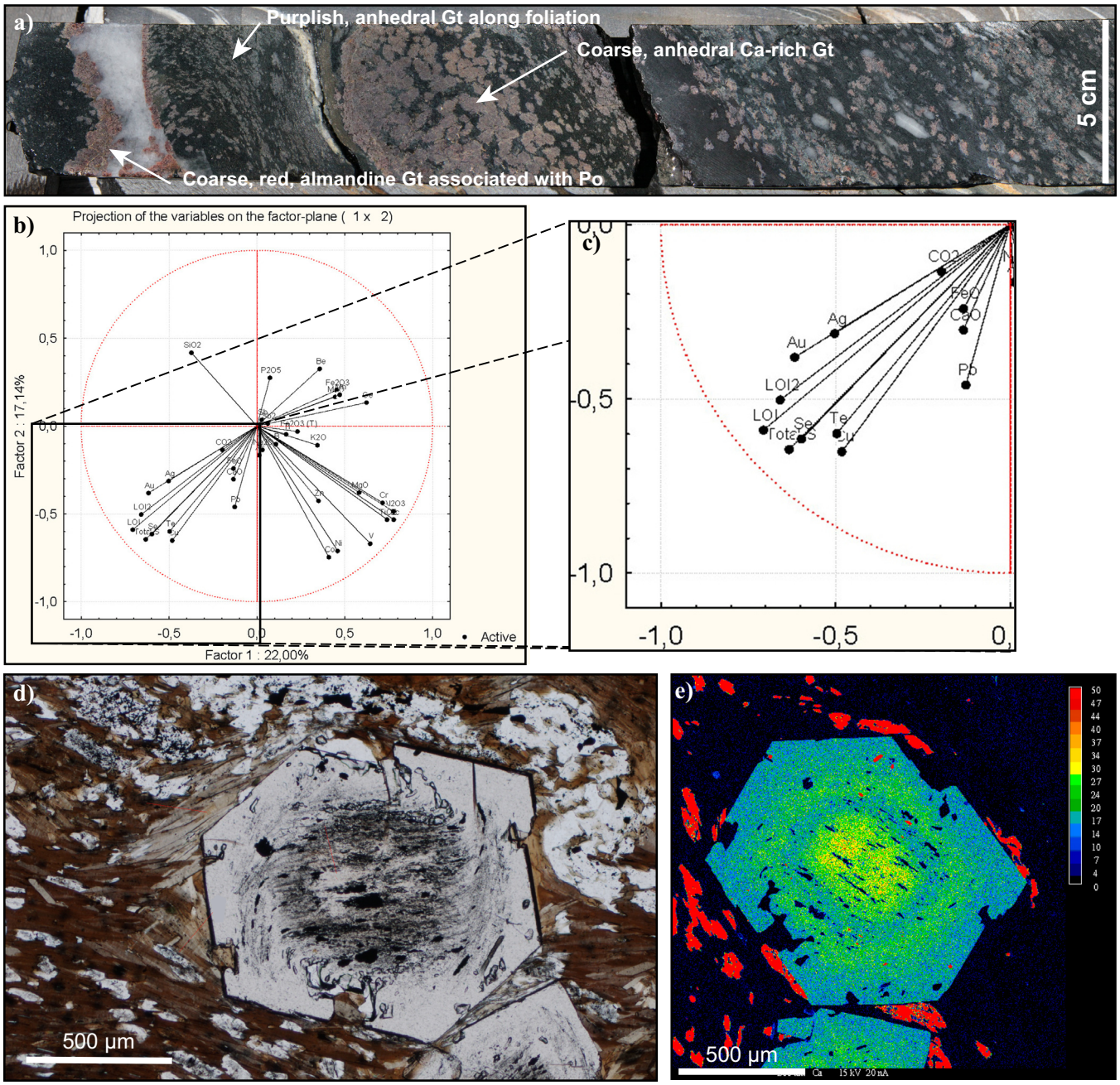

Figure 7. a) Photograph of drill-core sample containing three types of garnet (Gt): fine-grained, anhedral to subhedral, pale purple almandine distributed along the main foliation; coarse, subhedral, red almandine associated with pyrrhotite (po) in a quartz-dominated vein; and coarse, anhedral, pink to orange almandine associated with a calcite-rich veinlet. **b).** Principal component analysis (PCA) diagram for major elements and trace metals in the garnet-grunerite iron formation samples (4EA) using factors 1 and 2. **c)** Close-up of (b) showing the distinct association of trace metals with Au and S. **d)** Microphotograph of a garnet porphyroblast with a core containing folded inclusion trails marking an early fabric. **e)** Microprobe map of CaO content (percent) of the same garnet porphyroblast, note the halos of CaO enrichment concomitant with changes in orientation of inclusion trails.

may have reactivated a pre-existing unconformity.

The D_2 deformation is younger than 2846 Ma, which is the maximum age of the deformed ZHA (McNicoll et al., 2013). The D_2 deformation also deforms the margins of the 2870–2850 Ma North Caribou pluton and the 2860–2840 Ma Schade Lake gneissic complex (Breaks et al., 2001; Fig. 1). Competency contrast with the enclosed supracrustal rocks have induced strain partitioning during D_2 deformation and, thus, influenced the distribution and geometry of the BIF units during Au mineralization.

Recent geochronological work along the major shear zones of the area (Kelly et al., 2015) suggests that major faulting at ca. 2.75 to 2.71 Ga was followed by transpressive shear at ca. 2.60 to 2.56 Ga, and by late reactivation of pre-existing fault zones (e.g. Markop

shear zone: Fig. 1), occurring as late as 2.45 Ga. Field observations suggest this late reactivation event could correspond to the D_3 features that have been mapped in the present study area.

Mineralization and Alteration

Iron formations are extremely reactive to S-bearing fluids, thus Fe and S tend to combine to form pyrrhotite, which is the most abundant Au-associated sulphide at Musselwhite. The abundance of ore-related pyrrhotite at Musselwhite may originate from the metamorphic recrystallization of pyrite to pyrrhotite (Tomkins, 2010) or, more likely, because increasing metamorphic conditions favoured the crystallization of pyrrhotite during Au mineralization. Given the empirical correlation between pyrrhotite content and Au grade (1% pyrrhotite ≈ 1 ppm Au; W. McLeod, pers. comm., 2011) and the high Pearson correlation coefficient between Au and S in preliminary geochemical data (0.5–0.8), Au was most probably transported as thiocomplexes ($Au(HS)_2^-$ or $AuHS_0$; e.g. McCuaig and Kerrich, 1998), and released during pyrrhotite crystallization. In the silicate facies of the iron formation (unit 4EA), Fe is thought to have been derived from the breakdown of grunerite into Ca-amphibole, likely ferro-tschermakite and actinolite, which contain less Fe. In the adjacent clastic chert-magnetite facies of the iron formation (unit 4Bc), the large amount of magnetite provides a significant source of Fe to form pyrrhotite along with Fe-carbonate, especially ankerite. These replacements are interpreted to reflect the CaO enrichment usually associated with the alteration halo of orogenic Au mineralization (Dubé and Gosselin, 2007 and references therein).

The successive development of grunerite, almandine, and clinopyroxene indicate lower to mid-amphibolite-facies metamorphic conditions in iron formation (Klein, 2005). Relative timing of mineralization is best constrained by relationships with the structure and metamorphic paragenesis. Euhedral garnet porphyroblasts, e.g., at the Esker Docks exposure, have cores indicating a pre-existing foliation (S_1 or early S_2; Fig. 7d), and are characterized by an intermediate corona that recorded a subsequent progressive deformation, probably D_2, associated with increased Ca content (Fig. 7e). Euhedral outer rims that overprint the main S_2 foliation indicate late to post-D_2 growth and suggest that peak metamorphic temperature occurred during the latter stages of D_2 deformation. In high-grade zones, Au is present as inclusions and as fracture-filling in garnet porphyroblasts or in pressure-shadows developed along garnet crystals, suggesting that Au mineralization, or its local remobilization, occurred after the initiation of garnet porphyroblast crystallization during active D_2 deformation.

Stable isotope data (Isaac, 2008), coupled with the trace element signature of Au mineralization (e.g. Ag, Cu, Se, Te; Fig. 7b,c), suggest that the Musselwhite deposit is compatible with the metamorphic end-member of the greenstone-hosted Au deposit group (i.e. ore-fluids that are mainly of metamorphic origin; cf. Dubé and Gosselin, 2007). Syn-D_2 major compression (flattening-dominated) of rheologically contrasting units in the mine area induced the development of discrete subvertical high-strain zones in the iron formation, along with intense folding. Preliminary interpretations of our observations and data suggest that Au-bearing fluids were channelled into the high-strain zones and also migrated into adjacent F_2 fold hinge zones, which constituted areas of lower pressure suitable for trapping gold mineralization. Moreover, the Fe-rich, highly reactive 4EA NIF unit caused the destabilization of the Au-transporting agents and facilitated Au precipitation (a chemical trap). So, the rheological contrasts between the NIF and the surrounding igneous rocks (lithological/stratigraphic trap), at amphibolite-facies conditions, and its high-iron content (a chemical trap) explains the preferential deposition of Au in the iron formation at Musselwhite.

Biczok et al. (2012) published Sm-Nd isotopic analyses on several euhedral, red, almandine garnets spatially associated with Au that yielded a preferred age of 2690 ± 9 Ma, which is interpreted as the age of Au mineralization at Musselwhite. Newly acquired U-Pb SHRIMP (Sensitive High Resolution Ion Microprobe) in situ analyses of monazite grains in the garnet-biotite schist (unit 4F), conducted within this project, give a preliminary age of 2666 ± 6 Ma, which is interpreted to represent the timing of peak metamorphism. Analyzed monazite grains were located in the biotite matrix and in inclusion-poor outer rims of garnet porphyroblasts that appear to have grown during late- to slightly post-D_2 deformation, similar to the outermost rim of the garnet in Figure 6d. Given this relationship and the strong link between metamorphic paragenesis and mineralization, this monazite age is interpreted as a minimum age for the main Au mineralization event. As the D_2 deformation is younger than 2846 Ma, the bulk of the gold mineralization is bracketed between 2846 and 2666 Ma.

IMPLICATIONS FOR EXPLORATION

The interpretation of kilometre-scale F_1 folding in the Opapimiskan Lake area has implications for the location and geometry of prospective iron formation horizons and may thus provide new regional exploration targets. A strong D_2 strain gradient is documented in supracrustal rocks of the North Caribou greenstone belt, increasing northeastward toward the tight F_2 fold hosting the Musselwhite deposit and culminating at the

tectonic contact with the Shade Lake gneissic complex of the Island Lake Domain. This major first-order tectonic boundary, the early stage unconformity and/or thrust fault at the contact between the Opapimiskan-Markop and the adjacent Zeemel-Heaton assemblages, and the recently documented presence of polymictic conglomerate in the upper stratigraphic sequence (Fig. 1) are all critical features typically found in greenstone-hosted orogenic Au districts (e.g. Goldfarb et al., 2005; Robert et al., 2005; Dubé and Gosselin, 2007, Bleeker, 2012 and references therein). They provide targets for exploration throughout the greenstone belt, especially where associated with second-order D_2 structures affecting highly reactive BIF.

FUTURE WORK

Variations in mineral assemblages and chemistry between distal (barren) and proximal (mineralized) iron formation facies characterize the hydrothermal footprint of the deposit. Garnet porphyroblasts are present in various lithologies (Fig. 4a) and display multiple growth phases (Fig. 7d,e). Future work will include additional petrographic description to investigate relationships and timing of mineral growth. Mineral chemistry will also be used to better understand individual element variations in whole rock lithogeochemical data, such as the decoupling between Mn that is contained in the garnet cores, and thus isolated from subsequent hydrothermal events, and Mg that is contained in the matrix amphibole.

Ongoing spatial analysis and integration of the lithogeochemical database will allow characterization of the distribution and relative timing of the various types of alteration present at Musselwhite. Targeted LA-ICP-MS elemental mapping of sulphide minerals (cf. Cabri and Jackson, 2011) from samples of the ZHA will also document the evolution and distribution of trace metals during metamorphism and deformation, as was completed previously on pyrite nodules from an argillite unit of the West Antiform area (Jackson et al., 2013).

Multiple occurrences of polymictic conglomerates within the ZHA have been recently documented and subsequently sampled for geochronology study. The results will need to be interpreted in light of the geological setting of each outcrop and will likely impact the current stratigraphic model in the Opapimiskan Lake area.

ACKNOWLEDGEMENTS

This report emanates from the ongoing Ph.D. thesis undertaken by the first author (W. Oswald) at the Institut national de la recherche scientifique (INRS-ETE), as part of the Targeted Geoscience Initiative 4 (Lode Gold project) of Natural Resources Canada. Additional support is provided by Natural Sciences and Engineering Research Council of Canada (NSERC), Fonds de recherche du Québec (FRQNT) and Goldcorp Inc., through the Industrial Innovation Scholarship program (BMP/IIS) to the first author (W. Oswald). We sincerely thank Goldcorp Inc. Musselwhite Mine for access to the property, to drill core, and various data sets, and for chartered transport and accommodation. Rohan Millar, Jim Edwards, and Bill McLeod, as well as the entire production and exploration team of the Musselwhite Mine, are acknowledged for their time, operational support, interest in this project, and for sharing their unique knowledge of the deposit. The project has also benefited from the collaboration and discussions with Phil Thurston from the Laurentian University, Dave Schneider, Keiko Hattori, Colter Kelly, Emilie Gagnon, and Octavia Bath from the University of Ottawa and Wouter Bleeker of the GSC Ottawa. The manuscript has strongly benefited from Phil Thurston's constructive comments and suggestions.

REFERENCES

Baldwin, G.J., 2011. The sedimentology and geochemistry of banded iron formations of the Deloro assemblage, Barlett Dome area, Abitibi greenstone belt, Ontario, Canada: Implications for BIF deposition and greenstone belt formation; M.Sc. Thesis, Laurentian University, Sudbury, Ontario, 121 p.

Biczok, J., Hollings, P., Klipfel, P., Heaman, L., Maas, R., Hamilton, M., Kamo, S., and Friedman, R., 2012. Geochronology of the North Caribou greenstone belt, Superior Province Canada: Implications for tectonic history and gold mineralization at the Musselwhite mine; Precambrian Research, v. 192-195, p. 209−230.

Bleeker, W., 2012. Targeted Geoscience Initiative 4. Lode gold deposits in ancient deformed and metamorphosed terranes: The role of extension in the formation of Timiskaming basins and large gold deposits, Abitibi greenstone belt—A Discussion, *In:* Summary of field work and other activities 2012; Ontario Geological Survey, Open File Report 6280, p.47-1 to 47-12.

Breaks, F.W., Bartlett, J.R., Osmani, I.A., Finamore, P.F., and Wallace, H., 1985. Opapimiskan lake project: Precambrian and Quaternary geology of the North Caribou Lake area, district of Kenora, Patricia Portion, *In:* Summary of field work and other activities 1985; Ontario Geological Survey, Miscellaneous Paper 126, p. 268–276.

Breaks, F.W. and Bartlett, J.R., 1991. Geology of the Eyapamikama Lake Area; Ontario Geological Survey, Open File Report 5792, 132 p.

Breaks, F.W., Bartlett, J.R., de Kemp, E.A., and Osmani, I.A., 1991. Geology of the Doubtful-Akow lakes area, district of Kenora; Ontario Geological Survey, Open File Report 5795, 131 p.

Breaks, F.W., Osmani, I.A., and de Kemp, E.A., 2001. Geology of the North Caribou Lake area, northwestern Ontario; Ontario Geological Survey, Open File Report 6023, 80 p.

Cabri, L.J. and Jackson, S.E., 2011. New developments in characterization of sulphide refractory gold ores, In: Proceedings of the 50th Conference of Metallurgists, October 2-5, 2011, Montreal, Quebec, p. 51–62.

Couture, G., 1995. Stratigraphy, lithology, structural history and grade distribution of the Musselwhite gold prospect; unpublished report for Placer Dome Canada Limited, 102 p.

Cox, S. F., Knackstedt, M.A., and Braun, J., 2001. Principles of structural control on permeability and fluid flow in hydrothermal systems; Reviews in Economic Geology, v. 14, p. 1–24.

Davies, J.F., Whitehead, R.E.S., Cameron, R.A., and Duff, D., 1982. Regional and local patterns of CO_2-K-Rb-As alteration: A guide to gold in the Timmins area, *In:* Geology of Canadian Gold Deposits (ed.) R.W. Hodder and W. Petruk; Canadian Institute of Mining and Metallurgy, Special Volume 24, p.130–143.

Dubé, B., Mercier-Langevin, P., Castonguay, S., McNicoll, V.J., Pehrsson, S.J., Bleeker, W., Schetselaar, E.M., and Jackson, S., 2011. Targeted Geoscience Initiative 4. Lode gold deposits in ancient deformed and metamorphosed terranes – footprints and exploration implications: a preliminary overview of themes, objectives and targeted areas, *In:* Summary of field work and other activities 2011; Ontario Geological Survey, Open File Report 6270, p. 38-1 to 38-10.

Dubé, B. and Gosselin, P., 2007. Greenstone-hosted quartz-carbonate vein deposits, *In:* Mineral Deposits of Canada: A Synthesis of Major Deposit Types, District Metallogeny, the Evolution of Geological Provinces, and Exploration Methods, (ed.) W.D. Goodfellow; Geological Association of Canada, Mineral Deposits Division, Special Publication, No. 5, p. 49–73.

Duff, J., 2014. A geochemical and isotopic investigation of metasedimentary rocks from the North Caribou greenstone belt, western Superior Province, Canada; M.Sc. Thesis, University of Ottawa, Ottawa, Ontario, Canada, 189 p.

Goldfarb, R.J., Baker, T., Dubé, B., Groves, D.I., Hart C.J.R., and Gosselin, P., 2005. Distribution, character, and genesis of gold deposits in metamorphic terranes, *In:* Economic Geology 100th Anniversary Volume, (ed.) J.W. Hedenquist, J.F.H. Thompson, R.J. Goldfarb, and J.P. Richards; Society of Economic Geology, p. 407–450.

Gourcerol, B., Thurston, P.C., Kontak, D.J., and Côté-Mantha, O., 2014. Interpretations and implications of preliminary LA ICP-MS analysis of chert for the origin of geochemical signatures in banded-iron-formations from the Meadowbank gold deposit, western Churchill Province, Nunavut; Geological Survey of Canada, Current Research 2013-20, 22 p. doi:10.4095/293129

Gourcerol, B., Thurston, P.C., Kontak, D.J., Côté-Mantha, O., and Biczok, J., 2015. Depositional setting of Algoma-type banded iron formation from the Meadowbank, Meliadine and Musselwhite gold deposits, *In:* Targeted Geoscience Initiative 4: Contributions to the understanding of Precambrian lode gold deposits and implications for exploration, (ed.) B. Dubé and P. Mercier-Langevin; Geological Survey of Canada, Open File 7852, p. 55–68.

Hall, R.S. and Rigg, D.M., 1986. Geology of the West Anticline Zone, Musselwhite Prospect, Opapimiskan Lake, Ontario, Canada, *In:* Proceedings of Gold '86 Symposium, September 28th to October 1st, Toronto, Canada, p. 124–136.

Hollings, P. and Kerrich, R., 1999. Trace element systematics of ultramafic and mafic volcanic rocks from the 3 Ga North Caribou greenstone belt, northwestern Superior Province; Precambrian Research, v. 93, p. 257–279.

Isaac, C., 2008. Stable isotope (N, O, H) geochemistry, petrology and compositions of biotite of the Musselwhite Mine, Ontario: implications for mineralization; M.Sc. Thesis, Lakehead University, Thunder Bay, Ontario, 133 p.

Jackson S., Gao, J., and Dubé, B., 2013. Nouveaux développements applicables à l'analyse des éléments en traces dans les dépôts de minéraux et à la cartographie utilisée pour la recherche et l'exploration des gisements de minerai : exemples de gisements d'or du Québec et de l'Ontario, *In:* Résumés des conférences et des photoprésentations, Québec Mines, 11-14 Novembre, 2013, Québec, Québec, p. 16.

James, H.L., 1954. Sedimentary facies of iron-formations; Economic Geology, v. 49, p. 235–293.

Kalbfleisch, N., 2012. Crustal-scale shear zones recording 400 M.Y. of tectonic activity in the North Caribou greenstone belt, western Superior Province of Canada; M.Sc. Thesis, University of Ottawa, Ottawa, Ontario, 162 p.

Kamber, B.S., Greig A., and Collerson, K.D., 2005. A new estimate for the composition of weathered young upper continental crust from alluvial sediments, Queensland, Australia; Geochimica et Cosmochimica Acta, v. 69, p. 1041–1058.

Kelly, C.J. and Schneider, D.A., 2015. Insights into the timing of mineralization and metamorphism in the North Caribou greenstone belt, western Superior Province, *In:* Targeted Geoscience Initiative 4: Contributions to the understanding of Precambrian lode gold deposits and implications for exploration, (ed.) B. Dubé and P. Mercier-Langevin; Geological Survey of Canada, Open File 7852, p. 245–253.

Klein, C., 2005. Some Precambrian banded iron-formations (BIFs) from around the world: Their age, geologic setting, mineralogy, metamorphism, geochemistry, and origin; American Mineralogist, v. 90, p. 1473–1499.

McCuaig, C.T. and Kerrich, R., 1998. P-T-t-deformation-fluid characteristics of lode gold deposits: evidence from alteration systematics; Ore Geology Reviews, v. 12, p. 381–453.

McLean, T.J. and Barrett, W.H., 1993. Lithogeochemical techniques using immobile elements; Journal of Geochemical Exploration, v. 48, p. 109–133.

McNicoll, V., Dubé, B., Biczok, J., Castonguay, S., Oswald, W., Mercier-Langevin, P., Skulski, T., and Malo, M., 2013. The Musselwhite gold deposit, North Caribou greenstone belt, Ontario: new high-precision U-Pb ages and their impact on the geological and structural setting of the deposit, *In:* Program with Abstracts; Geological Association of Canada-Mineralogical Association of Canada joint annual meeting, May 22-24, 2013, Winnipeg, Manitoba, v. 36, p. 142.

McNicoll, V., Dubé, B., Castonguay, S., Oswald, W., Biczok, J., Mercier-Langevin, P., Skulski, T., and Malo, M., submitted. The world-class Musselwhite BIF-hosted gold deposit, Superior Province, Canada: new high-precision U-Pb geochronology and implications for the geological and structural setting of the deposit and gold exploration; Precambrian Research.

Moran, P., 2008. Lithogeochemistry of the Sedimentary Stratigraphy and Metosomatic Alteration in the Musselwhite Gold Deposit, North Caribou Lake Belt, Superior Province, Canada: Implications for Deposition and Mineralization: M.Sc. Thesis, Lakehead University, Thunder Bay, Ontario, 411 p.

Oswald, W., Dubé, B., Castonguay, S., McNicoll, V., Biczok, J., Mercier-Langevin, P., Malo, M., and Skulski, T., 2014a. New insights on the geological setting of the world-class Musselwhite gold deposit, Superior Province, northwestern Ontario, *In:* Program with Abstracts; Geological Association of Canada-Mineralogical Association of Canada joint annual meeting, May 21-23, 2014, v. 37, p. 311.

Oswald, W., Dubé, B., Castonguay, S., McNicoll, V., Biczok, J., Mercier-Langevin, P., Malo, M., and Skulski, T., 2014b. New insights on the structural and geological setting of the world-class Musselwhite gold deposit, Superior Province, Northwestern Ontario; Geological Survey of Canada Open File 7633, 1 poster.

Oswald, W, Castonguay, S., Dubé, B., Mercier-Langevin, P., Malo, M., Biczok, J., and McNicoll, V., 2014c. Targeted Geoscience Initiative 4. Lode gold deposits in ancient deformed and metamorphosed terranes: detailed mapping of key stripped outcrops in the Musselwhite Mine area, Northwestern Ontario, and implications for the geological and structural setting of the gold

mineralization, *In:* Summary of Field Work and other Activities 2014; Ontario Geological Survey, Open File Report 6300, p. 42-1 to 42-15.

Percival J.A., 2007. Geology and metallogeny of the Superior Province, Canada, *In:* Mineral Deposits of Canada: A Synthesis of Major Deposit Types, District Metallogeny, the Evolution of Geological Provinces, and Exploration Methods, (ed.) W.D. Goodfellow; Geological Association of Canada, Mineral Deposits Division, Special Publication No. 5, p. 903–928.

Piroshco, D.W., Breaks, F.W., and Osmani, I.A., 1989. The geology of gold prospects in the North Caribou Lake greenstone belt, district of Kenora, northwestern Ontario; Ontario Geological Survey, Open File Report 5698, 94 p.

Pitcairn, I., Damon, A., and Teagle, H., 2006. Sources of metals and fluids in orogenic gold deposits: Insights from the Otago and Alpine schists, New Zealand; Economic Geology, v. 101, p. 1525–1546.

Rayner, N., and Stott, G.M., 2005. Discrimination of Archean domains in the Sachigo Subprovince: a progress report on the geochronology, *In:* Summary of Field Work and other Activities 2005, Ontario Geological Survey, Open File Report 6172, p. 10-1 to 10-21.

Robert, F., Poulsen, K.H., Cassidy, K.F., and Hodgson, C.J., 2005. Gold metallogeny of the Superior and Yilgarn cratons, *In:* Economic Geology 100th Anniversary Volume, (ed.) J.W. Hedenquist, J.F.H. Thompson, R.J. Goldfarb, and J.P. Richards; Society of Economic Geology, p. 1001–1033.

Ross, P. S. and Bédard, J. H., 2009. Magmatic affinity of modern and ancient subalkaline volcanic rocks determined from trace-element discriminant diagrams; Canadian Journal of Earth Sciences, v. 46, p. 823–839.

Stott, G.M., Corkery, M.T., Percival, J.A., Simard, M., and Goutier, J., 2010. A revised terrane subdivision of the Superior Province, *In:* Summary of Field Work and other Activities 2010; Ontario Geological Survey, Open File Report 6260, p. 20-1 to 20-10.

Sun, S.-S. and McDonough, W.F., 1989. Chemical and isotope systematics of oceanic basalts: implications for mantle composition and processes, *In:* Magmatism in the Ocean Basins, (ed.) A.D. Saunders and M.J. Norry; Geological Society, London, Special Publication No. 42, p. 313–345.

Thurston, P., Osmani, I. and Stone, D., 1991. Northwestern Superior Province: review and terrane analysis, *In:* Geology of Ontario, Special Volume 4, Part 1, (ed.) P.C. Thurston, H.R. Williams, R.H. Sutcliffe, and G.M. Stott; Ontario Geological Survey, p. 80–142.

Tomkins, A., 2010. Windows of metamorphic sulfur liberation in the crust: Implications for gold deposit genesis; Geochimica et Cosmochimica Acta; v. 74, p. 3246–3259.

Van Lankvelt, A., 2013. Protracted magmatism within the North Caribou Terrane, Superior Province: petrology, geochronology, and geochemistry of Meso- to Neoarchean TTG suites; M.Sc. thesis, University of Ottawa, Ottawa, Ontario, 204 p.

GEOLOGICAL SURVEY OF CANADA
OPEN FILE 7852

Targeted Geoscience Initiative 4: Contributions to the Understanding of Precambrian Lode Gold Deposits and Implications for Exploration

Banded iron formation-hosted gold mineralization in the Geraldton area, northwestern Ontario: Structural setting, mineralogical characteristics, and geochronology

Zsuzsanna Tóth[1], Bruno Lafrance[1], Benoît Dubé[2], Vicki J. McNicoll[3], Patrick Mercier-Langevin[2], and Robert A. Creaser[4]

[1]Laurentian University, Sudbury, Ontario
[2]Geological Survey of Canada, Québec, Quebec
[3]Geological Survey of Canada, Ottawa, Ontario
[4]University of Alberta, Edmonton, Alberta

2015

Recommended citation

Tóth, Z., Lafrance, B., Dubé, B., McNicoll, V.J., Mercier-Langevin, P., and Creaser, R.A., 2015. Banded iron formation-hosted gold mineralization in the Geraldton area, northwestern Ontario: Structural setting, mineralogical characteristics, and geochronology, *In:* Targeted Geoscience Initiative 4: Contributions to the Understanding of Precambrian Lode Gold Deposits and Implications for Exploration, (ed.) B. Dubé and P. Mercier-Langevin; Geological Survey of Canada, Open File 7852, p. 85–97.

Publications in this series have not been edited; they are released as submitted by the author.

Contribution to the Geological Survey of Canada's Targeted Geoscience Initiative 4 (TGI-4) Program (2010–2015)

TABLE OF CONTENTS

Banded iron formation-hosted gold mineralization in the Geraldton area, northwestern Ontario: Structural setting, mineralogical characteristics and geochronology

Zsuzsanna Tóth[1]*, Bruno Lafrance[1], Benoît Dubé[2], Vicki J. McNicoll[3], Patrick Mercier-Langevin[2], and Robert A. Creaser[4]

[1]Mineral Exploration Research Centre, Department of Earth Sciences, Goodman School of Mines, Laurentian University, Sudbury, Ontario P3E 2C6
[2]Geological Survey of Canada, 490 rue de la Couronne, Québec, Quebec G1K 9A9
[3]Geological Survey of Canada, 601 Booth Street, Ottawa, Ontario K1A 0E8
[4]Department of Earth & Atmospheric Sciences, University of Alberta, 1-26 Earth Sciences Building, University of Alberta, Edmonton, Alberta T6G 2E3
*Corresponding author's e-mail: ztoth@laurentian.ca

ABSTRACT

Renewed exploration activities in the Beardmore-Geraldton belt in the Archean Superior Province, northwestern Ontario, produced large stripped outcrops and new drill cores that revealed a wealth of new information on the structural and lithological settings of gold mineralization in this past-producing mining camp. The aims of this project are to establish the key geological parameters that controlled the genesis and distribution of gold mineralization in the area and to define geological and exploration models that incorporate the revised knowledge of the geological and structural setting, relative timing, mineralogical characteristics and geochemical footprints of the gold mineralization to fill in knowledge gaps about the gold distribution and geometry in the belt. The Beardmore-Geraldton belt consists of 0.15 to 10 km-wide panels of Archean metasedimentary rocks alternating with 1 to 5 km-wide panels of metavolcanic rocks. The older, ca. 2725 Ma metavolcanic panels are in fault contact with the younger metasedimentary panels. The deposition of the sedimentary rocks started at <2700 Ma, as indicated by the youngest detrital zircons dated from the Central and Southern Metasedimentary units and was complete by 2694.0 ± 1.0 Ma, the crystallization age of the crosscutting quartz-feldspar porphyry.

The Beardmore-Geraldton belt underwent four deformation events. During D_1 deformation, the metavolcanic-metasedimentary sequences and the quartz-feldspar porphyry were thrust-imbricated and folded by F_1 folds. The D_1 event occurred between 2694 Ma, the age of the quartz-feldspar porphyry dyke in Geraldton, and 2690 ± 1 Ma, the age of the post-D_1 Croll Lake stock. During D_2 deformation, south-to-north shortening, regional-scale, west-plunging F_2 folds and axial-planar, east-trending, steeply dipping S_2 foliation were formed. The S_2 foliation has been folded by S-shaped F_3 folds that are associated with an east-trending, spaced axial-planar S_3 cleavage, indicating a previously unrecognized D_3 sinistral shear event in the belt. These three deformation events were overprinted by a D_4 dextral transpression event. In the Beardmore-Geraldton belt, gold mineralization is typically hosted by mudstone, sandstone, banded iron formation and quartz-feldspar porphyry. Gold mineralization is commonly associated with locally auriferous quartz-carbonate veins. The mineralized quartz-carbonate±tourmaline vein selvages are characterized by semi-massive sulphide-sericite-carbonate replacement alteration halos where hosted in banded iron formation. A similar alteration halo is present in veins that are hosted in mudstone, sandstone and quartz-feldspar porphyry, although the sulphides are less abundant than when the veins are hosted in banded iron formation.

At least two gold-mineralizing events, including possible remobilization, took place during the tectonic evolution of the belt. Gold-rich quartz-carbonate±tourmaline veins and the associated sericite-carbonate-sulphide alteration halos are folded by F_1 folds, suggesting that the first gold-bearing event is related to the early phases of the D_1 deformation. East-northeast- to east-trending, locally auriferous quartz-carbonate-tourmaline-sulphide veins cut F_2 fold hinges but are folded by S-shaped F_3 folds, suggesting a second, early D_3 auriferous episode in the district. Northwest-trending sulphide-rich veins, which cut across early D_3 tourmaline-rich veins and are folded by gentle Z-shaped F_4 folds, may also have carried or remobilized some gold mineralization during D_4 dextral transpression. An increase in gold grade is associated with elevated As, Te, Sb, and W concentrations and sericitization index. It is hoped that the new data and interpretation generated as part of this project will contribute to further mineral exploration success by defining new structural targets and establishing geochemical footprint vectors.

Tóth, Z., Lafrance, B., Dubé, B., McNicoll, V.J., Mercier-Langevin, P., and Creaser, R.A., 2015. Banded iron formation-hosted gold mineralization in the Geraldton area, northwestern Ontario: Structural setting, mineralogical characteristics, and geochronology, *In:* Targeted Geoscience Initiative 4: Contributions to the Understanding of Precambrian Lode Gold Deposits and Implications for Exploration, (ed.) B. Dubé and P. Mercier-Langevin; Geological Survey of Canada, Open File 7852, p. 85–97.

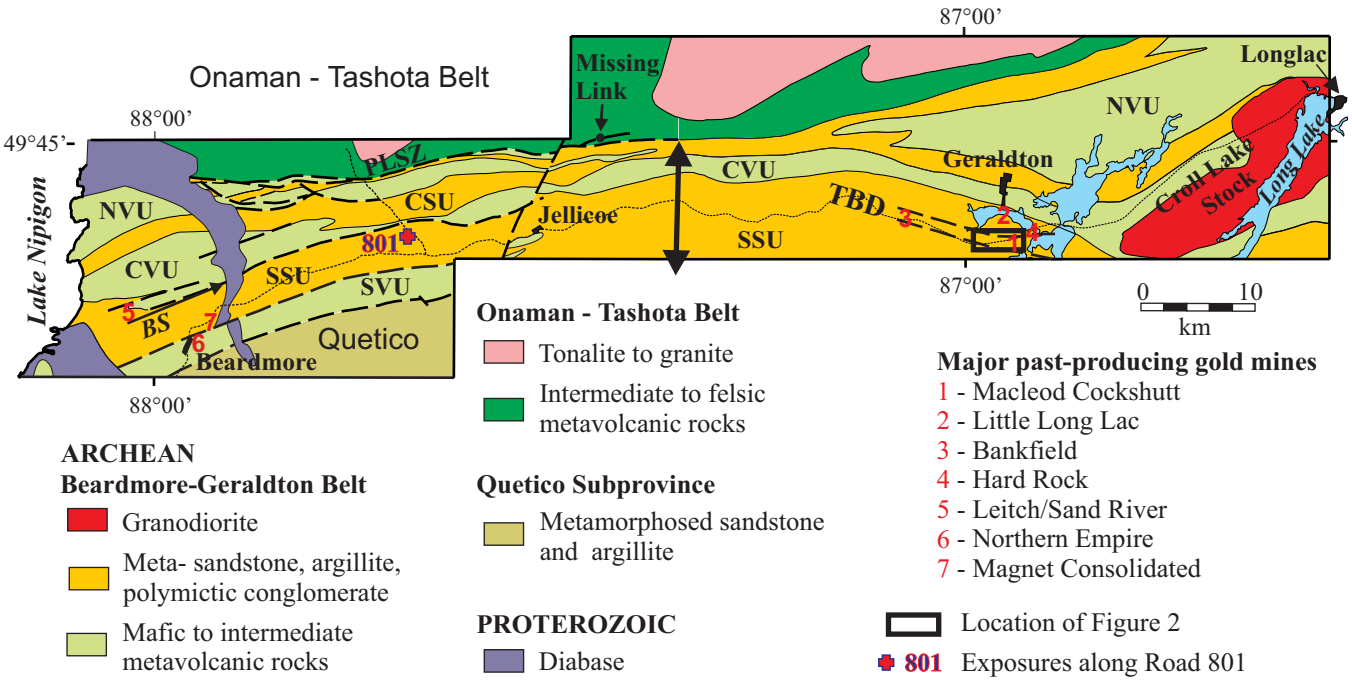

Figure 1. Regional geological map of the Beardmore-Geraldton greenstone belt (modified after Lafrance et al., 2004 and references therein). Abbreviations: BS = Beardmore syncline; NSU, CSU, SSU = Northern, Central, and Southern Metasedimentary units; NVU, CVU, SVU = Northern, Central, and Southern Metavolcanic units; PLSZ = Paint Lake Shear Zone; TBD = Tombill-Bankfield Deformation zone.

INTRODUCTION

The Beardmore-Geraldton belt (BGB) is a transitional terrane at the boundary between the Quetico and the Wabigoon subprovinces in the western Superior Province, northwestern Ontario (Devaney and Williams, 1989). Over 4.1 million ounces of gold were produced from several deposits between 1933 and 1970, after which mining ceased in the area (Pye, 1952; Horwood and Pye, 1955; Mason and McConnell, 1982; Mason and White, 1986). Renewed exploration has significantly increased the known gold resources in Geraldton. Premier Gold Mines Ltd. delineated an additional 4.87 Moz and 2.74 Moz in indicated and inferred resource categories, respectively, and, at the time this paper was written, is planning open-pit operations on two of the deposits (Press Release on July 8, 2014; www.premiergoldmines.com).

In order to better define the controls on gold mineralization and thereby refine existing geological and exploration models, new research activity was initiated in the BGB as part of the Lode Gold project of the Targeted Geoscience Initiative 4 program (TGI-4) of Natural Resources Canada (Dubé et al., 2011). The main objective of the project was to determine the geological parameters that controlled gold mineralization in the BGB and their relative timing, thereby contributing to a better understanding of lode gold deposits. Our specific objectives were to (1) determine the structural and lithological setting of the deposits; (2) characterize the geochemical footprint of the gold mineralization and its associated hydrothermal alteration envelope; (3) interpret the chronology of gold-mineralization event(s) relative to the tectonic evolution of the belt; and (4) develop tectonic and metallogenic models for the belt.

REGIONAL GEOLOGY

The BGB consists of six, east-trending, intercalated metavolcanic and metasedimentary units, which are separated by dextral shear zones (Fig. 1). The Northern (NVU), Central (CVU) and Southern Metavolcanic (SVU) units formed in back-arc, island arc, and oceanic crust environments, respectively (Tomlinson et al., 1996). The Northern (NSU), Central (CSU), and Southern (SSU) Metasedimentary units consist dominantly of polymictic conglomerate (NSU), conglomerate and turbiditic sandstone interbedded with Algoma-type banded iron formation (CSU), and turbiditic sandstone interbedded with polymictic conglomerate and banded iron formation (SSU) (Pye, 1952; Horwood and Pye, 1955; Mackasey, 1975, 1976; Barett and Fralick, 1985; Devaney and Fralick, 1985; Devaney and Williams, 1989). From north to south, the metasedimentary units represent alluvial fan or braided-plain fluvial environments (NSU), subaqueous fan and/or prodelta environments (CSU), and submarine fan and/or basin-plain environments (SSU) (Mackasey, 1975, 1976; Barrett and Fralick, 1985; Devaney and Williams, 1989; Fralick and Pufahl, 2006).

Previous structural studies documented three tectonic events across the BGB. The D_1 deformation is interpreted as a regional thrusting event, which imbricated the metavolcanic and metasedimentary units during closure of foreland basin, the Quetico subprovince, between the converging Wabigoon subprovince and the Wawa subprovince (Devaney and Williams, 1989; Williams, 1990). Outcrop-scale, isoclinal, F_1 folds with no associated cleavage formed during D_1 deformation (Williams, 1986, 1987a,b, 1989, 1990; Devaney and Williams, 1989; Lafrance et al., 2004), which was bracketed between 2696 ± 2 Ma, the youngest detrital zircon age in the Central and Southern Metasedimentary units (Hart et al., 2002; Fralick et al., 2006) and 2691 $^{+3}/_{-2}$ Ma, the crystallization age of a crosscutting quartz feldspar porphyry dyke (Anglin, 1987; Anglin et al., 1988; Lafrance et al., 2004). During the D_2 south-to-north shortening, the BGB underwent tight, upright, regional F_2 folding producing an east-trending, steeply dipping, axial-planar S_2 cleavage and a steeply plunging mineral stretching lineation (L_2) (Lafrance et al., 2004). During D_3 dextral transpression, the unit-bounding thrust faults were reactivated as dextral shear zones and a second regional cleavage formed axial-planar to asymmetrical, west-plunging F_3 folds (Lafrance et al., 2004). During the same progressive deformation event, F_3 and S_3 were refolded and overprinted by Z-shaped $F_{3'}$ folds and axial-planar $S_{3'}$ crenulation cleavage (Lafrance et al., 2004; DeWolfe et al., 2007).

Gold in the area occurs in quartz-carbonate veins and their hydrothermal alteration selvages. Previous work indicates that the veins are parallel to S_3 and overprint F_2 and F_3 fold hinges, and thus were interpreted to have been formed during the D_3 dextral transpression (Pye, 1952; Horwood and Pye, 1955; Beakhouse, 1984; Anglin and Franklin, 1985; Macdonald, 1988; Kresz and Zayachivsky, 1991; Lafrance et al., 2004; DeWolfe et al., 2007). Our work in the belt indicates that some of these interpretations may need to be revisited.

STRUCTURAL EVOLUTION OF THE BEARDMORE-GERALDTON BELT

Detailed mapping and description of 8 large stripped exposures, including lithology, primary texture, structure, veining, alteration and mineralization, were completed to improve the understanding of the relative timing of the gold mineralization, as well as the deformation history of the Beardmore-Geraldton belt. Mapping was aided by the use of a differential GPS, which proved to be essential for taking precise structural measurements on magnetic banded iron formation. Seven of these exposures are located south of Geraldton (Fig. 2), and the other is located west of Road 801, in the western part of the Beardmore-Geraldton greenstone belt (Fig. 1).

The complex, polyphased tectonic evolution of the BGB is summarized in Table 1. Excellent examples of F_1 folds (Fig. 3a) with an axial-plane S_1 cleavage are present in several outcrops. S_1 cleavage, which had not been recognized in previous studies, is expressed as a spaced, chlorite-defined cleavage parallel to bedding in metasedimentary rocks, as a continuous chloritic cleavage in mafic dykes (Fig. 3b), and as a strong crenulated, spaced cleavage (with an average spacing of ~1 mm) defined by sericite in quartz-feldspar porphyry dykes within the hinge of F_2 folds (Tóth et al., 2013a). During the D_2 compression, F_1 folds and the S_1 axial-planar foliation were refolded by regional, east-trending F_2 folds and overprinted by the associated S_2 axial-planar cleavage (Fig. 3c) (Lafrance et al., 2004; Tóth et al., 2013a, 2014b). S_2 cleavage is folded by tight to open S-shaped F_3 folds with an axial-planar, east-trending, and steeply dipping, S_3 crenulation cleavage (Fig. 3d). These structures formed during a previously unrecognized D_3 sinistral transcurrent shearing event (Tóth et al., 2013a). The D_4 dextral shearing event (D_3 of Lafrance et al., 2004) resulted in the formation of Z-shaped F_4 drag folds and an S_4 axial-planar cleavage (Fig. 3e) (Tóth et al., 2013a, 2014b). The S_4 cleavage is folded by Z-shaped $F_{4'}$ folds and overprinted by an $S_{4'}$ foliation in shear zones (Fig. 3f) (Lafrance et al., 2004; DeWolfe et al., 2007).

GOLD MINERALIZATION

Numerous samples were collected from stripped outcrops and drill core to characterize the host rocks, the nature of the gold mineralization and the associated hydrothermal footprint in the Geraldton area. Styles of gold mineralization differ according to their host rocks. In mudstone and sandstone, auriferous quartz-carbonate±tourmaline veins are surrounded by a strong yellow-brown sericite-Fe-carbonate-sulphide±chlorite alteration halo (Fig. 4a) (Tóth et al., 2013b, 2014b). In magnetite-rich banded iron formation, gold is associated with semi-massive sulphide-sericite-carbonate± chlorite alteration selvages surrounding quartz-carbonate±chlorite veins (Fig. 4b) (Tóth et al., 2013b). When hosted in quartz-feldspar porphyry, the auriferous quartz-carbonate±tourmaline veins are surrounded by a well developed sericite-iron-carbonate-sulphide alteration halo (Fig. 4c) (Tóth et al., 2013b, 2014b). Regardless of host rock, the dominant sulphide is pyrite; however, arsenopyrite, pyrrhotite and chalcopyrite are also present (Tóth et al., 2013b). Where arsenopyrite is present, the sulphides are zoned with a greater abundance of pyrite occuring next to the vein margins and a greater abundance of arsenopyrite further away from the vein margins (Tóth et al., 2013b). Gold occurs as fracture-fills or as inclusions in pyrite and arsenopyrite grains, but is also present as free grains in the veins (Tóth et al., 2013b).

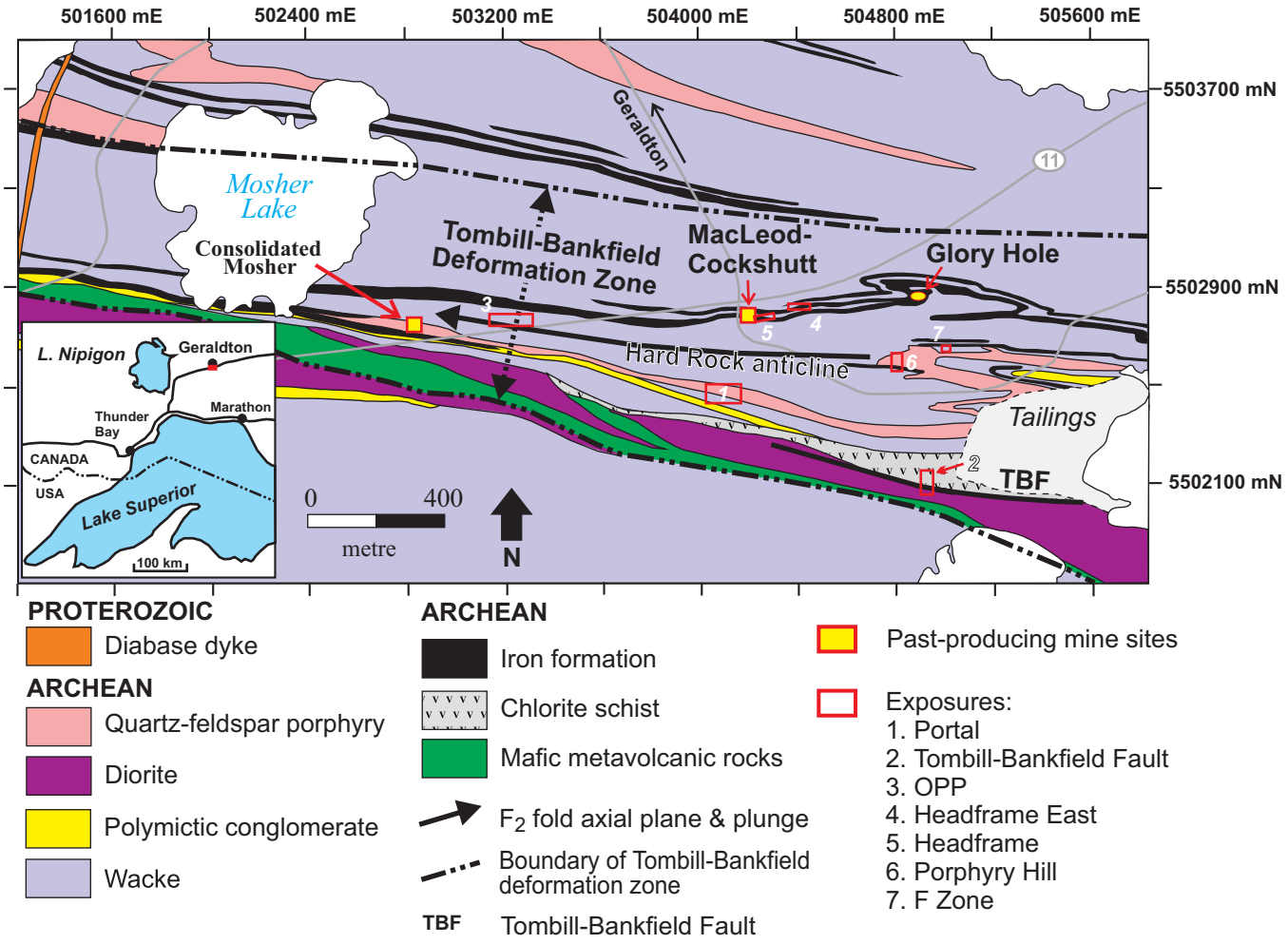

Figure 2. Simplified geological map of the Geraldton area showing the location of the mapped exposures (geology modified after Horwood and Pye, 1955, and Pye, 1952). The red rectangle in the inset shows the regional-scale location of the study area. Universal Transverse Mercator (UTM) co-ordinates are based on North American Datum 1927 (NAD27), zone 16.

Table 1. Summary of deformation and gold mineralization events in the Beardmore–Geraldton greenstone belt (Lafrance et al., 2004; Tóth et al., 2013a, 2014a,b). Abbreviations: ACW = anticlockwise; CW = clockwise; QFP = quartz-feldspar porphyry.

Regional Deformation Style	Description of Structures	
	Folding	Foliation
	Gold mineralization	
D_1 thrusting	Isoclinal, recumbent F_1 folds; up to 1 m in amplitude	Strong; appears in some mafic dykes and QFP; bedding-parallel in sedimentary rocks
D_2 north-south compression	Tight upright regional F_2 folds; plunge: 20–70°W; amplitude up to several km	East-trending, steeply-dipping S_2; axial-planar to F_2 folds; parallel or slightly CW/ACW of bedding
	Gold mineralization (or remobilization)	
D_3 sinistral transcurrent shear	Tight to open S-shaped F_3 folds; amplitude up to 10s of cm	East-trending, steeply-dipping S_3; axial-planar to F_3
	Gold mineralization (or remobilization)	
D_4 dextral transpression *(D3 in Lafrance et al., 2004)*	Z-shaped F_4 folds; plunge: 20–60°W; amplitude up to several km	East-northeast-trending, steeply-dipping regional S_4; axial-planar to F_4; oriented ACW to bedding
	Dextral east-trending shear zones localized along S_2 and lithological contacts	
	Z-shaped F_4' drag folds over-printing foliation in shear zones	Sinistral-slip S_4' crenulation clevage; axial-planar to F_4'

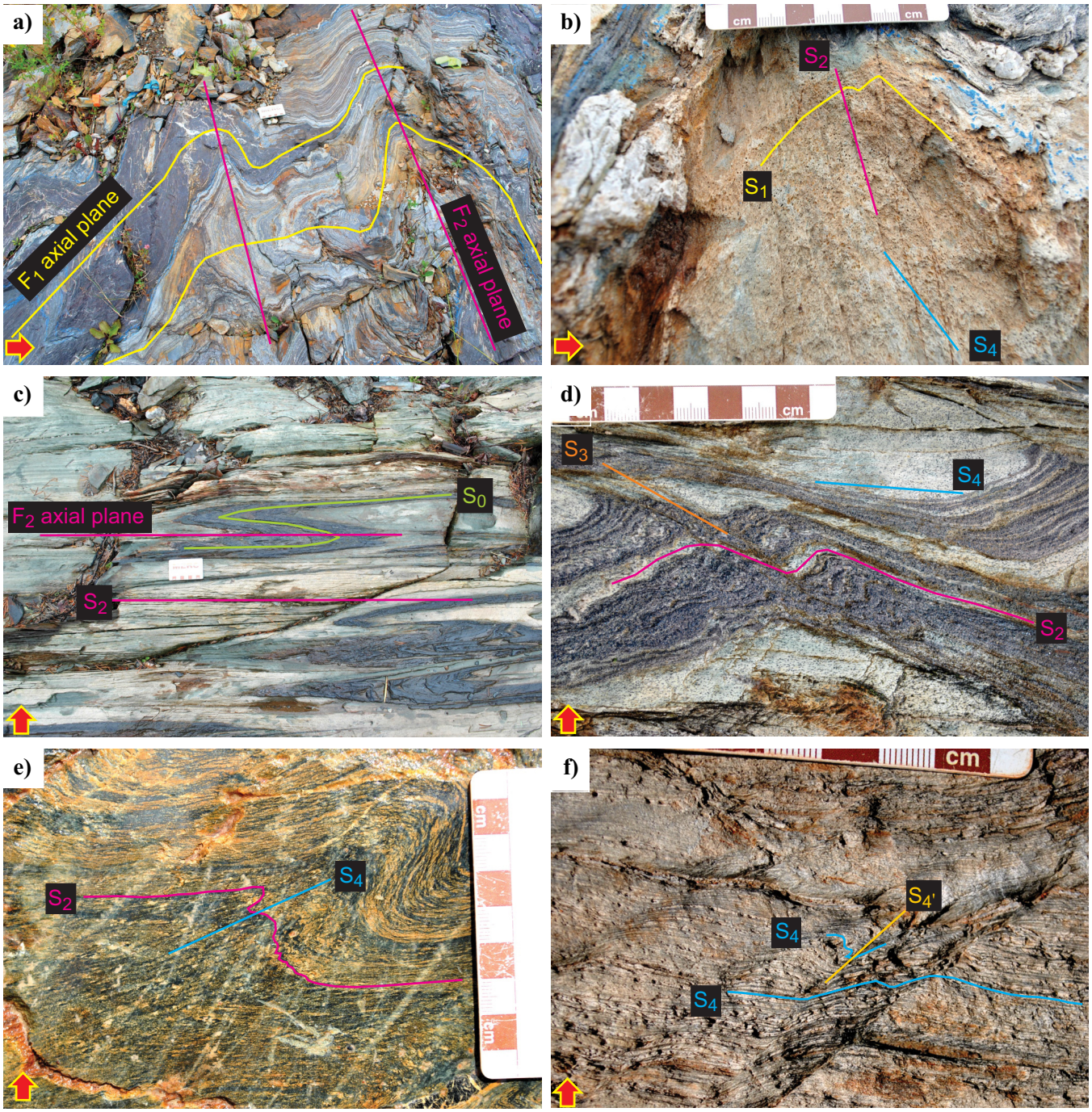

Figure 3. Structural elements in the Beardmore-Geraldton greenstone belt (Lafrance et al., 2004; DeWolfe et al., 2007; Tóth et al., 2013a, 2014b). The yellow-outlined red arrows indicate north on each photograph. **a)** F_1 folds refolded by west-plunging F_2 folds in banded iron formation. **b)** Strong chloritic S_1 cleavage folded by F_2 folds and overprinted by S_2 and S_4 foliation in a mafic dyke. **c)** Tight S-shaped F_2 folds with axial-planar S_2 foliation folding bedding (S_0) in banded iron formation. **d)** S_2 cleavage folded by S-shaped F_3 folds that are overprinted by S_4 foliation. **e)** Chloritic S_2 foliation folded by Z-shaped F_4 folds and overprinted by axial-planar S_4 cleavage. **f)** In shear zones, S_4 foliation is folded by another Z-shaped $F_{4'}$ fold generation that has axial-planar $S_{4'}$ sinistral-slip cleavage.

There were two main gold-mineralizing events that occurred during deformation. Iron-carbonatized beds and quartz-carbonate±tourmaline veins are folded by F_1 folds (Fig. 5a). Some of these early quartz-carbonate±tourmaline veins are surrounded by a strong sericite-carbonate-sulphide alteration halo (Fig. 5b) and commonly yield gold values between 2 and 15g/t (B. Cleland, Premier Gold Mines Ltd. pers. comm., 2014), suggesting that the first gold mineralization event occurred at the onset of the D_1 thrusting (Tóth et al., 2014b). Other banded iron formation-hosted quartz-carbonate veins associated with traces of pyrite

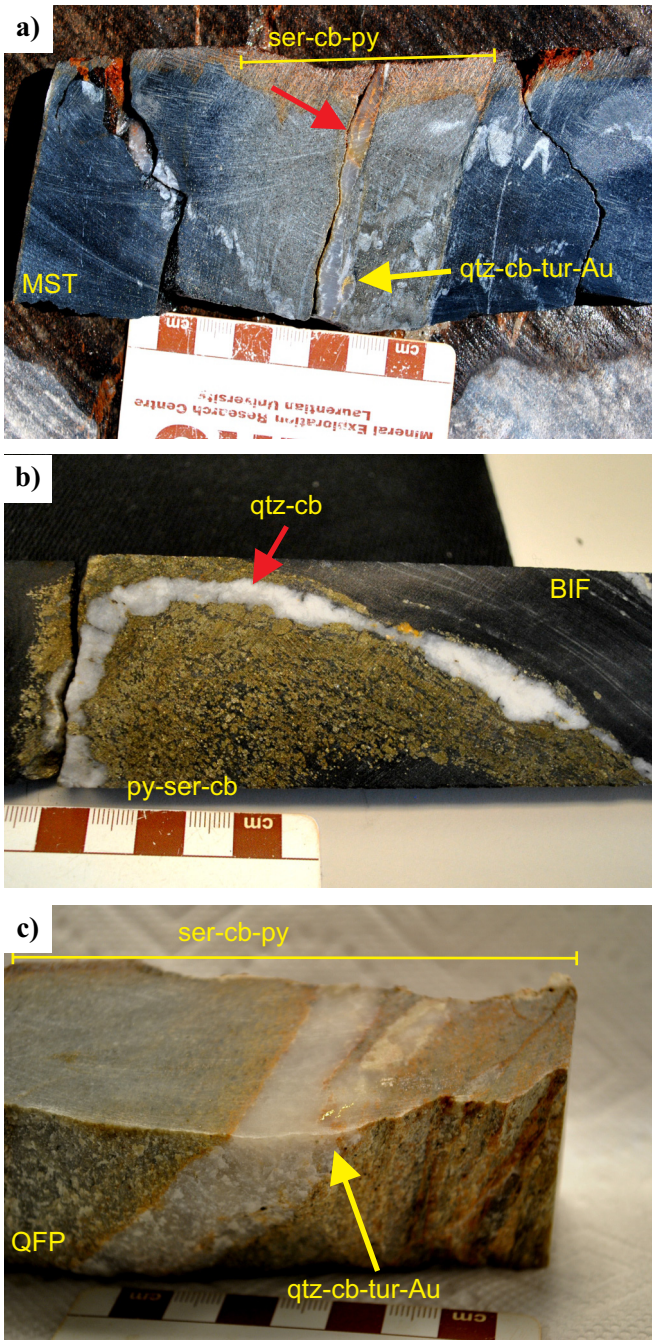

Figure 4. Photographs of mineralization styles. **a)** Auriferous quartz-carbonate-tourmaline vein surrounded by intense sericite-carbonate-pyrite alteration in turbiditic mudstone and sandstone (MST). **b)** Semi-massive pyrite-sericite replacement alteration surrounding a quartz-carbonate vein in banded iron formation (BIF). The semi-massive pyrite replacement yielded 65.1 g/t Au. **c)** Auriferous quartz-carbonate-tourmaline veins surrounded by sericite-carbonate-sulphide alteration in quartz-feldspar porphyry (QFP). Abbreviations (Siivola and Schmid, 2007): Au = gold; cb = carbonate; py = pyrite; qtz = quartz; ser = sericite; tur = tourmaline.

replacement cut the limbs of F_1 folds but are folded in the hinge of the same folds (Fig. 5c), suggesting that gold-bearing veins were emplaced throughout D_1 deformation. East-northeast- to northeast-trending tourmaline-rich (Fig. 5d) and auriferous quartz-carbonate-tourmaline-sulphide veins (Fig. 5e) and their carbonate-sericite-pyrite alteration halo cut F_2 fold hinges and are folded by S-shaped F_3 folds (Tóth et al., 2014b). These northeast-trending veins have an anticlockwise relationship with S_2, which is consistent with sinistral shearing parallel to S_2 during a syn-D_3 reactivation of the S_2 foliation. This suggests that the second gold-mineralizing event is syn-D_3 deformation (Tóth et al., 2014b). These results differ from previous studies that proposed a late-D_4 dextral transpression timing for the gold mineralization in the BGB (Lafrance et al., 2004; DeWolfe et al., 2007). Some quartz-sulphide veins, which fill northwest-trending tension gashes that cut across northeast-trending tourmaline-dominated veins, are folded by gentle Z-shaped F_4 folds (Fig. 5f) and were likely emplaced during D_4 dextral shear (Tóth et al., 2014b). Similar auriferous veins were described in the western part of the BGB (DeWolfe et al., 2007), implying a possible third gold-bearing event, or a syn-D_4 remobilization of gold.

GEOCHRONOLOGY

U-Pb Sensitive High Resolution Ion Microprobe (SHRIMP II) analyses of detrital zircon grains were completed at the Geological Survey of Canada (GSC) Geochronology Laboratory in Ottawa. Representative conglomerate and sandstone samples from the three BGB metasedimentary units and a sandstone sample from the Quetico Subprovince near the boundary with the BGB were selected for analysis. An auriferous quartz-feldspar porphyry dyke was dated using high-precision U-Pb isotope dilution thermal ionization mass spectrometry (ID-TIMS) techniques at the GSC. A gold-mineralized arsenopyrite-rich sample was dated using the Re-Os isotopic system in an attempt to directly date the gold-mineralizing event. These analyses were completed using isotope dilution negative thermal ionization mass spectrometry (ID-NTIMS) methods at the Canadian Centre of Isotopic Microanalysis (CCIM), University of Alberta.

Over three hundred U-Pb detrital zircon analyses reveal very similar age distributions in all samples. In the CSU and SSU sandstone samples, the youngest dominant detrital zircon populations were dated at ca. 2700 Ma. The youngest dominant zircon populations in the sandy matrix of the NSU conglomerate and the Quetico sandstone were determined to be ca. 2711 Ma (Tóth et al., 2014a). These U-Pb ages are consistent with the previous interpretation of the BGB as a transitional terrane between the Wabigoon and Quetico subprovinces (Devaney and Williams, 1989; Williams, 1990; Fralick et al., 2006). The deposition of the metasedimentary units therefore started at ≤2700 Ma

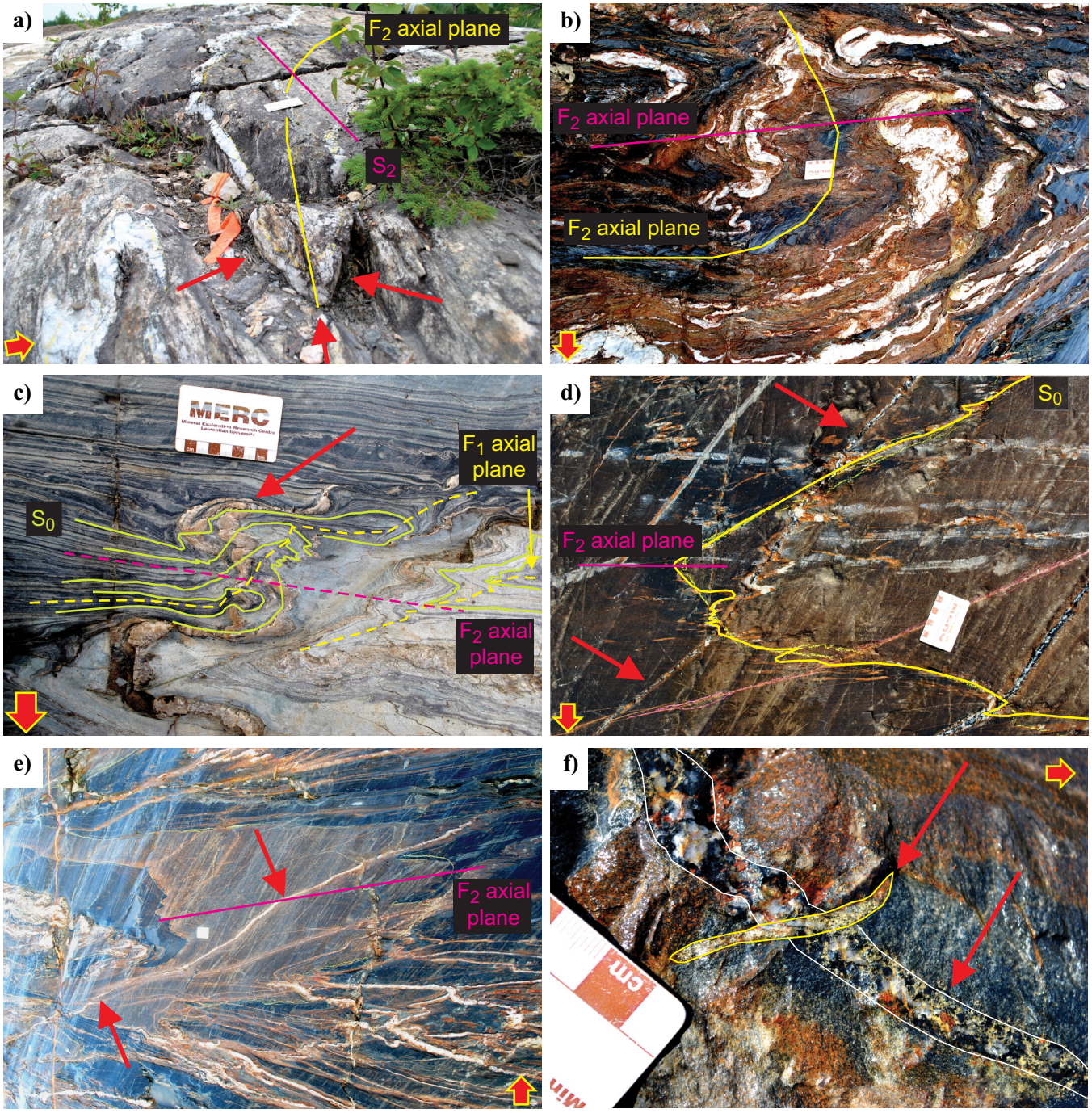

Figure 5. Field relationships between hydrothermal activity including gold mineralization events and the deformation history of the Geraldton area (Tóth et al., 2014b). The yellow-outlined red arrows indicate north on each photograph. **a)** Early quartz-carbonate-tourmaline vein folded by F_1 and refolded by F_2 folds in quartz-feldspar porphyry in the hinge of Hard Rock anticline. **b)** Gold-mineralized quartz-carbonate-tourmaline veins surrounded by intense sericite-carbonate-pyrite alteration that has been folded by F_1 and refolded by F_2 folds. **c)** Quartz-carbonate vein surrounded by traces of sulphidic alteration cuts across a F_1 fold hinge and is folded by a F_1 fold. **d)** Northeast- to east-northeast-trending tourmaline-rich veins cutting across a F_2 fold hinge. **e)** Gold-mineralized, east-northeast- to east-trending, quartz-carbonate-tourmaline vein cuts across a F_2 fold hinge and is locally folded by S-shaped F_3 folds. **f)** Northwest-trending quartz-pyrite vein (outlined by yellow) cuts across a northeast-trending tourmaline-rich vein (outlined by white) and is gently folded by a Z-shaped F_4 fold.

and ceased by 2694.0 ± 1.0 Ma, the crystallization age of the crosscutting quartz-feldspar porphyry that was sampled at the Porphyry Hill exposure south of Geraldton. The D_1 deformation event is younger than the 2694.0 ± 1.0 Ma quartz-feldspar porphyry, as indicated by its internal folding, but it is older than ca. 2690 ± 1 Ma (Corfu, 2000), the age of the post-D_1 Croll Lake stock that cuts the thrusted Northern Metavolcanic

(NVU), Northern Metasedimentary (NSU), and Central Metavolcanic units (CVU) (Kresz and Zayachivksy 1991) at the eastern boundary of the BGB.

Conglomerate in the NSU and SSU differ in clast composition and detrital zircon ages from Timiskaming conglomerate in the Abitibi greenstone belt, which contains alkali volcanic rocks (Bass, 1961; Legault, 1993) and that was deposited between 2676 and 2670 Ma (Ayer et al., 2005). Nevertheless, both the Timiskaming and the BGB conglomerates formed in similar, alluvial, fluvial and deltaic environments and represent similar regional-scale processes, such as syn-tectonic continental island arc-fed sedimentation (Mackasey, 1975, 1976; Barrett and Fralick, 1985; Devaney and Williams, 1989; Mueller et al., 1994; Born, 1995; Ayer et al. 2002; Fralick and Pufahl, 2006). The Timiskaming-like sedimentary rocks and the underlying unconformity are considered important features in many lode gold systems because they mark the beginning of major tectonic events that form pathways for gold-mineralizing hydrothermal fluids (Dubé and Gosselin, 2007).

A gold-mineralized sandstone sample (BGBZT 2013_362; 7.42 g/t Au) with abundant arseno-pyrite was collected from drillhole MM276 for Re-Os geochronology, yielding an age of 2579 ± 25 Ma. Lead isochron dating of pyrite samples collected from mineralized felsic porphyry bodies yielded a similar age of 2560 Ma (Anglin, 1987; Anglin and Franklin, 1989). These ages are not likely to represent the true radiogenic age of any of the gold-mineralizing phases because the tectonic evolution of the BGB is thought to have ceased much earlier, and no further processes have been identified that could have been responsible for such a late gold-bearing event. The meaning of the Re-Os age presented by this study will be further examined by detailed petrographic analysis to achieve a better interpretation.

HYDROTHERMAL FOOTPRINT (PRELIMINARY RESULTS)

A total of 216 samples were collected from drillholes and mapped exposures to characterize the footprint of the hydrothermal auriferous system in the Geraldton area. The samples were analyzed for major oxides, 46 trace elements, CO_2, total S, Au, As, Bi, Se, Sb, Te and FeO by Activation Laboratories Ltd. in Ancaster, Ontario.

As expected, there is a strong positive correlation between Au and total S, which is in agreement with the presence of pyrite in the ore zones (Tóth et al., 2013b). In addition, higher Au grades are typically accompanied by anomalous As and Te values (Tóth et al., 2013b). Gold is generally, but not exclusively, associated with high sericite alteration index values ($K_2O/(K_2O+Na_2O)$; Saeki and Date, 1980). Samples with elevated Au values are typically enriched in Sb as well, but elevated Sb values are not restricted to Au-mineralized samples, suggesting that Sb has a larger footprint than Au. Gold and W commonly show a positive correlation. However, non- to weakly mineralized, banded iron formation samples yielded higher W values than samples from the semi-massive sulphide replacement zone flanking iron-carbonate quartz veins in the iron formation.

MODEL FOR THE RELATIVE CHRONOLOGY BETWEEN HYDROTHERMAL ACTIVITY, GOLD MINERALIZATION, AND DEFORMATION EVENTS

The new data and interpretation presented herein suggest a much more complicated deformation and mineralization history than previously proposed. Quartz-feldspar porphyry dykes intruded the sedimentary rocks prior to any deformation (Tóth et al., 2013a, 2014b). The first gold mineralization event involving iron-carbonate alteration and gold-mineralized quartz-carbonate-tourmaline veins were emplaced parallel to bedding at the onset of D_1 deformation and were subsequently folded by F_1 folds (Tóth et al., 2014b) (Stage 1-2 on Fig. 6). Another set of quartz-carbonate veins, which are associated with a pyrite replacement halo, cut across F_1 fold hinges but are themselves folded when located in the F_1 fold hinges, which suggests late-D_1 timing for their formation. If these veins and their alteration halo carried gold, it would then imply that the first gold-bearing event might have extended throughout D_1 (Stage 2 on Fig. 6). During the D_2 north-south compression, F_1 folds and the first gold-bearing structures were refolded by regional F_2 folds, without significant hydrothermal activity (Stage 3 on Fig. 6). East-northeast- to northeast-trending tourmaline-dominated veins cut across F_2 fold hinges and are locally folded by F_3 folds; therefore they were introduced during early D_3 sinistral shear (Stage 4 on Fig. 6) (Tóth et al., 2014b). The second gold-mineralizing event occurred early during D_3 deformation and is characterized by a set of northeast- to east-trending quartz-carbonate-sulphide-tourmaline±gold veins (Stage 4 on Fig. 6) (Tóth et al., 2014b). Some short, northwest-trending quartz-sulphide-bearing tension gashes cut across northeast-trending tourmaline-rich veins and are folded by F_4 folds, suggesting a syn-D_4 timing of emplacement (Stage 5 on Fig. 6) (Tóth et al., 2014b). Based on analogies with the western part of the BGB (DeWolfe et al., 2007), these syn-D_4 veins might be gold-bearing (Tóth et al., 2014b). The geometry of auriferous veins, documented to be parallel to S_4 and overprinting F_2 and F_4 fold hinges (Pye, 1952;

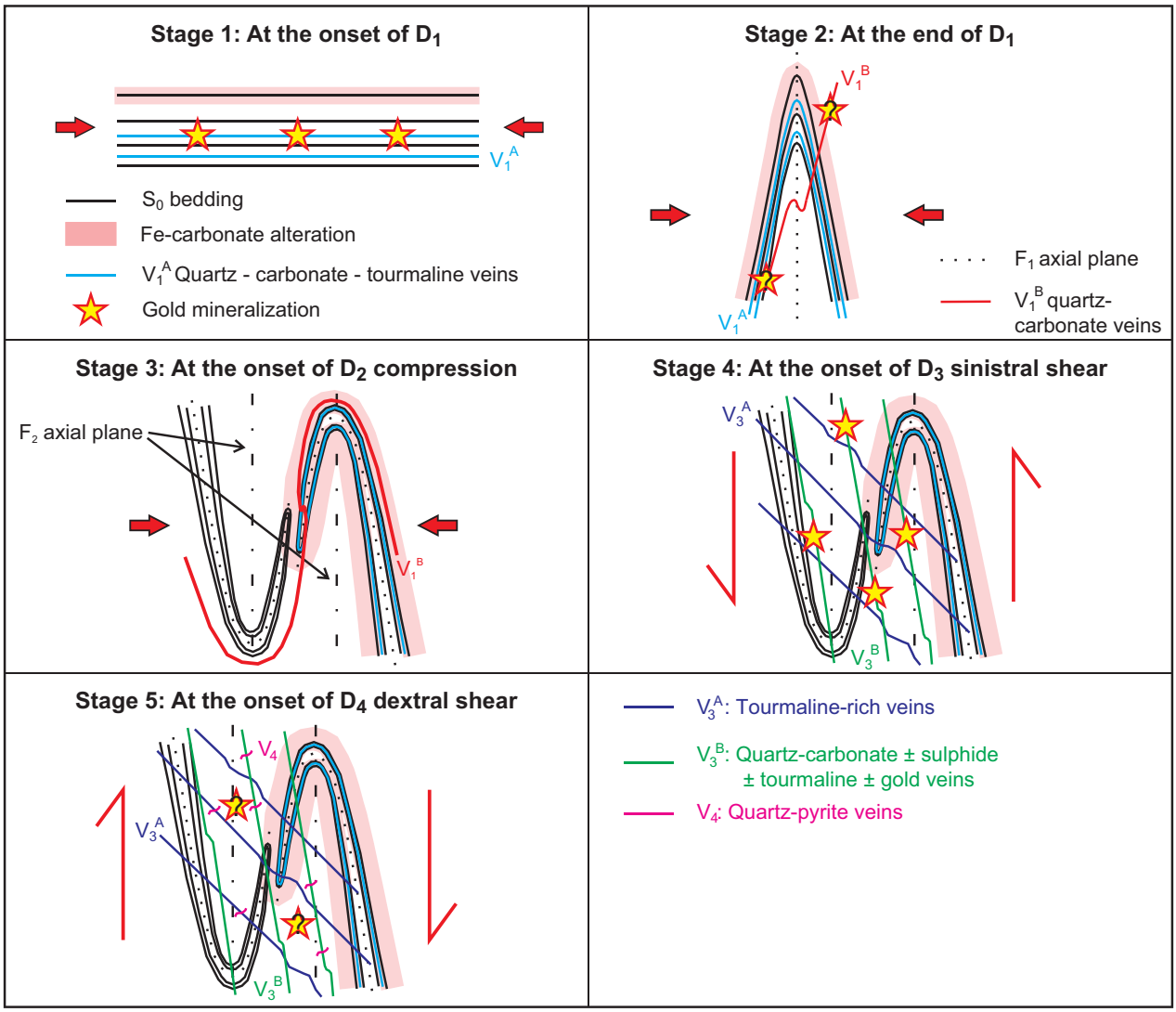

Figure 6. Summary of the hydrothermal activity, gold mineralization and deformation events in the Geraldton area (based on Tóth et al., 2014b). **Stage 1.** Iron-carbonate alteration and gold-mineralized quartz-carbonate-tourmaline veins were emplaced at the beginning of D_1 deformation. **Stage 2.** Oblique quartz-carbonate veins were emplaced late during D_1 deformation, but before the final closure of F_1 folds. Thus, these veins are also folded by F_1 folds in the fold hinges. **Stage 3.** Formation of regional F_2 folds by (re)folding older structural elements. **Stage 4.** Tourmaline-rich and auriferous quartz-carbonate-sulphide-tourmaline vein sets were introduced early during D_3 sinistral shear. **Stage 5.** Northwest-trending quartz-sulphide veins were emplaced syn-D_4. Analogies from the BGB suggest that these veins might also carry gold.

Horwood and Pye, 1955; Beakhouse, 1984; Anglin and Franklin, 1985; Macdonald, 1988; Kresz and Zayachivsky, 1991; Lafrance et al., 2004; DeWolfe et al., 2007), suggests that the majority of the gold mineralization was introduced during D_3 sinistral shear. The syn-D_1 and syn-D_3 timing of gold emplacement differs from that of other greenstone belts (e.g. Timmins-Val d'Or, Red Lake), where the bulk of the quartz-carbonate veining-related gold mineralization is commonly considered as having been emplaced during a main D_2 deformation event (Robert and Poulsen, 2001; Dubé et al., 2002; Robert et al., 2005).

IMPLICATIONS FOR EXPLORATION

This study presents detailed mapping of newly stripped outcrops and drill-core analysis placing new constraints on and interpretations of the chronology and structural setting of gold mineralization in the BGB. Based on this evidence, mineral exploration should focus on east- to northeast-trending vein systems emplaced in sinistral shear zones, rather than in late dextral shear zones. All the gold mineralization is expected to be deformed due to successive progressive deformation and mineralizing events. The early, syn- to late-D_1 auriferous veins will be strongly discontinuous and folded, whereas younger veins emplaced during the second, early to syn-D_3 mineralizing event occur as parallel veins that were locally S-folded during D_3 deformation and Z-folded during D_4 deformation. Both mineralization events produced similar mineralogy and

alteration halos and each deformation event is favourable for locally remobilizing gold.

FUTURE WORK

Future work includes the following:

- Additional optical and SEM petrography to fully characterize the mineralogical assemblages associated with the gold mineralization, in all host rock types;
- LA-ICP-MS study on mineralized samples to identify different generations of pyrite and arsenopyrite and the element associations related to gold;
- Final assessment of geochemical data;
- Submission of manuscripts to peer-reviewed journals about the structural geology of the BGB and the chronological, structural setting, and footprint of the gold mineralization in the BGB.

ACKNOWLEDGEMENTS

This project is part of a Ph.D. thesis undertaken by the lead author at Laurentian University, Sudbury, Ontario, with supervision by Bruno Lafrance (Laurentian University) and Benoît Dubé (Geological Survey of Canada). We gratefully acknowledge the funding from the Targeted Geoscience Initiative 4 Lode Gold project of Natural Resources Canada, as well as the support of the Ontario Geological Survey. We thank Premier Gold Mines Ltd. for access to its properties, drill cores and database, particularly Benjamin Cleland, Andrew Hackner, Daniel Grabiec, Thomas Salmi and the crew located in Geraldton. In addition, we greatly appreciate all discussions with the previously mentioned geologists, as well as with Kenneth Williamson, Dyane Duquette and Tim Twomey. We thank the entire crew of Premier Gold Mines Ltd. for the technical help provided during outcrop cleaning and sampling procedures.

REFERENCES

Anglin, C.D., 1987. Geology, structure and geochemistry of gold mineralization in the Geraldton area, Northwestern Ontario; M.Sc. thesis, Memorial University of Newfoundland, St. John's, Newfoundland, 283 p.

Anglin, C.D. and Franklin, J.M., 1985. Gold mineralization in the Beardmore-Geraldton area of northwestern Ontario: structural considerations and the role of iron formation; Geological Survey of Canada, Current Research Paper 85-1A, p. 193–201.

Anglin, C.D. and Franklin, J.M., 1989. Preliminary lead isotope studies of base metal and gold mineralization in the eastern Wabigoon Subprovince, northwestern Ontario; Geological Survey of Canada, Current Research Paper 89-1C, p. 285–292.

Anglin, C.D., Franklin, J.M., Loveridge, W.D., Hunt, P.A., and Osterberg, S.A., 1988. Use of zircon U-Pb ages of felsic intrusive and extrusive rocks in eastern Wabigoon subprovince, Ontario, to place constraints on base metal and gold mineralization; Geological Survey of Canada, Radiogenic Age and Isotopic Studies, Report 2, Paper 88-2, p. 109–115.

Ayer, J., Amelin, Y., Corfu, F., Kamo, S., Ketchum, J., Kwok, K., and Trowell, N., 2002. Evolution of the southern Abitibi greenstone belt based on U–Pb geochronology: autochthonous volcanic construction followed by plutonism, regional deformation and sedimentation; Precambrian Research, v. 115, p. 63–95.

Ayer, J., Thurston, P.C., Bateman, R., Dubé, B., Gibson, H.L., Hamilton, M.A., Hathway, B., Hocker, S.M., Houlé, M., Hudak, G.J., Ispolatov, V., Lafrance, B., Lesher, C.M., MacDonald, P.J., Péloquin, A.S., Piercey, S.J., Reed, L.E., and Thompson, P.H., 2005. Overview of results from the Greenstone Architecture Project: Discover Abitibi Initiative; Ontario Geological Survey, Open File Report 6154, 125 p.

Bass, M.N., 1961. Regional tectonics of part of the southern Canadian Shield; Journal of Geology, v. 69, p. 669–702.

Barrett, T.J. and Fralick, P.W., 1985. Sediment redeposition in Archean Iron Formation: Examples from the Beardmore-Geraldton Belt, Ontario; Journal of Sedimentary Petrology, v. 55, p. 205–212.

Beakhouse, G.P., 1984. Geology of the Grenville Lake Area, Thunder Bay District; Ontario Geological Survey, Open File Report 5513, 146 p.

Born, P., 1995. A sedimentary basin analysis of the Abitibi greenstone belt in the Timmins area, Northern Ontario, Canada; Ph.D. thesis, Carleton University, Ottawa, Ontario, 489 p.

Corfu, F., 2000. Extraction of Pb with artificially too-old ages during stepwise dissolution experiments on Archean zircon; Lithos, v. 53, p. 279–291.

Devaney, J.R. and Fralick, P.W., 1985. Regional sedimentology of the Namewaminikan Group, northern Ontario: Archean fluvial fans, braided rivers, deltas and an aquabasin; Geological Survey of Canada, Current Research Paper 85-1B, p. 125–132.

Devaney, J.R. and Williams, H.R., 1989. Evolution of an Archean subprovince boundary: a sedimentological and structural study of part of the Wabigoon–Quetico boundary in northern Ontario; Canadian Journal of Earth Sciences, v. 26, p. 1013–1026.

DeWolfe, J.C., Lafrance, B., and Stott, G.M., 2007. Geology of the shear-hosted Brookbank gold prospect in the Beardmore–Geraldton belt, Wabigoon Subprovince, Ontario; Canadian Journal of Earth Sciences, v. 44, p. 925–946.

Dubé, B. and Gosselin, P., 2007. Greenstone-hosted quartz-carbonate vein deposits, *In:* Mineral deposits of Canada: A Synthesis of Major Deposit Types, District Metallogeny, the Evolution of Geological Provinces, and Exploration Methods, (ed.) W.D. Goodfellow; Geological Association of Canada, Mineral Deposits Division, Special Publication no. 5, p. 49–73.

Dubé, B., Mercier-Langevin, P., Castonguay, S., McNicoll, V.J., Pehrsson, S.J., Bleeker, W., Schetselaar, E.M., and Jackson, S., 2011. Targeted Geoscience Initiative 4. Lode gold deposits in ancient, deformed and metamorphosed terranes – footprints and exploration implications: A preliminary overview of themes, objectives and targeted areas, *In:* Summary of Field Work and other Activities 2011; Ontario Geological Survey, Open File Report 6270, p. 38-1 to 38-10.

Dubé, B., Williamson, K., and Malo, M., 2002. Geology of the Goldcorp Inc. High Grade zone, Red Lake mine, Ontario: an update; Geological Survey of Canada, Current Research 2002-C26, 13 p.

Fralick, P. and Pufahl, P., 2006. Iron formation in Neoarchean deltaic successions and microbially mediated depositon of transgessive systems tracts; Journal of Sedimentary Research, v. 76, p. 1057–1066.

Fralick, P., Purdon, R.H., and Davis, D.W., 2006. Neoarchean transsubprovince sediment transport in southwestern Superior Province: sedimentological, geochemical and geochronological evidence; Canadian Journal of Earth Sciences, v. 43, p. 1055–1070.

Hart, T.R., terMeer, M., and Jolette, C., 2002. Precambrian Geology of Kitto, Eva, Summers, Dorothea and Sandra Townships, Northwestern Ontario: Phoenix Bedrock Mapping Project; Ontario Geological Survey, Open File Report 6095, 206 p.

Horwood, H.C. and Pye, E.G., 1955. Geology of Ashmore Township; Ontario Department of Mines, Annual Report, v. 60, Part 5, 105 p.

Kresz, D.U. and Zayachivsky, B., 1991. Precambrian Geology, northern Long Lake area; Ontario Geological Survey, Report 273, 77 p.

Lafrance, B., DeWolfe, J.C., and Stott, G.M., 2004. A structural reappraisal of the Beardmore-Geraldton Belt at the southern boundary of the Wabigoon subprovince, Ontario, and implications for gold mineralization; Canadian Journal of Earth Sciences, v. 41, p. 217–235.

Legault, M.I., 1993. Petrology and geochemistry of Timiskaming group sedimentary rocks, Kirkland Lake area, Abitibi greenstone belt; M.Sc. thesis, University of Ottawa, Ottawa, Ontario, 139 p.

Macdonald, A.J., 1988. The Geraldton Gold Camp: The role of the banded iron formation; Ontario Geological Survey, Open File Report 5694, 173 p.

Mackasey, W.O., 1975. Geology of Dorothea, Sandra, and Irwin Townships, District of Thunder Bay; Ontario Division of Mines, Geological Report 122, 83 p.

Mackasey, W.O., 1976. Geology of Walters and Leduc Townships, District of Thunder Bay; Ontario Division of Mines, Geological Report 149, 55 p.

Mason, J.K. and McConnell, C.D., 1982. Gold mineralization in the Beardmore-Geraldton area, *In:* The Geology of Gold in Ontario, (ed.) A.C. Colvine; Ontario Geological Survey, Miscellaneous Paper 100, p. 84¬¬–97.

Mason, J.K. and White, G., 1986. Gold occurrences, prospects and deposits of the Beardmore-Geraldton area, District of Thunder Bay and Cochrane; Ontario Geological Survey, Open File Report 5630, 680 p.

Mueller, W., Donaldson, J.A., and Doucet, P., 1994. Volcanic and tectono-plutonic influences on sedimentation in the Archean Kirkland Basin Abitibi greenstone belt, Canada; Precambrian Research, v. 68, p. 201–230.

Pye, E.G., 1952. Geology of Errington Township, Little Long Lac Area; Ontario Department of Mines, Annual Report, v. 60, Part 6, 140 p.

Robert, F. and Poulsen, H.K., 2001. Vein Formation and Deformation in Greenstone Gold Deposits, In: Structural Controls on Ore Genesis; Reviews in Economic Geology, v. 14, p. 111–155.

Robert, F., Poulsen, H.K., Cassidy, K.F., and Hodgson, C.J., 2005. Gold Metallogeny of the Superior and Yilgarn Cratons, *In:* 100th Anniversary Volume, (ed.) J.W. Hedenquist, J.F.H. Thompson, R.J. Goldfarb, and J.P. Richards; Society of Economic Geologists, p. 1001–1033.

Saeki, Y. and Date, J. 1980. Computer application to the alteration data of the footwall dacite lava at the Ezuru Kuroko deposits, Akita prefecture; Mining Geology, v. 30, p. 241–250. [(in Japanese with English abstract)

Siivola, J, and Schmid, R., 2007. A systematic nomenclature for metamorphic rocks: 12. List of mineral abbreviations. Recommendations by the IUGS Subcommission on the Systematics of Metamorphic Rocks; Recommendations, web version of 01.02.2007. (http://www.bgs.ac.uk/scmr/docs/papers/paper_12.pdf).

Tomlinson, K.Y., Hall, R.P., Hughes, D.J., and Thurston, P.C., 1996. Geochemistry and assemblage accretion of metavolcanic rocks in the Beardmore–Geraldton greenstone belt, Superior Province; Canadian Journal of Earth Sciences, v. 33, p. 1520–1533.

Tóth, Z., Lafrance, B., Dubé, B., and Mercier-Langevin, P., 2013a. Targeted Geoscience Initiative 4. Lode gold deposits in ancient deformed and metamorphosed terranes: Geological mapping and structural re-appraisal of the banded iron formation–hosted gold mineralization in the Geraldton area, Ontario, *In:* Summary of Field Work and other Activities 2013; Ontario Geological Survey, Open File Report 6290, p. 58-1 to 58-14.

Tóth, Z., Lafrance, B., Dubé, B., Mercier-Langevin, P., and McNicoll, V.J., 2013b. Geological setting of banded iron formation-hosted gold mineralization in the Geraldton area, Northern Ontario: preliminary results; Geological Survey of Canada, Open File 7370, 54 p.

Tóth, Z., Lafrance, B., Dubé, B., McNicoll, V.J. and Mercier-Langevin, P., 2014a. Stratigraphic and structural setting of banded-iron-formation-hosted gold mineralisation in the Geraldton area, Ontario, *In:* Program with Abstracts; Geological Association of Canada–Mineralogical Association of Canada, Fredericton, Joint Annual Meeting, v. 37, p. 272–273.

Tóth, Z., Lafrance, B., Dubé, B., Mercier-Langevin, P. and McNicoll, V.J., 2014b. Targeted Geoscience Initiative 4. Lode gold deposits in ancient deformed and metamorphosed terranes: Relative chronology between hydrothermal activity, gold mineralization and deformation events in the Geraldton area, NW Ontario, *In:* Summary of Field Work and Other Activities 2014; Ontario Geological Survey, Open File Report 6300, p. 40-1 to 40-10.

Williams, H.R., 1986. Structural studies in the Beardmore-Geraldton Belt, Northern Ontario; Ontario Geological Survey, Geoscience Research Grant Program, Summary of Research, 1985-1986, 235 p.

Williams, H.R., 1987a. Structural studies in the Wabigoon and Quetico subprovinces; Ontario Geological Survey, Open File Report 5668, 163 p.

Williams, H.R., 1987b. Structural Studies in the Beardmore-Geraldton Belt and in the Quetico and Wawa Subprovinces, *In:* Summary of Field Work and other Activities; Ontario Geological Survey, Open File Report 5668, p. 90–92.

Williams, H.R., 1989. Geological studies in the Wabigoon, Quetico and Abitibi-Wawa subprovinces, Superior Province of Ontario, with emphasis on the structural development of the Beardmore-Geraldton Belt; Ontario Geological Survey, Open File Report 5724, 189 p.

Williams, H.R., 1990. Subprovince accretion in the south-central Superior Province; Canadian Journal of Earth Sciences, v. 27, p. 570–581.

GEOLOGICAL SURVEY OF CANADA
OPEN FILE 7852

Targeted Geoscience Initiative 4: Contributions to the Understanding of Precambrian Lode Gold Deposits and Implications for Exploration

Setting, age, and hydrothermal footprint of the emerging Meliadine gold district, Nunavut

Christopher J.M. Lawley[1], Benoît Dubé[2], Patrick Mercier-Langevin[2], Vicki J. McNicoll[1], Robert A. Creaser[3], Sally J. Pehrsson[1], Sébastien Castonguay[1], Jean-Claude Blais[4], Marjorie Simard[4], William J. Davis[1], and Simon E. Jackson[1]

[1]Geological Survey of Canada, Ottawa, Ontario
[2]Geological Survey of Canada, Québec, Quebec
[3]University of Alberta, Edmonton
[4]Agnico Eagle Mines Ltd., Val D'Or, Quebec

2015

This publication is available for free download through GEOSCAN (http://geoscan.nrcan.gc.ca/)

Recommended citation

Lawley, C.J.M., Dubé, B., Mercier-Langevin, P., McNicoll, V.J., Creaser, R.A., Pehrsson, S.J., Castonguay, S., Blais, J.-C., Simard, M., Davis, W.J., and Jackson, S.E., 2015. Setting, age, and hydrothermal footprint of the emerging Meliadine gold district, Nunavut, *In:* Targeted Geoscience Initiative 4: Contributions to the Understanding of Precambrian Lode Gold Deposits and Implications for Exploration, (ed.) B. Dubé and P. Mercier-Langevin; Geological Survey of Canada, Open File 7852, p. 99–111.

Publications in this series have not been edited; they are released as submitted by the author.

Contribution to the Geological Survey of Canada's Targeted Geoscience Initiative 4 (TGI-4) Program (2010–2015)

TABLE OF CONTENTS

Setting, age, and hydrothermal footprint of the emerging Meliadine gold district, Nunavut

Christopher J.M. Lawley[1]*, Benoît Dubé[2], Patrick Mercier-Langevin[2], Vicki J. McNicoll[1], Robert A. Creaser[3], Sally J. Pehrsson[1], Sébastien Castonguay[1], Jean-Claude Blais[4], Marjorie Simard[4], William J. Davis[1], and Simon E. Jackson[1]

[1]Geological Survey of Canada, 601 Booth Street, Ottawa, Ontario K1A 0E8
[2]Geological Survey of Canada, 490 rue de la Couronne, Québec, Quebec G1K 9A9
[3]Department of Earth and Atmospheric Sciences, 1-26 Earth Sciences Building, University of Alberta, Edmonton, Alberta T6G 2E3
[4]Agnico Eagle Mines Ltd, 765 Chemin de la mine Goldex, Val D'Or, Quebec J9P 4N9
*Corresponding author's e-mail: clawley@nrcan.gc.ca

ABSTRACT

The Meliadine gold district comprises a combination of orogenic greenstone- and BIF-hosted gold mineralization. The largest gold deposits (Tiriganiaq, Wesmeg, Normeg, F Zone, Pump, Discovery, and Wolf) are cospatial with the northwest-trending Pyke Fault and its inferred east-trending splays, which cut amphibolite- to greenschist-facies rocks within the Rankin Inlet greenstone belt. New U-Pb detrital zircon ages suggest that turbiditic and mafic volcanic host rocks at Tiriganiaq were deposited ≤2.66 Ga. In contrast, a polymictic conglomerate south of the Pyke Fault, which is not known to host gold, yielded Paleoproterozoic U-Pb detrital zircons and was deposited at ≤2.50 Ga. These new ages confirm that the Rankin Inlet greenstone belt comprises intercalated Archean to Paleoproterozoic supracrustal successions. Deformed Paleoproterozoic conglomerates suggest that the Archean to Proterozoic Rankin Inlet stratigraphy was reworked during the Trans-Hudson Orogeny (1.9–1.8 Ga).

Gold in the district is associated with hydrothermally altered and sulphidized BIF and fault-fill quartz (± ankerite) veins. Hydrothermal alteration and pathfinder element enrichment (As-Te-Bi-Sb) can be mapped following a multivariate and probabilistic approach for 10s to 100s of meters beyond BIF-hosted replacement-style mineralization. Coarse-grained and idioblastic arsenopyrite crystals occur within and at the margins of folded quartz (± ankerite) veins and are also a good visual gold indicator. Gold is paragenetically late and occurs at arsenopyrite grain boundaries and/or as fracture fills. Clusters of gold inclusions coincide with recrystallized and sieve-textured arsenopyrite domains. These microtextures suggest that sulphide recrystallization liberated gold that was redistributed, at least locally, into low-strain microtextural sites along with other precious- and base-metals during a late fluid-assisted and deformation/metamorphic-driven remobilization. We propose that remobilization was concurrent with the growth of xenotime at ca. 1.86 Ga (new U-Pb ages), which postdates arsenopyrite and occurs together with gold in low-strain micro textural sites. New Re-Os arsenopyrite model ages range from 2.3 to 1.8 Ga and document a hitherto unrecognized pre-1.86 Ga hydrothermal and sulphide history. The range of Re-Os model ages tends to support partial open-system behaviour and/or mixing of disparate arsenopyrite generations that are evident from microtextures and in situ element mapping. Replicate analyses of the two most Re-rich and homogeneous arsenopyrite samples yield Re-Os model ages at ca. 2.27 and 1.90 Ga. We speculate that gold at the Meliadine gold district was initially introduced at 2.27 Ga and/or 1.90 Ga along with arsenopyrite and was subsequently remobilized, coupled with arsenopyrite recrystallization, during the Trans-Hudson Orogeny at 1.86–1.85 Ga.

INTRODUCTION

The Meliadine Gold District (MGD) research activity represents one component of the Banded Iron Formation (BIF)-hosted deposits subproject within the Lode Gold project of the Targeted Geoscience Initiative (TGI)-4 program (Dubé et al., 2011). Research at the MGD is conducted in close collaboration with Agnico-Eagle Mines Ltd. and focuses on further defining the setting, age, and hydrothermal footprint at this emerging gold district (2.8 Moz contained gold within an indicated and inferred resource of 5.8 Moz; www.agncioeagle.com). Prior to this study, the metallogenic model at the MGD emphasized a relatively late gold history (Carpenter and Duke, 2004;

Lawley, C.J.M., Dubé, B., Mercier-Langevin, P., McNicoll, V.J., Creaser, R.A., Pehrsson, S.J., Castonguay, S., Blais, J.-C., Simard, M., Davis, W.J., and Jackson, S.E., 2015. Setting, age, and hydrothermal footprint of the emerging Meliadine gold district, Nunavut, *In:* Targeted Geoscience Initiative 4: Contributions to the Understanding of Precambrian Lode Gold Deposits and Implications for Exploration, (ed.) B. Dubé and P. Mercier-Langevin; Geological Survey of Canada, Open File 7852, p. 99–111.

Carpenter et al., 2005). The model was based, in large part, on hydrothermal monazite U-Pb ages (1.85 Ga) that were interpreted to be cogenetic with gold at the Tiriganiaq deposit and correlative with the Trans-Hudson Orogeny (THO; 1.9–1.8 Ga; Carpenter et al., 2005). The apparent link between gold and late west-trending shear zones was taken as further evidence of late gold introduction at the MGD (Carpenter and Duke, 2004). However, the gold fertility of pre-THO structures was undocumented. Published geochronology for the Rankin Inlet greenstone belt was also limited to U-Pb zircon dating of a felsic band (originally interpreted as a porphyritic rhyolite) intercalated with mafic volcanic rocks at ca. 2.66 Ga (Tella et al., 1996). This sample was collected south of the major gold-bearing structure in the MGD (i.e. the Pyke Fault; Fig 1) and thus the ages of the rocks hosting the gold deposits remained speculative.

In this contribution, we briefly outline TGI-4 field and laboratory results that further constrain the setting, age, and hydrothermal footprint at the MGD. Critically, we document a hitherto unrecognized pre-1.85 Ga hydrothermal history at the MGD. The implications of 'early' auriferous hydrothermal activity to ongoing mineral exploration are also briefly discussed.

RESULTS AND DATA ANALYSIS

Setting

Regional Setting

West of Hudson Bay, the Western Churchill Province (WCP) is broadly divided into the Rae and Hearne cratons separated by the cryptic and polyorogenic Snowbird Tectonic Zone (Hoffman, 1988). However, more recent work has further subdivided the WCP into the Central Hearne subdomain and the Chesterfield Block (Berman et al., 2007, 2013; Pehrsson et al., 2013a, b). These authors placed the MGD at the boundary between the Central Hearne and the Chesterfield Block. Cratonic boundaries are widely recognized as first-order controls on the distribution of gold deposits and represent significant exploration targets.

Host Rocks

The MGD host rocks were originally assigned to the Rankin Inlet Group (Bannatyne, 1958) and later referred to as the Rankin Inlet greenstone belt (e.g. Aspler and Chiarenzelli, 1996). The district is dominated by volcanic rocks (basalt, andesite, and rare rhyolite), interflow volcaniclastic rocks and, more rarely, graded-bedded greywacke-siltstone-mudstone successions, quartzite and BIF. Metamorphosed and deformed granitic to tonalitic intrusions are intercalated with these supracrustal rock packages. Mafic volcanic and volcaniclastic rocks, known locally as the Wesmeg formation, represent the two main rock types at Wesmeg, Normeg, F Zone, and Pump and constitute the footwall at Tiriganiaq (Figs. 1–3). Graded-bedded greywacke-siltstone-mudstone rock assemblages are interpreted as turbidite sucessions and are known locally as the Sam and Tiriganiaq formations (Fig. 3a, b; Carpenter and Duke, 2004). Turbidite sequences comprise the hanging wall at Tiriganiaq and represent the dominant host rock at Discovery. Algoma-type BIF is interbedded with mafic volcanic and volcaniclastic rocks (i.e. oxide facies; Wesmeg, Pump, and F Zone deposits) and a greywacke-siltstone-chloritic mudstone rock assemblage (i.e. silicate facies; Tiriganiaq and Discovery deposits). Oxide-facies BIF is significantly more chert-rich than silicate-facies BIF.

Structure

The structural history of the MGD is broken into four distinct phases of deformation (Fig. 3a; Carpenter and Duke, 2004; Carpenter et al., 2005). The earliest recognizable deformation event (D_1) lacks a clear cleavage although it is linked to bedding-parallel thrusting and folding that may have resulted in the initial juxtaposition of volcanic-sedimentary packages (Tella et al., 1992; Carpenter and Duke, 2004). The largest gold deposits occur along the Pyke Fault and its associated splays (e.g. Lower Fault at Tiriganiaq; Figs. 1, 2). Carpenter and Duke (2004) have proposed that these faults may have developed during this earliest deformation event; however, the timing and nature of D_1, and especially its relationship to gold, remain poorly constrained.

A second deformation increment (D_2) resulted in bedding-parallel folding and thrusting and a penetrative northwest-trending foliation (S_2: 285/59; Carpenter and Duke 2004). This deformation event was likely coupled with shearing and reactivation of the Pyke Fault and associated west-trending fault splays (e.g. Lower Fault; Carpenter and Duke, 2004). TGI-4 fieldwork along the newly constructed all-season road between the town of Rankin Inlet and the Meliadine exploration camp identified that recumbent and isoclinals folds (F_1?) were refolded during D_2 to produce the dominant map pattern south of the Pyke Fault (Fig. 1; akin to Fig. 2 of Tella et al., 1992).

The dominant regional foliation (S_2) predates a west-trending cleavage (S_3) that is best developed within turbidite and represents the dominant fabric geometry at Tiriganiaq. Northeast-plunging regional- to outcrop-scale Z-shaped folding may have developed during this D_3 event (Carpenter and Duke, 2004). The relationship between asymmetric folding and D_3 reactivation of the Pyke and Lower faults and gold forms the basis for the late gold metallogenic model at the MGD (Carpenter and Duke, 2004; Carpenter et al., 2005).

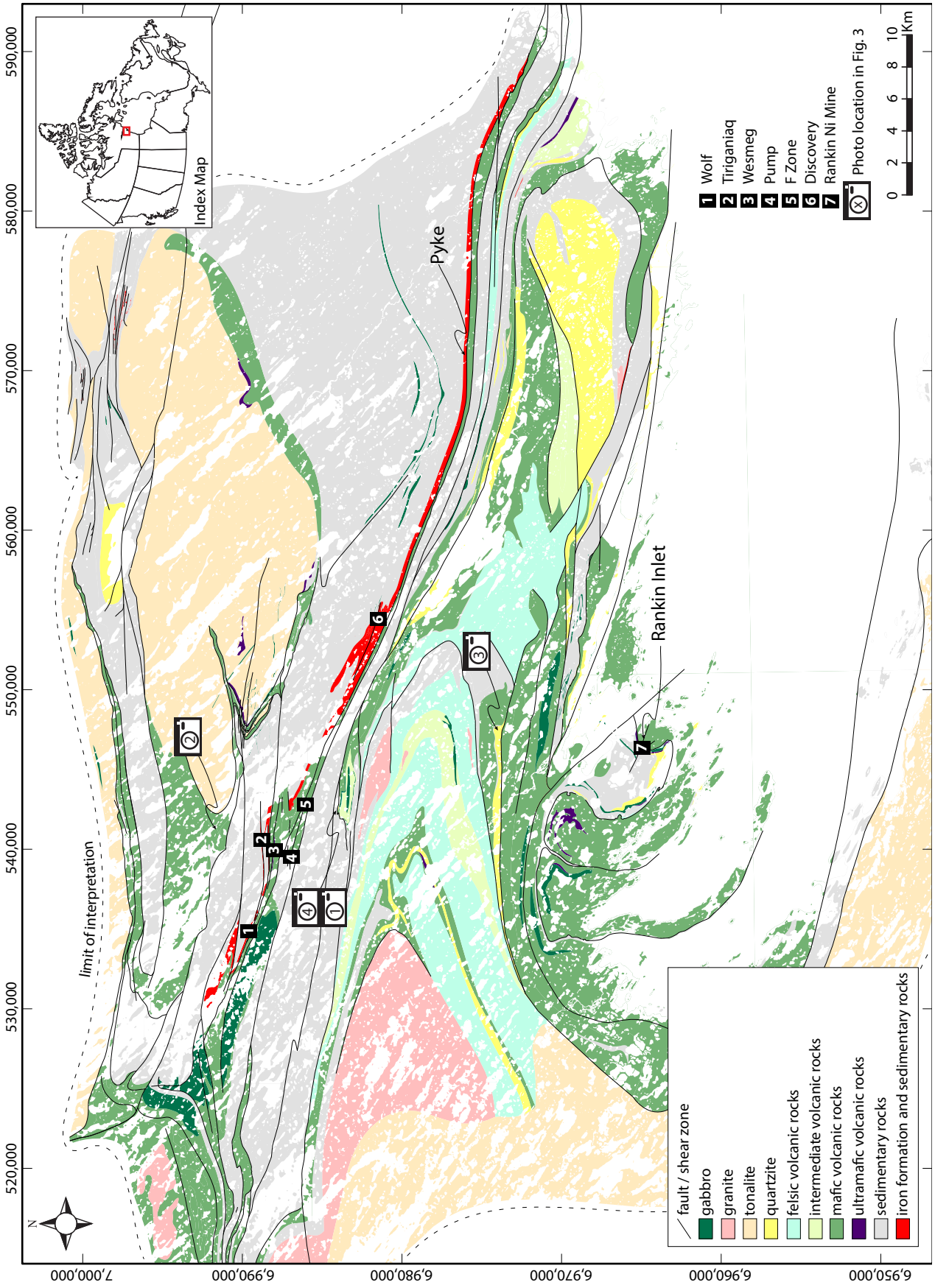

Figure 1. Local Meliadine gold district geology map (courtesy of Agnico-Eagles Mines Ltd.). The Pyke Fault, gold deposits, and the former Rankin Nickel Mine are shown for reference. Camera symbols correspond to outcrop photos presented in Figure 3.

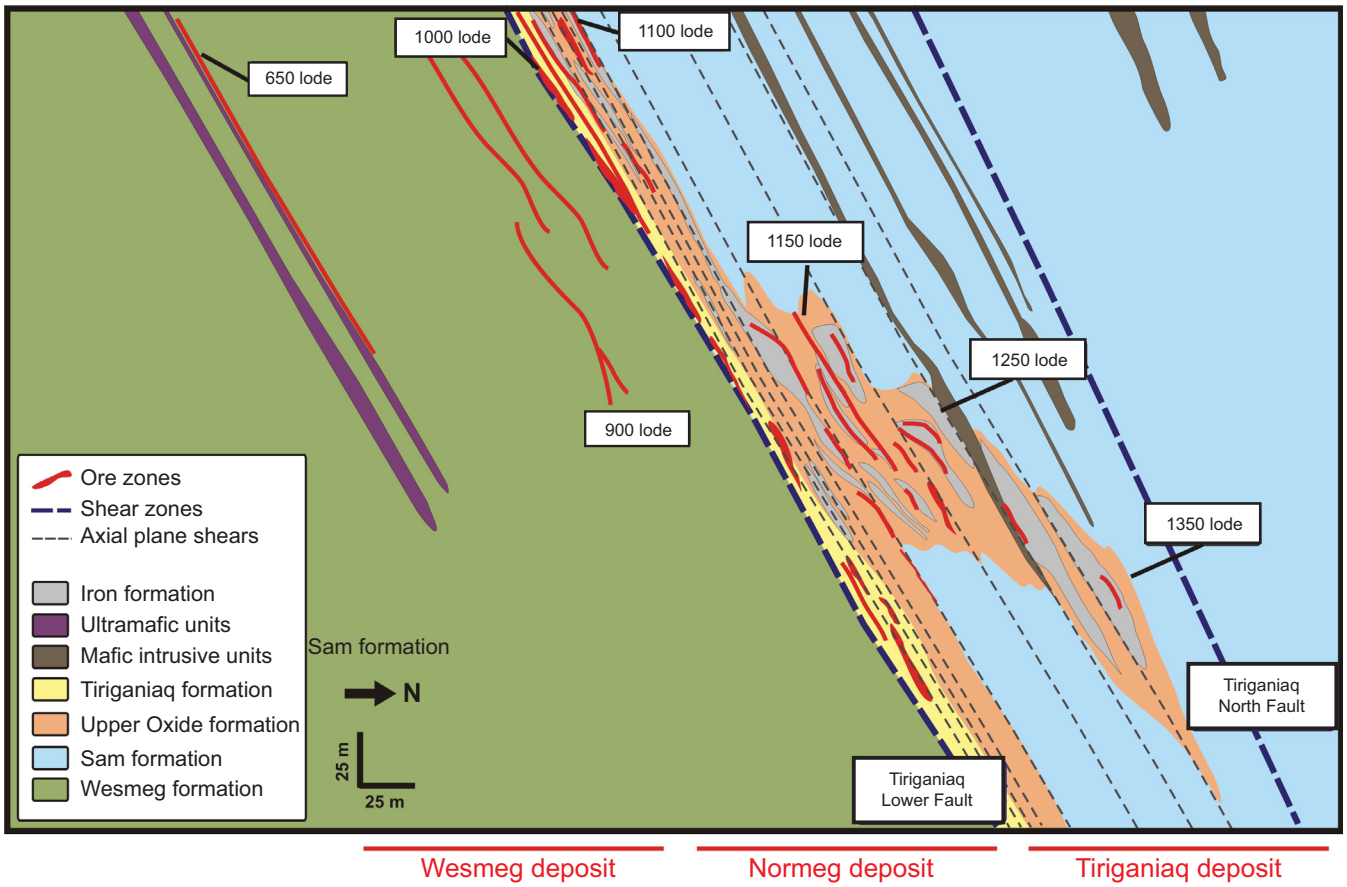

Figure 2. Simplified cross section showing the Tiriganiaq, Normeg, and Wesmeg deposits (courtesy of Agnico-Eagles Mines Ltd.). Section highlights folded BIF and turbidite (Sam and Upper Oxide formations) in the hanging wall at Tiriganiaq. Ore zones and BIF are transposed and axial planar to folds and are also parallel to the Lower Fault. Gold-rich intervals at Wesmeg locally occur along ultramafic and mafic volcanic (i.e. Wesmeg Formation) contacts.

At Tiriganiaq, auriferous quartz (± ankerite) veins are tightly folded, boudinaged, and transposed parallel to the main fabric (265/65N; Fig. 4a–d), which could represent (1) a locally penetrative S_3 fabric, developed subparallel to the west-trending and steeply dipping Lower Fault (Carpenter and Duke, 2004; Carpenter et al., 2005); (2) the main regional foliation (S_2) transposed into a west-trending orientation by D_3 strain (Miller et al., 1995); or (3) a composite S_2-S_3 fabric. The dearth of clear S_2-S_3 relationships underground at Tiriganiaq makes distinguishing between these possibilities equivocal. However, S_{main} is axial planar to tight folds in turbidite (Fig. 3b) and BIF, which is unlike S_3-S_0 relationships distal to D_3 shear zones (Fig. 3a). This relationship likely reflects transposed bedding adjacent to D_3 shear zones (e.g. Lower Fault), but could also suggest that the main deposit fabric at Tiriganiaq represents the dominant regional foliation (S_2) transposed into a west-trending orientation.

Asymmetric porphyroclasts and boudinaged quartz veins, coupled with the geometry of en echelon extension quartz (± ankerite) veins in the Tiriganiaq deposit structural hanging wall, suggests a component of reverse sense of motion during the main phase of deformation. This reverse component of motion postdates, or was synchronous with, auriferous quartz (± ankerite) veining (Fig. 4a–d). The main quartz vein at Tiriganiaq occurs within the Lower Fault and is interpreted as a fault-fill vein type (Fig. 4a, c; i.e., laminated appearance; included slivers of mylonitized wall rock; stylolites). Attendant flat-dipping extensional veins are also tightly folded, transposed by the main deposit fabric, and commonly occur as rootless folds (Fig. 4a). This suggests that these fault-fill and extensional quartz-ankerite veins were emplaced in an active deformation zone and thus contrast with the post-deformational vein timing (late D_3) proposed by Carpenter et al. (2005).

The final phase of deformation, D_4, is characterized by a northwest- to north-trending crenulation cleavage (S_4) and kink bands, which are best developed in fissile turbidite and mafic volcaniclastic successions (Fig. 3a). The late crenulation cleavage is generally steeply dipping and produces a strong vertical intersection lineation on S_2 foliation planes. This final phase of deformation does not significantly modify earlier structures, is not associated with mineralization, and likely postdates the introduction of gold (Carpenter and Duke,

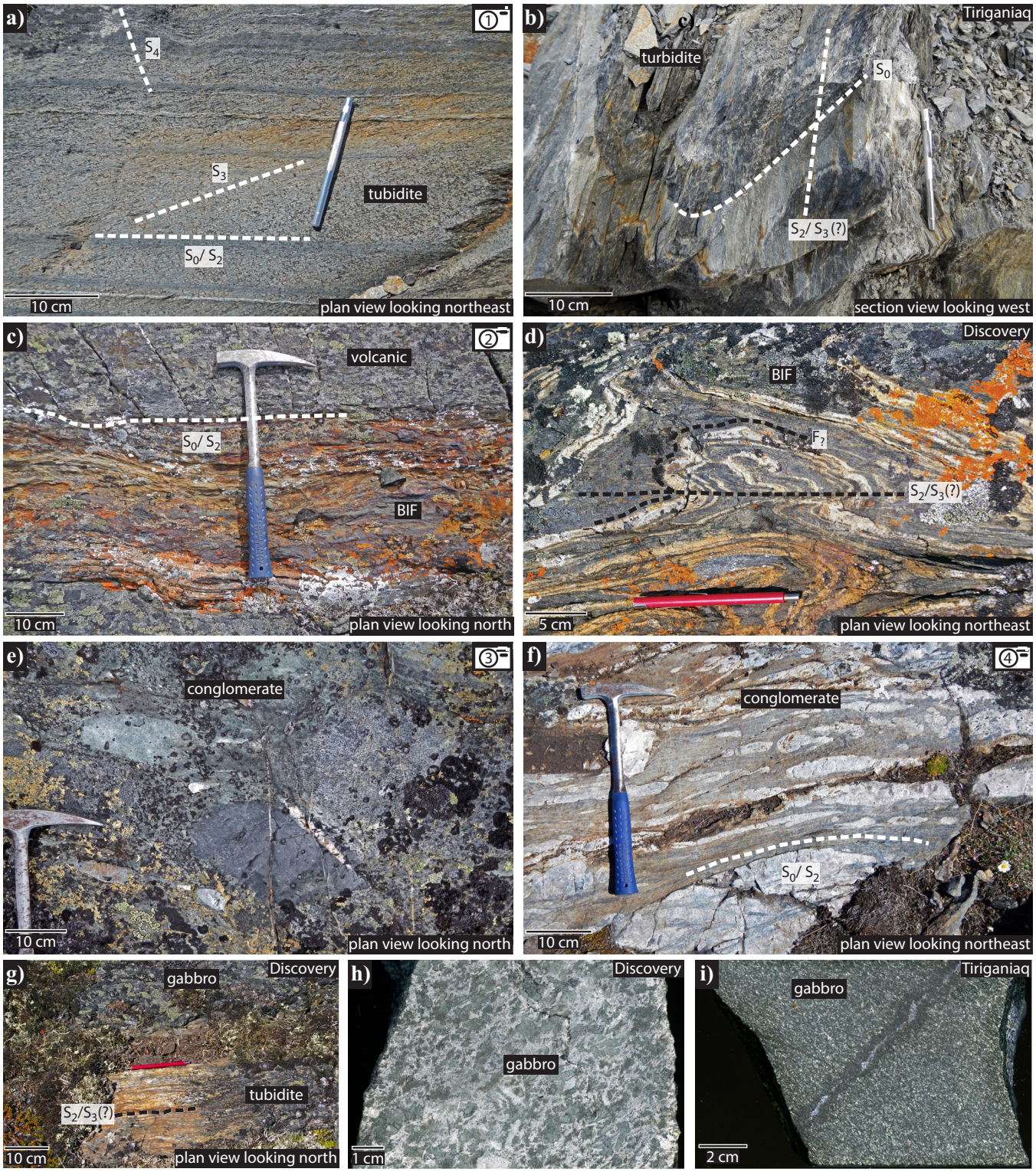

Figure 3. a) Turbidite showing three foliations (S_2–S_4) reported by Carpenter and Duke (2004). **b)** Turbidite bedding at Tiriganiaq. The main deposit fabric (S_2 or S_3) is axial planar to folded turbidite bedding at Tiriganiaq. **c)** BIF intercalated with mafic volcanic rock. **d)** Refolded BIF outcrop at Discovery. **e)** Polymictic conglomerate deposited ≤2.50 Ga. Conglomerate comprises muscovite schist, quartzite, metadiorite, and metabasalt clasts set in a siltstone matrix. **f)** Conglomerate deposited ≤2.66 Ga. The conglomerate comprises quartzite and tonalite/granodiorite clasts set in a siltstone matrix. **g–h)** A gabbroic dyke cutting the turbiditic host rocks at Discovery. The dyke is folded and transposed parallel to the main deposit fabric (S_2 or S_3). A zircon age of ca. 1.81 Ga obtained from the dyke most likely records the timing of metamorphism, or a hydrothermal event, as opposed to its emplacement age. **i)** Massive to foliated equigranular gabbroic dyke cutting turbiditic host rocks at Tiriganiaq. A U-Pb zircon crystallization age of ca. 90 Ma was obtained from this sample, significantly younger than any known magmatic activity in the Rankin Inlet region (Davis and Miller, 2001; N.B. veins were excluded prior to sample crushing).

2004). A deformed ≤2.155 Ga conglomeratic horizon south of the Pyke Fault is transposed parallel to the main regional foliation (S_2) and suggests that the Rankin Inlet Group was significantly reworked during the THO (Davis et al. 2008).

Structural Controls at the Tiriganiaq Deposit

Most of the mineralized zones (i.e. lodes) at the Tiriganiaq deposit are oriented parallel to the west-trending Lower Fault (Fig. 2), which is situated a few hundred metres to the north of the Pyke Fault (Fig. 1). These predominantly west-trending ore zones consist of folded quartz-carbonate-sulphide veins that cut sulphidized BIF and intercalated turbiditic rocks (Figs. 2, 4g). The 1100–1350 lodes are type examples of this mineralization style and extend into the Tiriganiaq hanging wall (Fig. 2). Auriferous quartz (± ankerite) veins within these lodes are predominately west- to west-southwest-trending and subparallel to the main deposit fabric at Tiriganiaq. The 1000 lode is hosted within the Lower Fault and corresponds to a wide (1–2 m) fault-fill quartz vein (Fig. 4a) that is folded, boudinaged, and transposed parallel to the main deposit fabric (Fig. 4a–d). Subordinate northwest- and north-trending quartz veins also host gold and are also folded by the main deposit fabric near the Lower Fault at Tiriganiaq. Mineralized BIF is tightly S-folded, probably during D_2, and further sheared especially along the Lower Fault, either late during D_2, and/or during D_3 dextral shearing (Fig. 2). Late movement along the Lower Fault cuts the southern limb of this S-shaped fold (Fig. 2). Two high-grade ore shoots are recognized at Tiriganiaq: (1) one ore trend plunges approximately 45º to the east and may correspond to the intersection between the main west-trending shear fabric and the axes of northeast-plunging folds (D_3?), and (2) a second ore trend plunges approximately 25º to the west, which parallels the hinge zone of the tightly S-folded BIF (Fig. 2).

Age

Regional U-Pb Zircon Geochronology

Six samples from the Rankin Inlet greenstone belt were targeted for U-Pb zircon dating (Lawley et al., in prep). Detrital zircons were analyzed from sedimentary and volcaniclastic samples using the SHRIMP (Sensitive High Resolution Ion Microprobe). Two of these samples (turbiditic hanging wall and mafic volcaniclastic footwall) host the Tiriganiaq deposit and yield detrital zircons with ages that range from 2.94 to 2.66 Ga, which suggests that both host rocks at Tiriganiaq were deposited ≤2.66 Ga (Lawley et al., in prep). A gabbroic dyke that cuts meta-turbiditic rocks at the Discovery deposit yield zircon crystals that were dated at ca. 1.81 Ga (U-Pb SHRIMP). This gabbroic dyke at Discovery (Fig. 3h; 'feather' gabbro of Carpenter and Duke, 2004) is folded and transposed parallel to the main foliation (Fig. 3g), which suggests that this fabric and the main MGD map pattern is the result of Paleoproterozoic reworking. However, zircons from this folded dyke are clearly metamict and contain significant common Pb. These zircon textures and compositions suggest that the zircon ages record the timing of metamorphism, or a hydrothermal event, rather than the crystallization age of the gabbroic dyke. A second gabbroic dyke that cuts meta-turbiditic host rocks at the Tiriganiaq deposit was dated at ca. 90 Ma (U-Pb ID-TIMS; Isotope Dilution-Thermal Ionization Mass Spectrometry; Fig. 3i). This crystallization age is significantly younger than any known Phanerozoic magmatism in the Rankin Inlet region (e.g. ca. 214 Ma kimberlite; Davis and Miller, 2001).

Two conglomerates were also dated south of the Pyke Fault. One of these samples is polymictic and

Figure 4 opposite. a) Underground photo of the 1000 lode at Tiriganiaq (photo credit to Agnico-Eagle Mines Ltd.). The main quartz vein occurs at the Lower Fault and is interpreted as a fault-fill vein. Dragging of the main fabric in the hanging wall is consistent with a reverse sense of motion postdating or synchronous with veining. Attendant extension veins are transposed and folded by Smain (S_2/S_3?). **b)** Underground photo of the 1000 lode at Tiriganiaq (photo credit to Agnico-Eagle Mines Ltd.). The main deposit fabric is parallel to transposed bedding. Auriferous quartz veins are folded and transposed. **c)** Underground wall photo at Tiriganiaq showing the high-grade 1000 lode (Smain is dipping towards the viewer). The main quartz vein is transposed, folded, and boudinaged parallel to S_{main}. **d)** Underground photo of transposed, folded, and boudinaged quartz (± ankerite) veins structurally above the 1000 lode at Tiriganiaq. **e)** Underground photo of lamprophyre dyke cutting mafic volcanic and quartz veins at Tiriganiaq. This dyke is apparently undeformed and clearly cuts S_{main}. Lamprophyre dykes in the MGD may be correlative with the 1.833 Ga Christopher Island Formation (Rainbird et al., 2006) and could suggest that the main regional foliation is ≥1.833 Ga. **f)** Core photo of a quartz vein and alteration halo at Pump. Arsenopyrite is concentrated within the vein's alteration halo along with chlorite-sericite-calcite. **g)** Core photo of a high-grade BIF interval at Tiriganiaq showing folded quartz veins and associated idioblastic arsenopyrite. **h)** Core photo of a folded quartz (± ankerite) and gold vein at Wolf. S_{main} appears axial planar to the fold. Idioblastic arsenopyrite crystals occur peripheral to the vein. **i)** Core photo of a folded quartz vein at Wesmeg. Idioblastic is concentrated within folded chloritic bands. **j)** Core photo at Wolf that highlights the challenge of unravelling the gold history in metamorphosed deposits. Gold occurs within a tightly folded quartz (± ankerite) vein. S_{main} is axial planar to the folded vein; however, a late pyrrhotite-quartz-calcite fracture cuts the folded quartz veins and could be associated with the gold. **k)** Core photo of a deformed quartz-ankerite-gold vein cutting BIF at Tiriganiaq. A late pyrite-rich fracture cuts the auriferous quartz vein (abbreviations: Ank = ankerite; Aspy = arsenopyrite; BIF = banded iron formation; Chl = chlorite; lamp = lamprophyre; Po = pyrrhotite; Py = pyrite; Qtz = quartz).

contains pebble- to boulder-sized clasts comprising muscovite schist, quartzite, granodiorite/tonalite, and metabasalt hosted by a metasiltstone matrix (Fig. 3e). The polymictic conglomerate yields detrital zircon ages that range from 3.37 to 2.50 Ga, suggesting that this conglomerate was deposited ≤2.50 Ga and confirms that Paleoproterozoic, or younger, sedimentary successions are intercalated and folded with Neoarchean volcanic rocks comprising the Rankin Inlet greenstone belt (Davis et al., 2008). The second dated conglomerate comprises pebble- to cobble-sized clasts of quartzite and granodiorite/tonalite (Fig. 3f) and yields detrital zircon ages that range from 2.86 to

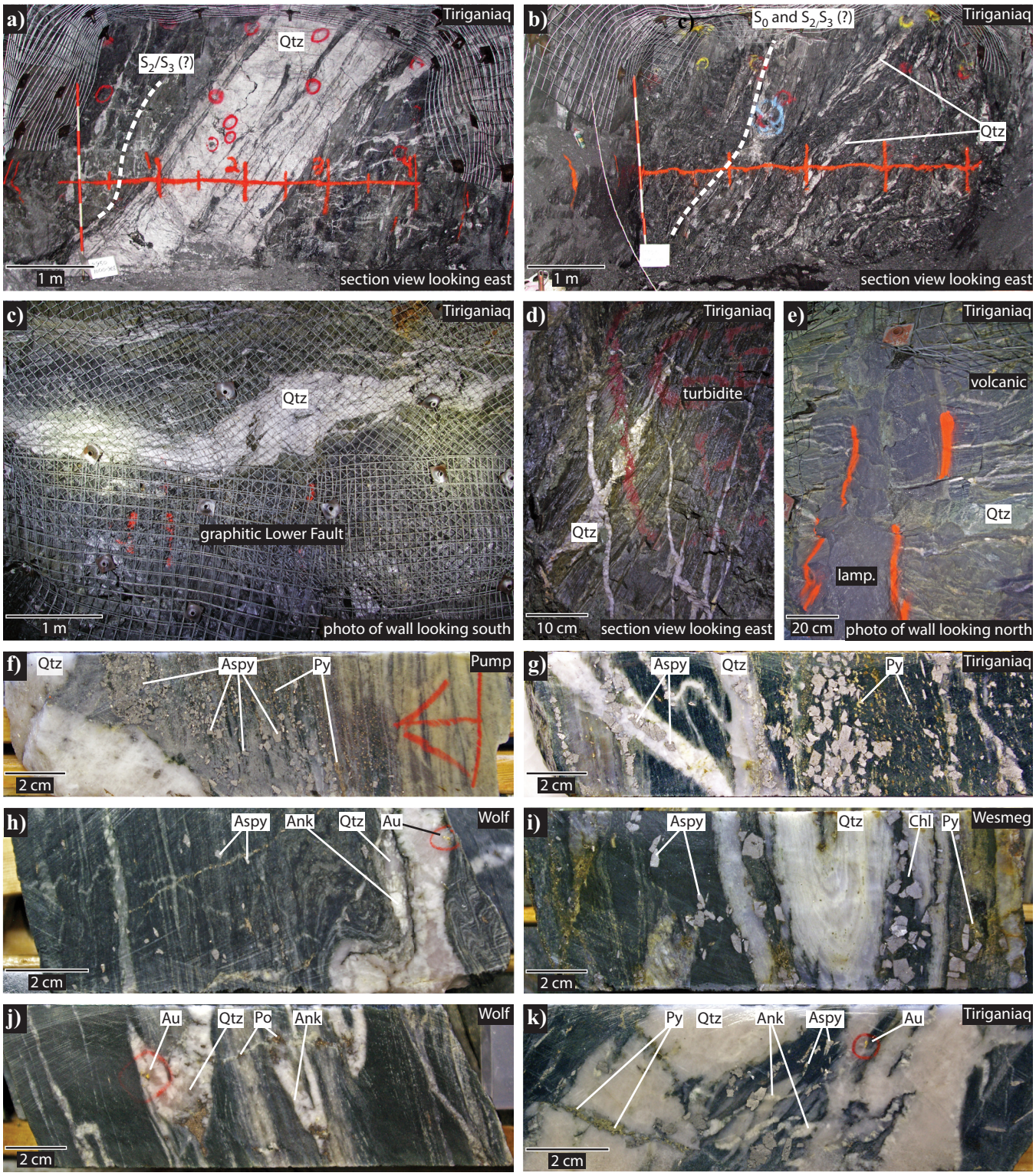

2.66 Ga, which suggests that this conglomerate was deposited at ≤2.66 Ga (Lawley et al., in prep).

Deposit U-Pb Xenotime Geochronology

Two auriferous quartz (± ankerite) vein samples cutting BIF and turbidite host rocks at Tiriganiaq were targeted for in situ U-Pb xenotime dating. Both samples were also dated via Re-Os arsenopyrite geochronology and compliment previously reported U-Pb monazite ages for the same deposit (Carpenter et al., 2005). Dated xenotime crystals postdate arsenopyrite (i.e. occur at arsenopyrite grain boundaries and fill arsenopyrite fractures) and yield a colinear array with an upper intercept Concordia age at 1862 ± 29 Ma (lower intercept = 117 ± 660 Ma; Mean Square Weighted Deviate, MSWD = 1.1; n = 15; 9 xenotime crystals). This upper intercept age is in excellent agreement with a weighted average $^{207}Pb/^{206}Pb$ age for all analyses at 1858 ± 10 Ma (MSWD = 1.1, n = 15; 9 xenotime crystals). Both age determinations are also in broad agreement with the previously reported preferred weighted mean $^{207}Pb/^{206}Pb$ monazite age at 1854 ± 6 Ma (MSWD = 1, n = 18; Carpenter et al., 2005). Undated ultrafine xenotime inclusions within arsenopyrite may represent an older, but undefined hydrothermal phosphate event(s) or could suggest that arsenopyrite crystals are locally ≤1.86 Ga.

Deposit Re-Os Arsenopyrite Geochronology

Arsenopyrite samples were collected from Tiriganiaq, Pump, F Zone, and Discovery. These samples share a similar paragenesis and occur with high-grade gold intervals at each of the targeted deposits (Fig. 4d–i). Gold fills arsenopyrite fractures and occurs at arsenopyrite crystal boundaries that, coupled with LA-ICP-MS in situ element mapping (Lawley et al., 2014a, b), provides evidence for late gold mobility and possible gold remobilization into low-strain microtextural sites. Arsenopyrite samples yield low Re-contents (0.5–6 ppb, n = 15) and are generally highly radiogenic (i.e. the Os isotopic composition is dominated by radiogenic ^{187}Os). Re-Os model ages range from 2.3 to1.8 Ga and point to complex Re-Os systematics that cannot be interpreted within the context of a single and cogenetic arsenopyrite sample suite. Replicate analyses of the two most Re-enriched samples yield the most uniform Re-Os model ages at 1899 ± 6 Ma (MSWD = 0.5, n =3) and 2269 ± 25 Ma (MSWD = 6, n = 5; Lawley et al., submitted a), respectively, whereas replicate analyses of Re-poor aliquots (≤1 ppb) yield variable Re-Os model ages between these two end-members.

We speculate that these homogeneous and reproducible Re-Os arsenopyrite ages are geologically meaningful and that arsenopyrite crystallization is significantly older than hydrothermal xenotime at ca. 1.86 Ga. If correct, new Re-Os ages are broadly concurrent with the Arrowsmith (2.4–2.3 Ga) and Snowbird (1.90 Ga) orogens (Berman et al., 2013) and record a hitherto unrecognized pre-1.86 Ga hydrothermal history at the MGD. Gold was likely introduced at ca. 2.27 and/or 1.90 Ga, whereas monazite and xenotime ages at ca. 1.86 Ga likely date phosphate and gold remobilization concomitant with the THO. Heterogeneous Re-Os arsenopyrite ages between 2.3 and 1.8 Ga could reflect partial open-system behaviour or mixing of disparate arsenopyrite generations that are evident from element mapping (Lawley et al., 2014b).

Hydrothermal Footprint

Fluid-rock interaction produces geochemical and mineralogical effects that can extend far beyond the economically viable portions of a hydrothermal ore deposit. This 'hydrothermal footprint' holds great promise as an exploration tool to vector from barren rock to high-grade gold ore and is a key tool in the search for new BIF-hosted gold deposits in metamorphosed and complexly deformed environments. As part of TGI-4 research at the MGD, we extended the probabilistic mapping approach, initially developed for geochemical survey studies, to hydrothermal footprint vectoring in the subsurface (Lawley et al., submitted b). Our conditional probability-based approach provides a framework to delineate domains of multivariate pathfinder-element enrichment and hydrothermally altered rock that extend 10s to 100s of meters beyond the gold ore zones. These anomalous domains occur in hanging wall and footwall rock devoid of gold (<5 ppb) and thus provide a possible vector to high-grade ore. At Tiriganiaq, hydrothermally altered and anomalous pathfinder-element concentrations extend for at least 200 m beyond the gold ore zone (Lawley et al., submitted b). We demonstrate that the accuracy and precision of portable X-Ray Fluorescence (pXRF) spectrometry on drill-core surfaces is sufficient to map multivariate hydrothermal footprints from the rock record in unprecedented detail and at a fraction of the cost and time compared to whole-rock analyses (Lawley et al., submitted b).

MULTISCALE IMPLICATIONS FOR EXPLORATION

Gold typically occurs in late fractures and other late and low-strain microtextural sites at orogenic deposits, which are the end-product of repeated hydrothermal stages linked to fluid-pressure cycling and episodic fluid infiltration in an active deformation zone (e.g. the fault-valve model; Sibson et al., 1988). Gold is expected to precipitate in multiple stages throughout this complex hydrothermal and deformation history and yet it typically occurs as the latest mineral phase at the microscale. This classic ore texture is the subject of

continued controversy and has been taken as evidence for (1) the relatively late timing for the bulk of the gold; (2) remobilized gold that was liberated from early and gold-rich sulphides and then redistributed during later fluid-assisted metamorphic and/or structural events; and/or (3) a mixture of these processes. Each scenario requires a tailored mineral exploration strategy and thus the absolute age of gold represents a key uncertainty for mineral explorationists. In the case of metamorphosed deposits, the current textural setting of gold is of great importance for defining deposit-scale ore shoots, but it likely reveals very little on how gold was initially introduced, which has major impacts on local- to regional-scale exploration models.

The late gold paragenesis at the MGD, coupled with U-Pb hydrothermal monazite ages at ca. 1.85 Ga, led to an inferred late gold model and a genetic link with the THO (1.9–1.8 Ga). Critically, the previous gold model implied that (1) MGD auriferous quartz veins are relatively undeformed; (2) idioblastic arsenopyrite crystals associated with gold are late and largely postdate the main regional foliation; and (3) late D_3 structures are prospective for gold, whereas D_2 folding and thrusting predate gold and thus were considered unprospective (Carpenter and Duke, 2004; Carpenter et al., 2005). Tiriganiaq and Pump are associated with D_3 east-trending shearing and Z-folding, respectively, and thus represent type examples of the late gold model (Fig. 1).

The link between gold and late reworking at the MGD is also supported by recent studies at other BIF-hosted gold deposits within the WCP (e.g. Three Bluffs, Davies et al., 2010; Meadowbank, Sherlock et al., 2004). Each of these studies proposed a genetic link between gold and the THO. This tectono-thermal event represents the latest Paleoproterozoic orogenic phase that is recorded across large swaths of the WCP. Accordingly, the Trans-Hudson Paleoproterozoic Metallotect has been tentatively correlated from northern Nunavut to Saskatchewan and Manitoba (e.g. Davies et al., 2010). In contrast, the gold fertility and prospectivity of orogenic episodes and fault-networks that predate the THO were undemonstrated.

Reproducible replicate analyses of the two most Re-rich samples yield the least evidence for disturbance and potentially record a pre-1.86 Ga gold-bearing sulphide history. If correct, arsenopyrite crystals may have initially crystallized concomitant with the Arrowsmith and/or Snowbird orogenies along with early arsenopyrite (i.e. 2.27 and/or 1.90 Ga). Gold was likely introduced along with early arsenopyrite and then remobilized during the later stages of the THO (i.e. 1.86–1.85 Ga). Late gold enrichment is also demonstrated by in situ LA-ICP-MS trace element mapping and spot analyses (Lawley et al., 2014b).

Idioblastic arsenopyrite crystals are also concentrated at the margins and within the halo of folded and transposed auriferous quartz (± ankerite) veins at each of the studied deposits. At Tiriganiaq, the main auriferous quartz vein, which occurs along the Lower Fault and shares similarities with fault-fill veins, is folded, boudinaged, and transposed subparallel to S_{main} (Fig. 4a, c). Smaller scale quartz (± ankerite) veins are also tightly folded and transposed subparallel to S_{main} in Tiriganiaq hanging wall and footwall rocks (Fig. 4b, d). Dated arsenopyrite crystals within and at the margins of these veins are wrapped by the bedding-parallel fabric and locally contain quartz strain fringes that point to post-crystallization strain across the MGD. These field and core observations at Tiriganiaq and the other deposits are at odds with the late gold metallogenic model proposed by Carpenter et al. (2005).

The 'early' gold model proposed here suggests that the Proterozoic Gold Metallotect as defined by Miller et al. (1994) in fact comprises several temporally distinct gold-bearing events. Differentiating between these events represents a critical step for effective mineral exploration. For example, the geometry of gold deposits is likely to have undergone variable degrees of structural reworking dependent, in part, on their timing relative to the WCP's polyorogenic Paleoproterozoic history and the extent of structural reactivation during each orogenic phase.

In the case of the MGD, the suggested pre-1.86 Ga hydrothermal and deformation history likely represent key factors in understanding the current geometry and occurrence of gold at the MGD, but are obscured by overprinting metamorphic/hydrothermal/deformation events related to the later stages of the THO. A metamorphosed, folded, and transposed gabbroic dyke at Discovery (Fig. 3h) contains metamict zircons that have been dated at ca. 1.81 Ga, which likely record the timing of metamorphism or a hydrothermal event, as opposed to its emplacement age. Undeformed lamprophyre dykes cut the main deposit fabric and folded quartz veining at Tiriganiaq (Fig. 4e) and, if correlative with the ca. 1.833 Ga Christopher Island Formation (Rainbird et al., 2006), provide a minimum age for the main deposit fabric (Carpenter and Duke, 2004; Carpenter et al., 2005). The deformed ≤2.155 Ga conglomerate south of the Pyke Fault further supports reworking from 2.155 to 1.833 Ga (Davis et al., 2008).

The MGD thus represents one of the few global examples of Proterozoic gold hosted at a reworked Archean cratonic margin. This geodynamic setting is distinct from classic orogenic gold deposits, which are hosted by Neoarchean granite-greenstone terranes that are broadly coeval (e.g. 10s Myr; Dubé and Gosselin, 2007) with auriferous fluids and spatially associated with terrane-bounding faults. At these deposits, gold is

intricately linked to basin development and subsequent reactivation during crustal shortening is linked to convergent tectonics and consanguineous metamorphism. An important corollary to this observation is that Neoarchean greenstone belts are also favourable gold exploration targets after reworking during much younger and overprinting tectono-thermal events. We consider that Archean basins, once formed, provide a crustal architecture (ground preparation) that facilitates subsequent reactivation and thus Archean fault networks represent zones of long-lived structural weakness. Archean basins in the WCP also comprise favourable host-rocks (e.g. mafic volcanic rocks, turbidite sequences, and BIF) that differ from granitoids and Proterozoic basins, which are comparatively gold-poor in the WCP. Together these apparent structural and lithostratigraphic gold controls likely contribute to the similar setting of Paleoproterozoic WCP gold districts to their Archean equivalents.

ACKNOWLEDGEMENTS

The MGD study is conducted under the auspices of Natural Resource Canada's Targeted Geoscience Initiative (TGI)-4. The authors would like to thank the cooperation and input from Agnico-Eagle Mines Ltd. throughout the study period. In particular, Denis Vaillancourt, Robert Fraser, Jérôme Lavoie, and Francine Fallara are thanked for sharing their knowledge and facilitating fieldwork logistics, assisting on site, and providing unpublished assays results, borehole logs, and geological plans/sections for the studied deposits.

REFERENCES

Aspler, L.B., and Chiarenzelli, J.R., 1996. Stratigraphy, sedimentology and physical volcanology of the Henik Group, central Ennadai-Rankin greenstone belt, Northwest Territories, Canada: Late Archean paleogeography of the Hearne Province and tectonic implications; Precambrian Research, v. 77, p. 59–89.

Bannatyne, M.J., 1958. The Geology of the Rankin Inlet Area and North Rankin Nickel Mines Limited, Northwest Territories; M.Sc. Thesis, University of Manitoba, Winnipeg, Manitoba.

Berman, R.G., Davis, W.J., and Pehrsson, S., 2007. The collisional Snowbird tectonic zone resurrected: Growth of Laurentia during the 1.9 Ga accretionary phase of the Trans-Hudson orogeny; Geology, v. 35, p. 911–914.

Berman, R.G., Pehrsson, S., Davis, W.J., Ryan, J.J., Qui, H., and Ashton, K.E., 2013. The Arrowsmith orogeny: Geochronological and thermobarometric constraints on its extent and tectonic setting in the Rae craton, with implications for pre-Nuna supercontinent reconstruction; Precambrian Research, v. 232, p. 44–69.

Carpenter, R.L. and Duke, N.A., 2004. Geological setting of the West Meliadine Gold Deposits, Western Churchill Province, Nunavut, Canada; Exploration and Mining Geology, v. 13, p. 49−65.

Carpenter, R.L., Duke, N.A., Sandeman, H.S., and Stern, R., 2005. Relative and absolute timing of gold mineralization along the Meliadine Trend, Nunavut, Canada: Evidence for Paleoproterozoic gold hosted in an Archean greenstone belt; Economic Geology, v. 100, p. 567−576.

Davies, T., Richards, J.P., Creaser, R., Heaman, L.M., Chacko, T., Simonetti, A., Williamson, J., and McDonald, D.W., 2010. Paleoproterozoic age relationships in the Three Bluffs Archean iron-formation-hosted gold deposits, Committee Bay Greenstone Belt, Nunavut, Canada; Exploration and Mining Geology, v. 19, p. 55–80.

Davis, W.J. and Miller, A.R., 2001. A Late Triassic Rb-Sr phlogopite isochron age for a kimberlite dyke from the Rankin Inlet area, Nunavut; Geological Survey of Canada, Radiogenic Age and Isotopic Studies Report 14, Current Research 2001-F3, 5 p.

Davis, W.J., Ryan, J.J., Sandeman, H.A., and Tella, S., 2008. A Paleoproterozoic detrital zircon age for a key conglomeratic horizon within the Rankin Inlet area, Kivalliq Region, Nunavut: Implications for Archean and Proterozoic evolution of the area; Geological Survey of Canada, Current Research 2008-8, 8 p.

Dubé, B. and Gosselin, P., 2007. Greenstone-hosted quartz-carbonate vein deposits, *In:* Mineral Deposits of Canada: A Synthesis of Major Deposit Types, District Metallogeny, the Evolution of Geological Provinces, and Exploration Methods, (ed.) W.D. Goodfellow; Geological Association of Canada, Mineral Deposits Division, Special Publication no. 5, p. 49–73.

Dubé, B., Mercier-Langevin, P., Castonguay, S., McNicoll, V.J., Pehrsson, S.J., Bleeker, W., Schetselaar, E.M., and Jackson, S., 2011. Targeted Geoscience Initiative 4. Lode gold deposits in ancient, deformed and metamorphosed terranes – footprints and exploration implications: A preliminary overview of themes, objectives and targeted areas, *In:* Summary of Field Work and other Activities 2011; Ontario Geological Survey, Open File Report 6270, p. 38-1 to 38-10.

Hoffman, P.F., 1988. United plates of America, the birth of a craton: Early Proterozoic assembly and growth of Laurentia; Annual Review of Earth and Planetary Sciences, v. 16, p. 543–603.

Lawley, C.J.M., Creaser, R.A., McNicoll, V., Dubé, B., Mercier-Langevin, P., Pehrsson, S., and Vaillancourt, D., 2014a. Re-Os arsenopyrite and U-Pb detrital zircon geochronology at the Meliadine Gold District, Nunavut: Implications for the geologic setting and age of the Tiriganiaq Deposit; Geological Survey of Canada, Open File 7510, 19 p. doi:10.4095/293939

Lawley, C.J.M., Dubé, B., Jackson, S., Yang, Z., Mercier-Langevin, P., and Vaillancourt, D., 2014b. Sulfide paragenesis and LA-ICP-MS arsenopyrite geochemistry at the Meliadine Gold District, Nunavut: Implications for Re-Os arsenopyrite geochronology and ore deposit genesis; Geological Survey of Canada, Open File 7491, 1 poster. doi:10.4095/293938

Lawley, C.J.M., Creaser, R., Jackson, S., Yang, Z., Davis, B., Pehrsson, S., Dubé, Mercier-Langevin, P., and Vaillancourt, D., submitted a. Unravelling the Western Churchill Province Paleoproterozoic Gold Metallotect: Constraints from Re-Os arsenopyrite and U-Pb Xenotime Geochronology and LA-ICP-MS arsenopyrite geochemistry at the BIF-Hosted Meliadine Gold District, Nunavut, Canada; Economic Geology.

Lawley, C.J.M., Dubé, B., Mercier-Langevin, P., Kjarsgaard, B., Knight, R., and Vaillancourt, D., submitted b. Defining and mapping hydrothermal footprints at the BIF-hosted Meliadine Gold District, Nunavut, Canada; Journal of Geochemical Exploration.

Lawley, C.J.M., McNicoll, V., Castonguay, S., Dubé, B., Mercier-Langevin, P., Pehrsson, S., in prep. Geology of the Meliadine Gold District.

Miller, A.R., Balog, M.J., Barham, B.A., and Reading, K.L., 1994. Geology of the Early Proterozoic gold metallotect, Hurwitz Group in the Cullaton-Griffin lakes area, central Churchill

Structural Province, Northwest Territories, *In:* Current Research 1994-C; Geological Survey of Canada, p. 135–146.

Miller, A.R., Balog, M.J., and Tella, S., 1995. Oxide iron-formation-hosted lode gold, Meliadine trend, Rankin Inlet Group, Churchill Province, Northwest Territories, *In:* Current Research 1995-C; Geological Survey of Canada, p. 163–174.

Pehrsson, S.J., Berman, R.G., and Davis, W.J., 2013a. Paleoproterozoic orogenesis during Nuna aggregation: A case study of reworking of the Rae craton, Woodburn Lake, Nunavut; Precambrian Research, v. 232, p. 167–188.

Pehrsson, S.J., Berman, R.G., Eglington, B., and Rainbird, R., 2013b. Two Neoarchean supercontinents revisited: The case for a Rae family of cratons; Precambrian Research, v. 232, p. 27–43.

Rainbird, R.H., Davis, W.J., Stern, R.A., Peterson, T.D., Smith, S.R., Parrish, R.R., and Hadlari, T., 2006. Ar-Ar and U-Pb geochronology of a late Proterozoic rift basin: Support for a genetic link with Hudsonian orogenesis, western Churchill Province, Nunavut, Canada; The Journal of Geology, v. 114, p. 1–17.

Sherlock, R., Pehrsson, S., Logan, A.V., Hrabi, R.B., and Davis, W.J., 2004. Geological setting of the Meadowbank Gold Deposits, Woodburn Lake Group, Nunavut; Exploration and Mining Geology, v. 13, p. 67–107.

Sibson, R.H., Robert, F., and Poulsen, K.H., 1988. High-angle reverse faults, fluid-pressure cycling, and mesothermal gold-quartz deposits; Geology, v. 16, p. 551-555.

Tella, S., Mikkel, S., Armitage, A.E., Seemayer, B.E., and Lemkow, D., 1992. Precambrian geology and economic potential of the Meliadine Lake-Barbour Bay region, district of Keewatin, Northwest Territories, *In:* Current Research, Part C; Geological Survey of Canada, Paper 92-1C, p. 1–11.

Tella, S., Roddick, J.C., and van Breemen, O., 1996. U-Pb zircon age for a volcanic suite in the Rankin Inlet Group, Rankin Inlet map area, District of Keewatin, Northwest Territories; Geological Survey of Canada, Radiogenic Age and Isotopic Studies Report 9, p. 11–15.

GEOLOGICAL SURVEY OF CANADA
OPEN FILE 7852

Targeted Geoscience Initiative 4: Contributions to the Understanding of Precambrian Lode Gold Deposits and Implications for Exploration

Geology, hydrothermal alteration, and genesis of the world-class Canadian Malartic stockwork-disseminated Archean gold deposit, Abitibi, Quebec

Stéphane De Souza[1], Benoît Dubé[1], Vicki J. McNicoll[2], Céline Dupuis[1], Patrick Mercier-Langevin[1], Robert A. Creaser[3], and Ingrid M. Kjarsgaard[4]

[1]Geological Survey of Canada, Québec, Quebec
[2]Geological Survey of Canada, Ottawa, Ontario
[3]University of Alberta, Edmonton, Alberta
[4]Consulting Mineralogist, Ottawa, Ontario

2015

This publication is available for free download through GEOSCAN (http://geoscan.nrcan.gc.ca/)

Recommended citation

De Souza, S., Dubé, B., McNicoll, V.J., Dupuis, C., Mercier-Langevin, P., Creaser, R.A., and Kjarsgaard, I.M., 2015. Geology, hydrothermal alteration, and genesis of the world-class Canadian Malartic stockwork-disseminated Archean gold deposit, Abitibi, Quebec, *In:* Targeted Geoscience Initiative 4: Contributions to the Understanding of Precambrian Lode Gold Deposits and Implications for Exploration, (ed.) B. Dubé and P. Mercier-Langevin; Geological Survey of Canada, Open File 7852, p. 113–126.

Publications in this series have not been edited; they are released as submitted by the author.

Contribution to the Geological Survey of Canada's Targeted Geoscience Initiative 4 (TGI-4) Program (2010–2015)

TABLE OF CONTENTS

Geology, hydrothermal alteration, and genesis of the world-class Canadian Malartic stockwork-disseminated Archean gold deposit, Abitibi, Quebec

Stéphane De Souza[1]*, Benoît Dubé[1], Vicki J. McNicoll[2], Céline Dupuis[1], Patrick Mercier-Langevin[1], Robert A. Creaser[3], and Ingrid M. Kjarsgaard[4]

[1]Geological Survey of Canada, 490 rue de la Couronne, Québec, Quebec G1K 9A9
[2]Geological Survey of Canada, 601 Booth Street, Ottawa, Ontario, K1A 0E8
[3]Department of Earth and Atmospheric Sciences, University of Alberta, Edmonton, Alberta T6G 2E3
[4]Consulting Mineralogist, 15 Scotia Place, Ottawa, Ontario K1S 0W2
*Corresponding author's e-mail: sdesouza@nrcan.gc.ca

ABSTRACT

The Canadian Malartic Mine consists of an Archean low-grade bulk tonnage gold deposit (reserves of 10.7 Moz Au @ 0.97 g/t) hosted by clastic metasedimentary rocks of the Pontiac Group and subalkaline porphyritic quartz monzodiorite and granodiorite located immediately south of the Larder Lake–Cadillac Fault Zone. The quartz monzodiorite and granodiorite yield syn-Timiskaming U-Pb zircon ages of 2677 and 2678 Ma, respectively. Gold mineralization is characterized by zones of quartz-carbonate vein stockwork and disseminated pyrite with a Au-Te-W-S-Bi-Ag±Pb±Mo metallic signature. These ore zones are dominantly oriented subparallel to the northwest-striking S_2 foliation and to the east-striking and south-dipping Sladen Fault, thus forming northwest-southeast and east-west mineralized trends. Molybdenite from high-grade ore yielded a Re-Os age of ca. 2664 Ma. In both the sedimentary rocks and the quartz monzodiorite, the proximal and distal alteration zones are characterized by the presence of calcite and ferroan dolomite, respectively. In the sedimentary rocks, the ore zones show a wide distal biotite alteration halo with proximal assemblages comprising albite and/or microcline. The quartz monzodiorite comprises a distal hematitic alteration zone that is overprinted by proximal microcline + albite + quartz replacement zones. This study suggests that at Canadian Malartic deposit, the gold mineralization and its distribution are largely controlled by D_2 faults, shear and high-strain zones developed in the hinge zone of F_2 folds, and by the Sladen Fault. A ≤2678 Ma syn-Timiskaming magmatic-hydrothermal early phase of gold mineralization can be inferred by the metallic signature or the ore, the presence of mineralized stockworks, the potassic alteration (biotite/microcline), and association with porphyritic intrusions. The main characteristics of the Canadian Malartic deposit is thus best explained by syn-D_2 deformation gold (ca. 2670–2660 Ma) superimposed onto, or remobilized from, a gold-bearing magmatic/hydrothermal system related to Timiskaming-age porphyritic intrusions emplaced along a major fertile fault zone.

INTRODUCTION

The Canadian Malartic open pit mine consists of an Archean low-grade bulk tonnage gold deposit (10.7 Moz Au, in 343.7 Mt @ 0.97 g/t Au; Belzile and Gignac, 2011) located in the Malartic mining district in the Abitibi region of Quebec (Figs. 1 and 2). The open pit mine was put into production in 2011 and is being developed on the grounds of three past-producing underground mines that exploited the same auriferous hydrothermal system but at average ore grades varying between 3.3 and 4.9 g/t (Trudel and Sauvé, 1992). The Canadian Malartic gold deposit is characterized by the presence of disseminated and stockwork mineralization, along with vein-hosted gold in turbiditic metasedimentary rocks and porphyritic intrusions (Sansfaçon and Hubert, 1990; Trudel and Sauvé, 1992; Helt et al., 2014; De Souza et al., in press). In the Abitibi greenstone belt, stockwork and disseminated sulphide mineralization are common features of Archean Au and Au-Cu deposits associated with, and/or hosted by Timiskaming-age (2680–2672 Ma) quartz-feldspar porphyry (Robert, 2001). Such deposits have been interpreted either as genetically related to the porphyritic intrusive host rocks (Sinclair, 1982; Robert, 2001; Helt et al., 2014), or as structurally controlled

De Souza, S., Dubé, B., McNicoll, V.J., Dupuis, C., Mercier-Langevin, P., Creaser, R.A., and Kjarsgaard, I.M., 2015. Geology, hydrothermal alteration, and genesis of the world-class Canadian Malartic stockwork-disseminated Archean gold deposit, Abitibi, Quebec, *In:* Targeted Geoscience Initiative 4: Contributions to the Understanding of Precambrian Lode Gold Deposits and Implications for Exploration, (ed.) B. Dubé and P. Mercier-Langevin; Geological Survey of Canada, Open File 7852, p. 113–126.

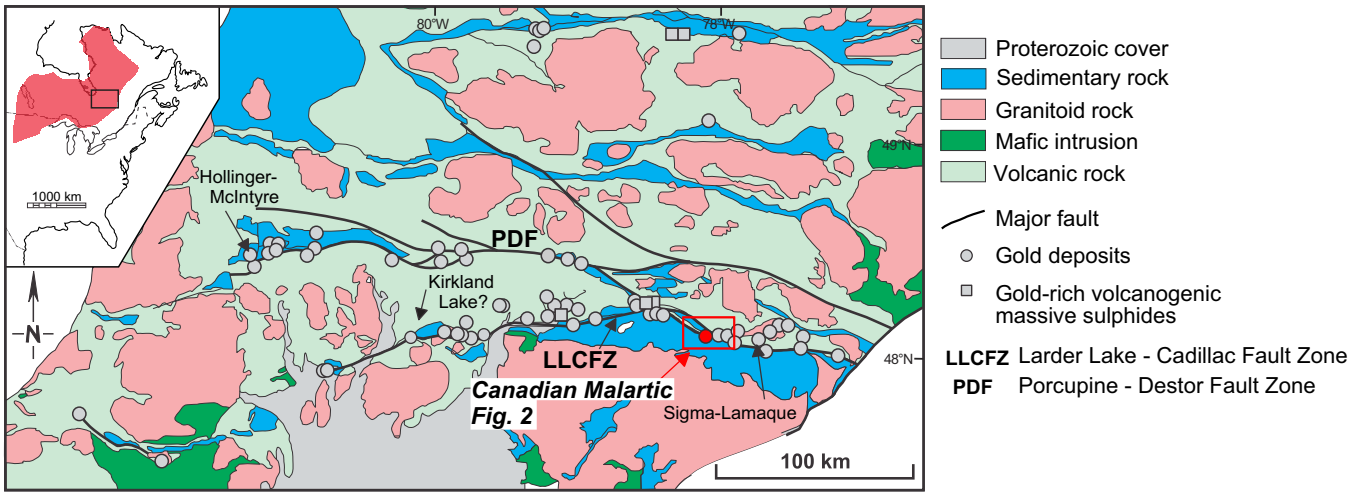

Figure 1. Simplified geological map of the Abitibi greenstone belt. Inset shows the location of the Superior Province. Adapted from Dubé and Gosselin (2007) and Poulson et al. (2000).

and, at least in part, contemporaneous with the main phase of deformation (Sansfaçon and Hubert, 1990; Trudel and Sauvé, 1992; Fallara et al., 2000; De Souza et al., 2013, in press; Zhang et al., 2014). At the Canadian Malartic Mine, calculated oxygen and hydrogen isotopic composition studies led to contrasting hypotheses on the origin of the Au mineralizing hydrothermal fluids, which are currently interpreted either as of magmatic (Helt et al., 2014) or metamorphic (Beaudoin and Raskevicius, 2014) origin. In this context, one of the main objectives of this project is to understand the geological parameters that control the distribution, genesis, and geological footprint of intrusion-associated gold deposits in deformed and metamorphosed Archean terranes.

The Canadian Malartic gold deposit is located within (Barnat zone) and immediately to the south (Canadian Malartic, Sladen and East Malartic zones) of the Larder Lake-Cadillac Fault Zone, which delineates the contact between the Abitibi Subprovince to the north and the Pontiac Subprovince to the south (Fig. 2). The fault zone is marked by volcanic and plutonic

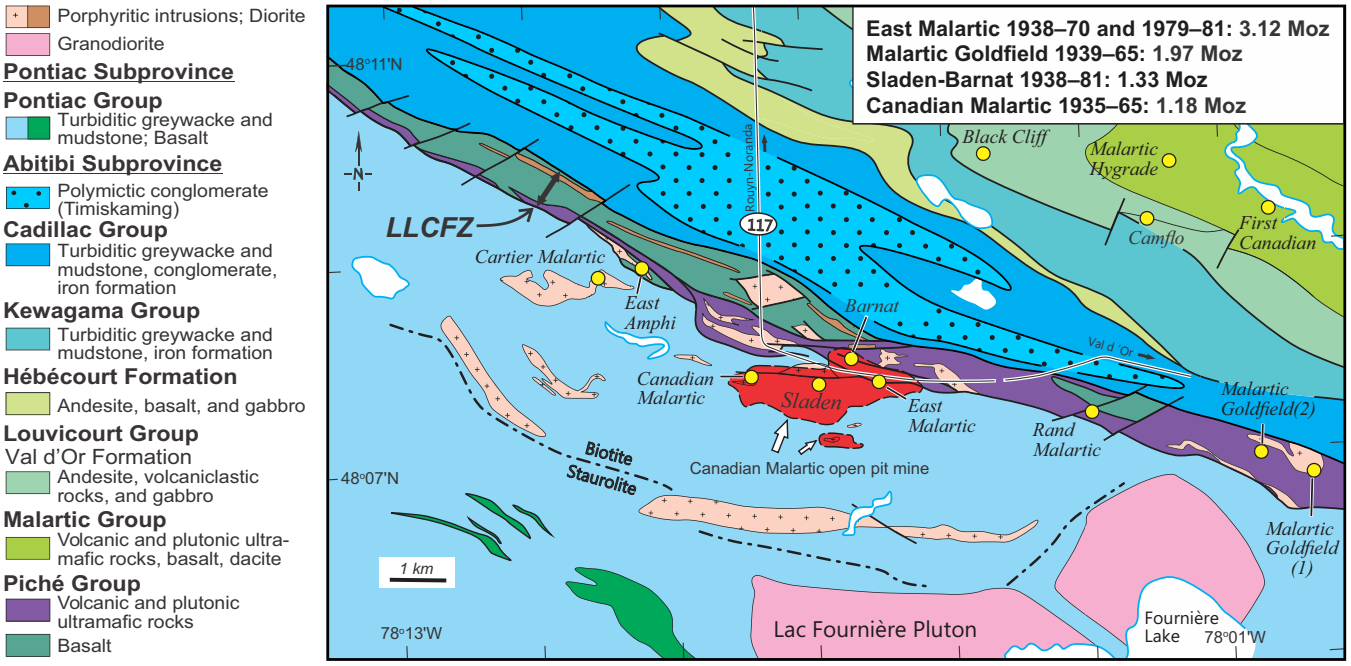

Figure 2. Geological map of the Malartic district showing the main past-producing gold mines and gold showings (yellow dots). The dash-dotted line corresponds to the staurolite isograd in the Pontiac Group sedimentary rocks. Geology is from this study and from Sansfaçon and Hubert (1990), Fallara et al. (2005), Grant et al. (2005), Pilote (2013), and Pilote et al. (2014). The final expected configuration of the Canadian Malartic open pit mine is shown in red. The gold production data for the past-producing East Malartic, Sladen-Barnat, Canadian Malartic, and Malartic Gold Fields are from Trudel and Sauvé (1992). LLCFZ: Larder Lake – Cadillac Fault Zone.

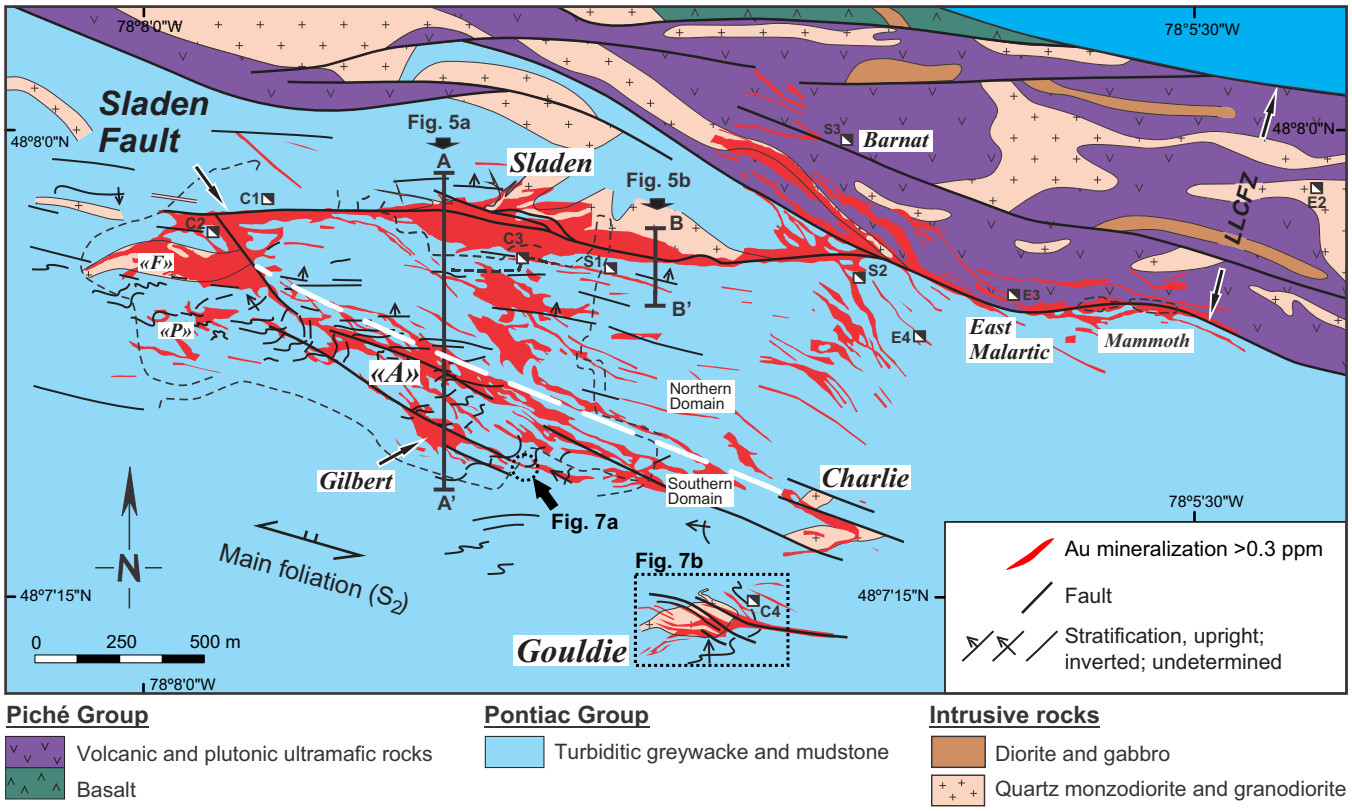

Figure 3. Geological map of the Canadian Malartic open pit gold mine. Geology from this study and from Derry (1939), Sansfaçon and Hubert (1990), and Fallara et al. (2000). Mineralized zones (≥0.3 g/t Au) are shown in red. The outline of the open pit mine, as of September 2012, is shown as a dashed line. The approximate limit between the northern and southern structural domains is identified by a white dashed line. Names of the main mineralized ore zones are identified in italic font. Location of the shafts of the past-producing mines: C = Canadian Malartic, E = East Malartic, S = Sladen-Barnat.

mafic-ultramafic rocks of the Piché Group (Fig. 2; Card, 1990; Daigneault et al., 2002). As in the Kirkland Lake and Timmins districts, Timiskaming-age polymictic conglomerate units have been recently identified immediately to the north of the Larder Lake-Cadillac Fault Zone and were dated at <2676 and 2678 Ma by Pilote et al. (2014). The Canadian Malartic gold deposit is mostly hosted by turbiditic greywacke and mudrock of the Pontiac Group (ca. 2685–2682; Davis, 2002) and by Timiskaming-age, ca. 2677–2678 Ma, porphyritic quartz monzodiorite to granodiorite intrusions (Helt et al., 2014; De Souza et al., in press). The metamorphic grade increases rapidly southward in the Pontiac Group (Sansfaçon and Hubert, 1990; Benn et al., 1994), from the biotite-chlorite zone along the southern contact of the Larder Lake-Cadillac Fault Zone, to garnet and staurolite zones within about 2 km to the south (Fig. 2). In the Malartic district, structural studies have shown that the Pontiac Group has undergone polyphase deformation and comprises a northeast-trending bedding-parallel S_1 foliation overprinted by a northwest-striking S_2 cleavage that represents the dominant foliation in the mine area (Sansfaçon and Hubert, 1990; Desrochers and Hubert, 1996; De Souza et al., in press).

GEOLOGY OF THE CANADIAN MALARTIC GOLD DEPOSIT

The Canadian Malartic open pit mine is mainly hosted by sedimentary rocks of the Pontiac Group (~70%; Fig. 3), which show a metamorphic paragenesis that comprises biotite, muscovite, oligoclase, chlorite, and epidote. Pyrite, pyrrhotite, ilmenite, magnetite, monazite and apatite are also present in variable proportions. These rocks are relatively weakly strained and show well preserved sedimentary structures. Sixty-five individual detrital zircon grains were collected from a sample of coarse-grained greywacke. The youngest U-Pb dating of which suggests a maximum age of ca. 2685 Ma (De Souza et al., in press), an age constraint similar to the one obtained by Davis (2002).

At the mine site, sedimentary rocks of the Pontiac Group are cut by dykes and sills of various compositions, all of which are known to show some evidence of hydrothermal alteration and to host, at least locally, ore-grade gold mineralization. These intrusive rocks include porphyritic quartz monzodiorite and granodiorite, intermediate and felsic dykes, and widespread lamprophyre dykes.

The quartz monzodiorite is mostly located in the

northern and western parts of the deposit and represents the main mineralized intrusive phase in the mine (Fig. 3). It is magnetite- and titanite-bearing and consists of perthitic orthoclase phenocrysts embedded within an equigranular groundmass composed of plagioclase, biotite, hornblende, epidote, quartz, and muscovite, with minor apatite, zircon, and ilmenite (Fig. 4a). The quartz monzodiorite can further be divided into low- and high-TiO_2 subtypes that are characterized by average TiO_2 values of ~0.34 and ~0.49 wt%, respectively. The low-TiO_2 subtype has normative compositions intermediate between quartz monzodiorite and granodiorite, but is referred to as quartz monzodiorite throughout the text. The porphyritic granodiorite is mostly present at the Gouldie zone (Fig. 3) and consists of 4 mm to 1 cm perthite phenocrysts that are set in an equigranular groundmass of quartz, plagioclase, muscovite, biotite, microcline, apatite, epidote, titanite, and pyrite. Molybdenite is locally present in the porphyritic granodiorite as disseminated flakes in the igneous groundmass, in "blue" quartz veins, or in molybdenite-pyrite-quartz veins.

Several samples of intrusive rocks were collected for U-Pb geochronology. The porphyritic quartz monzodiorite has yielded zircon and titanite ages of 2677 Ma and 2676 Ma, respectively, whereas zircons from the Gouldie zone granodiorite were dated at 2678 Ma. One felsic dyke from the open pit has yielded a zircon age of 2677 Ma. Thus, despite differences in composition of the intrusive rocks, geochronological studies indicate that the magmatic event(s) centred in the Malartic area happened in a restricted syn-Timiskaming 2678–2676 Ma time interval.

Structural Setting

In the mine area, S_2 is generally northwest-trending, northeast-dipping (65–90º) and is axial planar to F_2 open to closed folds that plunge steeply toward the east (Fig. 4b). F_2 folds form antiformal syncline and synformal anticline pairs, which are interpreted as the result of refolding of F_1 overturned folds. The S_1 foliation is only locally preserved in F_2 fold hinge zones and consists of a folded penetrative schistosity marked by white mica. The mine area has been divided into northern and southern structural domains based on the orientation of bedding relative to the S_2 cleavage (Fig. 3). The southern and northern domains represent the hinge zone and the long limb of a mine-scale S-type F_2 fold, respectively. Figure 5a also illustrates the distribution and geometry of the ore zones relative to the main structural features and host rocks. The east-trending Sladen Fault dips moderately to steeply (45–80º) toward the south and intersects the Piché Group in the eastern part of the deposit, where it is interpreted to locally mark the southern limit of the Larder Lake-Cadillac Fault Zone (Sansfaçon and Hubert, 1990). The Sladen Fault varies from a ~10 m-wide planar brittle±ductile deformation and alteration zone, to a ~100 m-wide fault zone comprising multiple subsidiary faults with evidence of both ductile and brittle strain increments. Banded porphyroclastic mylonite facies are present but discontinuous along and within ≤3 m into the footwall of the Sladen Fault, in the quartz monzodiorite. Hydrothermally altered fault breccia is also locally present, mostly in the quartz monzodiorite, and quartz breccia veins are common along the main fault segments in the sedimentary rocks. Cataclasite is locally superimposed on deformed and altered rocks and a 10 cm- to 2 m-wide zone of brittle deformation containing fault gouge, brecciated rock, and dismembered quartz veins generally marks a late fault plane.

Mineralization, Alteration, and Re-Os Dating

In the Canadian Malartic deposit, gold occurs mostly as <20 μm free gold grains and inclusions in pyrite, which are distributed in stockworks and veins (Fig. 4c) as well as disseminated in the altered host rocks (Fig. 4d). Gold is associated with trace amounts of Te-W-Bi±Ag and locally Mo±Pb (De Souza et al., in press). The mineralization is distributed according to two main trends forming east-west and northwest-southeast ore zones (Fig. 3). At the surface, the dominant east-west trace of the Sladen ore zone coincides with the position of the Sladen Fault and gold is hosted by quartz monzodiorite and by sedimentary rocks along and adjacent to the fault (Fig. 5). The surface trace of the northwest-southeast mineralized trend is subparallel to the S_2 cleavage. These northwest-trending ore zones dip steeply to moderately toward the northeast and are mainly hosted by sedimentary rocks and local dykes or sills. Mineralized rocks contain up to 5% disseminated pyrite with trace amounts of chalcopyrite, galena, scheelite, and telluride minerals. Molybdenite and sphalerite are locally present. Molybdenite from sedimentary rock-hosted high-grade gold mineralization was selected for Re-Os dating and yielded an age of ca. 2664 Ma.

Au-Related Veins

Among the different vein types documented during this study, three are closely related to auriferous hydrothermal alteration, and are present in the sedimentary rocks and in the quartz monzodiorite (V_1, V_2, and V_3 veins). The V_4 and V_5 veins are barren and post-date mineralization.

The V_1 veins are 1 mm to 3 cm in width, have low gold values (9 ppb to 0.44 ppm Au), and pre-date the main ore-forming stage. They are mainly composed of quartz with minor amounts of pyrite, albite, calcite, galena, molybdenite, biotite, and chlorite. The V_2 veins are related to the main stage of gold mineralization and

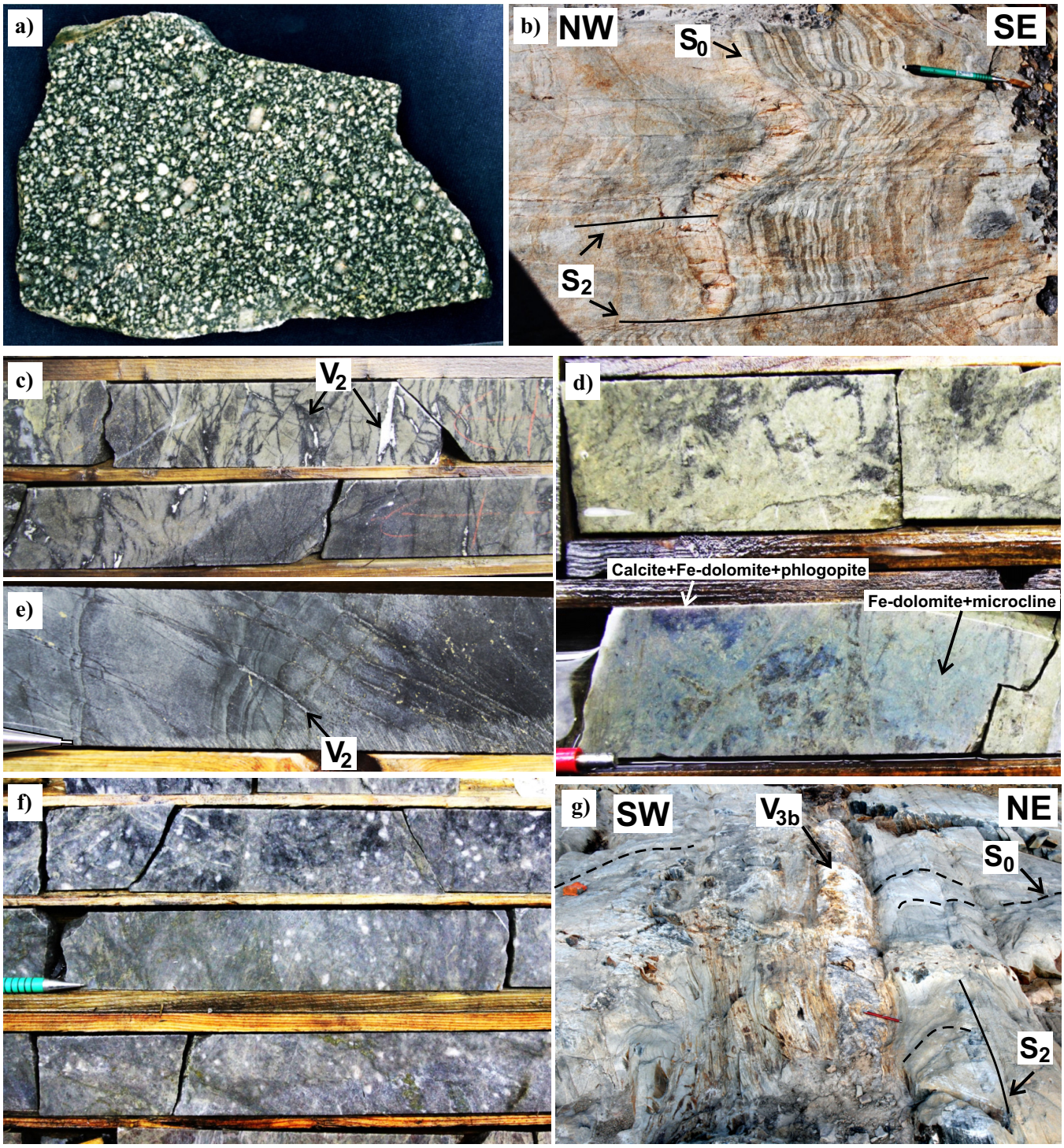

Figure 4. Field photographs. **a)** Least-altered quartz monzodiorite of the Sladen zone. **b)** F_2 folds in massive to laminated greywacke and mudstone of the Pontiac Group showing S_2 pressure-solution cleavage. Younging direction is to the northwest. **c)** Stockwork of V_2 veinlets and disseminated gold mineralization in altered greywacke. **d)** Proximal alteration in greywacke with ferroan dolomite coloured blue using carbonated staining technics. Notice the local presence of calcite (pinkish/purple) in biotite-rich zones. **e)** V_2 quartz veinlets with biotite-rich pyritized selvages in a distal alteration zone in sedimentary rocks. Veinlets are formed perpendicular to bedding. **f)** Proximal alteration zone in quartz monzodiorite, footwall of the Sladen Fault. **g)** High-grade laminated V_{3b} quartz vein in D_2 high-strain zone cutting the stratification at a high-angle. See Figure 7a for location.

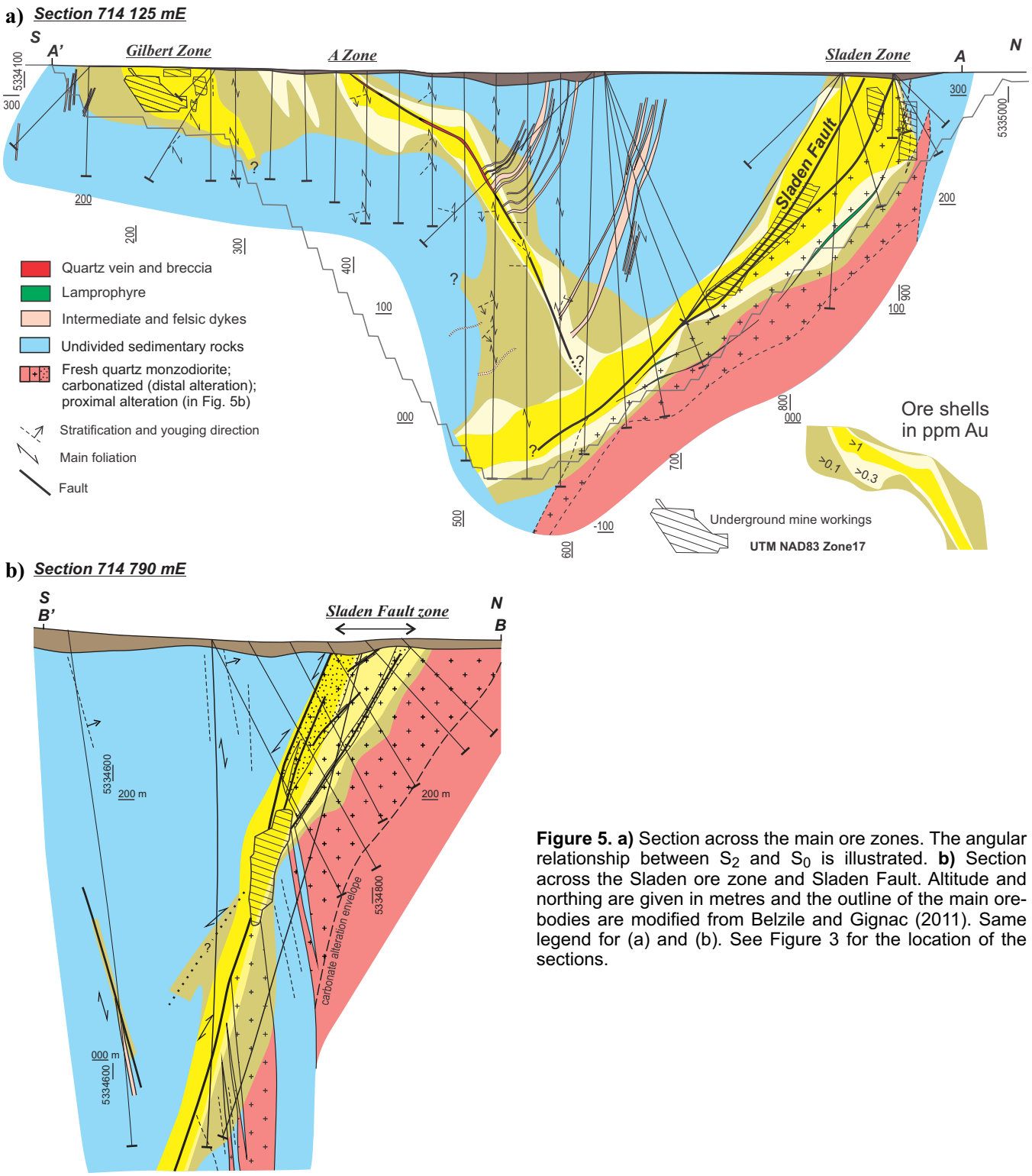

Figure 5. a) Section across the main ore zones. The angular relationship between S_2 and S_0 is illustrated. **b)** Section across the Sladen ore zone and Sladen Fault. Altitude and northing are given in metres and the outline of the main orebodies are modified from Belzile and Gignac (2011). Same legend for (a) and (b). See Figure 3 for the location of the sections.

are present in all rock types. These veins are 1 mm to 1 cm in width, generally show biotite selvages, and are composed of various proportions of quartz, calcite, ferroan dolomite, biotite, microcline, albite, chlorite, pyrite, and ankerite (Fig. 4c) with trace amounts of chalcopyrite, tellurides, gold, and scheelite. These V_2 veins occur as stockworks (Fig. 4c), as filled fractures and faults subparallel or at low-angle relative to the S_2 cleavage (Fig. 4e), or in some cases as crenulated veinlets at high-angle to S_2. The presence of deformed and undeformed V_2 veinlets suggests that they were emplaced syn- to late-D_2.

The V_3 veins cut V_2 veins and can be divided into three distinct subtypes: V_{3a}, V_{3b}, and V_c. The V_{3a}

veins are discontinuous, have well to poorly defined margins and in some cases are related to silica flooding of the host rocks. The V_{3a} veins consist of fine-grained white to grey saccharoidal quartz with finely disseminated pyrite and locally abundant molybdenite. The V_{3b} quartz-pyrite±galena veins are known to host high-grade Au values of up to 42.3 ppm. They form 1 cm- to 2 m-thick fault-fill laminated and breccia veins. The V_{3c} veins are mostly present in the quartz monzodiorite and granodiorite, and form 1 cm- to 30 cm-wide extensional veins that are dominated by quartz with variable proportions of coarse albite, muscovite, ankerite, calcite, biotite, pyrite, chlorite, and minor amounts of hematite, rutile, K-feldspar, tourmaline, galena, scheelite, native free gold, tellurides, and chalcopyrite. Derry (1939) described these veins as "pegmatitic", since grain size can reach up to 5 cm. Our analyses of such V_{3c} veins have yielded gold values of 0.013 to 6.7 ppm.

Distal and Proximal Hydrothermal Alteration Assemblages

Both the sedimentary and intrusive rocks are characterized by distal and proximal hydrothermal alteration assemblages with mineral compositions that are strongly influenced by the composition of the protolith. The main types of alteration that were documented are widespread carbonate alteration (calcite + ferroan dolomite ± ankerite) and sulphidation of the sedimentary and intrusive rocks. Biotite and K-feldspar potassic alteration is also important, whereas albitization and silicification are mostly developed in the sedimentary and intrusive rocks, respectively. Distal alteration zones are in excess of ~150 m. The proximal alteration haloes are up to 30 m wide, but larger zones containing almost continuous stockwork and/or proximal replacement zones over 70 m have also been documented.

In the sedimentary rocks, distal assemblages are composed of biotite, white mica, plagioclase, with minor amounts of pyrite and calcite (Fig. 4e). The carbonate and pyrite contents increase toward proximal alteration and ore zones. Carbonate minerals are mostly present in the greywacke facies and are almost absent from mudstone. The proximal assemblage in the sedimentary rocks is light beige and composed of fine-grained (5–20 um) albite and/or microcline with ferroan dolomite, calcite, quartz, phlogopite, and minor white mica (Fig. 4d). Phlogopite is F-rich (0.2–1.4 wt% F) and is absent from pervasively altered sedimentary rocks. Both the distal and proximal assemblages occur within D_2 high-strain zones, as replacement-style alteration controlled by protolith composition, and as selvages to V_2 and V_{3a-b} veins.

In the quartz monzodiorite, distal and proximal alteration assemblages are best developed in the high-TiO_2 subtype. The distal assemblage consists of a dark grey to reddish facies comprising calcite, hematite, biotite, and microcline, as well as magnetite, pyrite, chlorite, and rutile pseudomorphs after titanite and ilmenite. The proximal alteration consists of grey to pinkish (± hematite) microcline, albite, quartz, ferroan dolomite, rutile ± calcite assemblages that vary from vein selvages to a pervasive hydrothermal replacement (Fig. 4f). A fine-grained cherty subtype of the proximal grey alteration shows relict feldspar phenocrysts obscured by alteration, recrystallization, and by the local development of a mylonitic fabric.

At the Gouldie zone, hydrothermal alteration of the granodiorite is widespread and largely controlled by the presence of sheeted V_3 quartz veins and stockworks, whereas fresh granodiorite is seldom preserved. The dominant alteration facies is greenish to white-coloured and represented by a mineral assemblage consisting of calcite, ferroan dolomite, white mica, albite, microcline, quartz, pyrite and rutile. V_3 veins often show bleached selvages that are mainly composed of feldspar, quartz, and carbonate. Although in trace amounts overall, molybdenite is locally abundant in quartz veins, disseminated in the altered granodiorite, or as coating fractures.

Mass gain/loss in K_2O, Na_2O, and SiO_2 was calculated according to the isocon method of Grant (1986) for a set of samples collected from surface outcrops of the Sladen zone distributed ~150 m to the west and east of the section shown in Figure 5b. In the footwall of the Sladen Fault, the distal alteration assemblage hosted by the quartz monzodiorite shows negligible Na_2O variation and low K_2O increase of approximately 0 to +45 wt% related to variable Au values of <0.005 to 1.25 ppm. In the immediate footwall of the Sladen Fault, the proximal alteration assemblage shows marked increases in K_2O (+80 to +360 wt%) and SiO_2 (+30 to +250 wt%) and leaching of Na_2O (-2 to -80 wt%). In the sampled area, intense alteration of sedimentary rocks is mostly restricted to ca. 2 m within the hanging wall of the Sladen Fault, where sedimentary rocks are characterized by strong Na_2O enrichment (+40 to +330 wt%) and K_2O leaching in proximal altered zones (-15 to -40 wt%). Molar CO_2/CaO and CO_2/(CaO+MgO) ratios for these same samples suggest that, irrespective of the host rock type, ore-grade gold values (i.e. ≥0.30 ppm) are present in the samples with strongest carbonatization ($molCO_2$/(molCaO) >0.8; Fig. 6a), and that the wt% CO_2 content is largely dependent on the nature of the protolith and its capacity to react with the gold-bearing CO_2-rich fluid (Fig. 6b; e.g. Davies et al., 1982, 1990).

Characteristics of the Northwest-Southeast- and East-West-Trending Ore Zones

Northwest-southeast-trending ore zones include the P,

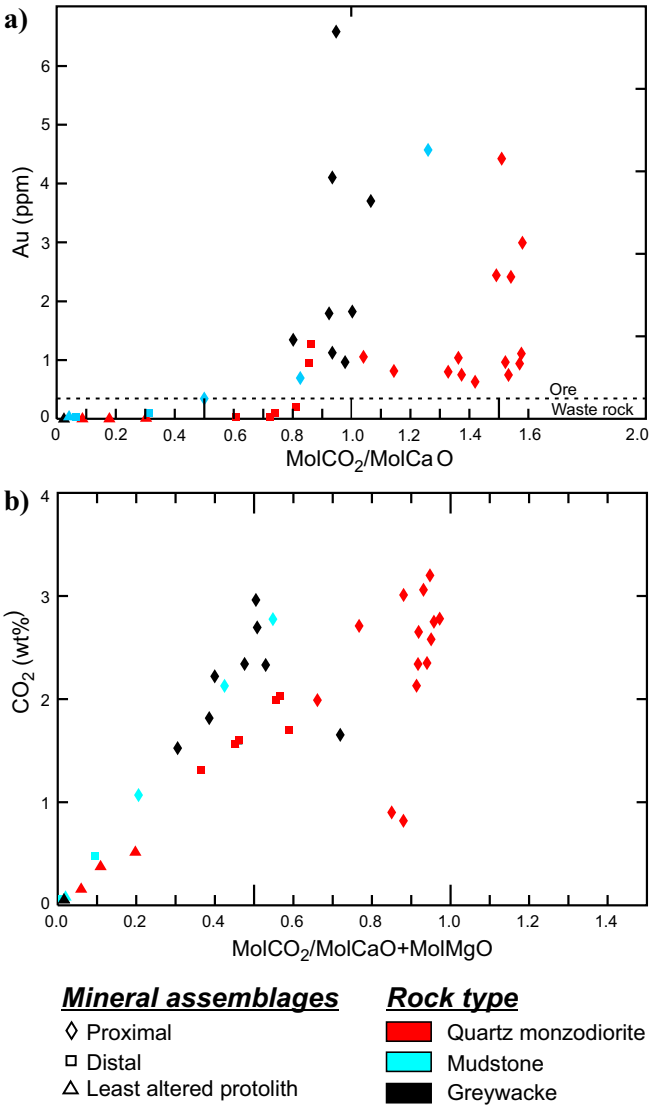

Figure 6. a) Au (ppm) vs molar CO_2/CaO ratio and **(b)** CO_2 wt% vs. molar CO_2/(CaO+MgO) diagrams for samples of greywacke, mudstone, and quartz monzodiorite from the Sladen ore zone.

A, Gouldie, and Gilbert zones, which show relatively similar alteration types and are discordant relative to bedding and to intrusive rocks. The P zone is, however, partly stratabound and controlled by the geometry of the folded strata (e.g. Sansfaçon et al., 1987). The Gilbert and A zones are subparallel, dip northward, and represent the main northwest-southeast-trending ore zones.

In the Gilbert zone, auriferous alteration zones are distributed in a series of subparallel, planar north-northeast-dipping D_2 high-strain zones varying from 5 cm to 3 m wide and developed at a high-angle to the folded bedding and felsic feldspar-phyric sill-like intrusions (Fig. 7a). The high-strain zones show closed to locally tight fold hinges that are dismembered by sets of parallel brittle faults filled by V_2 veinlets. Auriferous V_{3b} veins are present in some of the high-strain zones and yield up to 33.4 ppm Au (Fig. 4g). Distal and proximal alteration assemblages are present in the Gilbert zone as selvages of the V_2 veinlets and within high-strain zones, with gold values up to 6.11 ppm. The porphyritic felsic sill yields low gold values (<0.3 ppm) and shows minor carbonatization and sulphidation (mainly pyrite). An east-northeast-plunging mineral lineation with a steep pitch (~60–80º) is locally marked by biotite and by quartz fibres in V_{3b} veins (Fig. 7a). Kinematic indicators are scarce in the high-strain zones, but the dragging and displacement of the faulted dykes, together with the local occurrence of back-rotated quartz-vein boudins suggest a dominant top-to-the-southwest reverse sense of shear.

As shown in Figure 5a, the A-zone is centred on a D_2 fault zone that hosts V_{3a} and V_{3b} veins and clearly cuts south-dipping to subvertical dykes in the Pontiac Group. This fault zone also coincides with the transition from the northern to the southern structural domains. From the surface down to a depth of approximately 100 m, the A zone is marked by a sharp inflexion from a shallow to a steep dip. Considering the interpreted reverse sense of motion along D_2 faults, this inflexion can be interpreted as a dilational bend/jog structure or relay zone that may have acted as a preferential lower pressure fluid pathway during mineralization.

At the Gouldie zone, gold is distributed along and parallel to a north-dipping, west-northwest-trending, approximately ≤5- to 8-m-wide, D_2 high-strain zone formed at high-angle to the bedding in a F_2 hinge zone (Fig. 7b). This mineralized zone is continuous for >500 m along-strike toward the east-southeast and intersects a porphyritic granodiorite intrusion at its northwestern extremity. In the sedimentary rocks, the Gouldie zone shows typical alteration zonation with light-coloured proximal alteration and disseminated pyrite associated with V_2 veinlets and V_{3b} veins. However, V_{3b} veins are extensive and are locally up to 2 m wide. Detailed mapping has also revealed that D_2 faults and shear zones follow lamprophyre dykes, possibly due to competency contrasts between the dykes and the host rocks (Fig. 7b). The steep to moderate pitch (55–75º) of the northeast-plunging mineral lineation in the high-stain zone and the geometry of the quartz fibres in the quartz veins suggest a reverse sense of shear with a sinistral slip component (De Souza et al., in press).

Along east-west-trending ore zones, the quartz monzodiorite to the north of the Sladen Fault is strongly altered to proximal assemblages along the main fault segments. The distal alteration assemblage is developed as an alteration halo up to 100 m into the footwall of the Sladen Fault (Fig. 5b) and as selvages of V_1 veins. The main Sladen ore zone dips steeply to the south but westward it becomes shallow dipping at depth.

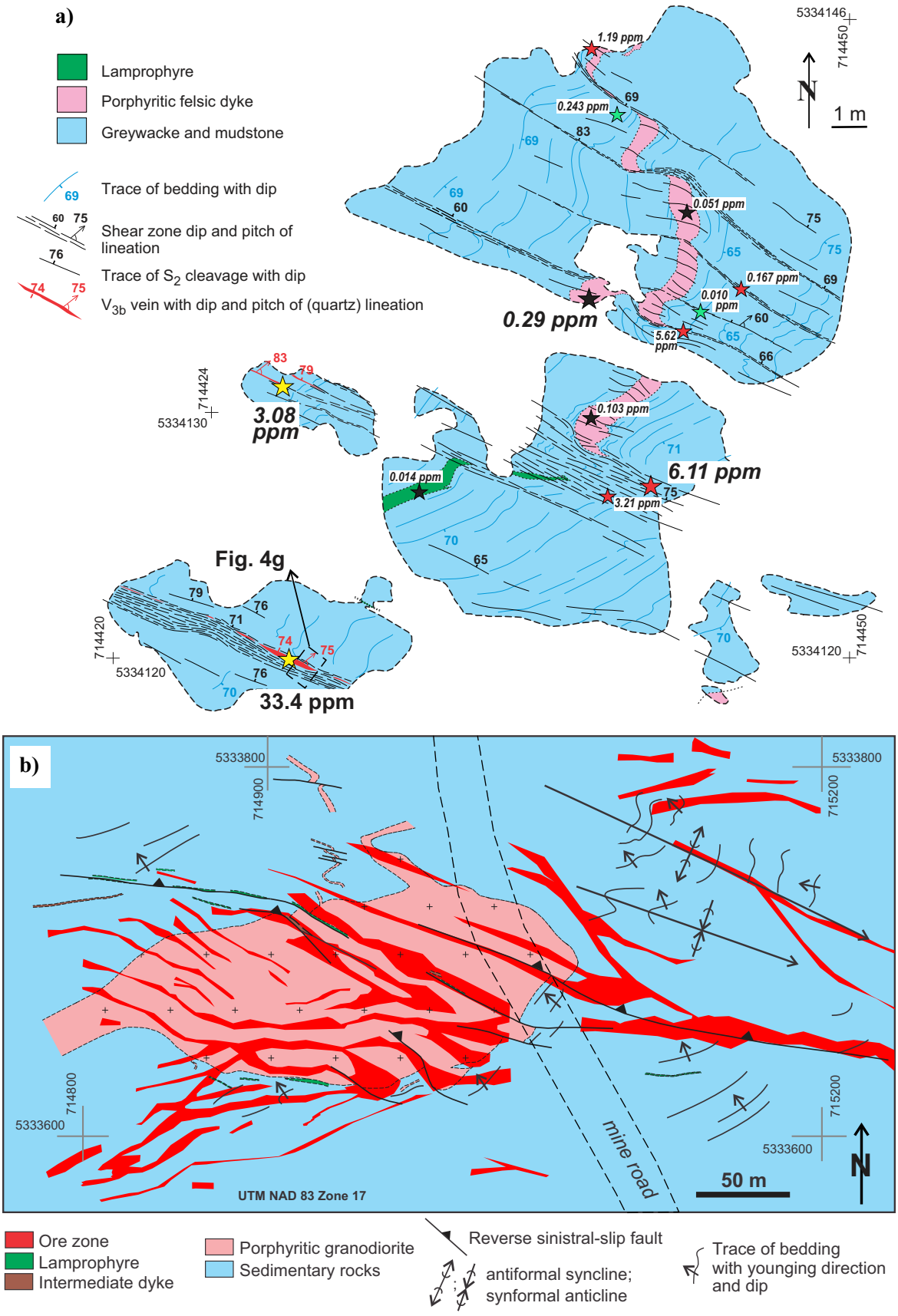

Figure 7. a) Detailed outcrop map of the southeastern extension of the Gilbert zone. Green, red, black, and yellow stars indicate the location and gold content of assayed samples of distal alteration, proximal alteration, dyke-hosted mineralization, and V_{3b} vein, respectively. **b)** Geological map of the Gouldie zone. See Figure 3 for locations.

DISCUSSION OF GENETIC MODELS

Compiled U-Pb ages and data presented herein clearly indicate that Timiskaming-age 2677–2678 Ma quartz monzodiorite and granodiorite, which host part of the mineralization at the Canadian Malartic Mine, were intruded into the Pontiac Group (ca. 2685–2682 Ma) metasedimentary rocks prior to D_2 main phase deformation and metamorphism in the southern Abitibi Subprovince (i.e. 2670–2660 Ma; Ayer et al., 2005; Robert et al., 2005, and references therein). An early magmatic-hydrothermal gold mineralization event, as originally proposed by Issigonis (1980), can be inferred based on the presence of widespread potassic alteration (microcline and biotite), the Au-Te-W-Bi±Ag±Mo±Pb metallic signature of the ore (e.g. Goldfarb et al., 2005; Hart, 2007), and by the spatial association of mineralization with porphyritic intrusions. Moreover, the Canadian Malartic deposit shares analogies with the structurally controlled sedimentary rock-hosted intrusion-related deposits, as described by Robert et al. (2007), especially in terms of host rock, metallic signature and alteration (feldspar, sericite, carbonate and biotite), but also because such deposits are commonly located in the core of anticlines cut by high-angle faults in proximity to a crustal scale fault. However, a simple magmatic-hydrothermal model at Canadian Malartic cannot entirely explain the northwest-southeast and east-west distribution of the ore zones, nor the interpreted chronology of mineralization relative to deformation and magmatism. Field evidence suggests that at least part of the alteration assemblages, disseminated orebodies, and vein networks are associated with widespread brittle and brittle-ductile structures formed as a result of D_2 deformation. V_2 veins emplaced along the S_2 cleavage and fractures/faults axial planar to F_2 folds, together with the presence of quartz veins (V_{3a} and V_{3c}), filling fractures, and faults at high angle to folded bedding, are indicative of gold-bearing hydrothermal fluids invading D_2 structures. A syndeformation stage of gold mineralization is also compatible with the ca. 2664 Ma Re-Os molybdenite age, which overlaps with the inferred age of the regional main phase D_2 deformation as well as with the bulk of lode gold mineralization (2670–2660 Ma) in the southern Abitibi (e.g. Ayer et al., 2005; Robert et al., 2005; Dubé and Gosselin, 2007). The D_2 deformation model is compatible with the widespread carbonate alteration that typifies a large number of gold deposits along the Larder Lake-Cadillac and Destor-Porcupine fault zones in the Abitibi greenstone belt (e.g. Dubé and Gosselin, 2007 and references therein). The main characteristics of the Canadian Malartic deposit are thus best explained by syn-D_2 deformation gold (ca. 2670–2660 Ma) superimposed onto, or partly remobilized from, an early gold-bearing magmatic/hydrothermal system related to Timiskaming-age porphyritic intrusions emplaced along a major fertile fault zone. Moreover, aside from the gold being mostly hosted by turbiditic clastic sedimentary rocks, the Malartic deposit exhibits several common features of Archean orogenic gold deposits (cf. Goldfarb et al., 2005), including a combination of widespread carbonate alteration, overall low Cu, Bi, Zn and Pb contents, CO_2, K_2O, Na_2O, and S hydrothermal metasomatism, and the spatial association with brittle-ductile faults and shear zones. Also, as illustrated by the distribution of the orebodies and the underground workings of the past-producing mines, the Sladen Fault has played a major role in the formation of the Canadian Malartic deposit, and represents one of the main conduits for the rising gold-bearing hydrothermal fluid(s). The close relationship between mineralization and a brittle fault next to the Larder Lake-Cadillac Fault Zone, as well as the association with calc-alkaline porphyritic intrusions emplaced in sedimentary rocks, the hydrothermal carbonate alteration and the positive correlation between Au and Te are similar to key features of the giant syenite-hosted Kirkland Lake gold deposit located further west along the Larder Lake-Cadillac Fault Zone (e.g. Ispolatov et al., 2008 and references therein).

IMPLICATIONS FOR EXPLORATION

As it is the case for the Canadian Malartic deposit and for most greenstone-hosted lode gold deposits, the proximity to a major fault and the association of porphyritic intrusions, carbonatized mafic to ultramafic rocks, and Timiskaming-like fluvial/alluvial sedimentary rocks are key geological parameters for the formation and preservation of major deposits (Poulsen et al., 1992; Hodgson, 1993; Goldfarb et al., 2005; Robert et al. 2005; Dubé and Gosselin, 2007; Bleeker, 2012). The identification of such key geological parameters is thus of major importance in exploration targeting. The lack of known gold mineralization more than ~2–3 km south of the Pontiac-Piché contact, which also corresponds to the transition from biotite zone metamorphism and brittle to brittle-ductile deformation, to higher grade garnet and staurolite zone metamorphism and dominantly ductile deformation, may also help to underline prospective gold corridors south of the Larder Lake-Cadillac Fault Zone. In this context, the Sladen Fault and brittle-ductile D_2 faults formed in fold hinges and along short limbs of drag folds, have proven to represent fertile hydrothermal conduits for the circulation of gold-bearing fluids. Alteration haloes in excess of 150 m that include a distal assemblage with calcite in variable amounts in both the sedimentary rocks and quartz monzodiorite, also provide useful vectors for exploration. The Au-Te-W-Bi±Ag metallic

signature of the ore and the potassic component of the alteration assemblages (biotite+muscovite and K-feldspar) are key features that can also be applied in geochemical prospecting.

ACKNOWLEDGEMENTS

This project is conducted in collaboration with P. Pilote and P. Roy of the Ministère de l'Énergie et des Ressources naturelles du Québec, and the Canada Mining and Innovation Council (CMIC) footprints project, including R. Linnen, G. Olivo, A. Galley, M. Lesher, F. Robert, A.E. Williams-Jones, and especially S. Perrouty, N. Gaillard, N. Piette-Lauzière, R. Enkin, N. Elgoumi, and C. Bérubé-Lafrenière, who are all gratefully acknowledged for collaborating in this joint project. Special thanks are also due to all of the Osisko and Mine Canadian Malartic exploration and production team. We are profoundly thankful to D. Gervais and F. Bouchard of the Mine Canadian Malartic partnership, and to R. Wares, P. de Chavigny, and L. Caron for sharing their knowledge of the Canadian Malartic deposit. S. Castonguay, S. Jackson, J.F. Gao, W. Bleeker, J. Moorehead, H.K. Poulsen, F. Robert, M. Bardoux, D. Sillitoe, D. Sinclair, J.-F. Couture, and J. Clark contributed to constructive discussions and are sincerely acknowledged.

REFERENCES

Ayer, J.A., Thurston, P.C., Bateman, R., Dubé, B., Gibson, H.L., Hamilton, M.A., Hathway, B., Hocker, S.M., Houlé, M.G., Hudak, G., Ispolatov, V.O., Lafrance, B., Lesher, C.M., MacDonald, P.J., Péloquin, A.S., Piercey, S.J., Reed, L.E., and Thompson, P.H., 2005. Overview of results from the Greenstone Architecture Project: Discover Abitibi Initiative; Ontario Geological Survey, Open File Report 6154, 146 p.

Belzile, E. and Gignac, L.P., 2011. Updated resource and reserve estimates for the Canadian Malartic project Malartic, Quebec; NI 43-101 Report, 261 p.

Beaudoin, G. and Raskevicius, T., 2014. Constraints on the genesis of the Archean oxidized, intrusion-related Canadian Malartic gold deposit, Quebec, Canada: A discussion; Economic Geology, v. 109, p. 2067–2068.

Benn, K., Miles, W., Ghassemi, M.R., and Gillett, J., 1994. Crustal structure and kinematic framework of the northwestern Pontiac Subprovince, Quebec: An integrated structural and geophysical study; Canadian Journal of Earth Sciences, v. 31, p. 271–281.

Bleeker, W., 2012. Targeted Geoscience Initiative 4: Lode gold deposits in ancient deformed and metamorphosed terranes: The role of extension in the formation of Timiskaming basins and large gold deposits, Abitibi greenstone belt – A discussion; Ontario Geological Survey, Open File Report 6280, p. 47-1 to 47-12.

Card, K.D., 1990. A review of the Superior Province of the Canadian Shield, a product of Archean accretion; Precambrian Research, v. 48, p. 99–156.

Daigneault, R., Mueller, W., and Chown, E.H., 2002. Oblique Archean subduction: Accretion and exhumation of an oceanic arc during dextral transpression, Southern Volcanic Zone, Abitibi Subprovince, Canada; Precambrian Research, v. 115, p. 261–290.

Davies, J.F., Whitehead, R.E.S., Cameron, R.A., and Duff, D., 1982. Regional and local patterns of CO_2-K-Rb-As alteration: A guide to gold in the Timmins area, *In:* Geology of Canadian Gold Deposits, (ed.) R.W. Hodder and W. Petruk; Canadian Institute of Mining and Metallurgy, Special Volume 24, p. 130–143.

Davies, J.F., Whitehead, R.E., Huang, J., and Nawaratne, S., 1990. A comparison of progressive hydrothermal carbonate alteration in Archean metabasalts and metaperidotites; Mineralium Deposita, v. 25, p. 65–72.

Davis, D.W., 2002. U-Pb geochronology of Archean metasedimentary rocks in the Pontiac and Abitibi Subprovinces, Quebec, Constraints on timing, provenance and regional tectonics; Precambrian Research, v. 115, p. 97–117.

Derry, D.R., 1939. The geology of the Canadian Malartic gold mine, N. Quebec; Economic Geology, v. 34, p. 495–523.

De Souza, S., Dubé, B., McNicoll, V., Mercier-Langevin, P., Dupuis, C., Creaser, R., de Chavigny, P., and Gervais, D., 2013. The Canadian Malartic mine, Abitibi, Quebec: Geological characteristics and relative timing of low-grade bulk-tonnage gold mineralization; Ministère des Ressources Naturelles du Québec, Québec-Mines, Abstracts, p. 28.

De Souza, S., Dubé, B., McNicoll, V., Dupuis, C., Mercier-Langevin, P., Creaser, R., and Kjarsgaard, I., in press, Geology, structure and timing of hydrothermal alteration at the Canadian Malartic Archean stockwork disseminated world-class gold deposit, Quebec, Canada, *In:* Archean Base and Precious Metal Deposits, Southern Abitibi Greenstone Belt, Canada, (ed.) T. Monecke, P. Mercier-Langevin, and B. Dubé; Society of Economic Geologists, Field guide book 46.

Desrochers, J.P. and Hubert, C., 1996. Structural evolution and early accretion of the Archean Malartic composite block, southern Abitibi greenstone belt, Quebec, Canada; Canadian Journal of Earth Sciences, v. 33, p. 1556–1569.

Dubé, B. and Gosselin, P., 2007. Greenstone-hosted quartz-carbonate vein deposits, *In:* Mineral Deposits of Canada: A Synthesis of Major Deposit Types, District Metallogeny, the Evolution of Geological Provinces and Exploration Methods, (ed.) W.D. Goodfellow; Geological Association of Canada, Mineral Deposits Division, Special Publication No. 5, p. 49–73.

Fallara, F., Ross, P.-S., and Sansfaçon, R., 2000. Caractérisation géochimique, pétrographique et structurale: Nouveau modèle métallogénique du camp minier de Malartic; Ministère des Ressources Naturelles du Québec, MB 2000-15, 41 p.

Fallara, F., Ross, P.-S., Sansfaçon, R., and Grant, M., 2005. Lac Fournière; Ministère des Ressources Naturelles du Québec, Geological compilation map, 32D01-200-0102, scale 1: 20,000.

Goldfarb, R.J., Baker, T., Dubé, B., Groves, D.I., Hart, C.J.R., Robert, F., and Gosselin, P., 2005. World distribution, productivity, character, and genesis of gold deposits in metamorphic terranes, *In:* One Hundredth Anniversary Volume, (ed.) J.W. Hedenquist, J.F.H. Thompson, R.J. Goldfarb, and J.P. Richards; Society of Economic Geologists, p. 407–450.

Grant, J.A., 1986. The isocon diagram – a simple solution to Gresens' equation for metasomatic alteration; Economic Geology, v. 81, p. 1976–1982.

Grant, M., Fallara, F., Ross, P.-S., and Sansfaçon, R., 2005. Malartic; Ministère des Ressources Naturelles du Québec, Geological compilation map, 32D01-200-0202, scale 1: 20,000.

Hart, C.J.R., 2007. Reduced intrusion-related gold systems, *In:* Mineral Deposits of Canada: A Synthesis of Major Deposit Types, District Metallogeny, the Evolution of Geological Provinces and Exploration Methods, (ed.) W.D. Goodfellow; Geological Association of Canada, Mineral Deposits Division, Special Publication No. 5, p. 95–112.

Helt, K.M., Williams-Jones, A.E., Clark, J.R., Wing, B., and Wares, R.P., 2014. Constraints on the genesis of the Archean oxidized, intrusion-related Canadian Malartic gold deposit, Quebec, Canada; Economic Geology, v. 109, p. 713–735.

Hodgson, C.J., 1993. Mesothermal lode-gold deposits, *In:* Mineral Deposit Modeling, (ed.) R.V. Kirkham; Geological Association of Canada, Special Paper 40, p. 635–678.

Ispolatov, V., Lafrance, B., Dubé, B., Creaser, R., and Hamilton, M., 2008. Geological and structural setting of gold mineralization in the Kirkland Lake-Larder Lake gold belt, Ontario; Economic Geology, v. 103, p. 1309–1340.

Issigonis, M.J., 1980. Occurrence of Disseminated Gold Deposits in Porphyries in Archean Abitibi Belt, NW Quebec, Canada; Institution of Mining and Metallurgy London, Transactions, Section B: Applied Earth Sciences, v. 89, p. 157–158.

Pilote, P., 2013. Géologie – Malartic; Ministère des Ressources naturelles du Québec, CG-32D01D-2013-01.

Pilote, P., Daigneault, R., David, J., and McNicoll, V., 2014. L'architecture des groupes de Malartic, de Piché et de Cadillac et de la Faille de Cadillac, Abitibi : révision géologique, nouvelles datations et interprétations; Ministère des ressources naturelles du Québec, Québec-Mines, Résumés, DV2014-07.

Poulsen, K.H., Card, K.D., and Franklin, J.M., 1992. Archean tectonic and metallogenic evolution of the Superior Province of the Canadian Shield; Precambrian Research, v. 58, p. 25–54.

Poulsen, K.H., Robert, F., and Dubé, B., 2000. Geological classification of Canadian gold deposits; Geological Survey of Canada, Bulletin 540, 106 p.

Robert, F., 2001. Syenite-associated disseminated gold deposits in the Abitibi greenstone belt, Canada; Mineralium Deposita, v. 36, p. 503–516.

Robert, F., Brommecker, R., Bourne, B.T., Dobak, P.J., McEwans, C.J., Rowe, R.R., and Zhou, X., 2007. Models and exploration methods for major gold deposit types, *In:* Proceedings of Exploration 07: Fifth Decennial International Conference on Mineral Exploration, (ed) Milkereit, B., p. 691-711.

Robert, F., Poulsen, K.H., Cassidy, D.F., and Hodgson, C.J., 2005. Gold metallogeny of the Superior and Yilgarn cratons, *In:* One Hundredth Anniversary Volume, (ed.) J.W. Hedenquist, J.F.H. Thompson, R.J. Goldfarb, and J.P. Richards; Society of Economic Geologists, p. 1001–1033.

Sansfaçon, R. and Hubert, C., 1990. The Malartic gold district, Abitibi greenstone belt, Quebec: Geological setting, structure and timing of gold emplacement at Malartic Gold Fields, Barnat, East Malartic, Canadian Malartic and Sladen Mines *In:* The Northwestern Quebec Polymetallic Belt, (ed.) A. Simard; Canadian Institute of Mining and Metallurgy, Special Volume 43, p. 221–235.

Sansfaçon, R., Grant, M., and Trudel, P., 1987. Géologie de la Mine Canadian Malartic – District de Val d'Or; Ministère des Ressources naturelles du Québec, MB 87-26, 44 p.

Sinclair, W.D., 1982. Gold deposits of the Matachewan Area, Ontario, *In:* Geology of Canadian Gold Deposits, (ed.) R.W. Hodder and W. Petruk; Canadian Institute of Mining and Metallurgy, Special Volume 24, p. 83–93.

Trudel, P., and Sauvé, P., 1992. Synthèse des caractéristiques géologiques des gisements d'Or du district de Malartic; Ministère des Ressources naturelles du Québec, MM89-04, 113 p.

Zhang, J., Lin, S., Linnen, R., and Martin, R., 2014. Structural setting of the Young-Davidson syenite-hosted gold deposit in the western Cadillac-Larder Lake deformation zone, Abitibi greenstone belt, Superior Province, Ontario; Precambrian Research, v. 248, p. 39–59.

GEOLOGICAL SURVEY OF CANADA
OPEN FILE 7852

Targeted Geoscience Initiative 4: Contributions to the Understanding of Precambrian Lode Gold Deposits and Implications for Exploration

Petrophysical signature of gold mineralization and alteration assemblages at the Canadian Malartic deposit, Quebec

Najib El Goumi[1], Stéphane De Souza[2], Randolph J. Enkin[1], and Benoît Dubé[2]

[1]Geological Survey of Canada, Sidney, British Columbia
[2]Geological Survey of Canada, Québec, Quebec

2015

This publication is available for free download through GEOSCAN (http://geoscan.nrcan.gc.ca/)

Recommended citation

El Goumi, N., De Souza, S., Enkin, R.J., and Dubé, B., 2015. Petrophysical signature of gold mineralization and alteration assemblages at the Canadian Malartic deposit, Quebec, *In:* Targeted Geoscience Initiative 4: Contributions to the Understanding of Precambrian Lode Gold Deposits and Implications for Exploration, (ed.) B. Dubé and P. Mercier-Langevin; Geological Survey of Canada, Open File 7852, p. 127–138.

Publications in this series have not been edited; they are released as submitted by the author.

Contribution to the Geological Survey of Canada's Targeted Geoscience Initiative 4 (TGI-4) Program (2010–2015)

TABLE OF CONTENTS

Petrophysical signature of gold mineralization and alteration assemblages at the Canadian Malartic deposit, Quebec

Najib El Goumi[1], Stéphane De Souza[2], Randolph J. Enkin[1]*, and Benoît Dubé[2]

[1]Paleomagnetism and Petrophysics Laboratory, Geological Survey of Canada, P.O. Box 6000, Sidney, British Columbia V8L 4B2
[2]Geological Survey of Canada, 490 rue de la Couronne, Québec, Quebec G1K 9A9
*Corresponding author's e-mail: renkin@nrcan.gc.ca

ABSTRACT

The rock physical properties of samples from the Canadian Malartic gold deposit in the Abitibi greenstone belt of Quebec have been measured to relate lithology and alteration assemblages to physical properties contrasts, and to provide geological interpretation of geophysical survey analyses for this type of ore deposit. Disseminated gold deposits are seldom directly characterized by a clear geophysical signature. However, we propose that a geophysical characterization of such ore deposits can be achieved by combining cost-effective geophysical surveys to identify zones of interest for gold exploration. This study has shown that the metasedimentary rocks and porphyritic intrusions that host the gold mineralization show similar variations in rock physical properties, probably because both rock types have similar geochemical and mineralogical compositions. However, the intrusive rocks show both magnetic and non-magnetic phases, and have a slightly lower density than metasedimentary rocks. Hydrothermal alteration produced continuous trends for magnetic susceptibility, density, and electric chargeability, but with no apparent variation in magnetic remanence and resistivity. These trends of decreasing density and magnetic susceptibility and increasing chargeability are correlated with alteration facies (carbonate saturation index), gold concentration, and proximity to ore. Based on this correlation, a principal component analysis petrophysical proxy has been established to represent this gradual hydrothermal mineralization process. This petrophysical proxy is a valid estimation of the variability of the rock physical properties inside the actual pit area of the Canadian Malartic deposit. Based on composite geophysical surveys (gravity, magnetic, and induced polarization) and inversion of the surface data for rock physical properties at depth, a petrophysical proxy, such as presented here, could help target zones of interest for orebodies similar to that at Canadian Malartic.

INTRODUCTION

Rock physical properties allow integration of geological and geophysical data and constitute an essential element of Common Earth Models (McGaughey, 2006). In the geological environment of a hydrothermal ore system, petrophysical characterization can play a key role for predicting geophysical methods that will be useful in mineral exploration.

The goal of this Geological Survey of Canada – Targeted Geoscience Initiative 4 (TGI-4) study is to define mutual relationships between physical properties (density, porosity, magnetic susceptibility and remanence, electrical resistivity and chargeability) and the local geological setting (lithology, alteration, structures, and metamorphism), to integrate data in geological models, and to constrain geophysical inversions. The project also aims to identify which combination of geophysical methods will give the best exploration results. This contribution presents a suite of rock property measurements from the Canadian Malartic low-grade, bulk-tonnage gold deposit and discusses implications for improvements in the use of geophysical methods in gold exploration.

The Archean Abitibi greenstone belt (700 km by 200 km) is located within the Superior Province and is known to host world-class gold and base metals deposits (Fig. 1; Poulsen et al., 1992, 2000; Robert et al., 2005; Dubé and Gosselin, 2007). The tectonic contact between the Abitibi and Pontiac subprovinces is marked by the Larder Lake - Cadillac Fault Zone, which is delineated by highly strained mafic and ultramafic rock slivers belonging to the Piché Group (Robert, 1989; Card, 1990; Daigneault et al., 2002). The Canadian Malartic gold deposit, which is located immediately to the south of the Larder Lake - Cadillac Fault Zone, is mainly hosted by turbiditic greywacke and mudstone of the Pontiac Group and by Timiskaming (2677–2678 Ma) porphyritic quartz monzodiorite with local granodiorite intrusions (Fig. 2; Sansfaçon and Hubert, 1990; De Souza et al., 2013, in press; Helt et al., 2014). In the mine area, the Pontiac Group was metamorphosed to biotite-chlorite facies

El Goumi, N., De Souza, S., Enkin, R.J., and Dubé, B., 2015. Petrophysical signature of gold mineralization and alteration assemblages at the Canadian Malartic deposit, Quebec, *In:* Targeted Geoscience Initiative 4: Contributions to the Understanding of Precambrian Lode Gold Deposits and Implications for Exploration, (ed.) B. Dubé and P. Mercier-Langevin; Geological Survey of Canada, Open File 7852, p. 127–138.

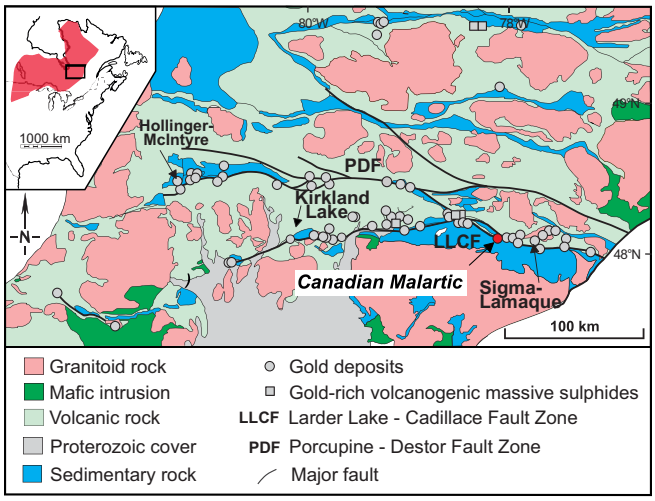

Figure 1. Simplified geological map of the Abitibi greenstone belt. The Canadian Malartic gold deposit is identified by a red dot. The inset shows the location of the Abitibi belt within the Superior Province (red). Map is adapted from Dubé and Gosselin (2007) and Poulson et al. (2000).

and has undergone polyphase deformation with a dominant S_2 pressure-solution cleavage that is related to the formation of open to tight F_2 folds and is northwest-striking and north-dipping (Fig. 2; Sansfaçon and Hubert, 1990; De Souza et al., 2015, in press). The orebodies are characterized by the presence of stockwork and disseminated gold mineralization. Ore minerals include disseminated pyrite (~ ≤5%) with traces of telluride, galena, chalcopyrite, sphalerite, and molybdenite. The main orebodies define northwest-southeast and east-west trends that correspond, respectively, to the orientation of the dominant S_2 foliation and to the Sladen Fault. The latter is a south-dipping brittle-ductile structure that controls the distribution of the east-west-trending ore (Sansfaçon and Hubert, 1990; De Souza et al., 2015, in press). The main auriferous hydrothermal alteration types documented at Canadian Malartic are widespread carbonate alteration (calcite+ferroan dolomite), albitization, potassic alteration (biotite+microcline), and local silicification (De Souza et al., 2015). The least altered sedimentary rocks and the quartz monzodiorite are composed of biotite-muscovite-oligoclase-chlorite ± pyrite-epidote-ilmenite-pyrrhotite-magnetite and orthoclase-oligoclase-quartz-biotite-hornblende-epidote-muscovite-magnetite-titanite assemblages, respectively. Distal alteration in the sedimentary rocks comprises biotite, calcite, muscovite, and pyrite, whereas proximal alteration consists of albite and/or microcline, quartz, carbonate (ferroan dolomite+calcite), phlogopite, rutile, and pyrite. Phlogopite is however absent in pervasively altered

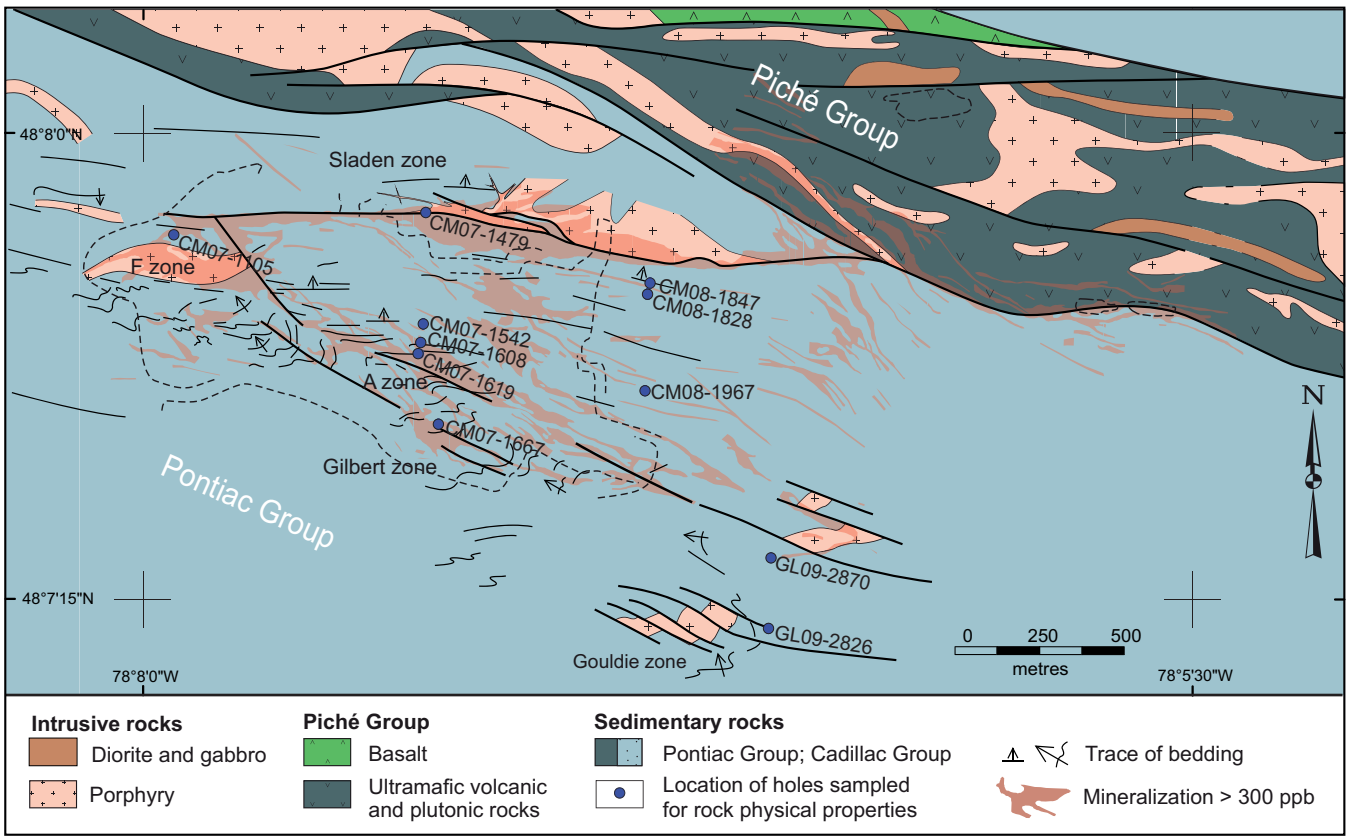

Figure 2. Geological setting of the Canadian Malartic gold deposit hosted by rocks of the Piché and Pontiac groups. Blue circles show the location of the drillholes that were sampled for rock physical properties measurements (adapted from De Souza et al., 2013).

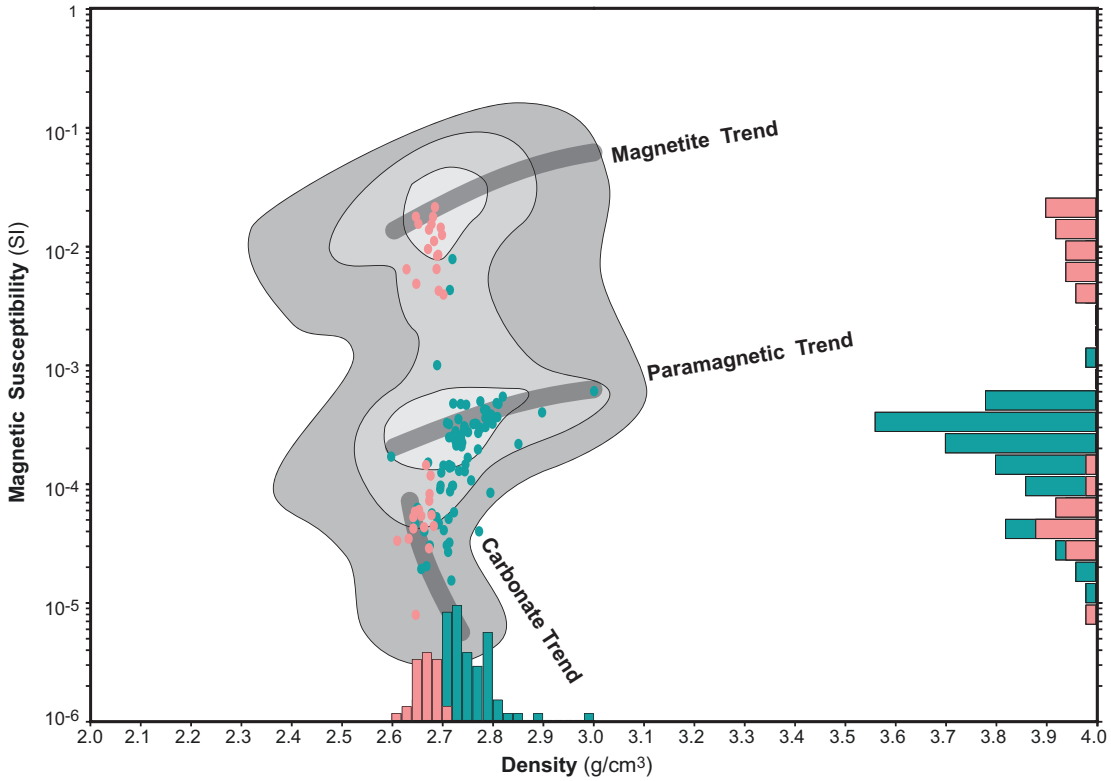

Figure 3. Bivariate plot of the distribution of density versus magnetic susceptibility, with distribution contours, and trends based on the British Columbia Rock Physical Property Database (3388 samples; Enkin, 2014). Density and magnetic susceptibility histograms show variations in metasedimentary (teal-green circles) and intrusive (salmon-pink circles) rocks.

rocks. Distal and proximal alteration assemblages in the quartz monzodiorite are composed of albite-K-feldspar-quartz-biotite-calcite-rutile-magnetite-pyrite-hematite and microcline-albite-ferroan dolomite- calcite-pyrite-rutile, respectively. Field relationships, the nature of the various alteration types, and the geometry of the Au-related veins suggest that gold is largely controlled by syn-D_2 structures and by the Sladen Fault (De Souza et al., 2015, in press). However, the Au-Te-W±Bi-Ag-Mo-Pb geochemical signature of the ore, the presence of stockwork-disseminated Au mineralization, and molybdenite together with potassic alteration, suggest that some of the gold might have been introduced during an early phase of magmatic-hydrothermal alteration that was followed by gold remobilization or a second-stage of gold introduction during D_2 deformation (De Souza et al., 2013, 2015, in press; Helt et al., 2014).

RESULTS AND DATA ANALYSIS

The physical properties were measured for 179 rock samples collected for the TGI-4 project from the Canadian Malartic mine. The collection of core samples was selected from holes drilled within the open pit area (Fig. 2) and is representative of the host lithologies, alteration assemblages, and various ore zones. The rock physical properties summarized in this report are publically accessible in the Canadian Rock Physical Property Database, which is published as a Geological Survey of Canada Open File.

Enkin et al. (2012) describe in detail the measurement protocols and methods. All measurements were conducted on paleomagnetism-size subsamples (2.5 cm diameter, 2.2 cm long cylinders). Samples were saturated with distilled water under vacuum and saturated bulk density was then measured by the weight in air-weight in water method, and porosity was derived from the difference between the dry and water-saturated weights. Magnetic susceptibility was measured using a Sapphire Instruments SI2B susceptibility metre and magnetic remanence was measured with an Agico JR5-A spinner magnetometer. Electrical resistivity and chargeability (Newmont standard time-domain decay) were derived from the complex impedance spectrum measured using a Solartron 1260 Frequency Response Analyser. Gold assays for 139 samples of the collection are also presented.

Magnetic and Density Properties

Metasedimentary rocks are weakly magnetic, with magnetic susceptibilities mostly spanning the range 2×10^{-5} to 5×10^{-4} SI and density varies from 2.65 to 2.85 g/cm^3 (Fig. 3). Unlike typical ore rocks containing high concentrations of sulphide and oxide minerals

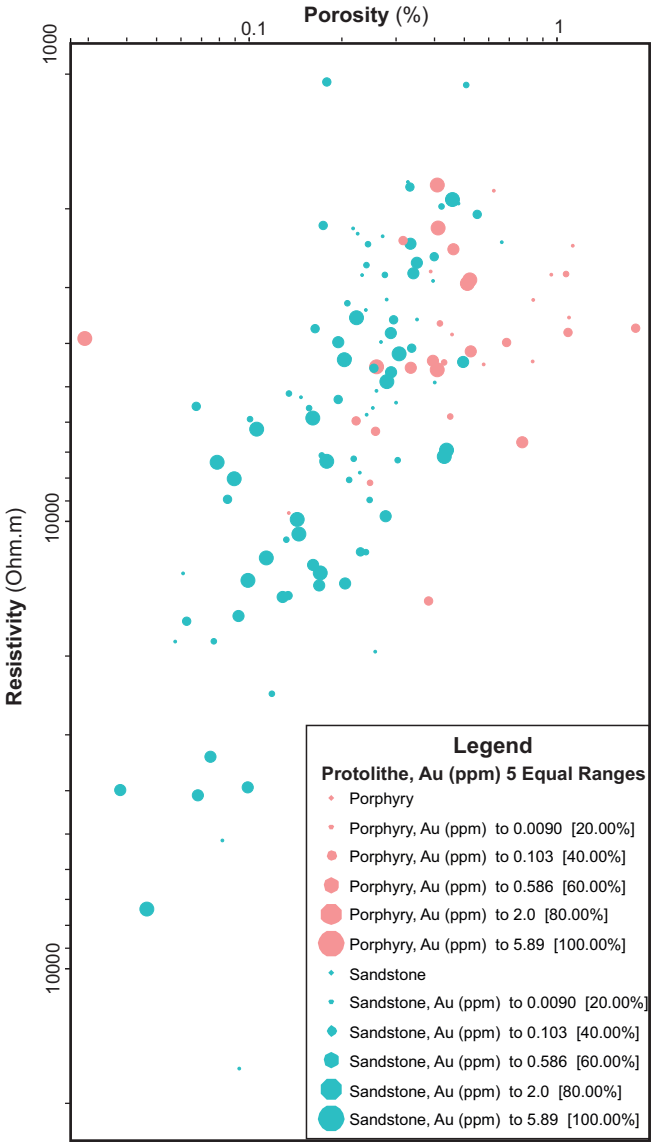

Figure 4. Bivariate diagram of porosity (log scale) and electric resistivity (log scale) revealing their negative correlation. Symbol size related to gold concentration is not correlated with neither porosity nor resistivity for metasedimentary (teal-blue) and intrusive (salmon-pink) rocks.

with densities well above 3.0 g/cm3, disseminated ore zones in the Canadian Malartic deposit have densities that rarely deviate from those of felsic minerals. The biplot of density against magnetic susceptibility does not align along the paramagnetic trend (Henkel, 1994) typical for sedimentary rocks (Fig. 3). Rather, the lower density samples (<2.7 g/cm^3) have magnetic susceptibilities that are anomalously lower by an order of magnitude.

The porphyritic intrusive rocks, mostly least altered quartz monzodiorite or altered quartz monzodiorite, display the typical bimodal magnetic susceptibility distribution of rocks belonging to Henkel's (1994) magnetic and paramagnetic trends, around 10^{-2} and 10^{-4} SI, respectively (Fig. 3). The densities have a restricted range of value of between 2.63 and 2.71 g/cm^3. The porosity was seldom above 1%, which is typical of metamorphosed environments, but we note that the median porosity of porphyries, 0.46%, is more than twice that of the sedimentary rocks, 0.22% (Fig. 4), and density increases with decreasing porosity.

The samples are unoriented, so we can only describe the magnitude rather than direction of the magnetic remanence. The Koenigsberger ratio, K_N, which describes the relative magnitude of magnetic remanence to induced magnetism, is almost always below unity for the higher susceptibility ferromagnetic-trend of the intrusive rock samples. The implication is that the rocks that dominate aeromagnetic survey map anomalies can be modelled accurately using the magnetic susceptibility without regard to the remanence. For the weakly magnetic paramagnetic-trend samples, 30% have K_N above unity but are too weak to markedly affect aeromagnetic results.

Electrical Properties

While porosity does not contribute much to variations in density, it does show a clear inverse correlation with the electrical resistivity (Fig. 4). Such porosity control indicates that these rocks conduct electricity dominantly by ionic conduction through their porosity-permeability rather than by galvanic conduction though networks of sulphide and oxide minerals.

Measurement of electric chargeability is important in disseminated ore systems because induced polarization methods can, in principle, detect the unconnected sulphide (conductive) and oxide (semi-conductive) minerals, as they play the role of electric capacitors interrupting the flow of ions through the rock permeability. In the Canadian Malartic deposit, chargeability has a unimodal distribution with a rather low median Newmont chargeability of 5 ms. The 15% of samples with relatively high chargeability (>10 ms) tend to have lower magnetic susceptibilities (<4×10^{-4} SI), but are otherwise unrelated to the other measured physical properties (Fig. 5).

DISCUSSION AND MODELS

Linking Rock Physical Properties to Hydrothermal Alteration

Native gold and sulphide concentrations are low at the Canadian Malartic deposit and the rock physical properties of the mineralized zones are largely controlled by the mineralogy and texture of the auriferous alterations. Geophysical targeting of such disseminated gold deposits can thus be achieved indirectly by examining rock physical properties of disseminated sulphide alteration and ore zones.

Whole-rock geochemical data give limited informa-

tion about mineralogy, but can be used to estimate mineral and alteration behaviour based on simple geochemical combinations, geochemical ratios, indexes, and assumptions. We make the initial assumption that sulphur concentration is dominated by pyrite. Gold in the Canadian Malartic deposit is hosted as free gold grains and inclusions in pyrite. Fieldwork and core logging indicate that increasing sulphur and gold contents follow the alteration pathway, from distal to proximal alteration zones.

Atypical of most geological environments, both density and porosity become lower with increasing sulphur and gold concentration. The increase in dense minerals, including pyrite, is apparently offset by an increase in less dense silicate and carbonate minerals. Along with the reduction in porosity, there is a slight increase in electrical resistivity of a factor 2 (Fig. 4). A small proportion (15%) of samples has Newmont chargeabilities above 10 ms, a threshold above which they can usually be imaged using induced polarization surveys. Most of the high-chargeability samples contain relatively high Au and S concentrations.

The porphyries display a bimodal magnetic susceptibility. The highly magnetic samples show low-sulphur content, and therefore pyrite content, and have chargeabilities mostly below 10 ms (median below 5 ms), which could be due to low pyrite and high magnetite content (Fig. 5). The low-magnetic samples contain higher sulphur, and therefore higher pyrite content. Chargeabilities are medium but trend toward higher values with increasing sulphur. The trend for magnetic to non-magnetic samples showing increasing values for chargeability is most likely linked to the destruction of primary magnetite and the increasing pyrite content.

In the sedimentary rocks, the distal to proximal alteration assemblages exhibit a trend from low-chargeability + medium-magnetic susceptibility to high-chargeability + low-magnetic susceptibility, which is related to increasing pyrite and gold content. The drop in magnetic susceptibility and increase in chargeability is possibly related to sulphidation, with destruction of magnetite and precipitation of pyrite. Further mineralogical and petrographic analyses should be undertaken to test this interpretation.

A Physical Properties Proxy for Gold Concentration and Hydrothermal Alteration

One of the major goals of the petrophysical study of rocks from a mineral deposit is to delineate rock properties of the ore zones that can be detected from surface geophysical surveys. It has long been noted that geophysical methods have been unsuccessful in delineating the Malartic deposit (Wares and Burzynski, 2011). Indeed the results of the current study reveal that the petrophysical contrasts in this collection are quite subtle.

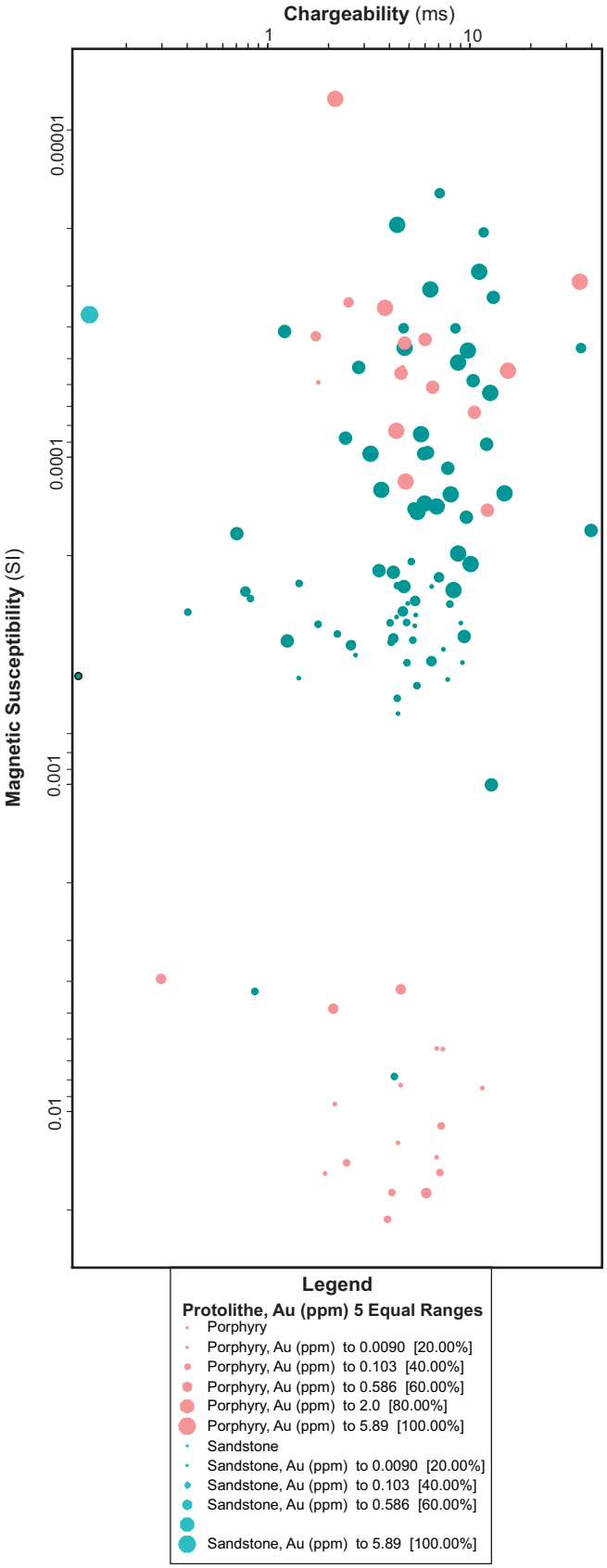

Figure 5. Bivariate diagram of chargeability versus magnetic susceptibility illustrates that highly auriferous samples have physical properties of higher chargeability and low magnetic susceptibility.

We propose that a more useful petrophysical proxy for gold mineralization is obtained by combining multiple physical rock properties, including density, magnetic susceptibility, and chargeability, rather than focusing individually on a single rock physical property.

As gold concentration in the metasedimentary rocks is roughly correlated with the electric chargeability and anti-correlated to the density and magnetic susceptibility, we performed principal component analysis (PCA) on these three physical properties. Since electric resistivity is largely independent of gold concentration, and there was no advantage to including that extra variable. Although gold concentrations are not used in the calculation, they will be used to test the validity of the result. Specifically, we used a robust principal component analysis (Campbell, 1980), with a "low outlier rejection" criterion, as enabled in the geochemical analysis program ioGAS®, which was developed by Reflex. Logarithmic transforms were first applied to the magnetic susceptibility and electric chargeability. The maximum eigenvector, or first PCA component, corresponds to the least-squares line that best fits the data. The proposed proxy is the projection of the measured (density, LOG(susceptibility), LOG(chargeability)) values along that axis:

(1) $PCA = -0.6268*(dens-2.74)-0.622*LOG(susc/1.64\times10^{-4}) +1.26*LOG(chrg/5.42)$

where density (dens) is measured in g/cm^3, magnetic susceptibility (susc) in SI units, and Newmont convention electric chargeability (chrg) in ms.

The plotted LOG (gold concentration) function of PCA (Fig. 6) shows that the proxy tracks most of the variation. The correlation coefficient is not strong (R=0.65), but with the removal of the furthest outliers, the correlation coefficient jumps to (R=0.84). The correlation with LOG (sulphur concentration) is however, less pronounced: R=0.62 and increases to R=0.71 after the furthest outliers are expelled. The suggestion is that a preliminary zonation of gold concentration can be accomplished using only surface geophysical measurements to target exploration drilling.

The direct linkage between geochemical, mineralogical and petrophysical data would be the base for innovative direct, remote, cost-effective methods that could be implemented for gold exploration in greenstone belts. In fact, the intensity and nature of alteration in such environments can be monitored by the combination of the carbonate saturation index (CSI) and the chlorite-carbonate-pyrite index (total Fe) (CCPI). The CSI corresponds to the molar ratio of CO_2/(CaO+MgO+FeO) and is calculated as

(2) $CSI=(CO_2/44.0095)/(CaO/56.0774+MgO/40.3044+FeO/71.8444)$

where C needs to be reported as CO_2, Fe can be

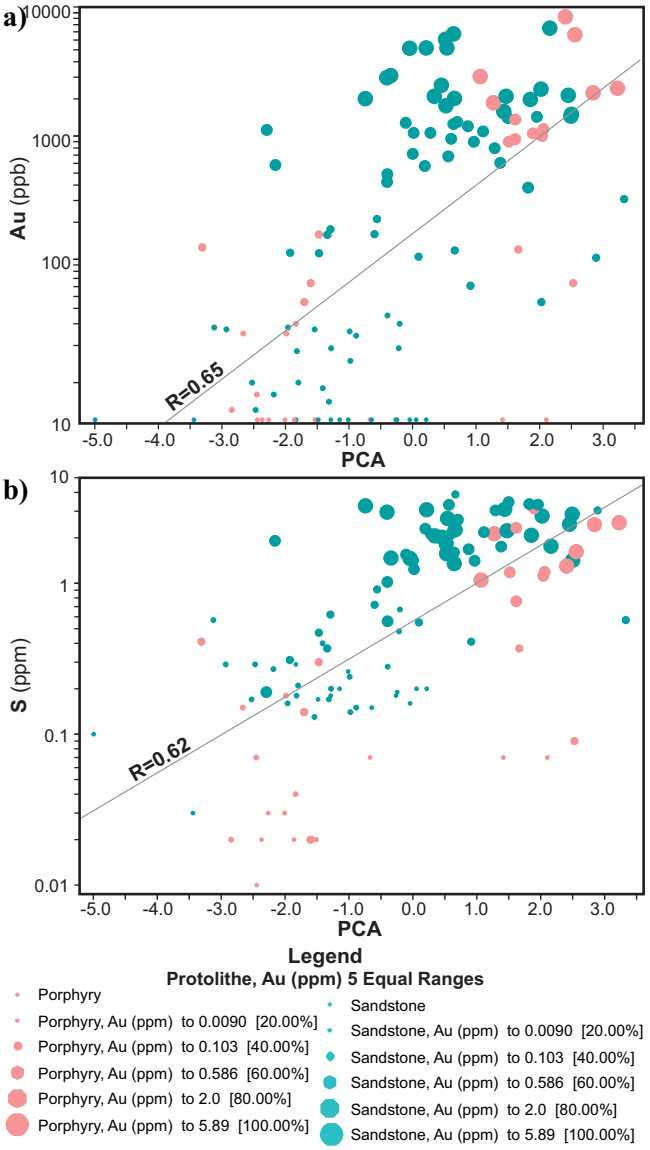

Figure 6. Bivariate diagrams of the petrophysical principal component analysis (CPA) parameter versus **(a)** gold and **(b)** sulphur concentration as a proxy for mineralization.

expressed either as FeO or Fe_2O_3 (Kishida and Kerrich, 1987). While, the calculation of CCPI (Large et al., 2001; Gemmell, 2007) is determined as

(3) $CCPI=100*(MgO+FeO)/(MgO+Na_2O+FeO+K_2O)$

where FeO is total (FeO + Fe_2O_3) content of the rock. The alteration indices (CSI and CCPI) and the petrophysical proxy are completely independent from each other but their correlations demonstrate that they monitor the same hydrothermal alteration processes related to gold mineralization.

Our proposed petrophysical proxy displays a strong positive correlation with CSI with R=0.71, which increases to R=0.73 if furthest outliers are removed. It is, however, negatively correlated with CCPI (R=-0.52), but would be strongly correlated if we reject the magnetic porphyry outliers (R=-0.8) (Fig. 7).

The implication is that gold and sulphide content are associated with alteration which lowers the density and magnetic susceptibility but increases the electric chargeability. Although pyrite represents the main ore mineral, it is usually present in minor amount (≤5%) and associated with a decrease in Fe of the biotite and breakdown of magnetite in the proximal alteration zones. As a result of hydrothermal alteration and interaction with a CO_2-rich fluid, biotite/phlogopite, plagioclase, epidote, titanite, magnetite, and ilmenite release Fe, Mg, and/or Ca that contribute in part to the formation of carbonate minerals and pyrite, which results in increasing the CSI, whereas increases of K and/or Na are associated with albite and microcline formation, which results in lowering the CCPI. This breakdown of magnetite and Ca-Fe-Mg silicate phases to form pyrite and less dense carbonate, quartz, and feldspar can be linked to the decreasing trends of magnetic susceptibility and density and increasing chargeability in the auriferous hydrothermally altered rocks. Thus petrophysical properties can be used to identify disseminated sulphide gold mineralization and related alteration.

IMPLICATIONS FOR EXPLORATION

Compilation of rock physical properties in national and international databases provides an important tool for mineral exploration. Geological processes that are usually inferred from difficult and costly chemical and mineralogical analyses can be derived from rapid, non-destructive, and inexpensive petrophysical measurements. These measurements contribute to the understanding of the physical change of rocks in ore systems due to alteration, structures, and other geological changes.

In order to assess the subtle change of physical properties in the Canadian Malartic deposit area, a tentative forward modelling of a simple geological model composed of a porphyry body intruded in metasedimentary rocks has been accomplished using the software package Potent®, which provides an interactive framework for 3-D modelling of magnetic and gravity data. A simple 100 m^3 sphere, representing the non-magnetic quartz monzodiorite mineralized body, has been assigned typical rock physical properties of mineralized samples (magnetic susceptibility = 10^{-4} SI and density =2.65 g/cm^3), and the host metasedimentary rocks have been assigned magnetic susceptibility = 8×10^{-4} SI and density = 2.75 g/cm^3. The forward model has taken into account parameters of the geomagnetic field (intensity=57489 nT; inclination = 75.4°; declination=-18.3°) without including magnetic remanence. The results shows that a subtle negative magnetic anomaly of -20 nT and a negative gravity anomaly of -0.17 mgal is to be expected if the top of the body occurs at the surface. If the body is buried (100 m depth), the magnetic anomaly is less than 1 nT and the gravity anomaly is less than -0.02 mgal (Fig. 8).

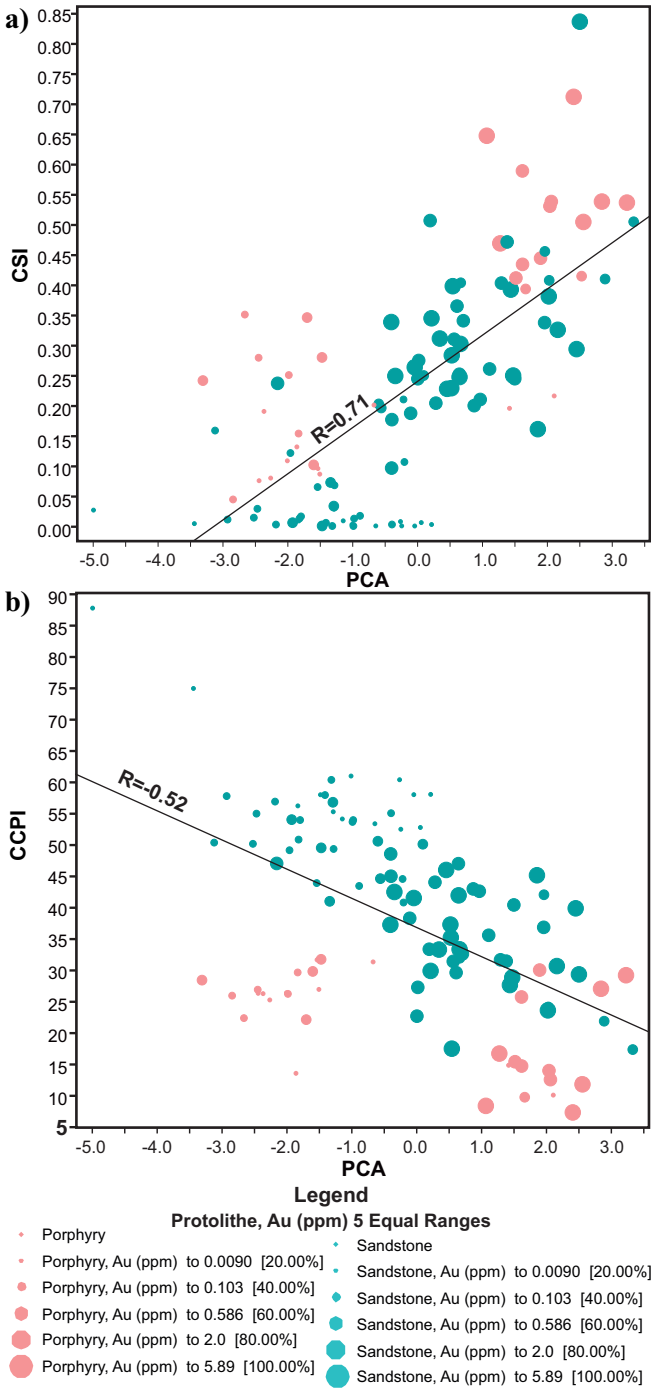

Figure 7. Bivariate diagrams showing the correlation between the principal component analysis (PCA) parameter (petrophysical proxy) versus the alteration indices **(a)** carbonate saturation index (CSI) and **(b)** chlorite-carbonate-pyrite index (CCPI).

Rock physical properties not only allow one to correlate and integrate geology to geophysics, but also can also allow one to optimize geophysical exploration for ore systems by defining the cost-effective geophysical

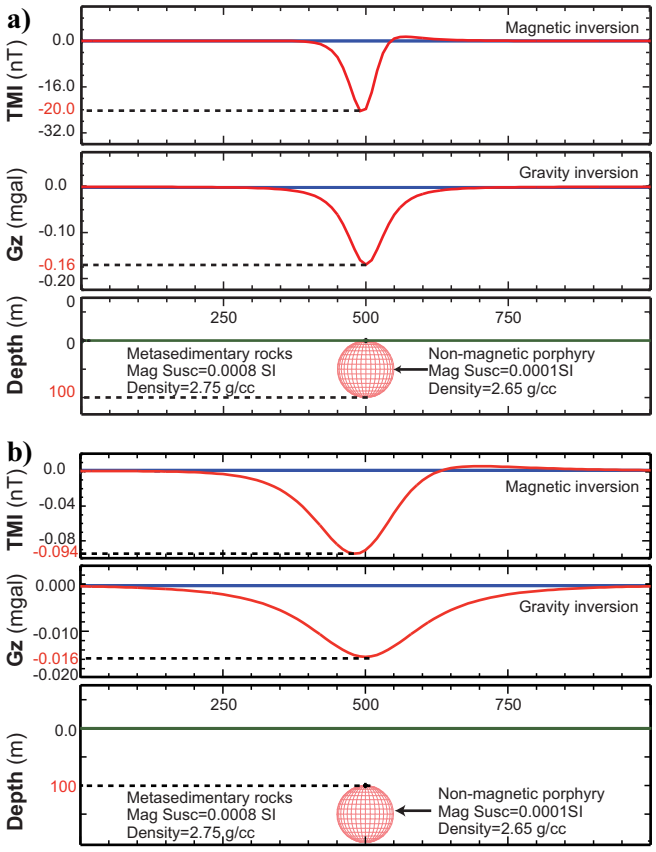

Figure 8. Two-dimensional magnetic and gravity forward modelling of a non-magnetic porphyry (100 m^3) intruded into metasedimentary rocks at depths of **(a)** 0 m and **(b)** 100 m using geomagnetic field parameters of magnetic field intensity of 57489 nT, declination of 18.3°, and inclination of 75.4°.

methods to implement. For the Canadian Malartic deposit area, no single geophysical technique, as demonstrated by forward modelling of gravity and magnetic surveys, can provide anomalies that are a useful measure of mineralization or gold content. However, a proxy can be developed through a combination of gravity, magnetic, and induced polarization survey results. We recommend this combination to define exploration targets over low-density, low-magnetic, and highly chargeable areas. The relationship between the PCA proxy and the different styles of hydrothermal alteration (distal and proximal) with linkage to gold concentration is presented here. Thus, a limit has been established between (1) a background level of gold associated with negative PCA values, including fresh rocks plus distal alteration and (2) a mineralized area with elevated gold concentrations associated with proximal alteration and positive PCA values. Distal alteration has no positive PCA value; petrophysically it is similar to fresh rocks, even if mineralogical differences exist (Fig. 9). The mineralogical and petrophysical border between fertile and non-fertile alteration is most likely the existence of hydrother-

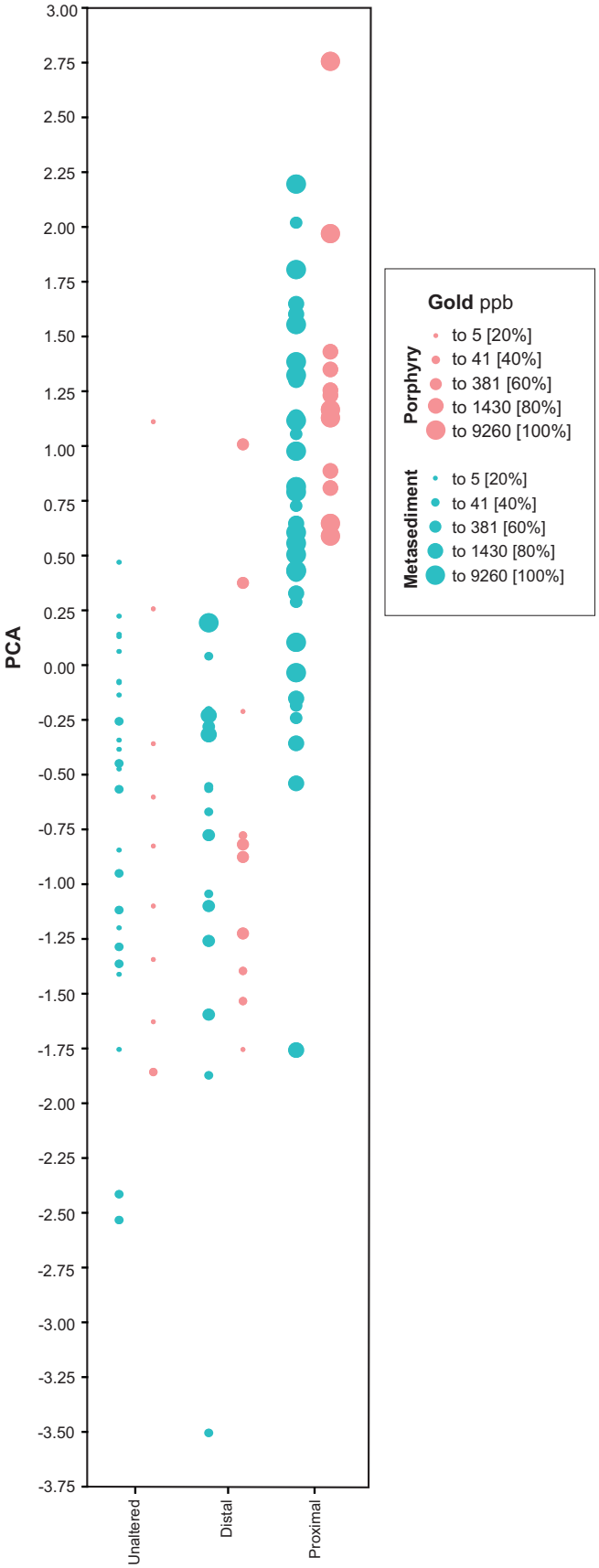

Figure 9. Correlation between the petrophysical proxy and alteration styles in the Canadian Malartic ore system.

mal biotite, as most of the Fe issued from biotite breakdown is going to be a combined with S to form finely disseminated pyrite, which is a good indicator of economic auriferous zones. A good knowledge of rock physical properties is important to constrain inversions, which allows for a better understanding of the correlations between the geological and geophysical data with fewer misleading results. A frequency-domain spectral induced polarization survey is recommended in this setting where time-domain induced polarization fails to discriminate between different conduction modes related to alteration types and mineral assemblages containing gold.

FUTURE WORK

Linking rock physical properties parameters to mineralogical data is our next step in order to refine and clarify integrated interpretations based on geochemical analyses. The integration of mineralogical and petrographic data with rock physical properties could lead to consistent and strong mineral, geochemical proxies for rock physical properties. A rock physical proxy for gold exploration in greenstone belts will also be improved.

ACKNOWLEDGEMENTS

This research work with the Geological Survey of Canada - Pacific Division was made possible by funding from the TGI-4 Lode Gold and Methodologies projects. We would like to thank the Canadian Malartic Partnership and the Osisko Mining Corporation for making data available and for logistical help. This study is conducted in collaboration with Canada Mining and Innovation Council (CMIC) Footprints project, including R. Linnen, G. Olivo, A. Galley, M. Lesher, and especially S. Perrouty, C. Bérubé-Lafrenière, and Michel Chouteau. Special thanks are due to Tark Hamilton and Michel Chouteau for their informative comments and suggestions.

REFERENCES

Campbell, N.A., 1980. Robust procedures in multivariate analysis. I: Robust covariance estimation; Applied Statistics., v. 29, p. 231–237.

Card, K.D., 1990. A review of the Superior Province of the Canadian Shield, a product of Archean accretion; Precambrian Research, v. 48, p. 99–156.

Daigneault, R., Mueller, W., and Chown, E.H., 2002. Oblique Archean subduction: Accretion and exhumation of an oceanic arc during dextral transpression, Southern Volcanic Zone, Abitibi Subprovince, Canada; Precambrian Research, v. 115, p. 261–290.

De Souza, S., Dubé, B., McNicoll, V., Mercier-Langevin, P., Dupuis, C., Creaser, R., de Chavigny, P., and Gervais, D., 2013. The Canadian Malartic mine, Abitibi, Québec: Geological characteristics and relative timing of low-grade bulk-tonnage gold mineralization; Ministère des Ressources naturelles du Québec, Québec-Mines, Abstracts, p. 28.

De Souza, S., Dubé, B., McNicoll, V.J., Dupuis, C., Mercier-Langevin, P., Creaser, R.A., and Kjarsgaard, I.M., 2015. Geology, hydrothermal alteration, and genesis of the world-class Canadian Malartic stockwork-disseminated Archean gold deposit, Abitibi, Quebec, *In:* Targeted Geoscience Initiative 4: Contributions to the Understanding of Precambrian Lode Gold Deposits and Implications for Exploration, (ed.) B. Dubé and P. Mercier-Langevin; Geological Survey of Canada, Open File 7852, p. 113–126.

De Souza, S., Dubé, B., Vicki, M., Dupuis, C., Mercier-Langevin, P., Robert, A., Creaser, R., and Kjarsgaard, I., in press. The Canadian Malartic gold deposit, *In:* Archean Base and Precious Metal Deposits, southern Abitibi Greenstone Belt, Canada, (ed.) T. Monecke and P. Mercier-Langevin; Society of Economic Geologists, Field Guide Book 46.

Dubé, B. and Gosselin, P., 2007, Greenstone-hosted quartz-carbonate vein deposits, *In:* Mineral Deposits of Canada: A Synthesis of Major Deposit Types, District Metallogeny, the Evolution of Geological Provinces and Exploration Methods, (ed.) W.D. Goodfellow; Geological Association of Canada, Mineral Deposits Division, Special Publication No. 5, p. 49–73.

Enkin, R.J., The rock physical property database of British Columbia, and the distinct signature of the Chilcotin basalts; Canadian Journal of Earth Sciences, v. 51, p. 327–338.

Enkin, R.J., Cowan, D., Tigner, J., Severide, A., Gilmour, D., Tkachyk, A., Kilduff, M., Vidal, B., and Baker, J., 2012. Physical Property Measurements at the GSC Paleomagnetism and Petrophysics Laboratory, including Electric Impedance Spectrum Methodology and Analysis; Geological Survey of Canada, Open File 7227, 42 p., doi:10.4095/291564

Helt, K.M., Williams-Jones, A.E., Clark, J.R., Wing, B., and Wares, R.P., 2014. Constraints on the genesis of the Archean oxidized, intrusion-related Canadian Malartic gold deposit, Québec, Canada; Economic Geology, v. 109, p. 713–735.

Henkel, H., 1994. Standard diagrams of magnetic properties and density – a tool for understanding magnetic petrology; Journal of Applied Geophysics, v. 32, p. 43–53. doi:10.1016/0926-9851 (94)90008-6

Gemmell, J.B., 2007. Hydrothermal alteration associated with the Gosowong epithermal Au-Ag deposit, Halmahera, Indonesia: Mineralogy, geochemistry, and exploration implications; Economic Geology, v. 102, p. 893–922.

Kishida, A. and Kerrich, R., 1987. Hydrothermal alteration zoning and gold concentration at the Kerr- Addison Archean lode gold deposit, Kirkland Lake, Ontario; Economic Geology, v. 82, p. 649–690.

McGaughey, J., 2006. The common Earth model: A revolution in mineral exploration data integration, *In:* GIS Applications in the Earth Sciences, (ed.) J.R. Harris; Geological Association of Canada Special Publication 44, p. 567–576.

Poulsen, K.H., Card, K.D., and Franklin, J.M., 1992. Archean tectonic and metallogenic evolution of the Superior Province of the Canadian Shield; Precambrian Research, v. 58, p. 25–54.

Poulsen, K.H., Robert, F., and Dubé, B., 2000. Geological classification of Canadian gold deposits; Geological Survey of Canada, Bulletin 540, 106 p.

Robert, F., 1989. Internal structure of the Cadillac tectonic zone southeast of Val d'Or, Abitibi greenstone belt, Quebec; Canadian Journal of Earth Sciences, v. 26, p. 2661–2675.

Robert, F., Poulsen, K. H., Cassidy, K. F., and Hodgson, C. J., 2005. Gold metallogeny of the Superior and Yilgarn cratons, *In:* 100th Anniversary Volume, (ed.) J.W. Hedenquist, J.F.H. Thompson, R.J. Goldfarb, and J.P. Richards; Society of Economic Geologists, v. 40, p. 1001–1033.

Large, R.R., Gemmell, J.B., Paulick, H., and Huston, D.L., 2001. The Alteration Box Plot: A simple approach to understanding

the relationship between alteration mineralogy and lithogeochemistry associated with volcanic-hosted massive sulfide deposits; Economic Geology, v. 96 p. 957–971.

Sansfaçon, R. and Hubert, C., 1990. The Malartic gold district, Abitibi greenstone belt, Québec: Geological setting, structure and timing of gold emplacement at Malartic Gold Fields, Barnat, East Malartic, Canadian Malartic and Sladen Mines; Canadian Institute of Mining and Metallurgy, v. 43, p. 221–235.

Wares, R. and Burzynski, J., 2011. The Canadian Malartic Mine, southern Abitibi Belt, Quebec, Canada: Discovery and development of an Archean bulk-tonnage gold deposit [online], http://www.tgdg.net/Resources/Documents/NEWGEN%20GOLD%20%20WaresBurzynski.pdf.

GEOLOGICAL SURVEY OF CANADA
OPEN FILE 7852

Targeted Geoscience Initiative 4: Contributions to the Understanding of Precambrian Lode Gold Deposits and Implications for Exploration

The Archean Côté Gold intrusion-related Au(-Cu) deposit, Ontario: A large-tonnage, low-grade deposit centred on a magmatic-hydrothermal breccia

Laura R. Katz[1], Daniel J. Kontak[1], Benoît Dubé[2], and Vicki J. McNicoll[3]

[1]Laurentian University, Sudbury, Ontario
[2]Geological Survey of Canada, Québec, Quebec
[3]Geological Survey of Canada, Ottawa, Ontario

2015

Recommended citation

Katz, L.R., Kontak, D.J., Dubé, B., and McNicoll, V.J., 2015. The Archean Côté Gold intrusion-related Au(-Cu) deposit, Ontario: A large-tonnage, low-grade deposit centred on a magmatic-hydrothermal breccia, *In:* Targeted Geoscience Initiative 4: Contributions to the Understanding of Precambrian Lode Gold Deposits and Implications for Exploration, (ed.) B. Dubé and P. Mercier-Langevin; Geological Survey of Canada, Open File 7852, p. 139–155.

Publications in this series have not been edited; they are released as submitted by the author.

Contribution to the Geological Survey of Canada's Targeted Geoscience Initiative 4 (TGI-4) Program (2010–2015)

TABLE OF CONTENTS

The Archean Côté Gold intrusion-related Au(-Cu) deposit, Ontario: A large-tonnage, low-grade deposit centred on a magmatic-hydrothermal breccia

Laura R. Katz[1]*, Daniel J. Kontak[1], Benoît Dubé[2], and Vicki J. McNicoll[3]

[1]Department of Earth Sciences, Laurentian University, Sudbury, Ontario P3E 2C6
[2]Geological Survey of Canada, 490 rue de la Couronne, Québec, Quebec G1K 9A9
[3]Geological Survey of Canada, 601 Booth Street, Ottawa, Ontario K1A 0E8
*Corresponding author's e-mail: lkatz@laurentian.ca

ABSTRACT

The recently discovered Côté Gold deposit, located in the southeast limb of the Swayze greenstone belt, Abitibi Subprovince, is an Archean low-grade, high-tonnage Au(-Cu) deposit. The deposit is hosted by the 2741 Ma Chester intrusive complex (CIC), a high-level, multi-phase, laccolithic-shaped synvolcanic intrusion composed of several tonalite and diorite phases. Although a close temporal and spatial relationship exists between the phases of the CIC, whole-rock geochemistry on least-altered samples suggests they are petrogenetically unrelated. Notably, the tonalite phases are characterized chemically as low-Al type, which is atypical of the tonalite-trondhjemite-granodiorite suites in the Archean Superior Province and elsewhere, but typical of primitive arc submarine environments. The mineralized system at the Côté Gold deposit is co-spatial with a multi-phase, magmatic-hydrothermal breccia body that contains multiple brecciation events and matrices and is overprinted by several alteration types (biotite, sericite, silica-sodic). Whole-rock geochemistry indicates that the deposit is Au(-Cu) only and is relatively depleted in other elements (e.g. As, F, Bi, Te). The overlap of Re-Os dates on syn-gold-deposition molybdenite (2739 ± 9 Ma) with the 2741 Ma CIC is consistent with field observations that suggest an overlap of magmatic and hydrothermal events. The results of this study have defined a new significant early stage gold metallogenic event in the Abitibi Subprovince at 2740 Ma and the deposit provides a guide for future exploration in other composite, subvolcanic, low-Al intrusions in the Archean.

INTRODUCTION

The recently discovered (2009/2010) Côté Gold deposit, located in the Archean Swayze greenstone belt, Abitibi Subprovince of northern Ontario, is a large-tonnage, low-grade Au(-Cu) deposit with an indicated resource of 269 Mt averaging 0.88 g/t Au (7.61 M oz) and an inferred resource of 44 Mt averaging 0.74 g/t Au (1.04 M oz) at a 0.3 g/t Au cut-off grade (IAMGOLD, 2013). The discovery of the Côté Gold deposit initiated a deposit-scale study that was undertaken as part of the Discover Abitibi Initiative. This study provided the first description of the host rocks and related alteration types and mineralization, whole-rock and alteration geochemistry, stable isotope geochemistry and U-Pb and Re-Os geochronology (Kontak et al., 2013). Two U-Pb zircon samples yielded ages of 2741.1 ± 0.9 and 2738.7 ± 0.8 Ma for a tonalite and tonalite breccia, respectively, which overlaps with two Re-Os molybdenite dates (avg. 2739 ± 9 Ma), one sample of which contained coarse gold. The significance of this discovery and initial study resulted in further studies, which included Ph.D. and M.Sc. theses that focused on a full characterization of the deposit and a structural synthesis of the ore system and surrounding area. The work is supported financially and logistically through Iamgold Corporation with funding for a comprehensive lithogeochemical and U-Pb geochronological study funded from Geological Survey of Canada through the TGI-4 Lode Gold Project. This article focuses on the aspects of the project associated with the TGI-4 mandate and therefore includes a general description of host rocks, nature and style of alteration and mineralization, U-Pb zircon geochronology, and geochemistry.

RESULTS AND DATA ANALYSIS

Geology of the Côté Gold Deposit

The Au(-Cu) Côté Gold deposit is located in the southern limb of the Swayze greenstone belt (SGB), part of the gold-rich Abitibi Subprovince (Fig. 1). The SGB

Katz, L.R., Kontak, D.J., Dubé, B., and McNicoll, V.J., 2015. The Archean Côté Gold intrusion-related Au(-Cu) deposit, Ontario: A large-tonnage, low-grade deposit centred on a magmatic-hydrothermal breccia, *In:* Targeted Geoscience Initiative 4: Contributions to the Understanding of Precambrian Lode Gold Deposits and Implications for Exploration, (ed.) B. Dubé and P. Mercier-Langevin; Geological Survey of Canada, Open File 7852, p. 139–155.

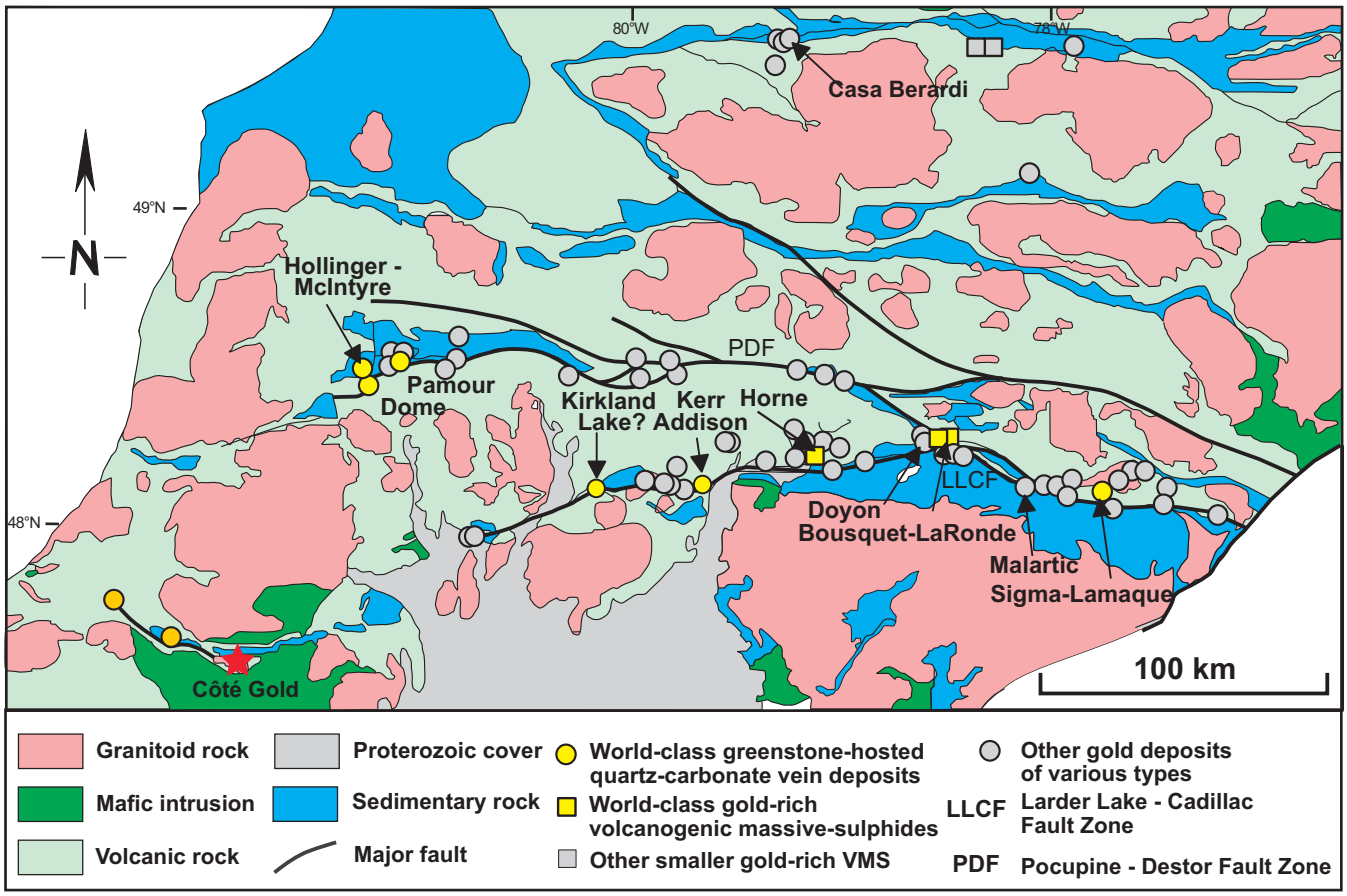

Figure 1. Simplified geological map of the Abitibi Subprovince showing the major gold deposits and fault zones. Red star shows the location of the Côté Gold deposit. Modified from Dubé and Gosselin (2007) and Poulson et al. (2000).

(2750–2670 Ma) contains many of the stratigraphic assemblages and structures typical of the southern Abitibi greenstone belt (AGB) based on lithology and geochronology criteria (Ayer et al., 2002; van Breemen et al., 2006). Several, regionally extensive, D_2 (ca. 2697–2675 Ma) high-strain zones transect the SGB. The D_2 deformation in the SGB, like in the AGB, is inferred to have been synchronous with the generation of orogenic style gold mineralization (Heather, 2001; van Breemen et al., 2006). Metamorphic grade within the southern Abitibi greenstone belt ranges from subgreenschist to greenschist. Peak metamorphism is estimated to have occurred from 2677 to 2643 Ma (Powell et al., 1995).

The deposit is hosted by the ca. 2741 Ma Chester intrusive complex (CIC), a multi-phase, locally layered, laccolithic-shaped, synvolcanic intrusion composed of tonalite and diorite (Fig. 2). The deposit is centred on a magmatic-hydrothermal breccia body that intrudes tonalitic and dioritic rocks.

The CIC intruded into the mafic volcanic rocks of the Arbutus Formation, which forms the basal formation in the Chester Group. The formation consists of low-K tholeiitic pillow basalts, mafic flows, and sills.

The Yeo Formation forms the upper formation in the Chester Group and overlies the CIC (Fig. 2). The Yeo Formation consists of intercalated felsic and intermediate volcanic rocks, clastic sedimentary and volcaniclastic rocks, iron formation and Fe-rich sedimentary rocks. The felsic and intermediate volcanic rocks range from poorly sorted to well bedded, monolithic and heterolithic lapilli to volcanic breccia tuffs, feldspar crystal ash tuffs, massive aphanitic flows and feldspar ± quartz phyric flows (Heather, 2001). Three previous U-Pb zircon dates were obtained from felsic lapilli tuffs at 2739 ± 2 and 2734 ± 2 Ma (Heather and Shore, 1999a,b), and 2739 ± 1 Ma (van Breemen et al., 2006; Fig. 2). Previous geochemical studies have interpreted the Yeo Formation to be the eruptive equivalent of the CIC (Heather et al., 1996; Berger, 2012).

The Chester Group is equivalent to the Pacaud Assemblage in the Abitibi greenstone belt. The Chester Group is inferred to have both ensimatic ocean basin and arc signatures (Ayer et al., 2002; van Breemen et al., 2006).

Host Rocks

The deposit is hosted by several phases of tonalite and diorite sills that display complex cross-cutting relation-

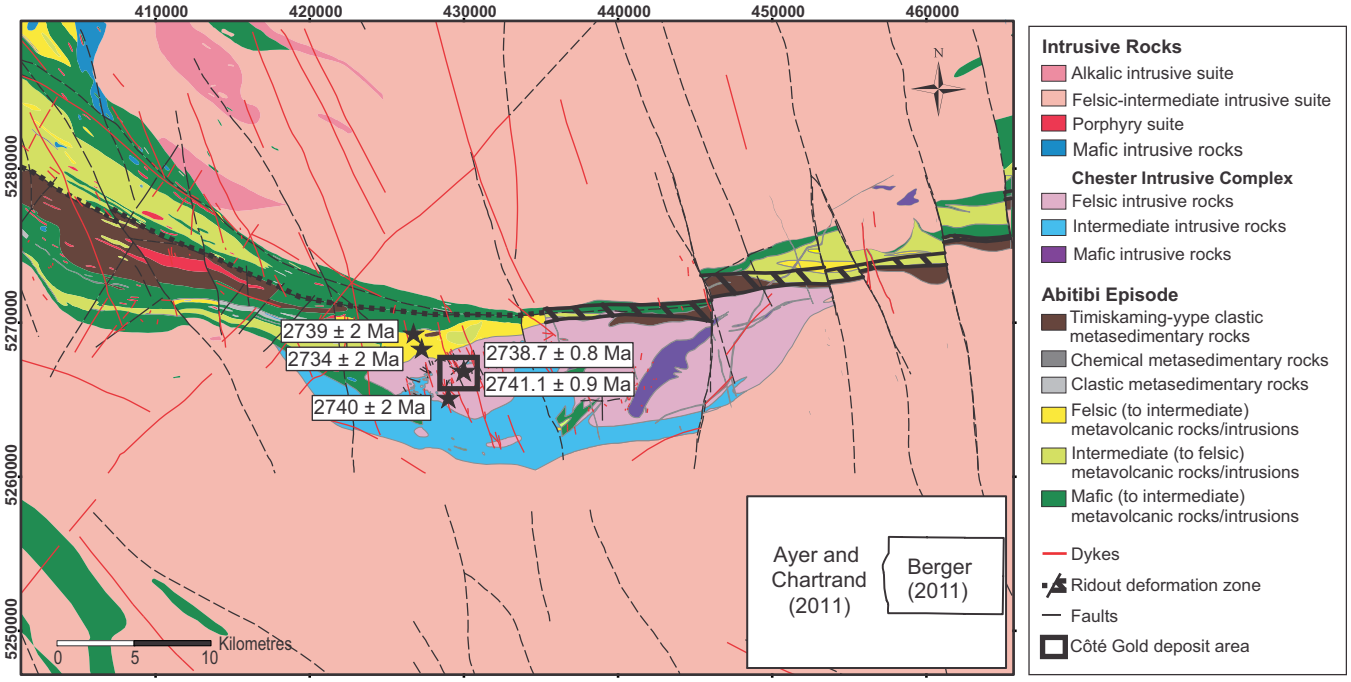

Figure 2. Simplified district-scale geological map of the Chester intrusive complex and the southeastern arm of the Swayze greenstone belt, compiled from Ayer and Chartrand (2011) and Berger (2011). Deposit area is shown in the black box. Location of previous geochronology dates are shown by black stars.

ships. Based on their relative timing and variable chemistry, five distinctive intrusive phases have been identified: (1) tonalite I; (2) diorite; (3) aphyric to quartz and/or plagioclase porphyritic quartz diorite; (4) tonalite II; and (5) hornblende-plagioclase ± quartz pegmatite. The Côté Gold deposit is centred on a mineralized magmatic-hydrothermal breccia body that intrudes tonalite and diorite rocks (Fig. 3a, c). Drill-core logging and detailed mapping of select exposures (e.g. North Breccia outcrop; Fig. 4) have established the basis for the relative timing of intrusive phases and the current nomenclature presented below.

Tonalite I, which forms sills with 10s to 100s of metres of apparent thickness, is a light grey, massive, equigranular rock composed of fine- to medium-grained plagioclase and quartz (Fig. 5a), with rare plagioclase or quartz phenocrysts. Accessory minerals include titanite, zircon, apatite, rutile, ilmenite, tourmaline, monazite, and xenotime. This unit has a hypidiomorphic granular texture with rare development of granophyre (Fig. 5b) and miarolitic cavities (Fig. 5c). Plagioclase has oscillatory zoning, polysynthetic twinning and rarely sieve textures. Miarolitic-like cavities include quartz ± sulphide, quartz-chlorite and quartz-plagioclase types that are typically oblate in shape and range from <5 mm to 10s of cm in diameter.

The diorite phase comprises sills of 5 to <150 metres in apparent thickness that intrude tonalite I and can be exhibit chilled margins. The contact between the diorite and tonalite I is commonly brecciated and, where this occurs, is termed a magmatic breccia with tonalite clasts in a dioritic matrix. The diorite is dark-green, massive to rarely foliated, equigranular to inequigranular and medium- to coarse-grained (Fig. 5d). The diorite contains variable amounts of plagioclase, amphibole, titanite, magnetite and ilmenite with accessory apatite, zircon, and tourmaline. This unit rarely has a granophyric texture and plagioclase shows primary oscillatory zoning and polysynthetic twinning.

Aphyric to quartz and/or plagioclase porphyritic quartz diorite consists of sills that range from 5 to <150 m in apparent thickness and intrudes into diorite. Quartz diorite is dark- to light-green, inequigranular, medium- to coarse-grained and is massive; locally it contains quartz phenocryst and rarely porphyritic plagioclase (Fig. 5e). The unit consists of plagioclase, amphibole, quartz, titanite, magnetite and ilmenite with accessory apatite, zircon, and tourmaline. The plagioclase contains primary oscillatory zoning, polysynthetic twinning and granophyric texture occurs.

The contact relationships of diorite and quartz diorite phases are variable, with both sharp and diffuse contacts. In both cases, diorite or quartz diorite clasts are present along the contact which gives a breccia texture whereby the more leucocratic quartz diorite matrix host melanocratic diorite clasts (Fig. 5e). This commonly observed cross cutting relationship suggests that diorite evolved over time, fractionating to more leucocratic quartz diorite.

Tonalite II forms sills of a few metres to 100s of metres in apparent thickness and is mineralogically and

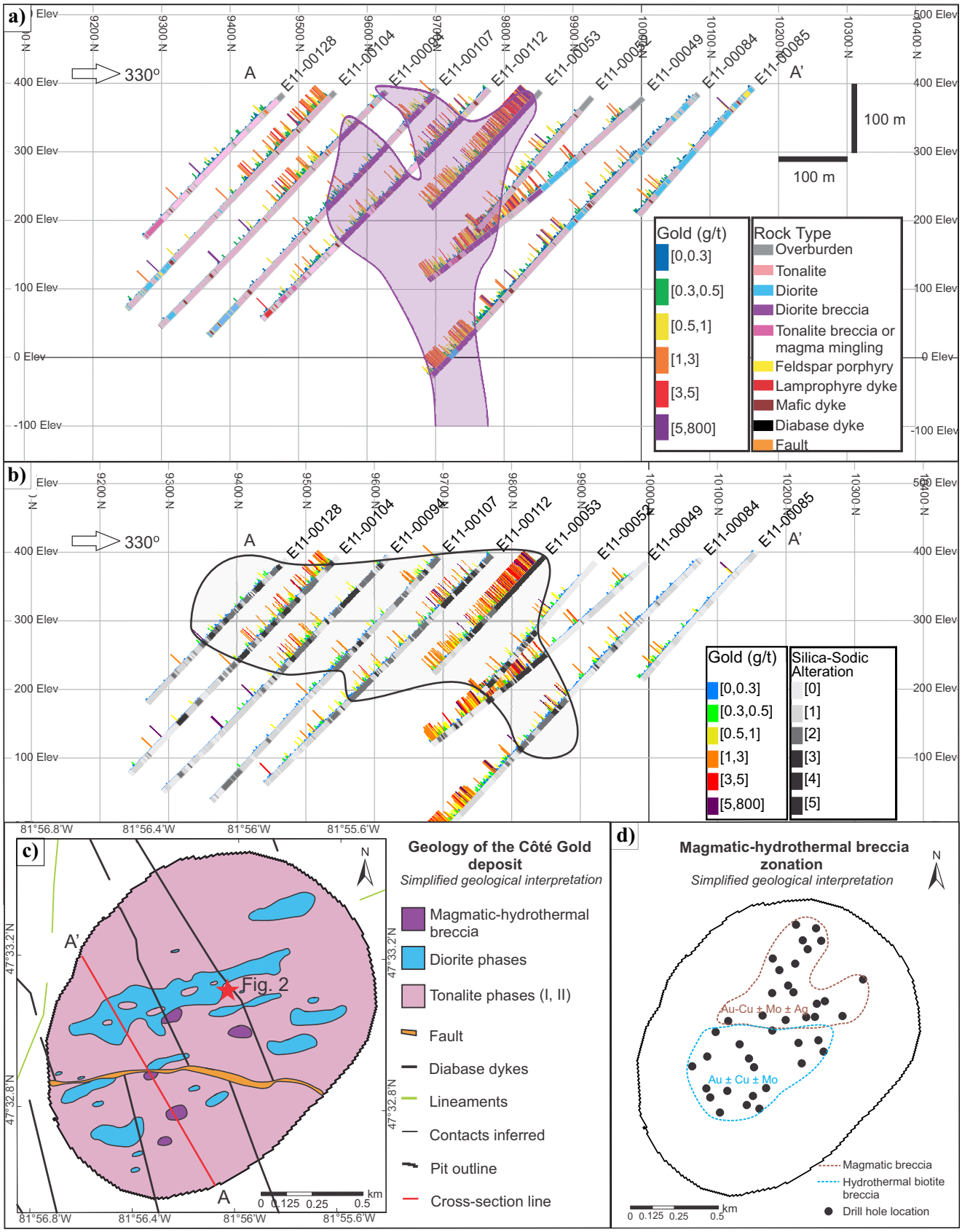

Figure 3 opposite page. a) Cross section of line 87+00 through the Côté Gold deposit showing the distribution of rock types. **b)** Extent of silica-sodic alteration. **c)** Plan-view map inside the proposed open pit. The location of cross-section A-A' is indicated by the red line and the location of the North Breccia outcrop (Fig. 4) is indicated by the star. Map was created using the first bedrock geology from 373 drillholes. **d)** Schematic plan view map of breccia matrix zonation and associated metals.

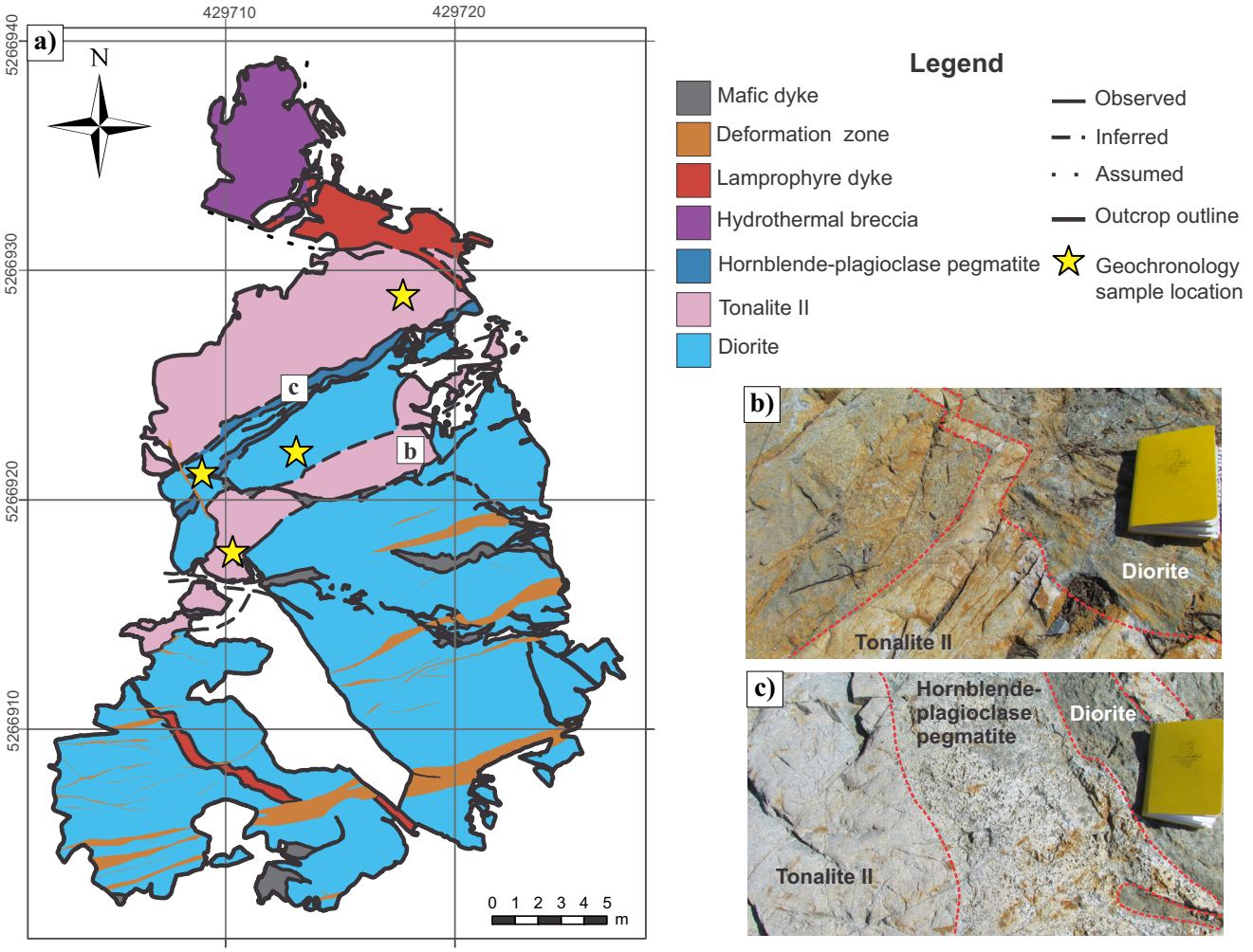

Figure 4. a) Geological map of the North Breccia outcrop showing the relative timing of the main geological units in the Côté Gold deposit. The locations of samples used for U-Pb zircon geochronology are indicated with stars. **b)** Field photograph of tonalite II cutting diorite. **c)** Field photograph showing the hornblende-plagioclase pegmatite intruding along the contact between the diorite and tonalite II. Book for scale is 19 x 12 cm.

texturally similar to tonalite I, but differs in terms of relative timing. The diorite and quartz diorite have sharp contacts with the older tonalite I phase and has transitional to sharp contacts with the younger tonalite II phase (Fig. 4b). The nature of the shape of the diorite clasts (millimetre- to metre-size; angular, rounded and scalloped contacts) in tonalite II suggests emplacement of tonalite II before the complete crystallization of dioritic phases.

Hornblende-plagioclase ± quartz pegmatite is the least abundant magmatic phase and generally occurs as small dykes of <1 m in apparent thickness. This unit is spatially associated with diorite and quartz diorite and has sharp to diffuse contacts with these phases (Fig. 4c). These pegmatitic dyke rocks are dark- to light-green, very coarse-grained (up to 2.5 cm) and inequigranular to massive. The mineralogy consists of plagioclase, hornblende, quartz, titanite, magnetite and apatite. Granophyric texture occurs and plagioclase is characterized by oscillatory zoning and polysynthetic twinning. This phase contains rare acicular amphibole grains (Fig. 5f).

Tonalite and diorite phases are intruded by a mineralized, sill-like magmatic-hydrothermal breccia body (~1200 m north-south and ~600 m east-west), on which the Au(-Cu) deposit is centred. The breccia body is complex, as both magmatic and hydrothermal variants occur as indicated by the nature of the matrix. Three types of matrices occur: (1) magmatic matrix with a dioritic mineralogy consisting of plagioclase-amphibole ± quartz (Fig. 5g) and rarely an evolved diorite consisting of quartz-plagioclase-biotite; (2) a rare amphibole-rich hydrothermal matrix consisting of amphibole-quartz ± biotite ± carbonate ± sulphides; and (3) a biotite-rich hydrothermal matrix. The biotite-rich breccia can be subdivided into three types based mainly on mineralogy and texture: (i) a biotite-quartz ± epidote ± carbonate ± pyrite ± chalcopyrite ± allanite ± magnetite, (ii) a biotite-quartz-magnetite-pyrite-chalcopyrite-carbonate ± allanite ± apatite, and a (iii)

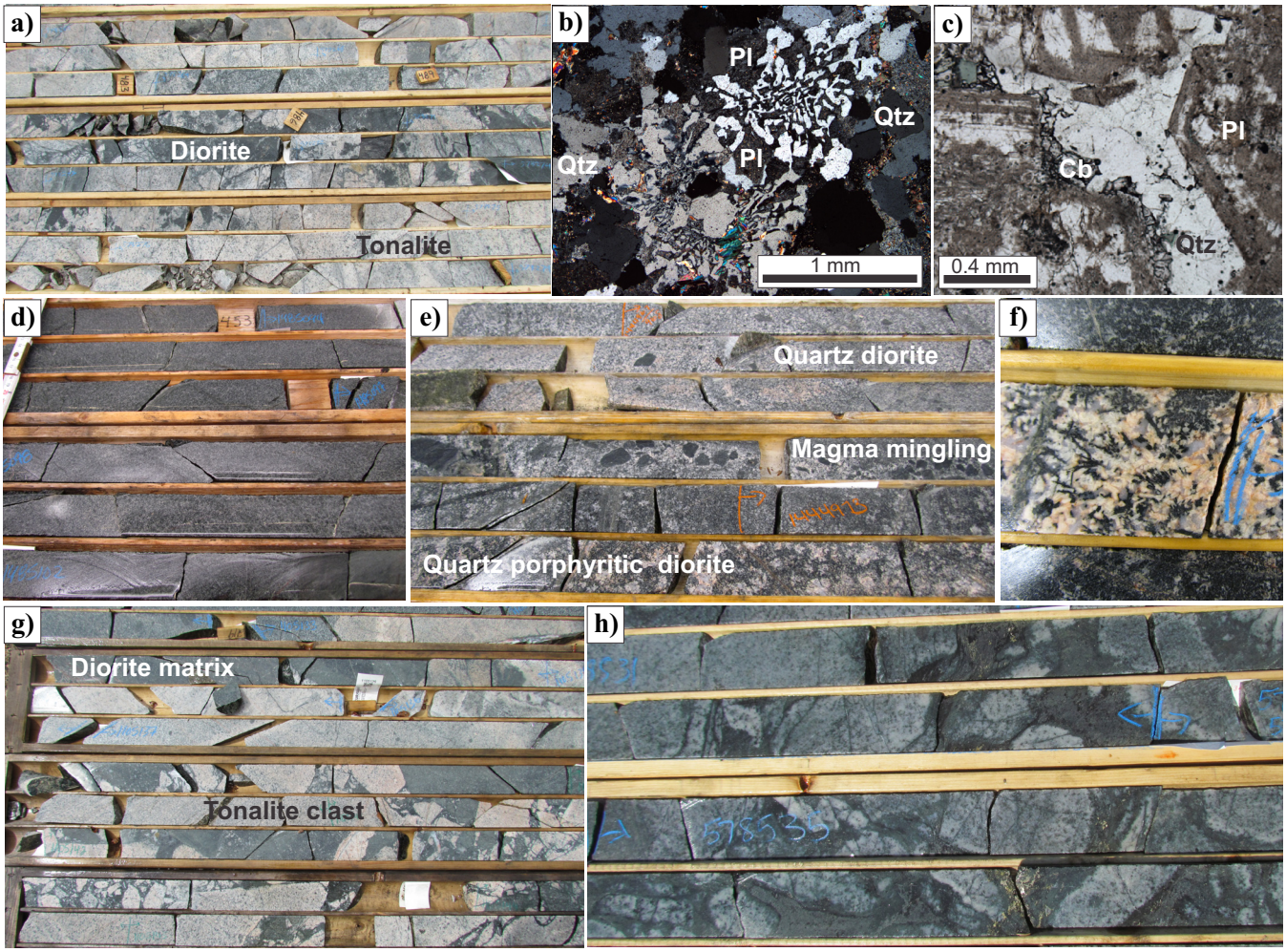

Figure 5. Drill-core and thin-section photographs showing the major rock types in the Côté Gold deposit. Width of drill core is 4.5 cm. **a)** Diorite intruding and brecciating (<5 m) tonalite I. **b)** Granophyric texture, which is common in the tonalite (Qtz = quartz, Pl = plagioclase). **c)** Miarolitic cavity in tonalite lined by carbonate (Cb) and filled with quartz. **d)** Section of homogeneous, medium-grained and equigranular melanocratic diorite. **e)** Contact between quartz diorite and quartz porphyritic diorite showing textural evidence for magma mingling. **f)** Hornblende-plagioclase-quartz pegmatite with acicular-textured amphibole grains. **g)** Section of magmatic breccia with tonalite clasts in a dioritic matrix. **h)** Section of biotite-rich hydrothermal matrix with clasts of tonalite.

biotite-quartz-carbonate-pyrite-chalcopyrite ± magnetite ± apatite (Fig. 5h).

The magmatic and biotite-rich hydrothermal breccia types can also be discriminated using geochemical parameters such as Zr/TiO_2 and CaO. The magmatic breccia is characterized by having relatively lower Zr/TiO_2 and elevated CaO values, thus similar to the chemistry of the diorite, whereas relatively higher Zr/TiO_2 and lower CaO values indicate a hydrothermal breccia. Using these indices (CaO and Zr/TiO_2), along with petrographic evidence, the data indicates an apparent zoning of breccia types exists in the deposit with the magmatic component occurring in the south and the biotite-rich hydrothermal breccia occurring in the north (Fig. 3d).

The division of breccia matrices in the deposit is also reflected in different metal associations, as illustrated in Figure 3d. The magmatic breccia is characterized by an Au ± Cu ± Mo association whereas the biotite-rich hydrothermal breccia is characterized by a Au-Cu ± Mo ± Ag association. There is, however, an overall lack of elemental associations in the Côté Gold deposit. Several bivariant elemental plots indicate there is no obvious correlation of Au mineralization with Cu, Mo, Te, F, Bi, or As in tonalite and diorite rocks (Fig. 6). However, in the breccia unit Au has a moderate positive correlation with Cu and Te, and a weak correlation with F.

The breccia body is characterized by the presence of tonalite I and II clasts. Rare dioritic clasts occur in the magmatic breccia. Tonalite, diorite, quartz diorite and hornblende-plagioclase pegmatite clasts are angular to rounded and variably sized, with dimensions from <1 mm to rarely >1 m in apparent length, and sharp to diffuse contacts. The breccia is typically matrix supported, but can rarely be clast-supported.

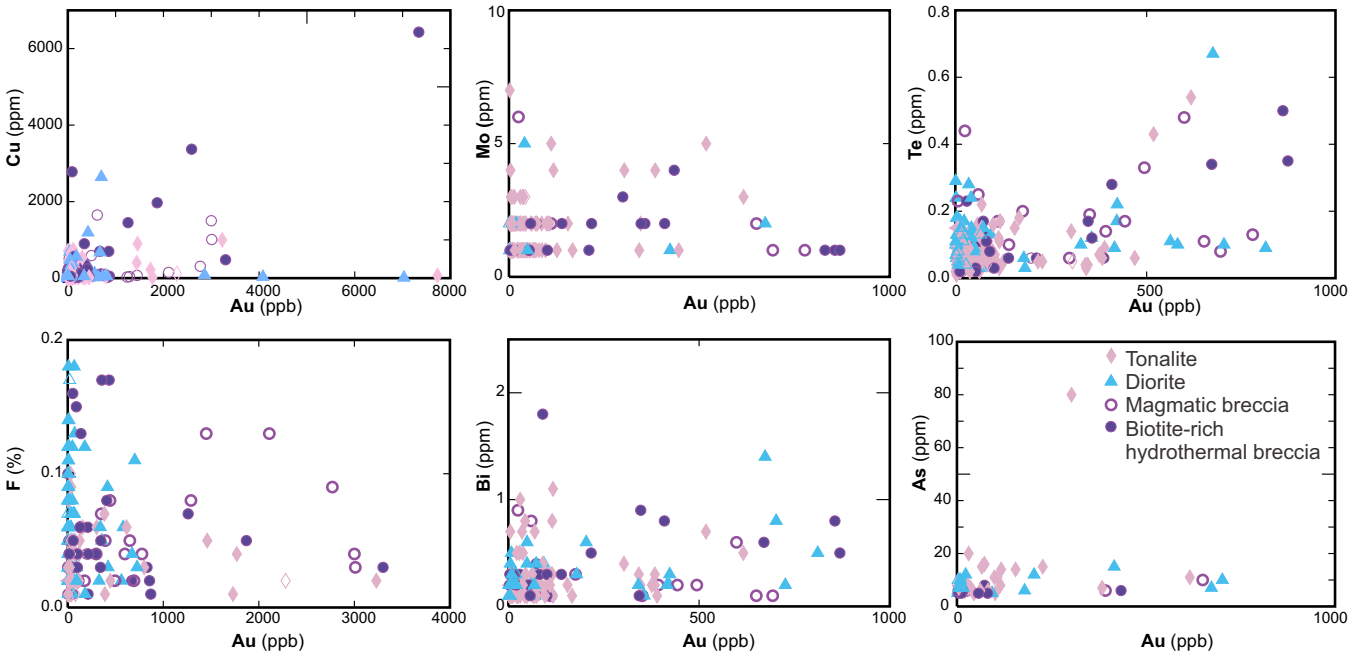

Figure 6. Binary element plots for all units in the Côté Gold deposit. The diagrams show that there is generally a poor correlation of all the elements with Au exception of the breccia unit where Au has a moderate association with Cu (correlation coefficient, R, of 0.76), moderate Au-Te association (R of 0.65) and weak Au-F association (R of 0.33).

Dyke Rocks

A variety of late, post-CIC dyke rocks cut the deposit. The dyke rocks are minor in total abundance and range in age from syn-SGB formation to post-deformation in age. Dyke rocks are not abundant in the deposit and are typically unmineralized. The dyke rocks include feldspar ± quartz porphyries, lamprophyre dykes and dioritic dykes, biotite-chlorite-quartz-carbonate dykes, diabase dykes, and tectonic breccias.

Geochemistry of Tonalitic and Dioritic Phases

A total of 455 samples were sampled to characterize the lithogeochemistry of the Côté Gold deposit. Included in the sample suite were major rock types, dykes, temporally-related volcanic rocks, as well as all alteration types and mineralization styles. Included in this summary herein are the least-altered tonalite and diorite samples. Table 1 presents a summary of analyses used in this study. The whole-rock geochemical data were obtained at Activation Laboratories, Ancaster, Ontario.

The intrusive rocks from the CIC are classified on the basis of their normative mineralogy (QAP) and the Zr/TiO_2 versus SiO_2 plot (Fig. 7a). In terms of their bulk compositions tonalite rocks equate to dacite and rhyolite. Some of the tonalite samples are notably enriched in silica (>74% SiO_2; Fig. 7a). The tonalite samples equate to the low-Al type (<15 wt% Al_2O_3) based on their Al_2O_3 contents at 70 wt% SiO_2 (Fig. 7b; Barker, 1979). This is atypical for these rocks, as the majority of Archean TTG are of high-Al type (>15 wt% Al_2O_3). The tonalite phases of the CIC have a range in terms of their Zr/Y versus Y ratios which equates to FII or FIIIa rhyolites (Fig. 7c). Importantly, the FII- and FIII-type rhyolites have been noted to be prospective for volcanic associated base-metal mineralization (Lesher et al., 1986). Tonalite samples contain a calc-alkaline to transitional affinity (Fig. 7d), with one tonalite sample plotting in the tholeiitic field.

The least-altered tonalite I and II are both characterized by relatively flat REE patterns with low (La/Yb)N ratios (Fig. 7e) and have moderate negative Eu anomalies (EuN/Eu*) of 0.30 to 0.77 and 0.27 to 0.63, respectively. In multi-element mantle-normalized plots tonalite I and II display similar patterns. Tonalite I and II display strong negative Ti, Eu P, Sr, with moderate Nb and Ta with variably negative Rb and Ba anomalies and positive Zr and Pb anomalies (Fig. 7f). The pronounced negative Eu anomalies and low Sr contents for both tonalite phases indicate plagioclase-dominated fractionation. On average, higher Ba, Sr and Ti occurs in tonalite II, which may be due to the presence of diorite clasts which are absent in tonalite I. These diorite clasts were originally amphibole-rich, but amphibole can be altered to biotite (Fig. 7f).

The diorite samples plot in the basalt to andesite field and quartz diorite samples plot in the andesite to dacite field in the Zr/TiO_2 versus SiO_2 plot (Fig. 7a). In terms of their normative mineralogy the quartz diorite phases rarely extend into the tonalite field as hornblende tonalites (Fig. 7a). Diorite is tholeiitic in nature and quartz diorite is tholeiitic to transitional in nature

Table 1. Average compositions of least altered major rocks from the Chester intrusive complex.

Rock Type	Tonalite I			Diorite			Tonalite II		
	Avg	STD	No.	Avg	STD	No.	Avg	STD	No.
SiO_2	77.07	2.56	6	56.11	5.53	15	71.87	2.55	6
Al_2O_3	11.94	0.62	6	14.91	1.09	15	13.39	1.00	6
Fe_2O_3	0.25	0.23	5	1.93	0.87	15	0.77	0.48	5
FeO_T	0.22	0.21	5	1.74	0.78	15	0.69	0.43	5
MnO	0.01	0.01	6	0.12	0.04	15	0.03	0.01	6
MgO	0.40	0.47	6	3.87	1.48	15	0.85	0.33	6
CaO	1.87	0.95	6	7.98	1.71	15	2.69	0.68	6
Na_2O	5.19	0.69	6	3.84	0.52	15	4.97	0.96	6
K_2O	0.60	0.14	6	0.66	0.46	15	0.98	0.41	6
TiO_2	0.315	0.017	6	1.489	0.471	15	0.532	0.311	6
P_2O_5	0.05	0.00	3	0.31	0.23	15	0.07	0.03	6
LOI	1.45	0.75	6	2.29	0.94	15	1.45	0.42	6
Total	99.97	0.67	6	100.19	0.53	15	99.47	0.79	6
Total S	0.08	0.06	5	0.07	0.10	14	0.05	0.04	5
CO_2	0.85	0.51	6	0.80	0.60	15	0.63	0.38	6
Cs	0.2	0.0	4	0.6	0.9	11	0.5	0.4	6
Rb	16	5	6	22	24	15	33	14	6
Ba	119	64	6	114	83	15	272	175	6
Th	7.93	2.64	6	2.68	1.21	15	7.35	2.36	6
U	1.80	0.33	6	0.94	0.64	15	1.85	0.44	6
Nb	7.1	2.0	6	9.1	4.0	15	12.1	7.0	6
Ta	0.85	0.16	6	0.75	0.73	15	0.89	0.09	6
Pb	7	1	2	3	2	9	3	1	5
Sr	103	43	6	254	72	15	160	76	6
Zr	269	32	6	141	51	15	259	46	6
Y	27.1	5.1	6	41.1	15.6	15	43.4	24.4	6
La	4.87	1.97	6	19.57	8.24	15	12.83	3.91	6
Ce	14.32	5.23	6	55.58	23.18	15	9.15	11.24	6
Pr	2.36	0.84	6	8.22	3.49	15	5.07	2.02	6
Nd	11.69	4.22	6	35.58	14.45	15	22.96	10.59	6
Sm	3.75	1.26	6	8.12	3.04	15	0.8	3.15	6
Eu	0.66	0.32	6	1.76	0.64	15	0.19	0.21	6
Gd	4.43	1.28	6	7.81	2.88	15	6.72	3.42	6
Tb	0.81	0.23	6	1.27	0.45	15	1.23	0.71	6
Dy	4.96	1.25	6	7.61	2.70	15	7.73	4.57	6
Ho	1.02	0.23	6	1.49	0.53	15	1.55	0.91	6
Er	3.10	0.68	6	4.33	1.45	15	4.65	2.65	6
Tm	0.49	0.10	6	0.65	0.22	15	0.74	0.43	6
Yb	3.21	0.57	6	4.22	1.43	15	4.72	2.7	6
Lu	0.437	0.060	6	0.605	0.196	15	0.647	0.355	6

Major elements as oxides in wt%, trace in ppm; Avg = average

(Fig. 7d). Both diorite and quartz diorite differ from a transitional to calc-alkaline nature for the tonalite samples.

The least altered diorite and quartz diorite have listric- or concave-shaped downwards LREE profiles with low La/YbN ratios and display weak negative Eu anomalies (EuN/Eu* = 0.43 to 0.89; Fig. 7g), hence they contrast markedly with the REE patterns for the tonalites. The multi-element mantle-normalized patterns for diorite and quartz diorite show weak negative Ti and Zr, moderate Rb, Ba, Nb, Ta, K, Sr, P anomalies and weak positive Pb anomalies (Fig. 7h). The mantle-normalized patterns for diorite differ from tonalite, the most obvious being the opposing Zr anomalies.

Post-Emplacement Veining and Alteration

Several types of magmatic-hydrothermal alteration are spatially associated with mineralization at the Côté Gold deposit. In paragenetic sequence, the dominant minerals associated to these alterations are amphibole, biotite, sericite, quartz-albite, epidote and chlorite (after biotite).

Amphibole alteration is rare in the deposit and occurs as a variety of amphibole-rich veins and breccias. Amphibole-bearing veins include amphibole, amphibole-quartz, amphibole ± apatite ± ilmenite ± titanite ± pyrite ± chalcopyrite assemblages (Fig. 8a). These veins cross cut the tonalite, diorite and the magmatic breccia and, therefore, post-date magmatic events. These amphibole-rich veins appear to be spatially restricted to the south of the deposit and represent the earliest hydrothermal alteration type associated with Au mineralization.

Biotite alteration is ubiquitous throughout the deposit and alters all intrusive phases. The biotite assemblage consists of biotite ± quartz ± magnetite ± epidote ± allanite ± carbonate ± pyrite ± chalcopyrite ± pyrrhotite ± titanite. This alteration assemblage occurs in the biotite-rich hydrothermal breccia (Fig. 8b), as disseminations in tonalite and diorite (Fig. 8c), in stockwork zones (Fig. 8d) and in sheeted veins (Fig. 8e). The biotite in the matrix of the biotite-rich hydrothermal breccia is not the result of alteration, but

Figure 7 (opposite page). Whole-rock geochemistry of least altered samples of tonalitic and dioritic phases of the Chester intrusive complex. **a)** A Zr/TiO_2 versus SiO_2 plot (Winchester and Floyd, 1975) for samples of diorite and tonalite, which was used to classify them chemically. Abbreviations: Alk-Bas = alkaline basalt, Bas/Trach/Neph = basanite/trachytes/nephelinite, Com/Pan = comendite/pantellite, Sub-AB = subalkaline basalt. The inset diagram shows the same samples plotted in the quartz-alkali feldspar-plagioclase (QAP) rock classification scheme. The pink shaded area shows tonalitic samples and the blue shaded area shows dioritic samples. Abbreviations: TT = tonalite-trondhjemite field and D = diorite/gabbro and quartz diorite/gabbro field. **b)** Plot of SiO_2 versus Al_2O_3 with the fields after Barker (1979) showing that the tonalite conforms to the low-Al type. **c)** Samples of tonalite plotted in the Y versus Zr/Y diagram, which shows their FII or FIIIa affinity. **d)** Samples of tonalite, diorite, and quartz diorite plotted on a Y versus Zr diagram; the fields for different magma associations from Galley and Lafrance (2014). **e)** Chondrite-normalized REE plot for samples of tonalite I and II. **f)** Multi-element mantle-normalized diagram for samples of tonalite I and II. **g)** Chondrite-normalized REE plot for samples of diorite and quartz diorite. **h)** Multi-element mantle-normalized diagram for samples of the different diorite and quartz diorite. The CI chondrite normalizing and primitive mantle values used are from Sun and McDonough (1989).

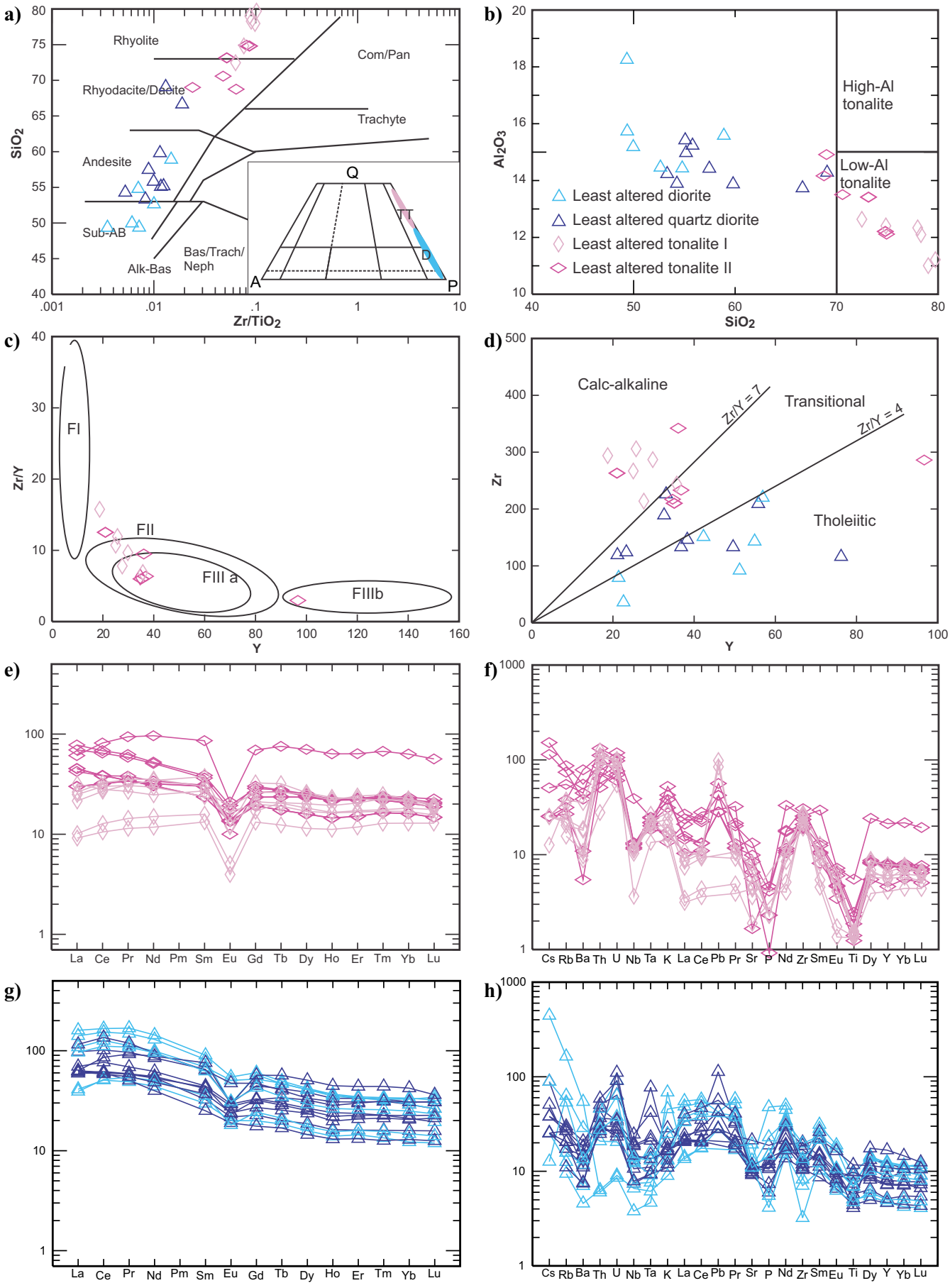
a)
Rhyolite
Com/Pan
Rhyodacite/Dacite
Trachyte
Andesite
Sub-AB
Alk-Bas
Bas/Trach/
Neph
Q
T
D
A
P
SiO2
Zr/TiO2
b)
High-Al
tonalite
Low-Al
tonalite
Least altered diorite
Least altered quartz diorite
Least altered tonalite I
Least altered tonalite II
Al2O3
SiO2
c)
FI
FII
FIII a
FIIIb
Zr/Y
Y
d)
Calc-alkaline
Transitional
Tholeiitic
Zr/Y = 7
Zr/Y = 4
Zr
Y
e)
La Ce Pr Nd Pm Sm Eu Gd Tb Dy Ho Er Tm Yb Lu
f)
Cs Rb Ba Th U Nb Ta K La Ce Pb Pr Sr P Nd Zr Sm Eu Ti Dy Y Yb Lu
g)
La Ce Pr Nd Pm Sm Eu Gd Tb Dy Ho Er Tm Yb Lu
h)
Cs Rb Ba Th U Nb Ta K La Ce Pb Pr Sr P Nd Zr Sm Eu Ti Dy Y Yb Lu

forms as a primary hydrothermal mineral. Disseminated biotite occurs as anhedral to subhedral, fine-grained (<1 to > 50%) disseminations that partly replace primary plagioclase and amphibole, as well as amphibole in veins and breccias. Sheeted veins consist of east-west trending, planar, subparallel, moderately to steeply dipping, closely (cm to 10s of cm apart) to widely (several metres apart) spaced veins that occur throughout the deposit. These veins are also found outside the deposit within the CIC. These sheeted veins contain quartz-biotite-pyrite ± chalcopyrite ± pyrrhotite ± carbonate ± titanite ± allanite and therefore inferred to be early, having formed during biotite alteration, but are typically overprinted by sericite alteration and deformation resulting in distinct sericite alteration haloes with or without shearing. The various types of biotite alteration noted above are partially to wholly altered by chlorite.

The sericite-bearing alteration assemblage consists of sericite-quartz ± carbonate ± pyrite ± chalcopyrite and occurs throughout the deposit. Sericite is light-grey to dark-grey and rarely green-grey with fine-grained, elongated to stubby grains that replace primary plagioclase. Sericite alteration is generally fracture-controlled as veins, disseminations and pervasive types. Sericite often forms alteration haloes surrounding stockworks (Fig. 8d) and sheeted veins (Fig. 8e,f), both of which contain an earlier biotite alteration assemblage. Although the extent of sericite alteration has not been fully determined, it is strongest within the centre of the deposit with its intensity decreasing with distance from the core of mineralization.

Silica-sodic alteration is a texturally-destructive alteration that occurs as vein-controlled (Fig. 8g) as well as a pervasive type that overprints earlier biotite and sericite alteration. The silica-sodic alteration envelope can be >200 m wide, moderately to steeply dipping to the north or northwest, and is most intensely developed towards the centre of the deposit. Figure 3b illustrates the distribution and intensity of the silica-sodic alteration, which also overprints the mineralized breccia body at depth. In drill core, the silica-sodic alteration is characterized by bleaching, destruction of primary textures, including grain boundaries, and replacement of mafic minerals. In thin section, this alteration is characterized by replacement of plagioclase by albite, grain-size reduction, and sutured grain boundaries due to dissolution of plagioclase and quartz. This alteration affects tonalite, diorite, quartz diorite, hornblende-plagioclase pegmatite, magmatic-hydrothermal breccia (Fig. 8h) and rarely dyke rocks. Gold mineralization can be spatially associated with this alteration (Fig. 8i), but it is typically inconsistent.

The epidote-bearing alteration, consisting of an epidote ± quartz ± carbonate ± chlorite assemblage, occurs as both disseminated and vein-controlled alteration (Fig. 8j). Epidote occurs as fine-grained anhedral disseminations in the groundmass replacing primary plagioclase and amphibole. An area of vein-controlled epidote alteration (Fig. 8j) is restricted to a ~300 m wide by 400 m long zone in the northern-most part of the deposit. Epidote alteration is rarely associated with Au mineralization. This alteration type appears to postdate the aforementioned alteration types based on limited crosscutting observations in drill core. This alteration is inferred to be syn-intrusion due to its spatial distribution in the deposit and that it is foliated, predating D_2 deformation.

Chlorite is ubiquitous throughout the deposit and occurs as disseminated, replacement and vein-controlled alteration. Petrographic observations indicate chlorite partially to wholly replace plagioclase, amphibole and secondary biotite. As a result of replacing biotite, titanium-bearing phases, such as rutile, form in association with chlorite. The timing of chlorite alteration is not fully constrained and therefore its importance in terms of deposit formation is unclear. Gold mineralization is spatially associated with hydrothermal chlorite alteration, but its genetic association is not fully understood as it pseudomorphs earlier, higher-temperature hydrothermal biotite.

The study and description of alteration types at the Côté Gold deposit is complicated by syn-tectonic alteration associated with regional D_2 deformation zones, including chlorite, sericite, silica, Fe- and Ca-carbonate, sulphidation and tourmaline alteration (Heather, 2001). At the deposit, syn-tectonic silica and sericite alteration are associated with D_2 deformation zones. Several discrete syn-tectonic shear zones, typically <3 m wide, cut through the deposit. Within the shear

Figure 8 (opposite page). Drill-core (width = 4.5 cm) and thin section photographs of alteration types and mineralization styles present at the Côté Gold deposit. **a)** Gold mineralized amphibole vein cutting through barren diorite. **b)** An example of mineralized, biotite-rich hydrothermal breccia with clasts of tonalite. **c)** Disseminated, light-brown to dark-brown, subhedral biotite (Bt) that replaces primary plagioclase (Pl) and more rarely quartz (Qtz). The opaque mineral is disseminated pyrite (Py). **d)** Stockwork developed in tonalite that is lined by biotite and quartz with sericite alteration haloes. **e)** Mineralized sheeted quartz-pyrite veins in tonalite. **f)** Close-up photograph of a multi-centimetre-thick quartz-pyrite-chalcopyrite-molybdenite vein with a sericite alteration halo in tonalite that forms part of a sheeted vein set. g) Example of fracture-controlled silica-sodic alteration overprinting disseminated and fracture-controlled biotite alteration. **h)** Example of the pervasive silica-sodic alteration of a breccia type of unknown magmatic or hydrothermal origin. **i)** An example of fracture-controlled silica-sodic alteration overprinting sericite alteration. j) An example of vein-controlled epidote alteration.

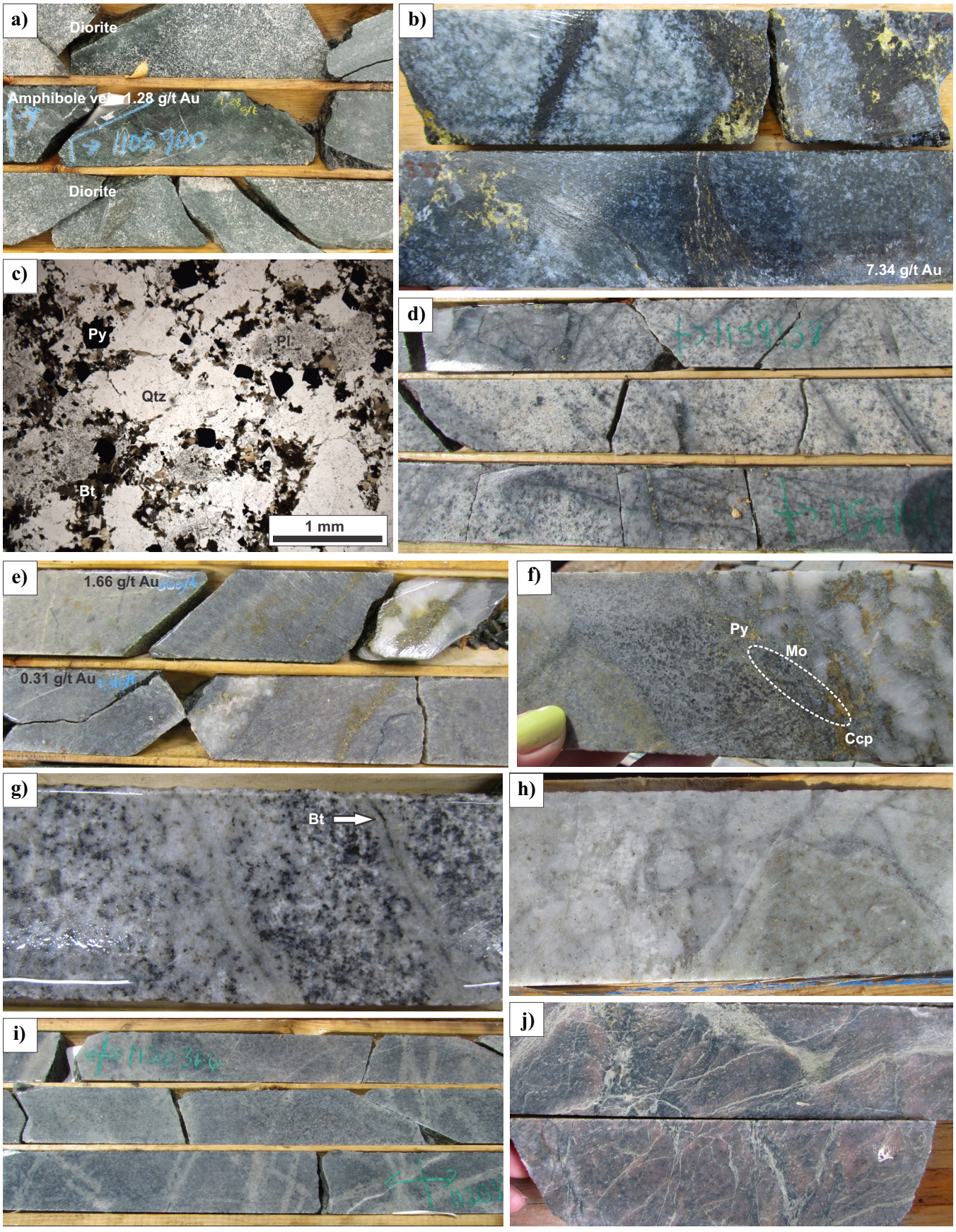
a)
Diorite
Amphibole ve
1.28 g/t Au
Diorite
b)
7.34 g/t Au
c)
Py
Pl
Qtz
Bt
1 mm
d)
e)
1.66 g/t Au
0.31 g/t Au
f)
Py
Mo
Ccp
g)
Bt
h)
i)
j)

zones there is the development of locally strong, pervasive sericite and silica alteration which overprints earlier syn-intrusion amphibole, biotite, sericite, silica-sodic and epidote alteration. Typically these shear zones do not contain mineralization. However, the shear zones can be mineralized when cutting through previously mineralized zones, such as a breccia unit or sheeted veins.

Mineralization

Several styles of Au mineralization are recognized within the Côté Gold deposit, and include disseminated, breccia-hosted and vein-type (Fig. 8). All of which are co-spatial with biotite (± chlorite), sericite and silica-sodic alteration.

Disseminated mineralization in the hydrothermal matrix of the breccia is the most important and consistent style of Au(-Cu) mineralization. This style consists of disseminated pyrite, chalcopyrite, magnetite, gold and molybdenite and is associated with primary hydrothermal biotite and chlorite after biotite (Fig. 8b). Similarly, disseminated mineralization in both tonalitic and dioritic rocks is associated with biotite or chlorite alteration (Fig. 8c). Although both biotite and chlorite are ubiquitous throughout the deposit, Au is not consistently associated with the two alteration types. Disseminated Au and chalcopyrite are intergrown with biotite/chlorite in the tonalite and breccia unit.

Several types and generations of veins host gold and molybdenite and include quartz, quartz-carbonate, quartz-biotite-pyrite ± chalcopyrite ± pyrrhotite ± carbonate ± titanite ± allanite, quartz-carbonate-titanite, quartz-tourmaline and quartz-epidote. The mineralized veins typically contain various proportions of pyrite and chalcopyrite. The nature of the veins and fractures vary from stockworks (Fig. 8d) to closely spaced, planar, subparallel sheeted vein sets (Fig. 8e, f). Stockwork mineralization cuts through all major rock types, but is most prominent in tonalite I and II versus the less competent dioritic unit. The mineralized sheeted veins and stockwork zones cut the hydrothermal breccia(s) and, therefore post-date the breccia-controlled mineralization. Miarolitic-like cavities, which consist of mm- to cm-size openings lined with feldspar, carbonate and sulphide, can also contain gold. Importantly, the gold-bearing sheeted and stockwork veins mineralization are not present in later post-CIC dykes suggesting a coeval syn-magmatic relationship.

Uranium-Lead Geochronology

The U-Pb zircon geochronology was done on four well-constrained samples collected from the North Breccia outcrop (Fig. 4 see location on Fig. 1c), and includes one diorite, two tonalites and one hornblende-plagioclase pegmatite. In addition, two feldspar-quartz porphyry dykes from drill core were sampled. Previous U-Pb zircon dating of tonalite I and II from the CIC includes 2740 ± 2 Ma (Heather and van Breemen, 1994; van Breemen et al., 2006; Fig. 2), 2741.1 ± 0.9 Ma, and 2738.7 ± 0.8 Ma (Kontak et al., 2013; Fig. 2).

Important field relationships mapped at the North Breccia outcrop are presented in Figure 4a–c. Diorite is the oldest rock type exposed and is intruded sharply by tonalite (Fig. 4b) that contains <1% dioritic clasts, which is characteristic of tonalite II. A hornblende-plagioclase pegmatite intrudes along the contact between diorite and tonalite II (Fig. 4c) and therefore postdates these phases. The results of the U-Pb zircon dating include (1) an age of 2741.5 ± 0.7 Ma for the diorite; (2) ages of 2741.7 ± 0.7 and 2741.4 ± 0.9 Ma for two tonalite samples; and (3) an age of 2741.0 ± 0.6 Ma for the pegmatite. The four samples constrain the age of crystallization of the CIC to 2741 Ma.

Two feldspar porphyry dykes that cross-cut mineralization were sampled to provide a minimum age for deposit formation. The first sample, an unaltered feldspar porphyry that cuts through a biotite altered tonalite (Fig. 9a), yielded an age of 2696.0 ± 0.9 Ma. The second sample, a sericite altered and deformed feldspar porphyry (Fig. 9b) cuts through a mineralized breccia unit, yielded a similar age of 2697.1 ± 0.8 Ma. These ages are among the youngest obtained for magmatic activity in the Swayze greenstone belt and do not constrain very well the minimum age for deposit formation.

Molybdenite Rhenium-Osmium Geochronology

Two samples previously analysed for molybdenite Re-Os dating were used to constrain the timing of mineralization (Kontak et al., 2013). The results yield ages of 2737 ± 11 Ma and 2741 ± 11 Ma for two tonalite-hosted samples, the former containing massive molybdenite in a fracture found in silica-sodic altered tonalite (Fig, 9c) and the latter containing visible molybdenite, chalcopyrite and gold in sericitized tonalite (Fig. 9d, e). Given that the two samples analysed yielded similar ages, the best estimate of the molybdenite Re-Os age is 2739 ± 9 Ma (Kontak et al., 2013). These two ages constrain the age of gold mineralization at the deposit.

DISCUSSION AND MODELS

Petrogenesis of Tonalite and Diorite

A previous geochemical study by Berger (2012) suggested that tonalite and diorite phases of the CIC are genetically related, however, geochemical evidence from this study suggests otherwise. The diorite contains slightly elevated LREE patterns compared to the less fractionated patterns and lower REE contents of tonalite. The less fractionated pattern of tonalite with moderate to strong negative Eu anomalies are inconsis-

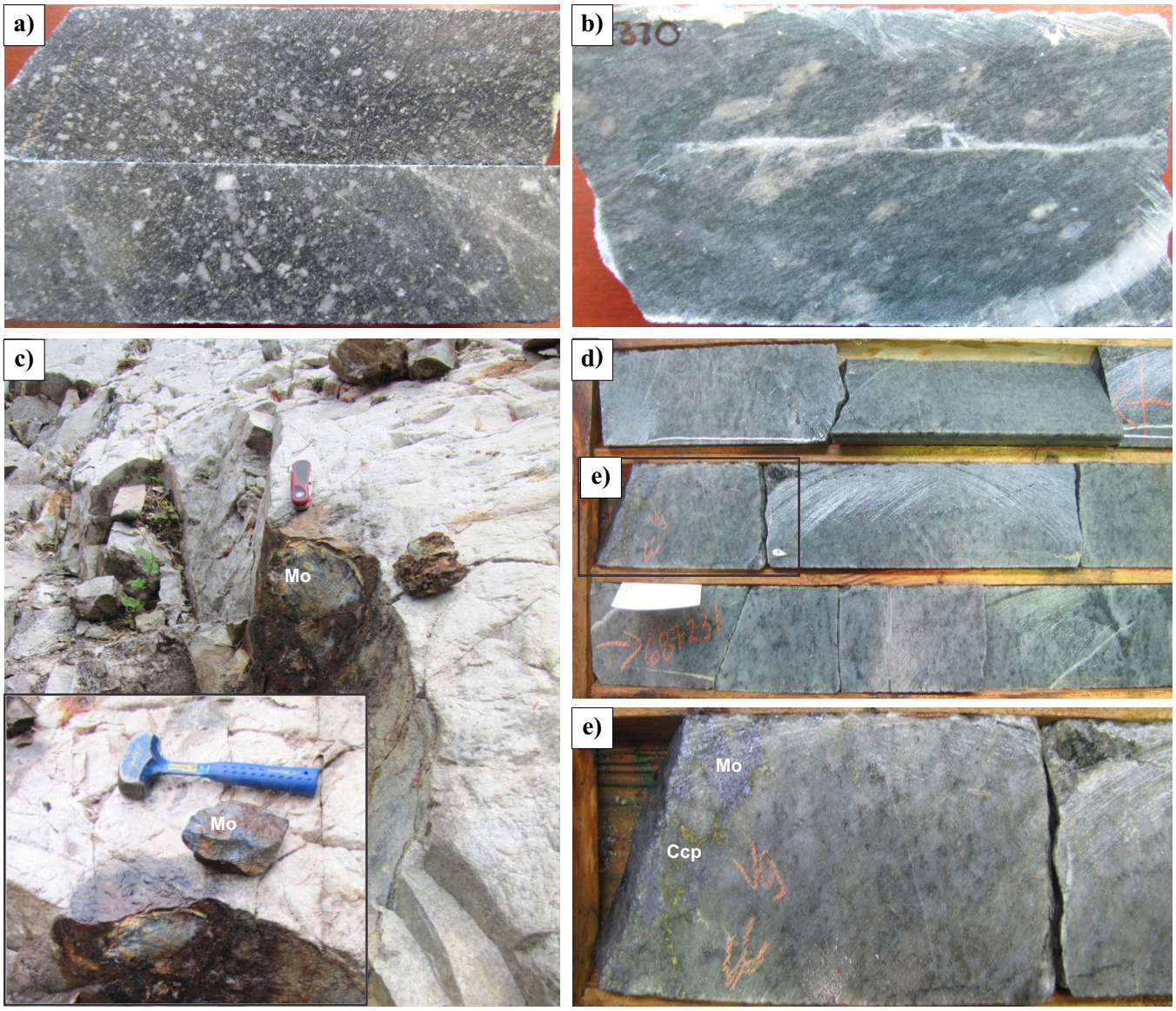

Figure 9. Field and drill-core (width = 4.5 cm) photographs of samples used for U-Pb and Re-Os geochronology. **a)** Unaltered feldspar porphyry. **b)** Sericite-altered and deformed feldspar porphyry dyke. **c)** Massive molybdenite (Mo) in a fracture in a silicified tonalite. In the inset, hammer for scale is 30 cm long. **d)** Molybdenite associated with chalcopyrite and gold in a veinlet cutting through a biotite altered tonalite that is overprinted by sericite alteration. **e)** Close-up photo of (d) showing molybdenite (Mo) intergrown with chalcopyrite (Ccp).

tent with being an evolved fractionate of the diorite, which is more elevated in the REEs and has a more fractionated pattern with a distinct listric- or concave-shaped downwards profile. Thus, although the tonalite and diorite are temporally related, this study suggests they are genetically unrelated.

The diorite and quartz diorite phases are tholeiitic to transitional in nature, whereas the tonalitic phases have a calc-alkaline to transitional affinity, based on their Zr/Y ratios. This spread of chemical affinity and, hence, petrogenetic associations for spatially associated rocks, in particular the quartz diorite-tonalite-trondhjemite suites, has been previously documented and could indicate that the intrusive suite consists of a composite of differentiated lithospheric mantle and lower-crust partial melts (Galley and Lafrance, 2014). Moreover, different petrogenetic associations is also supported by the differences in the primitive-mantle-normalized multi-element profiles between tonalite and diorite phases which suggests the involvement of two different magmas (i.e. mantle and crust; Galley, 2003). Both tonalite and diorite suites of the CIC display strong negative Ti, Eu P, and Sr, with moderate Nb and Ta, variably negative Rb and Ba anomalies, and positive Pb anomalies. The tonalite shows a decoupling between Nb and Zr which is typical of relatively reduced melts, whereas diorite shows a more sympathetic Nb/Zr decrease relative to primitive mantle, sug-

gesting a more evolved, oxidized source (Galley, 2003). This is consistent with petrographic evidence of accessory ilmenite in tonalite and accessory magnetite and ilmenite in diorite. The above evidence suggests a spread across petrogenetic origins for tonalitic and dioritic phases.

Metallogenic Implications

The known metallogenic events or epochs in the Abitibi greenstone belt were outlined by Robert (2001) and Robert et al. (2005) and occur in three main periods of gold mineralization which include (1) VMS from ca. 2728 to 2700 Ma; (2) syenite-associated from ca. 2680 to 2674 Ma; and (3) greenstone-hosted which spans from ca. 2671 to 2668 Ma. The U-Pb geochronology of this study constrains the intrusive phases of the CIC to ca. 2741 Ma which overlaps with the Re-Os dates of 2739 ± 9 Ma that constrain the age of molybdenite, some of which is associated with gold mineralization. These results, along with field and petrological evidence for syn-intrusion mineralization constrains the age of gold deposition. Therefore, at least some of the mineralization within the Côté Gold deposit defines a new and early-stage gold mineralization event within the Abitibi Subprovince. Possible later upgrading of this mineralization may have occurred due to structural overprinting, as has been documented at, for example, the Malartic intrusion-related gold deposit setting. This aspect of the Côté Gold deposit is being currently investigated given its significance for the deposit model.

IMPLICATIONS FOR EXPLORATION

Unlike the Abitibi greenstone belt that is rich in greenstone-hosted gold deposits, VMS, and syenite-associated gold deposits, few mineral deposits have been found so far in the SGB. Based on the similar geology of the two greenstone belts (Ayer et al., 2002), it seems reasonable to assume that the SGB should also be equally prospective for gold and base-metal deposits. Gold mineralization within the Abitibi Subprovince tends to be proximal to major faults, with the known deposits occurring in clusters (Dubé and Gosselin, 2007). Past exploration in the SGB focused on east-west trending, high-strain zones and greenstone-hosted quartz-carbonate vein-type deposits with minor success. The intrusion-related Côté Gold deposit is the first large gold deposit discovery in the SGB, and is similar to other low-Al composite suites described in the literature that have been documented to form in early arc rift environments that host VMS-style mineralization (Campbell et al., 1981; Galley, 2003). These subvolcanic, low-Al composite synvolcanic intrusions have also been documented to host porphyry-type Cu-Mo ± Au mineralization (Trowell 1974; Poulsen and Franklin, 1981; Galley, 2003). The Côté Gold deposit provides, therefore, a guide for future exploration activity for other low-Al composite, subvolcanic intrusive complexes within the SGB and other Archean terranes.

FUTURE WORK

The data reviewed here, which form part of a much more substantial data set, will be merged with other results and collectively assembled into three articles for submission to peer-reviewed journals. The tentative titles of each paper are as follows: (1) Geological setting, petrology and U-Pb zircon geochronology of an Archean large-tonnage, low-grade intrusion-related gold system: The Côté Gold Au(-Cu) deposit, Swayze greenstone belt, Ontario; (2) Mineral paragenesis, alteration and geochronology (U-Pb, Re-Os) of the Archean intrusion-related Côté Gold Au(-Cu) deposit, Ontario; and (3) Alteration lithogeochemistry of an Archean low-grade, large-tonnage intrusion-related gold deposit: The Côté Gold Au(-Cu) deposit, Swayze greenstone belt, Ontario.

ACKNOWLEDGEMENTS

This study is the outgrowth of support from several individuals and groups for which we are most appreciative. The initial work was supported by John Ayer and David Beilhartz and funded through Trelawney Mining and Exploration Inc. and the Discover Abitibi Program. Subsequently, Iamgold Corporation provided the considerable financial and logistical support needed to undertake this deposit-scale study and we sincerely acknowledge their financing and the input of staff, in particular Jamie Rogers, who made this project possible. We thank the financial support of the Geological Survey of Canada through the TGI-4 Lode Gold Project for providing funding and expertise for the lithogeochemical and geochronological component of this study. We also thank Alan Galley for a review and helpful comments.

REFERENCES

Ayer, J., Amelin, Y., Corfu, F., Kamo, S., Ketchum, J., Kwok, K., and Trowell, N., 2002. Evolution of the southern Abitibi greenstone belt based on U-Pb geochronology: autochthonous volcanic construction followed by plutonism, regional deformation and sedimentation; Precambrian Research, v. 115, p. 63–95.

Ayer, J.A. and Chartrand, J.E., 2011. Geological compilation of the Abitibi greenstone belt; Ontario Geological Survey, Miscellaneous Release Data 282.

Barker, F., 1979. Trondhjemites, Dacites and Related Rocks; Elsevier, New York, 659 p.

Berger, B.R., 2011. Geological investigations south of Gogama, In: Summary of Field Work and Other Activities 2011; Ontario Geological Survey, Open File Report 6270, 7 p.

Berger, B.R., 2012. Interpretation of Geochemistry in the south of Gogama area, In: Summary of Field Work and Other Activities 2012; Ontario Geological Survey, Open File Report 6280, 14 p.

Campbell, I.H., Franklin, J.M., Gorton, M.P., Hart, T.R., and Scott, S.D., 1981. The role of subvolcanic sills in the generation of massive sulfide deposits; Economic Geology, v. 76, p. 2248–2253.

Dubé, B. and Gosselin, P., 2007. Greenstone-hosted quartz-carbonate vein deposits, *In:* Mineral Deposits of Canada: A Synthesis of Major Deposit Types, District Metallogeny, the Evolution of Geological Provinces, and Exploration Methods, (ed.) W.D. Goodfellow; Geological Association of Canada, Mineral Deposits Division, Special Publication No. 5, p. 49–73.

Galley, A.G., 2003. Composite synvolcanic intrusions associated with Precambrian VMS-related hydrothermal systems; Mineralium Deposita, v. 38, p. 443–473.

Galley, A.G. and Lafrance, B., 2014. Setting and evolution of the Archean synvolcanic Mooshla Intrusive Complex, Doyon-Bousquet-LaRonde mining camp, Abitibi greenstone belt: Emplacement history, petrogenesis, and implications for Au metallogenesis; Economic Geology, v. 109, p. 205–229.

Heather, K.B. and van Breemen, O., 1994. An interim report on geological, structural, and geochronological investigations of granitoid rocks in the vicinity of the Swayze greenstone belt, southern Superior Province, Ontario, *In:* Canadian Shield; Geological Survey of Canada, Current Research 1994-C, p. 259–268.

Heather, K.B., Shore, G.T., and van Breemen, O., 1996, Geological investigations in the Swayze greenstone belt, southern Superior Province, Ontario: a final update, *In:* Canadian Shield; Geological Survey of Canada, Current Research 1996-C, p. 125–136.

Heather, K.B. and Shore, G.T., 1999a. Geology, Swayze Greenstone Belt, Ontario; Geological Survey of Canada, Open File 3384a, sheet 2, scale 1:50 000.

Heather, K.B. and Shore, G.T., 1999b. Geology, Gogama, Swayze Greenstone Belt, Ontario; Geological Survey of Canada, Open File 3384g, scale 1:50 000.

Heather, K.B., 2001. The geological evolution of the Archean Swayze Greenstone Belt, Superior Province, Canada; Ph.D. thesis, Keele University, Keele, England, 370 p.

IAMGOLD Corporation, 2013. IAMGOLD provides mineral resource update for Côté Gold and reports strongest quarter for production in 2012 with confirmed production guidance for 2013; IMG press release, January 22, 2013.

Kontak, D.J., Creaser, R.A., and Hamilton, M., 2013. Geological and geochemical studies of the Côté Lake Au(-Cu) deposit Area, Chester Township, Northern Ontario, *In:* Results from the Shining Tree, Chester Township and Matachewan Gold Projects and the Northern Cobalt Embayment Polymetallic Vein Project, (ed.) J.A. Ayer, D.J. Kontak, R.L. Linnen, and S. Lin; Ontario Geological Survey, Miscellaneous Release Data 294.

Lesher, C.M., Goodwin, A.M., Campbell, I.H., and Gorton, M.P., 1986. Trace-element geochemistry of ore-associated and barren, felsic metavolcanic rocks in the Superior Province, Canada; Canadian Journal of Earth Sciences, v. 23, p. 222–237.

Poulsen, K.H. and Franklin, J.M., 1981. Copper and gold mineralization in an Archean trondhjemitic intrusions, Sturgeon Lake, Ontario; Geological Survey of Canada, Paper 81-1a, p. 9–14.

Poulsen, K.H., Robert, F., and Dubé, B., 2000. Geological classification of Canadian gold deposits; Geological Survey of Canada, Bulletin 540, 106 p.

Powell, W.G., Carmichael, D.M., and Hodgson, C.J., 1995. Conditions and timing of metamorphism in the southern Abitibi greenstone belt, Québec; Canadian Journal of Earth Sciences, v. 32, p. 787–805.

Robert, F., 2001. Syenite-associated disseminated gold deposits in the Abitibi greenstone belt, Canada; Mineralium Deposita, v. 36, p. 503–516.

Robert, F., Poulsen, K.H., Cassidy, K.F., and Hodgson C.J., 2005. Gold metallogeny of the Yilgarn and Superior cratons, *In:* Economic Geology 100th Anniversary Volume: 1905–2005, (ed.) J.W. Hedenquist, J.F.H. Thompson, R.J. Goldfarb, and J.P. Richards; Society of Economic Geologists, Littleton, Colorado, p. 1001–1034.

Sun, S.S. and McDonough, W.F., 1989. Chemical and isotopic systematics of ocean basalts: Implications for mantle composition and process, *In:* Magmatism and Ocean Basins, (ed.) A.D. Saunders and M.J. Norry; Geological Society of London, p. 313–345.

Trowell, N.F., 1974. Geology of the Bell Lake-Sturgeon Lake area, districts of Thunder Bay and Kenora; Ontario Geological Survey, Report 113, 67 p.

Van Breemen, O., Heather, K.B., and Ayer, J.A., 2006. U-Pb geochronology of the Neoarchean Swayze sector of the southern Abitibi greenstone belt; Geological Survey of Canada, Current Research 2006-F1, 32 p.

Winchester, J.A. and Floyd, P.A., 1975. Geochemical magma type discrimination: Application to altered and metamorphosed basic igneous rocks; Earth and Planetary Science Letters, v. 28, p. 459–469.

GEOLOGICAL SURVEY OF CANADA
OPEN FILE 7852

Targeted Geoscience Initiative 4: Contributions to the Understanding of Precambrian Lode Gold Deposits and Implications for Exploration

Genesis of the Canadian Malartic, Côté Gold, and Musselwhite gold deposits: Insights from LA-ICP-MS element mapping of pyrite

Jian-Feng Gao[1], Simon E. Jackson[1], Benoît Dubé[2], Daniel J. Kontak[3], and Stéphane De Souza[2]

[1]Geological Survey of Canada, Ottawa, Ontario
[2]Geological Survey of Canada, Québec, Quebec
[3]Laurentian University, Sudbury, Ontario

2015

This publication is available for free download through GEOSCAN (http://geoscan.nrcan.gc.ca/)

Recommended citation

Gao, J.-F., Jackson, S.E., Dubé, B., Kontak, D.J., and De Souza, S., 2015. Genesis of the Canadian Malartic, Côté Gold, and Musselwhite gold deposits: Insights from LA-ICP-MS element mapping of pyrite, *In:* Targeted Geoscience Initiative 4: Contributions to the Understanding of Precambrian Lode Gold Deposits and Implications for Exploration, (ed.) B. Dubé and P. Mercier-Langevin; Geological Survey of Canada, Open File 7852, p. 157–175.

Publications in this series have not been edited; they are released as submitted by the author.

Contribution to the Geological Survey of Canada's Targeted Geoscience Initiative 4 (TGI-4) Program (2010–2015)

TABLE OF CONTENTS

Genesis of the Canadian Malartic, Côté Gold, and Musselwhite gold deposits: Insights from LA-ICP-MS element mapping of pyrite

Jian-Feng Gao[1], Simon E. Jackson*, Benoît Dubé[2], Daniel J. Kontak[3], and Stéphane De Souza[2]

[1]Geological Survey of Canada, 601 Booth Street, Ottawa, Ontario K1A 0E9
[2]Geological Survey of Canada, 490 rue de la Couronne, Québec, Quebec G1K 9A9
[3]Department of Earth Sciences, Laurentian University, Sudbury, Ontario P3E 2C6
*Corresponding author's e-mail: Simon.Jackson@NRCan-RNCan.gc.ca

ABSTRACT

Pyrite efficiently incorporates many key metals during progressive precipitation and thus records the chemical evolution of fluids from which it was deposited. To reveal this information, a new LA-ICP-MS mapping procedure has been developed to allow generation of 2-D trace element concentration maps of minerals in petrographic section. The technique has been applied to pyrite-/pyrrhotite-bearing Au ores from three major gold deposits.

Canadian Malartic is a low-grade bulk-tonnage deposit, which is located immediately south of the Larder Lake–Cadillac Fault Zone. It is hosted mainly by clastic metasedimentary rocks of the Pontiac Group, as well as by porphyritic quartz monzodiorite and granodiorite. Textural evidence and elemental mapping have revealed five types of pyrite. The pre-mineralization pyrite (py1) is likely diagenetic pyrite, with high Co, As, and Se, and low Ni, Te, Sb, Bi, and Pb. Gold-bearing pyrite 2, 3 and 4 (py2–py4) has covariant Co and Ni, high Au, Ag, Te, Bi, and Pb, and generally contains abundant potassic inclusions. Post-mineralization pyrite (py5) has high Co and Ni but is low in other metals. Pyrite from the ore zones distributed along the Sladen fault zone shows evidence of post-precipitation metal enrichment in fractures associated with Ca metasomatism. Though the elemental maps cannot unequivocally discriminate the deposit type, pyrite chemistry is consistent with a two-stage model comprising early syn-pyrite Au mineralization associated with potassium alteration and a later post-pyrite upgrading associated with Ca metasomatism.

The Côté Gold deposit is hosted by the Chester intrusive complex, a high-level, multi-phase synvolcanic intrusion composed of tonalite and diorite. Nickel, As, Sb, and Pb are generally relatively depleted in the cores and enriched in the rims of the pyrite grains, whereas Te and Ag are relatively enriched in the cores and depleted in the rims. Arsenopyrite grains have high Co, Ni, Se, Sb, and Te, but low Ag, Pb, and Bi. Gold is depleted both in pyrite and arsenopyrite, except locally in fractures, but is enriched in silicate minerals, possibly as nanoparticles, suggesting that gold mineralization is related to a hydrothermal event post-dating pyrite precipitation.

The Musselwhite deposit is a banded iron formation-hosted lode gold deposit in a sequence of volcanic and sedimentary rocks that include carbonaceous argillite locally hosting diagenetic pyrite nodules. Cobalt, Cu, Ni, Se, As, Ag, Sb, Te, Au, Tl, Pb, and Bi are enriched in the nodules but are depleted in recrystallized pyrite and pyrrhotite. Element and Pb-isotope maps are consistent with a model whereby at least some of the ore gold was derived from fluids that garnered Au liberated via metamorphic recrystallization of auriferous diagenetic pyrite and, probably, carbonaceous material in local argillite.

The elemental maps show that gold has multiple sources. The Musselwhite deposit provides evidence for local pyritic carbonaceous sedimentary rocks as one of the possible sources of Au. The Canadian Malartic and Côté deposits have a strong association with magmatic hydrothermal activity, although additional sources of Au may also have been important.

INTRODUCTION

Gold in ores may be visible or it may occur as so called "invisible gold" (Cook and Chryssoulis, 1990), either lattice-bound in sulphides or as nanoparticle inclusions (Deditius et al., 2011; Hough et al., 2011; Cook et al., 2013). Gold can partition into sulphide minerals during precipitation, or can be released from a sulphide lattice during later deformation, metamorphism, and recrystallization (Large et al., 2007, 2009). Cobalt and Ni can substitute for Fe in pyrite, whereas As, Se, and Te are likely to exchange with S in the pyrite lattice. Pyrite crystallized from fluids/melts with different Co, Ni, As,

Gao, J.-F., Jackson, S.E., Dubé, B., Kontak, D.J., and De Souza, S., 2015. Genesis of the Canadian Malartic, Côté Gold, and Musselwhite gold deposits: Insights from LA-ICP-MS element mapping of pyrite, *In:* Targeted Geoscience Initiative 4: Contributions to the Understanding of Precambrian Lode Gold Deposits and Implications for Exploration, (ed.) B. Dubé and P. Mercier-Langevin; Geological Survey of Canada, Open File 7852, p. 157–175.

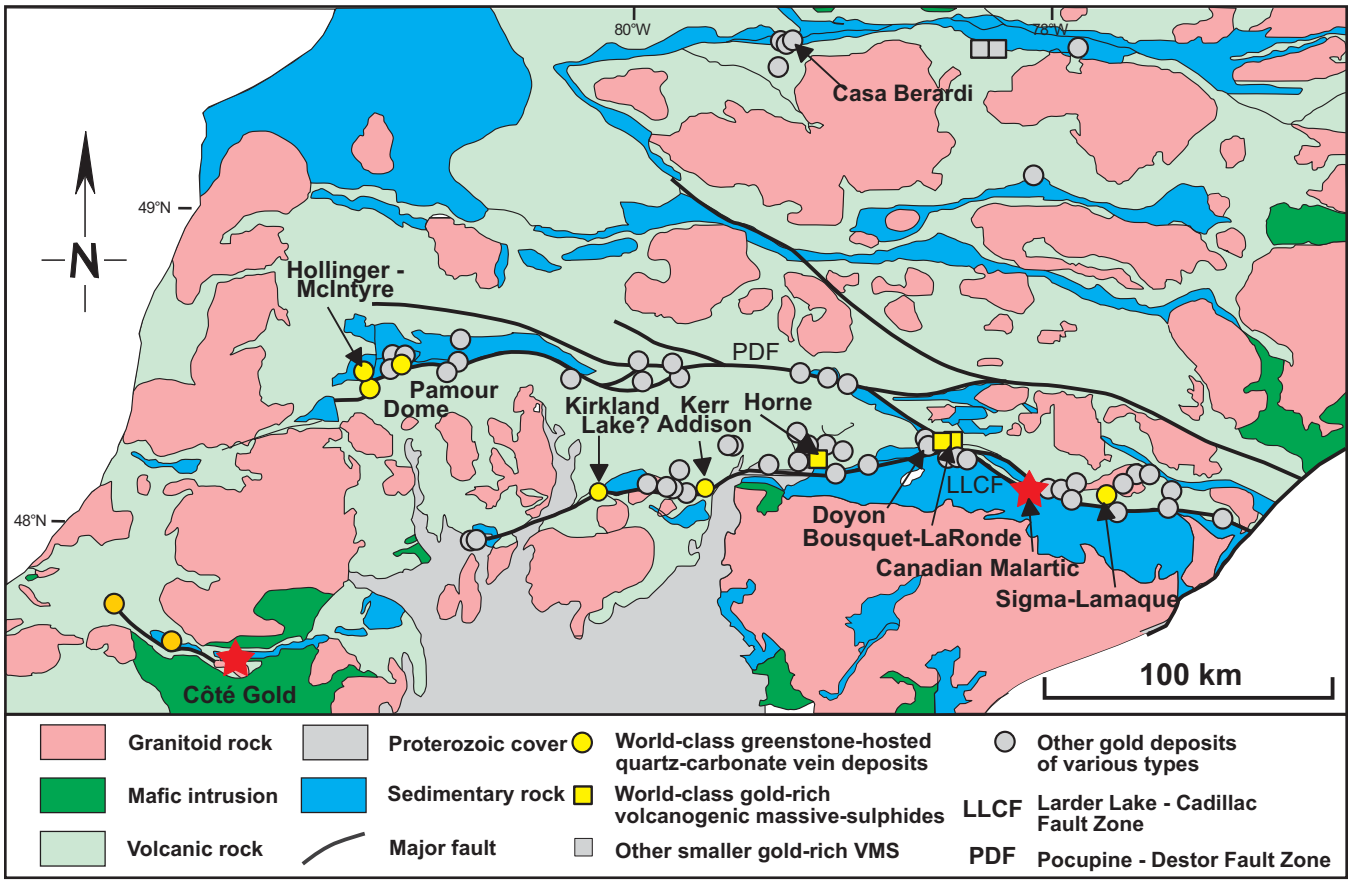

Figure 1. Simplified geological map of the Abitibi greenstone belt showing the distribution of major fault zones and gold deposits. Modified from Poulson et al. (2000) and Dubé and Gosselin (2007).

Se, and Te contents will contain different concentrations of these elements (Large et al., 2009; Koglin et al., 2010). Gold has similar geochemical characteristics to trace elements, such as Ag, As, Cu, Se, and Te, during pyrite precipitation but may show behaviour different to these elements during evolution of hydrothermal fluids (Chouinard et al., 2005; Large et al., 2009). In addition, previous studies on elemental distributions in pyrite have illustrated that it can contain highly variable contents of trace elements at the grain scale and that Au contents can correlate with different elements in different zones of a pyrite grain (Chouinard et al., 2005; Large et al., 2009; Deol et al., 2012; Agangi et al., 2013; Cook et al., 2013; Large et al., 2013). Thus, the textural and chemical differences among the pyrite grains have tremendous potential for providing information about the processes of gold mineralization (Koglin et al., 2010).

The Abitibi greenstone belt is a 750 km-long by 200 km-wide belt of metamorphosed volcanic, coeval subvolcanic, and intrusive rocks, locally derived clastic and chemical sedimentary rocks, and granitoid batholiths. It is the largest greenstone belt in the world and hosts world-class gold deposits of various styles, including greenstone-hosted quartz-carbonate Au vein, Au-rich VMS, syenite-associated disseminated gold, and intrusion-related deposits (Hodgson and McGeehan, 1982; Robert et al., 2005; Dubé and Gosselin, 2007, Dubé et al., 2007; Mercier-Langevin et al., 2007). Pyrite is the most common sulphide mineral in many of the gold ore assemblages. Due to different formation conditions in these various types of deposits, pyrite may have different morphologies and trace chemical compositions, which can record the paleofluid chemistry during its crystallization history.

In this study, we present new elemental maps of different types of pyrite from three gold deposits, including the intrusion-related stockwork-disseminated Canadian Malartic (Québec) and Côté Gold (Ontario) deposits located, respectively, in the Abitibi and Swayze greenstone belts, Abitibi Subprovince (Fig. 1), and the Musselwhite deposit (Ontario) of the North Caribou greenstone belt. Our aim is to combine these new data sets with detailed field mapping to help constrain the processes of gold mineralization in these deposits. This study demonstrates that quantitative elemental mapping of different generations of pyrite is a very powerful tool for interrogating minerals for the processes and physico-chemical evolution of their host hydrothermal systems and addressing the source(s) of

gold. This information can further our understanding of gold mineralizing processes and can be applied in gold exploration to vector toward potential ore zones.

RESULTS

Methodology

The application of LA-ICP-MS to 2-D trace element mapping of geological minerals has grown rapidly since its tremendous potential was first highlighted (Woodhead et al., 2007, 2008). However, because of calibration difficulties, most published examples have presented either signal intensity maps, or concentration maps of single mineral phases. For this study, 2-D element concentration maps of multi-phase mineral assemblages were required to allow quantitative interpretation of the distributions of Au and other elements. Additionally, because of the generally small grain size of hydrothermal minerals, methods were sought to improve the sampling resolution obtainable using the traditional line-scan sampling approach to LA-ICP-MS mapping (Woodhead et al., 2007, 2008), where constant sample stage translation and ablation aerosol mixing degrades resolution.

Firstly, the area mapped was sampled via thousands of discrete edge-to-edge square ablation spots. While collecting signal intensities for about 40 elements (typically, C, Na, Mg, Al, Si, P, S, K, Ca, Ti, V, Cr, Mn, Fe, Co, Ni, Cu, Zn, As, Se, Mo, Ag, Sb, Te, Ba, La, W, Au, Hg, Tl, Pb, Bi, U, plus about 5–7 of B, Ga, Sr, Zr, In, Sn, Cs, Ce, Nd, Sm, Gd, Yb, Lu, Th), each spot was in turn "pre-ablated" (3–5 laser pulses) to remove surface contaminants resulting from polishing and sample fallback from neighbouring spots. This material was flushed from the system (1.5 s) prior to ablation (2 s). The protocol was repeated until the entire selected area was sampled. The major advantage of this sampling protocol is that it produces true spot-size limited sampling resolution. It also removes surface contamination at each sampling site immediately prior to analysis.

To allow quantification of multi-phase mineral assemblages, standardization was achieved via external calibration against United States Geological Survey (USGS) synthetic basaltic glass reference material GSE-1G, coupled with ablation yield correction via normalization to 100% total element abundance (Halicz and Günther, 2004), performed on a spot-by-spot basis. To extend the calibration to S and C, which are not present in GSE-1G, surrogate calibration was applied using S/Fe and C/Ca sensitivity ratios determined by ablation of pure pyrrhotite and calcite, respectively. The methodology outlined above provides quantitative analysis without prior knowledge and input of internal standard element concentrations for each ablation spot and it is the most appropriate approach to calculating concentrations for spots that sample more than one mineral phase (e.g. small inclusions, grain boundaries). Lead isotope maps were also generated but in separate analytical sessions using a much reduced element list and calibration against GSE-1G.

Algorithms and software were developed to selectively integrate the ablation signals produced by each ablation spot and calculate concentrations via external standardization and internal normalization to 100%, including deconvolution calculations to determine, for each spot, O (and H) contents, which cannot be measured. The latter is complicated particularly by Fe, which may be present, in any ablation volume, as FeO and/or Fe_2O_3 and/or a Fe sulphide. The above was achieved by modification and full automation of in-house spreadsheet software, LAMTrace (Jackson, 2008) and its sister program, Convert (the latter subsequently rewritten as a VBA-driven Microsoft Excel® program). Another spreadsheet program (PixeLAte) was written to generate element concentration maps by displaying element concentrations for each spot as coloured pixels using a choice of colour schemes and scaling functions. A percentile scaling function is generally employed for displaying maps of low-abundance elements because it most effectively highlights subtle concentration differences. A logarithmic scaling function is generally employed for displaying more homogeneously distributed elements (e.g. major elements). A function was written that allows users to interrogate selected areas of the maps for statistical calculations of the values in the area selected (i.e. n, mean, median, standard deviation, standard error, relative standard deviation and relative standard error).

Canadian Malartic

The Canadian Malartic gold deposit, Val d'Or, Québec, is mainly hosted (~75%) in altered clastic (turbiditic) metasedimentary rocks of the Pontiac Group and in subalkaline porphyritic quartz monzodiorite and granodiorite located immediately south of the Larder Lake–Cadillac Fault Zone (De Souza et al., 2015, in press). Mineralization also occurs in dykes and sills of various compositions, but porphyritic quartz monzodiorite represents the main mineralized intrusive phase. The rocks have been deformed and metamorphosed to upper greenschist facies. Mineralization is distributed according to two main trends, forming east-west and northwest-southeast-trending ore zones (De Souza et al., 2015, in press). At the surface, the dominant east-west trend coincides with the position of the Sladen Fault and gold is hosted by quartz monzodiorite and by metasedimentary rocks along and adjacent to the fault zone. The surface trace of the northwest-southeast mineralized trend is subparallel to the S_2 cleavage, which is axial planar to F_2 folds. Though the Canadian

Malartic deposit shows some features suggestive of an intrusion-related deposit, including disseminated and stockwork mineralization associated with potassic alteration, the gold mineralization and its distribution are largely controlled by D_2 deformation structures, including faults, shear- and high-strain zones developed in the hinge zone of F_2 folds, and by the Sladen Fault. Some of the highest grade mineralization occurs along the Sladen Fault, which cuts the quartz monzodiorite and represents the main gold-bearing structure that was mined during the historical production at the Canadian Malartic, Sladen, and East Malartic mines (De Souza et al., 2015). The aim of this study is to determine whether element mapping of pyrite can shed any light on the origin(s) of the gold at Canadian Malartic.

Based on morphological and textural features, pyrite in the Canadian Malartic gold deposit can be subdivided into five types, which we refer to as py1 to py5. Element distributions in different types of pyrite are shown in Figures 2 to 5. Pyrite py1 is porous and has high Co, As, Se, but low Ni, Te, Sb, and Au concentrations and dominantly Ca-bearing inclusions. Pyrite py2, having sharp boundary with py1, features concentrically zoned, relatively K-rich inclusion trails and has similar Co contents as py1, but shows significant enrichment of Ni, Te, Sb Pb, and Au, and low As and Se contents (Fig. 2). Pyrite py3, containing abundant fine-grained inclusions, has transitional contacts with py1 and is characterized by relatively high Ag, Sb, Pb, and Au contents, low As, Co, and Ni contents, and is locally enriched in Cu (Fig. 3). It is noted that Zn, Mo, Tl, Ag, and Au, together with B, K_2O and SiO_2, are concentrated at the rim of some py3 grains. Pyrite py4 is characterized by large inclusions, again dominantly K-rich, and variable Co-Ni-Zn-Sb-Pb-Bi enrichment in the cores and depletion in the rims (Fig. 4). Py4 grains have relatively uniform As (~10 ppm), Se (~5 ppm), Te (~40 ppm), Mo (<0.1 ppm), and Tl (<0.1 ppm) concentrations and relatively high but variable Ag (~10 ppm) and Au (~2 ppm) concentrations. Pyrite py5, which occurs as inclusion-free rims to py1–py4, generally has high Co, Ni, and Se, and low As, Te, and Sb content. In general, it is extremely depleted in Cu, Au, Tl, Pb, and Bi (Figs. 3–5).

Pyrite from the Sladen zone (Fig. 5) shows late, post-pyrite-deposition fracturing. The fractures show enhanced concentrations of As, Mo, Ag, Sb, Te, Au, Pb, and Bi, accompanied by significant Ca- but not K-enrichment.

Côté Gold

The Côté Gold deposit, located in the Chester and Neville townships, occurs within the Swayze greenstone belt, to the southwest of the Abitibi greenstone belt. The Swayze belt contains a diversity of extrusive and intrusive igneous rock types, ranging in composition from ultramafic to felsic, as well as both chemical and clastic sedimentary rocks. These rocks underwent a complex and protracted history of metamorphism, folding, and development of ductile high-strain zones and late brittle faulting (Heather and van Breemen, 1994; Heather et al., 1996; Heather and Shore 1999a,b; Heather, 2001).

The Côté Gold deposit is hosted by the Chester intrusive complex (CIC), a high-level, multi-phase syn-volcanic intrusion composed of tonalite and diorite, and consists of low- to moderate-grade Au±Cu mineralization (Katz et al., 2015). The mineralized system is centred on a magmatic-hydrothermal breccia body overprinted by several alteration types (biotite, sericite, silica-sodic) (Katz et al., 2015). The overlap of Re-Os dates on syn-gold-deposition molybdenite with the age of the CIC, combined with stable isotopic data (S, O) and field relationships suggest that the deposit is a ca. 2,740 Ma intrusion-related Au(±Cu) deposit (Kontak et al., 2013; Katz et al., 2015). The aim of this study is to determine whether element mapping of pyrite could add new information about the origin(s) of the Côté Gold deposit.

Elemental maps of pyrite from the Côté Gold deposit (n=4) are presented in Figure 6. The study reveals that pyrite from the deposit is characterized by relatively homogeneous Co (>150 ppm), Se (>15 ppm), and Bi (>2 ppm) contents, but highly variable Ni, As, Sb, Te, and Ag contents. The arsenopyrite grain has a relatively homogeneous composition with high Co (>400 ppm), Ni (>200 ppm), Se (>20 ppm), Sb (>8 ppm), and Te (>1 ppm) but low Ag (<0.1 ppm), Au (<0.1 ppm), Pb (<2 ppm) and Bi (<0.3 ppm). Silver and Bi show slight enrichment in the rim of the arsenopyrite grain. Notably, Ag and Au content is extremely poor in pyrite and arsenopyrite grains (<0.1 ppm and <0.14 ppm, respectively), except locally in fractures. However, in three of the four samples mapped, gold is variably enriched (mostly >0.5 ppm) in silicate minerals (biotite, chlorite, and quartz).

Musselwhite

The Musselwhite gold deposit is located within the North Caribou Greenstone Belt of northwestern Ontario. The stratigraphy in the immediate vicinity of the mine is dominated by mafic and ultramafic volcanic rocks, banded iron formation, felsic volcanic rocks, siliciclastic sedimentary rocks (Biczok et al., 2012; Oswald et al., 2015), and local argillaceous units bearing diagenetic pyrite nodules that range up to >1 cm in diameter. All units in the immediate mine area have been deformed and metamorphosed at amphibolite facies. The bulk of the Au at Musselwhite is hosted

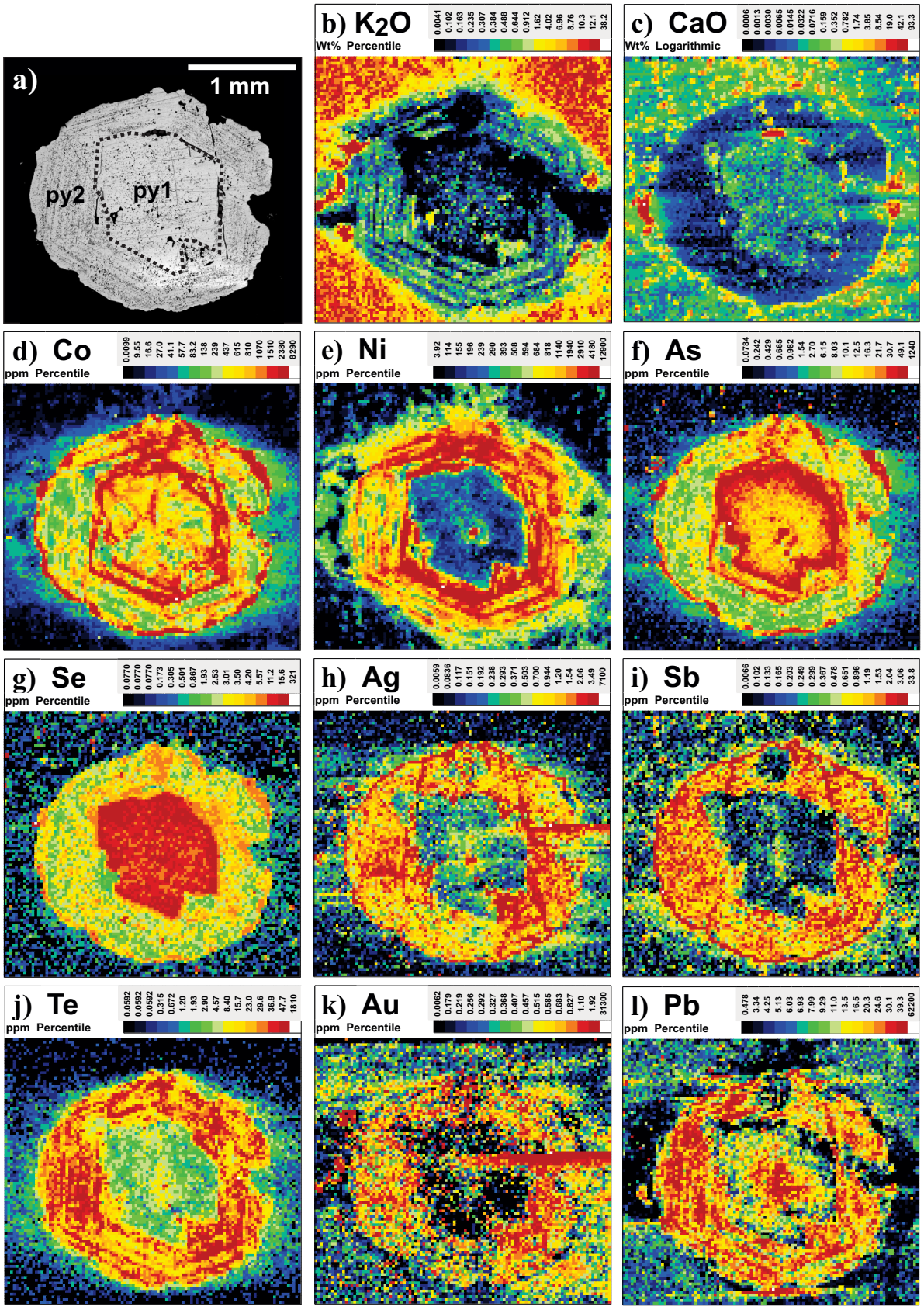

Figure 2. Photomicrograph and element concentration maps for pyrite from gold ore (sample CM7) in altered Pontiac sedimentary rocks from the A zone of the Canadian Malartic gold deposit. Scales are in ppm, with the exception of K_2O and CaO, which are in weight percent. The mapped pyrite is composed of py1 and py2. Note the calcic composition of the inclusions in py1 and the relatively potassic composition in py2.

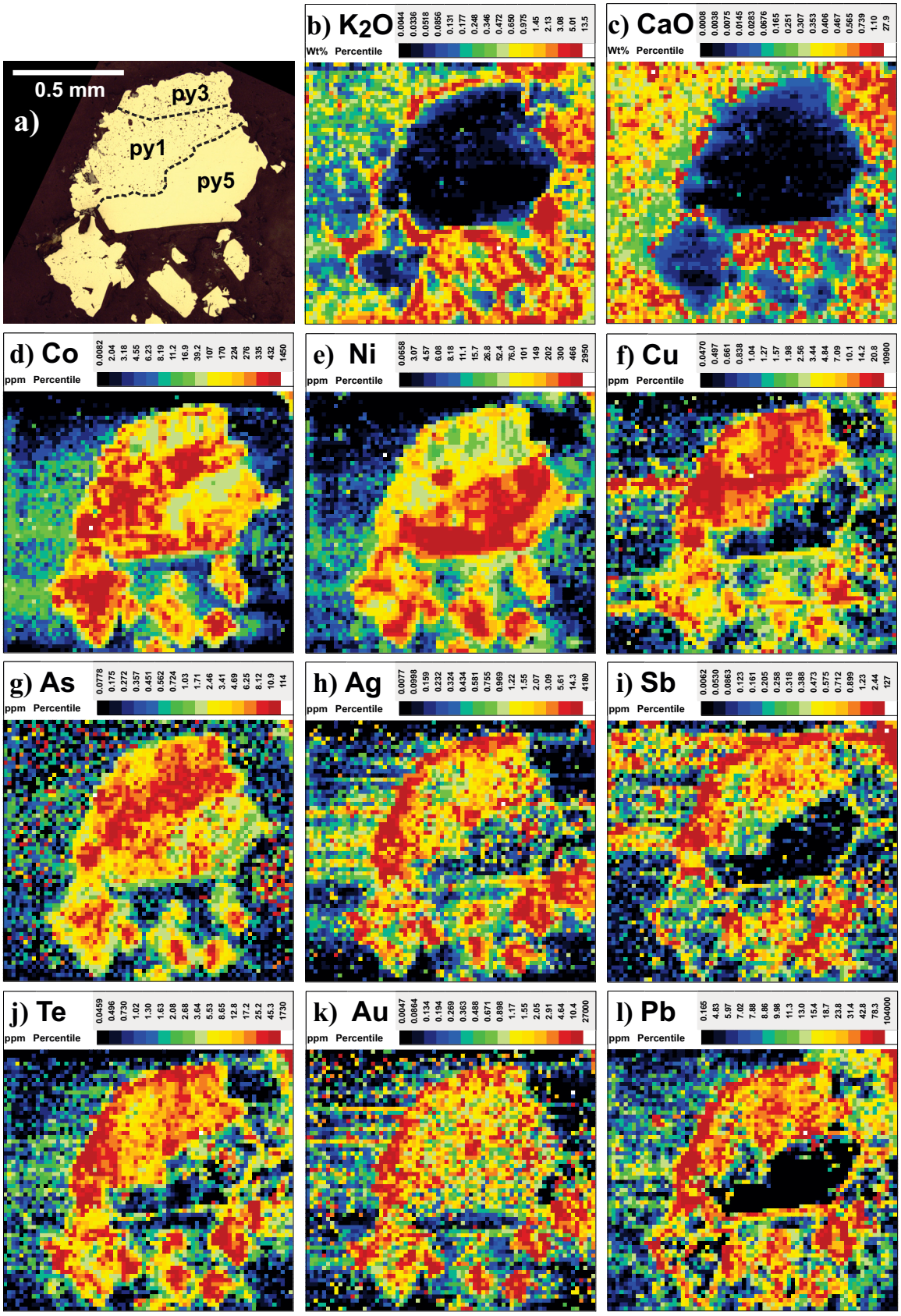

Figure 3. Photomicrograph and element concentration maps for pyrite from gold ore (sample CM6) in altered Pontiac sedimentary rocks from the A zone of the Canadian Malartic gold deposit. Scales are in ppm, with the exception of K_2O and CaO, which are in weight percent. The mapped pyrite consists of py1, py3, and py5.

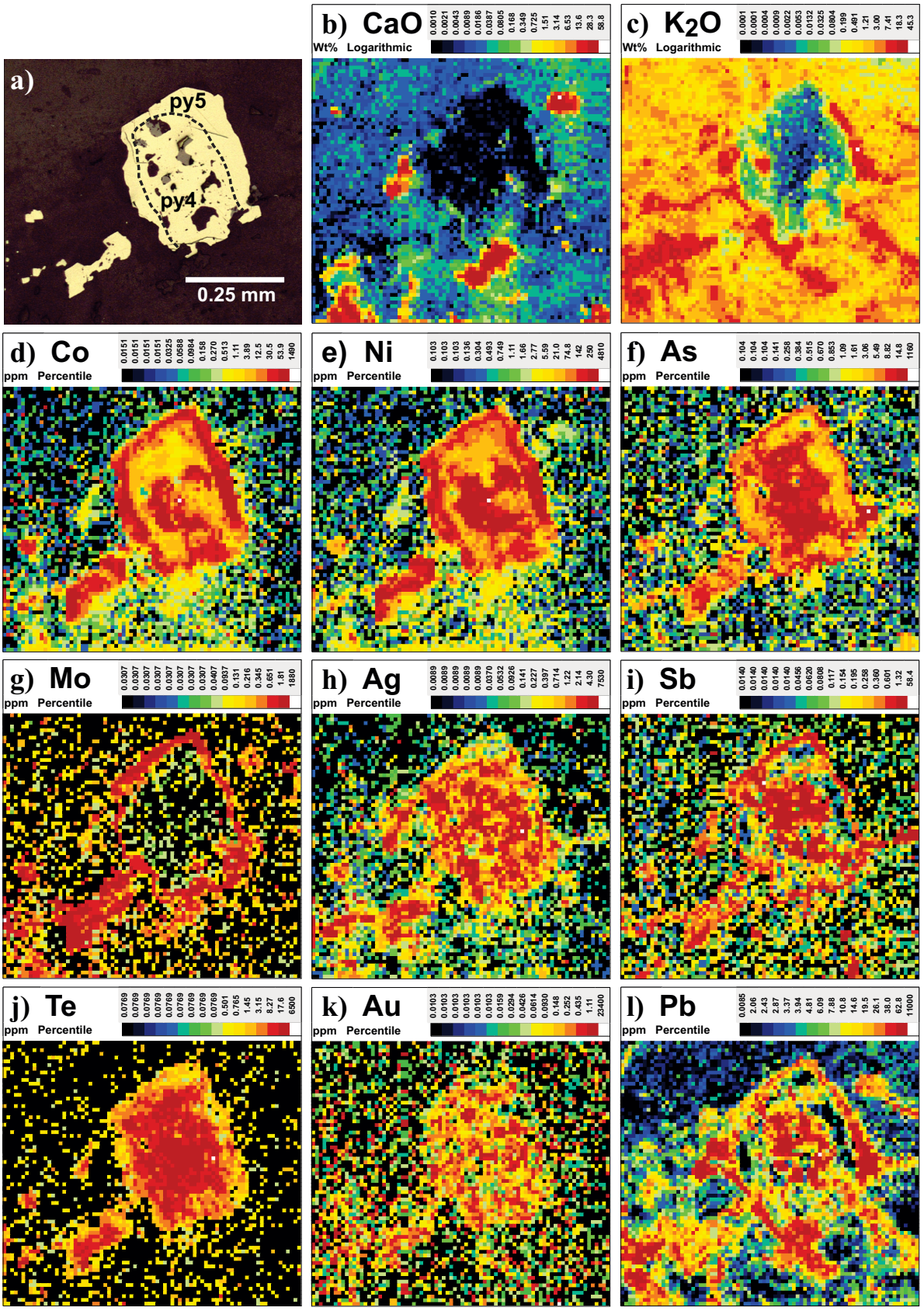

Figure 4. Photomicrograph and element concentration maps for pyrite from gold ore (sample CM17) in porphyry rocks of the Sladen zone, Canadian Malartic gold deposit. Scales are in ppm with the exception of K_2O and CaO, which are in weight percent. The mapped pyrite consists of py4 and py5. Note the potassic composition of the large inclusions in py4 and the matrix.

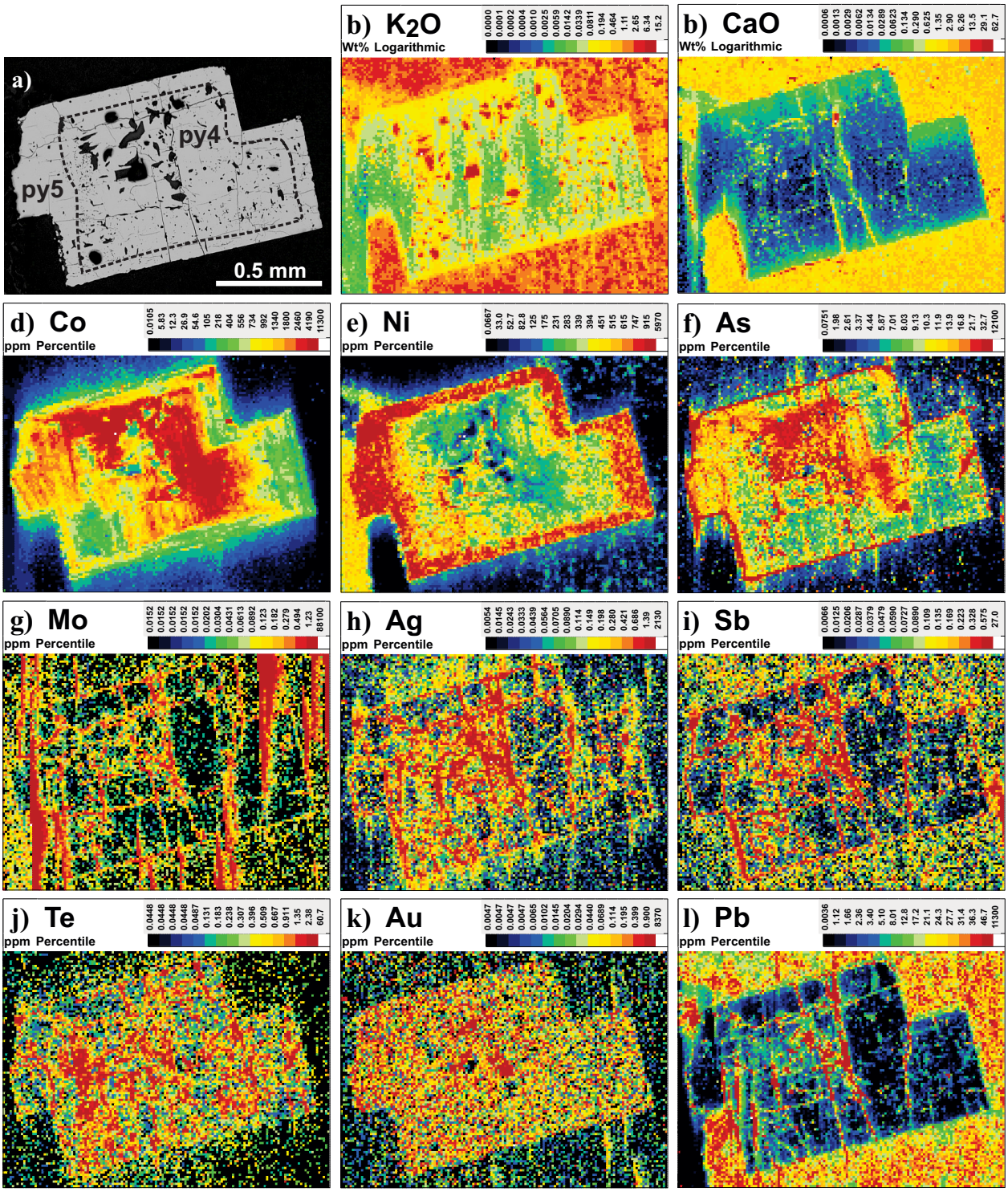

Figure 5. Photomicrograph and element concentration maps for pyrite from gold ore (sample CM25) in altered Pontiac sedimentary rocks from the Sladen zone, Canadian Malartic gold deposit. Scales are in ppm, with the exception of K_2O and CaO, which are in weight percent. The mapped pyrite shows late fracturing with metal and Ca enrichments along fractures, perhaps representing post-magmatic, structurally related hydrothermal overprinting.

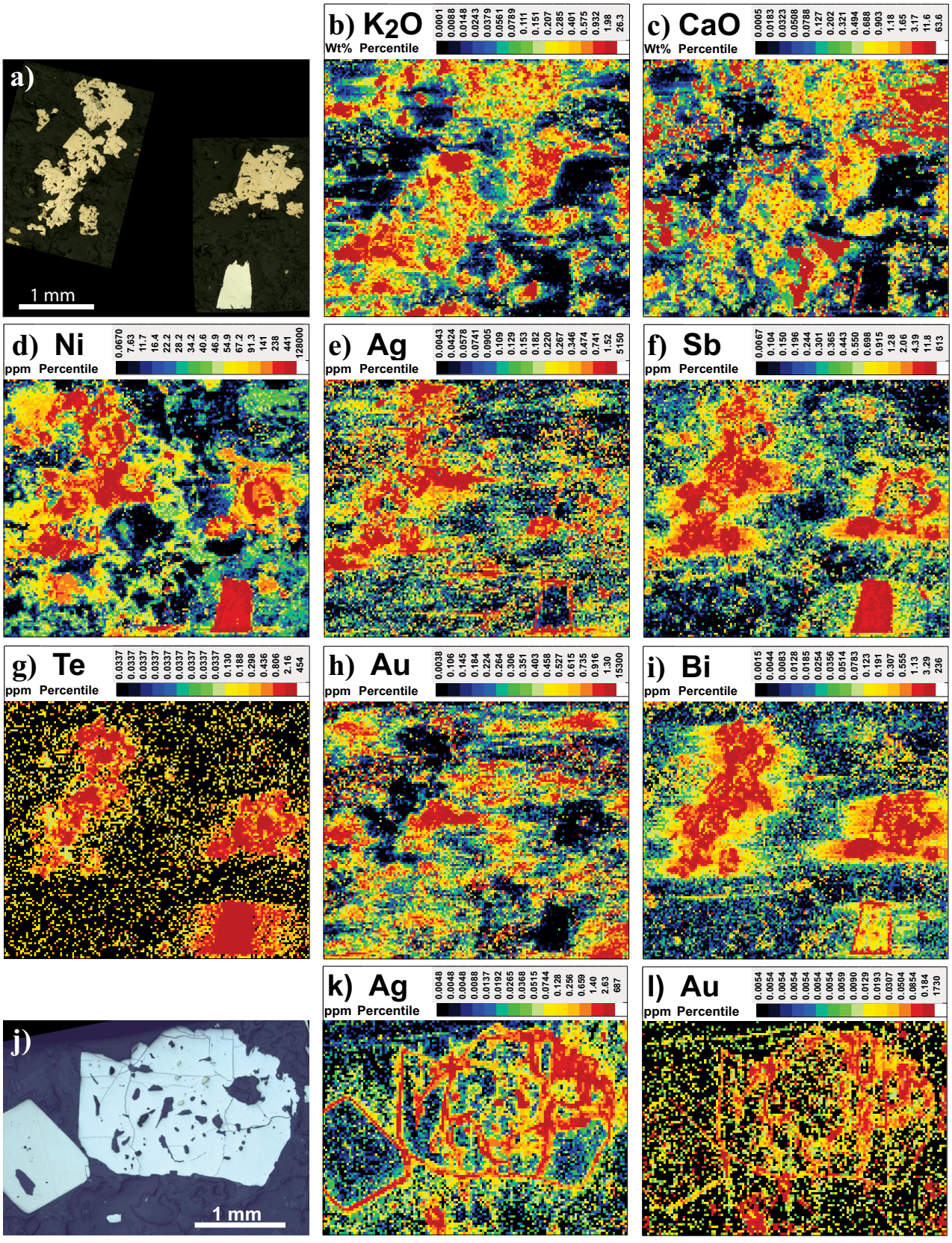

Figure 6. Photomicrograph and element concentration maps for two pyrite samples, CL13 (a-i) and CL10 (j-l) from the Côté Gold deposit. The sulphides in sample CL13 are pyrite (beige) and arsenopyrite (white). The sulphide in sample CL10 is pyrite. Scales are in ppm, with the exception of K_2O and CaO, which are in weight percent. Elemental maps show that gold is depleted in pyrite and arsenopyrite, but locally enriched in silicate minerals (quartz, biotite, and chlorite). In sample CL10, gold and other metals are locally enriched in fractures in pyrite, indicating late introduction or remobilization.

in silicate-rich banded iron formation and occurs in association with stratabound pyrrhotite replacements and silica flooding, with local discordant quartz± pyrrhotite veins. The ore zones are associated with D_2 high-strain zones that are preferentially developed along hinges and strongly attenuated fold limbs of tight F_2 folds (e.g. Biczok et al., 2012; Oswald et al., 2014, 2015).

This study focussed particularly on mapping diagenetic pyrite nodules in argillaceous sedimentary rocks from the mine area. The nodules range from millimetre to centimetre in size and frequently show concentric zoning that is accentuated locally by inclusions. The nodules show variable degrees of recrystallization to pyrrhotite and inclusion-free subhedral-euhedral pyrite, mostly at their margins but also as patches within the nodules. These features are interpreted to be the products of nodule recrystallization during metamorphism.

LA-ICP-MS element maps of selected elements in the nodules and secondary pyrrhotite and pyrite are presented in Figures 7 and 8. Element maps reveal significant enrichment of Co, Ni, As, Se, Ag, Sb, Te, Au, Tl, Pb, and Bi in the pyrite nodules. All elements show flattened concentric zoning, indicative of syngenetic metal incorporation. The zoning is often truncated by recrystallized pyrite and pyrrhotite. Gold values typically range between 20 and 50 ppb but are locally up to >1 ppm in Au-rich growth zones in the nodules. Also notable is that patches of the dark carbonaceous alumino-silicate-rich sediment matrix contain spotty Au enrichment at concentrations frequently >2 ppm. Indeed, the average Au content of the non-sulphide material in Figure 7 is ~1 ppm.

Gold and most metals (Sb, Te, Ag, Pb, Bi) are strongly depleted in recrystallized pyrrhotite and pyrite. Arsenic is variably enriched in recrystallized pyrite and Se and Ni are enriched in pyrrhotite (>200 ppm) but depleted in recrystallized pyrite (mostly <20 ppm).

Element maps of Musselwhite ore samples (Fig. 8) show that Au occurs largely in quartz and in microfractures in pyrrhotite, and, to a lesser degree, in fractures in garnet (Moran, 2008; Kolb, 2011; Biczok et al., 2012).

In an effort to determine the relationship, if any, between the metals concentrated in diagenetic sulphide nodules and Musselwhite ore, Pb-isotope ratios, $^{207}Pb/^{206}Pb$ and $^{208}Pb/^{206}Pb$, were mapped in a Musselwhite diagenetic pyrite nodule and a small area of relatively Pb-rich ore (Fig. 8). Mean Pb-isotope ratios for areas of representative values within the nodule and ore samples are indistinguishable within the uncertainty of the measurements.

DISCUSSION

Occurrence of Gold

Pyrite (and arsenopyrite) is one of the most common sulphide minerals associated with gold-ore assemblages, in which gold commonly occurs as sulphide lattice-bound gold or nanoparticle inclusions (Deditius et al., 2011; Hough et al., 2011; Cook et al., 2013). Auriferous pyrite at Canadian Malartic and auriferous nodular sedimentary pyrite at Musselwhite, although of different origin, have relatively uniform gold distribution, suggesting that Au partitions into the sulphide as lattice-bound Au. Almost all pyrite grains from the Côté Gold deposit are depleted in Au, but silicate minerals (quartz, biotite, chlorite) are locally enriched in Au (>0.5 ppm) with a spotty distribution, which suggests that Au occurs as nanoparticles in these minerals. This unusual occurrence of Au warrants further investigation (e.g. high-resolution TEM studies) to better characterize its localization in the silicate minerals. Similar spotty Au enrichment in carbonaceous material at Musselwhite suggests a nanoparticulate mode for some of this Au. Gold in the Musselwhite ores occurs largely in quartz and in association with pyrrhotite and garnet, although it appears largely as enrichments along micro-fractures.

In summary, LA-ICP-MS mapping has revealed that Au in the three deposits studied occurs either visibly in quartz, as lattice-bound Au in pyrite, as fracture-bound in pyrrhotite and garnet, and as nanoparticle inclusions in silicate minerals and carbonaceous sediments.

Evolution of the Hydrothermal Systems

Most gold mineralization-related elements, including Cu, Zn As, Ag, Sb, Te, W, Hg, Pb, and Bi, partition into pyrite. Thus, the distribution of elements in pyrite provides a record of the evolving composition and physico-chemistry of the hydrothermal fluids, which are very important for understanding the processes involved in the formation of the deposit and, as such, help define geological and exploration models. However, although elemental distributions within pyrite show significant potential for better understanding and perhaps isolating chemical trends that are prerequisite for gold mineralization, the behaviours of elements during pyrite crystallization (and recrystallization) are still poorly known due to the lack of supporting experimental data. For example, Ni and Co frequently show dramatic variations in concentrations during pyrite growth, the significance of which is largely unknown. The following interpretations are thus of an empirical nature based on our observations.

At the Canadian Malartic deposit, textural and quantitative elemental mapping has revealed five morphological and chemically distinct types of pyrite, which

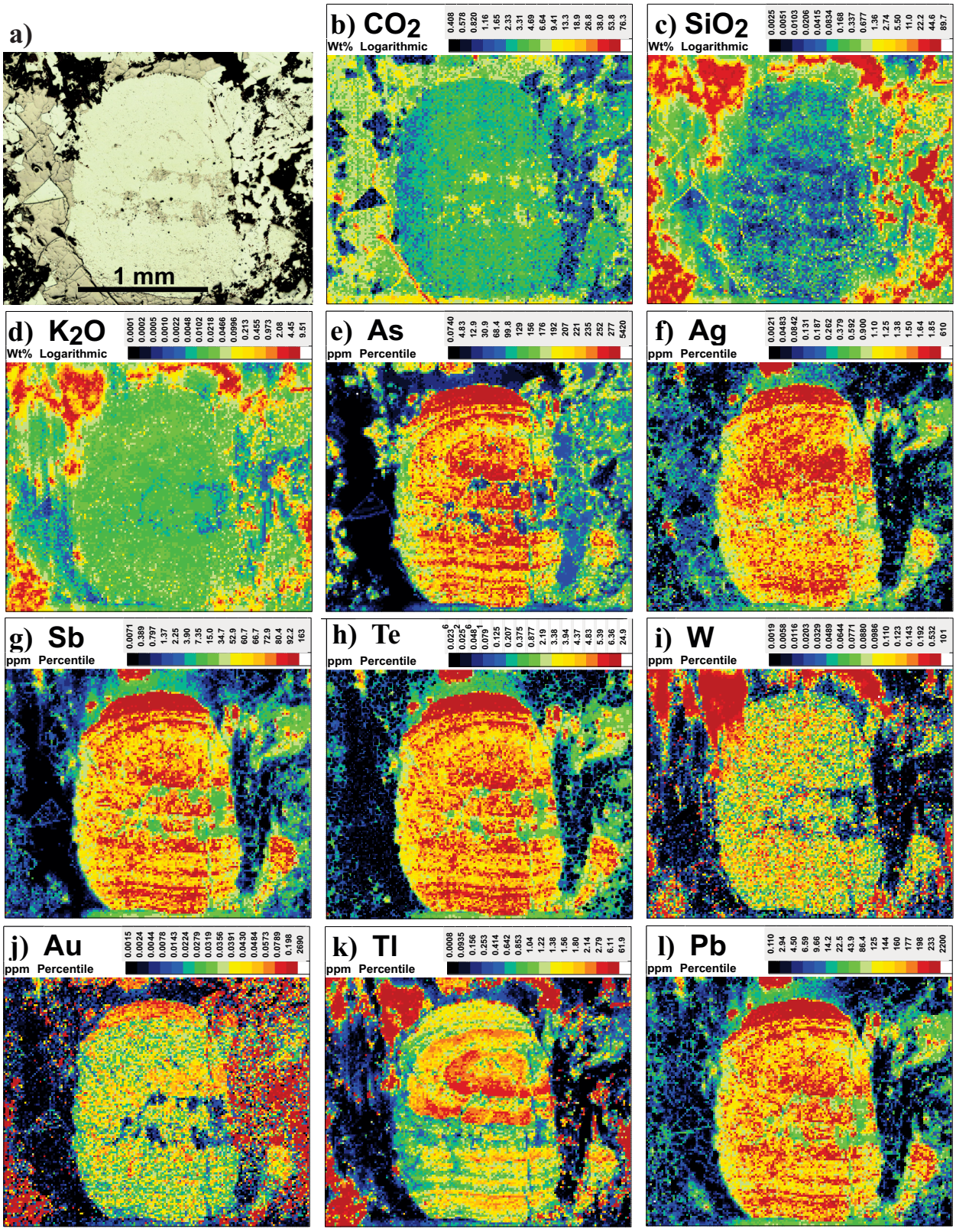

Figure 7. Photomicrograph and element concentration maps for a diagenetic pyrite nodule from sedimentary rocks in the vicinity of the Musselwhite deposit. Scales are in ppm, with the exception of K_2O and CaO, which are in weight percent. The element maps reveal concentric enrichment of metals in the nodule. Zoning is truncated by recrystallized pyrite (white, crystalline) and pyrrhotite (pink-brown) around and within the nodule. Also notable are patches of the dark carbonaceous alumino-silicate-rich sediment matrix that contain spotty Au enrichment in concentrations that are frequently >2 ppm. Gold and most metals (Ag, Sb, Te, Pb, Bi) are strongly depleted in recrystallized pyrrhotite and pyrite. A narrow vein in the pyrite nodule provides evidence for generation of an auriferous fluid during internal recrystallization of pyrite to pyrrhotite.

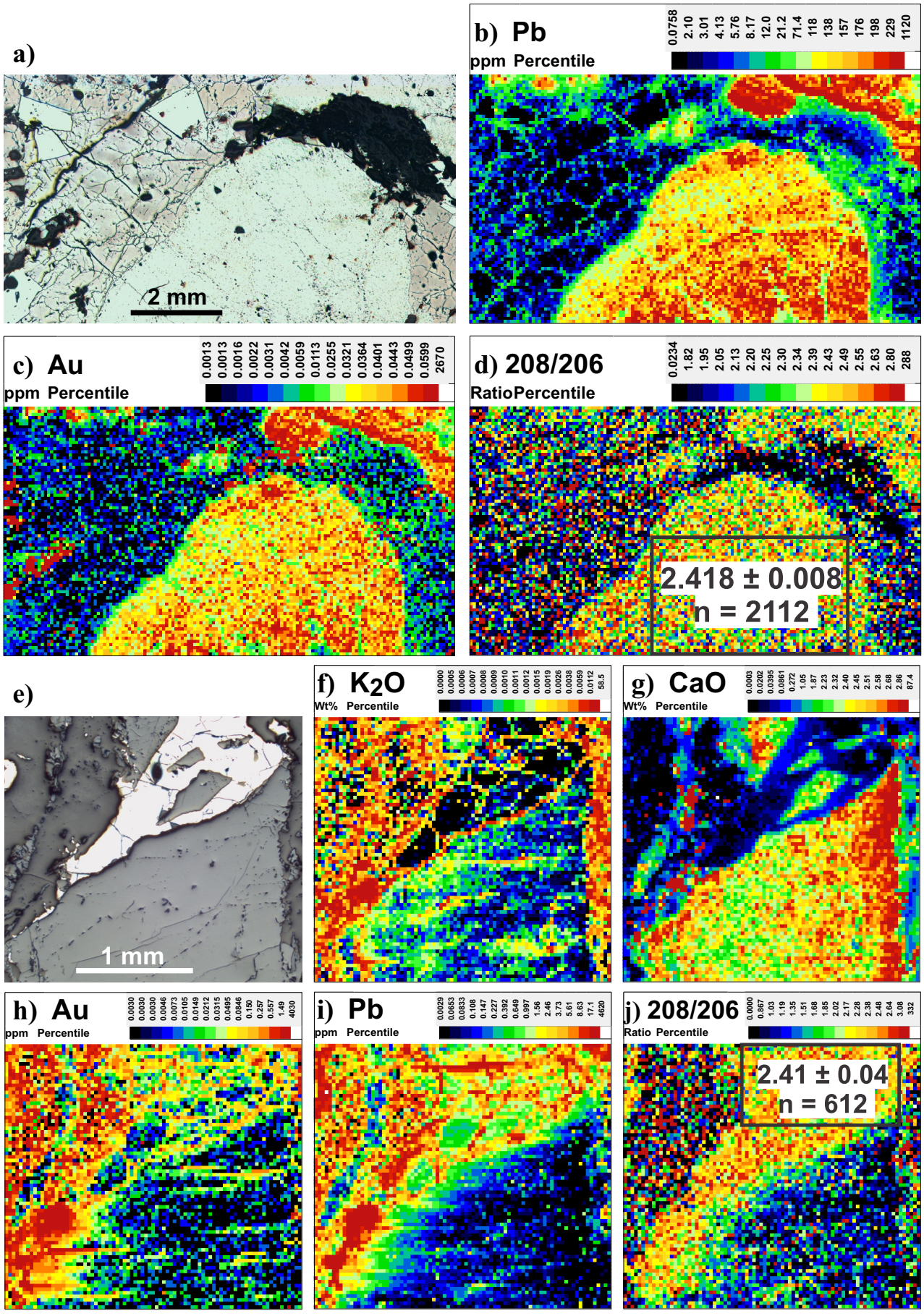
a)
2 mm
b) Pb
ppm Percentile
0.0758 2.10 3.01 4.13 5.76 8.17 12.0 21.2 71.4 118 138 157 176 198 229 1120
c) Au
ppm Percentile
0.0013 0.0013 0.0016 0.0022 0.0031 0.0042 0.0059 0.0113 0.0255 0.0321 0.0364 0.0401 0.0443 0.0499 0.0599 2670
d) 208/206
RatioPercentile
0.0234 1.82 1.95 2.05 2.13 2.20 2.25 2.30 2.34 2.39 2.43 2.49 2.55 2.63 2.80 288
2.418 ± 0.008
n = 2112
e)
1 mm
f) K2O
Wt% Percentile
0.0000 0.0005 0.0006 0.0007 0.0008 0.0009 0.0010 0.0011 0.0012 0.0015 0.0019 0.0026 0.0038 0.0059 0.0112 58.5
g) CaO
Wt% Percentile
0.0003 0.0202 0.0395 0.0861 0.272 1.05 1.87 2.23 2.32 2.40 2.45 2.51 2.58 2.68 2.86 87.4
h) Au
ppm Percentile
0.0030 0.0030 0.0030 0.0046 0.0073 0.0105 0.0149 0.0212 0.0315 0.0495 0.0846 0.150 0.257 0.557 1.49 4030
i) Pb
ppm Percentile
0.0029 0.0053 0.0833 0.108 0.147 0.227 0.392 0.649 0.997 1.56 2.46 3.73 5.61 8.63 17.1 4620
j) 208/206
Ratio Percentile
0.0000 0.867 1.03 1.19 1.35 1.51 1.68 1.85 2.02 2.17 2.28 2.38 2.48 2.64 3.08 332
2.41 ± 0.04
n = 612

are interpreted as related to three main stages of growth: (1) porous pyrite (py1), likely diagenetic pyrite, formed pre-mineralization; (2) Au-rich pyrite (py2–py4) crystallized during gold precipitation; each is enriched in Ag, Te, Au, Pb, and Bi and, in the latter part of this gold mineralization stage (py3, py4), Mo. Py3 and py4 are locally enclosed by, and/or contain inclusions of, K-rich silicate(s), suggesting that both precipitated from a K-rich fluid. This is consistent with, though not unequivocal evidence of, an intrusion-related magmatic-hydrothermal origin. After pyrite precipitation, there is evidence in the Sladen Fault zone for a post-pyrite fracture-related enrichment process associated with Ca-rich metasomatism, which may represent a syndeformational hydrothermal overprint.

Pyrite and arsenopyrite from the Côté Gold deposit are extremely depleted in Au; the Au enrichment occurs largely in hydrothermal silicate minerals (quartz, biotite, and chlorite) as possible nanoparticles of Au. Gold is also locally enriched in fractures cutting pyrite. These features suggest that gold mineralization in the breccia zone at the contact of tonalite and diorite mostly postdates pyrite crystallization, arguing for a relatively «late» introduction of Au. Later stage quartz-carbonate-pyrite veins in the deposit also often contain visible gold and have a high Au grade. However, the close spatial and temporal overlap of magmatic and hydrothermal events at Côté Gold argue strongly for a ca. 2,740 Ma magmatic-hydrothermal origin for the gold mineralization (Kontak et al., 2013; Katz et al., 2015). Based on these observations, it is suggested that gold mineralization at Côté Gold was the product of auriferous hydrothermal fluids released late in the evolution of the magmatic-hydrothermal system.

Element mapping of pyrite nodules in carbonaceous argillite at Musselwhite provide striking evidence for generation of Au-rich fluids during recrystallization and with similar element enrichments and Pb isotopic composition to the ore. This is discussed below.

Source of Gold

Archean greenstone-hosted orogenic gold deposits constitute one of the most important types of gold deposit; however, their origin and in particular, the source of gold remains controversial (e.g. Goldfarb et al., 2005). Most models for orogenic gold deposits propose a deep source for the Au; for example, the mantle, deep magmas, or deep crust. In the latter case, auriferous fluid was generated during prograde amphibolite- or granulite-facies metamorphism of subducted volcano-sedimentary terranes during accretionary or collisional tectonics (Kerrich et al., 2000; Goldfarb et al., 2005; Dubé and Gosselin, 2007). Recently, however, increasingly compelling evidence has been presented that gold in at least some orogenic, metasedimentary rock-hosted deposits is derived more locally from organic- and pyrite-rich shale in the host sedimentary basin during progressive diagenesis and metamorphism. Particularly, strong support has been provided by detailed LA-ICP-MS and fluid inclusion studies on a number of deposits (Large et al., 2007, 2009, 2011; Meffre et al., 2008; Thomas et al., 2011; Gaboury, 2013; Steadman et al., 2013, 2014; Bull and Large, 2014). These studies support a two-stage model for generation of some orogenic gold deposits: (1) Au, As, and other metals are introduced early into black shale and turbidite basins and are concentrated into early diagenetic arsenian pyrite; (2) during diagenesis and early metamorphism, the diagenetic pyrite is recrystallized to form coarser grained pyrite. Under higher grade metamorphism (lower greenschist facies and above) the arsenian pyrite is converted to pyrrhotite. These processes release Au, As, S, and other elements into a fluid phase, which is channelled into structural sites, such as shear zones and fold hinges, within or above the black shale sequence and precipitated by chemical reaction with reactive host rocks. Large et al. (2011) proposed that argillite beds with invisible Au contents of greater than 250 ppb in diagenetic pyrite were potential source rocks for economic gold deposits.

The sedimentary country rocks in the Musselwhite deposit area contain auriferous diagenetic pyrite. The following assesses the evidence that element mapping can provide answers as to whether these sedimentary units are one potential source of Au in these deposits. Three questions are addressed:

1. Is there evidence of auriferous diagenetic sulphides undergoing recrystallization and Au loss? The striking diagenetic pyrite nodules and carbonaceous lenses in argillite from Musselwhite locally contain >1 ppm Au, together with elevated concentrations of As, Mo, Ag, Sb, Te, W, Tl, Pb, and Bi. The con-

Figure 8 (opposite page). Photomicrographs and element concentration and Pb-isotope maps of a pyrite nodule and Pb-rich Au ore, Musselwhite deposit. **a)** Reflected light photomicrograph of a pyrite nodule in recrystallized sulphides, pyrrhotite (pink brown) and pyrite (white). **b, c)** Pb and Au concentration maps. **d)** $^{208}Pb/^{206}Pb$ map with mean ± uncertainty (2 S.E.) for rectangular area shown. **e)** Reflected light photomicrograph of gold ore showing quartz (darker grey), garnet (lighter grey), and pyrrhotite (white). **f–i)** K_2O, CaO, Au, and Pb concentration maps. **j)** $^{208}Pb/^{206}Pb$ map with mean ± uncertainty (2 S.E.) for rectangular area shown. Concentration scales are in ppm, with the exception of K_2O and CaO, which are in weight percent. Note that Pb and Au in the ore are concentrated largely in quartz and within fractures in pyrrhotite, suggesting likely co-precipitation. The mean Pb isotope value of the highlighted rectangular area of pyrrhotite (8f), chosen for its relatively consistent values, agrees within uncertainty with the pyrite nodule value (8d).

centric zonation of metal enrichments in the nodules is consistent with a syngenetic origin of metal concentration. By contrast, recrystallized pyrite and pyrrhotite are depleted in these elements. This is strikingly displayed in Figure 7, which shows a zone of incipient pyrrhotite recrystallization within a diagenetic pyrite nodule. The recrystallized zone is depleted in all metals, and even K, relative to the nodule, with the exception of Ni and Se, which are strongly sequestered by pyrrhotite. A narrow fracture through the nodule shows Au depletion (a gold-poor fluid entering the nodule?) to one side of the pyrrhotite and Au enrichment on the other side (a Au-rich fluid exiting the nodule?). This map provides strong evidence of Au and other metal remobilization and entrainment in a fluid during sulphide recrystallization.

Importantly, there are also spotty but strong enrichments of Au in the carbonaceous sedimentary matrix to the nodule. In fact, the matrix to the nodule has a mean Au content greater than 10 times the Au content of the nodule. Only Mo and W are similarly concentrated. The source and timing of introduction of this Au in the matrix are unclear but it appears to be Au sequestered by organic material. The carbon-associated gold greatly increases the potential of this rock to have been a Au source rock.

2. Is there evidence to link the metals in the diagenetic sulphides to the Au in the deposits? Figure 8 shows that Pb-isotope values for a nodule (100s ppm Pb) and Pb-rich (10s ppm) gold ore are indistinguishable within the uncertainties of the analyses. The close spatial relationship of Pb and Au enrichment in the ore clearly supports co-precipitation of the metals. This information is consistent with Musselwhite Pb, and by inference, at least some of the Au, being derived from the pyritic carbonaceous sedimentary rocks.
3. Is there sufficient pyritiferous carbonaceous argillite in the sedimentary basin at Musselwhite to provide the gold in the deposit? Pyritiferous shale units are a much richer potential source of Au than typical greenstones and porphyries. Our calculations show that a fluid extracting Au, with an efficiency of 50%, from as little as ~0.5 km^3 of argillite containing 0.1 ppm Au (e.g. a 5 km square layer(s) of argillite totalling 60 m thick) could have provided all of the ~6 Moz of Au at Musselwhite. The exposed thickness of pyritiferous argillite at Musselwhite totals only a few metres (Oswald et al., 2015). However, if additional layers exist at depth, they could potentially have made a significant contribution to the Au contained in the Musselwhite deposit.

Pre-mineralization pyrite at Canadian Malartic is poor in Au (~0.1 ppm) and is not likely to have been an important source for gold. Some Au-enriched pyrite at Canadian Malartic (py3 and py4) is associated with potassic alteration and elevated levels of Mo, consistent with deposition in a magmatic-hydrothermal system. Similarly, the Côté Gold deposit, which is hosted in magmatic and hydrothermal breccia, and where Au occurs in magmatic-hydrothermal silicate alteration minerals, is inferred to have been deposited from magmatic-hydrothermal fluids, although late in the evolution of the system.

Thus, the deposits that were studied have multiple gold sources: magmatic fluids were likely important at Côté Gold and Canadian Malartic, with metamorphic fluids, perhaps remobilizing early magmatic hydrothermal Au, potentially important at Canadian Malartic (De Souza et al., 2015), and Au derived, at least in part, from local pyritic, carbonaceous argillite, potentially important at Musselwhite.

IMPLICATIONS FOR EXPLORATION

Elemental mapping of pyrite and associated minerals can be helpful in fingerprinting the type of gold occurrence, the distribution of Au within the ores, and identifying potentially fertile sedimentary source rocks. In this study, we found that Au partitions strongly into pyrite and thus, as historically known, pyrite Au content is a generally good indicator of gold mineralization (e.g. Amaro et al., 1988). Pyrite in the samples studied from the Côté Gold deposit does not contain economic concentrations of Au; Au is, rather, hosted dominantly in silicate alteration minerals. The Musselwhite deposit is a BIF-hosted pyrrhotite-rich replacement-style gold deposit hosted in a volcano-sedimentary package that contains carbonaceous argillite-bearing auriferous diagenetic pyrite. In this type of gold deposit, carbonaceous shale and, especially, Au-rich diagenetic sulphide nodules in the sedimentary sequence, is potentially a regional-scale first-order indicator of potentially fertile exploration terrain (e.g. Large et al., 2009).

FUTURE WORK

The near-ubiquitous occurrence of pyrite in association with Au deposits and its demonstrated ability to concentrate elements and record the chemical history of its source hydrothermal system(s), and thus act as a vector to hidden mineralization, reinforces the evidence that pyrite chemistry requires further investigation. Future studies will concentrate on modelling element distributions in pyrite to determine compositional evolutionary fingerprints of productive systems and to develop chemical criteria of system fertility.

Because of its exploration significance, the connection between early Au enrichment in pyritic carbona-

ceous argillite and orogenic Au deposits requires much further investigation. Further work is currently in progress on diagenetic sulphide nodules in argillite using historical samples from the Hollinger-McIntyre and Owl Creek mines, Timmins.

Also still being evaluated are LA-ICP-MS data on zircon grains from the Côté Gold and Canadian Malartic gold deposits, which will provide important constraints on the oxidation state of the associated intrusions.

In situ isotopic compositions (e.g. Fe and S isotopes) of pyrite and other sulphides can provide potential constraints on the physico-chemistry of fluids/melts. Data collected from a Fe-isotope study of pyrite from the Côté Gold deposit are currently being evaluated. Furthermore, most Au deposits in the Abitibi greenstone belt have associated Ag and Te enrichments, so the stable isotopes of these metals may provide evidence to the source of Au and should be investigated in future studies, especially if combined with in situ elemental mapping and S- and Fe-isotope analyses.

ACKNOWLEDGEMENTS

This is a contribution to the Targeted Geoscience Initiative 4 (TGI-4) (2010-2015). We wish to thank Mine Canadian Malartic, Goldcorp, and Iamgold for supporting this study. Jian-Feng Gao thanks NSERC for the award of a visiting fellowship to the GSC. Dr. Zhaoping Yang's assistance with LA-ICP-MS analytical work and data processing is much appreciated.

REFERENCES

Agangi, A., Hofmann, A., and Wohlgemuth-Ueberwasser, C.C., 2013. Pyrite zoning as a Record of Mineralization in the Ventersdorp Contact Reef, Witwatersrand Basin, South Africa; Economic Geology, v. 108, p. 1243–1272.

Amaro, D., Ho, S., Groves, D., McNaughton, N., Dahl, N., Poll, N., and Grigson, M., 1988. The use of pyrite as an indicator of Archaean gold mineralization processes: examples from Western Australia, *In:* Abstracts; Bicentennial Gold 88, Geological Society of Australia, v. 23, p. 414–418.

Biczok, J., Hollings, P., Klipfel, P., Heaman, L., Maas, R., Hamilton, M., Kamo, S., and Friedman, R., 2012. Geochronology of the North Caribou greenstone belt, Superior Province Canada: Implications for tectonic history and gold mineralization at the Musselwhite mine; Precambrian Research, v. 192-195, p. 209–230.

Bull, S.W. and Large, R.R., 2014. Setting the stage for the genesis of the giant Bendigo ore system, *In:* Ore Deposits in an Evolving Earth, (ed.) G.R.T. Jenkin, P.A.J. Lusty, I. McDonald, I., M.P. Smith, A.J. Boyce, and J.J. Wilkinson; Geological Society of London, Special Publication No. 393, p. 1–31.

Chouinard, A., Paquette, J., and Williams-Jones, A.E., 2005. Crystallographic controls on trace-element incorporation in auriferous pyrite from the Pascua epithermal high-sulphidation deposit, Chile-Argentina; The Canadian Mineralogist, v. 43, p. 951–963.

Cook, N.J. and Chryssoulis, S.L., 1990. Concentrations of invisible gold in the common sulfides; The Canadian Mineralogist, v. 28, p. 1–16.

Cook, N.J., Ciobanu, C.L., Meria, D., Silcock, D., and Wade, B., 2013. Arsenopyrite-Pyrite Association in an Orogenic Gold Ore: Tracing Mineralization History from Textures and Trace Elements; Economic Geology, v. 108, p. 1273–1283.

Deditius, A.P., Utsunomiya, S., Reich, M., Kesler, S.E., Ewing, R.C., Hough, R., and Walshe, J., 2011. Trace metal nanoparticles in pyrite; Ore Geology Reviews, v. 42, p. 32–46.

Deol, S., Deb, M., Large, R.R., and Gilbert, S., 2012. LA-ICPMS and EPMA studies of pyrite, arsenopyrite and loellingite from the Bhukia-Jagpura gold prospect, southern Rajasthan, India: Implications for ore genesis and gold remobilization; Chemical Geology, v. 326-327, p. 72–87.

De Souza, S., Dubé, B., McNicoll, V.J., Dupuis, C., Mercier-Langevin, P., Creaser, R.A., and Kjarsgaard, I.M., 2015. Geology, hydrothermal alteration, and genesis of the world-class Canadian Malartic stockwork-disseminated Archean gold deposit, Abitibi, Quebec, *In:* Targeted Geoscience Initiative 4: Contributions to the Understanding of Precambrian Lode Gold Deposits and Implications for Exploration, (ed.) B. Dubé and P. Mercier-Langevin; Geological Survey of Canada, Open File 7852, p. 113–126.

De Souza, S., Dubé, B., McNicoll, V., Dupuis, C., Mercier-Langevin, P., Creaser, R., and Kjarsgaard, I., in press. Geology, structure and timing of hydrothermal alteration at the Canadian Malartic Archean stockwork disseminated world-class gold deposit, Quebec, Canada, *In:* Archean Base and Precious Metal Deposits, Southern Abitibi Greenstone Belt, Canada, (eds.) T. Monecke, P. Mercier-Langevin, and B. Dubé; Society of Economic Geologists, Field Guide Book 46.

Dubé, B. and Gosselin, P., 2007. Greenstone-hosted quartz-carbonate vein deposits, *In:* Mineral Deposits of Canada: A Synthesis of Major Deposit Types, District Metallogeny, the Evolution of Geological Provinces and Exploration Methods, (ed.) W.D. Goodfellow; Geological Association of Canada, Mineral Deposits Division, Special Publication No. 5, p. 49–73.

Dubé, B., Gosselin, P., Mercier-Langevin, P., Hannington, M., and Galley, A., 2007. Gold-rich Volcanogenic Massive Sulphide Deposits, *In:* Mineral Deposits of Canada: A Synthesis of Major Deposit Types, District Metallogeny, the Evolution of Geological Provinces and Exploration Methods, (ed.) W.D. Goodfellow; Geological Association of Canada, Mineral Deposits Division, Special Publication No. 5, p. 45–94.

Gaboury, D., 2013. Does gold in orogenic deposits come from pyrite in deeply buried carbon-rich sediments?: Insight from volatiles in fluid inclusions; Geology, v. 41, p. 1207–1210.

Goldfarb, R.J., Baker, T., Dubé, B., Groves, D.I., Hart, C.J.R., and Gosselin, P., 2005. Distribution, character, and genesis of gold deposits in metamorphic terranes, *In:* Economic Geology 100th Anniversary Volume, (ed.) J.W. Hedenquist, J.F.H. Thompson, R.J. Goldfarb, and J.P. Richards; Society of Economic Geologists, Littleton, Colorado, p. 407–450.

Halicz, L. and Günther, D., 2004. Quantitative analysis of silicates using LA-ICP-MS with liquid calibration; Journal of Analytical Atomic Spectrometry, v. 19, p. 1539–1545.

Heather, K.B. and van Breemen, O., 1994. An interim report on geological, structural, and geochronological investigations of granitoid rocks in the vicinity of the Swayze greenstone belt, southern Superior Province, Ontario, *In:* Canadian Shield; Geological Survey of Canada, Current Research 1994-C, p. 259–268.

Heather, K.B., Shore, G.T., and van Breemen, O., 1996. Geological investigations in the Swayze greenstone belt, southern Superior Province, Ontario: a final update, *In:* Canadian Shield;

Geological Survey of Canada, Current Research 1996-C, p. 125–136.

Heather, K.B. and Shore, G.T., 1999a. Geology, Swayze Greenstone Belt, Ontario; Geological Survey of Canada, Open File 3384a, sheet 2, scale 1:50 000.

Heather, K.B. and Shore, G.T., 1999b. Geology, Gogama, Swayze Greenstone Belt, Ontario; Geological Survey of Canada, Open File 3384g, scale 1:50 000.

Heather, K.B., 2001. The geological evolution of the Archean Swayze Greenstone Belt, Superior Province, Canada; Ph.D. thesis, Keele University, Keele, England, 370 p.

Hodgson, C.J. and MacGeehan, P.J., 1982. Geological characteristics of gold deposits in the Superior Province of the Canadian Shield, *In:* Geology of Canadian Gold Deposits, (ed.) R.W. Hodder and W. Petruks; Canadian Institute of Mining and Metallurgy, Special Volume 24, p. 211–229.

Hough, R.M., Noble, R.R.P., and Reich, M., 2011. Natural gold nanoparticles; Ore Geology Reviews, v. 42, p. 55–61.

Jackson, S.E., 2008. LAMTRACE data reduction software for LA-ICP-MS, *In:* Laser Ablation-ICP-Mass Spectrometry in the Earth Sciences: Current Practices and Outstanding Issues, (ed.) P. Sylvester; Mineralogical Association of Canada, Short Course Series, v. 40, p. 305–307.

Katz, L.R., Kontak, D.J., Dubé, B., and McNicoll, V.J., 2015. The Archean Côté gold intrusion-related Au(-Cu) deposit, Ontario, Canada: A large-tonnage, low-grade deposit centred on a magmatic-hydrothermal breccia, *In:* Targeted Geoscience Initiative 4: Contributions to the Understanding of Precambrian Lode Gold Deposits and Implications for Exploration, (ed.) B. Dubé and P. Mercier-Langevin; Geological Survey of Canada, Open File 7852, p. 139–155.

Kerrich, R., Goldfarb, R., Groves, D., and Garwin, S., 2000. The geodynamics of world-class gold deposits: characteristics, space-time distribution and origins, *In:* Gold in 2000, (ed.) S.G. Hagemann and P.E. Brown; Society of Economic Geologists, Reviews in Economic Geology, v. 13, p. 501–551.

Kolb, M., 2011. A microstructural study of Musselwhite Mine and Hammond Reef shear-zone-hosted gold deposits; M.Sc. thesis, Lakehead University, Thunder Bay, Ontario, 204 p.

Koglin, N., Frimmel, H., Lawrie Minter, W.E., and Brätz, H., 2010. Trace-element characteristics of different pyrite types in Mesoarchaean to Palaeoproterozoic placer deposits; Mineralium Deposita, v. 45, p. 259–280.

Kontak, D.J., Creaser, R.A., and Hamilton, M., 2013. Geological and geochemical studies of the Côté Lake Au(-Cu) deposit Area, Chester Township, Northern Ontario, *In:* Results from the Shining Tree, Chester Township and Matachewan Gold Projects and the Northern Cobalt Embayment Polymetallic Vein Project, (ed.) J.A. Ayer, D.J. Kontak, R.L. Linnen, and S. Lin; Ontario Geological Survey, Miscellaneous Release Data 294.

Large, R.R., Bull, S.W., and Maslennikov, V.V., 2011. A Carbonaceous Sedimentary Source-Rock Model for Carlin-Type and Orogenic Gold Deposits; Economic Geology, v. 106, p. 331–358.

Large, R.R., Danyushevsky, L., Hollit, C., Maslennikov, V., Meffre, S., Gilbert, S., Bull, S., Scott, R., Emsbo, P., Thomas, H., Singh, B., and Foster, J., 2009. Gold and Trace Element Zonation in Pyrite Using a Laser Imaging Technique: Implications for the Timing of Gold in Orogenic and Carlin-Style Sediment-Hosted Deposits; Economic Geology, v. 104, p. 635–668.

Large, R.R., Maslennikov, V.V., Robert, F., Danyushevsky, L.V., and Chang, Z., 2007. Multistage sedimentary and metamorphic origin of pyrite and gold in the Giant Sukhoi Log Deposit, Lena Gold Province, Russia; Economic Geology, v. 102, p. 1233–1267.

Large, R.R., Meffre, S., Burnett, R., Guy, B., Bull, S., Gilbert, S., Goemann, K., and Danyushevsky, L., 2013. Evidence for an intrabasinal source and multiple concentration processes in the formation of the Carbon Leader Reef, Witwatersrand Supergroup, South Africa; Economic Geology, v. 108, p. 1215–1241.

Meffre, S., Large, R.R., Scott, R., Woodhead, J., Chang, Z., Gilbert, S.E., Danyushevsky, L.V., Maslennikov, V., and Hergt, J.M., 2008. Age and pyrite Pb-isotopic composition of the giant Sukhoi Log sediment-hosted gold deposit, Russia; Geochimica et Cosmochimica Acta, v. 72, p. 2377–2391.

Mercier-Langevin, P., Dubé, B., Lafrance, B., Hannington, M., Galley, A., Moorhead, J., and Gosselin, P., 2007. Metallogeny of the Doyon-Bousquet-LaRonde Mining Camp, Abitibi Greenstone Belt, Quebec, *In:* Mineral Deposits of Canada: A Synthesis of Major Deposit Types, District Metallogeny, the Evolution of Geological Provinces and Exploration Methods, (ed.) W.D. Goodfellow; Geological Association of Canada, Mineral Deposits Division, Special Publication No. 5, p. 673–701.

Moran, P., 2008. Lithogeochemistry of the sedimentary stratigraphy and metasomatic alteration in the Musselwhite gold deposit. North Caribou Lake metavolcanic-metasedimentary belt, Superior Province, Canada: implications for deposition and mineralization; M.Sc. Thesis, Lakehead University, Thunder Bay, Ontario, 351 p.

Oswald, W., Castonguay, S., Dubé, B., Mercier-Langevin, P., Malo, M., Biczok, J., and McNicoll, V., 2014. Targeted Geoscience Initiative 4. Lode gold deposits in ancient deformed and metamorphosed terranes: detailed mapping of key stripped outcrops in the Musselwhite Mine area, Northwestern Ontario, and implications for the geological and structural setting of the gold mineralization, *In:* Summary of field work and other activities 2014; Ontario Geological Survey, Open File Report 6300, p. 42-1 to 42-15.

Oswald, W., Castonguay, S., Dubé, B., McNicoll, V.J., Biczok, J., Malo, M., and Mercier-Langevin, P., 2015. Geological setting of the world-class Musselwhite gold Mine, Superior Province, northwestern Ontario, and implications for exploration, *In:* Targeted Geoscience Initiative 4: Contributions to the Understanding of Precambrian Lode Gold Deposits and Implications for Exploration, (ed.) B. Dubé and P. Mercier-Langevin; Geological Survey of Canada, Open File 7852, p. 69–84.

Poulsen, K.H., Robert, F., and Dubé, B., 2000. Geological Classification of Canadian Gold Deposits; Geological Survey of Canada, Bulletin 540, 106 p.

Robert, F., Poulsen, K.H., Cassidy, K.F., and Hodgson, C.J., 2005. Gold metallogeny of the Superior and Yilgarn cratons, *In:* Economic Geology 100th Anniversary Volume, (ed.) J.W. Hedenquist, J.F.H. Thompson, R.J. Goldfarb, and J.P. Richards; Society of Economic Geologists, Littleton, Colorado, p. 1001–1033.

Steadman, J.A., Large, R.R., Meffre, S., and Bull, S.W., 2013. Age, origin and significance of nodular sulfides in 2680 Ma carbonaceous black shale of the Eastern Goldfields Superterrane, Yilgarn Craton, Western Australia; Precambrian Research, v. 230, p. 227–247.

Steadman, J.A., Large, R.R., Davidson, G.J., Bull, S.W., Thompson, J., Ireland, T. R., and Holden P., 2014. Paragenesis and composition of ore minerals in the Randalls BIF-hosted gold deposits, Yilgarn Craton, Western Australia: Implications for the timing of deposit formation and constraints on gold sources; Precambrian Research, v. 243, p. 110–132.

Thomas, H.V., Large, R.R., Bull, S.W., Maslennikov, V., Berry, R.F., Fraser, R., Froud, S., and Moye, R., 2011. Pyrite and

pyrrhotite textures and composition in sediments, laminated quartz veins, and reefs at Bendigo gold mine, Australia: insights for ore genesis; Economic Geology, v. 106, p. 1–31.

Woodhead, J.D., Hellstrom, J., Hergt, J.M., Greig, A., and Maas, R., 2007. Isotopic and elemental imaging of geological materials by laser ablation inductively coupled plasma-mass spectrometry; Geostandards and Geoanalytical Research, v. 31, p. 331–343.

Woodhead, J.D., Hellstrom, J., Paton, C., Hergt, J., Greig, A., and Maas, R., 2008. A guide to depth profiling and imaging applications of LA–ICP–MS; Mineralogical Association of Canada, Short Course Series, v. 40, p. 135–145.

GEOLOGICAL SURVEY OF CANADA
OPEN FILE 7852

Targeted Geoscience Initiative 4: Contributions to the Understanding of Precambrian Lode Gold Deposits and Implications for Exploration

The Archean Westwood Au deposit, southern Abitibi: Telescoped Au-rich VMS and intrusion-related Au systems

David Yergeau[1], Patrick Mercier-Langevin[2], Benoît Dubé[2], Michel Malo[1], Vicki J. McNicoll[3], Simon E. Jackson[3], Armand Savoie[4], and François La Rochelle[4]

[1]Institut national de la recherche scientifique – Centre Eau Terre Environnement, Québec, Quebec
[2]Geological Survey of Canada, Québec, Quebec
[3]Geological Survey of Canada, Ottawa, Ontario
[4]Iamgold Corporation, Westwood Mine, Rouyn-Noranda, Quebec

2015

Recommended citation

Yergeau, D., Mercier-Langevin, P., Dubé, B., Malo, M., McNicoll, V.J., Jackson, S.E., Savoie, A., and La Rochelle, F., 2015. The Archean Westwood Au deposit, southern Abitibi: Telescoped Au-rich VMS and intrusion-related Au systems, *In:* Targeted Geoscience Initiative 4: Contributions to the Understanding of Precambrian Lode Gold Deposits and Implications for Exploration, (ed.) B. Dubé and P. Mercier-Langevin; Geological Survey of Canada, Open File 7852, p. 177–191.

Publications in this series have not been edited; they are released as submitted by the author.

Contribution to the Geological Survey of Canada's Targeted Geoscience Initiative 4 (TGI-4) Program (2010–2015)

TABLE OF CONTENTS

The Archean Westwood Au deposit, southern Abitibi: Telescoped Au-rich VMS and intrusion-related Au systems

David Yergeau[1,4]*, Patrick Mercier-Langevin[2†], Benoît Dubé[2], Michel Malo[1], Vicki J. McNicoll[3], Simon E. Jackson[3], Armand Savoie[4], and François La Rochelle[4]

[1]Institut national de la recherche scientifique – Centre Eau Terre Environnement, 490 rue de la Couronne, Québec, Quebec G1K 9A9
[2]Geological Survey of Canada, 490 rue de la Couronne, Québec, Quebec G1K 9A9
[3]Geological Survey of Canada, 601 Booth Street, Ottawa, Ontario K1A 0E8
[4]Iamgold Corporation, Westwood Mine, C.P. 970, Rouyn-Noranda, Quebec J9X 5C8
*Corresponding author's e-mail: david_yergeau@iamgold.com
†Corresponding author's e-mail: pmercier@nrcan.gc.ca

ABSTRACT

The Westwood deposit (3.74 Moz Au) is part of the Doyon-Bousquet-LaRonde mining camp. The deposit is hosted in the 2699–2996 Ma Bousquet Formation that forms a moderately to highly-strained, steeply south-dipping and east-west-trending, upper greenschist/lower amphibolite facies, homoclinal volcano-plutonic sequence that faces south.

The Westwood deposit consists of three east-west-trending and steeply south-dipping mineralized corridors that are stacked from north to south: the Zone 2 Extension, the North Corridor, and the Westwood Corridor. The Zone 2 Extension consists of transposed centimetre- to decimetre-wide pyrite ± chalcopyrite-sphalerite-rich quartz veins and disseminations whereas the North Corridor consists of centimetre- to decimetre-wide quartz-pyrite-chalcopyrite ± sphalerite-galena-pyrrhotite veins and disseminations as well as thin, semi-massive to massive sulphide veins. The Westwood Corridor consists of discontinuous stratabound polymetallic semi-massive to massive sulphide lenses, veins and disseminations.

The Westwood and North corridors are associated with a large, semi-conformable to discordant Mn-rich garnet and biotite distal alteration halo that hosts a zone of more proximal sericite-dominated alteration. The Zone 2 Extension is characterized by a 2–10-m wide zone of intense biotite and sericite (± gypsum) alteration and local alteration zones composed of an assemblage of quartz-andalusite-kyanite-pyrophyllite. Mapping and 3-D modeling of the alteration zones strongly suggests that the Zone 2 Extension alteration overprints that of the North and Westwood corridors.

The Westwood and North corridors are considered to be subseafloor to seafloor (VMS-type) mineralization, whereas the Zone 2 Extension vein system is proposed to represent the eastward extension of the intrusion-associated Doyon Au deposit located less than 1.5 km west of Westwood. The Doyon system is rooted in, and possibly genetically related to, the polyphase Mooshla synvolcanic intrusive complex. The three mineralized corridors at Westwood were probably formed in a ≤2 Ma time span, as indicated by U-Pb zircon geochronology. By analogy with telescoped porphyry-epithermal systems, the three mineralized corridors of the Westwood deposit may represent various components of a submarine Archean auriferous synvolcanic magmatic-hydrothermal system, providing a unique opportunity to improve and expand metallogenic and exploration models for Archean greenstone belts.

INTRODUCTION

The Doyon-Bousquet-LaRonde (DBL) mining camp represents one of the largest Canadian gold and volcanogenic massive sulphide (VMS) districts and was the subject of numerous studies in the last few decades (Mercier-Langevin et al., 2007b). Two major types of Au systems are present in the Doyon-Bousquet-LaRonde (DBL) mining camp: Au-rich VMS deposits (i.e. Bousquet 1, Bousquet 2-Dumagami, LaRonde Penna, and possibly Mouska) and intrusion-related Au ± Cu deposits (i.e. Doyon) (Fig. 1; Mercier-Langevin et al., 2007b). Due to major deformation and conflicting characteristics, the timing of Au introduction in the DBL deposits has been debated for many years, and various models were proposed (Mercier-Langevin et al., 2007b and references therein). Recent models favour a synvolcanic/syngenetic origin for the bulk of the Au in the district (e.g. Dubé et al., 2007, 2014;

Yergeau, D., Mercier-Langevin, P., Dubé, B., Malo, M., McNicoll, V.J., Jackson, S.E., Savoie, A., and La Rochelle, F., 2015. The Archean Westwood Au deposit, southern Abitibi: Telescoped Au-rich VMS and intrusion-related Au systems, *In:* Targeted Geoscience Initiative 4: Contributions to the Understanding of Precambrian Lode Gold Deposits and Implications for Exploration, (ed.) B. Dubé and P. Mercier-Langevin; Geological Survey of Canada, Open File 7852, p. 177–191.

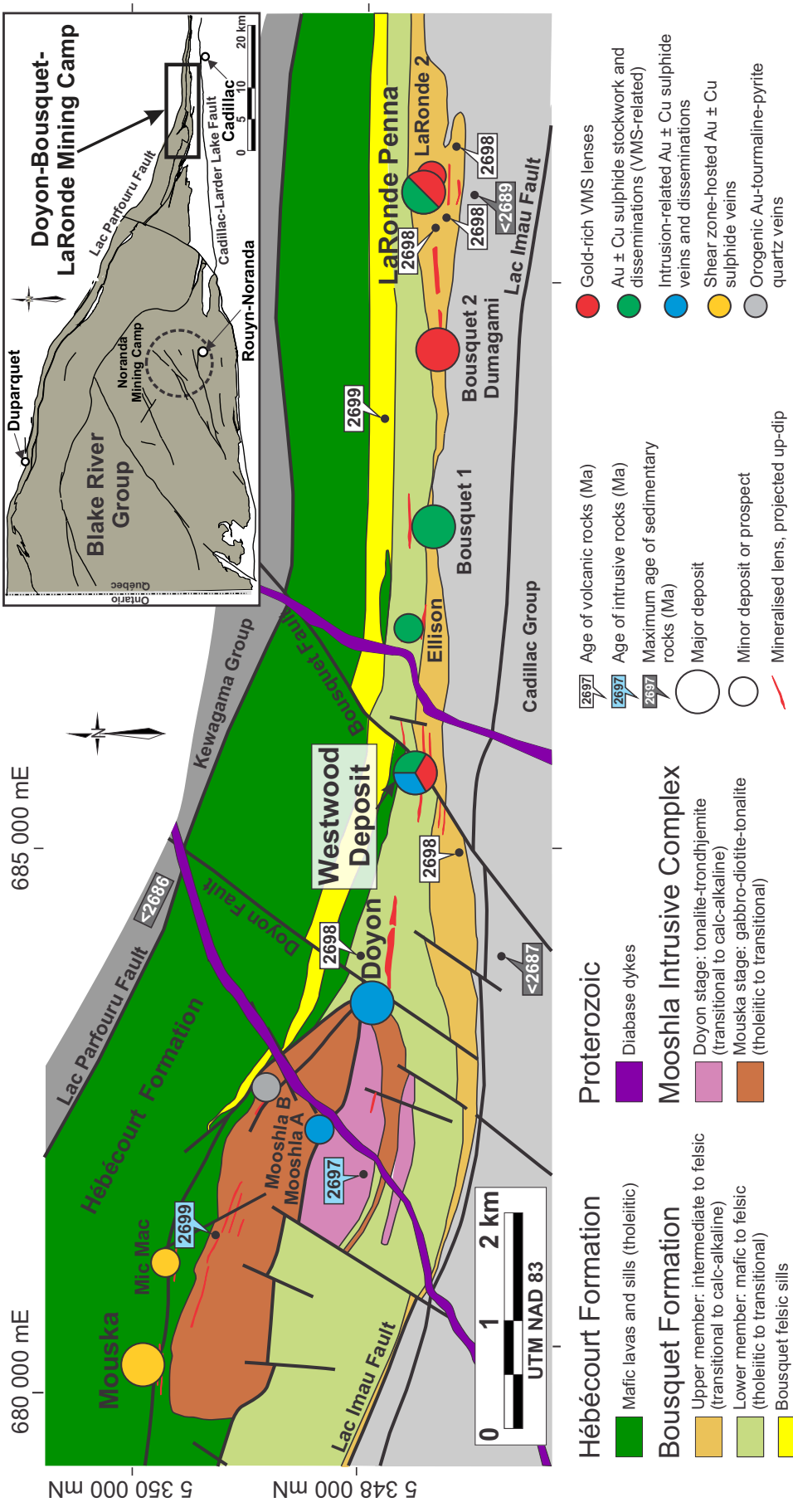

Figure 1. Simplified geological map of the Doyon-Bousquet-LaRonde (DBL) mining camp showing the types of deposits, the age of the rocks, and the location of the Westwood deposit. The inset shows the location of the DBL camp in the Blake River Group of the Abitibi greenstone belt. Modified from Mercier-Langevin et al. (2007a). U/Pb ages from Davis (2002), Lafrance et al. (2003, 2005), Mercier-Langevin et al. (2007a), and McNicoll et al. (2014).

Mercier-Langevin et al., 2007b; Wright-Holfeld, 2011; Galley and Lafrance, 2014), with extensive syntectonic reworking.

A genetic link between the intrusion-associated veins and the VMS-type deposits in the district has been proposed in the past, but this hypothesis has never been properly tested because of a lack of close spatial relationships between the different systems. The discovery, extensive drilling, and underground development of the Westwood deposit in the last decade has provided this opportunity, as both styles of mineralization are present and exposed in that area (Mercier-Langevin et al., 2009; Wright-Holfeld, 2011 and references therein). The reconstruction of the paleo-volcanic architecture and an exhaustive study of the ore zones and alteration halos, combined with a structural and metamorphic characterization of the Westwood deposit, were conducted through an M.Sc. project (Wright-Holfeld, 2011) and a Ph.D. project (Yergeau, 2015) as part of the Geological Survey of Canada TGI-4 Lode Gold project. A summary of our work at Westwood is presented here. Readers are referred to Yergeau (2015) and Wright-Holfeld (2011) for more details and complete referencing.

GEOLOGY AND LITHOGEOCHEMISTRY OF THE WESTWOOD AREA

The base of the host volcanic succession at Westwood consists of a kilometre-thick sequence of pillowed to massive tholeiitic basaltic flows and gabbro sills (map unit 1.0: Hébécourt Formation; Figs. 1 to 4). The Hébécourt Formation is in structural contact with the underlying sedimentary rocks of the ≤2686 Ma Kewagama Group (Davis, 2002).

Lower Member of the Bousquet Formation

The Hébécourt Formation is stratigraphically overlain by the lower member of the Bousquet Formation. The base of the lower member is composed of basaltic to andesitic porphyritic lapilli and block tuffs intercalated with andesitic to dacitic aphanitic lobes and sills (unit 3.0). This unit is tholeiitic (Figs. 3 and 4) and locally strongly altered with epidote- and quartz-filled amygdules (Fig. 5a).

The upper part of the Hébécourt Formation, as well as the base of unit 3.0, are injected by a series of metre-thick quartz- and feldspar-phyric massive tholeiitic rhyolitic sills (unit 2.0; 2698.6±1.5 Ma; Lafrance et al., 2003).

Unit 3.0 is overlain by the Bousquet heterogeneous unit (unit 4.4), which is composed mainly of pillowed to massive basaltic to andesitic lavas of tholeiitic to transitional affinity (Fig. 3). This unit becomes thinner and seems to be locally absent in the eastern part of the deposit. Unit 4.4 is more evolved than unit 3.0, with a

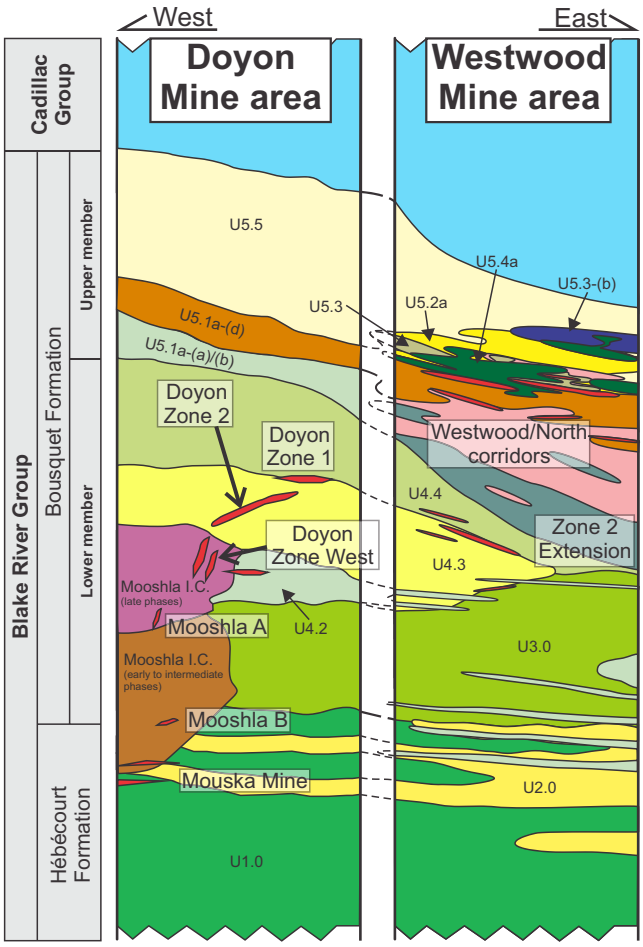

Figure 2. Schematic stratigraphic sections of the Westwood Mine and Doyon Mine areas. The Zone 2 Extension ore zone sits at the same level as the Doyon Mine zones 1 and 2. The North and Westwood corridors are hosted in the upper member of the Bousquet Formation. Modified from Mercier-Langevin et al. (2007a) and references therein.

significant depletion in heavy rare earth elements (HREE) ($[La/Yb]_N = 7.75$) combined with a strong Nb-Ta negative anomaly and a weak Zr-Hf negative anomaly (Fig. 4).

Units 3.0 and 4.4 are cut by a series of intermediate to felsic massive sills and transposed dykes (units 4.2 and 4.3), with the most prominent ones located near or directly at the contact between the two mafic units. Unit 4.2 (2698.3±0.9 Ma; Lafrance et al., 2005) is characterized by metre-thick feldspar-phyric andesitic-dacitic sills and dykes, whereas unit 4.3 is characterized by aphanitic rhyodacitic sills and dykes, with both units being of transitional affinity (Fig. 3). The largest sill of unit 4.3 is up to 200 metres thick and gradually thins and disappears in the eastern part of the Westwood deposit. The composition of these two intrusive units contrasts with the composition of the other units of the Bousquet Formation lower member, but is very similar to that of the Bousquet Formation upper volcanic member units (see below).

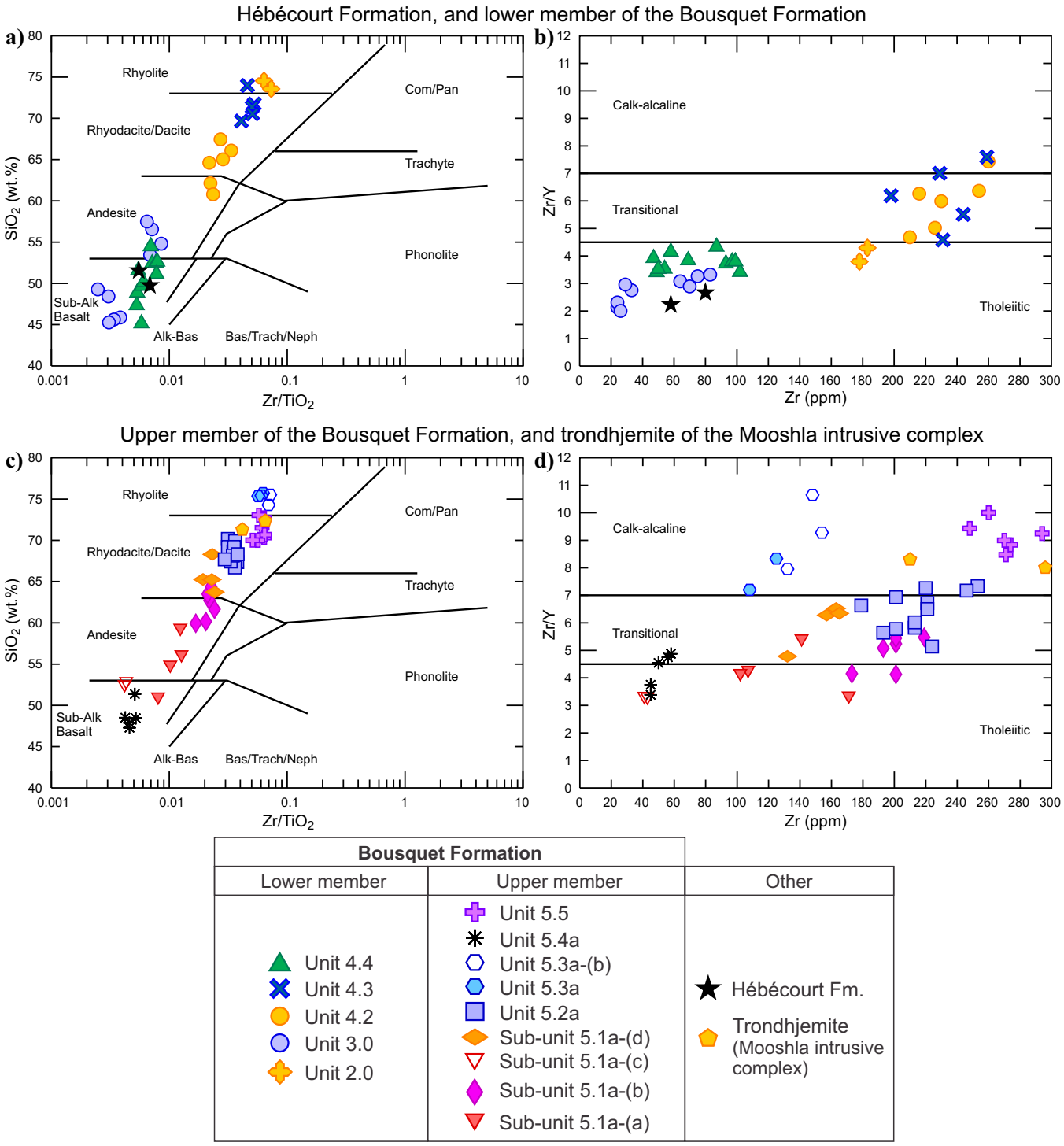

Figure 3. Major and trace element classification diagrams for the least-altered samples of the Westwood deposit host units. The Zr/TiO_2 vs SiO_2 (wt%) diagrams are from Winchester and Floyd (1977); the Zr (ppm) vs Zr/Y diagrams are from MacLean and Barrett (1993).

Upper Member of the Bousquet Formation

The upper member of the Bousquet Formation lies on top of units 4.4 or 3.0. The base of the upper member is composed of basaltic to andesitic (subunit 5.1a-(a)) and andesitic to dacitic (subunit 5.1a-(b)) volcanic rocks. Those two intercalated subunits consist mostly of amygdular and feldspar-phyric massive to brecciated flows. Both subunits are tholeiitic to transitional (Fig. 3), and characterized by a moderate to strong HREE depletion and Nb-Ta and Ti negative anomalies (Fig. 4).

The upper part of unit 5.1a contains spatially restricted dacitic domes and lobes (subunit 5.1a-(d)) intercalated with, or overlying, the two other subunits.

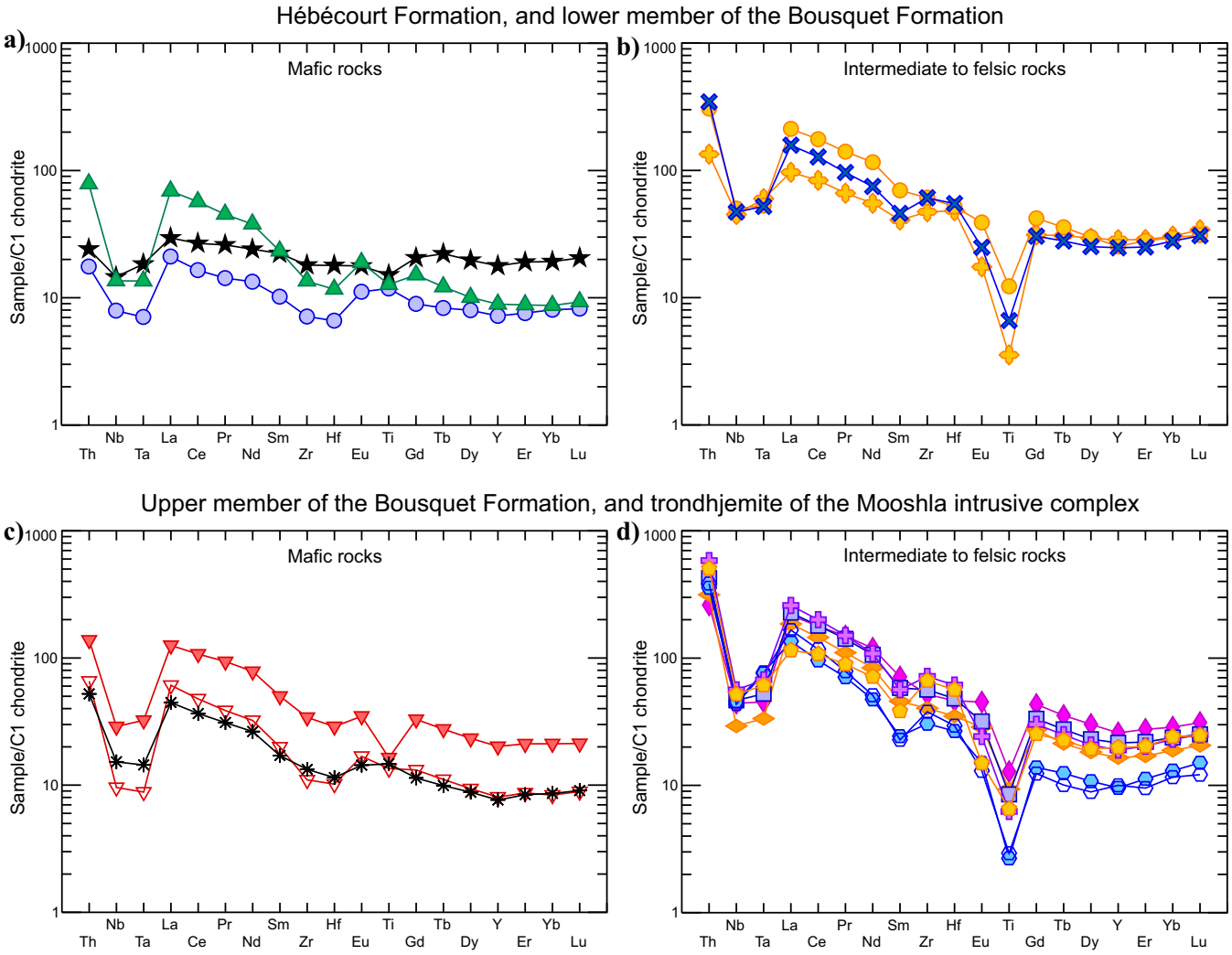

Figure 4. Chondrite-normalized trace and rare earth element diagrams for the Westwood deposit host units. C1 chondrite normalizing values from McDonough and Sun (1995). Unit symbols as in Figure 3.

It is mainly composed of aphanitic to feldspar-phyric volcaniclastic dacitic-rhyodacitic rocks (Fig. 5b) with local coherent facies. This transitional unit (Fig. 3) is significantly depleted in HREE ($[La/Yb]_N$ = 9.85) and has strong Nb-Ta and Ti negative anomalies (Fig. 4).

Unit 5.2a (2698.3±0.8 Ma; Mercier-Langevin et al., 2007a) overlies unit 5.1a and consists of a volcaniclastic and locally coherent volcanic feldspar-phyric dacitic-rhyodacitic rock sequence that is thicker in the central part of the deposit. Unit 5.2a is visually and geochemically similar to subunit 5.1a-(d) (Figs. 3 and 4) but it is slightly more felsic and generally much less altered (i.e. in the hanging wall of the VMS-type ore zones).

The uppermost effusive unit of the Bousquet Formation (unit 5.5; 2697.5±1.1 Ma; McNicoll et al., 2014) consists of rhyodacitic volcaniclastic rocks and locally massive lobes rich in feldspar phenocrysts and biotite microporphyroblasts. This unit is calc-alkaline (Fig. 3) and the rare earth element-high field strength elements (REE-HFSE) diagram shows depletion in HREE, strong negative Nb-Ta and Ti anomalies, and a positive Zr-Hf anomaly (Fig. 4).

Calc-alkaline, blue quartz- and feldspar-phyric rhyolitic dykes and sills (Fig. 3; 2697.8±1.0 Ma; Mercier-Langevin et al., 2007a), which are characterized by a pronounced negative Ti anomaly (unit 5.3a: Fig. 4), cut the felsic volcanic units (5.2a and 5.5) of the upper Bousquet Formation. All units of the upper member are subsequently cut by a series of synvolcanic, tholeiitic, basaltic to andesitic dykes and sills (Fig. 3 and 5c: subunit 5.1a-(c) and unit 5.4) that are geochemically similar to unit 4.4 (Figs. 3 and 4). A feldspar-phyric rhyolitic cryptodome (subunit 5.3a-(b)) is present within unit 5.5 in the eastern and upper part of the deposit. This unit has a similar geochemical signature to the unit 5.3a, but it does not contain blue quartz phenocrysts.

At least two centimetre- to decimetre-thick horizons of argillite are present in the upper Bousquet Formation. One of these horizons is located at the contact between

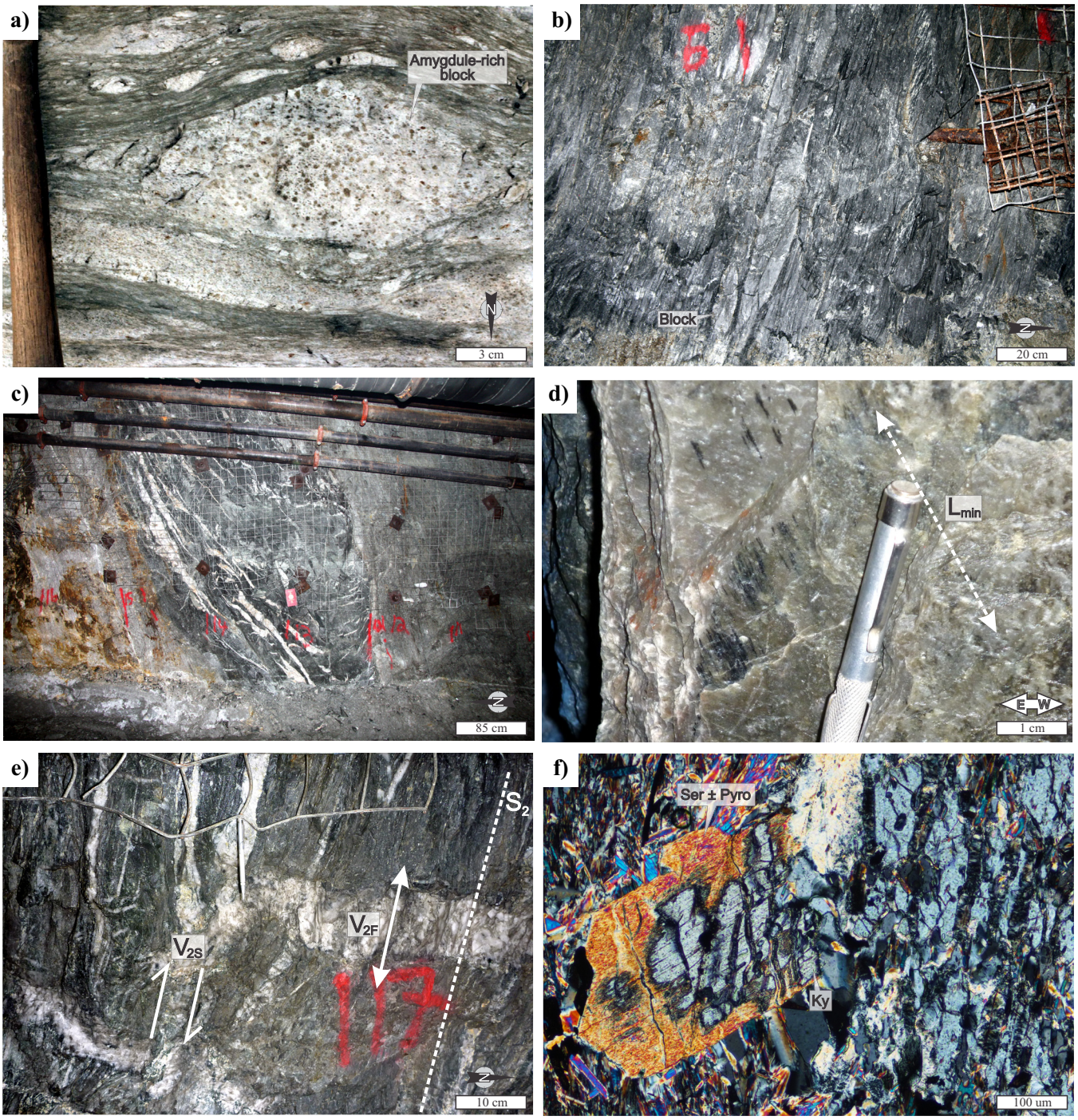

Figure 5. a) Mafic lapilli and block tuff of the Bousquet scoriaceous tuff (unit 3.0). The block shown contains 20% of epidote-quartz-filled amygdules. **b)** Felsic lapilli and block tuff of subunit 5.1a-(d) in the footwall of the Westwood Corridor. The matrix is altered in magnesian chlorite and sericite, whereas the fragments are weakly altered. **c)** Slightly altered mafic dyke of subunit 5.1a-(c) that crosscuts the intermediate volcanic rocks of subunit 5.1a-(b). **d)** Steeply west-dipping stretching lineation (L_{min}) on the S_2 plane characterized by the preferential orientation of chlorite. **e)** Extension flat quartz veins and S_2-parallel quartz veins (V_{2S}) generated during D_2 deformation. **f)** Kyanite crystal partially retrograded to sericite and pyrophyllite during the retrograde M_2 event. Abbreviations: Pyro = pyrophyllite, Ser = sericite.

unit 5.2a and the overlying unit 5.5, whereas a more spatially restricted horizon is located directly within unit 5.5 in the eastern part of the deposit. This argillite has a geochemical signature comparable to that of the upper member of the Bousquet Formation, and possibly represents sedimentation in local depressions during short volcanic hiatuses.

Less than 1 m-thick microcrystalline quartz-feldspar trondhjemite dykes of the Mooshla synvolcanic intrusive complex (Galley and Lafrance, 2014) crosscut unit

3.0 in the western, deep part of the Westwood deposit. The geochemistry of this unit is similar to that of felsic volcanic units 5.2a and 5.5 (Figs. 3 and 4).

The contact between the upper part of the Bousquet Formation and the overlying ≤2685 Ma Cadillac Group turbiditic sequence is characterized by a ≤1 m-thick horizon of massive pyrrhotite locally overlain by some argillite. The contact itself is traditionally interpreted as being structural or depositional (Mercier-Langevin et al., 2007b and references therein).

DEFORMATION AND METAMORPHISM OF THE WESTWOOD AREA

Deformation and related metamorphism are responsible for the modification of the primary geometry and mineralogy of the volcanic rocks, alteration zones, and ore zones. The first and most penetrative deformation event recognized (regional D_2 deformation) is characterized mainly by a penetrative east-west subvertical S_2 schistosity, a west-plunging stretching lineation (L_{min}; Fig. 5d), and local subhorizontal isoclinals folds (F_2). Those features are interpreted to be related to the major north-south shortening episode that characterizes the southern Abitibi greenstone belt (Dimroth et al., 1983). Two conjugate sets of quartz veins (flat subhorizontal veins (V_{2F}) and steeply dipping and boudinaged veins parallel to S_2 (V_{2S}); Fig. 5e) are also associated with D_2 deformation. Syn-D_2 stretching is responsible for the elongation of the ore zones and the development of perpendicular subhorizontal ore shoots. When the quartz veins cross-cut the ore zones, some of the most mobile elements (i.e. mostly Cu, Au, Ag, Pb, and Te) are remobilized in the quartz veins that are otherwise barren in the area. Free gold has also been found directly coating the S_2 plane within highly sericitized and schistose rocks adjacent to ore zones. Various structural elements that were discordant to the bedding (S_0) during D_2 deformation are highly transposed and folded, whereas those subparallel to S_0 are flattened and stretched (boudinaged). Although no specific fabric is attributed to the D_1 deformation in the Westwood area, it is interpreted as being responsible for the tilting of the volcanic sequence to the south (Yergeau, 2015).

Subsequent deformation events have had much less influence on the ore zones and the host rocks. The D_3 deformation is responsible for the development of a subvertical northeast-southwest cleavage in sericitized rocks that could have locally remobilized some metals. The D_4 deformation is associated with the development of three conjugated sinistral/dextral sets of discrete subvertical faults (northeast-southwest, northwest-southeast, and north-south) that locally displace ore zones over less than 3 m. The Bousquet Fault, a northeast-southwest brittle structure that divides the Westwood deposit in half with a ~250 m sinistral displacement is also associated with D_4. The final D_5 deformation event is associated with three sets of conjugate joints (subhorizontal, north-south/east-west subvertical) that locally remobilize some base and precious metals.

The M_1 prograde metamorphic event is syn- to late-D_2 deformation. Peak metamorphic conditions are estimated at 450–550ºC (upper greenschist), based on the presence of chlorite-epidote-actinolite-biotite ± hornblende in mafic volcanic rocks and biotite-sericite-chloritoid ± staurolite in sedimentary rocks in the upper part of the deposit. In the deeper part of the mine (>1500 m) on the eastern side of the Bousquet fault, the pressure-temperature (P-T) conditions are slightly more elevated, at 500–600ºC (lower amphibolite), with hornblende-biotite-garnet-epidote ± chlorite-actinolite-staurolite in mafic rocks and biotite-sericite-staurolite-garnet in sedimentary rocks. This gradual increase of the P-T conditions with increasing depth affects the mineralogy of the metamorphosed alteration assemblages. For example, aluminosilicate minerals (i.e. andalusite, kyanite, and Zn-staurolite) are present, along with sericite, in the argillic-style alteration (or phyllic) at depth, whereas the same alteration closer to surface consists exclusively of quartz and sericite. The coating by M_1 magnetite of S_2-flattened pyrite and pyrrhotite in the deeper part of the Westwood Corridor indicates that oxidation and desulphurization processes occurred at depth during metamorphism.

The M_1 prograde metamorphism is followed by a greenschist-facies retrograde metamorphism (M_2). This is indicated by the partial replacement of hornblende and biotite by chlorite, of Mn-garnet by chlorite and carbonate, and aluminosilicates (i.e. andalusite and kyanite) by sericite and pyrophyllite (Fig. 5f).

MINERALIZATION AND ALTERATION ZONES OF THE WESTWOOD DEPOSIT

This section presents a brief description of each mineralized corridor. The main features of each corridor are summarized in Table 1. A very detailed description of the ore and alteration zones at Westwood can be found in Yergeau (2015).

Zone 2 Extension

The Zone 2 Extension ore zones are spatially associated with the felsic to intermediate dykes and sills of units 4.2 and 4.3, which crosscut the mafic volcanic rocks of the lower member of the Bousquet Formation. The ore zones consist of sulphide-rich quartz veins, and zones/bands of sulphide dissemination that can locally form semi-massive sulphides. The veins and sulphide bands are deformed, boudinaged, and transposed within the main S_2 schistosity and locally seem to be overprinted by quartz veins that are themselves

Table 1. The main features of the Zone 2 Extension, North Corridor, and Westwood Corridor of the Westwood deposit.

	Zone 2 Extension	North Corridor	Westwood Corridor
Types of ore zones	Disseminated to semi-massive sulphides and sulphide-quartz veins	Massive to semi-massive sulphide veins/veinlets and disseminated sulphides	Massive to semi-massive sulphide veins/veinlets, disseminated sulphides, and massive sulphide lenses
Major host units	4.2, 4.3, and 4.4	5.1a-(a), and 5.1a-(b)	5.1a-(b), 5.1a-(d), 5.2a, 5.3a, and 5.4a
Thickness	0.1 m to <5 m	0.1 m to <1 m	0.1 m to 14 m (massive sulphide lenses)
Extent of ore zones	<500 m^2 to >200 m X 1 km	<500 m^2 to >200 m X 800 m	<500 m^2 to 300 m X 1.5 km
Major sulphide phases	Pyrite-Chalcopyrite	Pyrite-Sphalerite-Chalcopyrite	Pyrite-Sphalerite-Chalcopyrite± Galena
Accessory minerals	Sphalerite-Pyrrhotite	Pyrrhotite-Galena-Arsenopyrite	Pyrrhotite-Arsenopyrite-Stannite-Magnetite ± Gahnite-Cassiterite
Trace minerals	Galena-Gold-Melonite-Tellurobismuthite-Tetradymite	Gold-Electrum-Melonite-Tellurobismuthite-Tetradymite-Petzite-Sylvanite	Gold-Electrum-Melonite-Tellurobismithite-Tetradymite-Petzite-Sylvanite-Volynskite
Trace elements suite	B-Cd-Mo-Sb-Sn-W-As-Bi-In-Co-Hg-Se-Te	Sn-Bi-Sb-Mo-As-In-Cd-Hg-Se-Te	Bi-W-Sn-In-As-Cd-Sb-Hg-Se-Te
Metals associated with gold	Ag-Bi-Sb-W-Sn-Co-B-Mo-Te	Sb-Cd-Zn-Pb-Mo-Te	Cu-Bi-Ag-Te
Au/Ag ratio	2	1.95	0.26

deformed by D_2 (Fig. 6a). Sulphide-rich veins are thought in some cases to represent remobilization of disseminated sulphides during D_2 deformation. Replacement and breccia textures are commonly present and the vein contacts with the host rocks are usually gradational. At deposit scale, some of the ore zones seem to merge, forming a flattened, anastomosed pattern. The sulphides consist mainly of pyrite and/or chalcopyrite, although sphalerite and galena can constitute as much as 80% of the ore zones very locally. The sulphide-quartz veins/bands and disseminated sulphide zones are up to a metre wide but are laterally and vertically extensive, being transposed within the S_2 schistosity and subvertical stretching lineation. Native Au, electrum, and tellurides are common as microscopic trace minerals in association with the sulphides. Early pyrite grains, preserved from recrystallization, are enriched in Au, suggesting that Au was mainly within the pyrite lattice prior to the D_2 metamorphism (laser-ablation ICP-MS analysis). Gold-rich early pyrite is present in all three mineralized corridors (Yergeau, 2015). The most laterally extensive and richest veins are hosted in the main sill of unit 4.3, and close to, or at the contact with, the overlying unit 4.4. Several Zone 2 Extension ore zones are also associated with smaller satellite felsic dykes and sills located on both sides of the main unit 4.3 intrusion. The presence of these felsic dykes and sills seems to be an important element in the development of the Zone 2 Extension veins, as most of the veins are spatially associated with the dykes. A preliminary U/Pb ID-TIMS zircon crystallization age of 2699 Ma, obtained from an unaltered but strongly foliated mafic dyke that cuts the proximal alteration associated with the Z2-31 zone (Zone 2 Extension), suggests that the Zone 2 Extension mineralization is pre-D_2 deformation.

The Zone 2 Extension ore zones are accompanied by a sericite-quartz-pyrite ± gypsum-albite halo that can be up to a few tens of metres thick. Mass balance calculations indicate K-Ba-S-Fe gains and Ca-Na-Mn-Mg losses in that alteration halo. This assemblage is interpreted as a metamorphosed argillic- or phyllic-style alteration. This alteration overprints a much larger chlorite-carbonate-biotite-garnet alteration assemblage that is commonly associated with all the Doyon-Bousquet-LaRonde VMS-type ore zones (Fig. 6b; Mercier-Langevin et al., 2007b). Locally, some intensely leached zones (i.e. advanced argillic-style alteration) are present in the hanging wall of the ore zones and are characterized by a metamorphic assemblage of quartz-andalusite-kyanite-pyrophyllite ± sericite-gypsum where all mobile elements were leached.

North Corridor

North Corridor ore zones are preferentially hosted in the mafic to intermediate volcanic rocks of subunits 5.1a-(a) and 5.1a-(b) at the base of the upper member of the Bousquet Formation. This mineralized corridor is composed of semi-massive to massive sulphide veins and dissemination zones that can be up to a few metres wide, and characterized by pyrite and sphalerite with lesser amounts of quartz, chalcopyrite, and pyrrhotite with local traces of galena. Some veins are also exceptionally rich in chalcopyrite (i.e. >30%) or sphalerite. Gold is present as free Au, electrum, and tellurides. The North Corridor ore zones have strongly recorded the D_2 deformation, and consequently tight to isoclinal

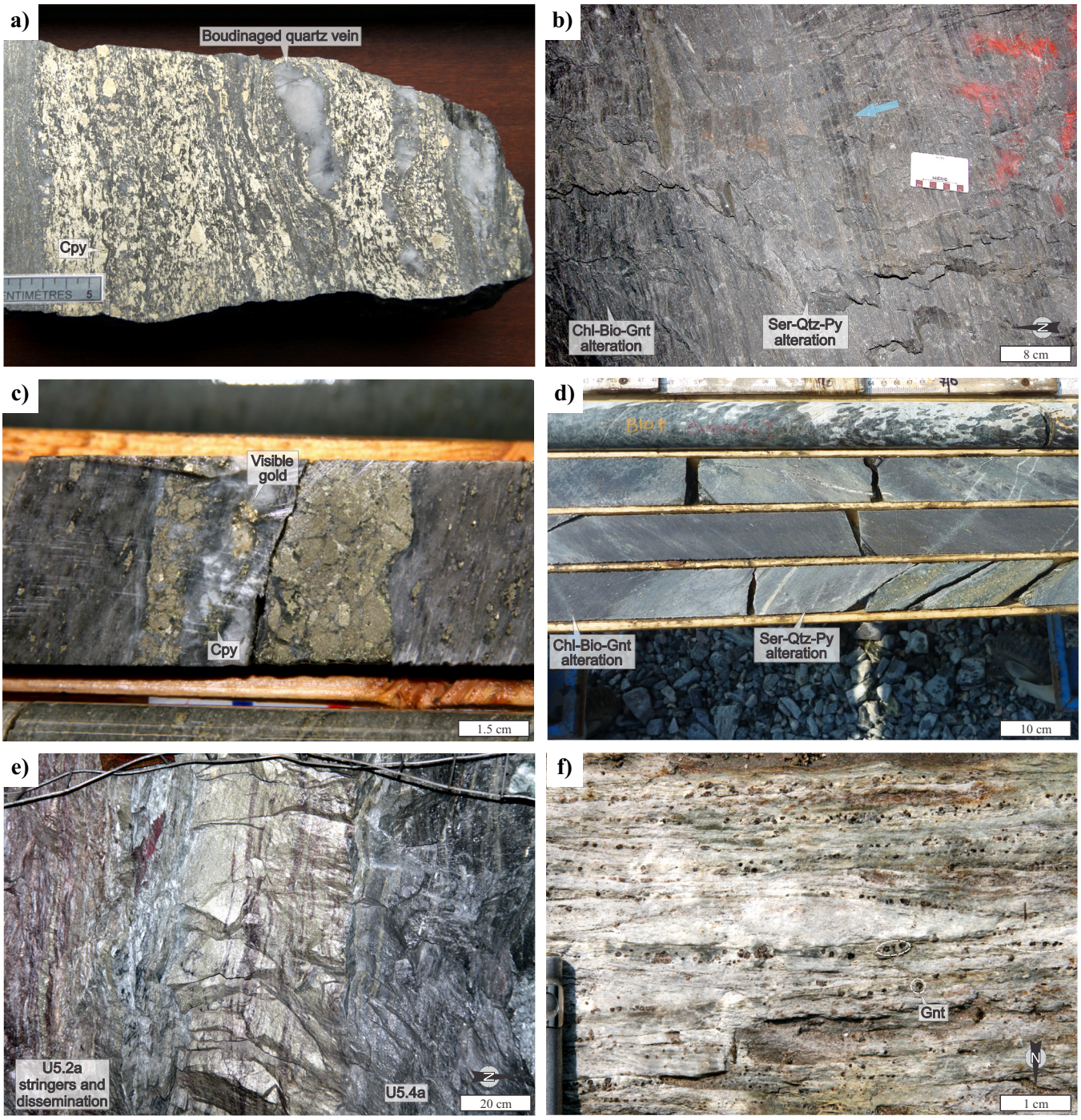

Figure 6. a) The Z2-30 (Zone 2 Extension) vein, composed mainly of pyrite with minor chalcopyrite, is strongly affected by the D_2 deformation event. Boudinaged orogenic quartz veins cut the Z2-30 in this sample. **b)** Sericite-quartz-pyrite alteration associated with the Zone 2 Extension overprinting the background chlorite-biotite-garnet alteration related to the North and Westwood corridors. A zone of background alteration is preserved in the sericite-dominated alteration (blue arrow). **c)** Deformed massive pyrite ± chalcopyrite vein of the North Corridor hosted within a sericitized andesite of subunit 5.1a-(b). A quartz vein crosscuts the sulphide vein and contains remobilized Au. **d)** Sericite-quartz-pyrite alteration halo surrounding a North Corridor ore zone. **e)** Banded pyrite-sphalerite massive sulphide lens of the Westwood Corridor overlain by a pyrite-sphalerite ± chalcopyrite stringer zone hosted in unit 5.2a. The footwall is composed of a mafic sill of unit 5.4a. **f)**. Manganiferous garnet alteration in a lapilli and block tuff of subunit 5.1a-(b) in the footwall of the Westwood Corridor. Abbreviations: Bio = biotite; Chl = chlorite; Cpy = chalcopyrite; Gnt = garnet; Py = pyrite; Qtz = quartz; Ser = sericite.

folding (shortening/transposition) of the veins and veinlets is common. Replacement and breccia textures are typical and sulphide-filling of volcanic vesicles is common in the vein selvages. The ore zones are preferentially developed within high-permeability rocks (i.e. mostly volcaniclastic rocks and vesicle-rich rocks) that are overlain by low-permeability cap rocks (i.e. massive lavas and intrusions). Syntectonic quartz veins that cut the ore zones are usually rich in Au and base metals as they caused, or are the locus of, some local metal remobilization in the three mineralized corridors (e.g. Fig. 6c). The North Corridor ore zones are spatially associated with the overlying mineralization of the Westwood Corridor that is less than 100 m higher in the stratigraphic sequence. The North Corridor mineralization is thought to represent a failed VMS-type system or a footwall replacement zone associated with the Westwood Corridor, which consists of more classic subseafloor to seafloor VMS-type mineralization, as described below.

The metamorphosed hydrothermal alteration surrounding the North Corridor ore zones consist of a few metres- to a few tens of metres-thick alteration halo characterized by a sericite-quartz-pyrite ± albite-biotite-carbonate-chlorite-Mn-garnet assemblage (Fig. 6d). Mass balance calculations indicate that this proximal alteration is marked by gains in K-Ba-Si-S-Fe-Mn-CO_2 and losses in Na-Ca-Mg.

Westwood Corridor

The Westwood Corridor is located at the same stratigraphic position as the massive sulphide lenses of the LaRonde Penna and Bousquet 2-Dumagami mines, which are located in the eastern part of the mining camp (Mercier-Langevin et al., 2009). The Westwood Corridor ore zones are mainly hosted in, or at the contact between, the volcanic intermediate to felsic units 5.1a-(b), 5.1a-(d) and 5.2a and the lower contact of, and locally within, the felsic and mafic dykes and sills of units 5.3a and 5.4a. The ore zones consist of sulphide-rich veins, disseminated sulphide zones, and stratabound semi-massive to massive sulphide lenses (Fig. 6e). Dissemination zones can be up to 10 m wide, whereas the veins are usually less than a metre thick. The massive sulphide lenses are up to 14 m thick. The veins, disseminated sulphide zones, and semi-massive sulphides can be laterally very extensive (i.e. > 800 m), whereas the massive sulphide lenses are spatially restricted and associated with felsic domes of subunit 5.1a-(d). Felsic breccia, rich in auriferous massive sulphide fragments, is also locally present. All ore zones are strongly affected by deformation; transposition, boudinage, and stretching, as well as piercement structures associated with D_2 deformation are common within the massive sulphide lenses. The massive sulphide lenses are elongated parallel to the stretching lineation, with subhorizontal Au-Ag-Cu-rich ore shoots which are perpendicular to the L_{min} lineations that are present within the lenses. Pyrite and sphalerite are the most abundant sulphides; chalcopyrite, galena, and pyrrhotite usually form less than 10% of the mineralized material, although some ore zones are locally quite rich in chalcopyrite and/or galena (i.e. >15%). Replacement of permeable volcanic rocks seems to be the main mineralizing process for the vein and disseminated sulphide zones. Free Au, electrum, tellurides, and primary pyrite are the main hosts for Au. Traces of stannite, arsenopyrite, gahnite, Zn-rich staurolite, and magnetite are locally present.

The metamorphosed hydrothermal alteration halo associated with the Westwood Corridor consists of a very extensive (<1 km), semi-conformable footwall chlorite-biotite-carbonate-Mn-rich garnet ± albite-tourmaline alteration assemblage. This alteration assemblage seems to be linked in time and space with the footwall alteration associated with the other VMS lenses of the district. Sodium leaching and gains in K, Ba, Mn, S, Fe, and CO_2 characterize this footwall alteration zone. The abundance of Mn-garnet generally increases toward the ore zones and can locally represent as much as 30 vol.% of the rock (Fig. 6f). The ore zones are wrapped in a plurimetric, proximal quartz-sericite-pyrite ± garnet-albite-tourmaline alteration envelope that overprints the distal alteration. Mass loss of Ca, Na, and Mg and gains of K, Ba, S, Fe, and Mn are associated with this alteration. At depth in the deposit (>1500 m), Zn-rich staurolite, kyanite, andalusite, gahnite, and magnetite are present in the alteration halos of the Westwood and North corridors ore zones. The development of aluminosilicate porphyroblasts is interpreted as being the result of a slight increase in the metamorphic grade at depth, combined with perhaps subtly more acidic hydrothermal alteration conditions in this part of the deposit. The presence of late-M_1 magnetite grains that partially replace pyrite and pyrrhotite is possibly related to the desulphurization and oxidation of sulphides during lower amphibolite-facies metamorphism.

SIMPLIFIED GENETIC MODEL

The Westwood deposit is characterized by different styles of Au ± base metals ore zones, which are stacked in the host stratigraphic succession. The lowermost ore zones consist of sulphide-rich quartz veins and disseminations that are thought to be an extension of the Doyon Mine intrusion-associated Au deposit to the west; whereas the uppermost ore zones are similar to the Au-rich VMS deposits of the Bousquet 2-Dumagami and LaRonde Penna mines to the east (Fig. 1). The intensity of the deformation in the Westwood

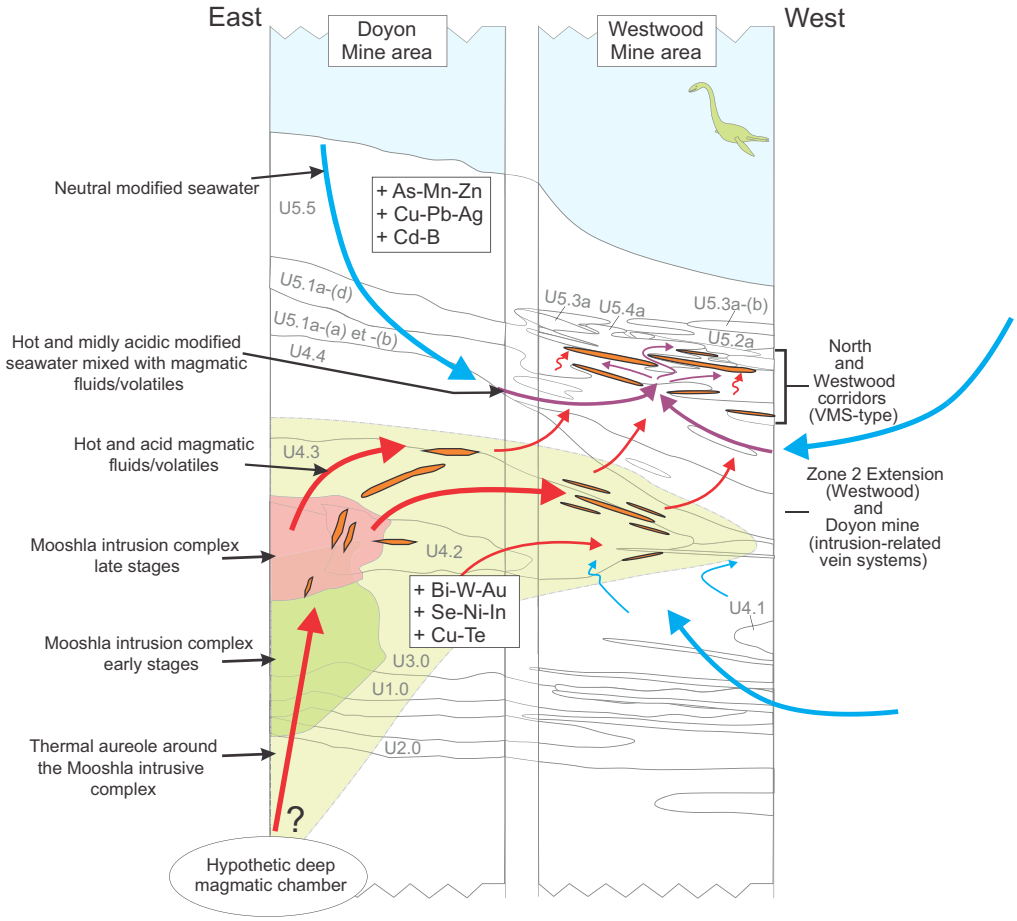

Figure 7. Schematic longitudinal section showing the origin of hydrothermal fluids that generated the Zone 2 Extension, Doyon mine ore zones, and North and Westwood corridors. The Zone 2 Extension represents the distal expression of the intrusion-related magmatic-hydrothermal system centred on the upper part of the Mooshla intrusive complex (i.e. Doyon Mine ore zones). The magmatic fluids/volatiles that were involved in the genesis of these ore zones were possibly exsolved from the crystallizing felsic late phases of the Mooshla intrusive complex. A deep magmatic chamber could also be the source of the fluids. The North and Westwood corridors result from the circulation of modified seawater within the volcanic edifice, in which a magmatic input from the Mooshla intrusion or from the passive degassing of the volcanic rocks might explain the anomalous Au enrichment of the fluids.

area is such that we can only speculate on the primary architecture of the system. Previous studies and our current work at Westwood, however, provide a number of geological, geochemical, and geochronological constraints that can be used to better understand the system prior to deformation.

The Zone 2 Extension ore zones (and those of the Doyon Mine) are spatially and interpreted as genetically associated with the Mooshla synvolcanic intrusive complex that generated (or channelled) magmatic volatiles/fluids during the crystallization of its late felsic calc-alkaline phases (e.g. Galley and Lafrance, 2014; Fig. 7). These magmatic volatiles, which possibly carried Au and Cu, escaped the intrusion and were transported into the overlying volcanic rocks of the lower Bousquet Formation, preferentially along the felsic sills and dykes of units 4.2 and 4.3. The seafloor and subseafloor-style mineralized zones of the Westwood and North corridors are associated with the development of a large hydrothermal cell comprising a dominant modified seawater component. This seawater-dominated hydrothermal system was fuelled by a temperature gradient associated with the hot volcanic and intrusive rocks of the Bousquet Formation. The presence of impermeable cap rocks (i.e. massive lavas and sills) is essential to the subseafloor maturation of the hydrothermal systems. The presence of felsic volcanic or talus breccias containing auriferous massive sulphide fragments suggests that at least some of the ore was potentially formed by exhalative activity on the seafloor. The presence of stacked semi-massive to massive sulphide lenses and disseminated sulphide zones at different stratigraphic levels suggests that the seafloor hydrothermal system was capped and became a subseafloor hydrothermal system during the evolution of the Bousquet Formation (e.g. replacement ore zones in the hanging wall of the seafloor massive sulphide lenses and laterally; Fig. 6e). By analogy with the neighbouring Bousquet 2-Dumagami and LaRonde Penna Au-rich VMS deposits (e.g. Dubé et al., 2007, 2014; Mercier-Langevin et al., 2007b), the Au enrichment of the VMS-type ore zones at Westwood is interpreted to be due to magmatic input into the circulating modified seawater. Geochronology indicates that the volcanic and intrusive rocks of the Bousquet Formation were emplaced in less than two million years, and crosscutting relationships and relative timing regarding deformation and metamorphism suggest that the intrusion-related and VMS-type hydrothermal systems are more or less coeval with volcanism. The mixing of fertile magmatic fluids/volatiles with modified seawater is, in this context, a viable hypothesis to explain the Au-rich VMS deposition (e.g. Dubé et al., 2014). In

light of what has been summarized here, previous work in the district, and an in-depth discussion on the nature of the Westwood deposit in Yergeau (2015), the Westwood deposit is interpreted as part of an Archean subaqueous, telescoped magmatic-hydrothermal system that shares some similarities with subaerial porphyry-epithermal systems that are generated in younger volcanic arcs (e.g. Hedenquist et al., 1998).

IMPLICATIONS FOR EXPLORATION

Transitional to calc-alkaline, basalt-andesite-dacite-rhyodacite-rhyolite volcanic and intrusive suites (i.e. more oxidized and fluid-rich "arc" magmas) represent good targets for synvolcanic gold deposits. At the district scale, the upper part of multiphase synvolcanic calc-alkaline intrusive complexes may represent favourable targets for Archean intrusion-related Au and Au-Cu deposits, especially if Au-rich VMS-style mineralization is present nearby. Manganiferous and potassic alteration halos combined with sodium depletion are good indicators of modified seawater circulation in the volcanic edifice, whereas combined positive barium and potassium anomalies are more commonly associated with intrusion-related ore zones. The presence of permeable volcaniclastic rocks facilitates fluid infiltration and efficient precipitation of sulphides in the subseafloor environment through replacement of the host rocks, whereas the presence of impermeable sills and dykes is key for the channelling of Au-enriched magmatic fluids.

ACKNOWLEDGEMENTS

The authors express their sincere gratitude to Iamgold Corporation and the Westwood Mine geology department for financial and logistical support, authorization to publish, and for sharing their unique knowledge of the deposit. Special thanks to the Ministère de l'Énergie et des Ressources Naturelles, and more specifically to J. Goutier for his precious help and advice. Additional support was provided to D. Yergeau by IAMGOLD Corp., by a Natural Sciences and Engineering Research Council of Canada (NSERC) and Fonds de recherche du Québec–Nature et technologies (FRQNT) Industrial Innovation Scholarship, by the Institut national de la Recherche scientifique, and by the DIVEX network. Thanks to A. Galley for is invaluable help during this project and his careful review of this manuscript.

REFERENCES

Davis, D.W., 2002. U-Pb geochronology of Archean metasedimentary rocks in the Pontiac and Abitibi subprovinces, Quebec, constraints on timing, provenance and regional tectonics; Precambrian Research, v. 115, p. 97–117.

Dimroth, E., Imreh, L., Goulet, N., and Rocheleau, M., 1983. Evolution of the south-central segment of the Archean Abitibi Belt, Quebec. Part II: Tectonic evolution and geomechanical model; Canadian Journal of Earth Sciences, v. 20, p. 1355–1373.

Dubé, B., Mercier-Langevin, P., Hannington, M.D., Lafrance, B., Gosselin, G., and Gosselin, P., 2007. The LaRonde Penna world-class Au-rich volcanogenic massive sulfide deposit, Abitibi, Quebec: Mineralogy and geochemistry of alteration and implications for genesis and exploration; Economic Geology, v. 102, p. 633–666.

Dubé, B., Mercier-Langevin, P., Kjarsgaard, I., Hannington, M., Bécu, V., Côté, J., Moorhead, J., Legault, M., and Bédard, N., 2014. The Bousquet 2-Dumagami world-class Archean Au-rich volcanogenic massive sulfide deposit, Abitibi, Quebec: Metamorphosed submarine advanced argillic alteration footprint and genesis; Economic Geology, v. 109, p. 121–166.

Galley, A. and Lafrance, B., 2014. Setting and evolution of the Archean synvolcanic Mooshla intrusive complex, Doyon-Bousquet-LaRonde mining camp, Abitibi greenstone belt: Emplacement history, petrogenesis and implications for Au metallogenesis; Economic Geology, v. 109, p. 205–229.

Hedenquist, J.W., Arribas, A., and Reynolds, T.J., 1998. Evolution of an intrusion-centered hydrothermal system: Far Southeast-Lepanto porphyry and epithermal Cu-Au deposits, Philippines; Economic Geology, v. 93, p. 373–404.

Lafrance, B., Moorhead, J., and Davis, D.W., 2003. Cadre géologique du camp minier de Doyon-Bousquet-LaRonde; Ministère des Ressources Naturelles du Québec, ET 2002-07, 44 p.

Lafrance, B., Davis, D. W., Goutier, J., Moorhead, J., Pilote, P., Mercier-Langevin, P., Dubé, B., Galley, A., and Mueller, W.U., 2005. Nouvelles datations isotopiques dans la portion québécoise du Groupe de Blake River et des unités adjacentes; Ministère des Ressources Naturelles et de la Faune du Québec, RP 2005-01, 15 p.

MacLean, W.H. and Barrett, T.J., 1993. Lithogeochemical techniques using immobile elements; Journal of Geochemical Exploration, v. 48, p. 109–133.

McDonough, W.F. and Sun, S.-S., 1995. The composition of the Earth; Chemical Geology, v. 120, p. 223–253.

McNicoll, V., Goutier, J., Dubé, B., Mercier-Langevin, P., Ross, P.-S., Dion, C., Monecke, T., Legault, M., Percival, J., and Gibson, H., 2014. U-Pb geochronology of the Blake River Group, Abitibi greenstone belt, Quebec, and implications for base metal exploration; Economic Geology, v. 109, p. 27–59.

Mercier-Langevin, P., Dubé, B., Hannington, M.D., Davis, D.W., Lafrance, B., and Gosselin, G., 2007a. The LaRonde Penna Au-rich volcanogenic massive sulfide deposit, Abitibi greenstone belt, Quebec: Part I. Geology and geochronology; Economic Geology, v. 102, p. 585–609.

Mercier-Langevin, P., Dubé, B., Lafrance, B., Hannington, M.D., Galley, A., Moorhead, J., and Gosselin, P., 2007b. Metallogeny of the Doyon-Bousquet-LaRonde mining camp, Abitibi greenstone belt, Quebec, *In:* Mineral Deposits of Canada: A Synthesis of Major Deposit Types, District Metallogeny, the Evolution of Geological Provinces, and Exploration Methods, (ed.) W.D. Goodfellow; Geological Association of Canada, Mineral Deposits Division, Special Publication 5, p. 673–701.

Mercier-Langevin, P., Wrigh-Holfeld, A., Dubé, B., Bernier, C., Houle, N., Savoie, A., and Simard, P., 2009. Stratigraphic setting of the Westwood-Warrenmac ore zones, Westwood Project, Doyon-Bousquet-LaRonde mining camp, Abitibi, Quebec; Geological Survey of Canada, Current Research 2009-3, 20 p.

Winchester, J.A. and Floyd, P.A., 1977. Geochemical discrimination of different magma series and their differentiation products using immobile elements; Chemical Geology, v. 20, p. 325–343.

Wright-Holfeld, A., 2011. The Geology and Geochemistry of the World-Class Westwood Deposit, Abitibi Subprovince, Québec;

M.Sc. thesis, Institut national de la recherche scientifique – Centre Eau Terre Environnement, Québec, Quebec, 166 p.

Yergeau, D., 2015. Géologie du gisement synvolcanique aurifère atypique Westwood, Abitibi, Québec; Ph.D. thesis, Institut national de la recherche scientifique – Centre Eau Terre Environnement, Québec, Quebec, 682 pages.

GEOLOGICAL SURVEY OF CANADA
OPEN FILE 7852

Targeted Geoscience Initiative 4: Contributions to the Understanding of Precambrian Lode Gold Deposits and Implications for Exploration

The Rainy River "atypical" Archean Au deposit, western Wabigoon Subprovince, Ontario

Mireille Pelletier[1], Patrick Mercier-Langevin[2], Benoît Dubé[2], Dean Crick[3], Justin Tolman[3], Vicki J. McNicoll[4], Simon E. Jackson[4], and Gary P. Beakhouse[5]

[1]Institut national de la recherche scientifique – Centre Eau Terre Environnement, Québec, Quebec
[2]Geological Survey of Canada, Québec, Quebec
[3]New Gold Inc., Barwick, Ontario
[4]Geological Survey of Canada, Ottawa, Ontario
[5]Ontario Geological Survey, Sudbury, Ontario

2015

This publication is available for free download through GEOSCAN (http://geoscan.nrcan.gc.ca/)

Recommended citation

Pelletier, M., Mercier-Langevin, P., Dubé, B., Crick, D., Tolman, J., McNicoll, V.J., Jackson, S.E., and Beakhouse, G.P., 2015. The Rainy River "atypical" Archean Au deposit, western Wabigoon Subprovince, Ontario, *In:* Targeted Geoscience Initiative 4: Contributions to the Understanding of Precambrian Lode Gold Deposits and Implications for Exploration, (ed.) B. Dubé and P. Mercier-Langevin; Geological Survey of Canada, Open File 7852, p. 193–207.

Publications in this series have not been edited; they are released as submitted by the author.

Contribution to the Geological Survey of Canada's Targeted Geoscience Initiative 4 (TGI-4) Program (2010–2015)

TABLE OF CONTENTS

The Rainy River "atypical" Archean Au deposit, western Wabigoon Subprovince, Ontario

Mireille Pelletier[1]*, Patrick Mercier-Langevin[2†], Benoît Dubé[2], Dean Crick[3], Justin Tolman[3], Vicki J. McNicoll[4], Simon E. Jackson[4], and Gary P. Beakhouse[5]

[1]Institut national de la recherche scientifique – Centre Eau Terre Environnement, 490 rue de la Couronne, Québec, Quebec, G1K 9A9
[2]Geological Survey of Canada, 490 rue de la Couronne, Québec, Quebec, G1K 9A9
[3]New Gold Inc., 317 Heatwole Road, RR#1, Barwick, Ontario, P0W 1N0
[4]Geological Survey of Canada, 601 Booth Street, Ottawa, Ontario, K1A 0E8
[5]Ontario Geological Survey, 933 Ramsey Lake Road, Sudbury, Ontario, P3E 6B5
*Corresponding author's e-mail: mireille.pelletier@ete.inrs.ca
†Corresponding author's e-mail: pmercier@nrcan.gc.ca

ABSTRACT

The Rainy River project, located in the western Wabigoon Subprovince in western Ontario, is an advanced Au exploration project with an estimated 6.2 Moz Au and 14.6 Moz Ag in reserves and resources (New Gold Inc). The bulk of the Au and Ag mineralization occurs with pyrite, chalcopyrite, and sphalerite in disseminated ± stockwork form, and part of the ore is within quartz-sulphide-tourmaline-carbonate veinlets that are subparallel to the main east-trending, south-dipping penetrative foliation (S_2). Folded and transposed veins of quartz, Fe-carbonate, and tourmaline contain higher Au values, with Au in its native form or as electrum. At deposit-scale, there is a relatively good correlation between Au and Ag values, and between Au and Zn contents. Mineralization is concentrated in six zones that are elongated parallel to the main foliation. Higher grade zones are aligned within the main foliation plane along a stretching lineation (L_2) plunging to the southwest.

The deposit is hosted mainly within dacitic to rhyodacitic calc-alkaline volcanic domes, flows, and associated flow breccia. The rocks were regionally metamorphosed to greenschist facies. The proximal to immediate alteration consists of a sericite ±Fe-carbonate overprinted to various degrees by chlorite. Manganiferous garnet, chloritoid, and kyanite are present locally, in proximity to, or within, mineralized zones.

There is a strong correlation between the spatial distribution of the mineralization and the sericite-dominated alteration. Moreover, there is a direct correlation of stronger alteration intensity, higher-grade and/or more extensive mineralization, and host rocks of higher initial porosity (i.e. fragmental units), suggesting an early Au-Ag mineralization controlled by volcanism-related hydrothermal activity. Cross-cutting field relationships, preliminary laser-ablation inductively coupled plasma mass spectrometry analyses (LA-ICP-MS) of pyrite grains, and U/Pb ID-TIMS zircon geochronology further support the hypothesis of a synvolcanic origin for at least part of the Au mineralization. Subsequent deformation and metamorphism are responsible for transposition of the mineralized zones and metals within the main foliation plane and the associated stretching lineation, and for the modification of the primary alteration mineralogy to its greenschist-facies metamorphic equivalent.

INTRODUCTION

The Rainy River project is an advanced exploration project located in western Ontario. It has measured and indicated resources of 177 million tonnes at 1.09 g/t Au and 2.6 g/t Ag, for a total of 6.2 Moz Au and 14.6 Moz Ag (New Gold Inc. website). Combined open pit and underground operations are planned, with lower cut-off criteria of 0.3–0.45 g/t Au and 2.5 g/t Au. In contrast to many conventional mining operations for Archean Au mineralization, such as orogenic greenstone-hosted quartz-carbonate veins or Au-rich VMS deposits, the "atypical" Rainy River has a large bulk tonnage. Wartman (2011) interpreted the mineralization at Rainy River to be an Archean analogue of a low-sulphidation epithermal deposit, such as those present worldwide in Phanerozoic volcanic belts.

As part of a federal-provincial-academia-industry collaborative geoscience program (TGI-4 program, Lode Gold project: Dubé et al., 2011), the Rainy River project was initiated in 2013 to better document and

Pelletier, M., Mercier-Langevin, P., Dubé, B., Crick, D., Tolman, J., McNicoll, V.J., Jackson, S.E., and Beakhouse, G.P., 2015. The Rainy River "atypical" Archean Au deposit, western Wabigoon Subprovince, Ontario, *In:* Targeted Geoscience Initiative 4: Contributions to the Understanding of Precambrian Lode Gold Deposits and Implications for Exploration, (ed.) B. Dubé and P. Mercier-Langevin; Geological Survey of Canada, Open File 7852, p. 193–207.

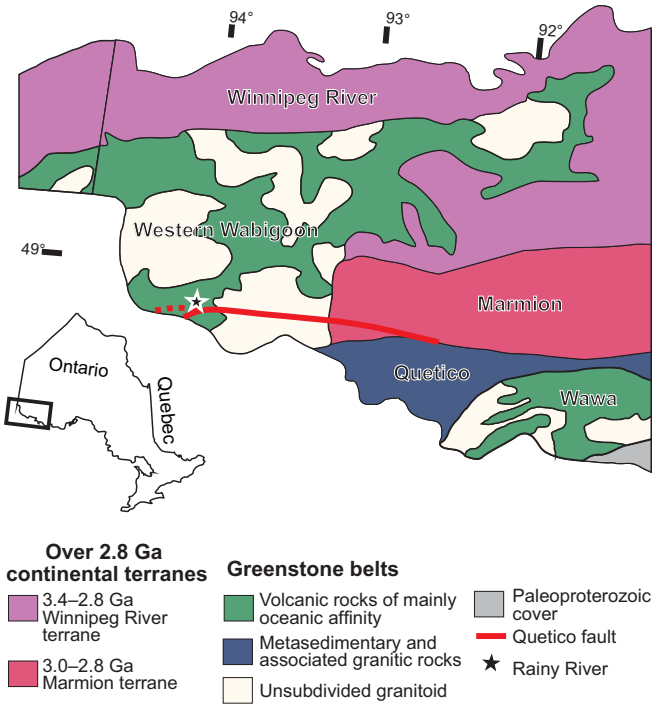

Figure 1. Regional geology of western Ontario, with emphasis on the western Wabigoon Subprovince. Adapted from (Percival, 2007).

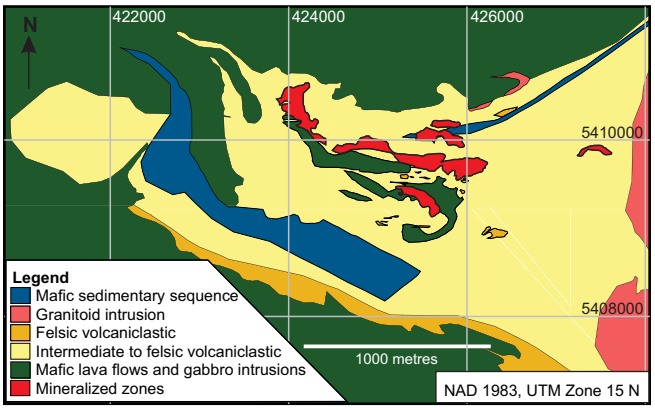

Figure 2. Geological map of the primary lithologies hosting the Rainy River deposit. Modified from a figure courtesy of New Gold Inc.

characterize this atypical Au system. The specific objectives at Rainy River were to identify key primary and secondary controls on Au mineralization as well as vectors to ore, with the intent to improve and update the exploration model for large volcanic-hosted Au deposits in the Superior Province. The current study builds on previous work by Wartman (2011) and Wartman et al. (2013), who characterized the volcanic setting and hydrothermal alteration at deposit scale.

This report presents preliminary findings of host volcanic facies at Rainy River, the metamorphosed hydrothermal alteration assemblages, geometry, and composition of the mineralized zones, and the deformation-related features and effects. A brief discussion on the relative timing of Au-bearing events is also presented, based on preliminary interpretations. This work is part of an ongoing Master's project by the lead author, M. Pelletier.

DESCRIPTION OF THE RAINY RIVER DEPOSIT

Geological Setting

The Rainy River project is located in the Archean Rainy River greenstone belt in the southern part of the western Wabigoon Subprovince (Fig. 1). This subprovince is bounded to the north by Meso-Archean, greenschist-facies, plutonic Winnipeg River terrane and, to the south, by the metasedimentary, amphibolite-facies Quetico Subprovince (Fig. 1). The western Wabigoon Subprovince is greenstone-dominated, with a restricted age span for submarine volcanism of 2745–2700 Ma (Percival et al., 2006) and with different geodynamic environments that include oceanic floor, plateau, island arc, and back-arc settings (Percival, 2007). Subsequent metaplutonic, mostly tonalitic rocks, crosscut the greenstone-dominated subprovince. Within the western part of the Wabigoon, structural elements reveal two major deformational events (D_1 and D_2), followed by late plutonism-related deformation (D_3) (Sanborn-Barrie, 1991; Percival et al., 2006; Percival, 2007).

On a local scale, the Rainy River project is located less than 5 km north of an east-trending fault, interpreted to be a splay of the domain-bounding Quetico fault (Fig. 1). This major fault is interpreted to be a subvertical shear zone with an overall dextral movement within a northwest-shortening transpressive regime (Davis et al., 1989; Fernández et al., 2013). The deposit is mainly hosted within an intermediate to felsic package, bounded to the north and south by mafic volcanic rocks of the Rainy River greenstone belt (Fig. 2). The Rainy River host sequence is cut by the Black Hawk quartz-monzonite stock located ~1–2 km east of the deposit (Wartman, 2011). The Black Hawk stock, which is affected by the main S_2 foliation, is dated at ca. 2698 Ma (New Gold Inc., unpublished data), whereas the volcanic rocks that host the Rainy River deposit are dated at approximately 2717 Ma (New Gold Inc., unpublished data). Greenschist-facies regional metamorphism affects all lithologies within the study area. Henceforth, the prefix "meta" is inferred in all succeeding descriptions. The area is characterized by up to 40 meters-thick glacial cover with very few exposed outcrops, especially proximal to the deposit area where information mostly comes from drill core.

Lithological Assemblages and Volcanic Facies

The Rainy River deposit is mainly hosted in felsic to

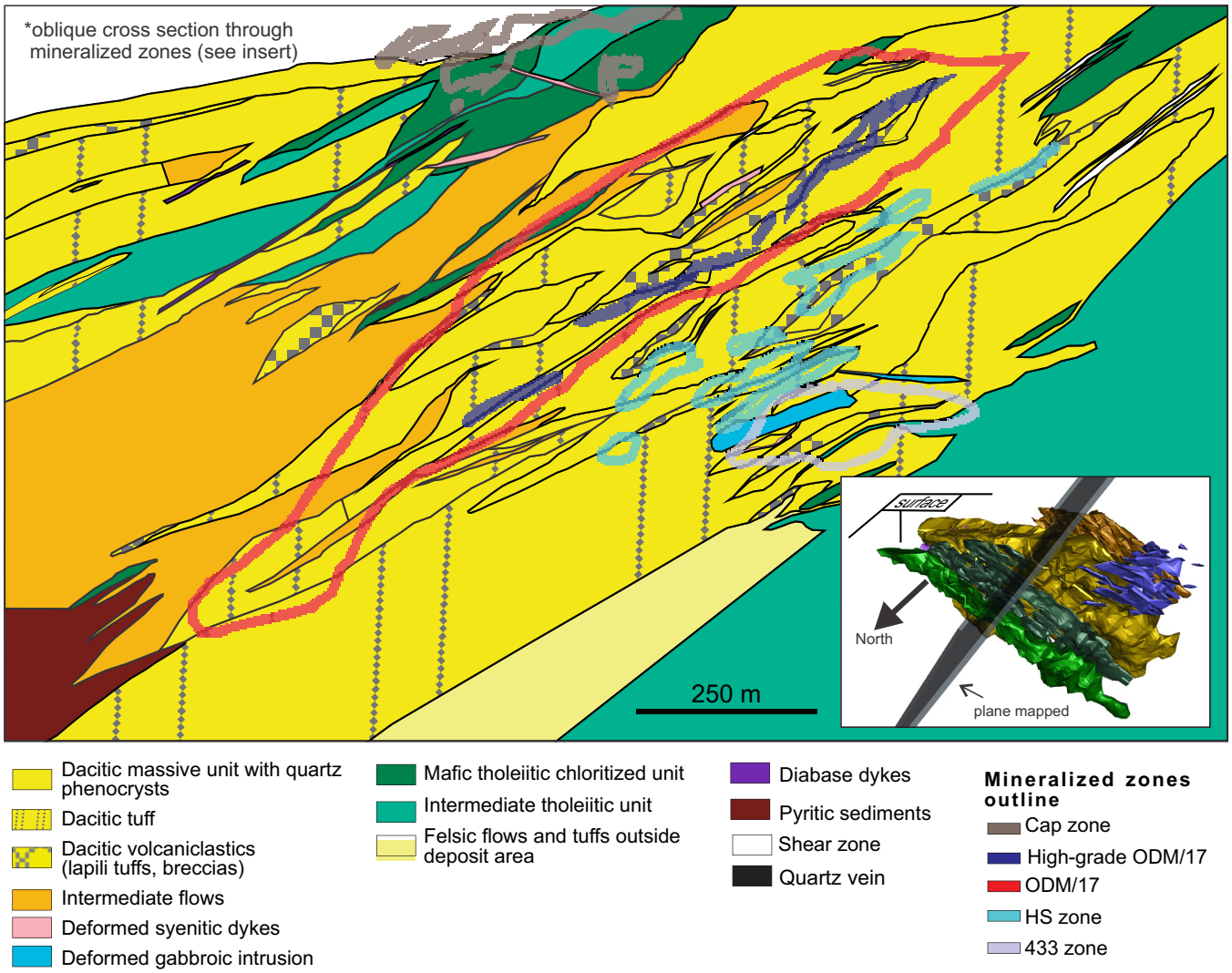

Figure 3. Preliminary geological map illustrating the distribution of the volcanic facies characterizing the dacitic units. This view represents an oblique section (323°/43°NE: Inset) that is perpendicular to the main foliation S_2 and stretching lineation L_2, both of which control mineralization. This map is based on drill-core observations and lithogeochemistry.

intermediate volcanic units in which, although overprinted by alteration and deformation of varying intensity, facies textures from massive (coherent) to volcaniclastic are still preserved (Wartman, 2011; Pelletier et al., 2014). Dacite and rhyodacite, which host the bulk of the deposit, have a distinct calc-alkaline affinity, though the basaltic to andesitic volcanic rocks, which bound the deposit to the north, west, and south (Figs. 2, 3), are of tholeiitic affinity (Wartman, 2011; Pelletier et al., 2014).

Outcrops of the structural footwall and hanging wall to the deposit were mapped in detail as part of this project and indicate an effusive intermediate to felsic volcanic environment of flows, domes, and associated volcaniclastic rocks (in situ and flow breccia) that formed in a subaqueous environment (Pelletier et al., 2014). An outcrop located in the structural footwall (north of the deposit) exposes well preserved flow bands (Fig. 4a) and transitional, curvilinear contacts between massive, amygdular flow units and monolithic to heterolithic, poorly sorted breccias (Fig. 4b). The breccia deposits contain disseminated, mostly matrix-controlled sulphide mineralization with anomalous Au values (0.1 g/t Au). These flows and associated breccias are also in sharp contact with pyrite-rich, mafic siliciclastic rocks. These sharp contacts are overprinted by the main S_2 foliation, indicating a pre main deformation control on their nature. The presence of flows and associated in situ flow breccia suggest a near-vent environment of deposition, whereas an outcrop mapped in the structural hanging wall (south of deposit) is characterized by a series of southward-younging, normally graded felsic tuff beds, possibly indicating a more distal position relative to the centre of effusive activity. On the same outcrop in the structural hanging wall, contact between the tuff beds and a porphyritic volcanic intrusion to the south is very irregular (Fig. 4c), characteristic of peperites that result

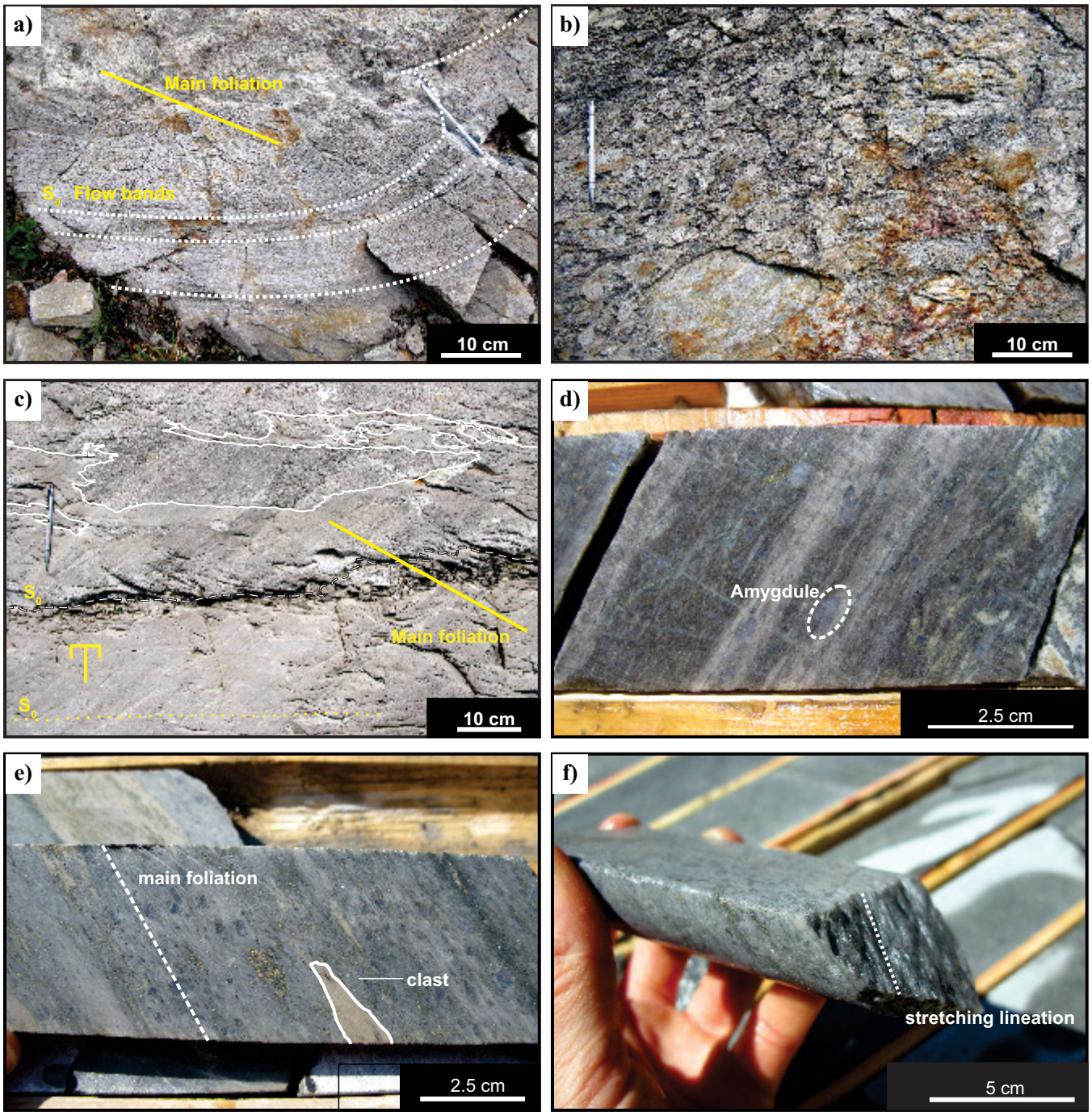

Figure 4. a) Flow bands (or flow foliations) in rhyodacite, with the main foliation (S_2) crosscutting the primary volcanic feature. **b)** Heterolithic, poorly sorted breccia with sulphide-bearing matrix and subangular clasts. **c)** Peperitic contact between a subaqueous synvolcanic sill or dyke (top of photo) and bedded tuff sequence (bottom of photo). **d)** Disseminated pyrite mineralization in a dacitic amygdular flow, with sericite and chlorite concentrated in millimetre- to centimetre-wide veinlets parallel to the main foliation plane. Sample from the ODM/17 zone. **e)** Disseminated granoblastic pyrite mineralization in heterolithic dacitic lapilli tuff from the HS zone. Clasts are flattened within the main foliation plane. **f)** Drill-core sample from the Cap zone structural hanging wall showing a well developed stretching lineation within the main foliation plane.

from the intrusion of lava into wet sediments (McPhie et al., 1993).

In addition to being noted in outcrop, primary volcanic textures were also observed in diamond-drill core (domes, lobes, and flow-breccia, e.g., Wartman, 2011; Pelletier et al., 2014). Massive felsic facies include aphanitic to strongly quartz ±plagioclase-phyric flow-banded lobes, amygdular flows, and flow breccia (Fig.4d) (Wartman et al., 2013; Pelletier et al., 2014). Primary plagioclase phenocrysts are only preserved in least-altered samples, and in all cases are partially replaced by sericite. Volcaniclastic rocks consist of

fine-grained to lapilli-sized, mainly monolithic fragmental units where clasts are flattened and stretched along the main S_2 foliation plane (Fig. 4e). Overall, similar volcanic facies were mapped at surface in the hanging wall and footwall of the deposit and in drill core from the immediate vicinity of the deposit.

Outside the deposit area, mafic units of tholeiitic affinity are mostly massive, with occasional pillowed textures (Wartman, 2011), indicating a subaqueous depositional environment for the volcanic sequences that hosts and surrounds the Rainy River deposit. The southernmost mineralized zone of the deposit, the Cap zone, is hosted in mafic volcanics. Variably altered and mineralized tholeiitic basalt intercalated with altered and mineralized dacitic to rhyodacitic flows are present in that area.

Deformation

Tectonic models generally regard the western Wabigoon as an oceanic terrane accreted to the Winnipeg River terrane during the Central Superior orogeny (Melnyk et al., 2006). This horizontal shortening event (D_1) generated north-trending upright F_1 folds. A subsequent deformation event (D_2) initiated transcurrent fault zones at the Quetico – western Wabigoon boundary, where the Rainy River project is located, resulting in a penetrative east-striking S_2 schistosity overprinting the D_1-related folds (Sanborn-Barrie, 1991; Percival et al., 2006). This steeply dipping S_2 foliation is the main penetrative fabric observed in the belt. Rare S_3 structures have been observed associated with the emplacement of relatively late intrusions (Sanborn-Barrie, 1991).

Up to five deformation events have been defined in the study area (e.g. Rankin, 2013). The main penetrative foliation, herein referred to as S_2, is oriented at 102°/51°SSW and is present in outcrop, diamond-drill core, and in thin section, (Figs. 4a, e). No clear evidence of an earlier tectonic fabric is present (or preserved) in the study area. A well developed stretching lineation (L_2: 225°/55°) is associated with the main S_2 foliation (Fig. 4f). This foliation is thought to result from a major north-south compression (Hrabi and Voss, 2010), or from an early east-verging thrusting and folding event superimposed by north-south shortening and east-southeast-trending upright folds (Rankin, 2013). The S_2 foliation and associated L_2 lineation have a strong influence on the current geometry of the mineralized zones.

The main S_2 foliation is characterized by discrete to extensive bands of aligned sericite ±chlorite, anastomosing around less altered clasts in volcaniclastic units. Deformation intensity is mostly dependent on alteration intensity; hence the presence of high-strain corridors focused in intensely altered rocks. Weakly developed interpreted C-S fabric (in unoriented drill core) is developed in areas of greater deformation, mainly within the HS zone. Late kink bands are common in the immediate hanging wall of the ODM zone.

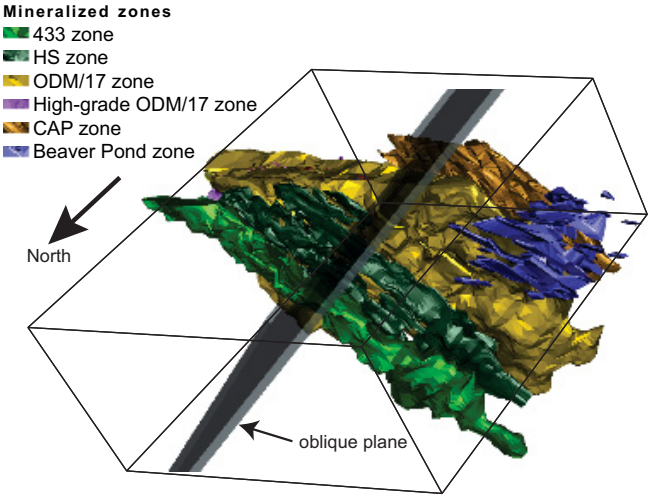

Figure 5. Three-dimensional view of the mineralized zones comprising the Rainy River deposit, with the oblique plane crosscutting the main mineralized zones at the predicted open-pit mining depth and perpendicular to the measured stretching lineation (L_2). View is looking east-southeast (mineralized zones dip 55° towards 192°N). Modified from a figure courtesy of New Gold Inc.

Brittle fractures with a sinistral movement, oriented at 195°/75°NW, crosscut the main fabric and are present in both drill core (unoriented) and outcrop. This late deformation offsets the mineralized zones at the metre scale, but does not seem to have generated any remobilization.

Mineralized Zones

Mineralization is distributed within a series of four main zones, which are, from north to south, the 433, HS, ODM/17, and Cap zones (Figs. 2, 5). They occur in a series of stacked bodies, all subparallel to the main east-west-trending, moderately south-dipping S_2 foliation (102°/51°SSW) (Figs. 2, 5). High-grade ore shoots within these zones are elongated subparallel to a southwest-plunging lineation (225°/55°) and contained within the main foliation plane. In addition, the Beaver Pond and Intrepid zones are satellites to the four main mineralized zones, flanking the ODM/17 zone respectively to the east and west.

The ODM/17, HS, and 433 zones are hosted by calc-alkaline dacite flows, tuffs and lapilli tuffs. The largest and richest mineralized zone on the Rainy River project is the ODM/17 zone; it is continuous over 1000 m along strike, can be up to 250 m thick, and extends from surface to a depth of ≥1000 m (Figs. 2, 3, 5). The HS zone defines a discontinuous, mainly low-grade zone with overprinting chlorite and an overall higher degree of sericitization and strain than the ODM/17

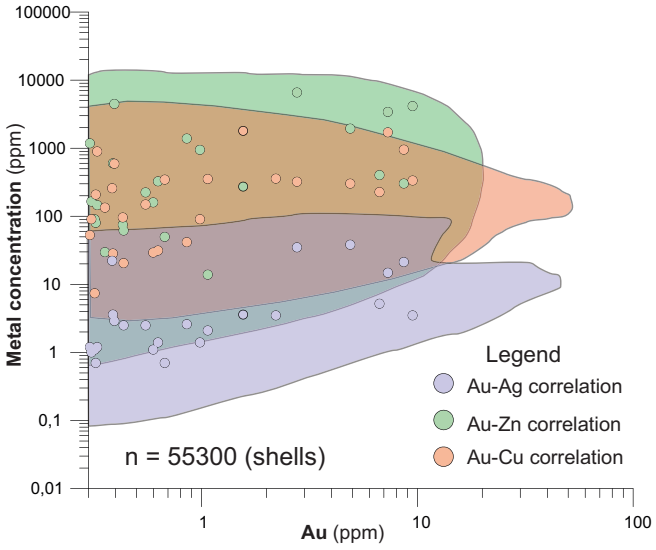

Figure 6. Scatter plot showing the correlation between Au (100 ppm > Au ≥0.3 ppm only) and Ag, Zn, and Cu. Data from New Gold inc. (n = 55,300) and this study (n = 27).

zone. Mineralization in the 433 zone is generally of higher grade than the ODM/17 zone, and has a more continuous and homogenous shape than the HS zone. The Cap zone is the only ore zone that is mainly hosted in tholeiitic basaltic-andesitic rocks.

The Rainy River deposit is characterized by a strong Au and Ag endowment in comparison to its base metal content. At the deposit scale, Au shows good affinity with Cu, Ag, and, to a lesser extent, Zn (Fig. 6). Zinc content greater than 0.7 ppm and/or Cu values greater than 3 ppm in the host rock are good indicators of the presence of Au and Ag.

The main Au zones are characterized by abundant disseminated auriferous pyrite (≤10 vol.%) and lesser sphalerite. Pyrite is flattened in the main S_2 foliation plane and it is commonly granoblastic (Figs. 4e, 7a, b, 8). Pyrite crystals are commonly characterized by complex zoning, usually with an early, inclusion-rich core and a later inclusion-free corona. The latter is probably the result of metamorphic recrystallization. Inclusions in pyrite consist primarily of chalcopyrite, which is also observed filling fractures in pyrite grains. This chalcopyrite fracture-filling is interpreted as late remobilization in low-strain zones (Fig. 8). A long list of trace elements is preferentially associated with the early pyrite phase (e.g. Cu, Zn, As, Ag, In, Sn Sb, Au, Pb: Fig. 8), whereas the recrystallized part has much lower trace element contents, usually with distinct Ni, Co, and Bi growth zones (Fig. 8).

Within the 4 main zones, Au and Ag also occur in pyrite-sphalerite-chalcopyrite±galena veinlets and veins, which are subparallel to the main S_2 foliation plane (Fig. 7c). Generally, these veinlets and veins are associated with higher precious metal values than the disseminated auriferous pyrite. The sphalerite in these veinlets varies in colour, but is generally yellowish, suggesting a high Zn/Fe ratio. In thin section, these polymetallic veinlets show a zonation with sulphides of lower ductility systematically rimmed by sulphides of increasing ductility; i.e., pyrite cores are successively rimmed by sphalerite, chalcopyrite, and finally galena. This zonation, based on variations in physical properties, is interpreted to be the result of partial remobilization during the main deformation and metamorphism event that affected the area.

Electrum, with variable Au content, is locally present within the main orebody (ODM/17 zone), especially in less than 100 m-wide, high-grade cigar-shaped zones oriented parallel to the stretching lineation and flattened within the main S_2 foliation plane (see the high-grade ODM/17 zone in Figs. 3, 5). It occurs in deformed sulphide-bearing veinlets and in folded quartz-Fe carbonate-tourmaline veins (Fig. 7d). These veinlets and veins are transposed within the main foliation plane, suggesting that they formed pre- to syn-main deformation. Furthermore, some diamond-drill core intercepts contain deformed electrum-bearing sulphide veins, which are crosscut by later deformed quartz-tourmaline veins (Fig. 7d). This basic crosscutting relationship suggests an early, pre-main-phase deformation, Au-precipitation event in host rocks that have undergone polyphase deformation. Such an interpretation is in agreement with the trace element distribution in the early pyrite. Gold-rich electrum is also present in brittle fractures (Fig. 7e), which is interpreted as the result of late, local remobilization of Au.

Figure 7 (opposite page). a) Ultrafine rutile dusting (pinkish hue) in tholeiitic-affinity andesite with granoblastic pyrite mineralization associated with deformed chlorite veins. Sample from the 433 zone. **b)** Deformed pyrite, sphalerite, and carbonate veinlets from the tholeiitic-affinity basalt of the Cap zone. **c)** Sphalerite, chalcopyrite, and galena stockwork veinlets flattened and transposed within the main foliation plane and associated with a deformed quartz-calcite-chlorite vein. Sample from the ODM/17 zone. **d)** Early, Au-bearing, deformed veinlet crosscut by a later quartz-tourmaline vein, which is also deformed, demonstrating an early gold-mineralization event followed by at least two deformation events. **e)** Visible gold locally remobilized within a late brittle fracture. **f)** Photomicrograph of a sericite-altered rhyodacitic lapilli tuff showing a pervasive foliation affecting white mica grains, with coarser grained chlorite overprinting the fabric. **g)** Photomicrograph of a spessartine garnet (25–28 wt% MnO) in a chlorite-sericite matrix. Sample from the ODM/17 zone. **h)** Photomicrograph of chloritoid minerals with bowtie texture and kyanite grains from the aluminosilicate-rich alteration zone within the ODM/17 mineralized body. Abbreviations: Au = gold, Chl = chlorite, Chld = chloritoid, Ky = kyanite, Py = pyrite, Qz = quartz, Sph = sphalerite, Tl = tourmaline.

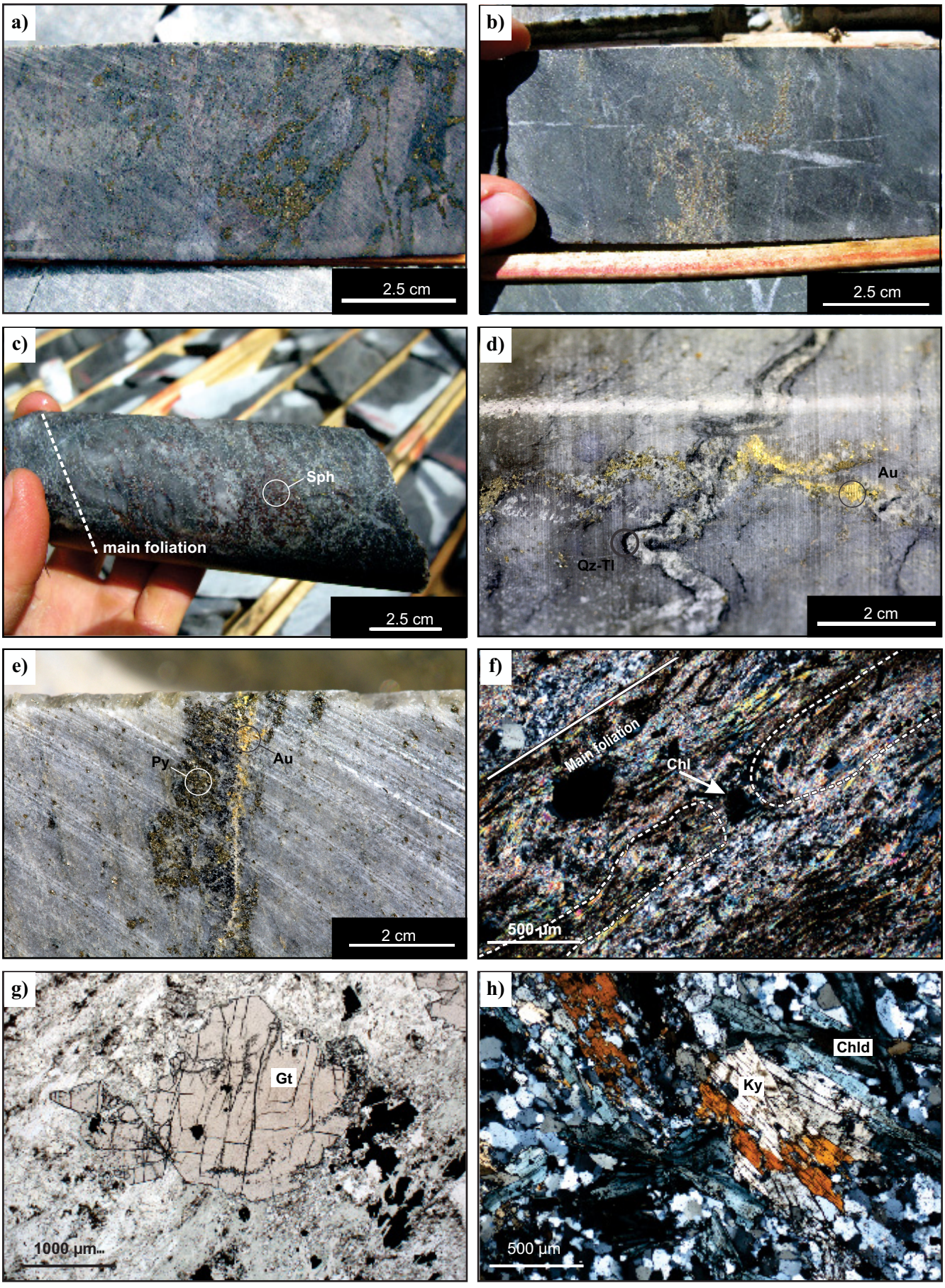
a)
2.5 cm
b)
2.5 cm
c)
Sph
main foliation
2.5 cm
d)
Au
Qz-Tl
2 cm
e)
Py
Au
2 cm
f)
Main foliation
Chl
500 µm
g)
Gt
1000 µm
h)
Chld
Ky
500 µm

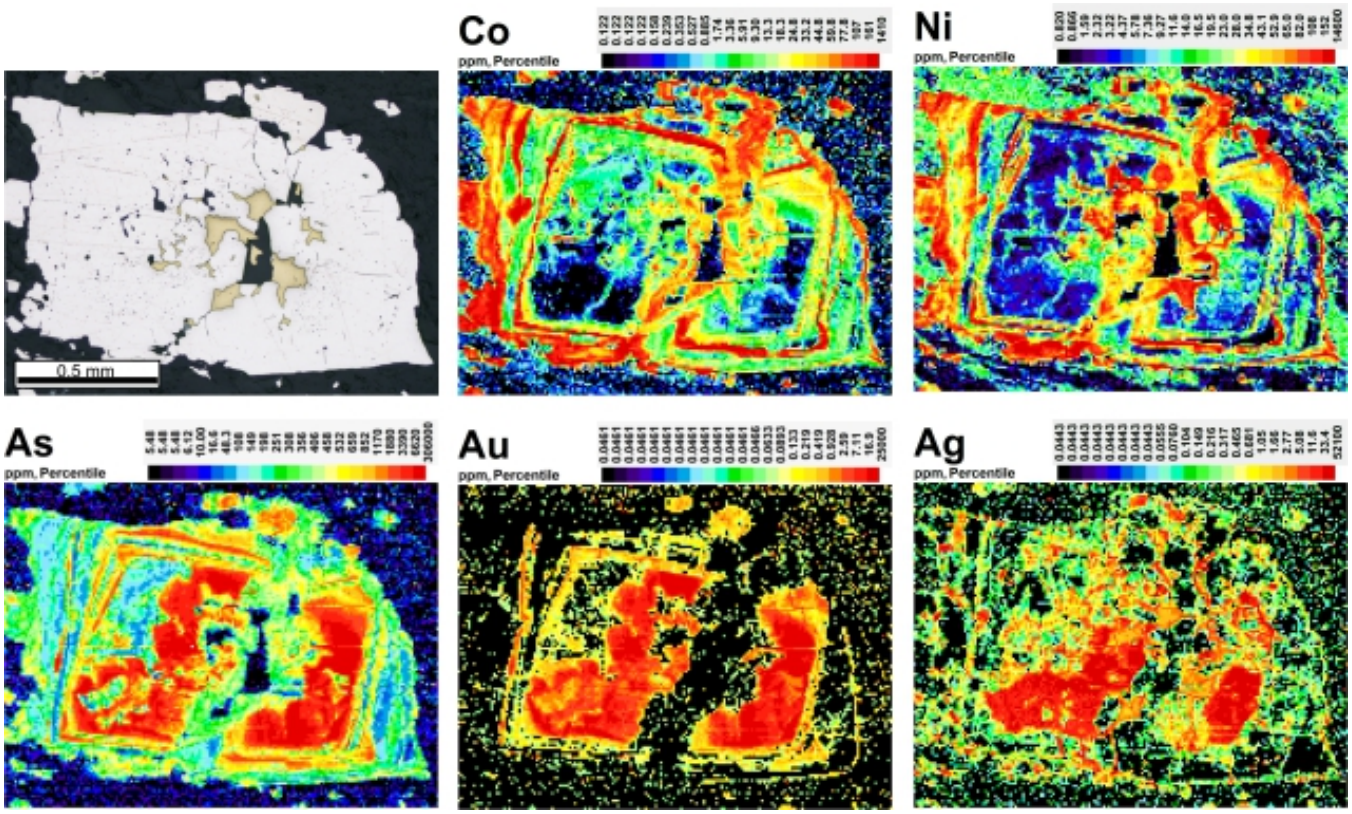

Figure 8. LA-ICP-MS element concentration maps (ppm) of a partly recrystallized pyrite grain from the ODM zone.

Alteration

The metamorphosed hydrothermal alteration assemblages associated with the Rainy River deposit were first described by Wartman (2011). Additional mineral phases have been documented in the current study, including kyanite and chloritoid, which suggests possible local zones of pre-metamorphism, advanced argillic-style alteration. When plotted on an alteration box plot (Large et al., 2001), the samples follow trends typical of VMS-related hydrothermal systems (Fig. 9). Most mineralized, calc-alkaline affinity samples (Fig. 9: represented by a star symbol), are located near the most altered ends of the muscovite, sericite+chlorite+pyrite, and sericite trends, and the most mineralized, tholeiitic affinity samples trend towards the ankerite and chlorite poles (Fig. 9).

Sericite Alteration

Sericite is ubiquitous throughout the deposit and represents the principal alteration mineral. Preliminary electron microprobe analyses indicate that most white mica (sericite) consists of muscovite. The sericite-dominated alteration seems to be better developed in volcaniclastic facies within the host dacite complex, suggesting a distribution controlled by primary composition of the protolith and porosity in the host rocks. Furthermore, drill core indicates that the spatial extent of the main mineralized body (ODM/17) is correlated with the spa-

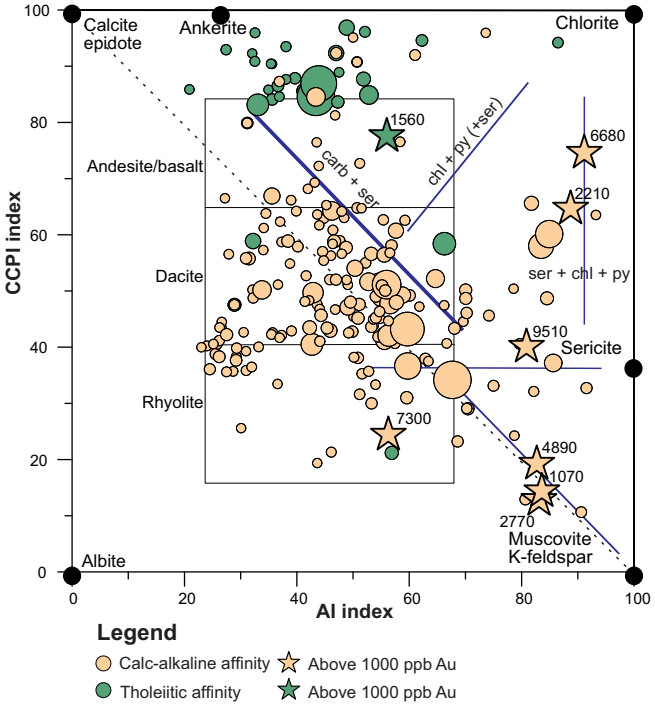

Figure 9. Alteration box plot (Large et al., 2001) with samples (n = 233) from this study sorted according to their magmatic affinity. Circle sizes are proportional to the Au content from 0 to 1 ppm. Ishikawa alteration index (AI) = $100(K_2O+MgO))/(K_2O+MgO+Na_2O+CaO)$. Chlorite-carbonate-pyrite index (CCPI) = $100(Mg+FeO)/(MgO+FeO+Na_2O+K_2O)$.

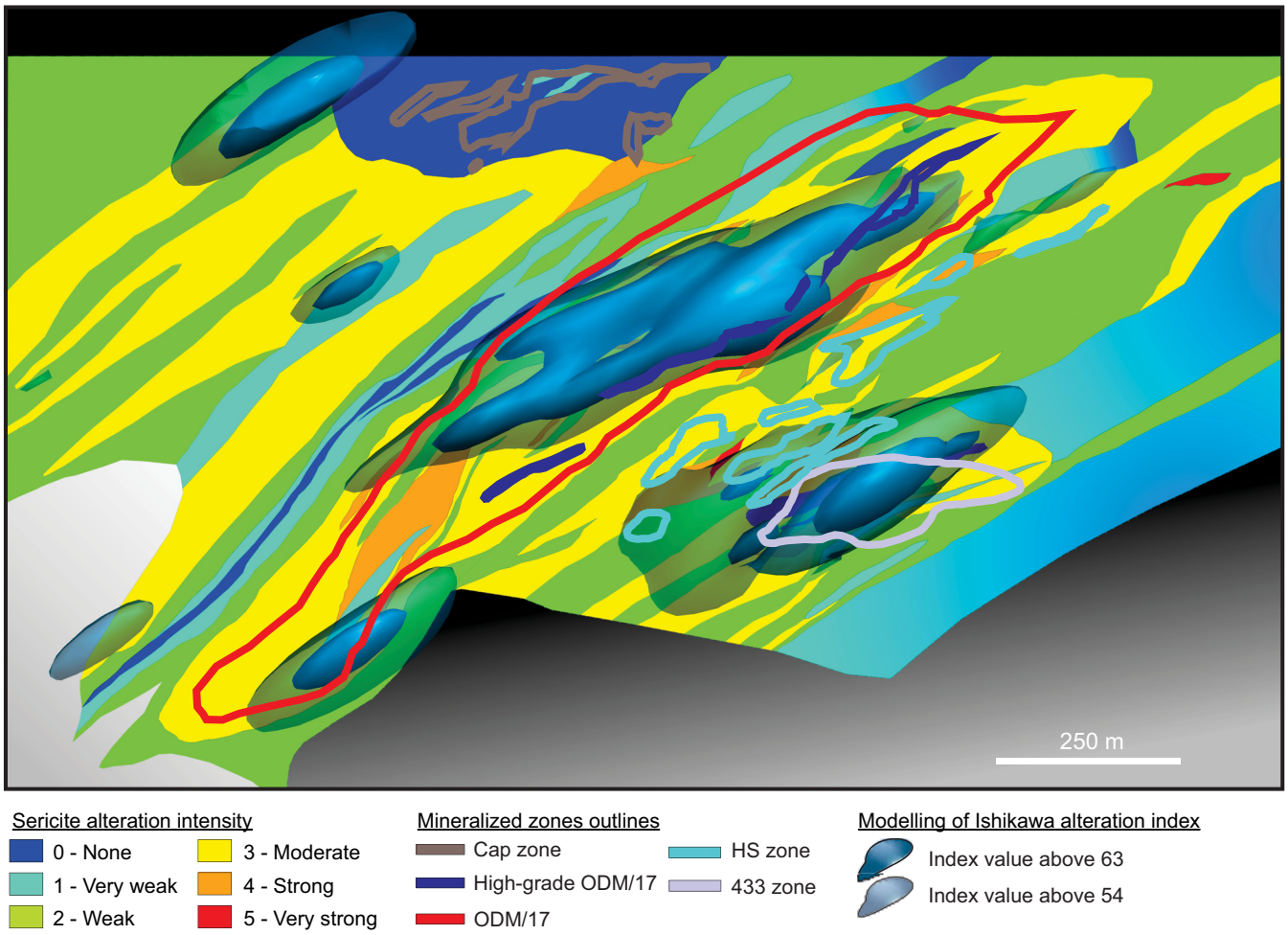

Figure 10. Implicit 3-D model of the distribution in space and intensity of the Ishikawa alteration index (AI = 100(K_2O+MgO))/(K_2O+MgO+Na_2O+CaO) plotted on the sericite-alteration intensity oblique map generated from visual observations of drill-core intercepts. This oblique plane is oriented 323°/43°NE and perpendicularly crosscuts the stretching lineation measured within the deposit. The outline of the main mineralized zones is also traced on the map. Implicit modelling was made with Leapfrog Mining© software (version 2.5.3.61) using lithogeochemical data from drill-core samples. It is constrained by the main stretching lineation trend (225°/55°). The outer shells correspond to a cut-off AI value of 54, the highest grade shell to a value of 63.

tial extent of a zone of well developed, pervasive to texturally destructive sericite alteration in the host dacite (Fig. 10), underpinning the role of hydrothermal processes in the generation of mineralized zones.

In the coherent dacite (lobes and/or domes), sericitization occurs as sparse to abundant bands and veinlets, with mica grains defining the main S_2 foliation plane (Fig. 7f). In addition, sericite partially to completely replaces relict feldspar phenocrysts. Fragmental facies composed of breccia and tuff show a similar distribution of sericite minerals, with the particularity of having sericite bands wrapping around more competent lapilli and clasts (Fig. 4e). In other cases where the lapilli and clasts were more prone to alteration, they are entirely replaced by sericite.

An implicit 3-D model of the distribution and intensity of the alteration index (AI = 100*(K_2O+MgO)/(K_2O+MgO+Na_2O+CaO: Ishikawa et al., 1976) was generated with Leapfrog Mining© software (version 2.5.3.61) using lithogeochemical data from drill-core samples (Fig. 10). Constrained by the main stretching lineation trend, this model further demonstrates the correlation between the main mineralized zones hosted in dacite and a zone with high AI values, plausibly caused by major replacement of volcanic glass and sodic plagioclase by sericite and chlorite.

Chlorite Alteration

Chlorite is the second most common mineral present in the alteration zones at the Rainy River deposit (Wartman, 2011). It is commonly associated with disseminated pyrite and quartz-carbonate veins and its abundance varies between 1 and 10% of the host rock, unlike sericite that can compose up to 65% of the rock. Chlorite can be observed rimming disseminated pyrite grains, or in very fine (≤1 mm) veinlets and rare ≤1 cm veins, both parallel to the main S_2 foliation. Replacement of relict feldspar phenocrysts with unori-

ented chlorite grains is locally present. Chlorite is generally coarser than sericite and tends to overprint an apparently earlier, more pervasive, sericite alteration (Fig. 7f). Chlorite distribution extends to most of the deposit, without displaying any specific zonation. Preliminary electron microprobe data reveal an Mg-rich tendency for chlorite throughout the deposit, with an additional population of Fe-rich chlorite restricted to the mafic rocks.

Sericite-Carbonate Alteration

Located within the ODM/17 zone is an area of sericite-carbonate alteration. Although this alteration assemblage is present elsewhere in the deposit, it is most continuous and strongest within the dacite-hosted main mineralized body. Chlorite is rare to absent in this alteration assemblage. The sericite-carbonate alteration is restricted to mineralized areas of the deposit and as such is commonly associated with veinlets or dissemination of pyrite, sphalerite, and chalcopyrite. Carbonate minerals are mainly Fe- to Mg-rich, although further work is underway to investigate a potential spatial zonation. Carbonate occurs as blebs or grains disseminated in the matrix, as very fine veinlets and, less commonly, as folded veins. In all cases, these carbonate is transposed within the main foliation plane.

Manganese-Rich Garnet Zone

Manganiferous garnet (spessartine: $Mn_3Al_2(SiO_4)_3$) is found sporadically as discontinuous small zones within dacite of the ODM/17, but mostly in a sliver-shaped zone in the immediate structural hanging wall of the ODM/17 zone (Fig. 7g). The garnet grains have a relatively homogenous major element composition and individual grains do not exceed 5 mm in size. The spessartine garnet zone is sericite- and chlorite-bearing, and garnet does not exceed 2 vol.% of the rock.

Kyanite-Chloritoid Zone

Slivers of kyanite, chloritoid and quartz, which are less than 25 m long and 2 m wide, occur within the ODM/17 zone. This assemblage, although well preserved, is very fine-grained (Fig. 7h). In other Archean synvolcanic (e.g. Headway-Coulee prospect: Osterberg et al., 1987) and hydrothermal-related deposits, such aluminosilicate zones, are interpreted as a metamorphic analogue to modern-day advanced argillic alteration assemblages found in hydrothermal activity zones characterized by low-pH fluids (e.g. Bousquet 2-Dumagami and LaRonde Penna Au-rich VMS deposit: Dubé et al., 2007b, 2014; Mercier-Langevin et al., 2007).

Rutile Zone

A <40 m-wide zone, located between the HS and 433 zones, is characterized by a very fine and pervasive rutile dusting. More patchy intervals are also present within the 433 zone associated with boudinaged pyrite, chalcopyrite, and chlorite veins that are folded and transposed within the main foliation (Fig. 7a). These rutile-altered rocks display a characteristic orange to pink hue, which is easily identified when logging (Fig. 7a). Rutile and titanite also occur in trace amounts in the dacite host rocks of the ODM/17 zone and can only be observed in thin section. Further work is underway to characterize the spatial distribution of these titanium oxides within the main mineralized body.

U-Pb Zircon Geochronology

Four samples were collected for high-precision U-Pb ID-TIMS zircon geochronology to further constrain the timing of magmatic and hydrothermal events. Samples from the host dacite and intrusive rocks were collected, as well as samples from an unaltered but deformed dyke that cuts the mineralization in the 433 zone. Preliminary results gave back an age of 2693 Ma for the dyke and 2716 Ma for the host dacite, constraining the main deformation to between >2716 and 2693 Ma, and the mineralization to >2693 Ma. These results also indicate that the host succession was emplaced at approximately 2716 Ma (including synvolcanic intrusions). More work is underway to refine these ages and the implications for the timing of events at Rainy River.

DISCUSSION

The Rainy River deposit is hosted in a calc-alkaline dacite to rhyodacite complex, bounded by geochemically distinct tholeiitic, intermediate to mafic volcanic and associated siliciclastic rocks of the western Wabigoon Subprovince. The current geometry of the mineralized zones is largely controlled by the main S_2 foliation and associated L_2 stretching lineation, but the presence of mineralization seems to be attributed to a pre-main-phase deformation fertile hydrothermal system. This is supported by a semi-conformable pervasive sericite-dominated alteration assemblage preferentially developed in fragmental rocks around the main ODM/17 mineralized zone, independent of strain distribution at property scale. However, with a stacking of relatively thick ore zones within a relatively compact felsic-intermediate volcanic centre, the geometry of the entire deposit does not appear to be solely controlled by the main deformation. Gold mineralization concentrated in primary generations of pyrite also reinforces the scenario of an early origin for at least part of the Au at the Rainy River deposit. Uranium-Pb geochronology results and crosscutting relationships are in agreement with an early hydrothermal system (≤2716 Ma and ≥2693 Ma). This interpretation is also in agreement with previous studies that interpret the Rainy River deposit as a syngenetic Au system (i.e. low-sulphida-

tion epithermal-style system: Wartman, 2011; Wartman et al., 2013). However, all evidence suggests that the deposit was formed in a subaqueous setting, and the bulk of the mineralization consists of disseminated pyrite ±sphalerite in a very large sericite-dominated alteration halo rather than an organized colloform-crustiform low-sulphidation-style vein system with fracture-controlled alteration, as would be expected for a low-sulphidation deposit *sensu stricto*. It is premature to propose a specific genetic model, but current work and geological features suggest that the Rainy River deposit is an atypical, pre-main-phase deformation Au deposit formed by a hydrothermal system similar to the ones involved in other known Archean VMS systems (e.g. LaRonde Penna, Westwood, Bousquet 1 deposits). There are possible analogues to Rainy River elsewhere in the Wabigoon Subprovince (e.g. Headway-Coulee prospect) and in the Superior Province (e.g. Bousquet district).

IMPLICATIONS FOR EXPLORATION

The specific characteristics of the 6 Moz Au, "atypical" bulk-tonnage Au mineralization at the Rainy River should be included in updated exploration model for Au deposits in the Superior Province. The updates to the exploration model would include incorporating geological characteristics and signatures previously documented for Archean Au-rich volcanogenic massive sulphide deposits (e.g. Morton and Franklin, 1987; Dubé et al., 2007a; Mercier-Langevin et al., 2007, 2011), although it would target mineralization with higher tonnage and high ratios of Au (ppm) to base metal (wt%).

Sericite-altered calc-alkalic dacite domes, flows, and flow breccia, bounded by tholeiitic mafic to intermediate volcanic rocks could define an exploration target for deposits similar to Rainy River. Another good indicator to mineralization at Rainy River, which could help further define future exploration targets, is the presence of alteration minerals such as Fe- to Mg-rich carbonate minerals, spessartine garnet, rutile, and aluminosilicate minerals, including chloritoid.

Though the Rainy River project can be considered as a large-tonnage and "low-grade"-style operation, it differs from many other "large-tonnage, low-grade"-style Au deposits recently discovered or put into production in the Superior Province, such as Côté Gold, Hammond Reef, Canadian Malartic, and Troilus, which implies that exploration strategies cannot be universally applied to such types of deposits. The ~10 Moz Hammond Reef deposit consists of a low-sulphide, syn-deformation quartz stockwork-type Au mineralization associated with shallowly dipping, anastomosed shear zones that crosscut the dominantly tonalitic Marmion batholith north of the Quetico fault, contrasting with the sulphide-associated Au at Rainy River. The ~7.6 Moz Au Côté Gold deposit is hosted in a calc-alkaline diorite-tonalite intrusive complex in the Swayze belt. The Coté Gold deposit is associated with a magmatic-hydrothermal breccia and Au±Cu mineralization that consists mainly of finely disseminated pyrite and chalcopyrite (±veins), this mineralization being considered syngenetic (Katz et al., 2014). This mineralization style contrasts with the volcanic host succession and the Au±Zn-Ag-Cu association at Rainy River. The ~10 Moz Au Canadian Malartic deposit consists of very finely disseminated auriferous pyrite and quartz-carbonate-pyrite veinlets and veins hosted in metagreywacke of the Pontiac Subprovince and late monzonitic porphyritic intrusions just south of the Cadillac-Larder Lake fault zone. The mineralization at Canadian Malartic is associated with potassic (biotite and potassium feldspar) and carbonate alteration zones and is considered as orogenic, with possible input from intrusions (de Souza et al., 2014, 2015), which again contrasts with the inferred early timing, volcanic setting, sericite-dominated alteration, and Au-base metal association at Rainy River. The ~2 Moz Au Troilus deposit in the Frotet-Evans belt is hosted in a calc-alkaline dioritic intrusion and is associated with a magmatic-hydrothermal pseudo-breccia that consists of early albitization crosscut by potassic alteration; the Au-Cu mineralization consists mainly of finely disseminated pyrite and chalcopyrite (±veins) and is interpreted as a reduced porphyry-style system (Rowins, 2011). This deposit is also in contrast to the volcanic setting and the Au±Zn-Ag-Cu association at Rainy River. The Mount Lyell mining district in Tasmania, hosted in the Cambrian Mount Read Volcanics, is a good example of a "large tonnage-low grade"-style Au deposit formed in the VMS environment. In this Cu-Au±Pb-Zn system, the bulk of the Cu-Au mineralization occurs as disseminated chalcopyrite-pyrite-bornite ore bodies associated with a >6 km-long pervasive sericite-chlorite-pyrite-silica alteration zone. Minor Pb-Zn-rich massive sulphide and limestone lenses characterize the exhalative zone above the Cu-rich orebodies and represent the upper part of an inferred hybrid magmatic-seawater system (Corbett et al., 2001). At Rainy River, the high Au/base metal ratio and the presence of both Cu and Zn mineralization within the main sericite-dominated alteration zone contrast with the Pb-Zn and Cu zonation at Mount Lyell.

FUTURE WORK

Current and future work will focus on analyzing the effects of structural deformation and hydrothermal activity on the distribution and grades of mineralization. In addition, sulphide chemistry, Cu and Zn isotopes, whole-rock oxygen isotope mapping, and U/Pb geochronology will help better define mineralization

style and timing, providing key tools to improve genetic and exploration models for similar "atypical" Archean Au systems at various scales.

ACKNOWLEDGEMENTS

The authors would like to express their sincere gratitude to New Gold Inc. for financial support, access to the property and samples, and for the authorization to publish. This research activity is part of an ongoing M.Sc. candidacy being undertaken by the lead author (M. Pelletier) at the Institut national de la recherche scientifque, centre Eau Terre Environnement (INRS-ETE). Additional support is provided to M. Pelletier through an Industrial Innovation Scholarship offered jointly by the Natural Sciences and Engineering Research Council of Canada (NSERC), Fonds de recherche du Québec- Nature et technologies (FRQNT), and New Gold Inc.

The authors would like to thank Darrell Hyde, Jason Pattison, Marilyn Rousseau, Amy Shute, and the Rainy River project staff for their precious help on site. We also want to thank George Hudak and Howard Poulsen for discussions on the geology and setting of the Rainy River deposit, and Alan Galley for his review of the manuscript.

REFERENCES

Corbett, K.D., 2011. New mapping and interpretations of the Mount Lyell mining district, Tasmania: a large hybrid Cu-Au system with an exhalative Pb-Zn top; Economic Geology, v. 96, p. 1089–1122.

Davis, D.W., Poulsen, H.K., and Kamo, S.L., 1989. New insights into Archean crustal development from geochronology in the Rainy Lake area, Superior Province, Canada; Journal of Geology, v. 97, p. 379–398.

De Souza, S., Dubé, B., McNicoll, V., Dupuis, C., Mercier-Langevin, P., and Creaser, R., 2014. Fracture-controlled hydrothermal alteration at the Canadian Malartic deposit: Toward a multi-phase model for Archean intrusion-related low-grade bulk tonnage gold deposits, *In:* Abstracts; Geological Association of Canada – Mineralogical Association of Canada Joint Annual Meeting, Fredericton, New Brunswick, May 2014, v. 37, p. 70.

De Souza, S., Dubé, B., McNicoll, V.J., Dupuis, C., Mercier-Langevin, P., Creaser, R.A., and Kjarsgaard, I.M., 2015. Geology, hydrothermal alteration, and genesis of the world-class Canadian Malartic stockwork-disseminated Archean gold deposit, Abitibi, Quebec, *In:* Targeted Geoscience Initiative 4: Contributions to the Understanding of Precambrian Lode Gold Deposits and Implications for Exploration, (ed.) B. Dubé and P. Mercier-Langevin; Geological Survey of Canada, Open File 7852, p. 113–126.

Dubé, B., Gosselin, P., Mercier-Langevin, P., Hannington, M., and Galley, A.G., 2007a. Gold-rich volcanogenic massive sulphide deposits, *In:* Mineral Deposits of Canada: A Synthesis of Major Deposit Types, District Metallogeny, the Evolution of Geological Provinces, and Exploration Methods, (ed.) W.D. Goodfellow; Geological Association of Canada, Mineral Deposits Division, Special Publication 5 p. 75–94.

Dubé, B., Mercier-Langevin, P., Hannington, M.D., Lafrance, B., Gosselin, P., and Gosselin, G., 2007b. The LaRonde Penna giant gold-rich volcanogenic massive sulfide deposit, Abitibi, Quebec: alteration footprint, genesis and implications for exploration; Economic Geology, v. 102, p. 633–666.

Dubé, B., Mercier-Langevin, P., Castonguay, S., McNicoll, V.J., Pehrsson, S.J., Bleeker, W., Schetwelaar, E.M., and Jackson, S., 2011. 38. Targeted Geoscience Initiative 4. Lode gold deposits in ancient, deformed and metamorphosed terranes - footprints and exploration implications: a preliminary overview of themes, objectives and targeted areas: Ontario Geological Survey, Open File Report 6272, p. 38-1 to 38-10.

Dubé, B., Mercier-Langevin, P., Kjarsgaard, I., Hannington, M., Bécu, V., Côté, J., Moorhead, J., Legault, M., and Bédard, N., 2014. The Bousquet 2-Dumagami World-Class Archean Au-Rich Volcanogenic Massive Sulfide Deposit, Abitibi, Quebec: Metamorphosed Submarine Advanced Argillic Alteration Footprint and Genesis; Economic Geology, v. 109, p. 121–166.

Fernández, C., Czeck, D.M., and Díaz-Azpiroz, M., 2013. Testing the model of oblique transpression with oblique extrusion in two natural cases: Steps and consequences; Journal of Structural Geology, v. 54, p. 85–102.

Hrabi, B. and Voss, I., 2010. Rainy River structural study, interim results - northwestern Ontario; SRK consulting Inc. confidential report to Rainy River Resources Ltd., unpublished report.

Ishikawa, Y., Sawaguchi, T., Iwaya, S., and Horiuchi, M., 1976. Delineation of prospecting targets for Kuroko deposits based on modes of volcanism of underlying dacite and alteration haloes; Mining Geology, v. 26, p. 12.

Katz, L.R., Kontak, D.J., Dubé, B., Rogers, J.R., McNicoll, V., and Creaser, R.A., 2014. The Archean Côté Gold intrusion-related Au-(Cu) deposit, Ontario, Canada: A large-tonnage, low-grade deposit centred on a magmatic-hydrothermal breccia, *In:* Abstracts; Geological Association of Canada - Mineralogical Association of Canada Joint Annual Meeting, Fredericton, May 2014, v. 37, p. 133–134.

Large, R.R., Gemmell, J.B., Paulick, H., and Huston, D.L., 2001. The Alteration Box Plot: A simple approach to understanding the relationship between alteration mineralogy and lithogeochemistry associated with volcanic-hosted massive sulfide deposits; Economic Geology, v. 96, p. 957–971.

McPhie, J., Doyle, M., and Allen, R.L., 1993. Volcanic Textures: A guide to the interpretation of textures in volcanic rocks; ARC Centre of Excellence in Ore Deposits, University of Tasmania, 197 p.

Melnyk, M., Davis, D.W., Cruden, A.R., and Stern, R.A., 2006. U-Pb ages constraining structural development of an Archean terrane boundary in the Lake of the Woods area, western Superior Province, Canada; Canadian Journal of Earth Sciences, v. 43, p. 967–993.

Mercier-Langevin, P., Dubé, B., Lafrance, B., Hannington, M., Galley, A.G., Moorhead, J., and Gosselin, P., 2007. Metallogeny of the Doyon-Bousquet-LaRonde mining camp, Abitibi greenstone belt, Quebec, *In:* Mineral Deposits of Canada: A Synthesis of Major Deposit Types, District Metallogeny, the Evolution of Geological Provinces, and Exploration Methods, (ed.) W.D. Goodfellow; Geological Association of Canada, Mineral Deposits Division, Special Publication 5, p. 673–701.

Mercier-Langevin, P., Hannington, M.D., Dubé, B., and Bécu, V., 2011. The gold content of volcanogenic massive sulfide deposits; Mineralium Deposita, v. 46, p. 509–539.

Morton, R.L. and Franklin, J.M., 1987. Two-fold classification of Archean volcanic-associated massive sulfide deposits; Economic Geology, v. 82, p. 1057–1063.

Osterberg, S.A., Morton, R.L., and Franklin, J.M., 1987. Hydrothermal alteration and physical volcanology of Archean rocks in the vicinity of the Headway-Coulee massive sulfide occurrence, Onaman area, Northwestern Ontario; Economic Geology, v. 82, 1505–1520.

Pelletier, M., Mercier-Langevin, P., Crick, D., Tolman, J., Beakhouse, G.P., and Dubé, B., 2014. 41. Targeted Geoscience Initiative 4. Lode Gold Deposits in Ancient and Deformed Terranes: Preliminary Observations on the Nature and Distribution of the Deformed and Metamorphosed Hydrothermal Alteration Associated with the Archean Rainy River Gold Deposit, Northwestern Ontario; Ontario Geological Survey, Open File Report 6300, p. 41-1 to 41-10.

Percival, J.A., 2007. Geology and metallogeny of the Superior Province, Canada, *In:* Mineral Deposits of Canada: A Synthesis of Major Deposit Types, District Metallogeny, the Evolution of Geological Provinces, and Exploration Methods, (ed.) W.D. Goodfellow; Geological Association of Canada, Mineral Deposits Division, Special Publication 5, p. 903–928.

Percival, J.A., Sanborn-Barrie, M., Skulski, T., Stott, G. M., Helmstaedt, H., and White, D.G., 2006. Tectonic evolution of the western Superior Province from NATMAP and Lithoprobe studies; Canadian Journal of Earth Sciences, v. 43, p. 1085–1117

Rankin, L.R., 2013. Structural setting of the Rainy River Au mineralization - NW Ontario; Geointerp confidential report 2013/08 for Rainy River Resources, unpublished internal report, 77 p.

Rowins, S.M., 2011. The Troilus Au-Cu deposit: A deformed Archean porphyry of the reduced variety, *In:* Abstracts; Geological Association of Canada – Mineralogical Association of Canada Joint Annual Meeting, Ottawa, Ontario, May 2011, v. 34, p. 189–190.

Sanborn-Barrie, M., 1991. Structural geology and tectonic history of the eastern Lake of the Woods grenstone belt, Kenora district; Ontario Geological Survey, Open File Report 5773, 137 p.

Tomlinson, K.Y., Davis, D.W., Stone, D., and Hart, T.R., 2003. U–Pb age and Nd isotopic evidence for Archean terrane development and crustal recycling in the south-central Wabigoon subprovince, Canada; Contributions to Mineralogy and Petrology, v. 144, p. 684–702.

Wartman, J.M., 2011. Physical volcanology and hydrothermal alteration of the Rainy River Gold Project, northwest Ontario; M.Sc. thesis, University of Minnesota, Duluth, Minnesota, 163 p.

Wartman, J., Morton, R., and Hudak, G.J., 2013. Physical volcanology and hydrothermal alteration at the Rainy River gold project, NW Ontario, *In:* Program with Abstracts; Geological Association of Canada - Mineralogical Association of Canada joint annual meeting, Winnipeg 2013, v. 36, p. 196.

GEOLOGICAL SURVEY OF CANADA
OPEN FILE 7852

Targeted Geoscience Initiative 4: Contributions to the Understanding of Precambrian Lode Gold Deposits and Implications for Exploration

Geology of the metamorphosed Roberto gold deposit (Éléonore Mine), James Bay region, Quebec: diversity of mineralization styles in a polyphase tectonometamorphic setting

Arnaud Fontaine[1], Benoît Dubé[2], Michel Malo[1], Vicki J. McNicoll[3], Tony Brisson[4], Dominique Doucet[5], and Jean Goutier[6]

[1]Institut national de la recherche scientifique – Centre Eau Terre Environnement, Québec, Quebec
[2]Geological Survey of Canada, Québec, Quebec
[3]Geological Survey of Canada, Ottawa, Ontario
[4]Goldcorp Inc., Éléonore mine, Rouyn-Noranda, Quebec
[5]Ressources Sirios, Montréal, Quebec
[6]Ministère de l'Énergie et des Ressources naturelles, Rouyn-Noranda, Quebec

2015

Recommended citation

Fontaine, A., Dubé, B., Malo, M., McNicoll, V.J., Brisson, T., Doucet, D., and Goutier, J., 2015. Geology of the metamorphosed Roberto gold deposit (Éléonore Mine), James Bay region, Quebec: diversity of mineralization styles in a polyphase tectonometamorphic setting, *In:* Targeted Geoscience Initiative 4: Contributions to the Understanding of Precambrian Lode Gold Deposits and Implications for Exploration, (ed.) B. Dubé and P. Mercier-Langevin; Geological Survey of Canada, Open File 7852, p. 209–225.

Publications in this series have not been edited; they are released as submitted by the author.

Contribution to the Geological Survey of Canada's Targeted Geoscience Initiative 4 (TGI-4) Program (2010–2015)

TABLE OF CONTENTS

Geology of the metamorphosed Roberto gold deposit (Éléonore Mine), James Bay region, Quebec: diversity of mineralization styles in a polyphase tectonometamorphic setting

Arnaud Fontaine[1], Benoît Dubé[2], Michel Malo[1], Vicki J. McNicoll[3], Tony Brisson[4], Dominique Doucet[5], and Jean Goutier[6]

[1]Institut national de la recherche scientifique – Centre Eau Terre Environnement, 490 rue de la Couronne, Québec, Quebec G1K 9A9
[2]Geological Survey of Canada, 490 rue de la Couronne, Québec, Quebec G1K 9A9
[3]Geological Survey of Canada, 601 Booth Street, Ottawa, Ontario K1A 0E9
[4]Goldcorp Inc., Éléonore mine, 853, boulevard Rideau, Rouyn-Noranda, Quebec J9Y 0G3
[5]Ressources Sirios, 1000, rue St-Antoine Ouest, bureau 415, Montréal, Quebec H3C 3R7
[6]Ministère de l'Énergie et des Ressources naturelles, 70, avenue Québec, Rouyn-Noranda, Quebec J9X 6R1
*Corresponding author's e-mail: arnaud.fontaine@ete.inrs.ca

ABSTRACT

The world-class Roberto gold deposit is a major discovery in the James Bay region. Hosted by <2675Ma (Timiskaming) sedimentary rocks, the deposit is located a few kilometres south of the tectonometamorphic contact between the Opinaca (paragneiss to migmatite) and the La Grande subprovinces (tonalitic basement, volcano-sedimentary belts and syn- to late-tectonic intrusions). Multiple deformation events, long-lived metamorphic event(s), and magmatic activity, including proximity to the migmatitic Opinaca domain, constitute a geological context that is favourable for long-lived hydrothermal systems or multiple mineralizing and/or remobilization events.

Detailed underground and surface mapping of the ore zones and host rocks of the Roberto gold deposit (Éléonore mine) provide new insights into host-rock variations, relationships between metamorphism and ore zones, syn- to post-mineralization structural events, and magmatic activity. These have led to a diversity of mineralization styles including i) stockwork of quartz, dravite (magnesian tourmaline) veinlets with microcline, phlogopite replacement zones with pyrrhotite, arsenopyrite, and löllingite (Roberto zone), ii) quartz, diopside, schorl (iron-rich tourmaline), arsenopyrite veins (East-Roberto zone), and iii) more atypical ore zones in migmatitic rocks or in biotite, amphibole schist (Lake zone). All of the mineralized zones are deformed (isoclinal folding, mylonitic shearing, boudinage) and some (e.g. Roberto zone) are locally strongly metamorphosed, suggesting that the bulk of the ore is pre-peak metamorphism (amphibolite facies). The timing of the mineralization relative to peak metamorphism and the complex geological setting are the dominant factors that influenced the nature of the Roberto deposit.

INTRODUCTION

Gold deposits located in deformed and metamorphosed terranes are associated with a wide range of host rocks originating from various crustal levels. Polyphase deformation and metamorphism have often obscured the primary characteristics and genetic history of these deposits (Poulsen et al., 2000; Goldfarb et al., 2005; Robert et al., 2005; Dubé and Gosselin, 2007 and references therein). Although most of these deposits occur in greenschist-facies metamorphic rocks (e.g. Hodgson, 1993; Groves et al., 1998; Goldfarb et al., 2005; Robert et al., 2005), some are also found in amphibolite and granulite metamorphic terranes (Barnicoat et al., 1991; McCuaig et al., 1993; Neumayr et al., 1993; Kisters et al., 1998; Dubé et al., 2000; Dubé and Gosselin, 2007). The temporal relationship between gold deposition and peak metamorphism is a critical feature to define metamorphic/hydrothermal processes, often involved in the genesis of gold deposits in these high-grade metamorphic terranes (Stüwe, 1998; Poulsen et al., 2000; Tomkins and Mavrogenes, 2002; Tomkins et al., 2004, 2006; Phillips and Powell, 2009). High metamorphic gradients, roughly coincident with large-scale tectonic contacts may represent important criteria for gold exploration (e.g. Thompson, 2003; Gauthier et al. 2007).

The world-class Roberto gold deposit is a relatively recent discovery in the less explored James Bay region with reserves of 4.97 Moz at 6.3 g/t Au, measured and indicated resources of 1.06 Moz at 6.34 g/t Au, and

Fontaine, A., Dubé, B., Malo, M., McNicoll, V.J., Brisson, T., Doucet, D., and Goutier, J., 2015. Geology of the metamorphosed Roberto gold deposit (Éléonore Mine), James Bay region, Quebec: diversity of mineralization styles in a polyphase tectonometamorphic setting, *In:* Targeted Geoscience Initiative 4: Contributions to the Understanding of Precambrian Lode Gold Deposits and Implications for Exploration, (ed.) B. Dubé and P. Mercier-Langevin; Geological Survey of Canada, Open File 7852, p. 209–225.

inferred resources of 2.80 Moz at 7.19 g/t Au (Goldcorp, 2014).

Previous work (Ravenelle et al., 2009, 2010; Ravenelle, 2013) on the Roberto deposit mainly focussed on the detailed surface mapping of the large stripped Roberto outcrop, supplemented by drill-core descriptions, U-Pb geochronology, and gOcad 3-D modeling, which uncovered the complex structural pattern, stratigraphic relationships, alteration assemblages, and timing of gold mineralization. Such a complex setting complicates the study of the genesis of the deposit and the definition of its geological and hydrothermal footprints.

The current project is part of a Ph.D. study by the first author, in progress at the Institut national de la recherche scientifique, Centre Eau Terre Environnement (INRS ETE) in collaboration with the Geological Survey of Canada (GSC), Goldcorp Inc. Éléonore Mine and Géologie Québec, under the umbrella of the Targeted Geoscience Initiative 4 - Lode Gold project of Natural Resources Canada (Dubé et al., 2011a). The study uses a multidisciplinary approach focussing on extensive detailed underground mapping, structural analysis, core logging, lithogeochemical analysis, U-Pb geochronology, and petrography to establish the various geological characteristics and processes involved in the genesis of the Roberto gold deposit. The main goal of this report is to provide an overview of the underground geology of the Roberto deposit.

REGIONAL GEOLOGY

The Superior Province is one of the most gold-rich Archean cratons with more than 375 Moz Au of estimated gold (Gosselin and Dubé, 2005a,b; B. Dubé and V. Bécu, unpub. data). The James Bay region is part of the Superior Province of the Canadian Shield (Card and Ciesielski, 1986; Percival et al., 2007), which is characterized by Neoarchean rocks with Meso- and Paleoarchean reworked domains (3.45–2.57 Ga; Goutier and Dion, 2004). The metamorphic grade increases quickly to the granulitic metasedimentary units of the Opinaca subprovince, which is interpreted as an injection complex (Morfin et al., 2013). Migmatization of the sedimentary rocks occurred between 2663 and 2637 Ma (Morfin et al., 2013). The La Grande subprovince comprises sedimentary rocks, local volcanic assemblages, and numerous intrusions (Franconi, 1978; Goutier et al., 2001; Moukhsil et al., 2003), underlain by an older Archean basement (Goutier et al., 2001; Bandyayera et al., 2010). The contact between the two subprovinces defines the first-order gold metallotect in the James Bay area as most known gold deposits and showings are located within about few kilometres of this contact (Fig. 1a), such as the Corvet-Est (Aucoin et al., 2011), the La Grande-Sud (Mercier-Langevin et al., 2012), and the turbidite-hosted Wabamisk (Beauchamp et al., 2015) projects. Since the discovery of the Roberto deposit by Mines d'or Virginia in 2004, this contact and, in particular, the adjacent polydeformed turbiditic basins are the current exploration targets in the James Bay region (Gauthier, 2000; Gauthier et al., 2007; Ravenelle et al., 2009, 2010; Ravenelle, 2013).

GEOLOGICAL SETTING OF THE DEPOSIT

Located near the boundary between the La Grande and Opinaca subprovinces, the deposit is hosted by a polydeformed <2675Ma (Timiskaming) turbiditic sequence, metamorphosed to amphibolite facies (Ravenelle et al., 2009, 2010; Ravenelle, 2013; Fontaine et al., 2014, and this study). The main part of the Éléonore property (La Grande subprovince, Fig. 1b) is composed of syn- to late-tectonic granodiorite, tonalite, diorite, and pegmatite, intruding the volcanic and sedimentary units of the Kasak and Low formations (Bandyayera and Fliszár, 2007). The Réservoir Opinaca pluton (Fig. 1b) is a polyphase intrusion composed of an early tonalitic phase (2708.9 ± 0.9 Ma: David et al., 2009) and a late dioritic phase (2703.5 ± 2.8 Ma: David et al., 2009). The Lac Ell intrusion (2705.6 ± 1.9 Ma: J. David, 2005) hosts Au-Ag-Cu-Mo mineralization (Bécu et al., 2007; Ravenelle et al., 2010). Pillowed lava and lapilli tuff of the Kasak Formation (2704 ± 1.1 Ma: Bandyayera and Fliszár, 2007) are unconformably overlain by <2702 ± 3 Ma polymictic clast-supported conglomerate (locally termed "ALow1"), which marks the base of the Low Formation (for details, see Ravenelle et al., 2010). Stratigraphically above, the turbiditic part of the Low Formation (termed "ALow2"; Bandyayera and Fliszár, 2007) comprises decimetre- to metre-thick lenses of arenite interbedded with an aluminosilicate-bearing greywacke. Detailed U-Pb work of the Low Formation in the Roberto deposit area has unravelled a structurally inverted stratigraphy involving an older sedimentary assemblage consisting of <2714 Ma massive greywacke (Ravenelle et al., 2010) intercalated with <2697 Ma aluminosilicate-bearing greywacke (Ravenelle, 2013) lying structurally above a younger sedimentary assemblage characterized by thinly bedded greywacke dated at <2675 Ma (Ravenelle et al., 2010) interbedded with massive greywacke. The gold mineralization is mainly hosted within the <2675 Ma thinly bedded greywacke at the top of the Low Formation (ALow2; Ravenelle et al., 2010). These sedimentary rocks are intruded by pegmatite dykes (Figs. 1, 2), and locally gradually evolve into paragneiss or migmatite towards the contact with the Opinaca subprovince (for details, see Ravenelle et al., 2010).

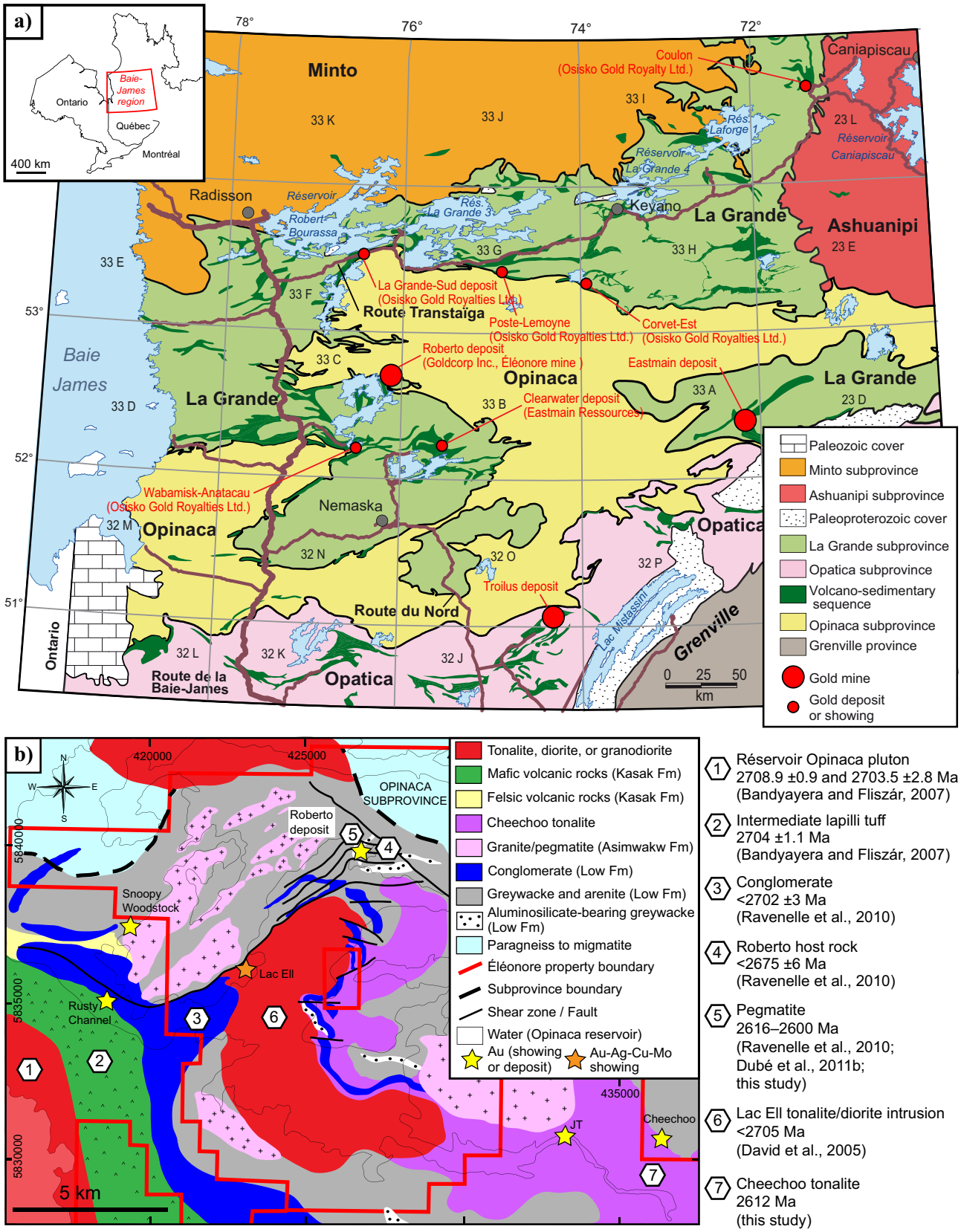

Figure 1. a) Simplified lithotectonic map of the James Bay region (modified after Thériault and Beauséjour, 2012; J. Goutier, 2014, work in progress). **b)** Geology of the Éléonore property with the location of the deposit/mine and geochronological data illustrating the complex tectonometamorphic framework and magmatic events associated with the Roberto gold deposit (modified after Bandyayera et al., 2010; Ravenelle et al., 2010; Ravenelle, 2013; and this study). Abbreviation: Fm = formation. Geographical coordinates: NAD83, UTM zone 18N.

STRUCTURAL FEATURES

Three main phases of regional deformation are recognized in the study area (Bandyayera and Fliszár, 2007; Bandyayera et al., 2010; Ravenelle et al., 2010; Ravenelle, 2013). The regional D_1 deformation consists of rare intrafolial folds, oriented north-northeast (Bandyayera and Fliszár, 2007). D_2 is the main phase of deformation associated with regional metamorphism. It is characterized by an east- to southeast-trending S_2 foliation associated with tight to isoclinal F_2 folds with steeply plunging hinge lines. An associated subvertical L_2 mineral lineation (biotite, aluminosilicate porphyroblasts) is preferentially present in aluminosilicate-bearing greywacke and conglomerate (Bandyayera et al., 2010; Ravenelle et al. 2010; this study). An S_3 crenulation cleavage locally reorients syn-D_2 metamorphic minerals (e.g. biotite, fibrous sillimanite, K-feldspar). F_3 folds have centimetric to metric wavelengths and are generally more open than F_2 folds (Bandyayera et al., 2010; Ravenelle et al., 2010; this study) and their interaction produces Type 3 fold interference patterns (Ramsay and Huber, 1987; Ravenelle, 2013). Ravenelle et al. (2010) have also documented sheath folds, which they interpret as related to the effect of continuous ductile deformation along D_2 high-strain zones on early F_2 folds.

At deposit scale, D_1 deformation is inferred by the repetition of the aluminosilicate-bearing greywacke along the southern limb of a kilometre-scale F_2 fold (Ravenelle et al., 2013). Although no evidence of D_1 deformation was observed in the 410 mine level (Fig. 2), the strongly deformed interbedded greywacke could be affected by early deformation event(s), as observed by the local presence of F_1 folds in the area close to the deposit (Ravenelle, 2013). The latter is characterized by a steeply dipping, roughly west-trending axial planar S_2 foliation, well displayed by the alignments of aluminosilicate porphyroblasts or biotite. These minerals define the L_2 lineation, commonly colinear with F_2 fold axes. F_2 folds are steeply plunging to subvertical and are commonly non-cylindrical and disharmonic. A steeply dipping northwest-trending S_3 crenulation cleavage locally deforms the S_2 foliation and is associated with non-coaxial strain reactivation of D_2 high-strain zones. The <2675 Ma thinly bedded greywacke (Fig. 3a) is strongly deformed by D_2 and D_3 fabrics on mine levels 410 and 380 (Figs. 2, 4). Similar deformation and chronology of events have been recorded by the quartzo-feldspathic veins in paragneiss, exposed 1 km east of the deposit. Two structural domains have been defined on the 410 mine level (Fig. 2): a southern domain, dominated by east-trending tight to isoclinal F_2 folds, where bedding is well preserved; and a northern domain dominated by a strongly developed S_3 crenulation cleavage axial planar to northeast-trending F_3 folds. The northern and southern domains are separated by D_2 high-strain zones. The latter may have been reactivated during D_3 deformation. Three structural domains are also defined based on the relative orientation of bedding versus S_2 foliation. A western domain is characterized by northwest-trending bedding though S_2 foliation is east-trending (Fig. 2, stereoplot 1). The central domain is marked by an irregular orientation of S_2 foliation (Fig. 2, stereoplot 2) probably related to the emplacement of pegmatitic material or F_3 folding (Fig. 2). Lastly, the eastern domain display S_2 foliations and bedding that are parallel to the east (Fig. 2, stereoplot 3) and is interpreted to be related to strong D_2 transposition along the contact of the aluminosilicate-bearing greywacke (< 2697 Ma) with the interbedded and more competent greywacke unit. This zone of strong transposition is well exposed on the large surface-stripped outcrop (Fig. 2b), although in some areas the original north-south orientation of the bedding is preserved (for details, see Ravenelle et al., 2010). Some of these D_2 high-strain zones contain elongated clasts of granitic pegmatite (e.g. near exploration shaft; Fig. 2) suggesting that these pegmatite units were intruded before or during D_2 deformation. These steeply dipping (79–88°) west to southwest-trending (N280°–N220°) high-strain zones intersect the east-trending and south-dipping orezone lenses located in the hanging wall of the main Roberto and Roberto East zones (Fig. 2).

Post-D_3 northwest- to east-trending conjugates sets of brittle faults (N310º and N340°) are marked by a coating of chlorite, epidote, and locally calcite and chalcopyrite and contain brecciated material with angular fragments of host rocks. Displacement along those late brittle faults ranges from a few centimetres to several metres and commonly shows brecciated material with angular fragments of the host rocks.

METAMORPHISM

Sedimentary rocks of the Low Formation (Fig. 3a,b) underwent prograde amphibolite-facies metamorphism, which sharply increases towards the contact with the Opinaca subprovince, as illustrated by the presence of (i) aluminosilicate (sillimanite), muscovite and K-feldspar porphyroblasts in metapelitic rocks, (ii) amphibole or biotite porphyroblasts in greywacke (Fig. 3c), (iii) an increasing proportion of quartzo-feldspathic veinlets with residual biotite selvages in greywacke, and (iv) paragneiss (Fig. 3d). Centimetre-sized amphibole porphyroblasts locally occur in the host rocks (Fig. 3c), near contacts with granitic pegmatite or feldspar-phyric monzonite (Fig. 3e,f). In the deposit area, the metamorphic gradient increases rapidly toward the northeast and with depth. These features suggest that isograds are probably southeast-trending with moderate dips of 45° to the southwest. In

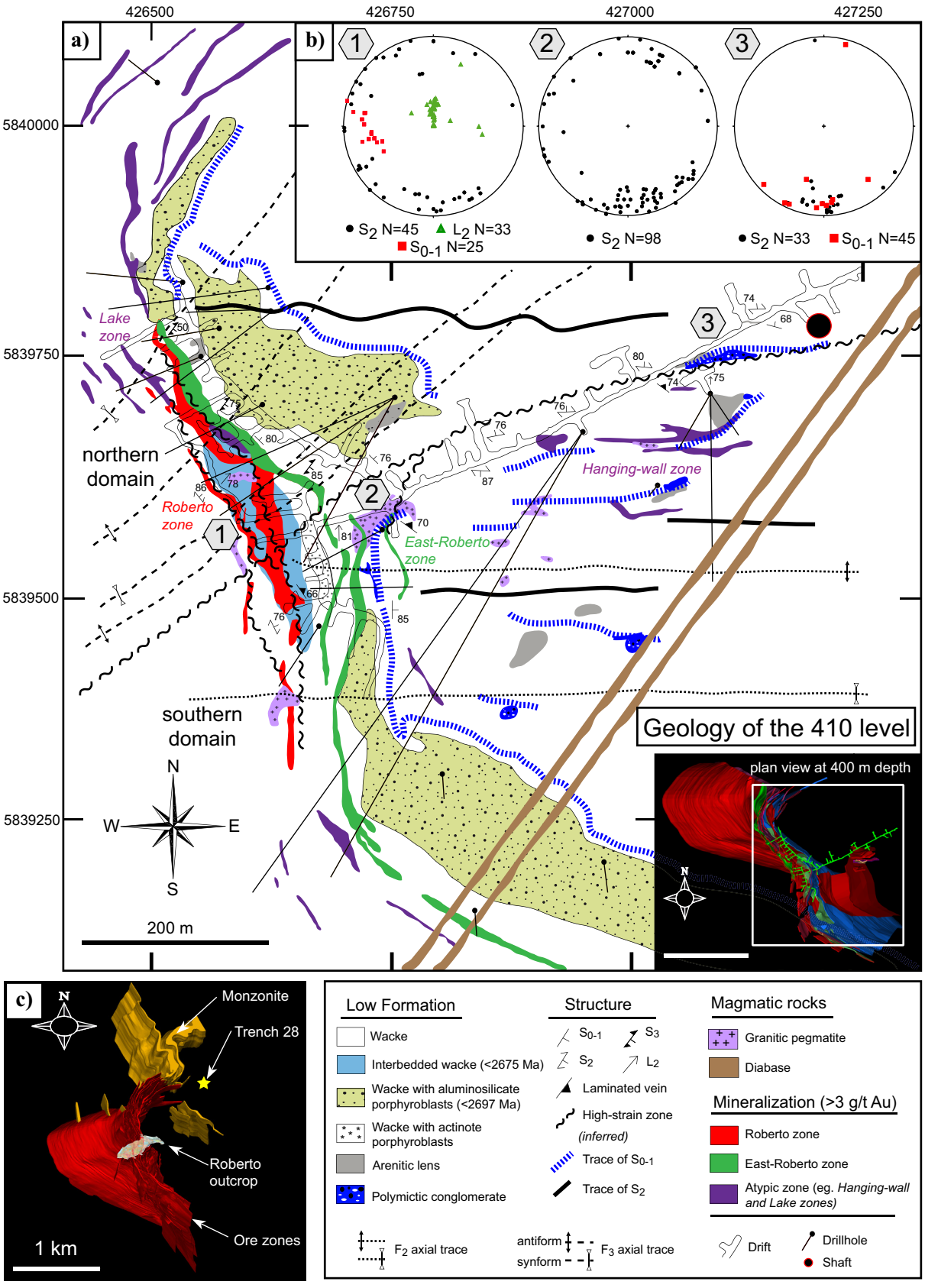

Figure 2. a) Simplified geological map of the 410 level (390 m depth) with main rock types and structures. **b)** Stereographic projections of fabrics associated with structural domains. **c)** Illustration of the geological model of the Roberto deposit with the location of Trench 28, monzonite, ore zones, Roberto outcrop, and Trench 28 (for details, see Fig. 6). Geographical coordinates: NAD83, UTM zone 18N.

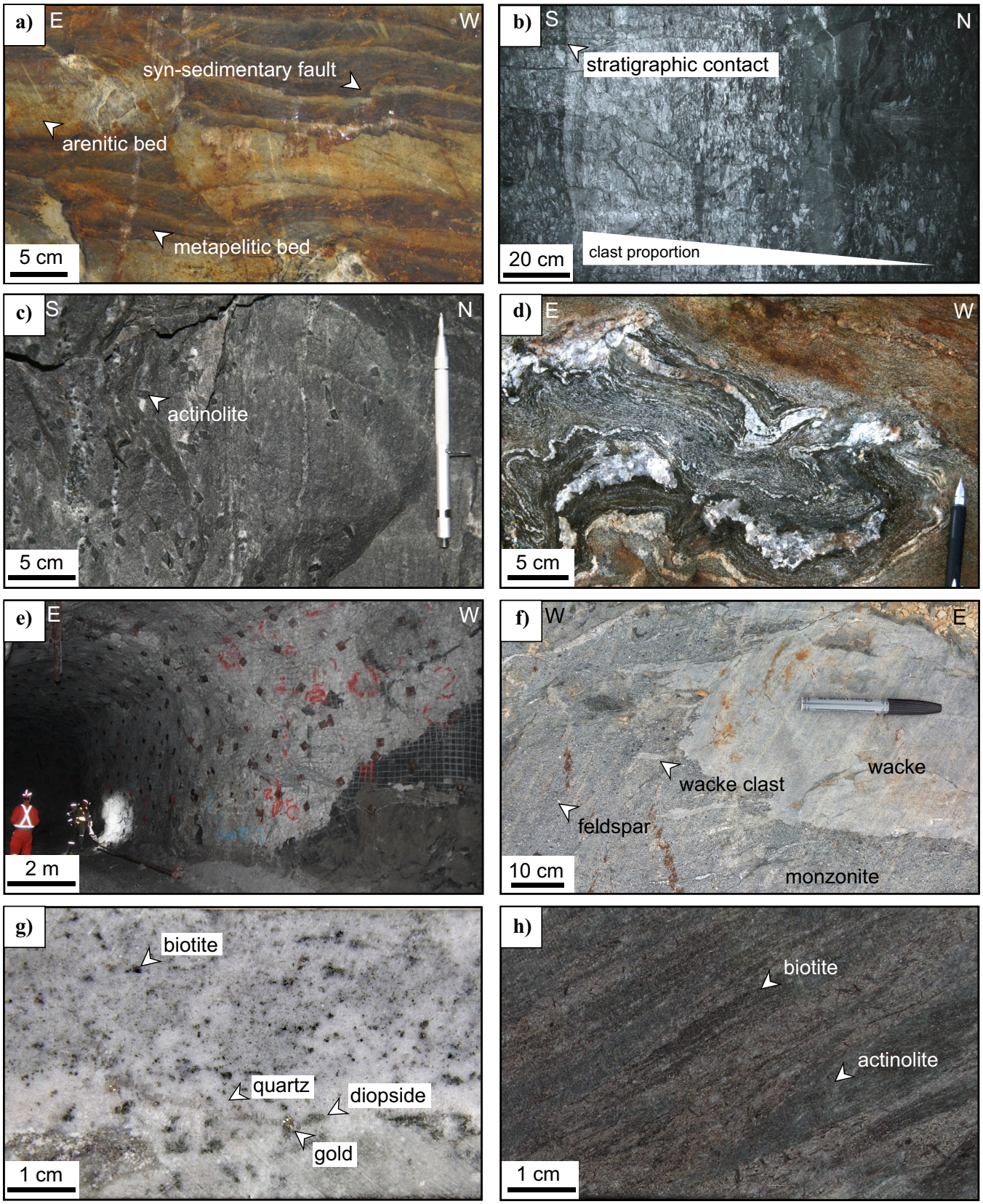

Figure 3. Photographs of **a)** interbedded greywacke with syn-sedimentary faults in the Trench 28; **b)** polymictic conglomerate (west wall at 600 m depth), facing north; **c)** amphibole-porphyroblasts wacke; **d)** paragneissic rocks; **e)** granitic pegmatite (at 400 m depth); **f)** monzonitic rocks; **g)** Cheechoo tonalite mineralization (photograph by Benoît Dubé, 2014; drillhole CH-919-12; 25.9 g/t Au, 136–137 m); and **h)** Lake Zone (biotite, amphibole schist).

some cases where partial melting occurred, residual biotite is present in association with hornblende in rims of quartzo-feldspathic veins (Fig. 3d).

Prograde metamorphism results in the breakdown of muscovite and growth of K-feldspar porphyroblasts (e.g. in the aluminosilicate-bearing greywacke) at depth possibly following the muscovite + quartz = K-feldspar + sillimanite + H_2O metamorphic reaction (Ravenelle, 2013). That reaction probably precludes migmatization in the stability field of the biotite, i.e., at a temperature of <800°C (Vielzeuf and Holloway, 1988) with the muscovite + plagioclase + quartz = melt + sillimanite + biotite melting reaction (Thompson and Tracy, 1979). This is well illustrated in a trench (Fig. 3d), where quartz-feldspar subparallel veinlets are associated with biotite, hornblende residual material in veinlet selvages.

Various generations of metamorphic and hydrothermal biotite are documented using petrography and mineral chemistry (#Mg versus Al^{iv}). Three preliminary groups are recognized: i) metamorphic biotite in metapelite and in the rims of K-feldspar, muscovite, sillimanite porphyroblasts (group 1), ii) residual biotite in paragneiss (group 2), and iii) hydrothermal phlogopite in pervasive calcium-bearing hydrothermal assemblages (group 3). Biotite thermometry data using titanium contents (Henry et al., 2005) of the first group (F ranging from 0.103 to 0.272 apfu) in metapelite of the interbedded greywacke gave metamorphic temperatures ranging from 542 to 705°C (RSD of 7.4% for n=32) with a mean value of 650 ± 16°C. This result is corroborated by preliminary garnet-biotite thermometry (Holdaway, 2000) data of biotite inclusions within M_2 garnet porphyroblasts in garnet-bearing sedimentary rocks found in the northern part of the deposit, which yielded a temperature estimate of 657°C.

MAGMATISM

Granitic, lithium-cesium-tantalum-enriched (LCT) pegmatite (Černý, 1991; Černý and Ercit, 2005), dated between ca. 2620 and 2600 Ma (U-Pb zircon age; Ravenelle et al., 2010; Dubé et al., 2011b; this study), occur as centimetric to metric dykes (Figs. 2, 3e) that locally display progressive transition with quartzo-feldspathic and quartz veins (Ravenelle, 2013; this study). Quartz and feldspar are present in various proportions in association with schorl, garnet, and rare traces of spodumene. Miarolitic cavities contain quartz, schorl, and spodumene crystals. Alkali feldspar and quartz occasionally show skeletal or graphic intergrowths. Coarse-grained quartz ± schorl-bearing dykes were injected within feldspar-garnet aplitic domains. They are commonly boudinaged and isoclinally folded (Ravenelle et al., 2010). U-Pb ages of these pegmatite dykes range from 2616 to 2603 Ma (Ravenelle, 2013). Furthermore, gold-bearing ca. 2600 Ma (ID-TIMS U-Pb preliminary age) granitic pegmatite located in the North zone (see below) contains acicular centimetric arsenopyrite-löllingite crystals in quartz-rich domains.

A feldspar-phyric monzonite sill (Fig. 2b), with a maximum age of ca. 2674 Ma, is mapped a few hundred metres north of the main ore zones, in the western part of the North zone (for details, see Alteration and Mineralization below). This intrusion (Fig. 3f), which displays irregular contacts with the host greywacke, is composed of quartz, amphibole, and biotite with local traces of pyrite, pyrrhotite, diopside, and rounded to elongated clasts of host rocks (e.g. greywacke, amphibolite, arenite). The monzonite is foliated by the S_2 fabric. A foliated feldspar porphyry intermediate dyke (~5 m wide) mapped next to the exploration shaft contains disseminated fine-grained pyrite and has a maximum U-Pb age of ca. 2688 Ma.

A tonalite intrusion that hosts the Cheechoo gold project (Fig. 1b; Ressources Sirios, 2014) is composed of local feldspar phenocrysts in a matrix of quartz, albite An_{10} microcline, biotite, and rare traces of diopside and actinolite. Preliminary petrographic and lithogeochemical data indicate that the intrusion is locally of granodioritic composition. The intrusion, locally cut by a stockwork of quartz veinlets, is deformed, recrystallized, and foliated, as shown by elongated biotite and chlorite. Textures vary from aplitic, granoblastic, gneissic, to nematoblastic. Locally, the tonalite evolves progressively to quartz-feldspar pegmatite dykes. The pegmatite dykes locally comprise strongly foliated amphibole- and biotite-rich mafic and greywacke clasts that contain traces of diopside, disseminated fine-grained arsenopyrite, pyrrhotite, and gold. The tonalite is the main host to the auriferous zones and drillhole intersections grade up to 7.24 g/t Au over 7.9 m (Ressources Sirios, 2014). The auriferous tonalite is silicified and/or K-altered, Na-altered and contain traces of disseminated fine-grained arsenopyrite and pyrrhotite and local quartz veinlets. Undeformed quartz-feldspar pegmatite is also locally auriferous. Visible gold locally occurs in grey quartz replacement zones or within quartz veinlets (Fig. 3g). A preliminary zircon age of ca. 2612 Ma (U-Pb Isotope Dilution Thermal Ionization Mass Spectrometry (ID-TIMS)) for the Cheechoo intrusion is interpreted as the crystallization age. This age is contemporaneous with some auriferous zones of the Roberto deposit dated at ca. 2615 to 2607 Ma (Ravenelle et al., 2010) and provide a maximum age for this phase of gold mineralization.

ALTERATION AND MINERALIZATION

The ore zones at Roberto are associated with a relatively large hydrothermal system characterized by a proximal potassium- to magnesium-bearing metaso-

matic alteration halo (0–75 m from ore zones; Fig. 4b) surrounded by an intermediate (75–100 m; Fig. 4e) or distal calcium-bearing alteration halo (≤100–250 m; Fig. 4c,f). From distal to proximal, the calcium-bearing metasomatism is characterized by replacement bands or diffuse zones with calcium-rich minerals (actinolite, diopside) in association with feldspar (20–60%), actinolite (25–30%), and a minor amount of coarse-grained biotite and quartz (Fig. 4e). Metasomatic layers/zones (Fig. 4f) are locally zoned with coarser minerals, suggesting open-space filling or possible recrystallization of the mineral phases during the prograde metamorphism (Fig. 4b,f). Diffuse replacement zones are characteristic of the distal hydrothermal footprint. The proportion of diopside and tourmaline (mainly schorl) strongly increases in proximity of ore zones (Ravenelle al., 2010). Also, the abundance and thickness of metasomatic material (e.g. replacement zones, veins, and veinlets) and deformation intensity also increase in the vicinity of high-grade zones (e.g. Roberto and East-Roberto). For example, veinlet networks evolve sharply to pervasive silica flooding with tourmaline enrichment approaching the East-Roberto zone. The presence of centimetric porphyroblasts of actinolite, phlogopite, and arsenopyrite, in association with microcline replacement zones and stockwork of quartz, dravite (magnesian tourmaline), are typical features of the proximal metasomatic alteration (Fig. 4b,c).

Several styles of mineralization have been documented from surface (Ravenelle, 2010) and underground mapping (this study). The Roberto stripped outcrop (Fig. 2b) exposes the richest domains of the gold mineralization (for details, see Ravenelle et al., 2010 and Ravenelle, 2013) where ore zones are preferentially hosted in thinly bedded greywacke adjacent to non-economic to barren massive greywacke. The Roberto style of mineralization (up to 25 g/t Au on 20 m) constitutes the bulk of the ore (Figs. 4b, 5d) and is characterized by a stockwork of quartz-sulphide veinlets and reddish-brown replacement zones (Ravenelle et al., 2010). The quartz-sulphide veinlets can form a chaotic (randomly oriented) stockwork/breccia in the massive greywacke or can be subparallel or at a high angle to the folded bedding in the interbedded greywacke. Biotite and dravite, in association with phlogopite and microcline, form replacement zones associated with the quartz-sulphides stockwork (Figs. 4d, 5a). Arsenopyrite, löllingite, and pyrrhotite (with gold inclusions) are present in the quartz-sulphide veinlets or as fine-grained disseminations in the replacement ore (Ravenelle et al., 2010). At depth, the Roberto zone is characterized by (i) an increasing proportion of microcline alteration in the selvages of the quartz-sulphide veinlets and in the matrix of the replacement ore (Fig. 4b); (ii) saccharoidal quartz ± feldspar; and (iii) recrystallized randomly oriented coarse-grained phlogopite porphyroblasts (Fig. 4b).

The East-Roberto zone (Fig. 5b,e) forms the eastern portion of the north-south mineralized corridor (Fig. 2a) and is characterized by massive or laminated quartz-diopside veins associated with silicification of host rocks, schorl veinlets, and disseminations of arsenopyrite. Underground, the East-Roberto mineralization appears spatially associated with silicified arenite lenses and local polymictic conglomerate (Fig. 5b).

Other mineralized zones of the Roberto deposit include the Lake, Hanging wall (Figs. 2a, 5c), and North zones (Fig. 6). These constitute an interesting but much smaller percentage of the deposit and result in ambiguous interpretations of ore process and genesis, most probably because of post-ore deformation and metamorphism. For instance, ore-bearing paragneiss shows progressive evolution to quartzo-feldspathic pegmatitic material (Ravenelle et al., 2010). The Lake zone is hosted by chlorite-amphibole-biotite schist (Fig. 3h) situated in the northern part of the main ore corridor. Along the northern limb of the F_2 fold, there is much higher strain intensity (Fig. 2). The Hanging-wall ore zones (Figs. 2, 5c) are located adjacent to D_2 high-strain zones and oriented subparallel to oblique to the overall trend of the S_2 foliation. They are characterized by quartz veins and local brecciated veins with pyrite, pyrrhotite, arsenopyrite and visible gold (up to 18.8 g/t over 9.6 m). Alteration assemblages around these veins share some similarities with the alteration associated with the East-Roberto and Roberto zones, suggesting similar gold-bearing fluids originating from a common deformed and metamorphosed hydrothermal system.

The North zone (Figs. 4f, 6), which is well exposed in Trench 28, is characterized by an up to 200 m thick "low-grade" envelope (1.3 g/t over 200 m). Located along the north limb of a kilometre-scale F_2 fold, the sedimentary sequence hosting the zone is mainly north-facing (Fig. 6); however, the bedding locally trends to the north, probably due to local parasitic folding. The S_2 metamorphic foliation is oriented northwest and was re-oriented by F_3 gentle to open folds. Gold mineralization occurs along the contact between the aluminosilicate-bearing greywacke and massive greywacke and within the interbedded greywacke (Fig. 6a). Exposed lithologies in Trench 28 include, from south to north, massive greywacke, overlain by aluminosilicate-bearing greywacke and interbedded greywacke (Fig. 6). Quartz-feldspar veins and veinlets lie parallel to the bedding (oriented north-south) or S_2 foliation (oriented north-west) in the aluminosilicate-bearing greywacke. The main ore zone, roughly oriented east-west, is composed of calcium-bearing mineral assem-

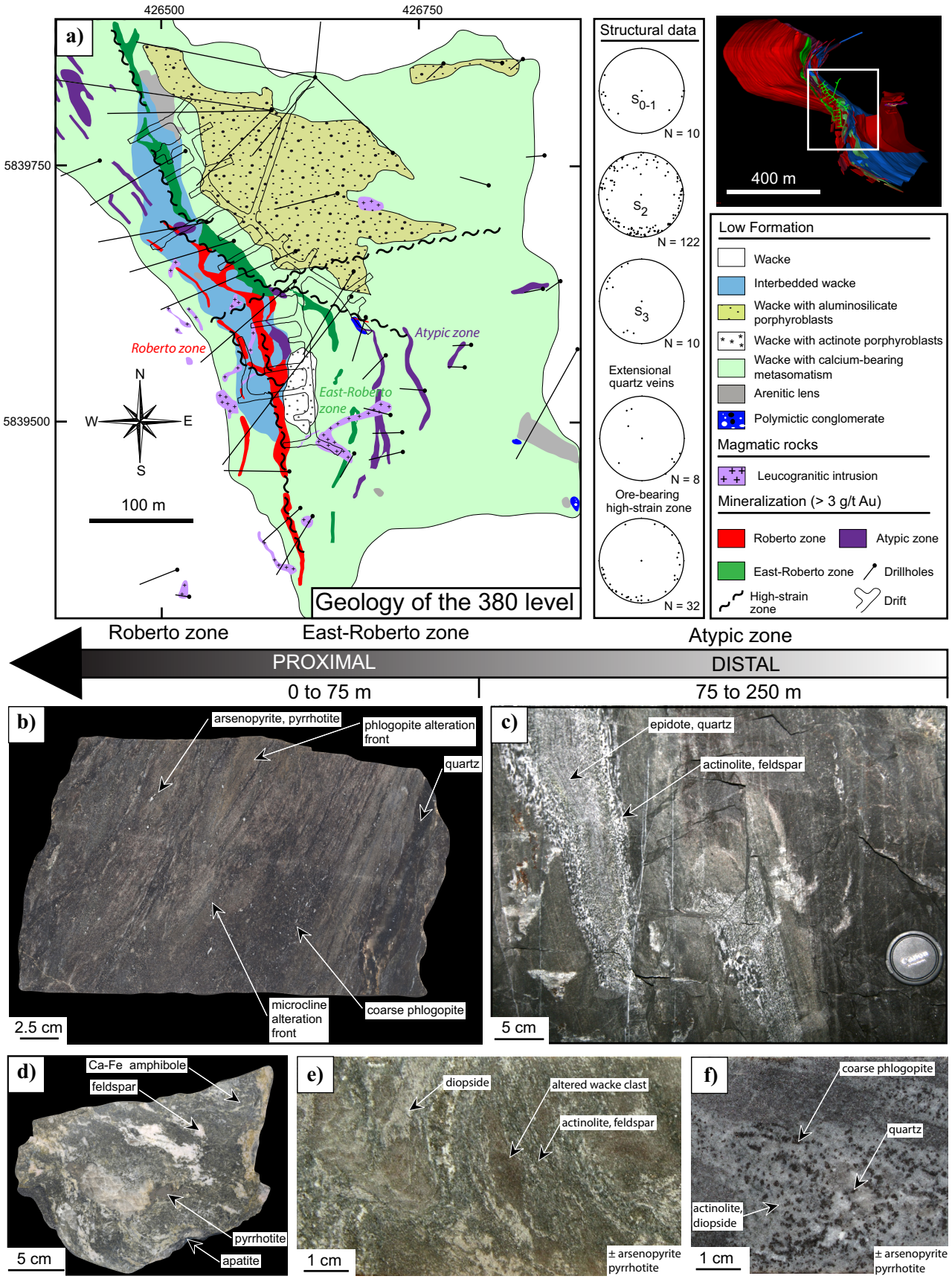

Figure 4. a) Geological map of the 380 level with stereographic projections of main structures. **b to f)** Photographs showing typical hydrothermal rocks, illustrating the zonality approaching main ore zones (East-Roberto and Roberto zones), separated into proximal (0–75 m), intermediate (75–100 m) and distal (>100–250 m). Geographical coordinates: NAD83, UTM zone 18N.

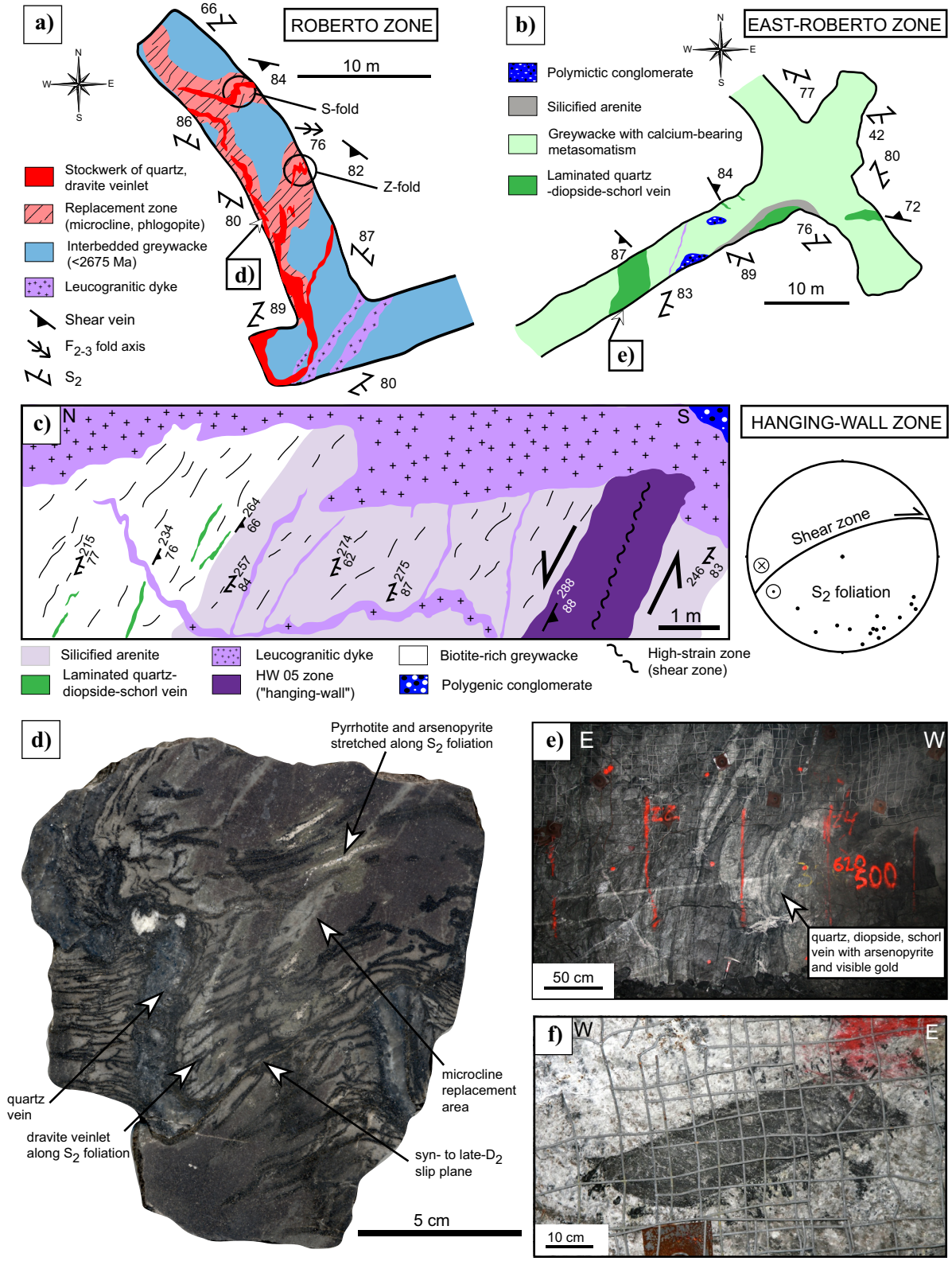

Figure 5. Simplified geological maps of **(a)** the Roberto zone (at 400 m depth) and **(b)** the East-Roberto zone (at 600 m depth). **c)** Vertical section map of the hanging-wall zone (at 600 m depth) and stereographic projections of average shear zone orientation (N=7) and S_2 foliation poles. **d)** Hand-sample showing the deformation affecting the Roberto zone. Dravite veinlets are transposed along the S_2 foliation though the quartz vein is not totally reoriented. The pyrrhotite and arsenopyrite aggregates have roughly the same structural position as the hanging-wall zones. **e)** Underground photograph of the south wall of the isoclinally folded East-Roberto zone (at 600 m depth; location highlighted in b) with several quartz generations in association with visible gold (236 g/t Au over 1 m). **f)** Underground photograph of the north wall (at 400 m depth; location highlighted in a) of the Roberto zone clast within a pegmatite that cuts across the Roberto zone.

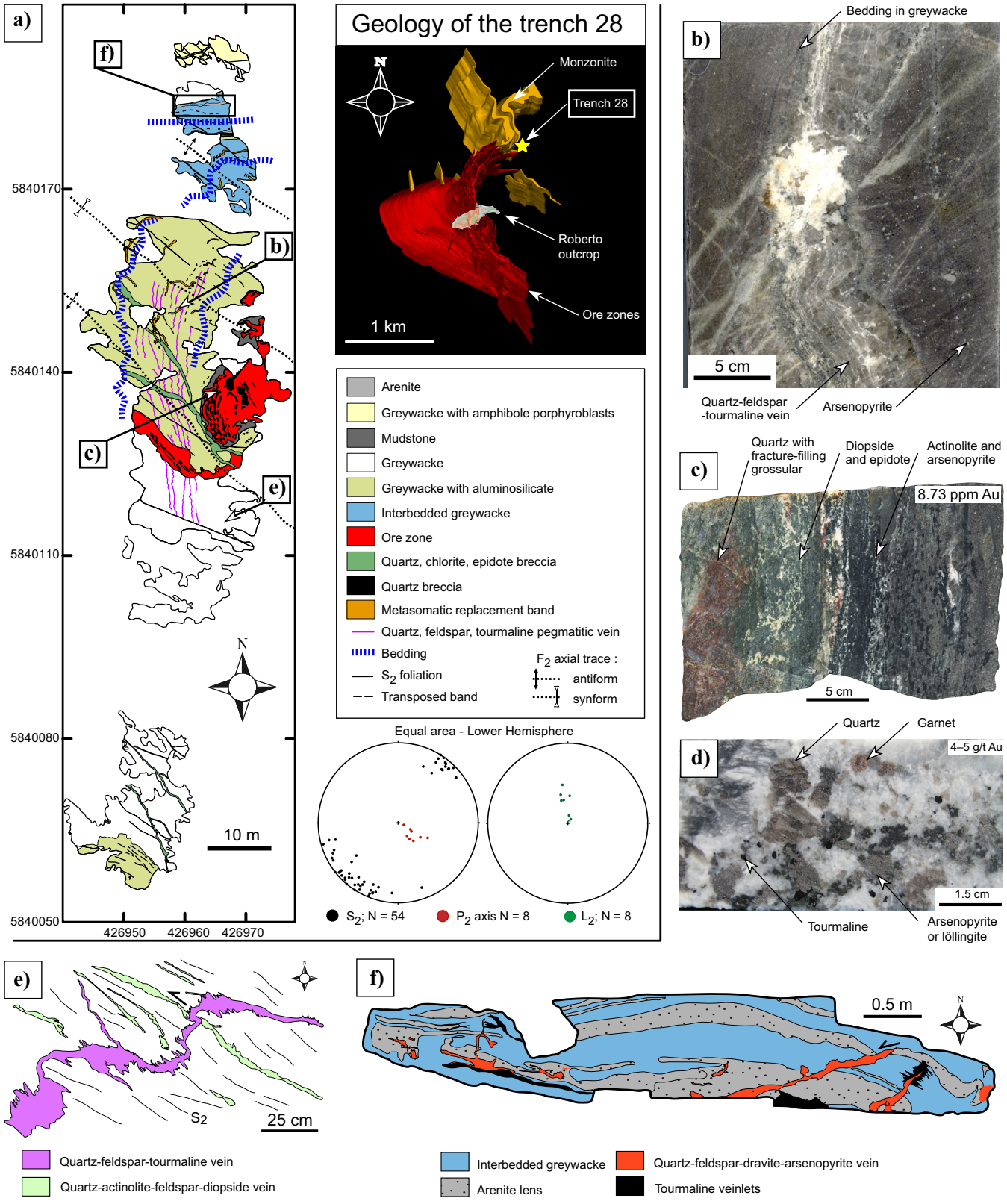

Figure 6. a) Geology of Trench 28. Note the locations of parts b, c, e, and f. Geographical coordinates: NAD83, UTM zone 18N. **b)** Quartz, feldspar, arsenopyrite-bearing vein (location highlighted in a). **c)** Hand sample of the calcium-bearing hydrothermally altered wacke in the middle of the trench (also called the Garnet Zone due to the presence of grossular). **d)** Gold-bearing pegmatite with garnet, schorl, and arsenopyrite (or löllingite). **e)** Sketch showing crosscutting relationships (see location in map a), which indicate that a quartz-feldspar-schorl vein cutting a quartz-actinolite-feldspar-diopside vein and suggesting apparent sinistral shearing along D_2-related high-strain zones. **f)** Simplified geology of the north part of the trench (see map a for location) with interbedded greywacke and decimetric arenitic lenses associated with quartz, arsenopyrite, schorl-bearing veins.

blages (grossular, diopside, carbonate, actinolite, and epidote) and disseminated coarse-grained arsenopyrite and pyrrhotite (Fig. 6c). Auriferous pegmatite dykes, locally documented in the North zone, have been intercepted in a drillhole beneath Trench 28 (19.15 g/t Au over 1.5 m). These pegmatite dykes (Fig. 6d) are zoned with feldspar-chlorite-rich walls with a predominance of quartz, feldspar, arsenopyrite, and löllingite in the cores. Such zoning, in particular quartz, feldspar, arsenopyrite, and löllingite, is interpreted to control the gold content. As this pegmatite was emplaced in barren sediment, its high gold content is not interpreted as a product of local gold remobilization but due to a magmatic gold-bearing event and/or to magma contamination during intrusion.

Most ore zones of the Roberto deposit are strongly deformed, north-trending, and located within the hinge zone of a non-cylindrical F_2 fold (Figs. 2, 4; Ravenelle et al., 2010). The geology of the north limb is more complex, as it is influenced by the presence of the monzonitic sill and the mineralized North zone. This zone, following stratigraphic contact, is strongly boudinaged and folded by F_2 and F_3 (Fig. 6a). For analogy, multiple strain increments are superimposed on the Roberto East ore zones and high-grade quartz veins have recorded isoclinal F_2 folding (Fig. 5e). On the Roberto stripped outcrop, the East-Roberto ore zone is deformed by late-D_2 oblique-dextral shearing (Ravenelle, 2013) along a steeply east-dipping high-strain zone or brittle fault with an apparent reverse component of motion, a feature that is not yet documented in underground drifts.

DISCUSSION

The main ore zones (Roberto and Roberto-East) are deformed by the main phase of deformation (D_2). This is illustrated by F_2 folds and late-D_2 slip planes deforming the Roberto stockwork (Fig. 5d), and by a S_2-foliated high-grade quartz vein of the East-Roberto mineralization isoclinally folded by F_2 (Fig. 5e). Clasts of foliated Roberto ore are found in an undeformed pegmatite cutting the main ore zone in the south part of the 410 mine level (Fig. 5f) attesting that the bulk of the mineralization was formed and deformed before the emplacement of the pegmatite. Mineralization and associated proximal alteration (e.g. diopside, microcline, phlogopite, schorl, dravite, and pyrrhotite) zones have recorded regional prograde and locally contact metamorphism. The metamorphic paragenesis and textures include (i) saccharoidal quartz in veins, (ii) biotite porphyroblasts, (iii) coarse-grained texture, and (iv) the increase of microcline alteration with depth and proximity of pegmatite. The presence of löllingite in the core of arsenopyrite (Ravenelle, 2013) and the coarse part of calcium-bearing assemblage also strongly supports the interpretation that the deposit has been metamorphosed.

The extensive magmatic activity in the study area is illustrated by several intrusive suites of tonalite (e.g. Cheechoo, Réservoir Opinaca), diorite (Lac Ell), LCT pegmatite, and feldspar-phyric monzonite. The Cheechoo tonalite is an example of the variability of rock types that host traces of diopside, actinolite, and gold mineralization (Fig. 3g). Lithium-cesium-tantalum granitic pegmatite displays various textures and mineralogy, suggesting that important segregation processes occurred during the emplacement of the granitic melt and that these variations can probably be used as good indicators for distinguishing if the pegmatite is gold-bearing (Fig. 6d). Some of granitic pegmatite dykes show progressive evolution with paragneiss rocks and some appear more evolved (spodumene-bearing pegmatite), suggesting various sources (Cheechoo tonalite, migmatite). In addition, the feldspar-phyric monzonite (Fig. 3f) shows a spatial association with the North zone (Figs. 4c,f, 6).

The calcium-bearing metasomatism, present for more than 400 m around the ore zones, is sometimes fracture-controlled (Fig. 4a,e) and with evolving mineralogy, thickness of veins or replacement zones, style and sulphide content. The integration of such variations in the metasomatic footprint represents an exploration vector (Fig. 4), which, notwithstanding metamorphic grade, is comparable to many sediment-hosted gold deposits worldwide (Sillitoe and Bonham, 1990). Also, the deposit is located a few kilometres from a migmatitic domain where partial melting (Morfin et al., 2013) and exhumation processes (Vry et al., 2010) may have been involved in the production of metamorphic fluids.

CONCLUDING REMARKS

This study illustrates the complex tectonometamorphic framework affecting the Low Formation, the host of the bulk of the gold mineralization at the Roberto deposit, which includes a wide range of mineralization styles: i) stockwork of quartz, dravite veinlets with microcline, phlogopite, and sulphides; ii) replacement zones (microcline, phlogopite, dravite) with traces of pyrrhotite, arsenopyrite, and rare löllingite (Roberto zone); ii) quartz, diopside, schorl, arsenopyrite veins (East-Roberto zone); iv) atypical ore zones in quartz-feldspathic veinlets, high-grade quartz veins, high-grade paragneiss (North zone and Hanging-wall zone); and v) local gold-bearing LCT pegmatite. The underground mapping provides new insights to the geology of the first world-class gold deposit in the James Bay region:

- The strong metamorphic gradient documented in the northeastern part of the deposit extends at

depth, suggesting that metamorphic isograds have a moderate dip to the southwest and intersect the subvertical mineralized envelope at approximately 1 km depth.

- High-strain zones are associated with all the mineralization styles, including high-grade paragneiss at depth, suggesting that hydrothermal alteration assemblages could play a role in focussing strain increments.
- The diversity of mineralization styles is due to a combination of factors: i) the superposition of gold deposition events or remobilization; ii) structural events obliterating primary hydrothermal features, and iii) the higher metamorphic grade affecting multiple host rocks, leading to atypical hydrothermal assemblages in contrast to those of classical greenschist-facies Archean gold deposits (Goldfarb et al., 2005, Robert et al., 2005; Dubé and Gosselin, 2007).
- Magmatic activity is spatially associated with the contact between Opinaca and La Grande subprovinces.
- Gold mineralizing event(s) occurred between 2675 Ma (e.g. maximum age of Low Formation) and ca. 2600 Ma (e.g. preliminary age of a gold-bearing pegmatite), a time span during which the turbiditic sequence was deposited, deeply buried, and exhumed.

IMPLICATIONS FOR EXPLORATION

The contact between the Opinaca and the La Grande subprovinces is a first-order gold exploration metallotect in the James Bay region (Fig. 1; Ravenelle et al., 2010; this study). Typified by a high metamorphic gradient (Gauthier et al., 2007), it has probably focused hydrothermal circulation, which occurred between deposition of the Low Formation deposition at <2675 Ma (Ravenelle et al., 2010) and the crystalization of a gold-bearing pegmatite at 2600 Ma (this study). During this 75 Ma time span, the turbiditic rocks were deeply buried, strongly tilted, and metamorphosed to amphibolite grade leading to the generation of aqueous fluids (from metapelitic units, mainly with muscovite or biotite breakdown mainly in metapelitic units). The discovery of gold mineralization hosted by the Cheechoo tonalite (Figs. 1b, 3g) suggests a second distinct gold mineralizing event in close proximity to the Roberto deposit, as proposed by Ravenelle et al. (2010). In terms of host rocks, the occurrence of aluminosilicate-bearing greywacke (Figs. 2, 4a), local conglomerate, and north-trending bedding, combined with the evidence of calcium-bearing metasomatism (Fig. 4a) are important geological parameters for gold exploration. Coupled with the proximity of the contact between the two subprovinces, west- and north-trending high-strain zones and kilometre-scale polyphase folds (Figs. 2, 4a) are structural targets for gold in James Bay region (Ravenelle et al., 2010; Ravenelle, 2013; this study).

FUTURE WORK

A lithogeochemical program to define the hydrothermal footprint of the deposit is currently underway in collaboration with Goldcorp Inc.'s exploration team and MERN (Ministère de l'Énergie et des Ressources naturelles). In addition, LA-ICP-MS mineral mapping is underway on gold-bearing sulphide assemblages. Magmatism (feldspar porphyry dykes, monzonite, granitic dykes) is also being geochemically investigated for its possible (active or passive) role on the genesis of the deposit. U-Pb geochronology and geothermobarometry is also being completed to constrain the pressure-temperature-time path of the Low Formation and characterize the long-lived metamorphic event. Data from some gold exploration projects around the Éléonore mine (e.g. Cheechoo, Éléonore Sud, Vieux Camp) will be integrated into a geological model.

ACKNOWLEDGEMENTS

Goldcorp Inc., Éléonore mine is gratefully acknowledged for logistics during fieldwork and underground access (staff from Geology Exploration Department and Geology Mine department, especially François Pulinckx, Catherine Vellet and David Bélisle), scholarship funding, and scientific support for the geology and new data obtained through mine production activity. Eric Fournier (Exploration Geologist at Goldcorp Inc.) is particularly thanked for technical, logistical, and scientific support on ArcGIS software. We are grateful to Julie Doyon, Luc Théberge, Peter Lauder, and Martin Perron for many constructive and enthusiastic discussions related to this scientific research. Ressources Sirios is also thanked for constructive discussions and sharing their knowledge on the geology of the Cheechoo project. INRS ETE, GSC, FRQNT (Fonds de recherche du Québec – Natures et technologies) and NSERC (Natural Sciences and Engineering Research Council of Canada) are also thanked for a scholarship funding related to the BMP (Bourse en milieu pratique) Innovation funding. We are grateful to the reviewer, Sébastien Castonguay, for helpful comments that improved the clarity of the manuscript.

REFERENCES

Aucoin, M., Beaudoin, G., Creaser, R.A., and Archer, P., 2012. Metallogeny of the Marco zone, Corvet Est, disseminated gold deposit, James Bay, Quebec, Canada; Canadian Journal of Earth Sciences, v. 49, p. 1154–1176.

Bandyayera, D. and Fliszár, A., 2007. Géologie de la région de la baie Kasipaskatch (33C09) et du lac Janin (33C16); Ministère des Ressources naturelles et de la Faune du Québec, RP 2007-05, 15 p.

Bandyayera, D., Rhéaume, P., Maurice, C., Bédard, E, Morfin, S., and Sawyer, E.W., 2010. Synthèse géologique du Secteur du Réservoir Opinaca, Baie-James; Ministère des Ressources naturelles et de la Faune du Québec, RG 2010-02, 44 p.

Barnicoat, A.C., Fare, R.J., Groves, D.I., and McNaughton, N.J., 1991. Syn-metamorphic lode-gold deposits in high-grade Archean settings; Geology, v. 19, p. 921–924.

Beauchamp, A-M., Dubé, B., Malo, M., McNicoll, V.J., Archer, P., Lavoie, J., and Chartrand, F., 2015. Geology, mineralization and alteration of the turbidite-hosted Mustang Au showing, Lower Eastmain greenstone belt, Superior Province, Quebec, *In:* Targeted Geoscience Initiative 4: Contributions to the Understanding of Precambrian Lode Gold Deposits and Implications for Exploration, (ed.) B. Dubé and P. Mercier-Langevin; Geological Survey of Canada, Open File 7852, p. 227–243.

Bécu, V., Ravenelle, J-F., Malo, M., Dubé, B., Gauthier, M., and Simoneau, J., 2007. Résultats préliminaires de l'étude de la minéralisation Cu-Au-Ag de l'indice du Lac Ell et de ses implications sur la genèse du gisement d'or Roberto, propriété Éléonore, Baie James; Rapport d'étape DIVEX, SC21, 40 p. http://www.divex.ca/projets/sc21.php

Card, K.D. and Ciesielski, A., 1986. Subdivisions of the Superior Province of the Canadian Shield; Geoscience Canada, v. 13, p. 5–13.

Černý, P., 1991. Fertile granites of Precambrian rare-element pegmatite fields: is geochemistry controlled by tectonic setting or source lithologies?; Precambrian Research, v. 51, p. 429–468.

Černý, P. and Ercit, T.S., 2005. The classification of granitic pegmatites revisited; The Canadian Mineralogist, v. 43, p. 2005–2026.

David, J., 2005. Rapport d'analyses géochronologiques sur des diorites provenant du secteur de la rivière Eastmain – avril 2005; Rapport interne, Virginia Mines Inc., 9 p.

David, J., Davis, D.W., Bandyayera, D., Pilote, P., and Dion, C., 2009. Datations U-Pb effectuées dans les sous-provinces de l'Abitibi et de La Grande en 2006-2007; Ministère des Ressources naturelles et de la Faune du Québec, RP 2009-02, 17 p.

Dubé, B. and Gosselin, P., 2007. Greenstone-hosted quartz-carbonate vein deposits, *In:* Mineral Deposits of Canada: A Synthesis of Major Deposit Types, District Metallogeny, the Evolution of Geological Provinces, and Exploration Methods, (ed.) W.D. Goodfellow; Geological Association of Canada, Mineral Deposits Division, Special Publication, No. 5, p. 49–73.

Dubé, B., Balmer, W., Sanborn-Barrie, M., Skulski, T., and Parker, J., 2000. A preliminary report on amphibolite facies, disseminated replacement-style mineralization at the Madsen gold mine, Red Lake, Ontario; Geological Survey of Canada, Current Research 2000-C17, 12 p.

Dubé, B., Mercier-Langevin, P., Castonguay, S., McNicoll, V., Pehrsson, S.J., Bleeker, W., Schetselaar, E.M., and Jackson, S., 2011a. Targeted Geoscience Initiative 4. Lode gold deposits in ancient, deformed and metamorphosed terranes – footprints and exploration implications: a preliminary overview of themes, objectives and targeted areas, *In:* Summary of field work and other activities 2011; Ontario Geological Survey, Open File Report 6270, p. 38-1 to 38-10.

Dubé, B., Ravenelle, J.-F., McNicoll, V., Malo, M., Nadeau, L., Creaser, R.A., and Simoneau, J., 2011b. The world-class Roberto gold deposit, Éléonore property, James Bay area, Superior province, Quebec: Insights from geology and geochronology, *In:* Program with Abstracts; Geological Association of Canada-Mineralogical Association of Canada-Society of Economic Geologists-Society for Geology Applied to Mineral Deposits (GAC-MAC-SEG-SGA) joint meeting, Ottawa, May 25-27, 2011, v. 34, p. 55.

Fontaine, A., Dubé, B., Malo, M., McNicoll, V., and Brisson, T., 2014. Géologie et caractéristiques structurales du gisement aurifère Roberto, Propriété Éléonore, Province du Supérieur, Baie-James, Québec, Canada, *In:* Abstracts; Québec Mines 2014, Ministère de l'Énergie et des Ressources naturelles du Québec, Québec, 17-20 novembre, 2014, DV 2014-04, p. 135.

Franconi, A., 1978. La bande volcanosédimentaire de la rivière Eastmain Inférieure; Ministère des richesses naturelles du Québec, DPV-574, 184 p.

Gauthier, M., 2000. Styles et répartition des gîtes métallifères du territoire de la Baie-James (Québec); Chronique de la recherche minière, N 539, p. 17–61.

Gauthier, M., Trépanier, S., and Gardoll, S., 2007. Metamorphic gradient: A regional-scale area selection criterion for gold in the northeastern Superior province, eastern Canadian Shield; Society of Economic Geologists Newsletter, v. 69, p. 1, 10–15.

Goldcorp, 2014. Reserves & Resources; http://www.goldcorp.com/English/Investor-Resources/Reserves-and-Resources/default.aspx (February 9th, 2015).

Goldfarb, R.J., Baker, T., Dubé, B., Groves, D.I., Hart, C.J.R., Robert, F., and Gosselin, P., 2005. World distribution, productivity, character, and genesis of gold deposits in metamorphic terranes, *In:* 100th Anniversary Volume, (ed.) J.W. Hedenquist, J.F.H. Thompson, R.J. Goldfarb, and J.P. Richards; Society of Economic Geologists, p. 407–450.

Gosselin, P. and Dubé, B., 2005a. Gold deposits and gold districts of the world; Geological Survey of Canada, Open File 4893, 1 sheet.

Gosselin, P. and Dubé, B., 2005b. Gold deposits of the world: distribution, geological parameters and gold content: Geological Survey of Canada, Open File 4895, 214 p., 1 CD-ROM.

Goutier, J. and Dion, C., 2004. Géologie et minéralisation de la Sous-province de La Grande, Baie-James, Dans: Résumés des conférences et des photoprésentations; Québec Exploration 2004, Ministère des Ressources naturelles et de la Faune du Québec, Québec, 22-25 novembre, 2004, DV 2004-06, p. 21.

Goutier, J., Dion, C., Ouellet, M.C., Mercier-Langevin, P., and Davis, D.W., 2001. Gélogie de la Colline Masson, de la Passe Awapakamich, de la Baie Caribellet et de la Passe Pikwahipanan (SNRC 33F/09, 33F/15 et 33F/16); Ministère des Ressources naturelles du Québec, RG-2000-10, 67 p.

Groves, D.I., Goldfarb, R.J., Gebre-Mariam, M., Hagemann, S.G., and Robert, F., 1998. Orogenic gold deposits: A proposed classification in the context of their crustal distribution and relationship to other gold deposit types; Ore Geology Reviews, v. 13, p. 7–27.

Henry, D.J., Guidotti, C.V., and Thomson, J.A., 2005. The Ti-saturation surface low-to-medium pressure metapelitic biotites: Implications for geothermometry and Ti-substitution mechanisms; American Mineralogist, v. 90, p. 316–328.

Hodgson, C.J., 1993. Mesothermal lode-gold deposits, *In:* Mineral Deposit Modelling, (ed.) R.V. Kirkham, W.D. Sinclair., R.I. Thorpe, and J.M. Duke; Geological Association of Canada, Special Paper 40, p. 635–678.

Holdaway, M.J., 2000. Application of new experimental and garnet Margules data to the garnet-biotite geothermometer; American Mineralogist, v. 85, p. 881–892.

Kisters, A.F.M., Kolb, J., and Meyer, F.M., 1998. Gold mineralization in high-grade metamorphic shear zones of the Renco Mine, southern Zimbabwe; Economic Geology, v. 93, p. 587–601.

Mercier-Langevin, P., Daigneault, R., Goutier, J., Dion, C., and Archer, P., 2012. Geology of the Archean intrusion-hosted La-Grande-Sud Au-Cu prospect, La Grande subprovince, James Bay Region, Québec; Economic Geology, v. 107, p. 935–962.

Morfin, S., Bandyayera, D., and Sawyer, E.W., 2013. Large volumes of anatectic melt retaine in granulite facies migmatites: An injection complex in northern Quebec; Lithos, v. 168-169, p. 200–218.

McCuaig, T.C., Kerrich, R., Groves, D.I., and Archer, N., 1993. The nature and dimensions of regional and local gold-related hydrothermal alteration in tholeiitic metabasalts in Norseman goldfields: The missing link in a crustal continuum of gold deposits?; Mineralium Deposita, v. 28, p. 420–435.

Moukhsil, A., Legault, M., Boily, M., Doyon, J., Sawyer, E., and Davis, D.W., 2003. Synthèse géologique et métallogénique de la ceinture de roches vertes de la Moyenne et de la Basse-Eastmain (Baie-James); Ministère des Ressources naturelles, de la Faune et des Parcs du Québec, ET 2002-06, 55 pages, 1 plan.

Neumayr, P., Cabri, L.J., Groves, D.I. Mikucki, E.J., and Jackman, J.A., 1993. The mineralogical distribution of gold and relative timing of gold mineralization in two Archean settings of high metamorphic grade in Australia; The Canadian Mineralogist, v. 31, p. 711–725.

Percival, J.A., 2007. Geology and metallogeny of the Superior Province, Canada, *In:* Mineral Deposits of Canada: A Synthesis of Major Deposit Types, District Metallogeny, the Evolution of Geological Provinces, and Exploration Methods, (ed.) W.D. Goodfellow; Geological Association of Canada, Mineral Deposits Division, Special Publication, No. 5, p. 903–928.

Phillips, G.N. and Powell, R., 2009. Formation of gold deposits: Review and evaluation of the continuum model; Earth-Sciences Reviews, v. 94, p. 1–21.

Poulsen, K.H., Robert, F., and Dubé B., 2000. Geological classification of Canadian gold deposits; Geological Survey of Canada, Bulletin 540, 106 p.

Ramsay, J. and Huber, M., 1987. The techniques of modern structural geology: Folds and fractures; Academic Press, London, 391 p.

Ravenelle J.-F., 2013. Amphibolite Facies Gold Mineralization: An example from the Roberto deposit, Eleonore property, James Bay, Quebec; Ph.D. thesis, Institut national de la recherche scientifique, Centre Eau Terre Environnement, Québec, Quebec, 283 p.

Ravenelle, J.-F., Dubé, B., Malo, M., McNicoll, V., and Nadeau, L., 2009. Geology of the amphibolite-facies world-class Roberto gold deposit, Eleonore property, James Bay, Canada, *In:* Proceeding; Tenth Biennial SGA Meeting, Townsville, Australia, August 17-20, 2009, p. 59–61.

Ravenelle J.-F., Dubé B., Malo M, McNicoll V., Nadeau L., Simoneau J., 2010. Insights on the geology of the world-class Roberto gold deposit, Eléonore property, James Bay area, Québec; Geological Survey Canada, Current Research 2010-1, 26 p.

Robert F., Poulsen K.H., Cassidy K. F., Hodgson C.J., 2005. Gold metallogeny of the Superior and Yilgarn cratons, *In:* 100th Anniversary Volume, (ed.) J.W. Hedenquist, J.F.H. Thompson, R.J. Goldfarb, and J.P. Richards; Society of Economic Geologists, p. 1001–1033.

Ressources Sirios, 2014. Press release; http://sirios.com/fr/chee-choo, (December 8th, 2014).

Sillitoe R.H. and Bonham H.F., 1990. Sediment-hosted gold deposits: Distal products of magmatic-hydrothermal systems; Geology, v. 18, p. 157–161.

Stüwe, K., 1998. Tectonic constraints on the timing relationships of metamorphism, fluid production, and gold-bearing quartz vein emplacement; Ore Geology Reviews, v. 13, p. 219–228.

Thériault, R. and Beauséjour, S., 2012. Carte géologique du Québec – édition 2012; Ministère des Ressources naturelles du Québec, DV 2012-06, 8 p., 1 carte et données numériques.

Thompson, A.B. and Tracy, R.J., 1979. Model systems for anatexis of pelitic rocks. II. Facies series melting and reaction in the system $CaO\text{-}KAlO_2\text{-}NAlO_2\text{-}Al_2O_3\text{-}SiO_2\text{-}H_2O$; Contributions to Mineralogy and Petrology, v. 98, p. 257–276.

Thompson, P.H., 2003. Toward a new metamorphic framework for gold exploration in the Red Lake greenstone belt; Ontario Geological Survey, Open File Report 6122, 52 p.

Tomkins, A.G. and Mavrogenes, J.A., 2002. Mobilization of gold as a polymetallic melt during pelite anatexis at the Challenger deposit, South Australia: a metamorphosed Archean gold deposit; Economic Geology, v. 97, p. 1249–1271.

Tomkins, A.G., Pattison, D.R.M., and Zaleski, E., 2004. The Hemlo gold deposit, Ontario: an example of melting and mobilization of a precious metal-sulfosalt assemblage during amphibolite facies metamorphism and deformation; Economic Geology, v. 99, p. 1063–1084.

Tomkins, A.G., Frost, B.R., and Pattison, D.R.M., 2006. Arsenopyrite melting during metamorphism of sulfide ore deposits; The Canadian Mineralogist, v. 44, p. 1045–1062.

Vielzeuf, D. and Holloway J.R., 1988. Experimental determination of fluid-absent melting relations in the pelitic system: consequences for crustal differentiation; Contributions to Mineralogy and Petrology, v. 98, p. 257–276.

Vry J., Powell, R., Golden, K.M., and Petersen, K., 2010. The role of exhumation in metamorphic dehydration and fluid production; Nature Geoscience, v. 3, p. 31–35.

GEOLOGICAL SURVEY OF CANADA
OPEN FILE 7852

Targeted Geoscience Initiative 4: Contributions to the Understanding of Precambrian Lode Gold Deposits and Implications for Exploration

Geology, mineralization, and alteration of the turbidite-hosted Mustang Au showing, Lower Eastmain greenstone belt, Superior Province, Quebec

Anne-Marie Beauchamp[1], Benoît Dubé[2], Michel Malo[1], Vicki J. McNicoll[3], Paul Archer[4], Jérôme Lavoie[4], and Francis Chartrand[4]

[1]Institut national de la recherche scientifique – Centre Eau Terre Environnement, Québec, Quebec
[2]Geological Survey of Canada, Québec, Quebec
[3]Geological Survey of Canada, Ottawa, Ontario
[4]Exploratrion Osisko - Baie James, Québec, Quebec

2015

This publication is available for free download through GEOSCAN (http://geoscan.nrcan.gc.ca/)

Recommended citation

Beauchamp, A.-M., Dubé, B., Malo, M., McNicoll, V.J., Archer, P., Lavoie, J., and Chartrand, F., 2015. Geology, mineralization, and alteration of the turbidite-hosted Mustang Au showing, Lower Eastmain greenstone belt, Superior Province, Quebec, *In:* Targeted Geoscience Initiative 4: Contributions to the Understanding of Precambrian Lode Gold Deposits and Implications for Exploration, (ed.) B. Dubé and P. Mercier-Langevin; Geological Survey of Canada, Open File 7852, p. 227–243.

Publications in this series have not been edited; they are released as submitted by the author.

Contribution to the Geological Survey of Canada's Targeted Geoscience Initiative 4 (TGI-4) Program (2010–2015)

TABLE OF CONTENTS

Geology, mineralization and alteration of the turbidite-hosted Mustang Au showing, Lower Eastmain greenstone belt, Superior Province, Quebec

Anne-Marie Beauchamp[1]*, Benoît Dubé[2]†, Michel Malo[1], Vicki J. McNicoll[3], Paul Archer[4], Jérôme Lavoie[4], and Francis Chartrand[4]

[1]Institut national de la recherche scientifique – Centre Eau Terre Environnement, 490 rue de la Couronne, Québec, Quebec G1K 9A9
[2]Geological Survey of Canada, 490 rue de la Couronne, Québec, Quebec G1K 9A9
[3]Geological Survey of Canada, 601 Booth Street, Ottawa, Ontario K1A 0E9
[4]Exploration Osisko -Baie James, 300 rue Saint-Paul, suite 200, Québec, Quebec G1K 7R1
*Corresponding author's e-mail: anne-marie.beauchamp@ete.inrs.ca
†Corresponding author's e-mail: bdube@nrcan.gc.ca

ABSTRACT

The Mustang gold showing is located on the Wabamisk property owned by Exploration Osisko - Baie James. The Mustang Vein (N240/80°) is located near the contact between the La Grande and Opinaca subprovinces in the Superior Province, 65 km southwest of the Éléonore gold mine. The gold zone is exposed on surface and can be traced through drillholes over a strike length of 570 m and to a depth of 225 m. The vein and its mineralized envelope range from a few centimetres to six metres in width. Gold values obtained for the vein reach 111.17 g Au/t over 2.6 m in channel sample and 22.65 g Au/t over 2.25 m in drillhole. More than 75 gold showings (Au >500 ppb) were discovered over a 10 by 10 km area around the Mustang Vein. The Mustang Vein is a quartz (±carbonate) laminated vein hosted in turbiditic metasedimentary rocks (greenschist facies) located near the top of an Archaean stratigraphic sequence of the Eastmain Belt. The preliminary results of U-Pb dating on detrital zircons of the metasedimentary rocks hosting the Mustang Vein indicate a maximum deposition age of 2709 ±4 Ma. The sedimentary sequence has undergone at least three deformation phases, including an initial phase of north-northwest-oriented folding with F_1 folds refolded by east-northeast-oriented F_2 folds. The S_2 foliation is oriented east-northeast with a steep dip and an axial plane with P_2 folds. The D_3 deformation phase is characterized by a moderate-dip, southwest-oriented crenulation cleavage. The Mustang Vein is subparallel to the bedding and folded into S shapes by the F_2 folds. It is interpreted as syn-D_2 regional deformation, along a F_2 fold limb. The vein and the altered walls (potassic alteration and carbonatization) contain 1–10% arsenopyrite, 5–10% pyrrhotite, with traces of pyrite, chalcopyrite, galena, and sphalerite. Locally, gold grains in the veins and altered host rock are disseminated and aligned on the main S_2 foliation planes.

The geological context and mineralization, alteration, and deformation styles at the Mustang showing are analogous to syn-deformation deposits hosted in turbidite sequences (e.g. Meguma in Nova Scotia and Central Victoria in Australia). Like the Roberto Gold Deposit (Éléonore Mine), the Mustang gold showing illustrates the potential for folded Archaean metasedimentary assemblages of the La Grande Subprovince proximal to the tectono-metamorphic boundary of the Opinaca Subprovince to host major gold deposits in the James Bay Region.

INTRODUCTION

Since the discovery of the Éléonore Mine's Roberto deposit (Goldcorp Inc.) by Virginia Mines Inc. in 2004, mining exploration companies have become increasingly interested in testing the gold potential of Archaean sedimentary rock sequences in the Superior Province. The Éléonore Mine is a world-class gold deposit (1.06 million ounces at 6.34 g Au/t of measured and indicated resources, 2.80 million ounces at 7.19 g Au/t of inferred resources, and 4.97 million ounces at 6.3 g Au/t of reserves: Goldcorp, 2014) that has recently been put into production. It is a metamorphosed gold deposit hosted in <2675 Ma metasedimentary rocks (Ravenelle et al., 2010; Fontaine et al., 2015) and located in the James Bay Region, about 65 km north-northeast of the Mustang gold showing (Figs. 1, 2). Discovered in the summer of 2012, the Mustang gold showing is a gold-quartz-carbonate vein that is

Beauchamp, A.-M., Dubé, B., Malo, M., McNicoll, V.J., Archer, P., Lavoie, J., and Chartrand, F., 2015. Geology, mineralization, and alteration of the turbidite-hosted Mustang Au showing, Lower Eastmain greenstone belt, Superior Province, Quebec, *In:* Targeted Geoscience Initiative 4: Contributions to the Understanding of Precambrian Lode Gold Deposits and Implications for Exploration, (ed.) B. Dubé and P. Mercier-Langevin; Geological Survey of Canada, Open File 7852, p. 227–243.

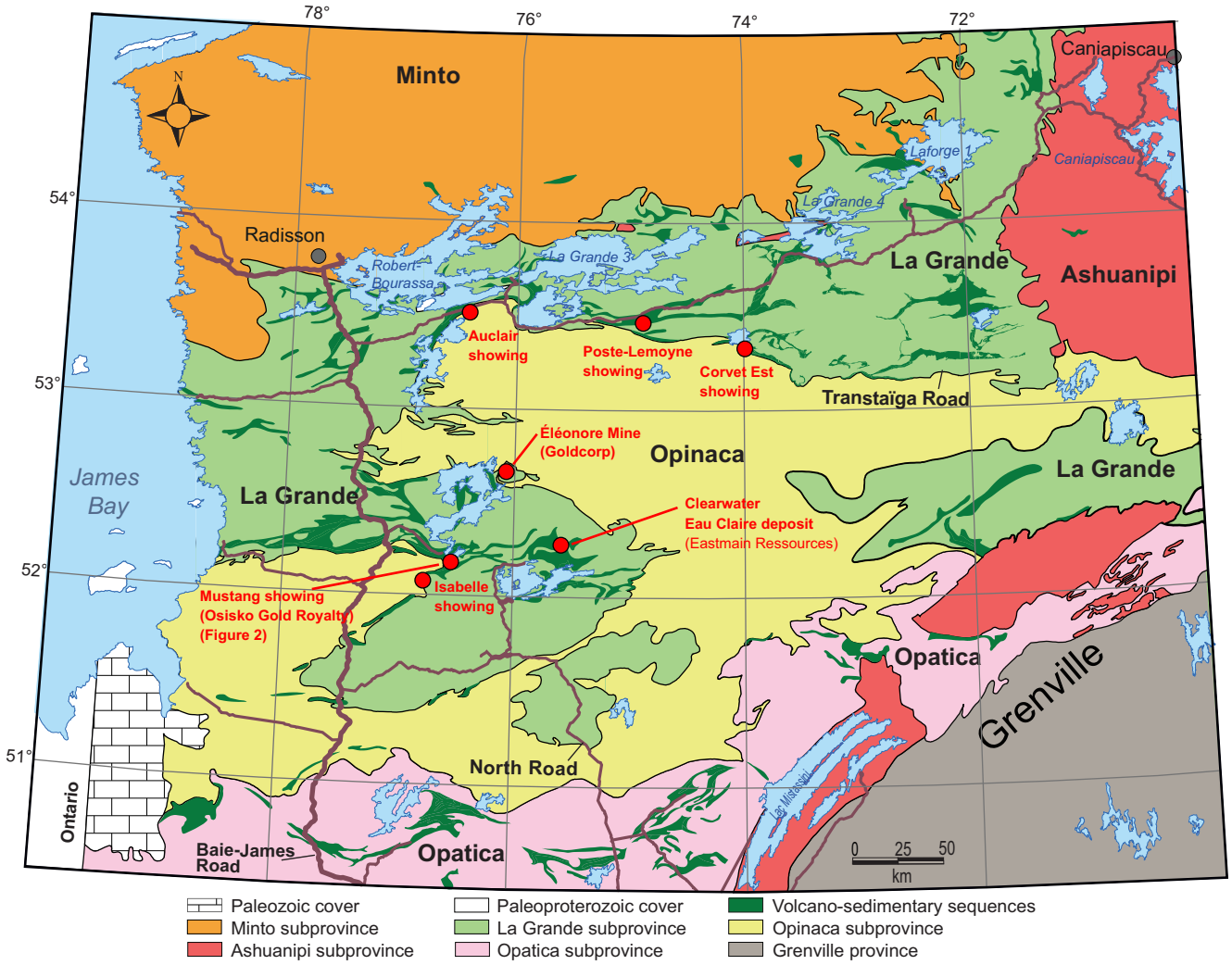

Figure 1. Location of the geological subprovinces of the Superior Province and position of the Mustang Au showing.

exposed at surface and can be intersected in drillhole over a strike length of 570 m, and to a depth of 225 m through mechanical excavation and drilling. The current study, which includes a Master's research project, was initiated under the umbrella of the Targeted Geoscience Initiative 4, Lode Gold Project of Natural Resources Canada (Dubé et al., 2011). The project objective is to document the geological and structural setting of the Mustang Vein and to define its metallic and hydrothermal signature in order to define the ore-forming controlling parameters and consequently improve geological and exploration models for the study area and elsewhere in the James Bay Region.

RESULTS AND DATA ANALYSIS

Regional Geology

The gold showing is located in the Lower Eastmain Greenstone Belt, which forms part of the La Grande Subprovince, near the contact with the Opinaca Subprovince in the central part of the Superior Province (Fig. 1).

The La Grande Subprovince contains volcano-sedimentary and plutonic assemblages overlying an old tonalitic basement (2.79–3.39 Ga) and consists of 85% syntectonic to post-tectonic plutonic rocks and 15% volcano-sedimentary rocks, which form the two volcanic belts of the La Grande and Eastmain rivers. The Middle and Lower Eastmain greenstone belt, which includes Eastmain Group rocks, extends along an east-west axis over 300 km and varies between 10 and 70 km in width (Franconi, 1978). The Eastmain Group comprises four volcanic cycles: (1) the 2,751.6 +0.6/-0.8 Ma Kauputauch Formation (Moukhsil et al., 2001); (2) the 2739 ±5 Ma Natel Formation (Moukhsil, 2000); (3) the 2723.1 ±2.2 Ma Anatacau-Pivert Formation (Moukhsil et al., 2001); and (4) the 2703 ±8 Ma to 2705 ±3 Ma Komo and the 2705 ±3 Ma Kasak formations (Moukhsil et al., 2001). The volcanism within the Lower Eastmain greenstone belt was produced during a relatively continuous interval of at least 50 Ma (Boily et al., 2003). The Eastmain Group volcanic rock, whose composition varies from komatiitic

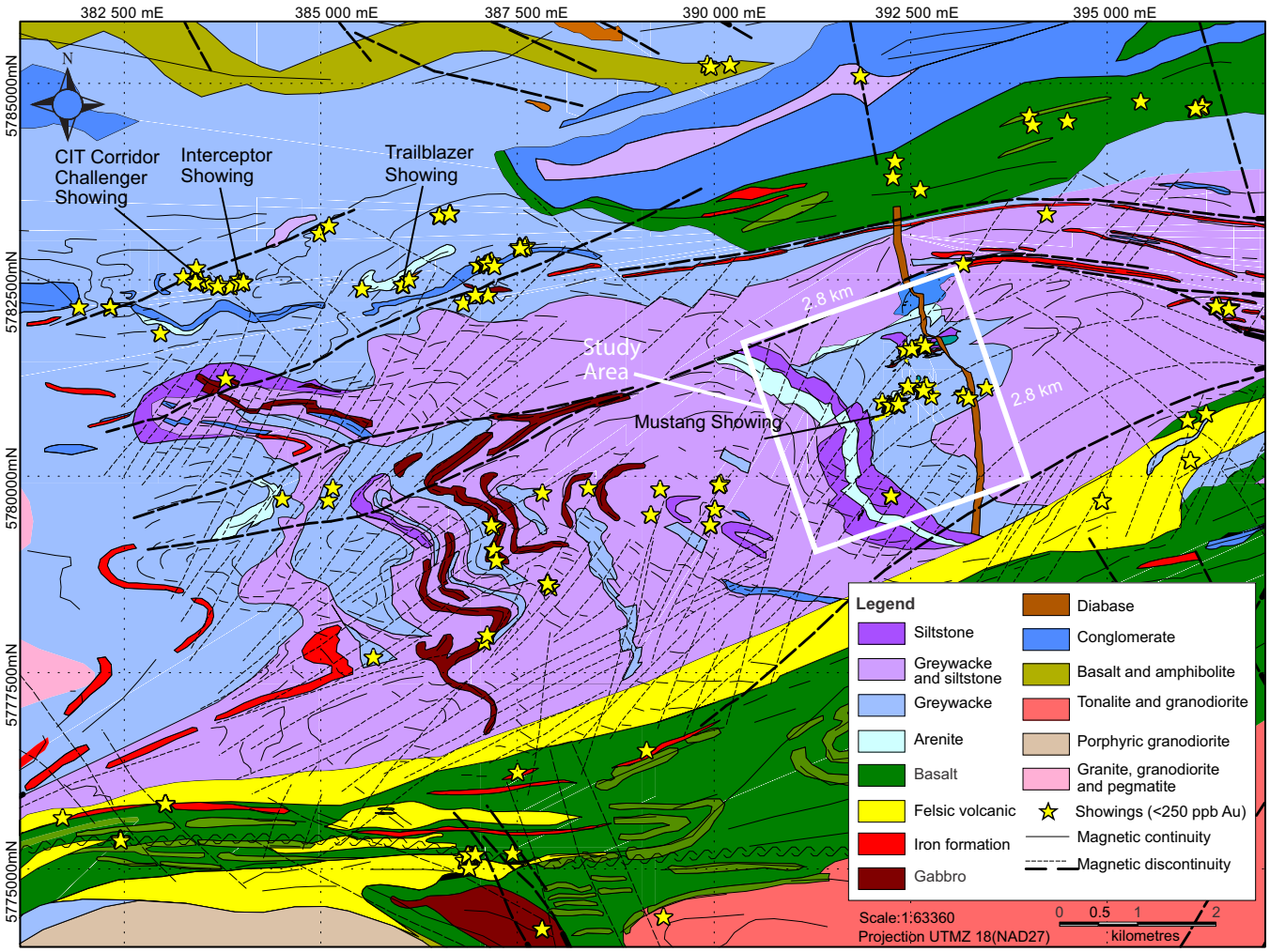

Figure 2. Regional geology of the Mustang area modified from SIGEOM by Pearson (2012), Lavoie (2013), and Beauchamp (2013) (internal data from Exploration Osisko - Baie James).

to rhyolitic, was created in an extensive ocean environment (Moukhsil et al., 2003). It is transected by various multi-phase intrusions of dioritic, tonalitic, granodioritic, and syntectonic to post-tectonic granitic composition.

The Opinaca Subprovince is a basin of Neo-Archaean sedimentary rock deposited on the La Grande Subprovince (Card and Ciesielski, 1986; Goutier et al., 2001). It consists mainly of migmatitic paragneiss and diatexite belonging to the Laguiche Complex (Bandyayera et al., 2010). The Opinaca Subprovince of the Superior Province is considered equivalent to the English River and Quetico metasedimentary subprovinces in Ontario (Card and Ciesielski, 1986; Goutier et al., 2001; Moukhsil et al., 2001; Doyon, 2004).

Three regional deformation phases (D_1, D_2, and D_3) are recognized within the Lower Eastmain greenstone belt. The large east-northeast to west-southwest regional structures are associated with D_2 deformation. In the study area, the La Grande Subprovince is characterized by tight, shallow-plunging large folds; the rocks of the Opinaca Subprovince are characterized by relatively scattered and detached domes-and-basins (Bandyayera et al., 2010). The rocks have been variable metamorphosed from greenschist to middle-amphibolite facies in the La Grande Subprovince and up to upper amphibolite and granulite facies of in the Opinaca Subprovince (Bandyayera et al., 2010).

There is a limited regional data available for the La Grande Subprovince - Opinaca Subprovince contact. The contact zone has been reported as a thrust zone (Gosselin and Simard, 1999), an unconformity (Gosselin and Simard, 1999), and characterized as a major fault zone (Bandyayera et al., 2010).

Deformation and Structural Style of the Mustang Gold Showing

The rocks in the vicinity of the Mustang gold showing have undergone several deformation phases. The D_1 deformation is characterized an S_1 schistosity, which is subparallel to the bedding (S_0) (Figs. 3a,b). The S_1

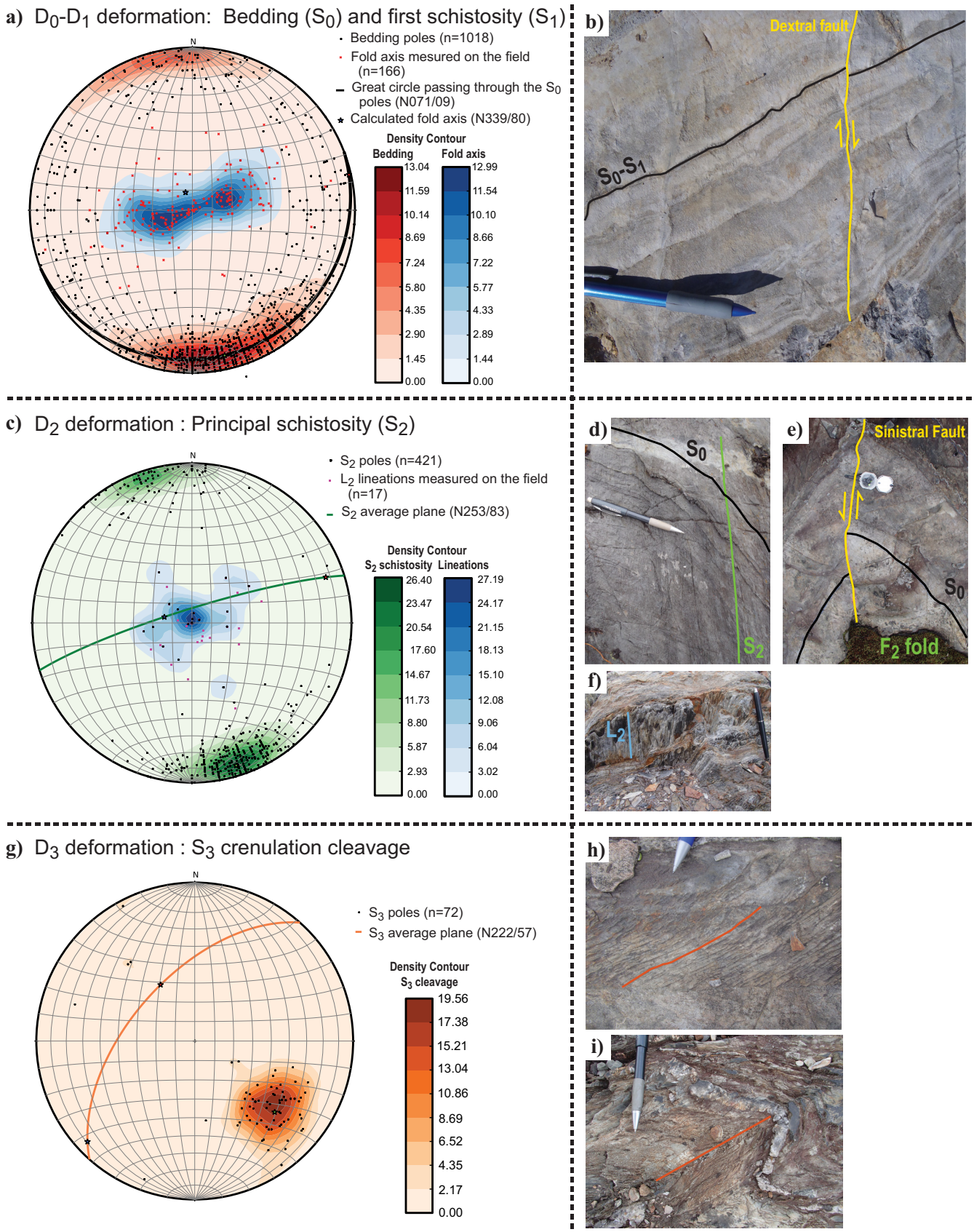

Figure 3. a) Stereonet of D_0-D_1 features. **b)** Photograph of well exposed primary bedding (S_0-S_1). **c)** Stereonet of D_2 features. **d)** Photograph of penetrative S_2 lineation that is axial planar to F_2 fold. **e)** Photograph of a F_2 fold that has been deformed by asinistral fault. **f)** Photograph of the subvertical L_2 lineation in a high-strain zone. **g)** Stereonet of D_3 feature. **h)** Photograph of typical S_3 renulation cleavage. **i)** Photograph of a F_3 kink fold.

schistosity is locally well preserved in the F_2 fold hinges. The D_2 deformation is characterized by regionally pervasive east-northest-trending S_2 schistosity (Fig. 3c), which is axial planar to the F_2 folds (Fig. 3c,e) and is defined by prograde metamorphic minerals (biotite, muscovite and ±chlorite). The S_2 foliation is better developed in the fine-grain facies (i.e. siltstone) than in the more massive and competent facies, such as greywacke. As shown in Figure 3a, the average attitude of the principal S_2 schistosity is N253/83° (n=421 measurements). The S_2 planes contain a subvertical stretching lineation (Fig. 3f). The flattening ratios of the conglomerate clasts exposed north of the Mustang gold showing vary from 1:5 to 1:15. The F_2 folds plunge sharply towards either the west or the east. This variation may be caused by the presence of earlier folds (F_1) that would have influenced the plunge of the F_2 folds axis. The F_2 folds vary from open to isoclinal (average 25º). Locally, these folds are faulted subparallel to the axial plane, which results in isolated hinge portions between the highly transposed limbs. The intensity of the D_2 deformation is not homogeneous but increases gradually as one gets closer to the D_2 shear zones. The D_3 deformation is characterized by a southwest-northeast crenulation cleavage (N222/57°) (Fig. 3g). Like the S_2 schistosity, the crenulation is better developed in the very fine-grained, aphanitic facies (i.e. siltstone) (Fig. 3h). The F_3 folds (Fig. 3i) are much less frequent than the F_2 folds and form chevron and kink-band folds. The metasedimentary rocks in the Mustang area are affected by greenschist-facies metamorphism.

Gold Mineralization

Gold mineralization in the area of the Mustang showing is mainly hosted in the quartz (±carbonate) veins and their immediate altered host rocks. The morphology and structural relationship make it possible to classify several types of the veins, the two most important being

1. The quartz (±carbonate) veins subparallel to bedding are folded, deformed, and usually laminated but are remarkably continuous. Their width ranges from centimetres to metres. The veins have fault-fill, crack-and-seal, and brecciated textures. The larger quartz (±carbonate) veins are preferentially located in the short limbs of the F_2 folds, indicating that the folding and deformation of the limbs (flexural slip) may have played a role in their formation. The bulk of the gold mineralization on the Wabamisk property (e.g. Mustang, Challenger, and Interceptor veins, Fig. 2) is associated with this type of quartz (±carbonate) vein.
2. Axial-planar quartz veins and the veins crosscutting bedding at high-angles and have been injected into extension fractures subparallel to the axial planes of the F_2 folds, subparallel to the S_2 foliation. These veins subparallel and sometimes boudinaged. These veins, which are abundant in the F_2 hinge zones are very rarely gold-bearing.

Other types of veins include (i) gold-bearing and barren extensional veins; (ii) gold-bearing and barren stockwork veins; (iii) gold-bearing and barren breccia; (iv) barren quartz (±plagioclase) veins with subhorizontal dip; and (v) quartz (±plagioclase) veins filling barren late faults.

Mustang Vein

The Mustang Vein is a quartz (±carbonate) laminated vein hosted in a grey-wacke and siltstone interlayered with 5% argillite beds (Fig. 4). On the surface, the vein is ~0.5 m wide. The direction of sedimentary polarity along the Mustang Vein is southward. The vein walls contain up to 10% sulphides, including coarse-grained arsenopyrite, aggregates and veinlets of crystalline pyrrhotite that are subparallel to the main schistosity, and pyrite with minor chalcopyrite, galena, and sphalerite. Hydrothermal alteration adjacent to the veins is pervasive or pseudo-fragmentary in texture consisting of host rock fragments partially replaced and elongated parallel to L_2 lineation. The alteration and mineralization are sometimes symmetrically distributed in the vein walls, but often the distribution is asymmetrical and limited to a few decimetres wide. The Mustang Vein consists of at least three generations of quartz (Fig. 4a): (1) white quartz distributed along the plane of the vein (about N240°); (2) smoky quartz that transects the white quartz and is oriented N270°; and (3) quartz in late fractures oriented at approximately N330° to N340°. The detailed map and structural analysis show that the Mustang Vein is syn-D_2 regional deformation, along a limb of an F_2 anticlinal fold, because it contains metric fragments of elongated, altered and probably foliated host rock fragments (S_2; Fig. 4c,e). However, the vein has recorded part of the D_2 deformation because it was folded into an S shape by the F_2 folds (Figs. 4b,g, 5a,b). In addition, the vein is broken up into a D_2 late ductile deformation zone. The shear zone is about 8 m wide and characterized by shear bands and the presence of protomylonite (Fig. 5d). The lineations measured in this highly deformed zone are subparallel to L_2, which suggests that the shear zone that deformed the Mustang Vein is syn to late D_2 (Fig. 5d). The highly deformed corridor is characterized by dismembered F_2 folds transposed into the S_2 schistosity. Locally, the vein is contained within a sheared corridor along the limbs of the major fold and several extensional quartz veinlets have developed. At the centre of the main stripped area (trench WB2012TR011; Fig. 4), there is an abrupt change in the general direc-

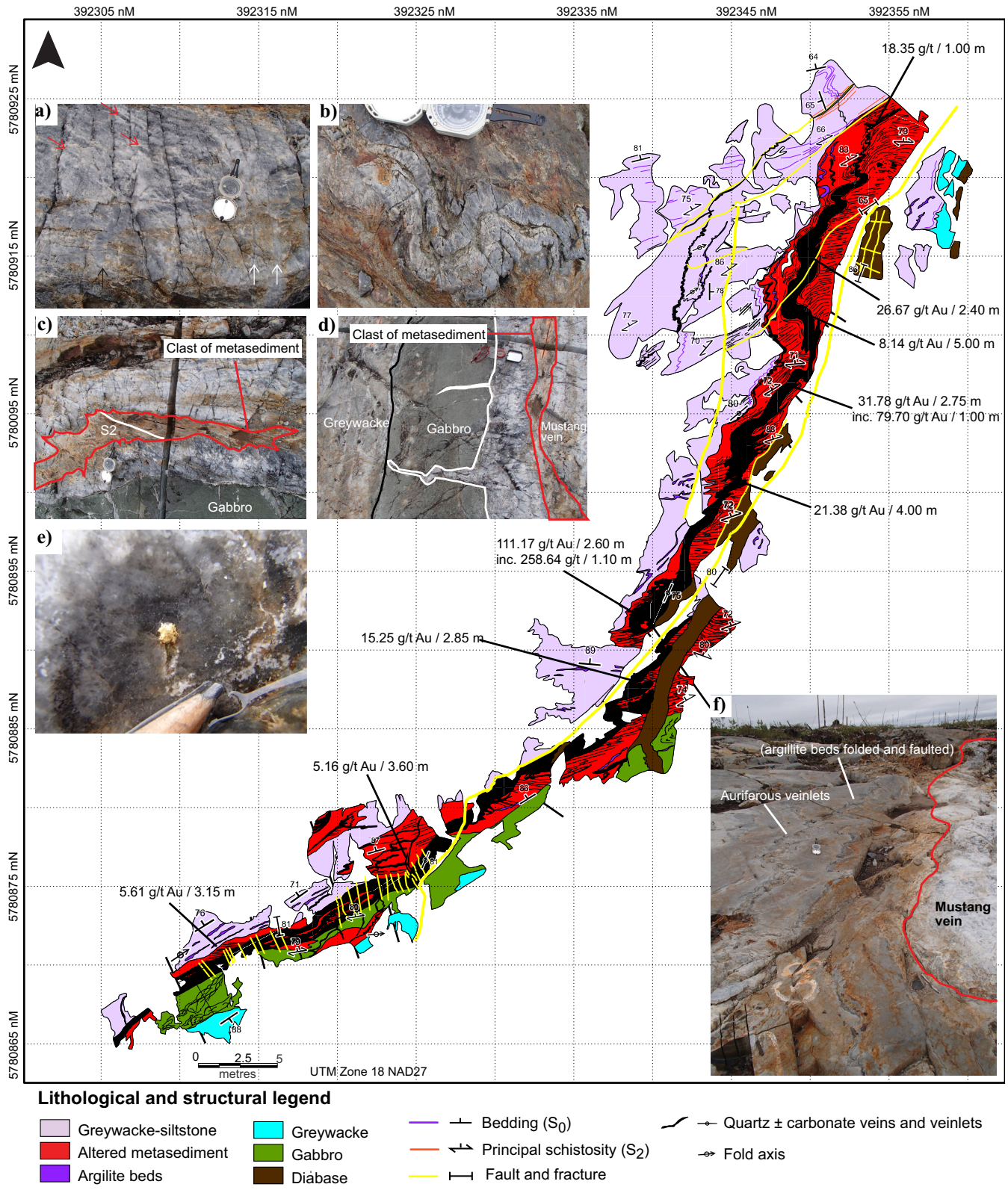

Figure 4. Geological map of Trench WB2012TR011 with some of the higher gold values obtained in channels (in 2012 and 2014); **a)** Red arrows indicate quartz generation #2 and black arrows indicate generation #3. **b)** Laminated Mustang Vein that has been folded by F_2. **c)** Altered and foliated (S_2) clast hosted in the Mustang Vein. **d)** Gabbro was in place before the Mustang Vein because the vein injects and cuts the dyke. **e)** Rounded visible gold grain (5 mm) in the Mustang Vein. **f)** The Mustang Vein and the auriferous veinlets are parallel to the folded bedding.

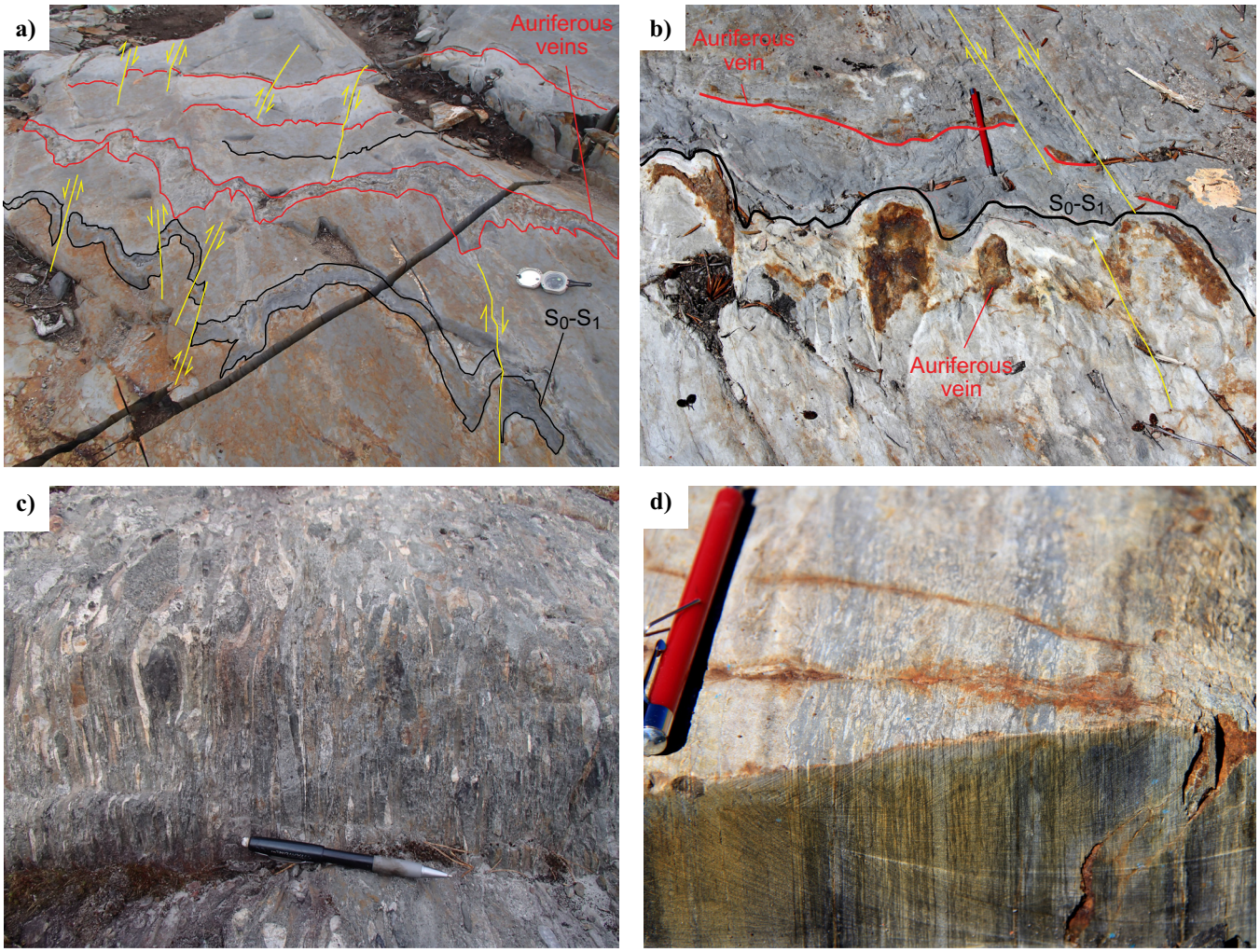

Figures 5. a and b) Auriferous veins and veinlets, a few metres north of the Mustang Vein, can be seen following the folded and faulted primary bedding (S_0-S_1). In photograph (b), the hinges of the rusty quartz vein are thickened (saddle reef), indicating that the folding mechanism played an important role in the implacement of the gold-bearing veins. **c)** Photograph of deformed polygenic conglomerate, 1 km north of the Mustang Vein. This conglomerate could correspond to an orogenic Timiskaming conglomerate, which is typically distributed along a major structure, and may have focused D_2 deformation and hydrothermal fluid circulation on a large scale. **d)** Photograph showing the strong stretching lineation of the protomylonite.

tion of the Mustang Vein. In the northeast part of the stripped area, the subvertical vein is folded by F_2, and its general orientation is N190°. At the centre of the stripped area, the vein becomes more rectilinear and its orientation is N240° in the south half of the stripped area. This sudden change of direction coincides with the presence of a magnesium-rich gabbro dyke in contact with the vein (Fig. 4c,d). The vein runs along the gabbro dyke for more than 300 m. The gabbro was emplaced before the Mustang Vein because the vein intrudes into and transects the dyke (Fig. 4d), which creates a strong rheological contrast (anisotropy) in the sedimentary sequence, which may have channeled or promoted the infiltration of hydrothermal auriferous fluid. This abrupt change in the general direction (flexure) coincides with the highest gold concentrations obtained in the channel samples and could control the formation and geometry of ore shoots.

Mineralization

The gold-bearing veins consist mainly of recrystallized quartz and 1–2% sulphides, mainly arsenopyrite, pyrite, and pyrrhotite, located for the most part in laminae and host-rock fragments. Free gold is visible in the quartz-carbonate veins (Fig. 4e) and forms aggregates. Gold is also found in altered wall rock and is closely associated with arsenopyrite, pyrite, galena, and sphalerite (Fig. 6a,b,c). Gold occurs as inclusions or as fracture-fillings in sulphides and as coatings on grain surfaces. Arsenopyrite and pyrite, which contain inclusions of visible gold, form coarse idiomorphic grains (up to 1 cm; Fig. 6a,b). These grains are accompanied by pressure shadows filled with quartz±carbonate± chlorite±sericite and pyrrhotite (Fig. 6e,f). This texture suggests that these sulphides are syn-deformation. The pyrrhotite is usually stretched and flattened within the

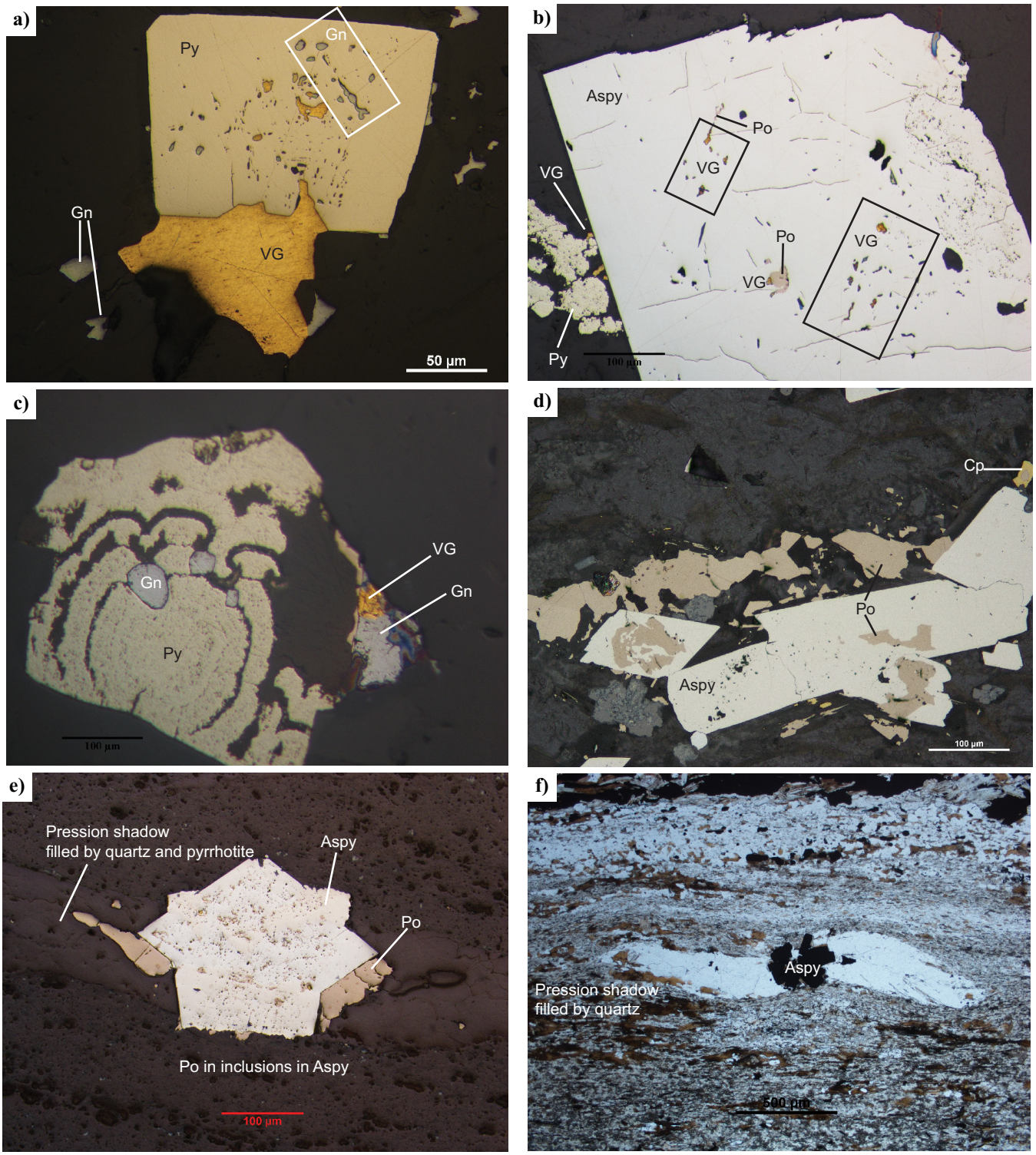

Figure 6. a) Visible gold within and in contact with inclusions in a euhedral pyrite grain. **b)** Gold, galena, and pyrrhotite occur as inclusions in coarse euhedral arsenopyrite. A few grains of gold are on the edge of an arsenopyrite grain that cuts hydrothermal pyrite. **c)** Gold associated with galena and colloidal (hydrothermal) pyrite. **d)** Pyrrhotite crystallized along the main foliation. Some arsenopyrite grains have grown from pyrrhotite. **e and f)** A typical pressure shadow within the mineralized zone suggests that the arsenopyrite and quartz are synkinematic. Abbreviations: Aspy = arsenopyrite; Cp = chalcopyrite; Gn = galena; Po = pyrrhotite; Py = pyrite; VG = visible gold.

main schistosity (Fig. 6d), which indicates that the bulk of the pyrrhotite has registered, at least partly, the D_2 deformation episode. Locally, cavities in the gold-bearing quartz veins contain framboidal pyrite of hydrothermal origin (Fig. 6c). This colloform pyrite is transected by pyrrhotite and arsenopyrite and by idiomorphic pyrite.

Hydrothermal Alteration

The 141 samples of metasedimentary rocks studied in the course of this project are distributed within a 2 km^2 area around the Mustang gold showing (Fig. 7). They consist in fresh and altered rock samples from outcrops and drillholes. The hydrothermal alteration associated with the Mustang gold showing system was characterized by petrography and mass balance calculation (Grant, 1986, 2005). Because the clastic, turbiditic metasedimentary rocks are very heterogeneous in terms of primary composition, finding a protolith with little alteration that is representative of the various types of metasedimentary rock is fundamental in performing mass balance calculations. A method developed by Trépanier (2011), based on the work of Sawyer (1986) and Fralick and Kronberg (1997), can be used to subdivide the metasedimentary rocks according to their source and degree of hydraulic sorting. For each subdivision (source/sorting combination), a relatively fresh protolith was selected and a mass balance was calculated (Trépanier, 2011). The fresh, or weakly altered, protoliths were selected upon petrographical observations and lithogeochemical results. All of the selected protoliths have low concentrations of CO_2 (<0.04 wt%), S (<0.4 wt%), LOI <3 wt%), Au (≤5 ppb, lower limit of detectability) and As (<25 ppm).

The Al_2O_3/TiO_2 diagram shows two relatively immobile major oxides preferentially concentrated in the clay fraction (Sawyer, 1986; Doyon, 2004). This diagram identifies various groups that may reflect potential sedimentary sources by means of straight lines passing through the sedimentary origin (Fig. 8a,c). According to this method, the 141 samples of metasedimentary rocks that were studied are divided into three groups (potential sources) represented by Group 1 (n=112), Group 2 (n=22), and Group 3 (n=7). Each group was then subdivided into subgroups based on their degree of hydraulic sorting (sandstone versus clay). To illustrate the hydraulic sorting phenomenon, it is necessary to compare a relatively immobile element that is preferentially concentrated in clays (e.g. Al_2O_3) with another element that is preferentially concentrated in sands (e.g. Zr; Fig. 8b). For each source/sorting combination, a protolith was selected in order to limit the primary variation of compositions. Group 1 rocks have undergone hydraulic sorting, which made it possible to subdivide them into three subgroups (three protoliths; Fig. 8d).Due to the small number of rocks in groups 2 and 3, no clear hydraulic sorting could be determined and thus a single protolith was attributed to each group.

The mass balances for all of the metasedimentary rock samples were calculated based upon their group (precursor). Samples from groups 1 and 2 were affected by hydrothermal alteration, though Group 3 samples were not altered. Hydrothermal alteration was indicated by sulphidization (arsenopyrite, pyrrhotite, pyrite ±galena, and sphalerite), which is present in the walls of the gold-bearing quartz (±carbonate) veins. The petrographic and lithogeochemical studies showed that potassic alteration (Figs. 9, 10a) and carbonatization (Figs. 9b,c,d, 11) were the two main types of alteration proximal to the gold-bearing quartz±carbonate veins. Potassic alteration is indicated primarily by sericite assemblages (Fig. 9a), biotite assemblages, and areas with high microcline content. The mass balance calculations indicate that the potassic alteration is characterized by gains in K_2O, Cr_2O_3, B, Se, Rb, Nb, Mo, Sb, Te, Ta, Pb, Bi, Th, U, CO_2, S, As, Au, and W, and by loss in Na_2O, P_2O_5, and MgO, and to a lesser extent, by decreased SiO_2, CaO, $Fe_2O_3{}^T$, FeO, and Zn content (Fig. 10).

Carbonatization is more difficult to identify in the field. The geochemistry and petrology help to better define this alteration. The carbonatization is characterized by a 5−15% content of carbonate (calcite ± iron carbonate) in the rocks. The carbonate is present in veinlet (±quartz) and replacement zones in the metasedimentary matrix of quartz-feldspars-biotite ± muscovite ± chlorite ± amphibole ± garnet (Fig. 9c). The carbonatization shows gains in CO_2, CaO, (K_2O or Na_2O), P_2O_5, B, Se, Mo, Sb, Te, S, As, Au, and W. Loss of mass affects concentrations of SiO_2, $Fe_2O_3{}^T$, FeO, (K_2O or Na_2O) and MgO (Fig. 11). This carbonatization is accompanied by either calcium-potassium gains (CO_2-Ca-K alteration) or calcium-sodium gains (CO_2-Ca-Na alteration).

A distal calcic-sodic alteration is present for 10−50 m from the gold-bearing veins. This alteration is characterized by gains in CaO, Na_2O, MgO, MnO, Cr_2O_3, Be, Mn, Se, Sr, Te, CO_2, S, As, Au, and W (Figs. 9e, 12). In the field, this alteration can be recognized in metasedimentary rocks by its white colour (Na plagioclase; $An_{10–30}$) containing 5−30% of non-oriented magnesiohornblende (Fig. 9e). Amphibole is abundant as replacement between beds, as veinlets, and as semi-pervasive replacements.

Chloritization and tourmalinization are additional alterations associated with the hydrothermal system.

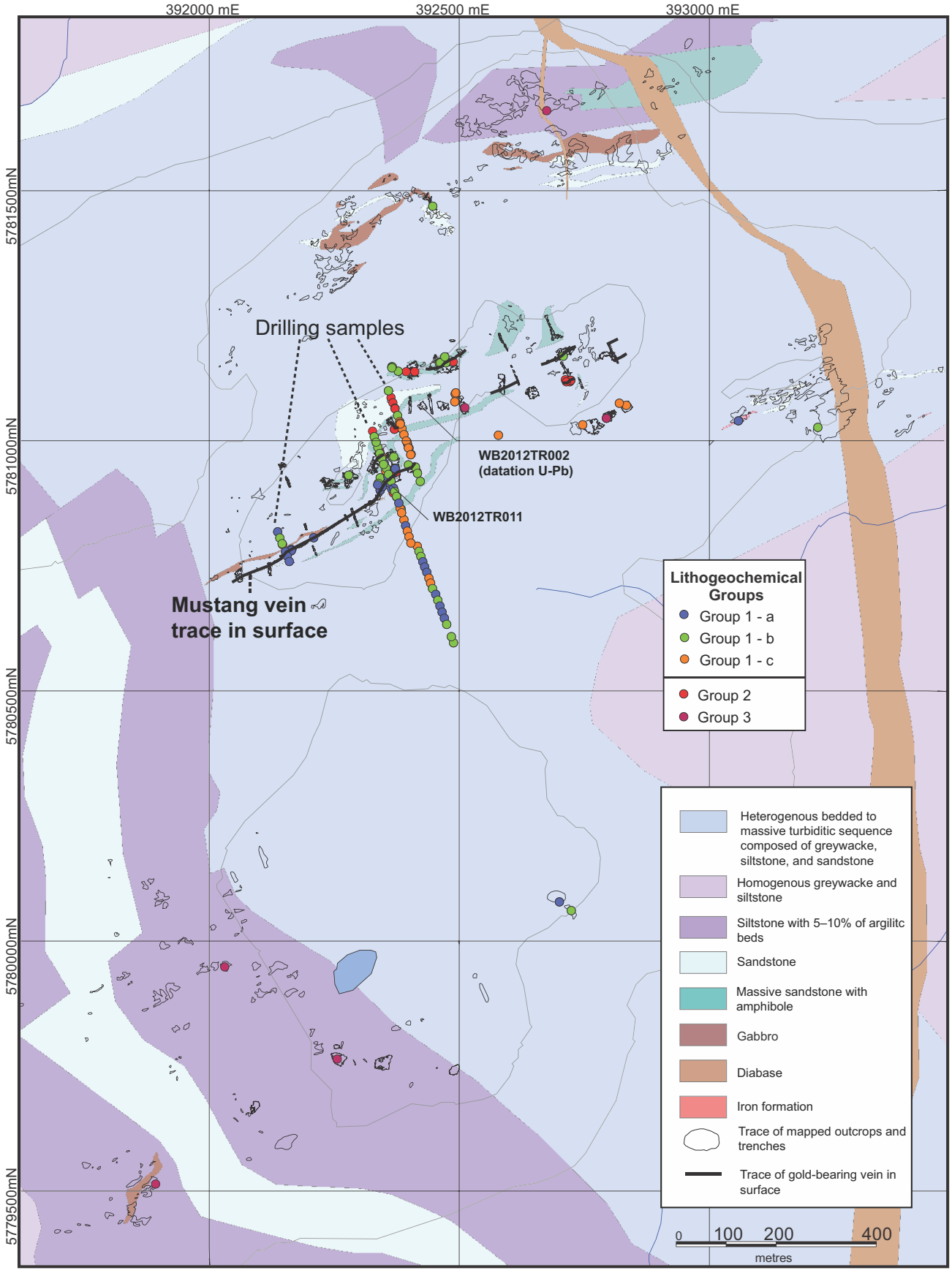

Figure 7. Metasedimentary lithogeochemical groups in the area of the Mustang showing.

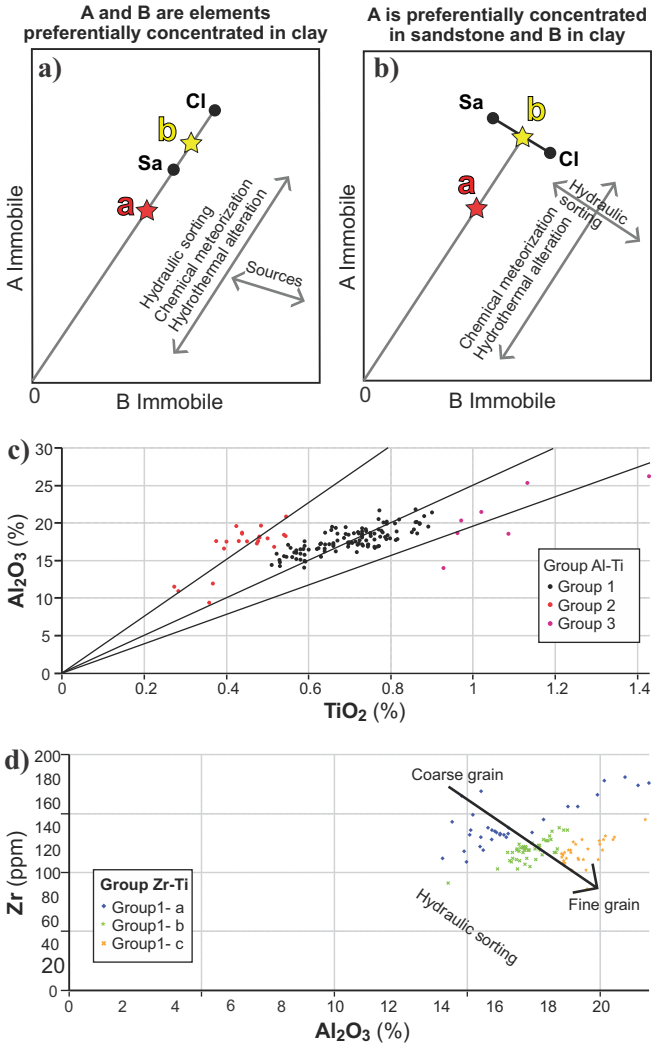

Figure 8. Theoretical scattergrams for assessing element mobility (Fralick and Kronberg, 1997). **a)** For immobile-immobile pairs preferentially located in the clay fraction, the starting composition 'a' moves during weathering as the total sediment mass is diminished. Composition 'b' splits into 'Cl' (clay) and 'Sa' (sand) due to hydraulic fractionation and forms a line extending to the origin. The lines define different sources. **b)** For an element preferentially concentrated in sandstone (ex. Zr, Y) versus one preferentially concentrated in clay (ex. Al, Ti), hydraulic fractionation will separate samples into different groups, either close to the x-axis or the y-axis. **c)** Al_2O_3-TiO_2 diagram defines 3 groups (potential sources) in the metasedimentary rocks from the Mustang area (n=141). **d)** A plot of Zr versus Al_2O_3 shows that the metasedimentary rocks from Group 1 were affected by hydraulic sorting (n=112).

U-Pb Geochronology

The preliminary results of U-Pb Sensitive High-Resolution Ion Microprobe (SHRIMP) dating of detrital zircons from the Mustang Vein host rock (greywacke) indicate a maximum sediment deposition age of 2709±4 Ma. The sample was collected 120 m north-northeast from the folded Mustang Vein, in the WB-2012-TR002 trench (Fig. 7). It is a thin, dismembered, massive, mid-grey, medium-grained greywacke horizon composed of quartz-feldspar-biotite-garnet with a strong stretching lineation. These results suggest that the host metasedimentary rocks are stratigraphically correlatable with the end of volcanic activity (Komo and Kasak formations) and the first sedimentation period (Wabamisk formation) in the La Grande Subprovince and that the gold mineralization is younger than 2709 Ma.

DISCUSSION

The Mustang gold-bearing vein contains previously foliated (S_2) host-rock fragments and has recorded part of the D_2 deformation (Fig. 4). The Mustang Vein, as well as other gold mineralization in the area, shows spatial-temporal relationships with the structural elements associated with D_2 deformation and is therefore interpreted as being synchronous with the principal D_2 deformation event. The Mustang Vein was created within a fragile-ductile system along the limb of an F_2 anticlinal fold through repeated episodes of shear failure and hydrothermal sealing. The idiomorphic arsenopyrite and pyrite that contain visible gold inclusions are accompanied by pressure shadows filled with quartz (±carbonate±chlorite±sericite) and sulphides (pyrrhotite and pyrite). These textures are compatible with a syndeformation model (Fig. 6f). The geochemistry combined with the petrography help to define proximal and distal hydrothermal alterations relative to the gold-bearing veins and are characteristic of those documented for gold-bearing deposits hosted in turbidite in Australia (e.g. Paleozoic Lachlan Fold Belt, Central Australia: Gao and Kwak, 1997; Bierlein et al., 1998; and Nova Scotia (Meguma Terrane); Ryan and Smith, 1998). Potassic alteration (sericite, biotite, and microcline), carbonatization (±Ca-Na or ±Ca-K) (Figs. 9a,b,c, 10, 11) and sulphidization occur proximal to the gold-bearing veins. Sericitization is restricted to the immediate walls of the gold-bearing veins. However, carbonatization and calcic metasomatism (CaO and CO_2 gains observed up to 50 m from the gold-bearing veins) are indicative of hydrothermal fluid circulation that may be associated with the gold-bearing veins. The proximal alterations are characterized by substantial gains of Se, Sb, Te, CO_2, S, As, Au, and W. A mafic magnesian dyke (gabbro) is spatially associated with the Mustang Vein. This spatial association has also been noted at four other gold-bearing veins (Isabelle, Bull, Chino and Contact gold showings) located less than 20 km from the Mustang gold showing (Vigneau, 2011). The competency contrast between these dykes and the adjacent metasedimentary rocks probably led to the development of high-strain zones and the circulation of gold-bearing hydrothermal fluids. The presence of these dykes may help to locate structural and

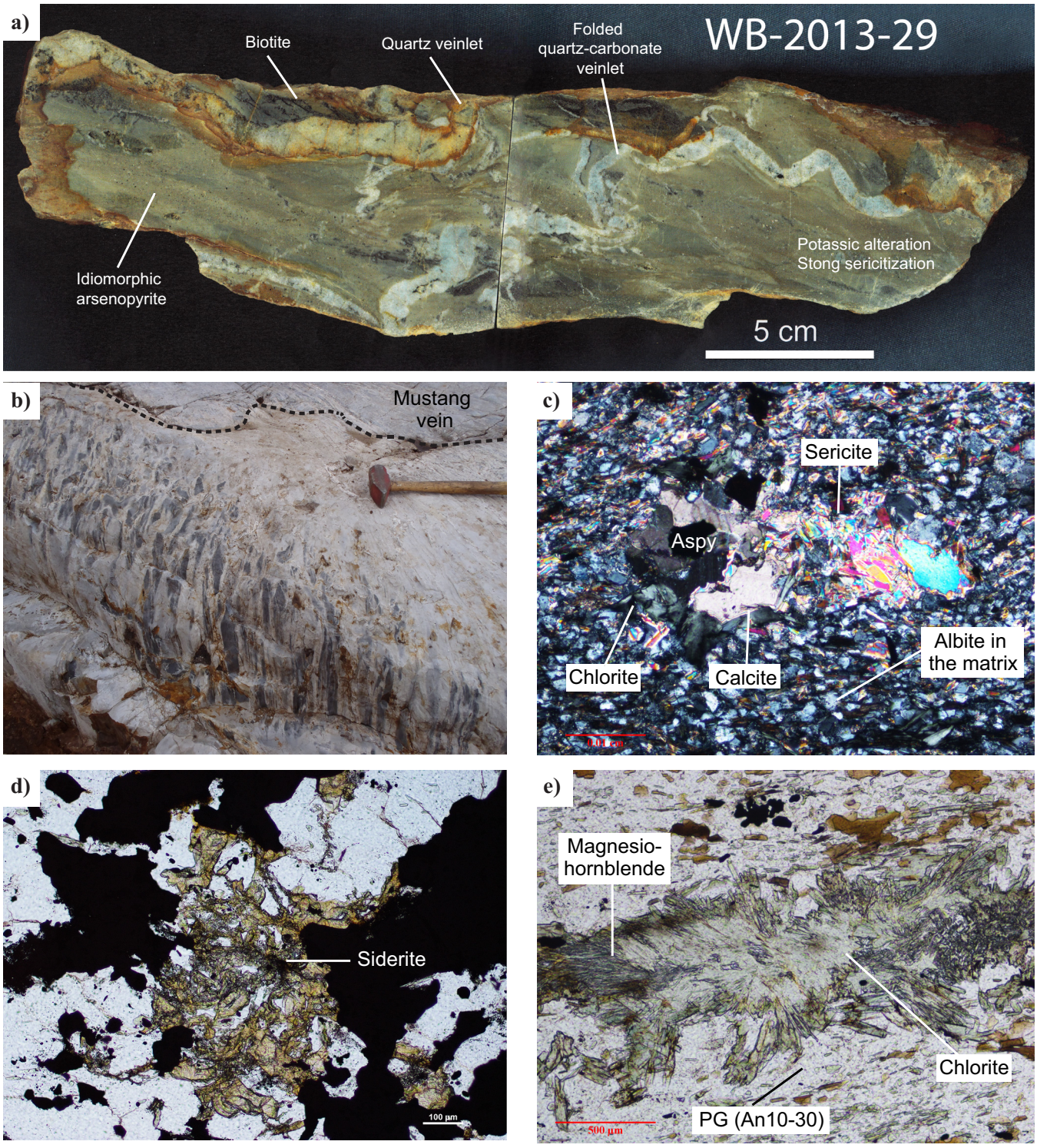

Figures 9. a) Photograph of a same showing the typical effect of strong potassic alteration (sericitization) in the proximal alteration zone associated with the gold-bearing Mustang Vein. **b)** Photograph of the Mustang Vein with the proximal pervasive and pseudo-fragmentary bleached alteration (carbonatization and calc-sodic alteration). **c)** Photograph of an outcrop showing the albite-sericite-chlorite-calcite assemblage (carbonatization and calci-sodic alteration) that defines the proximal bleached alteration of the Mustang Vein. **d)** Photomicrograph showing siderite (iron carbonate) that defines the carbonatization. **e)** Photomicrograph showing the typical assemblage of the distal calc-assemblage (sodic-plagioclase, magnesio-hornblende, chlorite) in a massive greywacke.

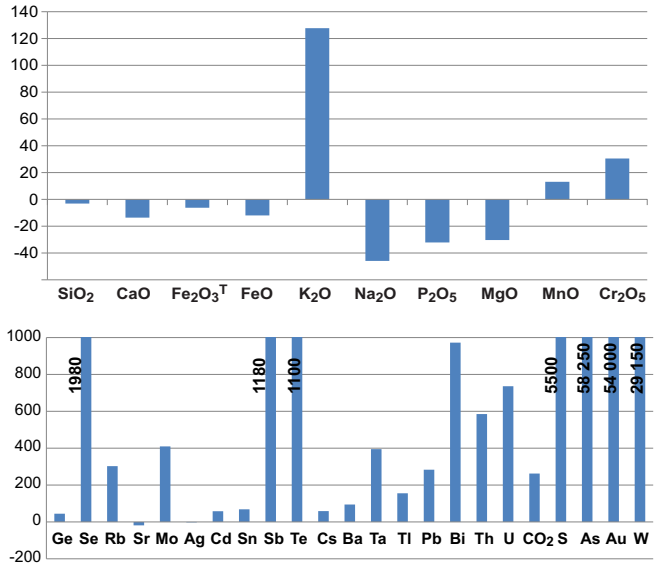

Figure 10. Mass balance (%) for proximal potassic alteration (mean; n=12).

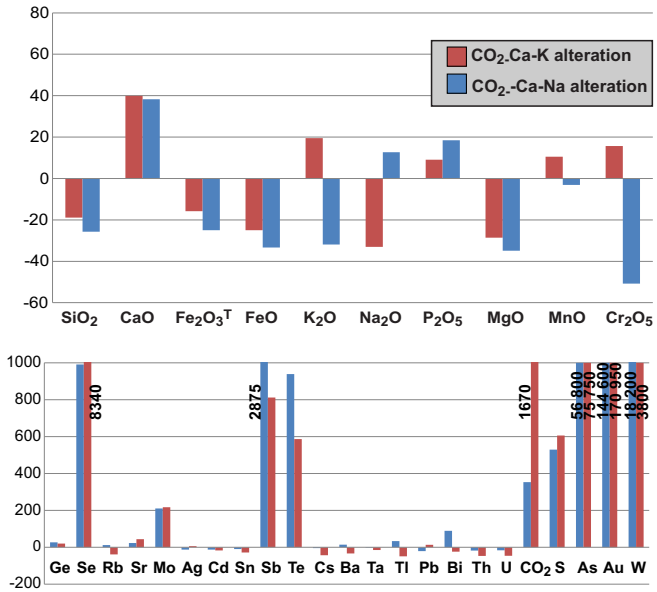

Figure 11. Mass balance (%) for proximal carbonatization (CO_2-Ca-Na and CO_2-Ca-K alterations) (mean; n=9).

lighological traps. In the proposed turbidite-hosted model, in addition to the fold limbs that may have developed D_2-related high-strain zones, the hinges of the F_2 folds are excellent geological structures for the development of extension fractures in the extrados of the folds and the channelling of gold-bearing hydrothermal fluids, thereby promoting the development of gold-bearing zones at high angles to the bedding. These fold hinges are thus excellent gold exploration targets in the Wabamisk property area.

The Mustang gold showing attests to the presence of a significant gold-bearing hydrothermal system. The deformed polygenetic conglomerate, 1 km north of the Mustang Vein (Figs. 5c, 7), may correspond to a

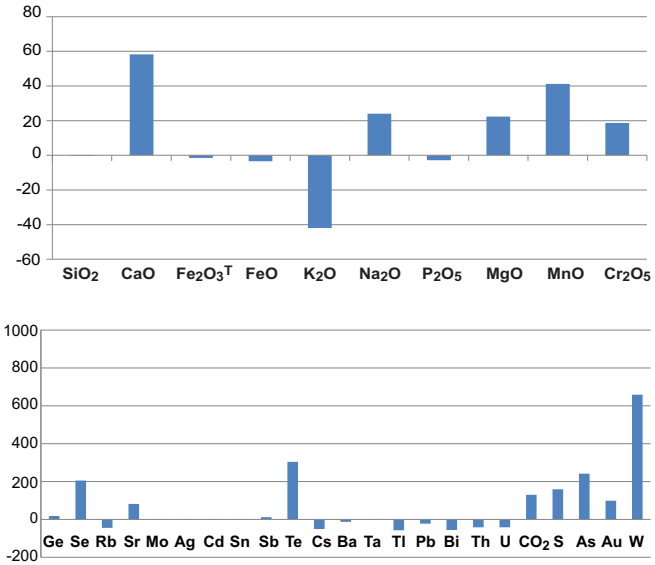

Figure 12. Mass balance (%) for distal calcic-sodic alteration (mean; n=5).

Timiskaming-type orogenic conglomerate that is typically distributed along the edge of a large structure that may have been the centre point of D_2 deformation and large-scale circulation of hydrothermal fluid.This type of structure may have controlled the formation and distribution of the principal gold-bearing zones, as documented in the case of the principal Archaean gold-bearing districts (Goldfarb et al., 2005; Robert et al., 2005; Dubé and Gosselin, 2007; Dubé et al., 2011). Similar to the Roberto gold-bearing system (Ravenelle et al., 2010; Fontaine et al., 2015), the Mustang Vein is hosted in clastic metasedimentary rocks, folded by F_2 folds, and located near the contact between two geological subprovinces (La Grande and Opinaca) (Fig. 1). The Roberto mineralized zone at the Éléonore Mine is primarily hosted in the upper part of the Low Formation, whose maximum deposition age is <2675 Ma (Ravenelle et al., 2010). A massive wacke zone located in the structural hanging wall of the Roberto/Roberto East zone has a maximum deposition age of 2714 Ma (Ravenelle et al., 2010). This age is similar to that of the host wacke of the Mustang Vein. These geological parameters not only highlight the similar geological context of Roberto and Wabamisk, but also the gold-bearing potential of the polydeformed metasedimentary rocks in the La Grande Subprovince, near the contact with the Opinaca Subprovince. However, the Roberto and Mustang gold showings are different in terms of ore type, degree of metamorphism, and gold content. The Mustang gold showing consists of a quartz±carbonate vein hosted in greenschist-facies metasedimentary rocks. Most of the gold mineralization is located in the Mustang quartz (±carbonate) vein and wall rocks at Wabamisk, whereas at Roberto gold is mainly hosted in a stockwork zone with quartz±

actinote±diopside±biotite-arsenopyrite/pyrrhotite veins, quartz-dravite-arsenopyrite veinlets, and a replacement zone with a high quartz-microcline-phlogopite-biotite-dravite content (Ravenelle et al., 2010). Roberto is an atypical gold deposit with amphibolite-facies metamorphism (Ravenelle et al., 2010). The Éléonore Mine, the Corvet Est, Poste Lemoyne, Auclair, and Isabelle gold showings and the Wabamisk property gold showings (such as the Mustang Vein) are located near the tectono-metamorphic contact between the La Grande and Opinaca subprovinces (Fig. 1). This contact zone is therefore a prime metallotect for gold exploration in the James Bay Region, as proposed by Gauthier et al. (2007) and Ravenelle et al. (2010).

FUTURE WORK

Re-Os arsenopyrite dating at the Mustang Vein is underway and may provide key information at local and regional scales to help define the age of the main gold event. The various generations of arsenopyrite and pyrite are undergoing LA-ICP-MS analysis by Simon Jackson of the Geological Survey of Canada in Ottawa. The trace element maps generated will be used to verify if there are zonations in the sulphides and invisible gold in the crystalline structure of the sulphides. The maps will help to define the metallogenic evolution of the Mustang gold showing. In addition, other methods for characterizing hydrothermal alteration, using CO_2/CaO and CO_2/(CaO+MgO) molar ratios, will be tested to further the characterization or mineralization in the Mustang Vein.

ACKNOWLEDGEMENTS

This report is based on results of an M.Sc. thesis undertaken by the first author at the Institut national de la recherche scientifique (INRS-ETE), as part of the Targeted Geoscience Initiative 4 (Lode Gold project) of Natural Resources Canada. Additional financial and operational support has been provided by Mines Virginia and DIVEX. We sincerely thank Virginia Mines, now Exploration Osisko - Baie James, for access to the property, to drill core, and various datasets, for accommodation, and for authorization to publish. The entire team of the Wabamisk project is acknowledged for their time, support, interest in this project, and for sharing their unique knowledge. The project has also benefited from discussions with S. Trépanier, M. Bardoux, J. Goutier, and A. Fontaine.

REFERENCES

Bandyayera, D., Rhéaume, P., Maurice, C., Bédard, É., Morfin, S., and Sawyer W.E., 2010. Synthèse géologique du secteur du réservoir Opinaca, Baie-James; Ministères des Ressources naturelles du Québec, RG 2010-02, 46 p.

Bierlein, F.P., Fuller, T., Stüwe, K., Arne, D.C., and Keays, R.R., 1998. Wallrock alteration associated with turbidite-hosted gold deposits. Examples from the Palaeozoic Lachlan Fold Belt in central Victoria, Australia; Ore Geology Reviews, v. 13, p. 345–380.

Boily, M. and Moukhsil, A., 2003. Géochimie des assemblages volcaniques de la ceinture de roches vertes de la Moyenne et de la Basse-Eastmain, province du Supérieur, Québec; Ministères des Ressources naturelles du Québec, ET 2002-05, 29 p.

Card, K. and Ciesielski, A., 1986. Subdivisions of the Superior province of the Canadian shield; Geoscience Canada, v. 13, p. 5–13.

Doyon, J., 2004. Comparaison de la composition des roches métasédimentaires archéennes dans six bassins de la province du Supérieur: une étude géochimique et statistique; M.Sc. thesis, Université du Québec à Chicoutimi, Chicoutimi, Québec, 214 p.

Dubé, B. and Gosselin, P., 2007, Greenstone-hosted quartz-carbonate vein deposits, *In:* Mineral Deposits of Canada: A Synthesis of Major Deposit Types, District Metallogeny, the Evolution of Geological Provinces and Exploration Methods, (ed.) W.D. Goodfellow; Geological Association of Canada, Mineral Deposits Division, Special Publication No. 5, p. 49–73.

Dubé, B., Mercier-Langevin, P., Castonguay, S., McNicoll, V.J., Pehrsson, S.J., Bleeker, W., Schetselaar, E.M., and Jackson, S., 2011. Targeted Geoscience Initiative 4. Lode gold deposits in ancient, deformed and metamorphosed terranes - footprints and exploration implications: A preliminary overview of themes, objectives and targeted areas, *In:* Summary of Field Work and other Activities 2011; Ontario Geological Survey, Open File Report 6270, p. 38-1 to 38-10.

Franconi, A., 1978. La bande volcanosédimentaire de la rivière Eastmain inférieure à l'ouest de la longitude 76º15'; Ministère des richesses naturelles du Québec, DVP 574, 177 p.

Fontaine, A., Dubé, B., Malo, M., McNicoll, V.J., Brisson, T., Doucet, D., and Goutier, J., 2015. Geology of the metamorphosed Roberto gold deposit (Éléonore Mine), James Bay Region, Québec: Diversity of mineralization styles in a complex tectono-metamorphic framework, *In:* Targeted Geoscience Initiative 4: Contributions to the Understanding of Precambrian Lode Gold Deposits and Implications for Exploration, (ed.) B. Dubé and P. Mercier-Langevin; Geological Survey of Canada, Open file 7852, p. 209–225.

Fralick, P.W. and Kronberg, B.I., 1997. Geochemical discrimination of clastic sedimentary rock sources; Sedimentary Geology, v. 113, p. 111–124.

Gao, Z.L. and Kwak, T.A.P., 1997. The geochemistry of wall rock alteration in turbidite-hosted gold vein deposits, central Victoria, Australia; Journal of Geochemical Exploration, v. 59, p. 259–274.

Gauthier, M., Trepanier, S., and Gardoll, S., 2007. Metamorphic Gradient: A Regional-Scale Area Selection Criterion for Gold in the Northeastern Superior Province, Eastern Canadian Shield; SEG Newsletter April 2007, No. 69, p. 10–15.

Goldcorp, 2014. Reserves & Resources webpage; http://www.goldcorp.com/English/Investor-Resources/Reserves-and Resources/default.aspx.

Goldfarb, R.J., Baker, T., Dube, B., Groves, D.I., Hart, C.J., and Gosselin, P., 2005. Distribution, character, and genesis of gold deposits in metamorphic terranes, *In:* 100th Anniversary Volume, (ed.) J.W. Hedenquist, J.F.H. Thompson, R.J. Goldfarb, and J.P. Richards; Society of Economic Geologists, v. 40, p. 407–450.

Gosselin, C. and Simard, M., 1999. Géologie de la région du lac Lichteneger (SNRC 33B); Ministère des Ressources naturelles du Québec, RG 98-15, 25 p.

Goutier, J., Dion, C., Ouellet, M.C., Mercier-Langevin, P., and Davis, D.W., 2001. Géologie de la région de la colline Masson

(33F/09), de la passe Awapakamich (33F/10), de la baie Caribellet (33F/15) et de la passe Pikwahipanan (33F/16); Ministère des Ressources naturelles du Québec, RG 2000-10, 68 p.

Grant, J.A., 1986. The isocon diagram; a simple solution to Gresens' equation for metasomatic alteration; Economic Geology, v. 81, p. 1976–1982.

Grant, J.A., 2005. Isocon analysis: A brief review of the method and applications; Physics and Chemistry of the Earth, Parts A/B/C, v. 30, p. 997–1004.

Moukhsil, A., 2000. Géologie de la région des lacs Pivert, Anatacau, Kauputauchechun et Wapamisk (SNRC 33C/01, 33C/02, 33C/07 et 33C/08); Ministère des Ressources naturelles du Québec, RG 2000-04, 47 p.

Moukhsil, A., Legault, M., Boily, M., Doyon, J., Sawyer, E., and Davis W.D., 2003. Synthèse géologique et métallogénique de la ceinture de roches vertes de la Moyenne et de la Basse-Eastmain (Baie-James), Québec; Ministère des Ressources naturelles du Québec, ET 2002-06, 55 p.

Moukhsil, A., Voicu, G., Dion, C., David, J.W. Davis, D., and Parent, M., 2001. Géologie de la région de la Basse-Eastmain centrale (33C/03, 33C/04, 33C/05 et 33C/06); Ministère des Ressources naturelles du Québec, RG 2001-08, 54 p.

Ravenelle, J.-F., Dubé, B., Malo, M., McNicoll, V., Nadeau, L., and Simoneau, J., 2010. Insights on the geology of the world-class Roberto gold deposit, Éléonore property, James Bay area; Geological Survey of Canada, Current Research, vol. 2010-1, p. 26.

Robert, F., Poulsen, K.H., Cassidy, K.F., and Hodgson, C.J., 2005. Gold metallogeny of the Superior and Yilgarn cratons, *In:* 100th Anniversary Volume, (ed.) J.W. Hedenquist, J.F.H. Thompson, R.J. Goldfarb, and J.P. Richards; Society of Economic Geologists v. 40, p. 1001–1033.

Ryan, R.J. and Smith, P.K., 1998. A review of the mesothermal gold deposits of the Meguma Group, Nova Scotia, Canada; Ore Geology Reviews, v. 13, p. 153–183.

Sawyer, E.W., 1986. The influence of source rock type, chemical weathering and sorting on the geochemistry of clastic sediments from the Quetico Metasedimentary Belt, Superior Province, Canada; Chemical Geology, v. 55, p. 77–95.

Trépanier, S., 2011. Une nouvelle méthode de calcul des bilans de masse pour caractériser l'altération associée à l'or dans les roches sédimentaires clastiques; Présentation du Forum Technologique de Consorem-Divex 2011 [online], https://consorem.uqac.ca/presentation_pub/forum_techno_2011/Trepanier%20Alteration%20Sediments%20Forum%202011.pdf, 29 p.

Vigneau, S., 2011. Métallogénie des minéralisations aurifères de la propriété Opinaca, Baie-James, Québec; M.Sc. thesis, Université du Québec à Chicoutimi, Chicoutimi, Québec, 307 p.

GEOLOGICAL SURVEY OF CANADA
OPEN FILE 7852

Targeted Geoscience Initiative 4: Contributions to the Understanding of Precambrian Lode Gold Deposits and Implications for Exploration

Insights into the timing of mineralization and metamorphism in the North Caribou greenstone belt, western Superior Province

Colter J. Kelly and David A. Schneider

University of Ottawa, Ottawa, Ontario

2015

Recommended citation

Kelly, C.J. and Schneider, D.A., 2015. Insights into the timing of mineralization and metamorphism in the North Caribou greenstone belt, western Superior Province, *In:* Targeted Geoscience Initiative 4: Contributions to the Understanding of Precambrian Lode Gold Deposits and Implications for Exploration, (ed.) B. Dubé and P. Mercier-Langevin; Geological Survey of Canada, Open File 7852, p. 245–253.

Publications in this series have not been edited; they are released as submitted by the author.

Contribution to the Geological Survey of Canada's Targeted Geoscience Initiative 4 (TGI-4) Program (2010–2015)

TABLE OF CONTENTS

Insights into the timing of mineralization and metamorphism in the North Caribou greenstone belt, western Superior Province

Colter J. Kelly* and David A. Schneider

Department of Earth Sciences, University of Ottawa, Ottawa, Ontario K1N 6N5
*Corresponding author's e-mail: ckell085@uottawa.ca

ABSTRACT

Secondary ion mass spectrometry (SIMS) U-Pb depth profiles of unpolished detrital zircon were used in an attempt to resolve the timing of metamorphism and mineralization in the North Caribou greenstone belt of northern Ontario, which hosts the Musselwhite gold mine. Eleven samples located 10–75 km from the mine site were collected from metasedimentary rocks adjacent to structures that may have promoted hydrothermal fluid flow. Zircon rim material is commonly characterized by decreased Th/U concentrations (up to an order of magnitude), as well as generally possessing concordant ages. Rim ages obtained via this technique range from 2788–2703 Ma, up to 250 m.y. younger than zircon cores. The timing of zircon rim recrystallization overlaps with the timing of potassic alteration in the surrounding plutons, as well as regional gold mineralization in the North Caribou Superterrane. These zircon rims may represent the timing and potential distribution of Au-bearing fluids within and regional to the Musselwhite deposit.

INTRODUCTION

The timing and nature of metamorphic and hydrothermal events is poorly understood at the Musselwhite gold mine, as well as elsewhere within in the North Caribou Greenstone Belt (NCGB) of the Western Superior Province. Peak metamorphic assemblages across the NCGB are apparently spatially correlated with positive magnetic highs, intrusive bodies, and areas of high strain (Kelly et al., 2013). Despite the relatively high-metamorphic grade of the NCGB, it has been a challenge to identify a suitable chronometer to date metamorphism and mineralization. Results of geochronology proximal to the mine site have resulted in ages that are >200 m.y. younger than major tectonic events in the region (Biczok et al., 2012; Kalbfleisch, 2012; Van Lankvelt, 2013). Biczok et al. (2012) reported a Sm-Nd garnet-whole rock age of 2.72–2.67 Ga for the ore-bearing unit at the Musselwhite mine, suggesting that this broadly resolves the timing of mineralization. In our study, we add to the growing geochronological framework of the Western Superior region by conducting U-Pb depth profiling of zircon from samples across the NCGB to determine the timing of thermal events. A coupled dissolution-reprecipitation of zircon by hydrothermal fluids has been shown to occur at the sub-micrometre to micrometer scale, resulting in rim material that has a unique geochemical and isotopic signature. Commonly, the rim possesses elevated U, Fe, and Al concentrations (e.g. Geisler et al., 2007), and the U-Pb isotopes record the timing of the event (Grove and Harrison, 1999; Carson et al., 2002; Mojzsis and Harrison, 2002; Schneider et al., 2012; Steely et al., 2014). Secondary ion mass spectrometry (SIMS) analysis has a lateral spatial resolution of <30 μm and depth resolution of 100 nm (Breeding et al., 2004; Kelly et al., 2014). By sputtering the primary beam normal to the fluid reaction front on unpolished zircon, SIMS U-Pb depth profiling is capable of detecting sub-micrometre isotopic changes within zircon grains that avoids significant domain mixing and produces geologically meaningful data, which has traditionally been overlooked. We hope to gain insight into the tectonothermal history of the NCGB with these data within the framework of existing geochronology of the Western Superior Province.

RESULTS AND DATA ANALYSIS

Sample Selection and Preparation

Eleven metasedimentary samples were collected across the NCGB (Fig. 1) to provide a broad spatial understanding of the thermal activity within the belt. Samples were specifically targeted adjacent to structures that may have fostered fluid activity, such as shear zones and intrusions. These targets were identified using a combination of metamorphic pattern observations (Breaks et al., 2001; Kelly et al., 2013), as well as the regional aeromagnetic anomalies. Metamorphic rocks that were sampled include siliciclastic sedimentary units ranging from mudstone to conglomerate, with metamorphic grades of greenschist

Kelly, C.J. and Schneider, D.A., 2015. Insights into the timing of mineralization and metamorphism in the North Caribou greenstone belt, western Superior Province, *In:* Targeted Geoscience Initiative 4: Contributions to the Understanding of Precambrian Lode Gold Deposits and Implications for Exploration, (ed.) B. Dubé and P. Mercier-Langevin; Geological Survey of Canada, Open File 7852, p. 245–253.

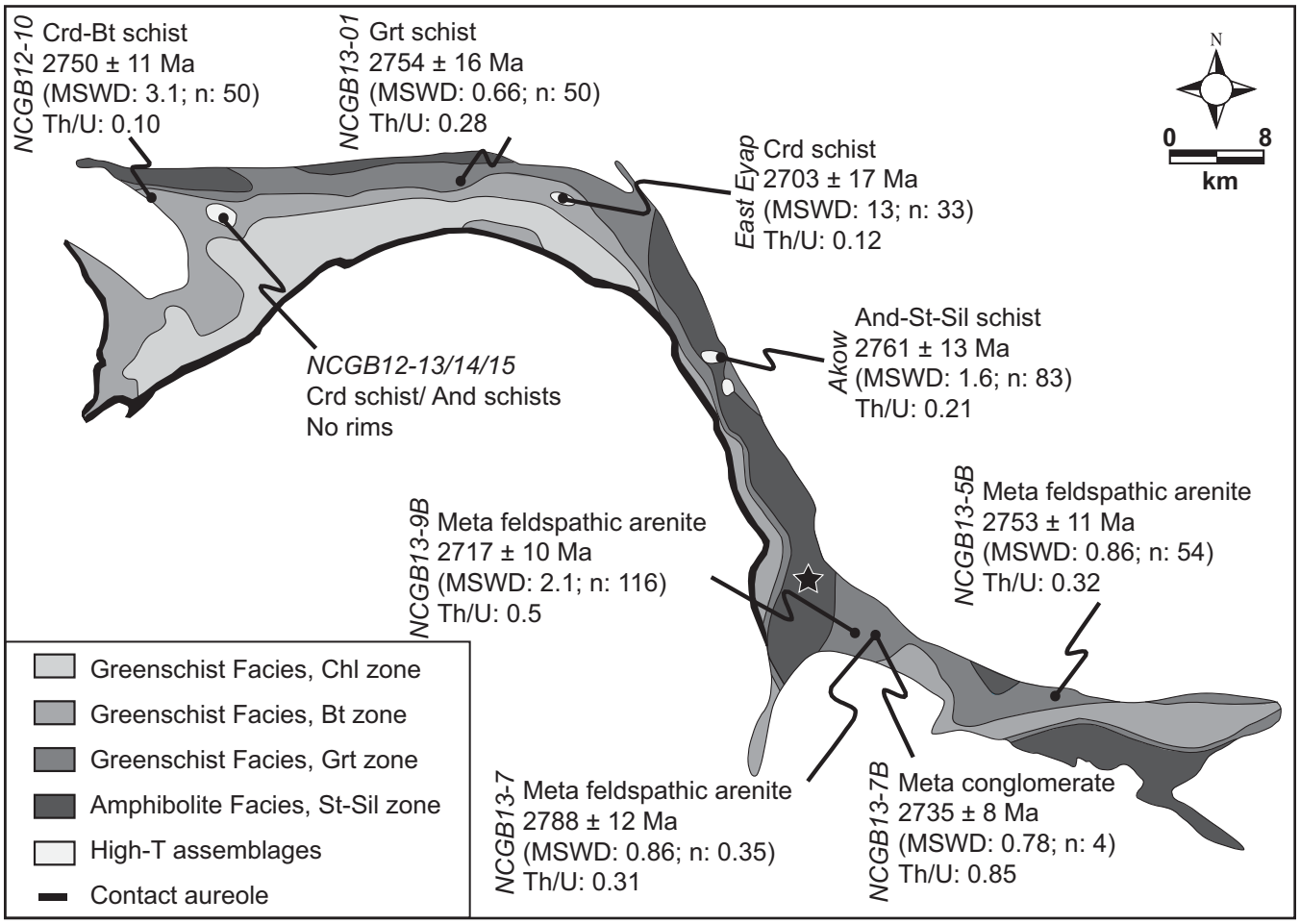

Figure 1. Metamorphic map of the North Caribou greenstone belt (modified from Breaks et al., 2001; Kelly et al., 2013) showing the locations of rock samples from this study (sample numbers NCGB12-10, NCGB12-13, NCGB12-14, NCGB12-15, NCGB13-01, East Eyap, Akow Lake, NCB13-9B, NCB13-7, NCB13-7B, NCB13-5B). Samples that exhibit U-Pb rim ages are reported as $^{207}Pb/^{206}Pb$ ages with the average Th/U values as described in the text. Metamorphic facies are variable within the belt, ranging from lower greenschist to upper amphibolite facies and apparent late high-temperature assemblages proximal to intrusions. Black star represents location of Musselwhite mine. Abbreviations: And = andalusite; Bt = biotite; Chl = chlorite; Crd = cordierite; Grt = garnet; MSWD = mean square weighted deviation; Sil = sillimanite; St = staurolite; T = temperature. Sample numbers are shown in italics.

to upper amphibolite facies, as well as localized high-temperature assemblages. Many of the samples possess well developed foliation, and at the metre-scale, folds, faults, and boudinage can be observed in the outcrops. Zircons were separated from the rocks, processed, and mounted as described by Kelly et al. (2014). The zircons were imaged before and after analysis with a JEOL6610LV scanning electron microscope (SEM; University of Ottawa, Ottawa, Canada) using secondary electron imaging in a high vacuum with a 1.7 kV beam to characterize the crystal structure, as well as to ensure that the analyzed volume was free of any fractured crystal faces or notable outgrowths. After SIMS analysis, a MicroXAM surface profilometer (University of California, Los Angeles, USA) was used to determine the pit dimensions of the material excavated from the zircon rims. We use the term rim in reference to an originally stable zircon that comes in contact with a fluid phase under fundamentally different pressure and temperature conditions. The zircon then begins to undergo coupled dissolution-reprecipitation, resulting in a recrystallized zircon rim that has re-equilibrated under these new conditions. Recrystallization commonly results in increased U concentrations, elevated light rare earth elements (LREE), and a reset isotopic age (Breeding et al., 2004; Geisler et al., 2007; Schneider et al., 2012; Kelly et al., 2014).

Analytical Methods and Data Reduction

SIMS U-Pb measurements were made using a CAMECA ims1270 ion microprobe (University of California, Los Angeles, USA) according to the methods published by Kelly et al. (2014). Our analyses were operated at beam intensities of 12 nA conducted over ~50 mass cycles resulting in ~30° µm diameter pits that are <5 µm in depth through a sputtering rate of ~100

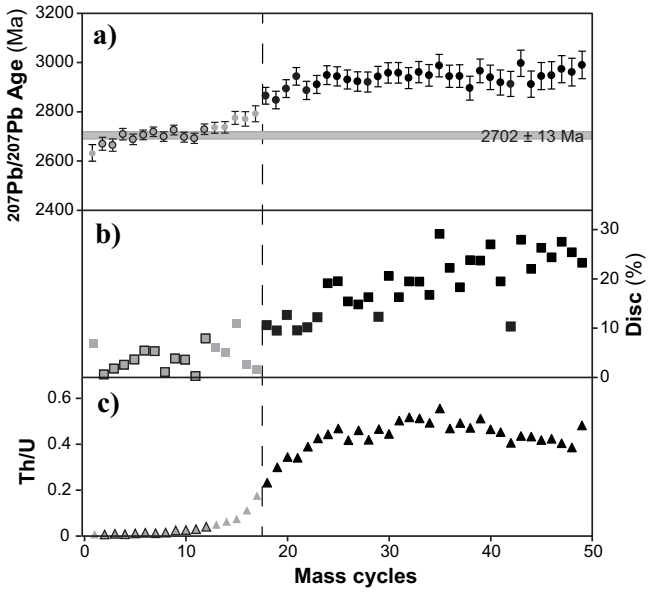

Figure 2. An example of a SIMS U-Pb zircon depth profile analysis from sample NCGB12-10, grain 8. **a)** ^{207}Pb/^{206}Pb age plotted against the number of mass cycles, which is a proxy for depth into the zircon crystal. Errors bars are 1σ and the vertical dashed line represents the cutoff used as the boundary between interior and rim material. Black symbols represent interior data; grey symbols represent younger (rim) data. Grey symbols with a black outline meet the criteria developed in the text as rim material and are therefore included in the rim calculation; the data points without the outline were ignored. In this example, the rim is 2702 ± 13 Ma (MSWD: 0.84; n: 11), consisting of 11 mass cycles and is ~1 µm thick. The interior of the crystal has an age of 2930 ± 15. Panel **(b)** illustrates the relationship between discordance and the mass cycle analyses. In this example, the rim is clearly more concordant. Panel **(c)** shows the changes of Th/U value with depth into the crystal. In this example, the rim material has an average Th/U ratio of 0.02, compared to the interior that has an average value of 0.44.

nm/mass cycle. The zircon reference material AS3 (^{206}Pb/^{238}U age: 1099 ± 1 Ma; Paces and Miller, 1993) was analyzed after every five unknowns, following the procedure of Schmitt et al. (2003). U-Pb ages were calculated from the measured ion intensities using UCLA's in-house ZIPS v3.0.4 software written by C.D. Coath and ISOPLOT v3.75 software (Ludwig, 2012). Uncertainties of individual mass cycles are reported at 1σ and integrated ages are reported at 2σ. By examining the ^{207}Pb/^{206}Pb ages (younger in rims), Th/U concentrations (often lower in rims), and percent discordance (often lower in rims) from all mass cycles as a function of depth into the crystal (Fig. 2), we are able to resolve sub-micron variations in the zircon rims. For internal consistency in the identification of rim material ^{207}Pb/^{206}Pb age and % discordance was plotted as a function of depth, allowing for core ages to be identified and eliminated. Rim ages were calculated through the interrogation of mass cycles identified as younger than the core. To be defined as fully re-equilibrated rim material, three criteria were used: (1) containing three or more contiguous mass cycles comprising more than 30% of the total cycles that are younger than the core material; (2) the probability of fit of the weighted mean of the rims is >5%; and (3) the ages of the outermost two mass cycles for either side of the identified rim must not be significantly different (at 1.8σ) than the weighted mean rim age (six or more cycles only). In addition, any mass cycles that have a discordance of >15% were not included in the age calculation (cf. Cottle et al., 2009; 2012). Rim ages reported here (with 2σ uncertainties) were assigned to an entire rock sample (comprising many zircon analyses) through a weighted average calculation inclusive of all mass cycles identified as rim material. Rims, when present, can range in thickness from 3 to 30 mass cycles (<3 µm).

Results

Below we report the results of 172 single zircon analyses from eleven samples (as summarized in Table 1), reporting only the ^{207}Pb/^{206}Pb rim ages in the text. Recrystallized rim material is commonly 0.1 to 1.5 µm thick, as determined by the Th/U values and young ages. Zircon interior or core ^{207}Pb/^{206}Pb ages range from ca. 2800 to 3045 Ma for all eleven samples. The full SIMS U-Pb data for each sample will be published in a forthcoming journal article authored by the Kelly and Schneider; we discuss the results of the rim analyses of each sample below.

A total of 34 zircon grains were analyzed from a cordierite-bearing biotite schist (sample NCGB12-10) collected on the northeastern shore of Miskeesik Lake. The sample is a metapelite with a mineral assemblage of quartz, plagioclase, orthoclase, and biotite, with foliation defined by biotite. The sample location is within mapped within upper greenschist rocks and the sample itself also contains cordierite relics, which are now chloritized (Kelly et al., 2013). Zircons in the sample are prismatic to subrounded. The interpreted rim age calculated from ten grains is 2750 ± 11 Ma (mean square weighted deviation (MSWD): 3.1; n: 50). The Th/U value for the rim material ranges from 0.01 to 0.46, with an average value of 0.1.

Three samples were collected at the western end of Eyapimikima Lake, within a high-temperature metamorphic aureole (cordierite facies; Kelly et al., 2013). The three samples, an andalusite schist, and two cordierite schists (samples NCGB12-13, NCGB12-14, and NCGB12-15, respectively) show no evidence of zircon rim material, despite evidence of alteration and mineralization within the rock (e.g. chlorite, sericite, pyrite). Zircons in the sample are prismatic to rounded.

Fourteen zircons were dated from a garnet schist (sample NCGB13-001) in a 1 km^2 sliver of sedimentary rocks to the east of Macgruer Lake. This foliated

Table 1. Summary of locations, descriptions, and SIMS U-Pb depth profile data of samples collected throughout the North Caribou greenstone belt.

Sample number	Location (NAD 83)	Rock name	Zircon with rims (# of zircons analyzed)	Zircon morphologies	Zircon rim data†	
					$^{207}Pb/^{206}Pb$ age (Ma)	Th/U
NCGB12-10	627540E, 5872755N (zone 15)	Cordierite-bearing biotite schist	10/(34)	Prismatic/subrounded	2750±11 (MSWD: 3.1; n: 50)	0.01–0.46 (0.1)
NCGB12-13	627909E, 5868746N (zone 15)	Andalucite schist	0/(4)	Prismatic/rounded		
NCGB12-14	626394E, 5869259N (zone 15)	Cordierite schist	0/(18)	Prismatic	No Rims	
NCGB12-15	627540E, 5869191N (zone 15)	Cordierite schist	0/(5)	Prismatic/subrounded/ rounded		
NCGB13-01	648708E, 5871865N (zone 15)	Garnet schist	5/(14)	Prismatic/subrounded	2754±16 (MSWD: 0.66; n: 50)	0.05–0.64 (0.28)
East eyap	657715E, 5868570N (zone 15)	Cordierite schist	7/(20)	Prismatic/subrounded	2703±17 (MSWD: 13; n: 33)	0.05–0.27 (0.12)
Akow Lake	670288E, 5850306N (zone 15)	Andalucite-bearing siliminite-staurolite schist	8/(27)	Subrounded/rounded	2761±13 (MSWD: 1.6; n: 83)	0.11–0.42 (0.21)
NCB13-9B	688250E, 5825109N (zone 15)	Meta-feldspathic aranite	9/(20)	Prismatic/subrounded/ rounded	2717±10 (MSWD: 2.1; n: 116)	0.16–1.22 (0.5)
NCB13-7	689548E, 5825474N (zone 15)	Meta-feldspathic aranite	3/(14)	Prismatic/subrounded	2788±12 (MSWD: 0.86; n: 35)	0.11–1.85 (0.31)
NCB13-7B	689548E, 5825474N (zone 15)	Meta-clast supported polymictic conglomerate	2/(14)	Prismatic/subrounded	2735±8 (MSWD: 0.78; n: 4)	0.5–1.37 (0.85)
NCB13-5B	300330E, 5820880N (zone 16)	Meta-feldspathic aranite	3/(17)	Prismatic/subrounded	2753±11 (MSWD: 0.86; n: 54)	0.16–0.64 (0.32)

† ages calculated from integrated $^{207}Pb/^{206}Pb$ ages of SIMS mass cycles (n) with low Th/U values, shown as ranges (and averages)

metapelite is dominated by quartz and feldspar with biotite defining, and garnet occurring along, the foliation. The location sample is within a mapped a garnet-zone greenschist-facies assemblage (Kelly et al. 2013). Zircons in the sample are prismatic to subrounded and have a rim age of 2754 ± 16 Ma (MSWD: 0.66; n: 50). Th/U values from the young rims range from 0.05 to 0.64, with an average value of 0.28.

A total of twenty zircon grains were analyzed from a cordierite-schist collected from the eastern shore of Eyapimikima Lake (East Eyap) within a high-temperature aureole (cordierite facies; Kelly et al., 2013). The metapelite is a weakly foliated rock characterized by a mineral assemblage of quartz, plagioclase, and biotite with centimetre-scale porphyroblasts of cordierite. Zircons in the sample are prismatic to subrounded and yield a rim age of 2705 ± 17 Ma (MSWD: 13; n: 33), with Th/U values from the rims of 0.04 to 0.27, with an average value of 0.12.

An andalusite-bearing sillimanite-staurolite schist from the shores of Akow Lake was sampled. The strongly foliated metapelite comprises quartz, plagioclase, and biotite with porphyroblasts of staurolite and andalusite that possess sillimanite overgrowths. Twenty-seven zircon subrounded to rounded grains were analyzed resolving a rim age of 2761 ± 8.4 Ma (MSWD: 1.6; n: 83) with Th/U values ranging from 0.11 to 0.42, with an average of 0.21.

A total of twenty zircon grains were analyzed from a gossanous metafeldspathic arenite (sample NCGB13-9B). The rock is a non-foliated metasedimentary unit that has a mineral assemblage dominated by feldspar as well as quartz and biotite. Mineralization is evinced by the presence of late pyrite. Zircons in the sample are prismatic to rounded. The rim age for this sample is 2717 ± 10 Ma (MSWD: 2.1; n: 116) with Th/U values ranging from 0.16 to 1.22, with an average of 0.5. Our data reduction scheme overlooks a population of ca. 2450 Ma ages, which can be resolved through the interrogation of the data on an individual cycle basis.

A metasedimentary unit adjacent to a gabbroic intrusion on the shores of the Pipestone River was sampled. Two sub-samples were identified (samples NCGB13-07 and NCGB13-07b) based on variation in grain size and presence of clasts (sand-sized metafeldspathic arenite and a clast-supported polymictic metaconglomerate, respectively). The feldspathic arenite is characterized by mineralogy of plagioclase, quartz, and orthoclase with a very weak foliation defined by biotite. Alteration is evinced by sericitization of feldspar as well as secondary biotite. Zircons in the sample are prismatic to subrounded. The rim age calculated through the analysis of fourteen zircon grains is 2788 ± 12 Ma (MSWD: 0.86; n: 35) and with Th/U ratios ranging from 0.11 to 1.85, with an average of 0.31. The conglomerate is characterized by a sand-sized matrix not unlike the feldspathic arenite described previously, whereas clast-size ranges from centimetre to decime-

tre. Zircons in the sample are prismatic to subrounded. Fourteen zircon grains from the conglomerate yield a rim age of 2735 ± 89 (MSWD: 0.78; n: 4) with Th/U values ranging from 0.5 to 1.37, with an average of 0.85.

Seventeen zircon grains were analyzed from a weakly foliated metafeldspathic arenite (sample NCGB13-05b) sampled adjacent to a granitic intrusion. The primary mineralogy includes plagioclase, quartz, and orthoclase with a weak foliation defined by biotite and muscovite. Secondary mineral phases include sericite, chlorite, and oxides. Zircon grains in the sample range from prismatic to subrounded. A calculated rim age of 2753 ± 11 Ma (MSWD: 0.86; n: 54) is resolved from the rims of three grains. The Th/U values range from 0.16 to 0.64, with an average value of 0.32. These zircons in particular are characterized by elevated U concentrations (up to 5000 ppm for single mass cycles). This may have been outside of the calibration range of the reference material, which may explain the abundance of discordant mass cycles for this particular sample.

DISCUSSION AND MODELS

All of the samples presented in this study from across the belt have integrated zircon rim age populations between ca. 2790 and 2700 Ma. Despite the intensity of metamorphism ranging from hornfels and greenschist to upper amphibolite, the presence of recrystallized zircon rims occurring throughout the belt suggests that the rim-forming process is apparently independent of metamorphic facies. The lack of well-defined zircon rim material in western Eyapamikima Lake suggests that the occurrence of rims, and therefore fluid activity, is not pervasive over the entire belt. One sample (NCGB12-9B) from the Markop shear zone, south of Musselwhite mine, possesses a zircon rim population of ca. 2450 Ma, which has been observed in total-Pb monazite ages from NCGB (Kalbfleisch, 2012), Ar-Ar ages from the Musselwhite mine (Biczok et al., 2012), and zircon rims from the Abitibi (Schneider et al. 2012). This enigmatic event remains unresolved and we will not address this event further in the report.

Conventional interpretation of zircon Th/U values <0.2 suggest the neo- or recrystallized zircon material formed under metamorphic or hydrothermal conditions, likely in the presence of a crystallizing Th-bearing phase (i.e. monazite, apatite). Conversely Th/U values >0.2 occur because of primary igneous processes or in metamorphic rocks where Th-bearing phases are not present or actively crystallizing (Moeller et al., 2003). The average Th/U values in the northwestern and central portion of the NCGB average 0.175. In the southeastern portion of the belt, values are typically greater (>0.3), where monazite total-Pb ages are younger than 2600 Ma (Kalbfleisch, 2012). The elevated zircon Th/U values suggest that monazite was not present during zircon recrystallization, which is consistent with the relatively young (late) monazite ages. Additional work is required to understand the controls of bulk-rock geochemistry on the zircon rim recrystallization.

Some of the scatter in our data, represented by moderate MSWD values, is no doubt higher than expected. One explanation may be the inclusive approach to data reduction we took, and by including all of the relatively concordant data younger than the zircon core, we have sacrificed some statistical quality at the cost of a consistent data-reduction scheme. Samples with larger MSWDs can be interpreted as having thinner rim material (<300 nm) while MSWDs closer to unity are indicative of thicker rims (0.5–1.5 μm).

Regional Age Correlations

Our goal was to help resolve the timing of metamorphism and mineralization within the NCGB. Gold mineralization within the Western Superior Province occurs at 2720–2690 Ma within the Red Lake camp (Corfu and Stone, 1998; Dubé et al., 2004) and between 2730–2700 Ma at the Pickle Lake camp (Young et al., 2006). The North Caribou Greenstone Belt has a protracted history of igneous activity and thermal events. This is punctuated by three intrusive episodes at ca. >2950 Ma, 2870–2850 Ma, and 2730–2716 Ma (Biczok et al., 2012; Van Lankvelt, 2013). Within these plutons surrounding the greenstone belt, Van Lankvelt (2013) has identified a potassic alteration event at 2760–2680 Ma, as resolved from U-Pb zircon and titanite analyses. Biczok et al. (2012) suggest that gold mineralization at the Musselwhite mine may have occurred between 2720 and 2670 Ma, as determined by Sm-Nd analyses of hydrothermal garnets believed to be coeval with mineralization. Regionally within the North Caribou Superterrane (Thurston et al., 1991) and coincident with the Uchian orogeny (Percival et al., 2006), the Berens River Intrusive event affected zircon and apatite ages, resulting in 2750 to 2685 Ma U-Pb ages (Corfu and Stone, 1998). Ernst and Jowitt (2013) describe the widespread Bird River large igneous province at ca. 2735 Ma, which may have additionally acted as a driver for the hydrothermal fluid circulation. Though our results cannot explicitly resolve between the different regional tectonic episodes, they indicate that the NCGB has witnessed a metamorphic and mineralization episode broadly coeval with that of the Western Superior region.

IMPLICATIONS FOR EXPLORATION

The age of zircon rim recrystallization within the North Caribou Greenstone belt is similar to the timing of

potassic alteration in the adjacent plutons and broadly correlative to mineralization within the North Caribou Superterrane. This synchronicity across a range of scales suggests that we may have determined the timing of hydrothermal events responsible for the gold mineralization within the Musselwhite mine, adding to a growing set of observations of pervasive lower temperature tectonism across the Western Superior Province. Although the zircon depth-profiling technique is likely not a primary exploration tool, it can be used as a secondary method to resolve the timing of fluid flow within Archean greenstone belts. For example, the lack of significant zircon rim material at the western end of Eyapimikima Lake probably suggests that this is a region of low economic interest, since it is an area of relatively low fluid-mineral interaction.

FUTURE WORK

The authors are currently pursuing a couple of geochronology-geochemistry methodologies, using LA-ICPMS to resolve rare earth element depth-profiles in combination with the U-Pb age depth-profiles. Moreover, we are conducting LA-ICPMS trace element mapping on the unpolished zircon grains to determine the extent of rim recrystallization, since it is apparent that not all of the zircon we examined possessed a recrystallized rim. We believe alkaline fluids are, in part, responsible for the recrystallization, and potentially the armoring effects of adjacent refractory mineral phases prohibit complete rim recrystallization.

ACKNOWLEDGEMENTS

We would like to thank Émilie Gagnon for her insights into the metamorphic history of the belt as well as assisting in the collection of samples with John Biczok (Musselwhite mine). Dr. Axel Schmitt (UCLA) is thanked for his assistance and advice in the operation of the SIMS. Constructive reviews by Vicki McNicoll (GSC) are appreciated. Funding for this project was generously provided by Musselwhite gold mine and by a research grant from the Natural Resource Canada's Targeted Geoscience Initiative-4.

REFERENCES

Biczok, J., Hollings, P., Klipfel, P., Heaman, L., Maas, R., Hamilton, M., Kamo, S., and Friedman, R., 2012. Geochronology of the North Caribou greenstone belt, Superior Province of Canada: implications for tectonic history and gold mineralization in the Musselwhite Mine; Precambrian Research, v. 192–195, p. 209–230.

Breaks, F.W., Osmani, I.A., and de Kemp, E.A., 2001. Geology of the North Caribou Lake area, northwestern Ontario; Ontario Geological Survey, Open File Report 6023, 80 p.

Breeding, C.M., Ague, J.J., Grove, M., and Rupke, A.L., 2004. Isotopic and chemical alteration of zircon by metamorphic fluids: U-Pb age depth-profiling of zircon crystals from Barrow's garnet zone, northeast Scotland; American Mineralogist, v. 89, p. 1067–1077.

Carson, C.J., Ague, J.J., Grove, M., Coath, C.D., and Harrison, T.M., 2002. U-Pb isotopic behavior of zircon during upper-amphibolite facies fluid infiltration in the Napier complex, east Antarctica; Earth and Planetary Science Letters, v. 199, p. 287–310.

Corfu, F. and Stone, D., 1998. The significance of titanite and apatite U-Pb ages: constraints for the post-magmatic thermal-hydrothermal evolution of a batholithic complex, Berens River area, northwestern Superior Province, Canada; Geochimica et Cosmochimica Acta, v. 62, p. 2979–2995.

Cottle J.M., Horstwood, M.S.A., and Parrish, R.R., 2009. A new approach to single shot laser ablation analysis and its application to in situ Pb/U geochronology; Journal of Analytical Atomic Spectrometry, v. 24, p. 1355–1363.

Cottle, J.M., Kylander-Clark, A.R., and Vrijmoed, J.C., 2012. U-Th/Pb geochronology of detrital zircon and monazite by single shot laser ablation inductively coupled plasma mass spectrometry (SS-LA-ICPMS); Chemical Geology, v. 332-333, p. 136–147.

Dubé, B., Williamson, K., McNicoll, V., Malo, M., Skulski, T., Twomey, T., and Sanborn-Barrie, M., 2004. Timing of Gold Mineralization at Red Lake, Northwestern Ontario, Canada: New Constraints from U-Pb Geochronology at the Goldcorp High-Grade Zone, Red Lake Mine, and the Madsen Mine; Economic Geology, v. 99, p. 1611–1641.

Ernst, R.E. and Jowitt, M., 2013. Large Igneous Provinces (LIPs) and metallogeny, *In:* Tectonics, Metallogeny, and Discovery: The North American Cordillera and Similar Accretionary Settings, (ed.) M. Colpron, T. Bissig, B.G. Rusk, and J.F.H. Thompson; Society of Economic Geologists, Special Publication 17, p. 17–51.

Geisler, T., Schaltegger, U,. and Tomashek, F., 2007. Re-equilibration of zircon in aqueous fluids and melts; Elements, v. 3, p. 43–50.

Grove, M. and Harrison, T.M., 1999. Monazite Th/Pb age depth-profiling; Geology, v. 27, p. 487–490.

Kalbfleisch, N., 2012. Tectonometamorphic evolution of the North Caribou belt and implications for Au mineralization; M.Sc. Thesis, University of Ottawa, Ottawa, Ontario, 162 p.

Kelly, C., Gagnon, É., and Schneider, D.A., 2013. Redefining the pattern and timing of metamorphism in the North Caribou greenstone belt, *In:* Summary of Fieldwork and other Actvities 2013; Ontario Geological Survey, Open File Report 6290, p. 59-1 to 59-8.

Kelly, C.J., McFarlane, C., Schneider, D.A., and Jackson, S., 2014. Dating micrometer-thin rims using a LA-ICP-MS depth-profiling technique on zircons from an Archean metasediment: comparison with the SIMS depth-profiling method; Geostandards and Geoanalytical Research, v. 38, p. 389–407.

Ludwig, K.R., 2012. User's manual for ISOPLOT 3.75: A Geochronological Toolkit for Microsoft Excel; Berkeley Geochronological Centre Special Publication no 5, 75 p.

Moeller, A., O'Brien, P.J., Kennedy, A., and Kroner, A., 2003. Linking growth episodes of zircon and metamorphic textures to zircon chemistry: an example from the ultrahigh-temperature granulites of Rogaland (SW Norway); Geological Society, London, Special Publications, v. 220, p. 65–81.

Mojzsis, S.J. and Harrison, T.M., 2002. Establishment of a 3.83 Ga magmatic age for the Akilia tonalite (southern west Greenland); Earth and Planetary Science Letters, v. 202, p. 563–576.

Paces, J.B. and Miller, J.D., 1993. Precise U-Pb ages of Duluth complex and related mafic intrusions, northeastern Minnesota: Geochronological insights to physical, petrogenetic, paleomagnetic, and tectonomagmatic processes associated with the 1.1 Ga Mid-continent Rift System; Journal of Geophysical Research, v. 98, p. 13,997–14,013.

Percival, J.A., Sandborn-Barrie, M., Skulski, T. Stott, G.M., Helmstaedt, H., and White, D.J., 2006. Tectonic evolution of the western Superior Province from NATMAP and Lithoprobe studies; Canadian Journal of Earth Sciences, v. 43, p. 1085–1117.

Schmitt, A.K., Grove, M., Harrison, T.M., Lovera, O.M., Hulen, J., and Waters, M., 2003. The Geysers-Cobb Mountain magma system, California (Part 1): U-Pb zircon ages of volcanic rocks, conditions of zircon crystallization and magma residence times; Geochimica et Cosmochimica Acta, v. 67, p. 3422–3442.

Schneider, D.A., Bachtel, J., and Schmitt, A.K., 2012. Low temperature zircon alteration and timescales of fluid flow at Pamour and Hoyle Pond mines, Abitibi granite greenstone belt: applying depth profiling techniques on zircon; Economic Geology, v. 107, p. 1043–1072.

Steely, A.N., Hourigan, J.K. and Juel, E., 2014. Discrete multi-pulse laser ablation depth profiling with a single-collector ICP-MS: Sub-micron U–Pb geochronology of zircon and the effect of radiation damage on depth-dependent fractionation; Chemical Geology, v. 372, p. 92–108.

Thurston, P., Osmani, I., and Stone, D., 1991. Northwestern Superior Province: review and terrane analysis, *In:* Geology of Ontario, (ed.) Thurston, P.C., Williams, H.R., Sutcliffe, R.H., Stott, G.M.; Ontario Geological Survey, Special Volume 4, Part 1, p.80–142.

Van Lankvelt, A., 2013. Protracted magmatism within the North Caribou Terrane, Superior Province: petrology, geochronology, and geochemistry of Meso- to Neoarchean TTG suites; M.Sc. Thesis, University of Ottawa, Ottawa, Ontario, 208 p.

Young, M.D., McNicoll, V., Helmstaedt, H., Skulski, T., and Percival, J.A., 2006. Pickle Lake revisited: new structural, geochronological and geochemical constraints on greenstone belt assembly, western Superior Province, Canada; Canadian Journal of Earth Sciences, v. 43, p. 821–847.

GEOLOGICAL SURVEY OF CANADA
OPEN FILE 7852

Targeted Geoscience Initiative 4: Contributions to the Understanding of Precambrian Lode Gold Deposits and Implications for Exploration

Geology of the banded iron formation-hosted Meadowbank gold deposit, Churchill Province, Nunavut

Vivien Janvier[1], Sébastien Castonguay[2], Patrick Mercier-Langevin[2], Benoît Dubé[2], Michel Malo[1], Vicki J. McNicoll[3], Robert A. Creaser[4], Benoît de Chavigny[5], and Sally J. Pehrsson[3]

[1]Institut national de la recherche scientifique – Centre Eau Terre Environnement, Québec, Quebec
[2]Geological Survey of Canada, Québec, Quebec
[3]Geological Survey of Canada, Ottawa, Ontario
[4]University of Alberta, Edmonton, Alberta
[5]Agnico-Eagle Mines Ltd., Ottawa, Baker Lake, Nunavut

2015

Recommended citation

Janvier, V., Castonguay, S., Mercier-Langevin, P., Dubé, B., Malo, M., McNicoll, V.J., Creaser, R.A., de Chavigny, B., and Pehrsson, S.J., 2015. Geology of the banded iron formation-hosted Meadowbank gold deposit, Churchill Province, Nunavut, *In:* Targeted Geoscience Initiative 4: Contributions to the Understanding of Precambrian Lode Gold Deposits and Implications for Exploration, (ed.) B. Dubé and P. Mercier-Langevin; Geological Survey of Canada, Open File 7852, p. 255–269.

Publications in this series have not been edited; they are released as submitted by the author.

Contribution to the Geological Survey of Canada's Targeted Geoscience Initiative 4 (TGI-4) Program (2010–2015)

TABLE OF CONTENTS

Geology of the banded iron formation-hosted Meadowbank gold deposit, Churchill Province, Nunavut

Vivien Janvier[1]*, Sébastien Castonguay[2]†, Patrick Mercier-Langevin[2], Benoît Dubé[2], Michel Malo[1], Vicki J. McNicoll[3], Robert A. Creaser[4], Benoît de Chavigny[5], and Sally J. Pehrsson[3]

[1]Institut national de la recherche scientifique – Centre Eau Terre Environnement, 490 rue de la Couronne, Québec, Quebec G1K 9A9
[2]Geological Survey of Canada, 490 rue de la Couronne, Québec, Quebec G1K 9A9
[3]Geological Survey of Canada, 601 Booth Street, Ottawa, Ontario K1A 0E8
[4]University of Alberta, 116 Street and 85 Avenue, Edmonton, Alberta T6G 2R3
[5]Agnico-Eagle Mines ltd, Meadowbank Division, P.O. Box 540, Baker Lake, Nunavut X0C 0A0
*Corresponding author's e-mail: vivien.janvier@ete.inrs.ca
†Corresponding author's e-mail: sebastien.castonguay@RNCan-NRCan.gc.ca

ABSTRACT

The Meadowbank gold deposit is hosted in ca. 2711 Ma banded iron formation (BIF) successions within the polydeformed and metamorphosed Woodburn Lake Group. This volcano-sedimentary sequence comprises several similar BIF successions of which only one contains economical gold mineralization. Deposit host rocks consist of greenschist- to amphibolite-facies, intermediate to felsic volcaniclastic rocks, mafic and ultramafic rocks, quartzite and BIF. Notwithstanding cryptic and strongly overprinted Archean tectonism, four phases of Proterozoic Trans-Hudsonian deformation have been regionally documented. In the Meadowbank deposit area, several generations of structures are recognized: 1) isoclinal F_1 folds and D_1 faults strongly overprinted by 2) south-trending isoclinal F_{2a} folds and associated D_2 fault zones that cut mineralized zones. Late D_2 deformation consists of north-trending gentle F_{2b} folds, 3) open to closed south-west-plunging megascopic F_3 folds, and 4) south-verging shallowly to moderately inclined, open to tight, chevron-style F_4 folds.

The bulk of the gold is hosted in BIF and is associated with pyrrhotite ±pyrite and traces of chalcopyrite and arsenopyrite. Gold-rich quartz-pyrrhotite ±pyrite veins cut intercalated intermediate to felsic volcaniclastic rocks. The ore-associated mineral assemblage includes grunerite and chlorite within BIF, whereas muscovite, chlorite, and pyrite represent the dominant mineral assemblage of altered volcaniclastic rocks. Biotite, Fe-Mg amphibole, and garnet occur in variable modal abundance in the southern part of the deposit, where metamorphic grade is higher.

Crosscutting relationships suggest that most of the gold was preferentially introduced along D_1 faults and was likely remobilized during D_2 deformation, especially along sheared contacts and F_{2a} fold limbs. Deposit- and regional-scale lithogeochemistry coupled with new U-Pb zircon ages indicate that the Meadowbank deposit is located at or near the boundary between two distinct lithological assemblages (2711 Ma and 2717 Ma), which are separated by long-lived fault zones that potentially controlled the occurrence and geometry of the Meadowbank deposit.

INTRODUCTION

The Meadowbank Mine, owned and operated by Agnico Eagle Mines Ltd., is located approximately 70 km north of the community of Baker Lake (Fig. 1a). Approximately 4.2 million ounces of gold, including 1.3 Moz produced from 2010 to 2013, 1.8 Moz in reserve, and 1.2 Moz in resources are comprised in the Portage-Goose and Vault deposits (Agnico Eagle Mines website end of December 2014). Most of the gold is hosted in banded magnetite-chert iron formations, but a significant amount of gold is also associated with quartz veins that cut intercalated intermediate to felsic volcaniclastic rocks. The mineralized succession is part of the polydeformed and metamorphosed Neoarchean Woodburn Lake Group (Sherlock et al., 2004).

In the Meadowbank mine area, the Woodburn Lake Group comprises several major banded iron formations (BIF), including the East BIF, the Central BIF, and the West BIF (Fig. 1b). Despite their mineralogical and textural similarities (e.g. Gourcerol et al., 2014, 2015), only the Central BIF contains economic gold concentration (Portage-Goose deposit), suggesting that key elements and ore-forming processes were specific to that particular BIF interval. Establishing the nature of these key ore-forming event(s) at Meadowbank could

Janvier, V., Castonguay, S., Mercier-Langevin, P., Dubé, B., Malo, M., McNicoll, V.J., Creaser, R.A., de Chavigny, B., and Pehrsson, S.J., 2015. Geology of the banded iron formation-hosted Meadowbank gold deposit, Churchill Province, Nunavut, *In:* Targeted Geoscience Initiative 4: Contributions to the Understanding of Precambrian Lode Gold Deposits and Implications for Exploration, (ed.) B. Dubé and P. Mercier-Langevin; Geological Survey of Canada, Open File 7852, p. 255–269.

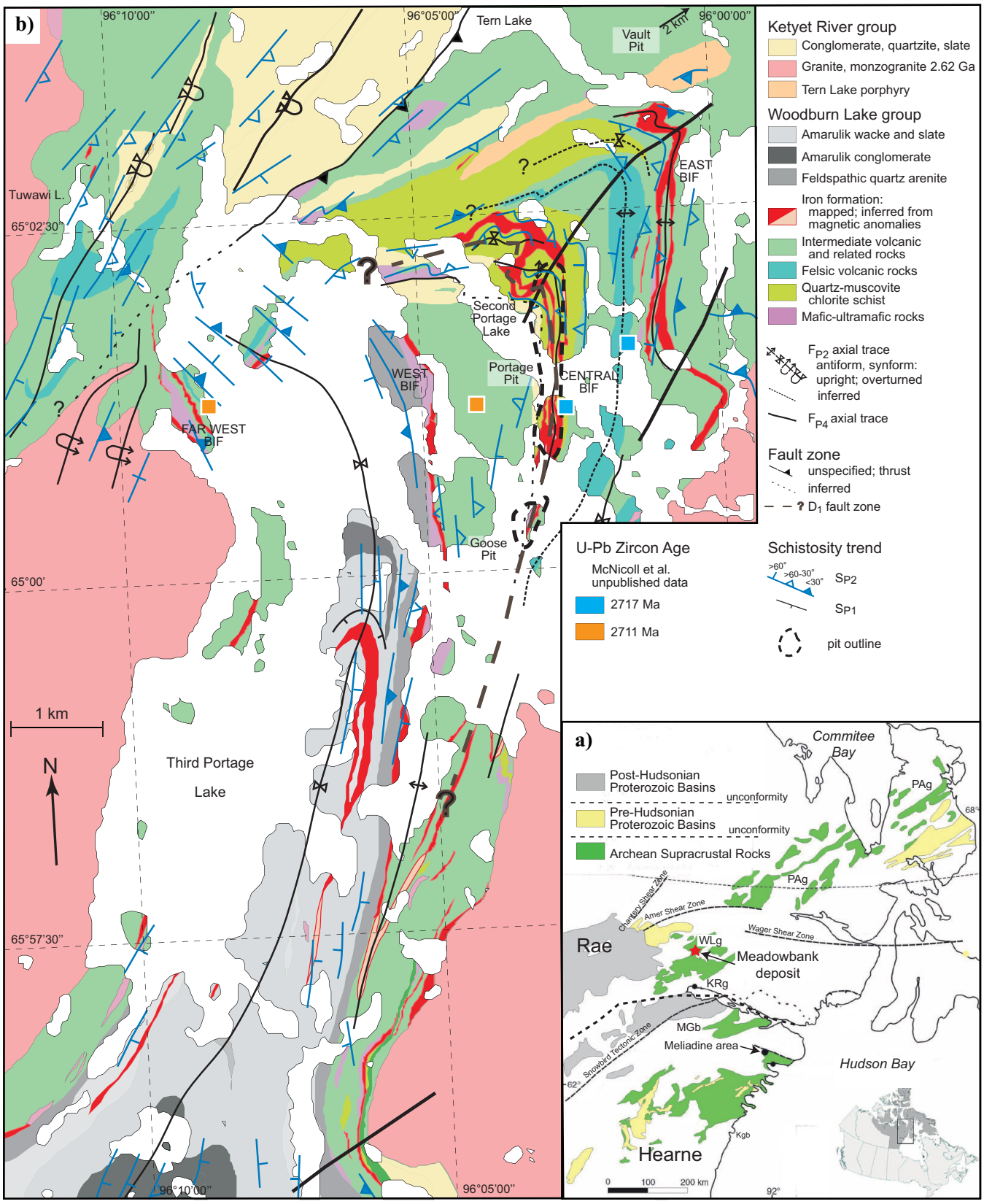

Figure 1. a) Geology and structure of the Meadowbank gold deposit area (modified map and structural nomenclature of Pehrsson et al., 2013). **b)** Simplified geological map of the western Churchill Province (modified from Hrabi et al., 2003). Abbreviations: KGb = Kaminak greenstone belt; KRg = Ketyet River Group; MGb = MacQuoid-Gibson belt; PAg = Prince Albert Group; WLg = Woodburn Lake Group. U-Pb ages from Davis and Zaleski (1998) and McNicoll et al. (unpublished data).

have a major impact on exploration models as well as genetic models for other BIF-hosted gold deposits.

Our field-based research includes geological mapping of the open-pit deposit, detailed description of several drillhole sections, and geochemical characterization of host rocks and their alteration (Castonguay et al., 2012, 2013; Janvier et al., 2013). Geochronology of key units in and around the deposit (Castonguay et al., 2013) and a study of the Vault gold deposit, 10 km north of Portage-Goose deposit (Dupuis et al., 2014), were also undertaken. The present report synthesizes the main geological features of the Portage deposit.

GEOLOGICAL SETTING

The Meadowbank deposit is situated within the Rae domain of the western Churchill Province (Fig. 1a). The Rae domain is dominated by Meso- to Neoarchean granodioritic-tonalitic orthogneiss and supracrustal rocks (Hoffman, 1989; Zaleski et al., 1997, 1999b; Skulski et al., 2003; Berman et al., 2005). The Meadowbank deposit is hosted by the 2.71 Ga Pipedream-Third Portage sequence, the third of five assemblages comprising the ca. 2.73–2.68 Ga Woodburn Lake Group (Fig. 1b; Henderson et al., 1991; Zaleski et al., 1997, 2001; Pehrsson et al., 2013). The Woodburn Lake Group constitutes part of a greenstone belt including greenschist- to amphibolite-facies, ultramafic to mafic volcanic rocks, intermediate volcanic rocks, BIF, quartzite, and oligomictic conglomerate, overlain by Paleoproterozoic (2.3–1.9 Ga) sedimentary rocks of the Ketyet River Group.

Rocks comprising the Woodburn Lake Group in the Meadowbank mine area were likely deformed during the Archean (Ashton, 1988; Zaleski et al., 1999a, 2003; Berman et al., 2005, 2007). However, Archean fabrics are mainly cryptic in the Meadowbank area. Proterozoic reworking, concomitant with the Trans-Hudson Orogeny (1.9–1.8 Ga), is extensive and developed during at least four phases (Hrabi et al., 2003; Sherlock et al., 2004; Pehrsson et al., 2004, 2013; Fig. 1b). The first two Proterozoic deformation phases/increments [D_{P1} and D_{P2}; following Pehrsson et al. (2013), in which the subscript P is used to identify deformation phases of Proterozoic age] are characterized by tight to isoclinal folds. In areas less affected by younger deformation, F_{P1} and F_{P2} folds verge to the south and northwest, respectively. In areas of strong D_{P2} strain or along long limbs of F_{P2} folds, the S_{P1} and S_{P2} axial-planar foliations become generally coplanar, and are thus difficult to differentiate and are often described as a composite S_{P1-2} fabric (Pehrsson et al., 2013). Fault zones associated with these two major episodes of deformation have an impact on the distribution and geometry of ore zones, which will be discussed below. The third Proterozoic deformation (D_{P3}) comprises shallowly to moderately north- to northwest-inclined, open to tight, chevron-style mesoscopic folds, locally marked by an axial-planar S_{P3} crenulation cleavage. The D_{P4} regional deformation consists of megascopic upright southeast- or northeast-plunging chevron folds (Fig. 1b).

DEPOSIT HOST ROCKS

The Meadowbank deposit comprises several variably altered, intensely deformed and metamorphosed rock units (Sherlock et al., 2001a). From east to west, rock units consist of intermediate volcaniclastic rocks (unit 1), intermediate to felsic (unit 2) and felsic (unit 3) volcaniclastic rocks intercalated with BIF, mafic volcanic rocks (unit 4), ultramafic rocks (unit 5) and quartzite with mafic (unit 6) to intermediate volcanic rocks (unit 7; Sherlock et al., 2001a; Fig. 2). Unit 1 consists of massive intermediate volcaniclastic rocks that form the structural footwall at the Meadowbank deposit. Volcaniclastic rocks comprise quartz and plagioclase grains within a groundmass of fine-grained quartz, plagioclase, and biotite. Unit 2 comprises medium- to fine-grained, intermediate to felsic volcaniclastic rocks, commonly intercalated with BIF, and quartz ±plagioclase with a significant amount of muscovite and chlorite. Unit 3 is characterized by felsic volcaniclastic rocks, commonly muscovite-altered and intensely foliated, forming distinct muscovite schists. BIF comprises millimetre- to centimetre-thick magnetite and chert layers (1 mm to 3 cm) along with lesser grunerite/cummingtonite, chlorite, greenalite, and stilpnomelane. Mafic and ultramafic volcanic rocks (units 5 and 4, respectively) generally occur in the structural hanging wall of the ore zones. A massive quartzite, locally underlain by a basal polymictic conglomerate, structurally overlies the deposit host succession (Fig. 2). Minor mafic (unit 6) and intermediate (unit 7) volcanic rocks, respectively, consisting of chlorite and biotite schists, occur as conspicuous layers within the quartzite.

GEOCHEMISTRY OF PROTOLITHS

Rocks proximal to mineralized zones are strongly altered and their primary geochemical signatures (especially mobile major oxides and trace elements) are commonly obscured. Although visual recognition of the rock units allows for a preliminary classification, lithogeochemical data and more specifically least mobile elements such as Zr, Ti, Al, Y, Cr, Ni, Sc, V, and rare-earth elements (REE) are essential to further differentiate the subtle lithological variations, characterize distinct protoliths, and thus facilitates mapping of individual units. Lithogeochemical data and analysis of Janvier et al. (2015) are summarized herein.

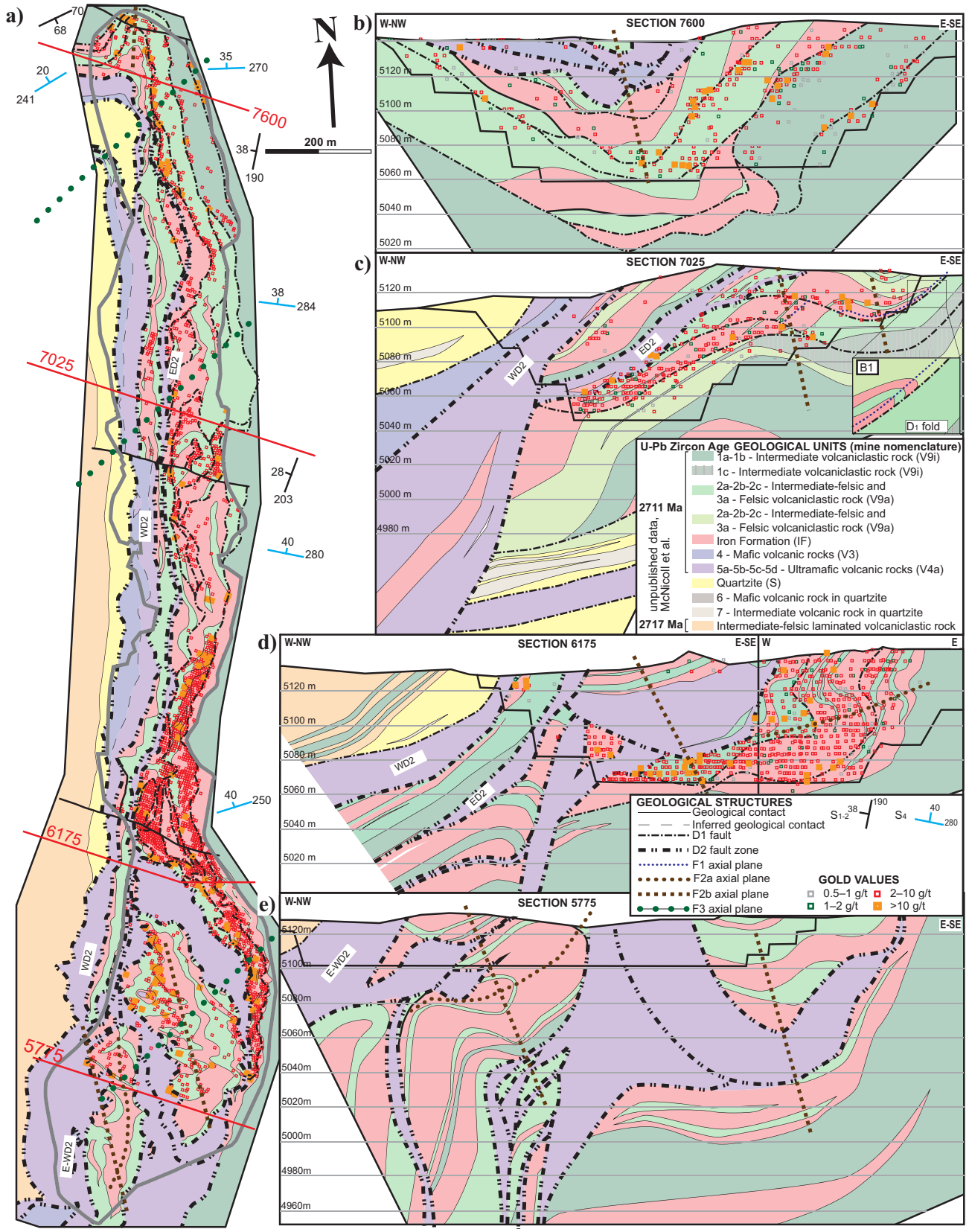

Figure 2. a) Geological map (based on drill sections, pit mapping, and geochemical characterization) of the Portage deposit (Meadowbank mine) at level 5102 m. Interpreted geology of sections **(b)** N7025, **(c)** N7600, **(d)** N5775, and **(e)** N6175 across the Portage deposit showing the complex fault imbrications and the distribution of gold. The gold values are from blast holes and are present inside the pit outline. Gold values are not available for section N5775. Mine-scale structural nomenclature modified from Pehrsson et al., 2013. U-Pb ages from Davis and Zaleski (1998) and McNicoll et al (unpublished data).

The Zr/TiO_2 versus Al_2O_3/TiO_2 binary diagram is useful to discriminate the main groups of volcanic rocks and various sub-units (Fig. 3a). Intermediate (unit 1: 1a, 1b, 1c) to felsic (unit 2: 2a, 2b, 2c), volcanic and/or volcaniclastic units yield andesitic and calc-alkaline compositions (Fig. 3b,c. Felsic volcaniclastic rocks (unit 3) yield trachyte and calc-alkaline compositions (Fig. 3b,c). Mafic (unit 4) and ultramafic units (unit 5) yield transitional to tholeiitic magmatic affinities (Fig. 3b) and a high-Fe basalt and basaltic komatiite compositions (Fig. 3d), respectively. Chondrite-normalized trace and rare-earth elements plots further help to differentiate units and subunits. Units 1 and 2 (Fig. 3e,f) have an arc-like signature with negative Nb, Ta, and Ti anomalies. Intermediate sub-units have elevated heavy-REE concentrations relative to intermediate to felsic sub-units (Fig. 3e,f). Mafic units yield flat REE patterns that range from 10 to 30 times chondritic compositions (Fig. 3g); whereas sub-units 5a, 5b, and 5c have generally lower REE values than mafic units (Fig. 3h), with depleted to enriched light-REE relative to heavy-REE. Unit 3 is distinct with much higher Zr/TiO_2 and Al_2O_3/TiO_2 ratios (Fig. 3a) and yield rhyodacitic to rhyolitic compositions (Fig. 3b) and a calc-alkaline affinity (Fig. 3c). Chondrite-normalized trace and REE plots for this unit show variable patterns with a moderate negative slope, and slightly negative Zr and strongly negative Ti anomalies (Fig. 3f).

STRUCTURE

The structural setting of Meadowbank deposit is highly complex and ore zones are strongly deformed (e.g. Sherlock et al., 2001a,b, 2004; Pehrsson et al., 2004, 2013; Janvier et al., 2013, 2015). Detailed mapping of the Portage and Goose open pits has delineated seven generations of structures defined on the basis of structural style, orientation, and relative crosscutting relationships. Each deformation increment is described below in apparent chronological order: 1) Along the eastern wall of the Portage open pit, a penetrative bedding-/layering-parallel schistosity, S_1, is generally south-trending and dips shallowly to moderately (~30°) to the west (Fig. 2a). The S_1 schistosity is associated with isoclinal folds (F_1). One of the F_1 folds, apparently east-verging, is mapped in the western part of the Portage open pit, as shown on section 7025 (Fig. 2c). 2) A large fault zone consisting of a series of discrete D_1 faults occurs in the Portage open pit causing the imbrication of volcaniclastic rocks, iron formation, and quartzite (Fig. 2). No reliable kinematic indicators have been identified for these faults. However, based on the interpreted section 7025 (Fig. 2c), the latter are apparently east-directed. The relative timing of such early faults is difficult to determine, but they are clearly folded and faulted by D_2 structures and are therefore termed D_1 faults (Fig. 2). 3) Tight to isoclinal F_{2a} folds with sub-horizontal south-trending axes occur in the southeastern part of the Portage open pit (Fig. 2a,e) and eastward, where asymmetric F_{2a} folds affect mineralized BIFs and intermediate to felsic rocks (Fig. 2d). Mesoscopic isoclinal F_{2a} folds have an apparent eastward vergence. An axial planar S_{2a} foliation is mostly developed along the limbs of F_{2a} folds, where it is coplanar to the S_1 schistosity and forms a composite $S_{1\text{-}2}$ fabric (Fig. 4a). 4) A network of late D_2 fault zones is distinctively outlined by ultramafic rocks in the Portage open pit. Two of these, termed the western and eastern fault zones, are subparallel and mapped along parts of the western wall (Figs. 2, 4b). These structures, which cut D_1 faults and the ore zones, are affected by F_{2b}, F_3, and F_4 folds (Fig. 2). Although kinematic indicators are rare in volcanic units, some found in sheared ultramafic rocks suggest a down-to-the-west motion (inverted/folded thrust?). 5) North-trending upright gentle folds or undulations, termed F_{2b} folds herein, deform previous structures such as D_1 (Fig. 2a,c) or D_2 fault zones (Fig. 2e). Two late folding events are also differentiated by their vergence and wavelength. 6) In the northern part of the Portage open pit, the mine sequence turns abruptly to the west, affected by a shallow southwest-plunging, southeast-verging megascopic F_3 chevron-style synform, without a penetrative axial-planar fabric (Fig. 2a). Southward, along the long limb of this megascopic fold, minor F_3 folds occur in the Portage open pit, where they produce slight undulations of the lithological contacts and main fabric (Fig. 2). The structure of the southern part of the Portage open pit is dominated by a dome-and-basin pattern, resulting from the interference of F_3 and F_{2b} folds (Fig. 2). 7) D_4 deformation is characterized by mesoscopic shallowly to moderately inclined, south-verging, open to tight folds. The conspicuous axial-planar crenulation cleavage (S_4) is roughly west-trending and dips between 10 and 45° to the north (Fig. 2a).

ORE ZONES: MINERAL ASSEMBLAGES AND DISTRIBUTION

Banded Iron Formation-Hosted Gold

The bulk of the gold in the Meadowbank deposit is hosted in Algoma-type, banded magnetite-chert iron formations (BIF). Ore-bearing BIFs are intensely deformed, with pyrrhotite ±pyrite as the main ore-related minerals, together with lesser chalcopyrite and arsenopyrite. Grunerite is common in chert bands (Fig. 4c,d). In general, pyrrhotite/pyrite replace magnetite bands (Fig. 4c) and occur within high-strain zones (Fig. 4a) or as a transposed stockwork in magnetite and chert bands along with chlorite alteration (Fig. 4d). The gold-rich intersections (≥2 g/t) are often intensely deformed and primary layering of the host BIF is transposed or disrupted, forming dismembered masses of

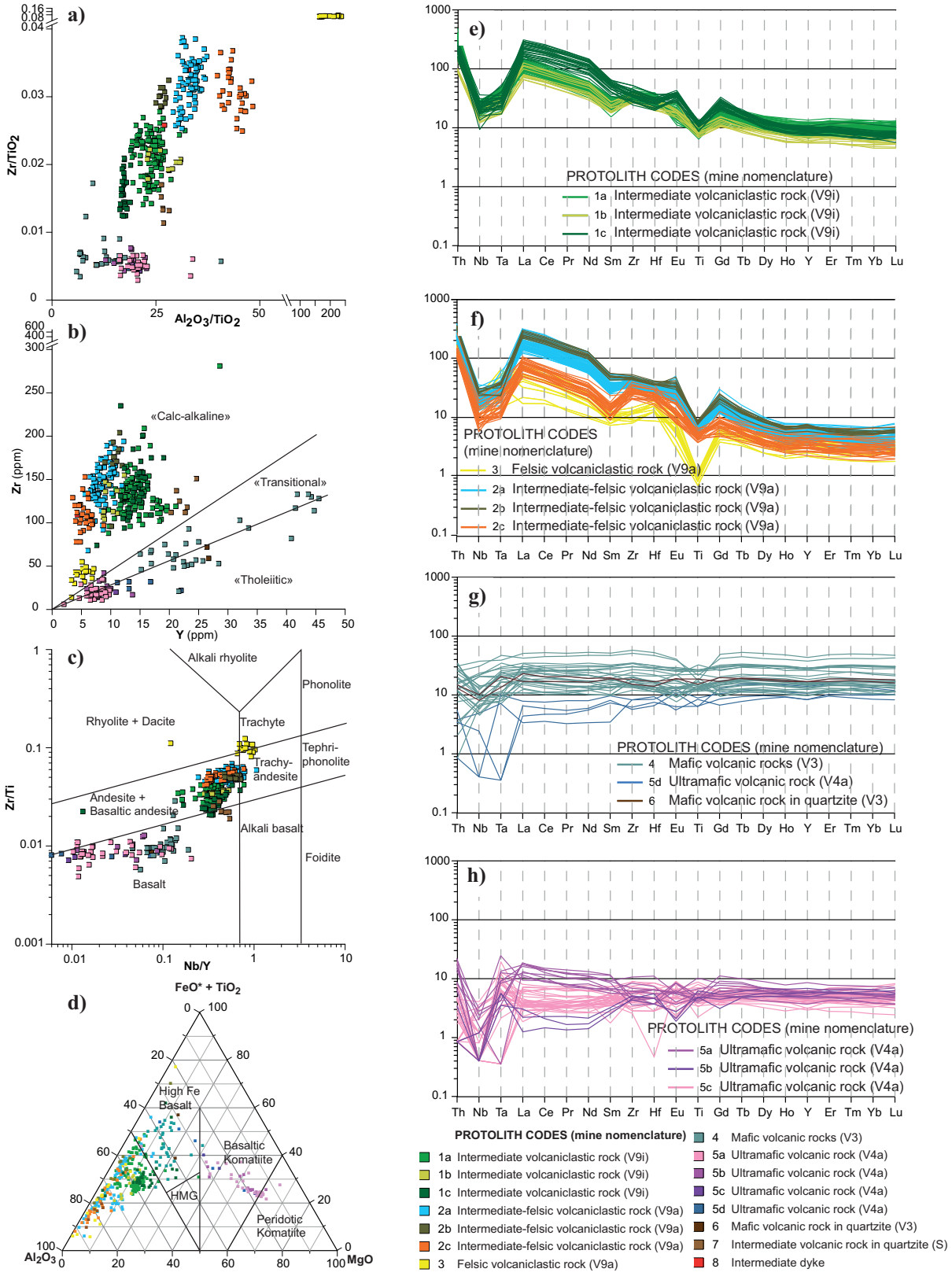

Figure 3. Geochemical diagrams for the volcanic and volcaniclastic rocks of the Meadowbank deposit area. **a)** Zr/TiO_2 versus Al_2O_3/TiO_2; **b)** Zr versus Y magmatic affinity diagram from MacLean and Barrett (1993); **c)** Zr/Ti versus Nb/Y classification diagram (Winchester and Floyd, 1977); **d)** AFM ternary diagram from Jensen (1976). Geochemical plots for volcanic and volcaniclastic rocks of the host rocks of the Meadowbank deposit. Abbreviation: HMG = high-magnesium tholeiite (basalt). **e)** C1 chondrite normalized (McDonough and Sun, 1995) multi-elements patterns for units 1a, 1b and 1c; **f)** units 2a, 2b, 2c, and 3; **g)** units 4, 5d, and 6; and **h)** units 5a, 5b, and 5c.

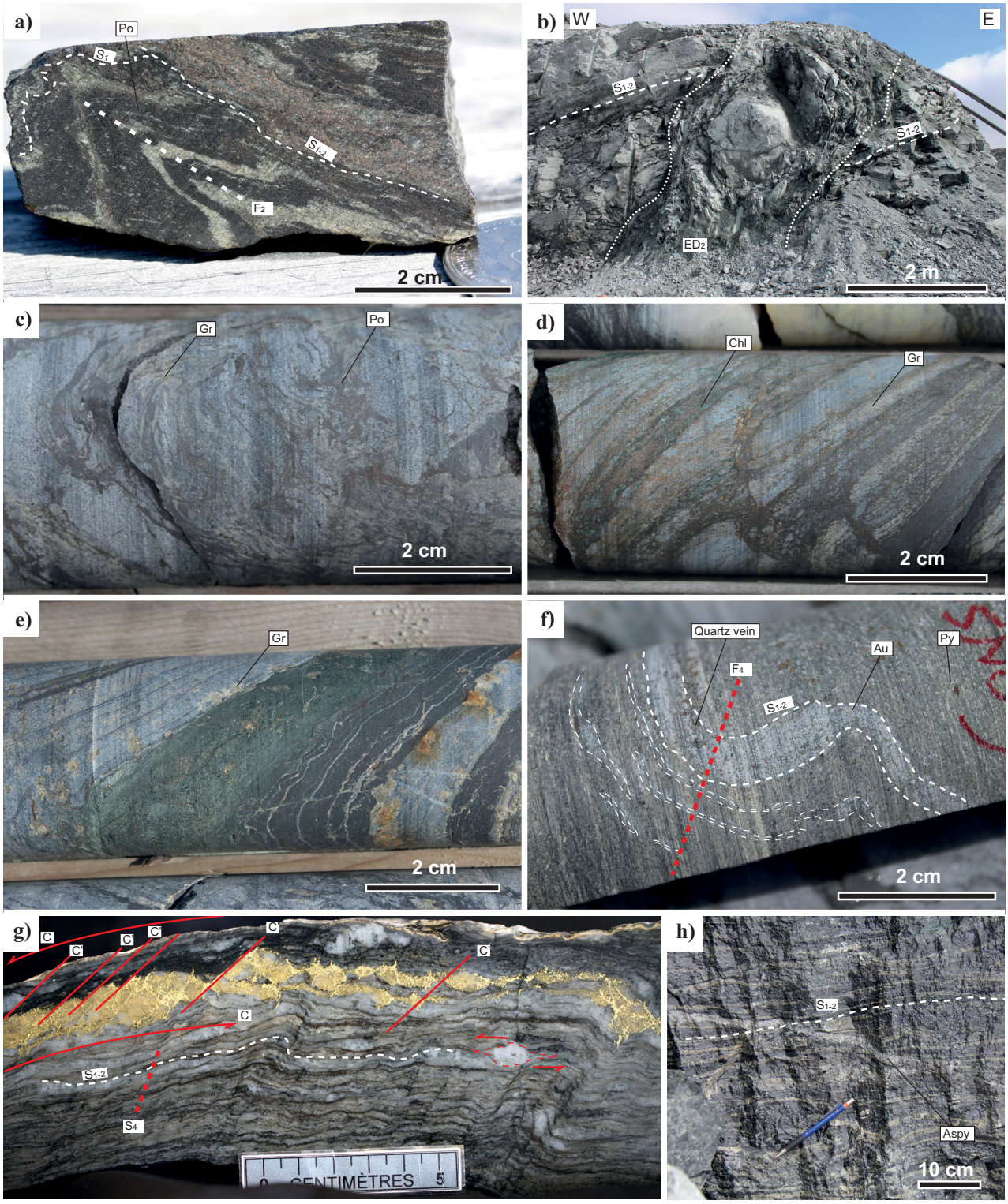

Figure 4. Representative photographs of mineralized and barren banded iron formations (BIFs) and volcaniclastic rocks with associated mineral assemblages of the Meadowbank deposit. **a)** BIF with pyrrhotite (Po) replacing magnetite layers along the S_1 fabric and remobilized along a sheared F_2 fold limb. **b)** The Eastern D_2 fault zone (ED2) marked by ultramafic rocks cutting the composite S_{1-2} fabric in the volcaniclastic rocks. **c)** Mineralized and strongly deformed BIF; note the thin disseminated grunerite (Gr) where pyrrhotite (Po) replaces magnetite. **d)** Transposed pyrrhotite and pyrite stockwork in BIF-chert layers with minor chlorite (Chl) alteration. **e)** Barren BIF with chlorite-rich bands and acicular grunerite at the margins of Fe-oxide bands. **f)** Intermediate to felsic volcaniclastic rock with a pyrite-chlorite- muscovite assemblage adjacent to a quartz-gold vein deformed by F_4 folding. **g)** Felsic schist showing the composite S_{1-2} fabric and transposed (C: shear plane) and boudinaged (C': synthetic riedel or secondary shear plane) gold-quartz veins, affected by the S_4 crenulation cleavage). **h)** Arsenopyrite (Aspy) vein (arrow) cutting the BIF layering and affected by the S_{1-2} fabric. (Mine-scale structural nomenclature).

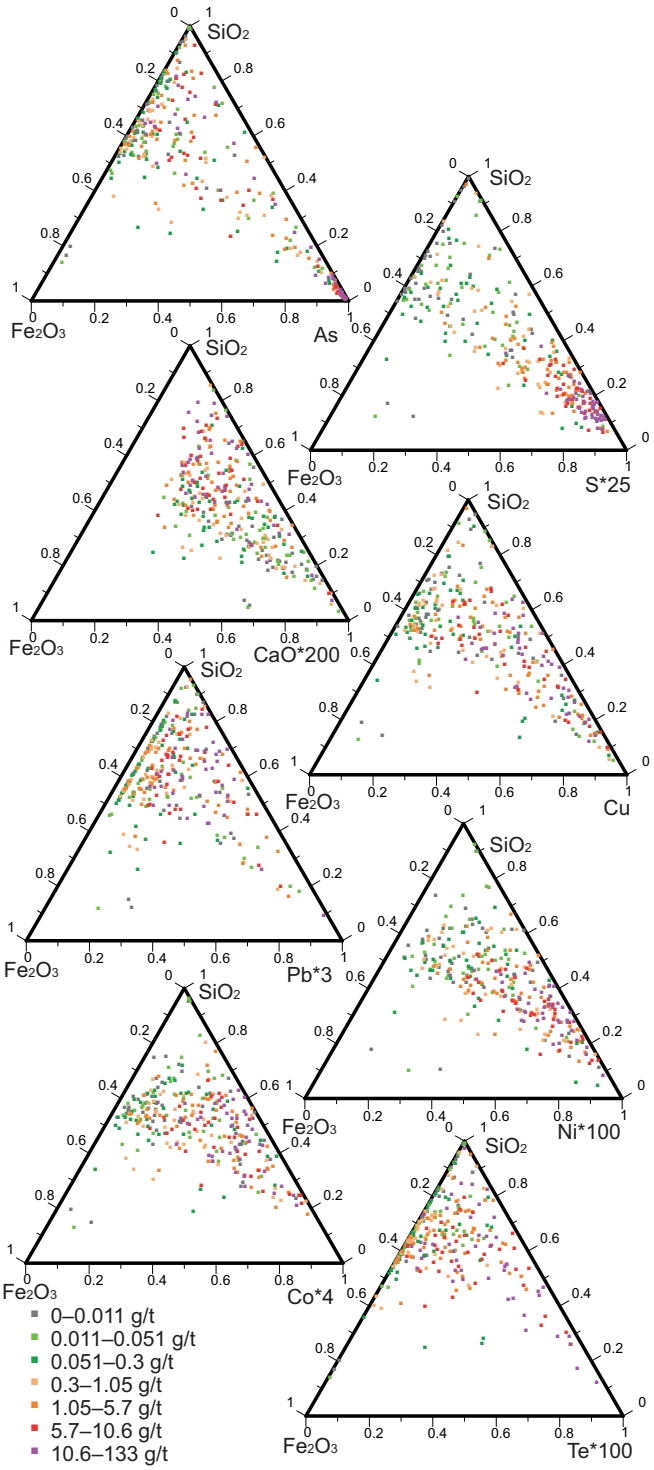

Figure 5. SiO_2-Fe_2O_3-X ternary diagrams representing the relative abundance of various elements versus gold grade of iron formation samples.

quartz, pyrrhotite, and relict magnetite (Fig. 4a,c). Arsenic, S, Cu, Pb, Ni, Co, and Te are anomalous in auriferous BIF, whereas Ca seems to have been leached (Fig. 5). Barren BIFs are much less deformed and have dark green chlorite-rich layers and coarse-grained acicular grunerite (Fig. 4e).

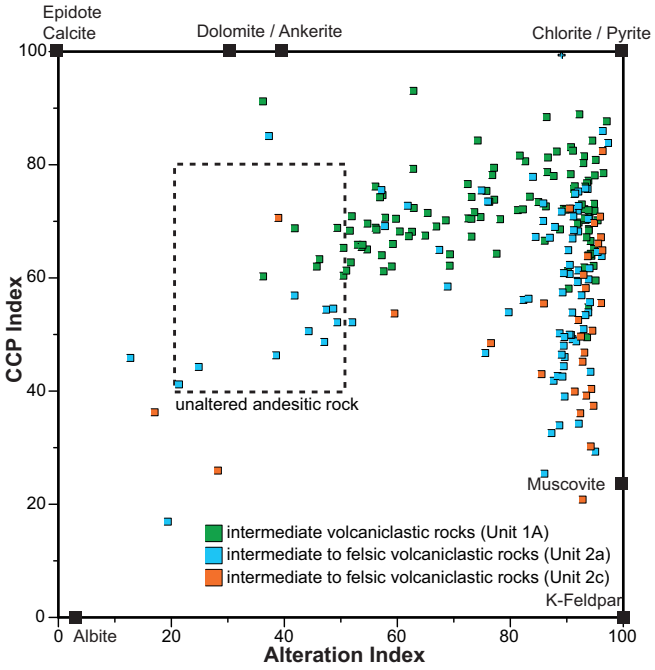

Figure 6. Al-CCPI alteration box plot illustrating chlorite/pyrite and muscovite alteration poles. Al (Ishikawa alteration index) = $100(MgO+K_2O)/(MgO+K_2O+CaO+Na_2O)$ (Ishikawa et al., 1976); CCPI (chlorite-carbonate-pyrite index) = $100(FeO+MgO)/(FeO+MgO+Na_2O+K_2O)$ (modified from Large et al., 2001). Such a diagram has been principally developed for Kuroko-style volcanogenic massive sulphide deposits, and is used herein as a first-order analysis of our data.

Volcaniclastic Rock-Hosted Gold

A second style of mineralization consists of gold-bearing quartz-pyrrhotite ±pyrite veins hosted by intermediate to felsic volcaniclastic rocks (Fig. 4f). This style of mineralization is locally associated with spectacular high-grade ore (Fig. 4g). Auriferous veins are transposed, sheared, and boudinaged sub-parallel to the composite $S_{1\text{-}2}$ schistosity and pre-date the S_4 fabric (Fig. 4f). Disseminated pyrite commonly occurs in the selvages of these veins (Fig. 4f), which are marked by metre-scale chlorite-muscovite alteration halos. An alteration boxplot diagram (Fig. 6; Large et al., 2001) supports this observation and shows that altered samples plot towards the chlorite/pyrite and muscovite poles. Following the single precursor method of MacLean and Barrett (1993), mass changes resulting from alteration were calculated using protoliths that were selected based on low loss-on-ignition values and petrographic observations. Intermediate (subunit 1a) and intermediate to felsic rock (subunit 2a) samples show a loss in Na_2O and CaO (~75–100%), reflecting a strong feldspar destruction, and a gain in K_2O (~25–75%), attributed to the muscovite alteration (Fig. 7). Such mass gain of 0.89 to 5.41 wt% K_2O and loss of 0.67 to 3.66 wt% Na_2O are predominantly observed in subunit 2a, which may be explained by its spatial asso-

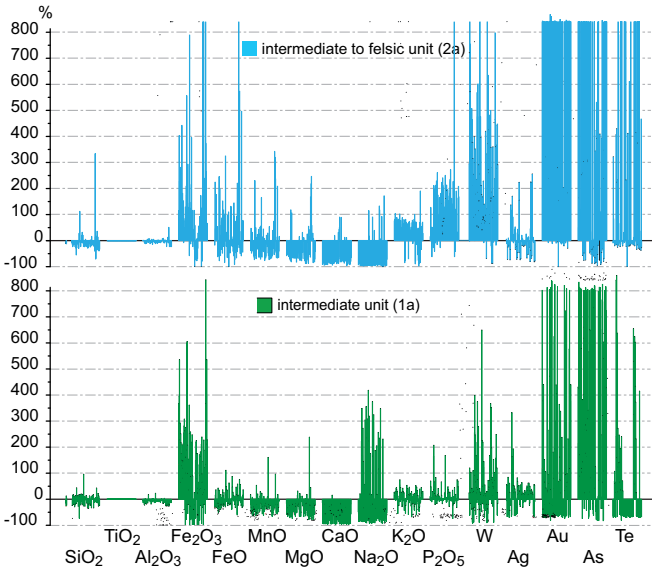

Figure 7. Mass balance diagram (based on the method of MacLean and Barrett, 1993) showing the gains and losses (in percentage) of major elements for intermediate and intermediate to felsic rock samples compared to least altered samples.

ciation with the ore zone (Fig. 8). The mass balance diagram also shows strong gains in Fe_2O_3, P_2O_5, W, As, and Te (Fig. 7). Although some disseminated calcite occurs in subunit 1c, no carbonate alteration is associated with the Portage-Goose deposit. Metamorphic grade transitions from greenschist facies at Portage to amphibolite facies at Goose, which is reflected by a change in the dominant hydrothermal mineral alteration assemblage (i.e. chlorite-muscovite vs. biotite± Fe-Mg amphibole ±garnet; Pehrsson et al., 2004; Sherlock et al., 2004).

Gold Distribution

There are important spatial relationships between the ore zones and some of the earliest structures of the deposit. In the southern part of the Portage open pit (sections 5775 and 6175; Fig. 2a,d,e), the ore zones are hosted in iron formation and occur along D_1 faults and/or proximal to D_2 fault/shear zones. Northward in the Portage open pit, gold mineralization is also hosted, in part, by volcaniclastic rocks and occurs along several subparallel planar ore zones (Fig. 2a,b,c). These ore zones are discordant to lithological contacts, locally coincide with truncations of units, and are thus interpreted to mark discrete D_1 faults. The concentration of sulphides along sheared F_{2a} fold limbs (Fig. 4a) suggests that part of the ore was remobilized or introduced during early- to syn-D_2 deformation. Late idioblastic arsenopyrite veins pre-date the $S_{1\text{-}2}$ fabric and also suggest an early- to syn-D_2 mineralizing event (Fig. 4h). Preliminary Re-Os dating of this arsenopyrite gave an age of ca. 1899 Ma (Janvier et al., in prep.).

DISCUSSION

The analysis of the «immobile elements» has allowed for the identification of several, previously undifferentiated, distinctive volcanic subunits. Three intermediate subunits (i.e. 1a, 1b and 1c), three intermediate to felsic subunits (i.e. 2a, 2b and 2c), one felsic unit (i.e. 3), one mafic unit (i.e. 4), and four ultramafic subunits (i.e. 5a, 5b, 5c and 5d) have been identified. This detailed subdivision has allowed for better definition of the lithostratigraphic and structural settings of the Portage-Goose deposit. Characterization of the primary composition of the host units of the Portage-Goose deposit have allowed us to identify and quantify a potassic alteration proximal to the ore zones that is substantiated by an abundance of muscovite in the volcanoclastic rocks. Such an alteration is typical of lode-gold deposits (Poulsen et al., 2000). The mine-scale protoliths defined herein correlate with those established regionally (Zaleski et al., 1999b; Pehrsson et al., 2013), despite the use of different data sets. As such, regional protolith determination can be used as a regional exploration tool to outline the specific prospective stratigraphic horizons and trace key geological structures.

The various generations of structures defined in the Meadowbank deposit area can be correlated with the regional deformation phases of Pehrsson et al. (2013), although some apparent structural vergence or crosscutting relationships appear to be contradictory. D_1 fabrics (schistosity, isoclinal folds and faults) correlate with the D_{P1} deformation phase of Pehrsson et al. (2013). However, the apparent eastward vergence of the discrete D_1 faults mapped at the Portage deposit contrasts with the overall south vergence of the regional D_{P1} deformation (Pehrsson et al., 2013). Incremental deposit-scale D_2 structures, comprising D_{2a} folds, D_2 fault zones, and D_{2b} gentle folds, are all interpreted to be associated with the regional D_{P2} deformation (Pehrsson et al., 2013). The actual dip and apparent down-to-the-west motion of D_2 fault zones are interpreted as resulting from D_3 folding and are otherwise compatible with the regional northwest-directed D_{P2} thrusting documented by Pehrsson et al. (2013). The two late phases of folding (D_3 and D_4) are also correlated with the regional D_{P3} and D_{P4} folding events (Pehrsson et al., 2013), however, their relative timing established by deposit-scale crosscutting relationships appears to be contradictory and reversed (i.e. deposit-scale F_3 and F_4 folds correspond to the regional F_{P4} and F_{P3} folds, respectively). The consistent orientation of S_4 crenulation cleavage at the mine scale suggests that D_4 deformation represents the youngest folding phase.

Establishing the relationships and controls between structural geology and gold mineralization is a key aspect of the present study. Our study indicates that

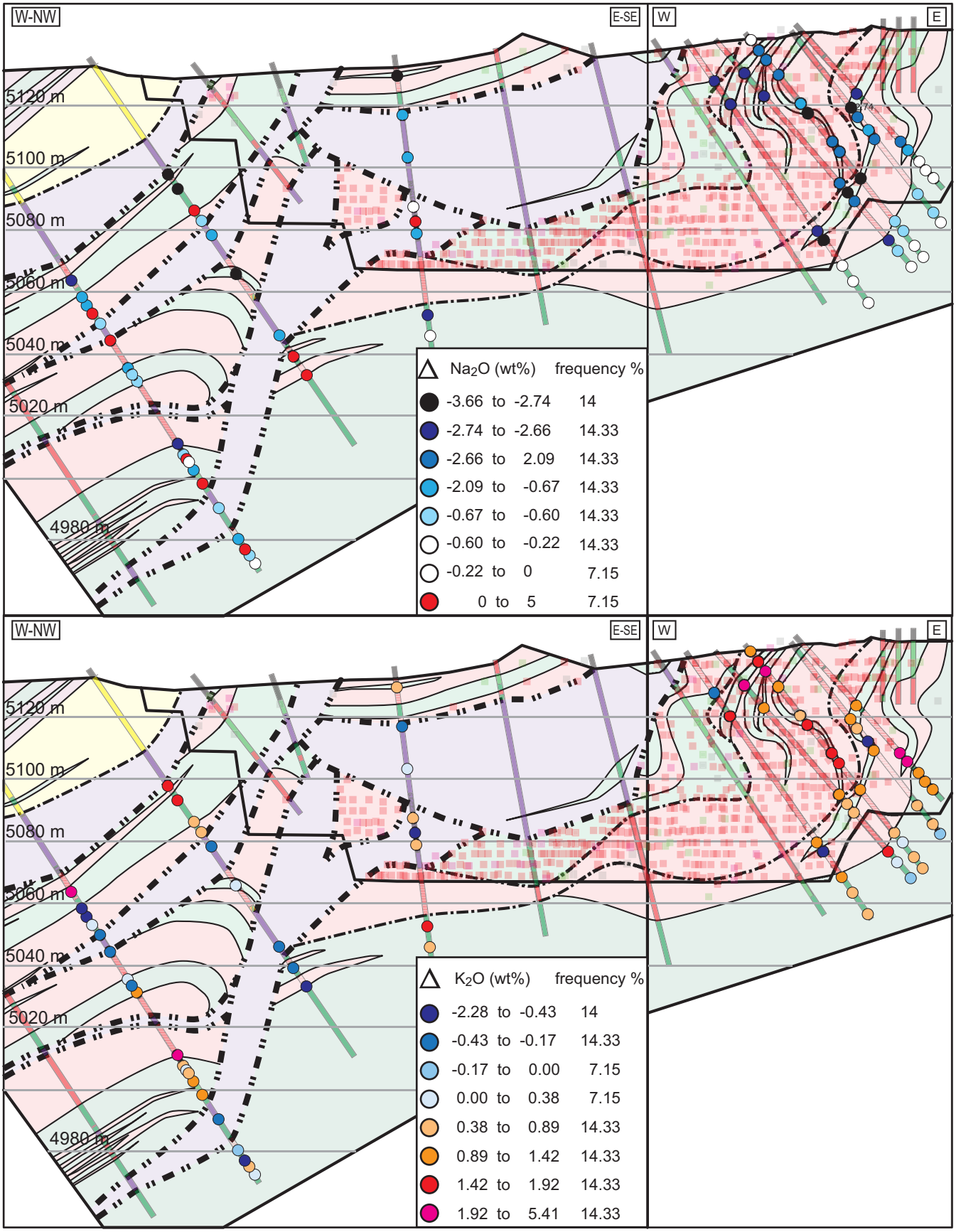

Figure 8. Calculated mass changes in Na_2O and K_2O in absolute weight percent (based on the method of MacLean and Barrett, 1993) of samples of drill section 6175

lithological (BIF) and structural traps (network of D_1 and D_2 fault zones) have clearly exerted a control on the location and geometry of the gold-rich ore at Meadowbank. Competence contrasts between BIF and volcaniclastic and ultramafic rocks contributed to strain localization and/or partitioning and fluid circulation in the highly reactive BIF, allowing gold to precipitate. Previous research (e.g. Armitage et al., 1996; Sherlock et al., 2004) has proposed that gold was introduced during the regional D_{P2} deformation at ca. 1.83 Ga. We propose that gold mineralization occurred prior to, or very early during D_{P2} based on the following reasoning: 1) the occurrence of transposed-boudinaged (remobilized) high-grade gold-quartz veins into the composite $S_{1\text{-}2}$ foliation (Fig. 4g) suggest that gold-quartz veins were introduced either during D_1 or early during D_2; 2) D_2 fault zones cut planar ore zones (D_1 faults) affected by composite $S_{1\text{-}2}$ fabric (Figs. 2c, 4b); 3) S_1-foliated magnetite layers (S_0) are replaced by pyrrhotite and are folded by mesoscopic F_2 folds (Fig. 4a); 4) at the pit-scale, gold is spatially associated with D_1 faults (Fig. 2), which are folded by both sets of F_2 folds (Fig. 2c,e); and 5) a preliminary Re-Os age of an auriferous arsenopyrite vein cutting the $S_{1\text{-}2}$-foliated chert-magnetite layering yielded an age of ca. 1899 Ma, which is contemporaneous with the older published age constraints for D_{P1} and D_{P2} (i.e. 1.91–1.83 Ga; Pehrsson et al., 2013; Fig. 4h).

IMPLICATIONS FOR EXPLORATION

Access to open-pit workings, new outcrops, exploration and delineation drilling, and mining data, coupled with in-depth geochemical characterization of the Meadowbank deposit host rocks provides new constraints on the lithostratigraphic setting and structure of the Meadowbank deposit. The bulk of the gold mineralization in the Meadowbank deposit is accompanied by pyrrhotite, grunerite, and minor chlorite, and hosted in strongly deformed BIF, within or adjacent to fault/shear zones. A significant amount of the gold also occurs in quartz veins in adjacent muscovite-altered volcaniclastic rocks, in association with disseminated pyrite, muscovite, and chlorite. Elevated P_2O_5, W, As, Cu, Pb, Ni, Co, and Te represent the hydrothermal footprint of the Meadowbank auriferous system. Contrary to other shear-zone-related gold deposits, there is no significant carbonate alteration at Meadowbank.

Hitherto undocumented fault zones (D_1 and D_2) represent important controls on the geometry of the gold at the ore-zone to deposit scales. Crosscutting relationships and preliminary Re-Os arsenopyrite ages suggest that gold mineralization occurred prior to the peak of D_{P2} deformation. We propose that D_{P1} fault zones played a major control on the actual ore distribution and probably the genesis of the deposit. Deposit- and regional-scale mapping, lithogeochemistry, and U-Pb zircon geochronology indicate that the Meadowbank BIF-hosted deposit is located at or very near the boundary between two petrographically and geochemically distinct rock packages (2711 Ma and 2717 Ma; Fig. 1; McNicoll et al (unpublished data)), which are separated by long-lived fault zones (D_{P1}) (or reactivated Archean structures?). Such an interpretation may explain why gold is confined to the central BIF (Figs. 1, 2). Identifying and following such early structures may constitute regional exploration vectors. Research results presented herein suggest that some of the gold mineralization processes are older than previously thought, which may have implications for exploration strategies in Archean sequences affected by younger Proterozoic deformation.

FUTURE WORK

On-going work at Meadowbank aims to 1) better constraining the relative and absolute timing of the ore-forming events and the geochemical and mineralogical signatures of the gold-bearing hydrothermal event(s); and 2) extrapolate the structural model for the Meadowbank deposit at the scale of the Woodburn Lake Group in order to identify and follow structures or favourable geological settings for gold mineralization.

ACKNOWLEDGEMENTS

This contribution emanates mainly from the Ph.D. thesis research of lead author (V. Janvier) at the Institut national de la recherche scientifique (INRS-ETE), as part of the Targeted Geoscience Initiative 4 (Lode Gold project) of Natural Resources Canada. We thank Agnico Eagle Mines Ltd for access to the property, to drill cores and various databases, and for chartered transport and accommodation during fieldwork. The staffs of the AEM Meadowbank and Exploration divisions are acknowledged for their time, full operational and scientific support and interest in this project. We thank Christopher Lawley for his constructive comments and suggestions.

REFERENCES

Armitage, A.E., James, R.S., and Goff, S.P., 1996. Gold mineralization in Archean banded iron formation, Third Portage Lake area, Northwest Territories, Canada; Exploration and Mining Geology, v. 5, p. 1–15.

Ashton, K.E., 1988. Precambrian geology of the southeastern Amer Lake area (66H/1), near Baker Lake, N.W.T.: a study of the Woodburn Lake Group, an Archean orthoquartzite-bearing sequence in the Churchill structural province; Ph.D. thesis, Queen's University, Kingston, Ontario, 335 p.

Berman, R.G., Sanborn-Barrie, M., Stern, R.A., and Carson, C.J., 2005. Tectonometamorphism at ca. 2.35 and 1.85 Ga in the Rae domain, western Churchill Province, Nunavut, Canada: insights from structural, metamorphic and in situ geochrono-

logical analysis of the southwestern Committee Bay Belt; The Canadian Mineralogist, v. 43, p. 409–442.

Berman, R.G., Davis, W.J., and Pehrsson, S., 2007. Collisional Snowbird tectonic zone resurrected: Growth of Laurentia during the 1.9 Ga accretionary phase of the Hudsonian orogeny; Geology, v. 35, p. 911–914.

Castonguay, S., Janvier, V., Mercier-Langevin, P., Dubé, B., McNicoll, V., Malo, M., Pehrsson, S., and Bécu, V., 2012. Recognizing optimum banded-iron formation-hosted gold environments in ancient, deformed and metamorphosed terranes: preliminary results from the Meadowbank deposit, Nunavut, *In:* Program with Abstracts; 40th Annual Yellowknife Geoscience Forum, Yellowknife, Northwest Territories.

Castonguay, S., Janvier, V., Mercier-Langevin, P., Dubé, B., McNicoll, V., Malo, M., Pehrsson, S., and Bécu, V., 2013. Recognizing optimum banded iron formation (BIF)-hosted gold environments: preliminary results from the Meadowbank deposit, *In:* Program with Abstracts 2013; Nunavut Mining Symposium, Iqaluit, Nunavut.

Davis, W.J. and Zaleski, E., 1998. Geochronological investigations of the Woodburn Lake group, western Churchill Province, Northwest Territories: preliminary results, *In:* Radiogenic Age and Isotopic Studies, Report 11; Geological Survey of Canada, Current Research no. 1998-F, p. 89–97

Dupuis, C., Mercier-Langevin, P., McNicoll, Janvier, V., Dubé, B., Castonguay, S., de Chavigny, B., Pehrsson, S., and Côté-Mantha, O., 2014. The Vault gold deposit, Meadowbank area, Nunavut: Preliminary results on the nature and timing of mineralization, *In:* Program with Abstracts; Geological Association of Canada – Mineralogical Association of Canada annual joint meeting, Fredericton, New Brunswick, v. 37, p. 81.

Gourcerol, B., Thurston, P.C., Kontak, D.J., and Côté-Mantha, O., 2014. Interpretations and implications of preliminary LA ICP-MS analysis of chert for the origin of geochemical signatures in banded iron-formations from the Meadowbank gold deposit, western Churchill Province, Nunavut; Geological Survey of Canada, Current Research 2014-1, 22 p.

Gourcerol, B., Thurston, P.C., Kontak, D.J., Côté-Mantha, O. and Biczok, J., 2015. Depositional setting of Algoma-type banded iron formation from the Meadowbank, Meliadine and Musselwhite gold deposits, *In:* Targeted Geoscience Initiative 4: Contributions to the understanding of Precambrian lode gold deposits and implications for exploration, (ed.) B. Dubé and P. Mercier-Langevin; Geological Survey of Canada, Open File 7852, p. 55–68.

Henderson, J.R., Henderson, M.N., Pryer, L.L., and Cresswell, R.G., 1991. Geology of the Whitehills-Tehek area, District of Keewatin: an Archean supracrustal belt with iron formation-hosted gold mineralization in the central Churchill Province, *In:* Current Research, Part C; Geological Survey of Canada, Paper 91-01C, p. 149–156.

Hoffman, P.F., 1989. Precambrian geology and tectonic history of North America In: The Geology of North America – An Overview: The Geology of North America, Part A; Geological Society of America, p. 447–512.

Hrabi, R.B., Barclay, W.A., Fleming, D., and Alexander, R.B., 2003. Structural evolution of the Woodburn Lake group in the area of the Meadowbank gold deposit, Nunavut; Geological Survey of Canada, Current Research 2003-C27, p. 10.

Ishikawa, Y., Sawaguchi, T., Iwaya, S., and Horiuchi, M., 1976. Delineation of prospecting targets for Kuroko deposits based on modes of volcanism of underlying dacite and alteration halos; Mining Geology, v. 26, p. 105–117 (in Japanese with English abstract).

Janvier, V., Castonguay, S., Mercier-Langevin, P., Dubé, B., McNicoll, V., Malo, M., Pehrsson, S.J., and Bécu, V., 2013. Recognizing optimum banded-iron formation-hosted gold environments in ancient, deformed and metamorphosed terranes: Preliminary results from the Meadowbank deposit, Nunavut, Canada; Geological Survey of Canada, Open File 7407. doi:10.4095/292589

Janvier, V., Castonguay, S., Mercier-Langevin, P., Dubé, B., McNicoll, V., Pehrsson, S., Malo, M., De Chavigny, B., and Côté-Mantha, O., 2015. Geology of the Portage deposit, Meadowbank gold mine, Churchill Province, Nunavut; Geological Survey of Canada, Current Research 2015-2, 18 p.

Jensen, L.S., 1976. A new cation plot for classifying subalcalic volcanic rocks; Ontario Division of Mines, Miscellaneous Paper 66, 21 p.

Large, R.R., Gemmell, J.B., Paulick, H., and Huston, D.L., 2001. The alteration box plot: A simple approach to understanding the relationship between alteration mineralogy and lithogeochemistry associated with volcanic-hosted massive sulfide deposits; Economic Geology, v. 96, p. 957–971.

MacLean, W.H. and Barrett, T.J., 1993. Lithogeochemical techniques using immobile elements; Journal of Geochemical Exploration, v. 48, p. 109–133.

Pehrsson, S.J., Wilkinson, L., and Zaleski, E., 2004. Geology of the Meadowbank gold deposit area, Nunavut: Geological Survey of Canada, Open File 4269, scale 1:20,000.

Pehrsson, S.J., Berman, R.G., and Davis, W.J., 2013. Paleoproterozoic orogenesis during Nuna aggregation: A case study of reworking of the Rae craton, Woodburn Lake, Nunavut; Precambrian Research, v. 232, p. 167–188.

Poulsen, K.H., Robert, F., and Dubé, B., 2000. Geological classification of Canadian gold deposits; Geological Survey of Canada, Bulletin 540, 106 p.

Sherlock, R.L., Alexander, R.B., March, R., Kellner, J., and Barclay, W.A., 2001a. Geological setting of the Meadowbank iron-formation-hosted gold deposits, Nunavut; Geological Survey of Canada, Current Research 2001-C11, 10 p.

Sherlock, R., Alexander, B., March, R., and Kellner, J., 2001b. Geologic setting of the Meadowbank iron formation hosted gold deposits; Geological Survey of Canada, Open file 3149, scale 1:10,000.

Sherlock, R., Pehrsson, S.J., Logan, A.V., Hrabi, R.B., and Davis, W.J., 2004. Geological Setting of the Meadowbank Gold Deposits, Woodburn Lake Group, Nunavut; Exploration and Mining Geology, v. 13, p. 67–107.

Skulski, T., Sandeman, H., Sanborn-Barrie, M., MacHattie, T., Young, M., Carson, C., Berman, R., Brown, N., Rayner, D., Pangapko, D., Byrne, D., and Deyell, C., 2003. Bedrock geology of the Ellice Hills map area and new constraints on the regional geology of the Committee Bay area, Nunavut; Geological Survey of Canada, Paper 2003-C22, 11 p.

Winchester, J.A. and Floyd, P.A., 1977. Geochemical discrimination of different magma series and their differentiation products using immobile elements; Chemical Geology, v. 20, p. 325–343.

Zaleski, E., Henderson, J.R., Corrigan, D., Jenner, G.A., Kjarsgaard, B.A., and Kerswill, J.A., 1997. Preliminary results of mapping and structural interpretation from the Woodburn project, western Churchill Province, Northwest Territories, *In:* 1996 Exploration Overview; Northwest Territories Geoscience Office, p. 3.43–3.44.

Zaleski, E., Duke, N., L'Heureux, R., and Wilkinson, L., 1999a. Geology, Woodburn Lake group, Amarulik Lake to Tehek Lake, Kivalliq Region, Nunavut; Geological Survey of Canada, Open File 3743, scale 1:50,000.

Zaleski, E., L'Heureux, R., Duke, N., and Wilkinson, L., 1999b. Komatiites and felsic volcanic rocks overlain by quartzite, Woodburn Lake group, Meadowbank River area, western

Churchill Province, Northwest Territories (Nunavut); Geological Survey of Canada, Current Research 1999-C, p. 9–18.

Zaleski, E., Davis, W.J., and Sandeman, H.A., 2001. Continental extension, mantle magmas and basement/ cover relationships, In: Extended Abstracts; Fourth International Archaean Symposium, Perth, Australia, p. 374–376.

Zaleski, E., Pehrsson, S., and Kerswill, J.A., 2003. Geology, Half Way Hills and Whitehills Lake area, Nunavut; Geological Survey of Canada, Map 1234A, scale 1:50,000.

GEOLOGICAL SURVEY OF CANADA
OPEN FILE 7852

Targeted Geoscience Initiative 4: Contributions to the Understanding of Precambrian Lode Gold Deposits and Implications for Exploration

A global database of gold deposits: quantification of multi-element ore signatures

Eric C. Grunsky[1], Benoît Dubé[2], Steffen Hagemann[3], and Carl W. Brauhart[3]

[1]Geological Survey of Canada, Ottawa, Ontario
[2]Geological Survey of Canada, Québec, Quebec
[3]University of Western Australia, Perth, West Australia, Australia

2015

This publication is available for free download through GEOSCAN (http://geoscan.nrcan.gc.ca/)

Recommended citation

Grunsky, E.C., Dubé, B., Hagemann, S., and Brauhart, C.W., 2015. A global database of gold deposits: quantification or multi-element ore signatures, *In:* Targeted Geoscience Initiative 4: Contributions to the Understanding of Precambrian Lode Gold Deposits and Implications for Exploration, (ed.) B. Dubé and P. Mercier-Langevin; Geological Survey of Canada, Open File 7852, p. 271–285.

Publications in this series have not been edited; they are released as submitted by the author.

Contribution to the Geological Survey of Canada's Targeted Geoscience Initiative 4 (TGI-4) Program (2010–2015)

TABLE OF CONTENTS

A global database of gold deposits: quantification of multi-element ore signatures

Eric C. Grunsky[1]*, Benoît Dubé[2], Steffen Hagemann[3], and Carl W. Brauhart[3]

[1]Geological Survey of Canada, 601 Booth Street, Ottawa, Ontario K1A 0E9
[2]Geological Survey of Canada, 490 rue de la Couronne, Québec, Quebec G1K 9A9
[3]Centre for Exploration Targeting, University of Western Australia, 35 Stirling Highway Crawley, Perth, Western Australia 6009, Australia
*Corresponding author's e-mail: Eric.Grunsky@NRCan-RNCan.gc.ca

ABSTRACT

A new approach to characterizing and classifying mineral deposits based on whole-rock geochemistry is currently being developed jointly by the mineral exploration industry, the University of Western Australia, and the Geological Survey of Canada.

Based on 24 elements (Fe, Co, Ni, Re, Pd, Pt, Cu, Ag, Au, Zn, Cd, In, Tl, Pb, Hg, As, Sb, Bi, Te, Mo, W, Sn, La, U), a centred log-ratio transformation is used for representative samples of mineral deposits. Success of this approach requires the use of rigorous analytical protocols that have also been established for this project.

A component of this project is focused on the development of a statistical classification approach to cataloguing ore deposit styles. Research done to date, shows that this methodology has successfully identified a wide range of mineral deposit types including porphyry, lode gold, PGE, skarn, sedimentary rock-hosted massive sulphides, volcanic-hosted massive sulphides and Mississippi-type lead-zinc deposits. This contribution focuses solely on gold deposits.

Geochemical data of unknown metallogenic affinities can be classified and existing classifications can be enhanced/re-defined. The results indicate that trends and differences of a spectrum of gold deposits can be successfully classified using statistical methodologies and metrics for expressing ore chemistry. In conjunction with geological knowledge, this database and associated methodologies will enhance the recognition and classification of a range of lode gold deposit types and could be useful in both greenfields and brownfields exploration programs.

INTRODUCTION

Ore Samples Normalized to Average Crustal Abundance (OSNACA) is part of a broad initiative to characterize ore deposit signatures in a unique way such that geochemical similarities and differences between mineral deposit types can be quantified and classified. The OSNACA international project is a new approach jointly developed by the mineral exploration industry, the Centre for Exploration Targeting, University of Western Australia, and the TGI-4 Lode Gold project to characterize and classify ore samples from various mineral deposit types based on whole rock geochemistry. A technique (Brauhart et al., 2015) has been developed that quantifies differences in multi-element signatures or ore-deposit chemistry and defines a "magmato-hydrothermal space". Twenty-four elements define the mathematical space where an ore geochemical signature is defined by its "enrichment vector". Every sample must be analysed for every element used in the calculations. The database that comprises these ore samples is part of a larger database being assembled and defined by the OSNACA project (Brauhart et al., 2015) Research is being conducted on the development of a suitable metric to study ore-deposit chemistry.

Numerous workers have suggested a continuum between different ore-deposit classes such as Mississippi Valley type (MVT) and sedimentary-hosted massive sulphide (SHMS) (e.g. Leach et al., 2005), volcanic-hosted massive sulphide (VHMS) and epithermal (e.g. Hannington et al., 1999), porphyry and high-sulphidation epithermal (Sillitoe, 1989), orogenic Au, Carlin Au, and epithermal (Nesbitt, 1988), and even a link between iron oxide-copper-gold (IOCG) deposits and mantle-related mineralization (Groves et al., 2010). The integration of the deposits into a metric space has been termed the "Magmato-Hydrothermal Space". The latter is presented as a new means to document and quantitatively describe both the range and statistical uniqueness of ore-deposit types and clans.

Grunsky, E.C., Dubé, B., Hagemann, S., and Brauhart, C.W., 2015. A global database of gold deposits: quantification or multi-element ore signatures, *In:* Targeted Geoscience Initiative 4: Contributions to the Understanding of Precambrian Lode Gold Deposits and Implications for Exploration, (ed.) B. Dubé and P. Mercier-Langevin; Geological Survey of Canada, Open File 7852, p. 271–285.

Although the broader goals of the OSNACA project are to incorporate all deposit types into a geochemical metric, this report is limited to four main types of gold deposits: Carlin (Car), epithermal, high-sulphidation epithermal (HSEpi), low-sulphidation epithermal (LSEpi), and orogenic greenstone-hosted (OGs) (Table 1). The OSNACA database also contains seven gold deposits that are "intrusion-related". This population was considered too small to be considered for a statistical evaluation of gold deposits and these data were not included in this study. Two methodologies described for the OSNACA project include (1) examining the ratios of ore-deposit chemistry against average crustal abundance; and (2) centred log-ratio transformations (Aitchison, 1986). This study examines the centred log-ratio (clr) metric for characterization and classification of gold deposits. Geochemical data are compositional in nature and thus to identify patterns and features of the data that are not related to the data closure problem, a centred log-ratio transform was employed (Aitchison, 1986). Data discovery methods, including principal component analysis (PCA) and multi-dimensional scaling (MDS), were applied to the transformed data to assist in characterizing the different deposit types. Finally, a classification methodology (linear discriminant analysis; LDA) was applied to test the uniqueness of the established deposit classifications.

The results presented here represent a global collection of gold deposit samples, which includes many samples from Canada as part of the Targeted Geoscience Initiative 4 (TGI-4) Lode Gold Project. The samples contributed to the project are listed in Table 1.

Analytical Methods

Ore deposit samples were obtained from world-wide sources according to the following prerequisites.

- Ore samples must be from a substantial body of mineralization that could be mined profitably through modern mining techniques;
- Samples must be devoid of weathering effects;
- Samples must be from different parts of the ore deposit, with "run of the mill" samples preferred to obscure and unusual samples of the deposit;
- A minimum of 500 g of sample is recommended, but samples as small as 200 g were also analyzed; and
- The ore deposit is located by longitude and latitude [datum: WGS84] coordinates.

Samples were prepared on a diamond saw to produce a reference sample and an assay subsample of (ideally) more than 250 g. Samples were cut across layering or any dominant vein direction so that the assay sample and reference sample are as similar as possible. The entire assay sample was crushed at Bureau-Veritas – Ultratrace in a steel jaw crusher and then milled in a tungsten-carbide mill with a barren quartz wash between each sample. Four analytical techniques were performed:

1. 50 g Pb-collection fire assay with ICP-MS finish;
2. 20 g aqua regia digest with ICP-MS finish;
3. 0.15 g "four-acid" digest with ICP-MS and ICP-OES finish; and
4. 0.25 g peroxide fusion digest with ICP-MS and ICP-OES finish.

The first three analytical techniques are tailored to the 24 elements used in this paper, but we recognize that the OSNACA database has many different potential uses and therefore it is desirable to also capture all of the major elements and a wide suite of trace elements. The analytical techniques listed above are ideal for analysing for many of these additional elements, but not all. For example, major elements would better be analyzed by XRF but the extra cost is not warranted for the entire OSNACA collection.

Samples were submitted in batches of 48 with an additional blank sample and assay standard. All data is available at http://www.cet.edu.au/OSNACA.

The amount of publicly available geochemical data for ore deposits is extensive, but analytical techniques, detection limits, and above all, assay suites, vary widely. The subset of publically available datasets containing analyses for all 24 ore and pathfinder elements used here, with appropriate detection limits, is extremely limited. In response to this gap in available data, researchers at the Centre for Exploration Targeting at the University of Western Australia created the OSNACA database, a publicly available online resource providing consistent high-quality data of ore-deposit samples from around the world (OSNACA, 2013).

RESULTS AND DATA ANALYSIS

The results presented here represent a global collection of 178 gold deposit samples from a total of 431 analyses that currently comprise the OSNACA database. The TGI-4 Lode Gold Project provided 18 samples, mainly from Canadian orogenic gold deposits (see Table 1).

In the application of statistical methods requiring estimates of the mean and other moments, sample populations with censored data (data reported at less than the lower limit of detection) are biased. This is due values of less than the lower limit of detection are all reported only as that value. In order to minimize this bias, a replacement methodology (EM algorithm), which has documented by Palarea-Albaladejo et al. (2008), was used to find suitable replacement values.

Table 1. Listing of the gold deposit chemistry used in this study. Geochemical data available from the Ore Samples Normalized to Average Crustal Abundance (OSNACA) website (http://www.cet.edu.au/OSNACA).

Sample	Deposit Name	CharCode	Country	State	Class	SubClass	WClass	Longitude	Latitude
700077	Betze-Post	BZP	USA	Nevada	Carlin Au	Carlin Au	Car	-116.376037	40.980021
700078	Betze-Post	BZP	USA	Nevada	Carlin Au	Carlin Au	Car	-116.376037	40.980021
700079	Gold Quarry	GQY	USA	Nevada	Carlin Au	Carlin Au	Car	-116.215976	40.782255
700080	Gold Quarry	GQY	USA	Nevada	Carlin Au	Carlin Au	Car	-116.215976	40.782255
700081	Rain	RAI	USA	Nevada	Carlin Au	Carlin Au	Car	-116.011442	40.613802
700107	Gold Quarry	GQY	USA	Nevada	Carlin Au	Carlin Au	Car	-116.215976	40.782255
700108	Gold Quarry	GQY	USA	Nevada	Carlin Au	Carlin Au	Car	-116.215976	40.782255
700109	Rain	RAI	USA	Nevada	Carlin Au	Carlin Au	Car	-116.011442	40.613802
700110	Rain	RAI	USA	Nevada	Carlin Au	Carlin Au	Car	-116.011442	40.613802
700111	Betze-Post	BZP	USA	Nevada	Carlin Au	Carlin Au	Car	-116.376037	40.980021
700112	Betze-Post	BZP	USA	Nevada	Carlin Au	Carlin Au	Car	-116.376037	40.980021
700138	Mount Olympus	MTO	Australia	WA	Carlin Au	Carlin Au	Car	117.900151	-23.432301
700139	Mount Olympus	MTO	Australia	WA	Carlin Au	Carlin Au	Car	117.900151	-23.432301
700140	Mount Olympus	MTO	Australia	WA	Carlin Au	Carlin Au	Car	117.900151	-23.432301
700141	Mount Olympus	MTO	Australia	WA	Carlin Au	Carlin Au	Car	117.900151	-23.432301
700142	Mount Olympus	MTO	Australia	WA	Carlin Au	Carlin Au	Car	117.900151	-23.432301
700143	Mount Olympus	MTO	Australia	WA	Carlin Au	Carlin Au	Car	117.900151	-23.432301
700144	Mount Olympus Peake	MTO	Australia	WA	Carlin Au	Carlin Au	Car	117.873183	-23.43358
700244	Florida Canyon	FLC	USA	Nevada	Carlin Au	Carlin Au	Car	-118.242	40.574
700245	Florida Canyon	FLC	USA	Nevada	Carlin Au	Carlin Au	Car	-118.242	40.574
700246	Twin Creeks	TWC	USA	Nevada	Carlin Au	Carlin Au	Car	-117.172802	41.245
700247	Gold Quarry	GQY	USA	Nevada	Carlin Au	Carlin Au	Car	-116.216	40.7823
700248	Gold Quarry	GQY	USA	Nevada	Carlin Au	Carlin Au	Car	-116.216	40.7823
700251	Gold Quarry	GQY	USA	Nevada	Carlin Au	Carlin Au	Car	-116.216	40.7823
700252	Betze-Post	BZP	USA	Nevada	Carlin Au	Carlin Au	Car	-116.376037	40.980021
700253	Betze-Post	BZP	USA	Nevada	Carlin Au	Carlin Au	Car	-116.376037	40.980021
700046	Equity	EQU	USA	Colorado	Epithermal	Low-Sulphidation Epithermal	LSEpi	-106.959618	37.939382
700047	Equity	EQU	USA	Colorado	Epithermal	Low-Sulphidation Epithermal	LSEpi	-106.959618	37.939382
700294	Lake Cowal	LCW	Australia	NSW	Epithermal	Low-Sulphidation Epithermal	LSEpi	147.404323	-33.639494
700295	Lake Cowal	LCW	Australia	NSW	Epithermal	Low-Sulphidation Epithermal	LSEpi	147.404168	-33.639397
700296	Lake Cowal	LCW	Australia	NSW	Epithermal	Low-Sulphidation Epithermal	LSEpi	147.404034	-33.639324
700297	Lake Cowal	LCW	Australia	NSW	Epithermal	Low-Sulphidation Epithermal	LSEpi	147.405683	-33.637445
700298	Lake Cowal	LCW	Australia	NSW	Epithermal	Low-Sulphidation Epithermal	LSEpi	147.405741	-33.637816
700357	Lake Cowal	LCW	Australia	NSW	Epithermal	Low-Sulphidation Epithermal	LSEpi	147.404544	-33.635096
700358	Lake Cowal	LCW	Australia	NSW	Epithermal	Low-Sulphidation Epithermal	LSEpi	147.404781	-33.635956
700359	Lake Cowal	LCW	Australia	NSW	Epithermal	Low-Sulphidation Epithermal	LSEpi	147.404802	-33.635052
700360	Lake Cowal	LCW	Australia	NSW	Epithermal	Low-Sulphidation Epithermal	LSEpi	147.404762	-33.635162
700361	Lake Cowal	LCW	Australia	NSW	Epithermal	Low-Sulphidation Epithermal	LSEpi	147.406022	-33.634852
700362	Lake Cowal	LCW	Australia	NSW	Epithermal	Low-Sulphidation Epithermal	LSEpi	147.406252	-33.634843
700363	Lake Cowal	LCW	Australia	NSW	Epithermal	Low-Sulphidation Epithermal	LSEpi	147.405539	-33.639371
700181	Lake Cowal	LCW	Australia	NSW	Epithermal	Low-Sulphidation Epithermal	LSEpi	147.408087	-33.638148
700182	Lake Cowal	LCW	Australia	NSW	Epithermal	Low-Sulphidation Epithermal	LSEpi	147.405551	-33.637239
700183	Lake Cowal	LCW	Australia	NSW	Epithermal	Low-Sulphidation Epithermal	LSEpi	147.405482	-33.637487
700184	Lake Cowal	LCW	Australia	NSW	Epithermal	Low-Sulphidation Epithermal	LSEpi	147.407125	-33.636367

Table 1 continued.

Sample	Deposit Name	CharCode	Country	State	Class	SubClass	WClass	Longitude	Latitude
700185	Lake Cowal	LCW	Australia	NSW	Epithermal	Low-Sulphidation Epithermal	LSEpi	147.407158	-33.636391
700186	Lake Cowal	LCW	Australia	NSW	Epithermal	Low-Sulphidation Epithermal	LSEpi	147.407137	-33.63636
700187	Lake Cowal	LCW	Australia	NSW	Epithermal	Low-Sulphidation Epithermal	LSEpi	147.40721	-33.636532
700188	Lake Cowal	LCW	Australia	NSW	Epithermal	Low-Sulphidation Epithermal	LSEpi	147.407241	-33.63657
700189	Lake Cowal	LCW	Australia	NSW	Epithermal	Low-Sulphidation Epithermal	LSEpi	147.407156	-33.63646
700163	Hishikari	HIS	Japan	Kagoshima	Epithermal	Epithermal Low-Sulphidation	HSEpi	130.696207	32.013132
700164	Hishikari	HIS	Japan	Kagoshima	Epithermal	Epithermal Low-Sulphidation	HSEpi	130.696207	32.013132
700059	Akeshi	AKH	Japan	Kagoshima	Epithermal	High-Sulphidation Epithermal	HSEpi	130.380279	31.309986
700060	Akeshi	AKH	Japan	Kagoshima	Epithermal	High-Sulphidation Epithermal	HSEpi	130.380279	31.309986
700061	Kasuga	KAS	Japan	Kagoshima	Epithermal	High-Sulphidation Epithermal	HSEpi	130.256945	31.270014
700062	Kasuga	KAS	Japan	Kagoshima	Epithermal	High-Sulphidation Epithermal	HSEpi	130.256945	31.270014
700063	Kasuga	KAS	Japan	Kagoshima	Epithermal	High-Sulphidation Epithermal	HSEpi	130.256945	31.270014
700064	Castle Mountain	CAM	USA	California	Epithermal	High-Sulphidation Epithermal	HSEpi	-115.100184	35.284472
700065	Castle Mountain	CAM	USA	California	Epithermal	High-Sulphidation Epithermal	HSEpi	-115.100184	35.284472
700066	Ohakuri	OHA	New Zealand	Waikato	Epithermal	High-Sulphidation Epithermal	HSEpi	176.086035	-38.404594
700067	Ohakuri	OHA	New Zealand	Waikato	Epithermal	High-Sulphidation Epithermal	HSEpi	176.086035	-38.404594
700068	Ohakuri	OHA	New Zealand	Waikato	Epithermal	High-Sulphidation Epithermal	HSEpi	176.086035	-38.404594
700069	Martha	MAR	New Zealand	Waikato	Epithermal	High-Sulphidation Epithermal	HSEpi	175.842267	-37.386383
700070	Martha	MAR	New Zealand	Waikato	Epithermal	High-Sulphidation Epithermal	HSEpi	175.842267	-37.386383
700441	Chelopech	CLP	Bulgaria		Epithermal	High-Sulphidation Epithermal	HSEpi	24.073247	42.695752
700462	Chesney	CSY	Australia	NSW	Epithermal	High-Sulphidation Epithermal	HSEpi	145.85	-31.52
700463	Chesney	CSY	Australia	NSW	Epithermal	High-Sulphidation Epithermal	HSEpi	145.85	-31.52
700464	Chesney	CSY	Australia	NSW	Epithermal	High-Sulphidation Epithermal	HSEpi	145.85	-31.52
700087	Brewer	BRW	USA	Alaska	Epithermal	High-Sulphidation Epithermal	HSEpi	-80.417197	34.653015
700093	Haile	HAI	USA	South Carolina	Epithermal	High-Sulphidation Epithermal	HSEpi	-80.533613	34.580796
700094	Haile	HAI	USA	South Carolina	Epithermal	High-Sulphidation Epithermal	HSEpi	-80.533613	34.580796
700442	Rosia Montana	RSM	Romania		Epithermal	High-Sulphidation Epithermal	HSEpi	23.122895	46.298785
700443	Rosia Montana	RSM	Romania		Epithermal	High-Sulphidation Epithermal	HSEpi	23.122895	46.298785
700090	Fort Knox	FTK	USA	Alaska	Orogenic - Intrusion-Related Au	High-Sulphidation Epithermal	IR	-147.360601	64.992228
700091	Fort Knox	FTK	USA	Alaska	Orogenic - Intrusion-Related Au	Intrusion-Related Au	IR	-147.360601	64.992228
700092	Fort Knox	FTK	USA	Alaska	Orogenic - Intrusion-Related Au	Intrusion-Related Au	IR	-147.360601	64.992228
700397	Boddington	BOD	Australia	WA	Intrusion-Related	Intrusion-Related	IR	116.349488	-32.747333
700513	Westwood-Warrenmac	WWW	Canada	Quebec	Intrusion-Related	Intrusion-Related and VMS	IR	-78.502908	48.256229
700494	Canadian Malartic	CMA	Canada	Quebec	Intrusion-Related/Orogenic Au	Intrusion-Related/Orogenic Au	OGs	-78.135621	48.135039
700495	Canadian Malartic	CMA	Canada	Quebec	Intrusion-Related/Orogenic Au	Intrusion-Related/Orogenic Au	OGs	-78.135621	48.135039
700048	Co-O	COO	Phillippines	Mindano	Epithermal	Low-Sulphidation Epithermal	LSEpi	126.02829	8.241732
700051	Co-O	COO	Phillippines	Mindano	Epithermal	Low-Sulphidation Epithermal	LSEpi	126.02829	8.241732
700052	Co-O	COO	Phillippines	Mindano	Epithermal	Low-Sulphidation Epithermal	LSEpi	126.02829	8.241732
700053	Hishikari	HIS	Japan	Kagoshima	Epithermal	Low-Sulphidation Epithermal	LSEpi	130.696207	32.013132
700054	Hishikari	HIS	Japan	Kagoshima	Epithermal	Low-Sulphidation Epithermal	LSEpi	130.696207	32.013132
700055	Hishikari	HIS	Japan	Kagoshima	Epithermal	Low-Sulphidation Epithermal	LSEpi	130.696207	32.013132
700056	Creede	CRE	USA	Colorado	Epithermal	Low-Sulphidation Epithermal	LSEpi	-106.927191	37.868586
700057	Creede	CRE	USA	Colorado	Epithermal	Low-Sulphidation Epithermal	LSEpi	-106.927191	37.868586
700058	Creede	CRE	USA	Colorado	Epithermal	Low-Sulphidation Epithermal	LSEpi	-106.927191	37.868586
700151	Pajingo	PAJ	Australia	QLD	Epithermal	Low-Sulphidation Epithermal	LSEpi	146.450347	-20.526569

Table 1 continued.

Sample	Deposit Name	CharCode	Country	State	Class	SubClass	WClass	Longitude	Latitude
700207	Big Bell	BBL	Australia	WA	Orogenic Au	Orogenic Au	IR	117.6544	-27.3212
700208	Big Bell	BBL	Australia	WA	Orogenic Au	Orogenic Au	IR	117.6544	-27.3212
700082	Ridgeway	RID	Australia	NSW	Orogenic Au	Orogenic Au	OGs	148.976738	-33.436361
700083	Ridgeway	RID	Australia	NSW	Orogenic Au	Orogenic Au	OGs	148.976738	-33.436361
700084	Ridgeway	RID	Australia	NSW	Orogenic Au	Orogenic Au	OGs	148.976738	-33.436361
700085	Silver King	SIL	USA	Arizona	Orogenic Au	Orogenic Au	OGs	-111.08933	33.330743
700086	Kensington	KEN	USA	Alaska	Orogenic Au	Orogenic Au	OGs	-135.061958	58.846117
700088	Stawell	STW	Australia	VIC	Orogenic Au	Orogenic Au	OGs	142.780037	-37.054903
700089	Stawell	STW	Australia	VIC	Orogenic Au	Orogenic Au	OGs	142.780037	-37.054903
700101	Eersteling	EER	South Africa	Limpopo	Orogenic Au	Orogenic Au	OGs	29.271313	-24.121195
700102	Eersteling	EER	South Africa	Limpopo	Orogenic Au	Orogenic Au	OGs	29.271313	-24.121195
700103	Maybell	MAY	Australia	WA	Orogenic Au	Orogenic Au	OGs	121.793098	-32.370098
700104	Maybell	MAY	Australia	WA	Orogenic Au	Orogenic Au	OGs	121.793098	-32.370098
700105	Wallaby	WAL	Australia	WA	Orogenic Au	Orogenic Au	OGs	122.307714	-28.851087
700106	Wallaby	WAL	Australia	WA	Orogenic Au	Orogenic Au	OGs	122.307714	-28.851087
700113	Murchison	MUR	South Africa	Limpopo	Orogenic Au	Orogenic Au	OGs	30.686216	-23.89998
700114	Astoria	AST	Canada	Quebec	Orogenic Au	Orogenic Au	OGs	-79.025522	48.179638
700115	Crixas	CRX	Brazil	Goias	Orogenic Au	Orogenic Au	OGs	-49.964828	-14.573218
700116	Crixas	CRX	Brazil	Goias	Orogenic Au	Orogenic Au	OGs	-49.964828	-14.573218
700117	Crixas	CRX	Brazil	Goias	Orogenic Au	Orogenic Au	OGs	-49.964828	-14.573218
700118	Renco	REN	Zimbabwe	Masvingo	Orogenic Au	Orogenic Au	OGs	31.167202	-20.625731
700119	Renco	REN	Zimbabwe	Masvingo	Orogenic Au	Orogenic Au	OGs	31.167202	-20.625731
700120	Luziania	LUZ	Brazil	Goias	Orogenic Au	Orogenic Au	OGs	-48.008587	-16.233755
700121	Luziania	LUZ	Brazil	Goias	Orogenic Au	Orogenic Au	OGs	-48.008587	-16.233755
700162	Telfer	TEL	Australia	WA	Orogenic Au	Orogenic Au	OGs	122.209869	-21.721615
700190	Paddington	PDT	Australia	WA	Orogenic Au	Orogenic Au	OGs	121.3445	-30.4898
700191	Paddington	PDT	Australia	WA	Orogenic Au	Orogenic Au	OGs	121.3445	-30.4898
700192	Golden Mile	GMK	Australia	WA	Orogenic Au	Orogenic Au	OGs	121.503695	-30.77755
700193	Darlot	DLT	Australia	WA	Orogenic Au	Orogenic Au	OGs	121.269999	-27.889861
700194	Darlot	DLT	Australia	WA	Orogenic Au	Orogenic Au	OGs	121.269999	-27.889861
700195	Westonia	WTN	Australia	WA	Orogenic Au	Orogenic Au	OGs	118.698996	-31.290779
700196	Chalice	CHL	Australia	WA	Orogenic Au	Orogenic Au	OGs	121.5155	-31.8168
700197	Griffins Find	GFA	Australia	WA	Orogenic Au	Orogenic Au	OGs	118.3189	-33.0694
700198	Chalice	CHL	Australia	WA	Orogenic Au	Orogenic Au	OGs	121.5155	-31.8168
700201	Griffins Find	GFA	Australia	WA	Orogenic Au	Orogenic Au	OGs	118.3189	-33.0694
700202	Wiluna	WIL	Australia	WA	Orogenic Au	Orogenic Au	OGs	120.2386	-26.6219
700203	Wiluna	WIL	Australia	WA	Orogenic Au	Orogenic Au	OGs	120.2386	-26.6219
700204	Wiluna	WIL	Australia	WA	Orogenic Au	Orogenic Au	OGs	120.2386	-26.6219
700205	Warronga - Agnew	WGA	Australia	WA	Orogenic Au	Orogenic Au	OGs	120.5052	-28.0061
700206	Warronga - Agnew	WGA	Australia	WA	Orogenic Au	Orogenic Au	OGs	120.5052	-28.0061
700209	Hill 50	H50	Australia	WA	Orogenic Au	Orogenic Au	OGs	117.8087	-28.0429
700210	Hill 50	H50	Australia	WA	Orogenic Au	Orogenic Au	OGs	117.8087	-28.0429
700211	Lawlers	NWH	Australia	WA	Orogenic Au	Orogenic Au	OGs	120.5401	-28.0795
700212	Lawlers	NWH	Australia	WA	Orogenic Au	Orogenic Au	OGs	120.5401	-28.0795
700213	Transvaal	TVL	Australia	WA	Orogenic Au	Orogenic Au	OGs	119.3205	-31.2698

Table 1 continued.

Sample	Deposit Name	CharCode	Country	State	Class	SubClass	WClass	Longitude	Latitude
700214	Redeemer	RDM	Australia	WA	Orogenic Au	Orogenic Au	OGs	120.4833	-28.0658
700215	Macraes	MCR	New Zealand	Otago	Orogenic Au	Orogenic Au	OGs	170.4573	-45.3763
700216	Harbour lights	HBL	Australia	WA	Orogenic Au	Orogenic Au	OGs	121.3224	-28.8754
700217	Harbour lights	HBL	Australia	WA	Orogenic Au	Orogenic Au	OGs	121.3224	-28.8754
700218	Sunrise Dam	SNR	Australia	WA	Orogenic Au	Orogenic Au	OGs	122.416	-29.0808
700219	Sunrise Dam	SNR	Australia	WA	Orogenic Au	Orogenic Au	OGs	122.416	-29.0808
700220	Lindsays	LND	Australia	WA	Orogenic Au	Orogenic Au	OGs	121.1717	-30.943
700221	Three Mile Hill	3MH	Australia	WA	Orogenic Au	Orogenic Au	OGs	121.1982	-30.9264
700222	Three Mile Hill	3MH	Australia	WA	Orogenic Au	Orogenic Au	OGs	121.1982	-30.9264
700223	Three Mile Hill	3MH	Australia	WA	Orogenic Au	Orogenic Au	OGs	121.1982	-30.9264
700224	Porphyry	PRY	Australia	WA	Orogenic Au	Orogenic Au	OGs	122.2856	-29.7807
700225	Porphyry	PRY	Australia	WA	Orogenic Au	Orogenic Au	OGs	122.2856	-29.7807
700226	Jupiter	JUP	Australia	WA	Orogenic Au	Orogenic Au	OGs	122.2186	-28.8077
700227	Jupiter	JUP	Australia	WA	Orogenic Au	Orogenic Au	OGs	122.2186	-28.8077
700228	Mount Wilkinson	MWK	Australia	WA	Orogenic Au	Orogenic Au	OGs	120.2154	-26.7576
700229	Mount Wilkinson	MWK	Australia	WA	Orogenic Au	Orogenic Au	OGs	120.2154	-26.7576
700230	Golden Mile	GMK	Australia	WA	Orogenic Au	Orogenic Au	OGs	121.503695	-30.77755
700231	Golden Mile	GMK	Australia	WA	Orogenic Au	Orogenic Au	OGs	121.503695	-30.77755
700239	Karonie	KNE	Australia	WA	Orogenic Au	Orogenic Au	OGs	122.5611	-31.0346
700240	Karonie	KNE	Australia	WA	Orogenic Au	Orogenic Au	OGs	122.5611	-31.0346
700241	Karonie	KNE	Australia	WA	Orogenic Au	Orogenic Au	OGs	122.5611	-31.0346
700242	Nathans Labouchere	NLB	Australia	WA	Orogenic Au	Orogenic Au	OGs	118.31	-25.3199
700243	Micky Doolan Meekatharra	MDM	Australia	WA	Orogenic Au	Orogenic Au	OGs	118.5025	-26.6184
700254	Sheba	SHB	South Africa	Mpumalanga	Orogenic Au	Orogenic Au	OGs	31.076549	-25.733161
700263	Mount Morgans	MMG	Australia	WA	Orogenic Au	Orogenic Au	OGs	122.06944	-28.771032
700264	Golden Mile	GMK	Australia	WA	Orogenic Au	Orogenic Au	OGs	121.503695	-30.77755
700265	Golden Mile	GMK	Australia	WA	Orogenic Au	Orogenic Au	OGs	121.503695	-30.77755
700266	Golden Mile	GMK	Australia	WA	Orogenic Au	Orogenic Au	OGs	121.503695	-30.77755
700267	Kanowna Belle	KBL	Australia	WA	Orogenic Au	Orogenic Au	OGs	121.5765	-30.6112
700268	Hunt	HNT	Australia	WA	Orogenic Au	Orogenic Au	OGs	121.6802	-31.2185
700269	Marvel Loch	MVL	Australia	WA	Orogenic Au	Orogenic Au	OGs	119.4969	-31.4693
700270	Meekatharra Prohibition	MKP	Australia	WA	Orogenic Au	Orogenic Au	OGs	118.5051	-26.6047
700271	Randalls	RDL	Australia	WA	Orogenic Au	Orogenic Au	OGs	122.1993	-31.0814
700272	Randalls	RDL	Australia	WA	Orogenic Au	Orogenic Au	OGs	122.1993	-31.0814
700273	Junction	JCT	Australia	WA	Orogenic Au	Orogenic Au	OGs	121.8383	-31.4576
700274	Griffins Find	GFA	Australia	WA	Orogenic Au	Orogenic Au	OGs	118.3189	-33.0694
700275	Hunt	HNT	Australia	WA	Orogenic Au	Orogenic Au	OGs	121.6802	-31.2185
700276	Granny Smith	GSM	Australia	WA	Orogenic Au	Orogenic Au	OGs	122.4223	-28.8127
700285	Lancefield	LFD	Australia	WA	Orogenic Au	Orogenic Au	OGs	122.3813	-28.548
700286	Lancefield	LFD	Australia	WA	Orogenic Au	Orogenic Au	OGs	122.3813	-28.548
700287	Copperfield	CFD	Australia	WA	Orogenic Au	Orogenic Au	OGs	120.4658	-29.0979
700288	Hunt	HNT	Australia	WA	Orogenic Au	Orogenic Au	OGs	121.6802	-31.2185
700289	WIluna	WIL	Australia	WA	Orogenic Au	Orogenic Au	OGs	120.2386	-26.6219
700290	Youanmi	YOU	Australia	WA	Orogenic Au	Orogenic Au	OGs	119.3119	-27.9898
700383	Golden Kilometre	GKM	Australia	WA	Orogenic Au	Orogenic Au	OGs	121.236397	-30.519227

Table 1 continued.

Sample	Deposit Name	CharCode	Country	State	Class	SubClass	WClass	Longitude	Latitude
700384	Ora Banda	OBA	Australia	WA	Orogenic Au	Orogenic Au	OGs	121.064859	-30.38315
700385	Mount Charlotte	MCT	Australia	WA	Orogenic Au	Orogenic Au	OGs	121.480993	-30.746367
700386	Mount Charlotte	MCT	Australia	WA	Orogenic Au	Orogenic Au	OGs	121.480993	-30.746367
700387	Mount Charlotte	MCT	Australia	WA	Orogenic Au	Orogenic Au	OGs	121.480993	-30.746367
700388	Kanowna Belle	KBL	Australia	WA	Orogenic Au	Orogenic Au	OGs	121.576513	-30.611192
700389	Kanowna Belle	KBL	Australia	WA	Orogenic Au	Orogenic Au	OGs	121.576513	-30.611192
700390	Chalice	CHL	Australia	WA	Orogenic Au	Orogenic Au	OGs	121.515495	-31.816816
700391	Chalice	CHL	Australia	WA	Orogenic Au	Orogenic Au	OGs	121.515495	-31.816816
700392	Copperhead	CHD	Australia	WA	Orogenic Au	Orogenic Au	OGs	119.124928	-30.976901
700393	Copperhead	CHD	Australia	WA	Orogenic Au	Orogenic Au	OGs	119.124928	-30.976901
700394	Frasers	FRA	Australia	WA	Orogenic Au	Orogenic Au	OGs	119.331119	-31.239256
700395	Harlequin	HLQ	Australia	WA	Orogenic Au	Orogenic Au	OGs	121.794567	-32.114448
700396	Kings Cross	KCX	Australia	WA	Orogenic Au	Orogenic Au	OGs	121.181542	-30.952687
700398	Nevoria	NEV	Australia	WA	Orogenic Au	Orogenic Au	OGs	119.585022	-31.507187
700401	Victory	VTY	Australia	WA	Orogenic Au	Orogenic Au	OGs	121.771659	-31.323771
700402	Sons of Gwalia	SOG	Australia	WA	Orogenic Au	Orogenic Au	OGs	121.333425	-28.918846
700404	Redeemer	RDM	Australia	WA	Orogenic Au	Orogenic Au	OGs	120.48372	-28.063396
700405	Ballarat Last Chance WA	BLX	Australia	WA	Orogenic Au	Orogenic Au	OGs	121.611619	-30.596082
700426	Victory	VTY	Australia	WA	Orogenic Au	Orogenic Au	OGs	121.771659	-31.323771
700427	Nevoria	NEV	Australia	WA	Orogenic Au	Orogenic Au	OGs	119.585022	-31.507187
700492	Salt Creek	SCK	Australia	WA	Orogenic Au	Orogenic Au	OGs	122.0206183	-31.1083
700493	Beaufor	BFR	Canada	Quebec	Orogenic Au	Orogenic Au	OGs	-77.555914	48.159333
700496	Detour Lake	DTL	Canada	Ontario	Orogenic Au	Orogenic Au	OGs	-79.718391	50.017776
700497	Detour Lake	DTL	Canada	Ontario	Orogenic Au	Orogenic Au	OGs	-79.718391	50.017776
700498	Dome Mine	DOM	Canada	Ontario	Orogenic Au	Orogenic Au	OGs	-81.241391	48.462964
700501	Dome Mine	DOM	Canada	Ontario	Orogenic Au	Orogenic Au	OGs	-81.241391	48.462964
700502	Francoeur	FCR	Canada	Quebec	Orogenic Au	Orogenic Au	OGs	-79.275215	48.158702
700503	Giant	GIA	Canada	NWT	Orogenic Au	Orogenic Au	OGs	-114.359302	62.499779
700504	Lac Herbin	LHB	Canada	Quebec	Orogenic Au	Orogenic Au	OGs	-77.650808	48.134823
700505	Meadowbank	MDB	Canada	Nunavut	Orogenic Au	Orogenic Au	OGs	-96.070482	65.021028
700506	Musselwhite	MSW	Canada	Ontario	Orogenic Au	Orogenic Au	OGs	-90.366311	52.611458
700507	Meliadine Tiriganiaq deposit	MTG	Canada	Nunavut	Orogenic Au	Orogenic Au	OGs	-92.17885	63.027055
700508	Pine Cove	PCV	Canada	Newfoundland	Orogenic Au	Orogenic Au	OGs	-56.130003	49.959586
700509	Rice Lake	RLK	Canada	Manitoba	Orogenic Au	Orogenic Au	OGs	-95.675197	51.021385
700510	Rice Lake	RLK	Canada	Manitoba	Orogenic Au	Orogenic Au	OGs	-95.675197	51.021385
700511	Timmins West	TMW	Canada	Ontario	Orogenic Au	Orogenic Au	OGs	-81.557712	48.390235
700512	Thunder Creek	TCK	Canada	Ontario	Orogenic Au	Orogenic Au	OGs	-81.55185	48.384038
700097	Hemlo Williams	HWL	Canada	Ontario	Intrusion-Related Au	Transition Intrusion-Related to Epithermal	IR	-85.92856	48.697006
700098	Hemlo Williams	HWL	Canada	Ontario	Intrusion-Related Au	Transition Intrusion-Related to Epithermal	IR	-85.92856	48.697006

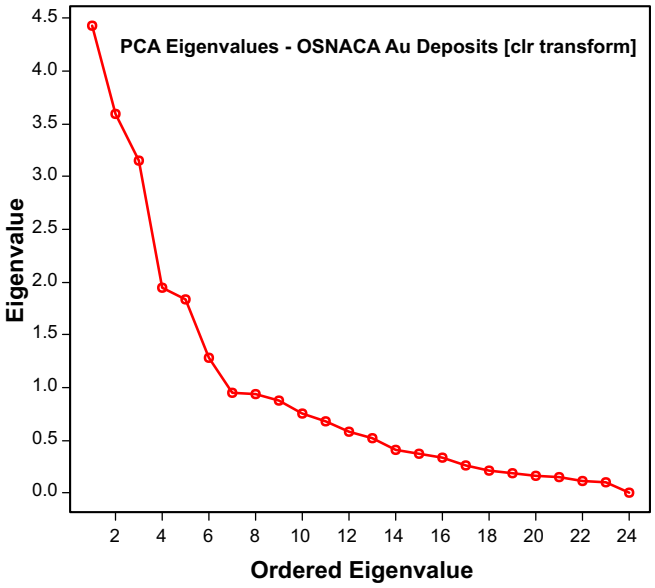

Figure 1. Screeplot of order eigenvalues derived from centred log-transformed geochemical data from the database of three types of gold deposits.

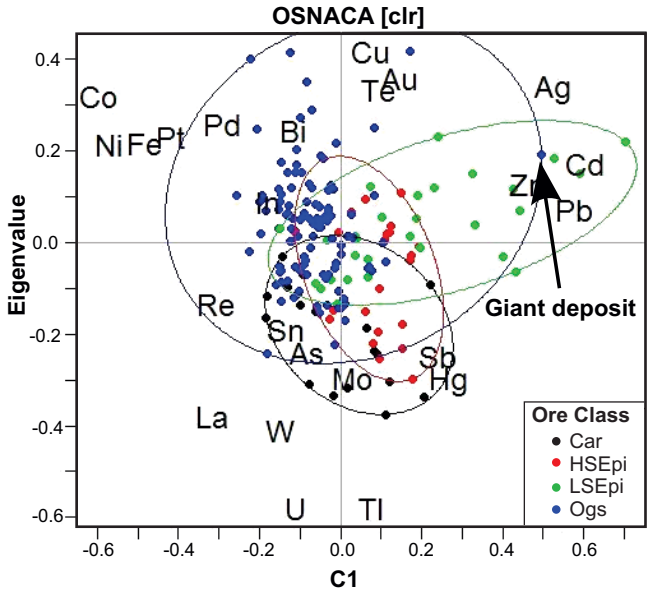

Figure 2. Biplot of principal components PC1 and PC2 for the four gold deposit types. The loadings of the elements are scaled to fit on the same diagram as the scores of the individual samples (observations). A convex ellipsoid hull encompasses the range of values for each gold deposit type and enhances the view of overlap and range. The Giant deposit (Yellowknife, Canada) is shown because of its distinct departure from the other orogenic greenstone-hosted gold deposits. See text for more details on the significance of the elements and observations. Abbreviations: Car = Carlin; HSEpi = high-sulphidation epithermal; LSEpi = low-sulphidation epithermal; OGs = orogenic greenstone-hosted.

The methods used in this study were applied in the R programming environment (R Core Team, 2014).

The data were then transformed using a centred log-ratio, as documented by Aitchison (1986) and others (Egozcue et al., 2003; Buccianti et al., 2006; Pawlowsky and Buccianti, 2011). The use of log-ratios overcomes the problem of data closure (constituents summing to a constant) and opens the data into the real number space rather than being confined to the positive number space, known as the simplex. This transformation permits the application of standard statistical methodology.

Process Discovery

A principal component analysis (PCA) was applied to the log-centred (clr) data. The results are shown in Table 2 and Figures 1 and 2. Table 2 shows that the first 8 components account for more than 76% of the variation of the data. The R-scores provide the coordinates of the elements on the biplots (Fig. 2). The relative contributions indicate the percentage that each component contributes to the variability of a specific element. The absolute contributions indicate the percentage that each element contributes to a given component. The first three components account for 47% of the data variability. As Figure 2 illustrates, there are distinct element associations with specific deposit types. The low-sulphidation (LSEpi) gold deposits show a contrast of relative enrichment of Ag-Cd-Zn-Pb at a sub-horizontal angle to the PC1 axis. High-sulphidation epithermal deposits are associated with relative enrichment in Sb-Hg-As-Sn-Mo. Carlin-type gold deposits yield relatively low PC2 scores, which correspond to As-Sn-Sb-Hg (key geochemical signature) and also Mo-U-Tl-W-La-Re element assemblages. Orogenic greenstone-hosted (OGs) gold deposits show a range of relative enrichment in Co-Ni-Fe-Pt-Pd-Cu-Te, which likely represents a mafic host-rock association, as seen along the positive PC2 axis. There is a corresponding relative depletion of these elements towards the origin of the figure. These trends require more detailed interpretation within the context of the geology of the deposits, which is beyond the scope of this initial study. It is also important to note that there is significant overlap between ore geochemistry at each of the deposit types. This is emphasized through the addition of ellipses (convex hulls) around the range of the samples that define each class. As noted in Figure 2, the. Giant gold mine, (Yellowknife, Northwest Territories, Canada) appears to have a closer association with low-sulphidation epithermal deposits.

Another method for investigating the dominant associations and trends in multivariate data is multidimensional scaling (MDS). This method (see Venables and Ripley, 2002, p. 306) provides a measure of optimum distribution of observations within a defined dimensional space. Typically MDS is rendered in two or three dimensions. Figure 3 shows a plot of the two MDS coordinates derived from the application of a two-dimensional MDS. As in the PCA biplot of Figure

Table 2. Summary of principal component analysis. Only the first 10 principal components are shown (for brevity). See text for detailed explanation. R-scores are contrasted by red (values > 0) and blue (<=0). Bold red values are highlighted for relative and absolute contributions of >10.

Eigenvalues

	PC1	PC2	PC3	PC4	PC5	PC6	PC7	PC8	PC9	PC10
λ	4.4400	3.5900	3.1500	1.9500	1.8400	1.2900	0.9500	0.9400	0.8700	0.7600
λ%	18.6085	15.0461	13.2020	8.1727	7.7117	5.4065	3.9816	3.9396	3.6463	3.1852
Σλ%	18.6085	33.6547	46.8567	55.0293	62.7410	68.1475	72.1291	76.0687	79.7150	82.9003

R-Scores

	PC1	PC2	PC3	PC4	PC5	PC6	PC7	PC8	PC9	PC10
Fe	-0.6057	0.2705	-0.2491	0.0321	0.1320	-0.4479	0.1137	0.0682	0.0877	-0.1391
Co	-0.7469	0.4000	-0.1807	0.0404	0.0642	-0.1777	0.0399	-0.0472	0.1164	-0.2642
Ni	-0.7142	0.2673	0.2863	-0.0418	0.1590	0.1361	0.0670	0.1424	-0.0294	-0.3238
Re	-0.3826	-0.1658	-0.0975	-0.4794	0.1884	0.0582	0.1820	0.2725	0.3888	0.4057
Pd	-0.3626	0.3248	0.5970	0.1969	0.2231	0.3764	0.0552	-0.1102	-0.0165	0.2151
Pt	-0.5223	0.2873	0.5323	0.2311	0.2268	0.3423	0.0158	-0.1298	-0.0250	0.1284
Cu	0.0952	0.5227	-0.3013	0.3836	-0.3489	0.0529	0.1331	0.2299	0.2179	-0.0315
Ag	0.6588	0.4180	0.0538	-0.3261	-0.0003	0.0307	0.1611	-0.1434	-0.0466	0.0762
Au	0.1872	0.4497	0.2756	-0.5640	-0.0739	-0.0744	-0.0485	-0.1793	-0.2896	0.0490
Zn	0.5792	0.1586	-0.2824	0.2692	0.5404	-0.1806	0.0129	-0.0259	0.1011	0.0002
Cd	0.7557	0.2160	-0.1240	0.2514	0.3568	0.0060	0.0165	0.0055	0.1557	0.0473
In	-0.2216	0.1121	-0.4959	0.3661	-0.2864	-0.1586	0.1870	-0.2907	-0.1355	0.1819
Tl	0.0956	-0.7251	0.2283	-0.0501	0.0168	0.1325	-0.1298	-0.1821	0.0784	-0.2967
Pb	0.7207	0.0912	-0.2095	0.2182	0.2768	0.1738	0.1581	0.0843	-0.1874	-0.2019
Hg	0.3355	-0.3795	0.3856	-0.1107	-0.3312	0.1252	0.0402	-0.0985	0.4332	-0.2718
As	-0.1003	-0.3007	0.5099	0.3136	-0.1071	-0.5296	-0.2433	0.2708	-0.1567	0.0781
Sb	0.3028	-0.3097	0.5956	0.2421	-0.3443	-0.1591	0.0683	0.2077	-0.1487	0.1752
Bi	-0.1435	0.3058	-0.4965	-0.0128	-0.3824	0.4169	-0.2037	0.2026	-0.3276	-0.0929
Te	0.1198	0.4179	-0.1621	-0.4972	-0.0882	-0.2296	-0.4539	-0.2100	0.1043	0.0414
Mo	0.0366	-0.3698	-0.4133	-0.4509	-0.0757	0.1296	0.2215	0.4135	-0.1139	-0.0013
W	-0.1838	-0.5108	-0.0411	-0.1409	-0.0901	-0.1603	0.5571	-0.3489	-0.1948	-0.0409
Sn	-0.1671	-0.2383	-0.4707	0.2953	-0.4907	0.1876	-0.1348	-0.2534	0.2105	0.1777
La	-0.3954	-0.4726	-0.4215	0.0031	0.4547	-0.0209	-0.1541	-0.1138	-0.1249	0.0914
U	-0.1374	-0.7247	-0.3332	0.0776	0.3106	0.1772	-0.2340	0.0117	-0.0927	0.0337

Relative Contributions

	PC1	PC2	PC3	PC4	PC5	PC6	PC7	PC8	PC9	PC10
Fe	**36.8961**	7.3601	6.2390	0.1035	1.7536	**20.1776**	1.2989	0.4674	0.7731	1.9446
Co	**56.0980**	**16.0885**	3.2824	0.1644	0.4139	3.1753	0.1605	0.2244	1.3621	7.0223
Ni	**51.2935**	7.1848	8.2419	0.1756	2.5425	1.8632	0.4520	2.0387	0.0871	**10.5459**
Re	**14.7209**	2.7656	0.9555	**23.1103**	3.5697	0.3409	3.3322	7.4675	**15.2037**	**16.5546**
Pd	**13.2194**	**10.6078**	**35.8478**	3.8986	5.0061	**14.2458**	0.3066	1.2222	0.0275	4.6515
Pt	**27.4363**	8.2987	**28.4927**	5.3729	5.1719	**11.7814**	0.0250	1.6930	0.0628	1.6573
Cu	0.9114	**27.4797**	9.1274	**14.7951**	**12.2451**	0.2819	1.7828	5.3158	4.7768	0.0999
Ag	**43.6405**	**17.5695**	0.2916	**10.6970**	0.0000	0.0947	2.6101	2.0679	0.2183	0.5841
Au	3.5227	**20.3418**	7.6367	**31.9926**	0.5495	0.5565	0.2362	3.2348	8.4320	0.2414
Zn	**33.7380**	2.5307	8.0203	7.2867	**29.3664**	3.2813	0.0168	0.0675	1.0287	0.0000
Cd	**57.4243**	4.6938	1.5456	6.3582	**12.8003**	0.0037	0.0274	0.0031	2.4385	0.2247
In	4.9404	1.2631	**24.7333**	**13.4814**	8.2492	2.5298	3.5163	8.4967	1.8471	3.3272
Tl	0.9183	**52.8799**	5.2408	0.2529	0.0283	1.7663	1.6954	3.3351	0.6175	8.8517
Pb	**52.2297**	0.8359	4.4122	4.7882	7.7036	3.0372	2.5135	0.7139	3.5310	4.0984
Hg	**11.3214**	**14.4830**	**14.9514**	1.2322	**11.0324**	1.5751	0.1623	0.9756	**18.8708**	7.4274
As	1.0108	9.0923	**26.1518**	9.8895	1.1536	**28.2057**	5.9512	7.3733	2.4685	0.6133
Sb	9.2230	9.6439	**35.6756**	5.8928	**11.9221**	2.5455	0.4686	4.3379	2.2241	3.0852
Bi	2.0716	9.4052	**24.7923**	0.0166	**14.7085**	**17.4775**	4.1731	4.1295	**10.7954**	0.8683
Te	1.4432	**17.5625**	2.6430	**24.8611**	0.7828	5.2993	**20.7187**	4.4356	1.0939	0.1722
Mo	0.1349	**13.7519**	**17.1817**	**20.4421**	0.5764	1.6885	4.9323	**17.1936**	1.3035	0.0002
W	3.3990	**26.2442**	0.1702	1.9961	0.8173	2.5850	**31.2069**	**12.2404**	3.8160	0.1680
Sn	2.8071	5.7124	**22.2772**	8.7668	**24.2112**	3.5376	1.8263	6.4560	4.4577	3.1748
La	**15.7205**	**22.4624**	**17.8642**	0.0010	**20.7918**	0.0438	2.3870	1.3018	1.5692	0.8404
U	1.8995	**52.8104**	**11.1639**	0.6056	9.6994	3.1587	5.5061	0.0138	0.8644	0.1145

Absolute Contributions

	PC1	PC2	PC3	PC4	PC5	PC6	PC7	PC8	PC9	PC10
Fe	8.2723	2.0384	1.9685	0.0527	0.9474	**15.6110**	1.3629	0.4930	0.8798	2.5497
Co	**12.5774**	4.4558	1.0357	0.0838	0.2236	2.4567	0.1684	0.2367	1.5502	9.2074
Ni	**11.5002**	1.9899	2.6005	0.0895	1.3736	1.4415	0.4743	2.1504	0.0991	**13.8274**
Re	3.3005	0.7660	0.3015	**11.7801**	1.9286	0.2637	3.4963	7.8766	**17.3025**	**21.7059**
Pd	2.9639	2.9379	**11.3107**	1.9872	2.7046	**11.0217**	0.3217	1.2892	0.0313	6.0990
Pt	6.1513	2.2984	8.9900	2.7387	2.7942	9.1151	0.0262	1.7858	0.0715	2.1730
Cu	0.2043	7.6107	2.8799	7.5415	6.6156	0.2181	1.8706	5.6071	5.4362	0.1310
Ag	9.7844	4.8660	0.0920	5.4526	0.0000	0.0732	2.7387	2.1812	0.2485	0.7659
Au	0.7898	5.6338	2.4095	**16.3077**	0.2969	0.4305	0.2479	3.4120	9.5960	0.3165
Zn	7.5642	0.7009	2.5306	3.7143	**15.8655**	2.5387	0.0176	0.0712	1.1707	0.0000
Cd	**12.8748**	1.3000	0.4877	3.2410	6.9155	0.0028	0.0287	0.0032	2.7751	0.2946
In	1.1077	0.3498	7.8038	6.8719	4.4567	1.9572	3.6895	8.9622	2.1021	4.3626
Tl	0.2059	**14.6454**	1.6536	0.1289	0.0153	1.3665	1.7789	3.5179	0.7028	**11.6060**
Pb	**11.7101**	0.2315	1.3921	2.4407	4.1619	2.3498	2.6373	0.7530	4.0184	5.3737
Hg	2.5383	4.0112	4.7174	0.6281	5.9604	1.2187	0.1703	1.0291	**21.4759**	9.7386
As	0.2266	2.5182	8.2514	5.0410	0.6232	**21.8222**	6.2442	7.7773	2.8093	0.8042
Sb	2.0678	2.6709	**11.2563**	3.0038	6.4410	1.9694	0.4917	4.5756	2.5312	4.0453
Bi	0.4645	2.6048	7.8224	0.0085	7.9464	**13.5220**	4.3787	4.3558	**12.2857**	1.1384
Te	0.3236	4.8641	0.8339	**12.6725**	0.4229	4.1000	**21.7391**	4.6786	1.2449	0.2257
Mo	0.0302	3.8087	5.4212	**10.4200**	0.3114	1.3064	5.1752	**18.1357**	1.4835	0.0002
W	0.7621	7.2685	0.0537	1.0175	0.4415	2.0000	**32.7438**	**12.9111**	4.3428	0.2203
Sn	0.6294	1.5821	7.0289	4.4687	**13.0804**	2.7369	1.9163	6.8098	5.0731	4.1627
La	3.5246	6.2211	5.6365	0.0005	**11.2330**	0.0339	2.5045	1.3732	1.7858	1.1019
U	0.4259	**14.6262**	3.5224	0.3087	5.2402	2.4438	5.7772	0.0146	0.9837	0.1501

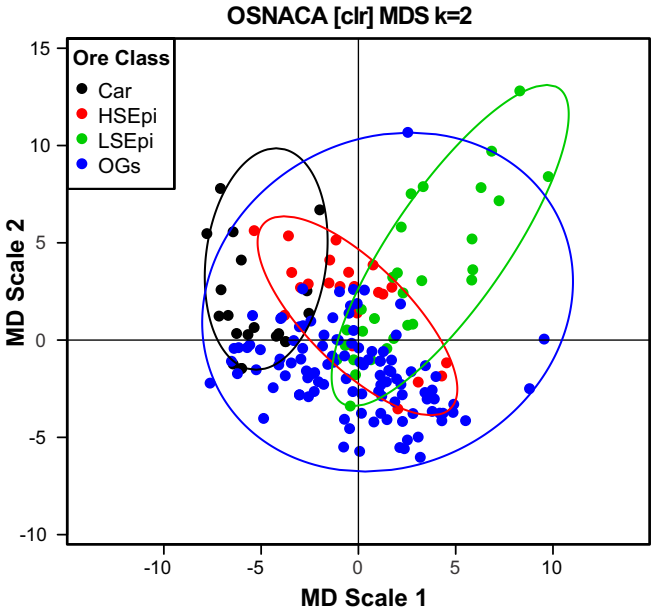

Figure. 3. Multidimensional scaling plot of reduced dimensionality of the data (2 dimensions). As in Figure 2, the overlap and relationship between the four gold deposit classes is enhanced by convex ellipsoid hulls that encompass each deposit type. Abbreviations: Car = Carlin; HSEpi = high-sulphidation epithermal; LSEpi = low-sulphidation epithermal; OGs = orogenic greenstone-hosted.

2, there is significant overlap of the four classes. The extended range of the orogenic greenstone-hosted (OGs) deposits is due to three individual deposits shown in the figure: one of which is the Giant gold mine, discussed previously. The chemistry of these three deposits may be different due to wall-rock contamination or they have been misclassified. Similarly, three Carlin-type deposits occur within the field dominated by high-sulphidation epithermal deposits. This overlap may be the result of misclassification or an insufficient range of Carlin-type deposit geochemistry. However, these deposit types share some analogies in terms of low-pH fluid chemistry and strong silicification (jasperoid versus massive silica), which may explain at least part of the geochemical overlap. Several of the deposits are close to the origin of the plot, suggesting that they are compositionally similar and highlights the fact that knowledge of the geology of the deposits and the associated paragenesis is critical in characterizing and classifying gold deposits.

Process Validation

Assessing the statistical uniqueness of the gold deposit types can be performed through an analysis of variance (Venables and Ripley, 2002). The four types of gold deposits were subjected to an analysis of variance, based on the centred log-transformed data and the principal component scores derived from the centred log-transform of the data. A graphical summary of the results are shown in Figures 4 and 5. Figure 4 shows

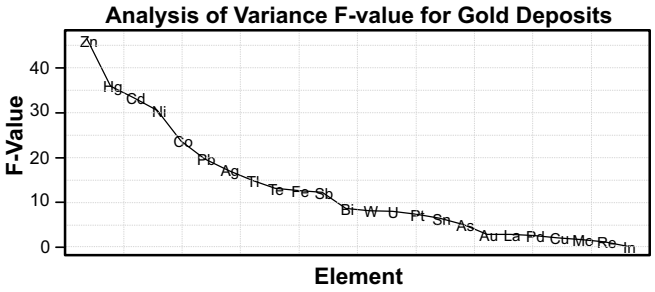

Figure 4. Ordered plot of F-values for each element based on analysis of variance on log centred transform geochemical data for each of the four gold deposit types. High F-values indicate better group separability. Co and Cd are better at discriminating between the four gold deposits types, whereas Sn and Mo are poor at discriminating between the types of gold deposits.

that Zn-Hg-Cd-Ni-Co-Pb-Ag-Tl-Te-Fe-Sb account for most of the discriminating power between the three of the deposit types. Since all deposits contain Au, it is expected to see that Au has low discriminating power. Figure 5 shows the results of a discriminant analysis applied to the principal components. In contrast to Figure 4, principal components 1, 5, and 2 account for most of the discriminating power between the four deposit types. Table 2 shows that both the relative and absolute contributions to PC5 are dominated by Zn (low-temperature Au deposition?). Since principal components represent linear combinations of the elements, they can typically reflect the stoichiometric controls that govern the associations of the minerals. These linear combinations result in fewer numbers of variables being required to define the variation in the data. In this case, the three principal components listed above (principal components 1, 5, and 2) are sufficient for the purposes of classification of the gold deposits.

An interesting feature of the multi-element chemistry of the gold deposits included in this study is the dominance of Zn as a significant element in defining deposit class separation (Fig. 4). This implies that Zn may represent a proxy for the deposition of Au in low-temperature environments.

The four groups of deposit types were classified using a linear discriminant procedure (lda, see Venables and Ripley, 2002). Cross-validation procedures (e.g. Venables and Ripley, 2002, section 12.6) were used, which sampled the dataset 20 times, from which average classification accuracy was established. The results of this classification are shown in Table 3. The overall classification accuracy is 80.9%, with individual class accuracies ranging from 50.0 to 96.3%. Overlap and/or misclassification are shown in the off-diagonal elements of the accuracy matrix of Table 3. Carlin-type (Car) deposits show overlap/misclassification with high-sulphidation epithermal (HSEpi) deposits and orogenic greenstone-hosted (OGs)

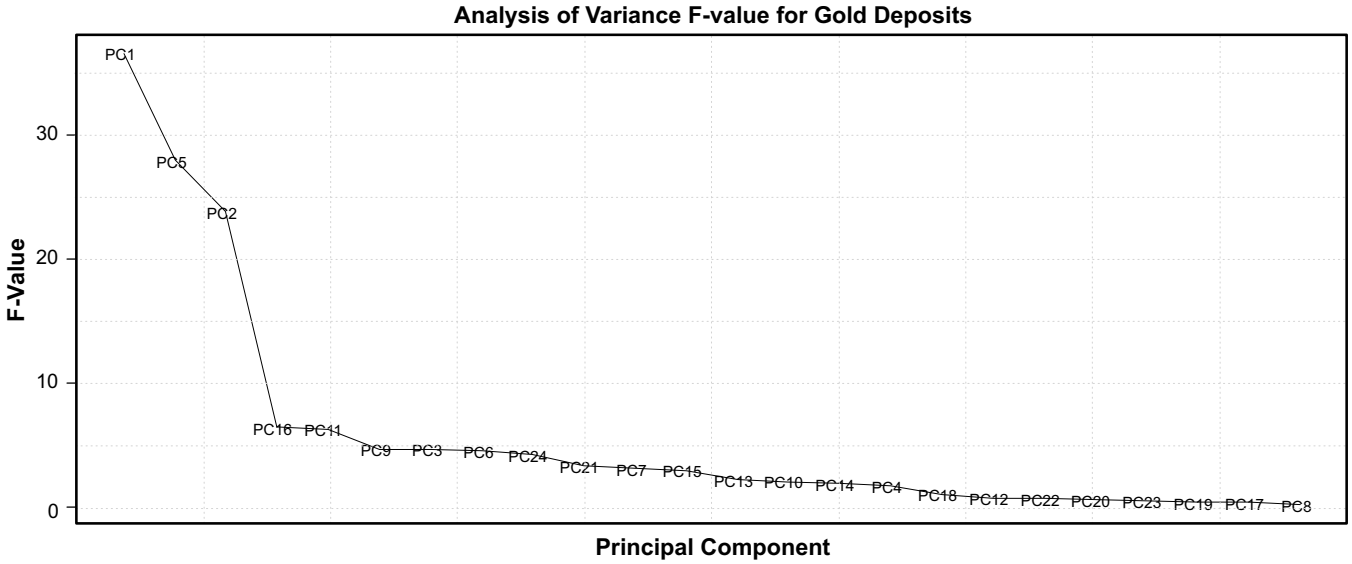

Figure. 5. Ordered plot of F-values for each principal component based on analysis of variance for the four types of gold deposits. High F-values indicate better group separability. The plot shows that PC1 and PC2 are much better at discriminating between the four types of gold deposits than any of the other components.

deposits. High-sulphidation epithermal (HSEpi) deposits show overlap/misclassification with Carlin-type, and orogenic greenstone-hosted deposits. Low-sulphidation epithermal gold deposits show overlap with orogenic greenstone-hosted deposits. Orogenic greenstone-hosted deposits show overlap with all of the other classes and intrusion-related deposits show minor overlap/misclassification with orogenic greenstone-hosted gold deposits. These associations are graphically shown in Figure 6 as a plot of the first two linear discriminant scores. The colour of each observation defines the deposit class to which the sample was initially assigned. The symbol defines the class to which each observation from the linear discriminant procedure was assigned. All four deposit classes occupy unique regions of the plot. The convex hull ellipsoid provides a measure of the overlap between the classes after the classification by the "lda" procedure. The "misclassification" of the Giant deposit is highlighted in this figure.

DISCUSSION

The methodology presented here provides a framework in which high-quality geochemical data from a database of ore geochemistry can be used for characterizing well known mineral deposit types. The results presented in this study are restricted to four types of gold deposits. Other types of gold deposits (e.g. skarn, porphyry, volcanic-hosted, paleoplacer) can be studied as well. The methods employed in this study are based solely on geochemistry and the resulting overlap between classes and apparent misclassification (e.g. Giant deposit) indicates that geochemistry alone is

Table 3. Accuracy of the prediction of gold deposit types based on a 20-fold cross-validation linear discriminant analysis.

Count Accuracy	Car	HSEpi	LSEpi	OGs
Car	11	1	0	6
HSEpi	4	11	0	7
LSEpi	0	0	17	12
OGs	1	2	1	105

% Accuracy	Car	HSEpi	LSEpi	OGs
Car	61.11	5.56	0	33.33
HSEpi	18.18	50.00	0	31.82
LSEpi	0	0	58.62	41.38
OGs	0.92	1.83	0.92	96.33

Overall Accuracy (%) 80.9

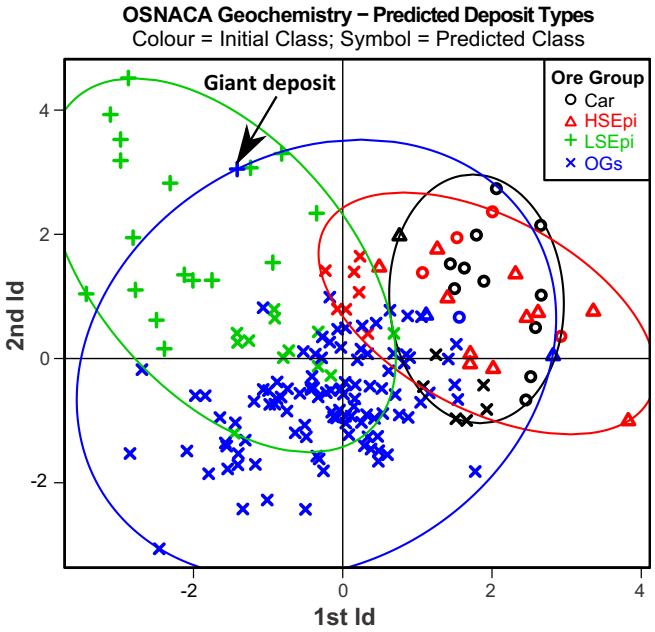

Figure 6. Plot of linear discriminant scores 1 and 2 for the three types of gold deposits. The linear discriminant scores were determined from the principal components shown in Figure 5, namely: PC1, PC5, and PC2. See Table 3 for the accuracy of the linear discriminant model. Abbreviations: Car = Carlin; HSEpi = high-sulphidation epithermal; LSEpi = low-sulphidation epithermal; OGs = orogenic greenstone-hosted.

insufficient to uniquely classify ore deposits. Hodgson and Troop (1988) provide details on criteria for gold deposit exploration based on computer based methods using a database of key gold deposit characteristics. Studies by Drew and Menzie (1993) detail the importance of the regional geological/tectonic framework in defining metrics for ore-deposit classification. Poulsen et al. (2000) provide a decision tree based on geological characteristics that can helpful to classify the gold deposit type. Our results suggest that ore geochemistry can support these classifications schemes and also highlight that ore deposits clans define a "magmato-hydrothermal space".

IMPLICATIONS FOR EXPLORATION

The approach used in this study demonstrates the geochemical distinctiveness of the major types of gold deposits derived from a global database of ore deposits. Despite demonstrated overlap between the four gold deposit types studied herein, the framework establishes a baseline for testing unknown samples for the potential affinity with the environments of gold deposit formation.

Currently, the OSNACA database does not have sufficient numbers of representative ore sample chemistry for the less common mineral deposit types, which creates difficulty when applying statistical methods. An ongoing study at the Centre for Exploration Technology, University of Australia, is involved in the characterization and classification of a broader suite of mineral deposits. Preliminary results (Grunsky et al., 2013) show that a consistent methodological approach together with carefully chosen ore-deposit samples and exacting laboratory standards and protocols will create a reliable database that can be used for a variety of research and mineral exploration purposes.

FUTURE WORK

Further work is required to gather more data from the global inventory of ore-deposit samples and research more detailed relationships within the data. As the database grows, both the distinctiveness and overlap that exists as a continuum between gold deposits will evolve and become more refined. A continuum of other ore deposit styles, i.e., the magmato-hydrothermal space, is the subject for further study. These data are also available from the OSNACA database and may be used for future studies.

ACKNOWLEDGEMENTS

Support from the Targeted Geoscience Initiative 4 – Gold Deposits, the Centre for Exploration Technology, University of Western Australia and SIPA Resources, Perth, Australia is gratefully acknowledged. The authors wish to thank Chris Lawley for his thoughtful and helpful review of the manuscript.

REFERENCES

Aitchison, J., 1986. The statistical analysis of compositional data. Monographs on statistics and applied probability; Chapman & Hall Ltd., London, 416 p.

Brauhart, C.W., Grunsky, E.C., Hagemann, S., and Dubé, B., 2015. OSNACA Project website, Centre for Exploration Technology, University of Western Australia, Australia, http://www.cet.edu.au/research-projects/special-projects/projects/osnaca-ore-samples-normalised-to-average-crustal-abundance.

Buccianti, A., Mateu-Figueras, G., and Pawlowsky-Glahn, V., 2006. Compositional Data Analysis in the Geosciences: From Theory to Practice; Geological Society, Special Publication 264, 212 p.

Drew, L.J. and Menzie, D.W., 1993; Is there a metric for mineral deposit occurrence probabilities?; Nonrenewable Resources, v. 2, p. 92–105.

Egozcue, J.J., Pawlowsky-Glahn, V., Mateu-Figueras, G., and Barcelo-Vidal, C., 2003. Isometric Logratio Transformations for Compositional Data Analysis; Mathematical Geology, v. 35, p. 279–300.

Groves, D.I., Bierlein, F.P., Meinert, L.D., and Hitzman M.W., 2010. Iron Oxide Copper-Gold (IOCG) deposits through Earth history: Implications for origin, lithospheric setting, and distinction from other epigenetic iron oxide deposits; Economic Geology, v. 105, p. 641–654.

Grunsky, E.C., Brauhart, C., Mueller, U., Dubé, B., and Hagemann, S., 2013. Ore samples normalized to average crustal abundance (OSNACA): a global online database and a new technique for quantifying multi-element ore deposit signatures; PDAC-SEG Canada Student Chapter Minerals Colloquium, Prospectors and Developers Association of Canada Meeting, March 4, 2013, poster.

Hannington, M.D., Poulsen, K.H., Thompson, J.F.H., and Sillitoe, R.H., 1999. Volcanogenic gold in the massive sulfide environment, *In:* Volcanic-Associated Massive Sulfide Deposits: Processes and Examples in Modern and Ancient Settings, (ed.) C.T. Barrie and M.D. Hannington; Society of Economic Geologists, Reviews in Economic Geology 8, p. 325–356.

Hodgson, C.J. and Troop, D.G., 1988. A new computer-aided methodology for area selection in gold exploration: a case study from the Abitibi Greenstone Belt, Ontario; Economic Geology, v. 83, p. 952–977.

Leach, D.L., Sangster, D.F., Kelley, K.D., Large, R.R., Garven, G., Allen, C.R., Gutzmer, J., and Walters, S.G., 2005. Sediment-hosted lead-zinc deposits: A global perspective, *In:* 100th Anniversary Volume, (ed.) J.W. Hedenquist, J.F.H. Thompson, R.J. Goldfarb, and J.P. Richards; Society of Economic Geologists, v. 40, p. 561–607.

Nesbitt, B.E., 1988. Gold deposit continuum: A genetic model for lode Au mineralization in the continental crust; Geology, v. 16, p. 1044–1048.

OSNACA, 2013. OSNACA: Ore samples normalized to average crustal abundance, http://www.cet.edu.au/research-projects/special-projects/projects/osnaca-ore-samples-normalised-to-average-crustal-abundance.

Palarea-Albaladejo J. and Martin-Fernandez J.A., 2008. A modified EM alr-algorithm for replacing rounded zeros in compositional data sets; Computers & Geosciences, v. 34, p. 902–917

Pawlowsky-Glahn, V. and Buccianti, A. (ed.), 2011. Compositional Data Analysis, Theory and Applications; Wiley & Sons, New York, 378 p.

Poulsen, K.H., Robert, F., and Dubé, B., 2000. Geological classification of Canadian gold deposits; Geological Survey of Canada, Bulletin 540, 106 p.

R Core Team, 2014. R: A language and environment for statistical computing; R Foundation for Statistical Computing, Vienna, Austria. URL (http://www.R-project.org/).

Sillitoe, R.H., 1989. Gold deposits in western Pacific island arcs: The magmatic connection, *In:* The Geology of Gold Deposits: The Perspective in 1988, (ed.) R.R. Keays, W.R., Ramsay, and D.I. Groves; Society of Economic Geologist, Monograph 6, p. 274–291.

Venables, W.N. and Ripley, B.D., 2002. Modern Applied Statistics with S (Fourth Edition); Springer, Berlin, 495 p.

Appendix

Refereed Publications Related to theTGI-4 Lode Gold Ore Systems Project

PUBLICATIONS IN SCIENTIFIC JOURNALS

Dubé, B., Mercier-Langevin, P., Kjarsgaard, I., Hannington, M., Bécu, V., Côté, J., Moorhead, J., Legault, M., and Bédard, N. 2014. The Bousquet 2-Dumagami world-class Archean Au-rich volcanogenic massive sulfide deposit, Abitibi, Quebec: metamorphosed submarine advanced argillic alteration footprint and genesis, *In:* A Special Issue on Archean Magmatism, Volcanism, and Ore Deposits – Part 2; Economic Geology, v. 109, p. 121–166. doi:10.2113/econgeo.109.1.121

Lawley, C.J.M., Creaser, R., Jackson, S., Yang, Z., Davis, B., Pehrsson, S., Dubé, Mercier-Langevin, P., and Vaillancourt, D., submitted. Unravelling the Western Churchill Province Paleoproterozoic gold metallotect: constraints from Re-Os arsenopyrite and U-Pb xenotime geochronology and LA-ICP-MS arsenopyrite geochemistry at the BIF-hosted Meliadine gold district, Nunavut, Canada; Economic Geology.

Lawley, C.J.M., Dubé, B., Mercier-Langevin, P., Kjarsgaard, B., Knight, R., and Vaillancourt, D., in press. Defining and mapping hydrothermal footprints at the BIF-hosted Meliadine Gold District, Nunavut, Canada; Journal of Geochemical Exploration. Available online.

McNicoll, V., Dubé, B., Castonguay, S., Oswald, W., Biczok, J., Mercier-Langevin, P., Skulski, T., and Malo, M., submitted. The world-class Musselwhite BIF-hosted gold deposit, Superior Province, Canada: new high-precision U-Pb geochronology and implications for the geological and structural setting of the deposit and gold exploration; Precambrian Research.

Mercier-Langevin, P., Hannington, M.D., Dubé, B. and Bécu, V., 2011. The gold content of volcanogenic massive sulfide deposits; Mineralium Deposita, v. 46, p. 509–539. doi:10.1007/s00126-010-0300-0

Mercier-Langevin, P., Houlé, M.G., Dubé, B., Monecke, T., Hannington, M.D., Gibson, H.L., and Goutier, J., 2012. A special issue on Archean magmatism, volcanism, and ore deposits: Part 1. Komatiite-associated Ni-Cu-(PGE) sulfide and greenstone-hosted Au deposits — Preface; Economic Geology, v. 107, p. 745–753. doi:10.2113/econgeo.107.5.745

Mercier-Langevin, P., Daigneault, R., Goutier, J., Dion, C., and Archer, P., 2012. Geology of the Archean intrusion-hosted La-Grande-Sud Au-Cu Prospect, La Grande Subprovince, James Bay Region, Québec, *In:* A Special Issue on Archean Magmatism, Volcanism, and Ore Deposits – Part 1; Economic Geology, v. 107, p. 935–962. doi:10.2113/econgeo.107.5.935

Mercier-Langevin, P., McNicoll, V., Allen, R., Blight, J., and Dubé, B., 2013. The Boliden gold-rich volcanogenic massive sulfide deposit, Skellefte District, Sweden: new U-Pb age constraints and implications at deposit and district scale; Mineralium Deposita, v.48, p. 485–504. doi:10.1007/s00126-012-0438-z

Mercier-Langevin, P., Lafrance, B., Bécu, V., Dubé, B., Kjarsgaard, I., and Guha, J., 2014. The Lemoine auriferous volcanogenic massive sulfide deposit, Chibougamau camp, Abitibi greenstone belt, Québec, Canada: geology and genesis, *In:* A Special Issue on Archean Magmatism, Volcanism, and Ore Deposits – Part 2; Economic Geology, v. 109, p. 231–269. doi:10.2113/econgeo.109.1.231

GOVERNMENT REPORTS

Bleeker, W., 2012. Targeted Geoscience Initiative 4. Lode gold deposits in ancient deformed and metamorphosed terranes: the role of extension in the formation of Timiskaming Basins and large gold deposits, Abitibi Greenstone Belt—A discussion, *In:* Summary of Field Work and other Activities 2012; Ontario Geological Survey, Open File Report 6280, p. 47-1 to 47-12.

Bleeker, W., Atkinson, B.T., and Stalker, M., 2014. A "New" Occurrence of Timiskaming sedimentary rocks in the Northern Swayze Greenstone Belt, Abitibi Subprovince—with implications for the western continuation of the Porcupine–Destor Fault Zone and nearby gold mineralization, *In:* Summary of Field Work and Other Activities 2014; Ontario Geological Survey, Open File Report 6300, p. 43-1 to 43-10.

Dubé, B., Mercier-Langevin, P., Castonguay, S., McNicoll, V.J., Pehrsson, S.J., Bleeker, W., Schetselaar, E.M., and Jackson, S., 2011. TGI-4 lode gold deposits in ancient, deformed and metamorphosed terranes – footprints and exploration implications: a preliminary overview of themes, objectives and targeted areas, *In:* Summary of Field Work and other Activities 2011; Ontario Geological Survey, Open File Report 6270, p. 38-1 to 38-10.

Gourcerol, B., Thurston, P., Kontak, D.J., and Côté-Mantha, O., 2014. Interpretations and implications of preliminary LA ICP-MS analysis of chert for the origin of geochemical signatures in banded iron-formations (BIFs)

Appendix: Refereed publications related to the TGI-4 Lode Gold Ore Systems Project, *In:* Targeted Geoscience Initiative 4: Contributions to the Understanding of Precambrian Lode Gold Deposits and Implications for Exploration, (ed.) B. Dubé and P. Mercier-Langevin; Geological Survey of Canada, Open File 7852, p. 287–293.

from the Meadowbank gold deposit, Western Churchill Province, Nunavut; Geological Survey of Canada, Current Research 2014-1, 26 p. doi:10.4095/293129

Gourcerol, B., Thurston, P.C., Kontak, D.J., Côté-Mantha, O., and Biczok, J.,2015. Distinguishing primary and mineralization-related signatures of chert from the banded iron formation-type gold deposits at Musselwhite, Ontario and Meadowbank, Nunavut; Geological Survey of Canada, Current Research 2015-1, 21 p.

Grunsky, E.C., Brauhart, C., Hagemann, S., and Dubé, B., 2015. The magmato-hydrothermal space: a new metric for geochemical characterization of ore deposits; Geological Survey of Canada, Open File 7487, 1 sheet. doi:10.4095/295662

Janvier, V., Castonguay, S., Mercier-Langevin, P., Dubé, B., McNicoll, V., Malo, M., Pehrsson, S., and Bécu, V., 2013. Recognizing optimum Banded-Iron Formation-hosted gold environments in ancient, deformed and metamorphosed terranes: Preliminary results from the Meadowbank deposit, Nunavut, Canada; Geological Survey of Canada, Open File 7407, 1 sheet. doi:10.4095/292589

Janvier, V., Castonguay, S., Mercier-Langevin, P., Dubé, B., McNicoll, V., Pehrsson, S., Malo, M., De Chavigny, B., and Côté-Mantha, O., 2015. Preliminary results of the geology of the Portage deposit, Meadowbank gold mine, Churchill Province, Nunavut; Geological Survey of Canada, Current Research 2015-2, 21 p. doi:10.4095/295532

Kelly, C.J., Gagnon, É, and Schneider, D.A., 2013. Redefining the pattern and timing of metamorphism in the North Caribou greenstone belt. Ontario Geological Survey, *In:* Summary of Field Work and other Activities 2013; Ontario Geological Survey, Open File Report 6290, p. 59-1 to 59-8.

Lafrance, B., Tóth, Z., Dubé, B., and Mercier-Langevin, P., 2012. Geological setting of banded iron formation-hosted gold mineralization in the Geraldton area, Northern Ontario, *In:* Summary of Field Work and other Activities 2012; Ontario Geological Survey, Open File Report 6280, p. 48-1 to 48-10.

Lawley, C.J.M., Creaser, R.A., McNicoll, V., Dubé, B., Mercier-Langevin, P., Pehrsson, S., and Vaillancourt, D., 2014. Re-Os arsenopyrite and U-Pb detrital zircon geochronology at the Meliadine Gold District, Nunavut: implications for the geologic setting and age of the Tiriganiaq Deposit; Geological Survey of Canada, Open File 7510, 19 p. doi:10.4095/293939

Lawley, C.J.M., Dubé, B., Jackson, S., Yang, Z., and Mercier-Langevin, P., 2014. Sulfide paragenesis and LA-ICP-MS arsenopyrite geochemistry at the Meliadine Gold District, Nunavut: implications for Re-Os arsenopyrite geochronology and ore deposit genesis; Geological Survey of Canada, Open File 7491, 1 sheet. doi:10.4095/293938

Lawley, C.J.M., Creaser, R.A., Jackson, S., Yang, Z., Davis, B., Dubé, B., Mercier-Langevin, P., Pehrsson, S., and Vaillancourt, D., 2015. Protracted Paleoproterozoic gold history at the Archean BIF-hosted Meliadine Gold District, Nunavut; Geological Survey of Canada, Open File 7743, 23 p. doi:10.4095/295629

Lawley, C.J.M., Dubé, B., Mercier-Langevin, P., Kjarsgaard, B.A., and Knight, R.D., 2015. Whole-rock lithogeochemistry and pXRF data from the Meliadine gold district, Nunavut, Canada; Geological Survey of Canada, Open File 7711, 1 .zip file. doi:10.4095/296223

Lawley, C.J.M., Dubé, B., Mercier-Langevin, P., and Vaillancourt, D., 2015. Mapping hydrothermal footprints: case studies from the Meliadine Gold District, Nunavut; Geological Survey of Canada, Open File 7744, 22 p. doi:10.4095/295920

Mercier-Langevin, P., Goutier, J., Ross, P.-S., McNicoll, V., Monecke, T., Dion, C., Dubé, B., Thurston, P., Bécu, V., Gibson, H., Hannington, M., and Galley, A., 2011. The Blake River Group of the Abitibi greenstone belt and its unique VMS and gold-rich VMS endowment, GAC-MAC-SEG-SGA Annual Meeting, Ottawa, Ontario, May 2011, Field Trip 02B guidebook; Geological Survey of Canada, Open File 6869, 61 p.

Oswald, W., Dubé, B., Castonguay, S., McNicoll, V., Biczok, J., Mercier-Langevin, P., Malo, M., and Skulski, T., 2014. New insights on the structural and geological setting of the world-class Musselwhite gold deposit, Superior Province, Northwestern Ontario; Geological Survey of Canada, Open File 7633, 1 sheet. doi:10.4095/294817

Oswald, W, Castonguay, S., Dubé, B., Mercier-Langevin, P., Malo, M., Biczok, J., and McNicoll, V., 2014. Targeted Geoscience Initiative 4. Lode gold deposits in ancient deformed and metamorphosed terranes: detailed mapping of key stripped outcrops in the Musselwhite Mine area, Northwestern Ontario, and implications for the geological and structural setting of the gold mineralization, *In:* Summary of Field Work and Other Activities 2014; Ontario Geological Survey, Open File Report 6300, p. 42-1 to 42-15.

Oswald, W., Castonguay, S., Dubé, B., McNicoll, V., Biczok, J., Malo, M., and Mercier-Langevin, P., in press. New insights on the geological and structural settings of the Musselwhite banded iron formation-hosted gold deposit, North Caribou greenstone belt, Superior Province, Ontario; Geological Survey of Canada, Current Research 2015-3, 19 p.

Pelletier, M., Mercier-Langevin, P., Crick, D., Tolman, J., Beakhouse, G.P., and Dubé, B., 2014. Preliminary observations on the nature and distribution of the deformed and metamorphosed hydrothermal alteration associated with the Archean Rainy River gold deposit, northwestern Ontario; Ontario Geological Survey, Open File Report 6300, p. 41-1 to 41-10.

Tóth, Z., Lafrance, B., Dubé, B., Mercier-Langevin, P., and McNicoll, V, 2013. Geological setting of banded iron formation-hosted gold mineralization in the Geraldton area, Northern Ontario: preliminary results; Geological Survey of Canada, Open File 7370, 54 p. doi:10.4095/292558

Tóth, Z., Lafrance, B., Dubé, B., Mercier-Langevin, P., and McNicoll, V., 2013. Targeted Geoscience Initiative 4. Lode gold deposits in ancient deformed and metamorphosed terranes: geological mapping and structural reappraisal of the banded iron formation-hosted gold mineralization in the Geraldton area, Ontario, *In:* Summary of Field Work and other Activities 2013; Ontario Geological Survey, Open File Report 6290, p. 58-1 to 58-14.

Tóth, Z., Lafrance, B., Dubé, B., Mercier-Langevin, P., and McNicoll, V.J., 2014. Targeted Geoscience Initiative 4. Lode gold deposits in ancient deformed and metamorphosed terranes: relative chronology between hydrothermal activity, gold mineralization and deformation events in the Geraldton area, NW Ontario, *In:* Summary of Field Work and Other Activities 2014; Ontario Geological Survey, Open File Report 6300, p. 40-1 to 40-10.

Wright-Holfeld, A., Mercier-Langevin, P., and Dubé, B., 2011. Mass changes and element mobility associated with the Westwood deposit ore zones, Doyon-Bousquet-LaRonde mining camp, Abitibi, Quebec; Geological Survey of Canada, Current Research 2011-8, 19 p. doi:10.4095/288023

Yergeau, D., Mercier-Langevin, P., Dubé, B., Jackson, S., Malo, M., Bernier, C., and Simard, P., 2014. Synvolcanic Au-Cu±Ag-Zn-Pb massive sulphides, veins and disseminations of the Westwood deposit, Abitibi greenstone belt, Québec; Geological Survey of Canada, Open File 7482, 54 p. doi:10.4095/293117

STUDENT THESES

Beauchamp A.-M., en préparation. Géologie, styles de minéralisation et d'altération de l'indice aurifère Mustang, Ceinture de roches vertes de la Basse-Eastmain, Province du Supérieur, Québec; Mémoire de maîtrise (M.Sc.), Institut national de la recherche scientifique – Centre Eau Terre Environnement, Québec, Québec.

Fontaine, A., en préparation. Géologie et genèse de la mine Éléonore, gisement aurifère Roberto, Baie James, Province du Supérieur, Québec, Canada; Thèse de doctorat (Ph.D.), Institut national de la recherche scientifique – Centre Eau Terre Environnement, Québec, Québec.

Goucerol, B., in preparation. Banded-Iron Formation primary geochemistry signatures, and exploration implications for BIF-hosted Au deposits; Ph.D. thesis, Laurentian University, Sudbury, Ontario.

Janvier, V., en préparation. Géologie et caractéristiques structurales du gisement aurifère Meadowbank, Nunavut, Canada; Thèse de doctorat (Ph.D.), Institut national de la recherche scientifique – Centre Eau Terre Environnement, Québec, Québec.

Katz, L., in preparation. The geology, alteration and mineralization of the Archean intrusion-related Côté Gold Au(-Cu) deposit; Ph.D. thesis, Laurentian University, Sudbury, Ontario.

Kelly, C.J., in prep. Dating the metamorphic veil of the North Caribou Superterrane via SIMS depth-profiling; Ph.D. thesis, University of Ottawa, Ottawa, Ontario.

Oswald, W., in prep. Structural and geological setting of the world-class Musselwhite gold deposit, Superior Province, Northwestern Ontario; Ph.D. thesis, Institut national de la recherche scientifique – Centre Eau Terre Environnement, Québec, Québec.

Pelletier, M., in prep. Geologic and structural controls on ore style and distribution in the Archean Rainy River Gold deposit, Wabigoon Subprovince, Ontario; M.Sc. thesis, Institut national de la recherche scientifique – Centre Eau Terre Environnement, Québec, Québec.

Ravenelle, J.-F., 2013. Amphibolite-facies gold mineralization: an example from the Roberto deposit, Eleonore property, James Bay, Quebec; Ph.D thesis, Institut national de la recherche scientifique – Centre Eau Terre Environnement, Québec, Québec, 283 p.

Tóth, Z., in prep. Banded iron formation-hosted gold mineralization – Beardmore-Geraldton area: structural setting, footprint(s), and exploration implications; Ph.D. thesis, Laurentian University, Sudbury, Ontario.

Yergeau, D., 2015. Géologie du gisement synvolcanique aurifère atypique Westwood, Abitibi, Québec; thèse de doctorat (Ph.D.), Institut national de la recherche scientifique – Centre Eau Terre Environnement, Québec, Quebec, 682 p.

CONFERENCE PROCEEDINGS/ABSTRACTS

Beauchamp, A.-M., Dubé, B., Malo, M., Archer, P., Chartrand, F., and Lavoie, J., 2014. Geology of the turbidite-hosted Mustang gold showing, lower Eastmain greenstone belt, Superior Province, Quebec, *In:* Program with Abstracts; Geological Association of Canada – Mineralogical Association of Canada Annual Joint Meeting, Fredericton, New Brunswick, May 2014, v. 37, p. 22.

Beauchamp, A.M., Dubé, B., Malo, M., Archer, P., Chartrand, F., and Lavoie, J., 2014. Geology of the turbidite-hosted Mustang gold showing, lower Eastmain greenstone belt, Superior Province, Quebec: preliminary results, *In:* Abstracts; Prospectors and Developers Association of Canada – Society of Economic Geologists Student Minerals Colloquium, Prospectors

and Developers Association of Canada International Trade Show and Investors Exchange, Toronto, Ontario, March 3rd, 2014. Available on-line at https://cmic-footprints.ca/pdac-smc/2014

Beauchamp, A.-M., Dubé, B., Malo, M., Archer, P., Lavoie, J. et Chartrand, F., 2015. Géologie, styles de minéralisation et d'altération de l'indice aurifère Mustang, Ceinture de roches vertes de la Basse-Eastmain, Province du Supérieur, Québec, Dans: Résumés des conférences et des photoprésentations; Québec Mines 2014, Ministère de l'Énergie et des Ressources naturelles du Québec, Québec, novembre 2014, DV 2015-03, p. 67.

Beaudoin, G., Mercier-Langevin P., Dubé, B., and Taylor, B.E., 2011. Low-temperature hydrothermal alteration at the world-class gold-rich VMS LaRonde Penna mine, Abitibi, Québec: An oxygen isotope study, *In:* Program with Abstracts; Geological Association of Canada – Mineralogical Association – Society of Economic Geologists – Society for Geology Applied to Mineral Deposits Annual Joint Meeting, Ottawa, Ontario, May 2011, v. 34, p. 13.

Bleeker, W., 2013. Major faults, synorogenic clastic deposits, and gold mineralization in Archean cratons: syn-orogenic extension followed by thick-skinned thrust burial, and final strike-slip, *In:* Program with Abstracts; Geological Association of Canada – Mineralogical Association of Canada Annual Joint Meeting, Winnipeg, Manitoba, May 2013, v. 36, p. 70–71.

Bleeker, W., 2014. The Abitibi breaks: Syn-orogenic extensional faults inverted as thick-skinned thrusts, and explaining the link with economic gold mineralization, Canada, *In:* Program with Abstracts; Geological Association of Canada – Mineralogical Association of Canada Annual Joint Meeting Fredericton, New Brunswick, May 2014, v. 37, p. 32–33.

Boudreau, C., Mercier-Langevin, P. Goutier, J. et Dubé, B., 2013. Caractérisation des unités volcaniques felsiques et des brèches de coulée à fragments de sulfures de la partie supérieure de la Formation de Rouyn-Pelletier, Rouyn-Noranda, Québec, Dans: Résumés des conférences et des photoprésentations; Québec Mines 2012, Ministère des Ressources naturelles du Québec, Quebec, novembre 2012, DV 2013-03, p. 51.

Castonguay, S., Janvier, V., Mercier-Langevin, P., Dubé, B., McNicoll, V., Malo, M., Pehrsson, S. and Bécu, V., 2012. Recognizing optimum Banded-Iron Formation-hosted gold environments in ancient, deformed and metamorphosed terranes: Preliminary results from the Meadowbank deposit, Nunavut, *In:* YKGSF Abstracts Volume, (comp.) D.M. Watson; 40th Annual Yellowknife Geoscience Forum, Northwest Territories Geoscience Office, Yellowknife, NWT, November 2012, v. 2012, p. 54.

De Souza, S., Dubé, B., McNicoll, V., Mercier-Langevin, P., de Chavigny, P., Gervais, D. et Caron, L., 2013. La mine Canadian Malartic, Abitibi: Observations préliminaires des caractéristiques géologiques et de la chronologie relative des minéralisations aurifères archéennes à basse teneur et fort tonnage, Dans: Résumés des conférences et des photoprésentations; Québec Mines 2012, Ministère des Ressources naturelles du Québec, Québec, novembre 2012, DV 2013-03, p. 45.

De Souza, S., Dubé, B., McNicoll, V., Mercier-Langevin, P., Dupuis, C., Creaser, R., de Chavigny, P. and Gervais, D., 2014. La mine Canadian Malartic, Abitibi, Québec: caractéristiques géologiques et chronologie relative de la minéralisation aurifères à basse teneur et fort tonnage, Dans: Résumés des conférences et des photoprésentations; Québec Mines 2013, Ministère des Ressources naturelles du Québec, Québec, novembre 2013, DV 2014-03, p. 16.

De Souza, S., Dubé, B., McNicoll, V., Dupuis, C., Mercier-Langevin, P. and Creaser, R., 2014. The Canadian Malartic world-class gold deposit: toward a multiphase model for Archean sediment- and porphyry-hosted low-grade large tonnage gold deposit, *In:* Abstracts; Prospectors and Developers Association of Canada – Society of Economic Geologists Student Minerals Colloquium, Prospectors and Developers Association of Canada International Trade Show and Investors Exchange, Toronto, Ontario, March 3rd, 2014. Available on-line at https://cmic-footprints.ca/pdac-smc/2014

De Souza, S., Dubé, B., McNicoll, V., Dupuis, C., Mercier-Langevin,P., and Creaser, R., 2014. Fracture-controlled hydrothermal alteration at the Canadian Malartic deposit: Toward a multiphase model for Archean intrusion-related low-grade bulk tonnage gold deposits, *In:* Program with Abstracts; Geological Association of Canada – Mineralogical Association of Canada Annual Joint Meeting, Fredericton, New Brunswick, May 2014, v. 37, p. 70.

De Souza, S., Dubé, B., Dupuis, C., Mercier-Langevin,P., McNicoll, V. et Creaser, R., 2015. Altération hydrothermale à la mine Canadian Malartic: distribution, minéralogie et géochimie d'un système aurifère archéen complexe et multiphasé, Dans: Résumés des conférences et des photoprésentations; Québec Mines 2014, Ministère de l'Énergie et des Ressources naturelles du Québec, Québec, novembre 2014, DV 2015-03, p. 45.

Dubé, B., Ravenelle, J.F., McNicoll, V., Malo, M., Nadeau, L., Creaser, R.A., and Simoneau, J., 2011. The world-class Roberto gold deposit, Éléonore property, James Bay area, Superior province, Quebec: Insights from geology and geochronology, *In:* Program with Abstracts; Geological Association of Canada – Mineralogical Association – Society of Economic Geologists – Society for Geology Applied to Mineral Deposits Annual Joint Meeting, Ottawa, Ontario, May 2011, v. 34, p. 55–56.

Dubé, B., Ravenelle, J.F., McNicoll, V., Malo, M., Nadeau, L., Creaser, R.A., and Simoneau, J., 2011. The world-class Roberto gold deposit, Éléonore property, James Bay area, Superior province, Quebec: Insights from geology and geochronology, *In:* Program with Abstracts; Geological Association of Canada –

Mineralogical Association – Society of Economic Geologists – Society for Geology Applied to Mineral Deposits Annual Joint Meeting, Ottawa, Ontario, May 2011, v. 34, p. 55–56.

Dupuis, C., Mercier-Langevin, P., McNicoll, V., Janvier, V., Dubé, B., Castonguay, S., de Chavigny, B., Pehrsson, S., and Côté-Mantha, O., 2014. The Vault gold deposit, Meadowbank area, Nunavut: Preliminary results on the nature and timing of mineralization, Canada, *In:* Program with Abstracts; Geological Association of Canada – Mineralogical Association of Canada Annual Joint Meeting, Fredericton, New Brunswick, May 2014, v. 37, p. 81.

Fontaine, A., Dubé B., Malo, M., McNicoll, V., and Brisson, T., 2014. Roberto gold deposit, Eleonore project, Superior Province, James Bay, Quebec, diversity of styles related to structural-metamorphic settings, *In:* Program with Abstracts; Geological Association of Canada – Mineralogical Association of Canada Annual Joint Meeting, Fredericton, New Brunswick, May 2014, v. 37, p. 93–94.

Fontaine, A., Dubé, B., Malo, M., McNicoll, V., and Brisson, T., 2014. Roberto gold deposit, Eleonore project Superior Province, James Bay, Quebec: relationships between tectono-metamorphic settings and ore bodies diversity, *In:* Abstracts; Prospectors and Developers Association of Canada – Society of Economic Geologists Student Minerals Colloquium, Prospectors and Developers Association of Canada International Trade Show and Investors Exchange, Toronto, Ontario, March 3rd, 2014. Available on-line at https://cmic-footprints.ca/pdac-smc/2014

Fontaine, A., Dubé, B., Malo, M., McNicoll, V. et Brisson, T., 2015. Géologie et caractéristiques structurales du gisement aurifère Roberto, propriété Éléonore, Province du Supérieur, Baie-James, Québec, Canada, Dans: Résumés des conférences et des photoprésentations; Québec Mines 2014, Ministère de l'Énergie et des Ressources naturelles du Québec, Québec, novembre 2014, DV 2015-03, p. 68.

Gagnon, E., Schneider, D.A., Hattori, K., and Biczok, J., 2013. Regional Metamorphism and Deformation of the North Caribou Belt (W. Superior Province) and the Relationship with the Lode Gold Mineralization at Musselwhite Mine, *In:* Abstracts; Society of Economic Geologists Annual Meeting, Whistler, British-Columbia, September 2013. Available on-line at http://www.segweb.org/SEG/Events/SEG_Conference_Website_Archives/SEG/_Events/SEG_Conference_Website_Archives

Gao, J.-F., Jackson S.E., and Dubé, B., 2013. Multi-stage gold mineralization at the Hollinger-McIntyre deposit: A LA-ICPMS mapping study, *In:* Goldschmidt 2013 conference abstracts; Mineralogical Magazine, v. 77, p. 1139.

Gao, J.-F., Jackson, S.E., Dubé, B., and De Souza, S., 2014. Gold mineralization in the Canadian Malartic deposit, Canada: Insights from textural and quantitative elemental mapping of pyrite, *In:* Program with Abstracts; Geological Association of Canada – Mineralogical Association of Canada Annual Joint Meeting, Fredericton, New Brunswick, May 2014, v. 37, p. 97–98.

Gourcerol, B., Thurston, P.C., Konak, D.J., and Côté-Mantha, O., 2014. The geochemistry of banded iron formation (BIFs) at the Meadowbank gold deposit, Churchill Province: Implications for the origin of gold mineralization in BIF deposits, *In:* Program with Abstracts; Geological Association of Canada – Mineralogical Association of Canada Annual Joint Meeting, Fredericton, New Brunswick, May 2014, v. 37, p. 107-108.

Gourcerol, B., Thurston, P.C., Kontak, D.J., and Côté-Mantha, O., 2014. The geochemistry of banded iron formation (BIFs) at the Meadowbank gold deposit, Churchill Province: implications for the sources of fluids in gold-mineralized in BIF deposits, *In:* Abstracts; Prospectors and Developers Association of Canada – Society of Economic Geologists Student Minerals Colloquium, Prospectors and Developers Association of Canada International Trade Show and Investors Exchange, Toronto, Ontario, March 3rd, 2014. Available on-line at https://cmic-footprints.ca/pdac-smc/2014

Gourcerol, B., Thurston, P.C., Kontak, D.J., Côté-Mantha, O., and Biczok, J., 2015. Depositional setting of Algoma-type Banded Iron Formation from the Meadowbank, Meliadine and Musselwhite gold deposits, *In:* Abstracts; Prospectors and Developers Association of Canada – Society of Economic Geologists Student Minerals Colloquium, Prospectors and Developers Association of Canada International Trade Show and Investors Exchange, Toronto, Ontario, March 2nd, 2015. Available on-line at http://cmic-footprints.ca/pdac-smc/2015

Jackson, S., Dubé, B., Chapman, J., and Gao, J.-F., 2013. Applications of LA-ICP-MS element mapping in mineral deposit research and exploration, *In:* Proceedings; 12th Biennial Society for Geology Applied to Mineral Deposits Meeting, Uppsala, Sweden, August 2013, v.1, p. 201–204.

Jackson, S., Gao, J. et Dubé, B., 2014. Nouveaux développements applicables à l'analyse des éléments en traces dans les dépôts de minéraux et cartographie utilisée pour la recherche et l'exploration des gisements de minerai: exemples de gisements d'or du Québec et de l'Ontario, Dans: Résumés des conférences et des photoprésentations; Québec Mines 2013, Ministère des Ressources naturelles du Québec, Québec, novembre 2013, DV 2014-03, p. 16.

Janvier, V., Castonguay, S., Mercier-Langevin, P., Dubé, B., Malo, M., McNicoll, V., Pehrsson, S., De Chavigny, B., and Côté-Mantha, O., 2014, Geology of the banded iron formation-hosted Meadowbank gold deposit, Nunavut, Canada, *In:* Program with Abstracts; Geological Association of Canada – Mineralogical Association of

Canada Annual Joint Meeting, Fredericton, New Brunswick, May 2014, v. 37, p. 127.

Janvier, V., Mercier-Langevin, P., Castonguay, S., Dubé, B., McNicoll, V., Pehrsson, S., Malo, M., de Chavigny, B., and Côté-Mantha, O., 2014. Geology and structural relationships of the Meadowbank BIF-hosted gold deposit, Nunavut, Canada, *In:* Abstracts; Prospectors and Developers Association of Canada – Society of Economic Geologists Student Minerals Colloquium, Prospectors and Developers Association of Canada International Trade Show and Investors Exchange, Toronto, Ontario, March 3rd, 2014. Available on-line at https://cmic-footprints.ca/pdac-smc/2014

Katz, L., Kontak, D.J., Dubé, B., McNicoll, V., Creaser, R., and Hamilton, M., 2013. The Archean Coté Gold deposit, Ontario, Canada: A large tonnage, low-grade deposit centred on a 2740 Ma magmatic-hydrothermal diorite breccia complex; *In:* Abstracts; Society of Economic Geologists Annual Meeting, Whistler, British-Columbia, September 2013. Available on-line at http://www.segweb.org/SEG/Events/SEG_Conference_Website_Archives/SEG/_Events/SEG_Conference_Website_Archives

Katz, L.R., Kontak, D.J., and Dubé, B., 2014. Chemical fingerprinting of the Archean Côté Gold deposit: A large-tonnage, low-grade intrusion-related deposit system, Ontario, Canada, *In:* Program with Abstracts; Geological Association of Canada – Mineralogical Association of Canada Annual Joint Meeting, Fredericton, New Brunswick, May 2014, v. 37, p. 134–135.

Katz, L.R., Kontak, D.J., and Dubé, B., 2014. The Archean Côté Gold intrusion-related Au (-Cu) deposit, Ontario, Canada: A largetonnage, low-grade deposit centred on a magmatic-hydrothermal breccia, *In:* Program with Abstracts; Geological Association of Canada – Mineralogical Association of Canada Annual Joint Meeting, Fredericton, New Brunswick, May 2014, v. 37, p. 133-134.

Katz, L.R., Kontak, D.J., Dubé, B., Rogers, J.R., McNicoll, V, and Creaser, R.A., 2014. The Côté Gold Au(-Cu) deposit, Ontario, Canada: an Archean large-tonnage, low-grade deposit centered on a magmatic-hydrothermal breccia, *In:* Abstracts; Prospectors and Developers Association of Canada – Society of Economic Geologists Student Minerals Colloquium, Prospectors and Developers Association of Canada International Trade Show and Investors Exchange, Toronto, Ontario, March 3rd, 2014. Available on-line at https://cmic-footprints.ca/pdac-smc/2014

Kelly, C., Schneider, D., Hattori, K., Biczok, J., and Schmitt, A., 2013. Resolving the Timing of Fluid Flow within Metamorphosed Terranes: U-Pb Age Depth-Profiles of Zircon from the North Caribou Greenstone Belt, Canada, *In:* Abstracts; Society of Economic Geologists Annual Meeting, Whistler, British-Columbia, September 2013. Available on-line at http://www.segweb.org/SEG/Events/SEG_Conference_Website_Archives/SEG/_Events/SEG_Conference_Website_Archives

Kontak, D.J., Katz, L., Creaser, R., and Hamilton, M., 2013. The Archean Côté Gold Au(-Cu) deposit of northern Ontario, Canada : A large tonnage, low-grade Au deposit centred on a 2740 Ma magmatic-hydrothermal diorite complex, *In:* Program with Abstracts; Geological Association of Canada – Mineralogical Association of Canada Annual Joint Meeting, Winnipeg, Manitoba, May 2013, v. 36, p. 122–123.

Lawley, C.J.M., Dube, B., Jackson, S., and Mercier-Langevin, P., 2013. Sulfide paragenesis and LA-ICP-MS arsenopyrite geochemistry at the Meliadine Gold District, Nunavut: Implications for Re-Os arsenopyrite geochronology and ore deposit genesis, *In:* Abstracts; Society of Economic Geologists Annual Meeting, Whistler, British-Columbia, September 2013. Available on-line at http://www.segweb.org/SEG/Events/SEG_Conference_Website_Archives/SEG/_Events/SEG_Conference_Website_Archives SEG-Whistler2013

McNicoll, V., Dubé, B., Biczok, J., Castonguay, S., Oswal, W., Mercier-Langevin, P., Skulski, T., and Malo, M., 2013. The Musselwhite gold deposit, North Caribou greenstone belt, Ontario: new high precision U-Pb ages and their impact on the geological and structural setting of the deposit, *In:* Program with Abstracts; Geological Association of Canada – Mineralogical Association of Canada Annual Joint Meeting, Winnipeg, Manitoba, May 2013, v. 36, p. 142.

Mercier-Langevin, P., Dubé, B., Yergeau, D., Galley, A., Wright-Holfeld, A., and Hannington, M., 2011. The Archean Westwood gold deposit, Abitibi: contrasting styles of auriferous mineralization and hydrothermal alteration, *In:* Program with Abstracts; Geological Association of Canada – Mineralogical Association of Canada – Society of Economic Geologists – Society for Geology Applied to Mineral Deposits Annual Joint Meeting, Ottawa, Ontario, May 2011, v. 34, p. 140.

Mercier-Langevin, P., Hannington, M., Dubé, B., and Bécu, V. 2011. The gold content of volcanogenic massive sulphide deposits, *In:* Conference Guide; Conference of Metallurgists 2011, World Gold 2011 meeting, Montreal, October 2011, p. 47–48.

Mercier-Langevin, P., Hannington, M., Dubé, B., McNicoll, V., Goutier, J., and Monecke, T., 2011. Geodynamic influences on the genesis of Archean world-class gold-rich VMS deposits: examples from the Blake River Group, Abitibi greenstone belt, Canada, *In:* Proceedings; 11th Biennal Society for Geology Applied to Mineral Deposits Meeting, Antofagasta, Chile, September 2011, p. 85–87.

Mercier-Langevin, P., Hannington, M., Dubé, B., McNicoll, V., Goutier, J., and Monecke, T., 2013. Geodynamic influences on the genesis of Archean world-class gold-rich VMS deposits: examples from the Blake River Group, Abitibi greenstone belt, Canada, *In:* Program with Abstracts; Geological Association of Canada-

Mineralogical Association of Canada Annual Joint Meeting, Winnipeg, Manitoba, May 2013, v. 36, p. 144–145.

Mercier-Langevin, P., Dubé, B., Hannington, M., and Bécu, V., 2012. The gold content of VMS deposits: Key features and controlling parameters, with implications for exploration in the Appalachain orogen, *In:* Program with Abstracts; Geological Association of Canada – Mineralogical Association of Canada Annual Joint Meeting, St-John's, Newfoundland, May 2012, v. 35, p. 91.

Mercier-Langevin, P., Lafrance, B., Bécu, V., Dubé, B., Kjarsgaard, I., Guha, J., and Ross, P.-S., 2013. Geology, alteration and mineralization of the Lemoine auriferous VMS deposit, Chibougamau camp, Abitibi greenstone belt, Quebec: Geologic evidence for a magmatic input, *In:* Program with Abstracts; Geological Association of Canada – Mineralogical Association of Canada Annual Joint Meeting, Winnipeg, Manitoba, May 2013, v. 36, p. 145.

Oswald, W., Dubé, B., Castonguay, S., McNicoll, V., Biczok, J., Mercier-Langevin, P., Malo, M., and Skulski, T., 2014. New insights on the geological setting of the world-class Musselwhite gold deposit, Superior Province, northwestern Ontario, *In:* Program with Abstracts; Geological Association of Canada – Mineralogical Association of Canada Annual Joint Meeting, Fredericton, New Brunswick, May 2014, v. 37, p. 311.

Oswald, W., Dubé, B., Castonguay, S., McNicoll, V., Biczok, J., Mercier-Langevin, P., Malo, M., and Skulski, T., 2014. New insights on the structural and geological setting of the world-class Musselwhite gold deposit, Superior Procvince, Northwestern Ontario, *In:* Abstracts; PDAC-SEG Student Minerals Colloquium, Prospectors and Developers Association of Canada International Trade Show and Investors Exchange, Toronto, Ontario, March 3rd, 2014. Available on-line at https://cmic-footprints.ca/pdac-smc/2014

Pelletier, M., Mercier-Langevin, P., Tolman, J., McNicoll, V., Dubé, B., Richer-Laflèche, M. and Beakhouse, G., 2014. Geologic and structural controls on ore style and distribution in the Archean Rainy River Gold deposit, Wabigoon Subprovince, Ontario: Preliminary results, *In:* Program with Abstracts; Geological Association of Canada – Mineralogical Association of Canada Annual Joint Meeting, Fredericton, New Brunswick, May 2014, v. 37, p. 218–219.

Pelletier, M., Mercier-Langevin, P., Tolman, J., McNicoll, V., Dubé, B., Richer-Laflèche, M., and Beakhouse, G., 2014. The Rainy River gold project, Wabigoon Subprovince, Ontario: preliminary observations on ore zone's geometry and style, and associated alteration, *In:* Abstracts; PDAC-SEG Student Minerals Colloquium, Prospectors and Developers Association of Canada International Trade Show and Investors Exchange, Toronto, Ontario, March 3rd, 2014. Available on-line at https://cmic-footprints.ca/pdac-smc/2014

Smith, J., Lafrance, B., and Kontak, D., 2014. A comparative study of the deformation history of auriferous quartz veins in the Archean Côté Gold deposit and the structural evolution of the spatially-related Ridout Deformation Zone, Swayze Greenstone Belt, northern Ontario, *In:* Program with Abstracts; Geological Association of Canada – Mineralogical Association of Canada Annual Joint Meeting, Fredericton, New Brunswick, May 2014, v. 37, p. 257–258.

Tóth, Z., Lafrance, B., Dubé, B., McNicoll, V.J., and Mercier-Langevin, P., 2014. Stratigraphic and structural setting of banded-iron-formation-hosted gold mineralisation in the Geraldton area, Ontario, *In:* Program with Abstracts; Geological Association of Canada – Mineralogical Association of Canada Annual Joint Meeting, Fredericton, New Brunswick, May 2014, v. 37, p. 272–273.

Tòth, Z., Lafrance, B., Dubé, B., Mercier-Langevin, P., and McNicoll. V., 2014. Structural setting, mineralogical characteristics and geochemical footprints of banded-iron-formation-hosted gold mineralisation in the Geraldton area, Ontario, *In:* Abstracts; Prospectors and Developers Association of Canada – Society of Economic Geologists Student Minerals Colloquium, Prospectors and Developers Association of Canada International Trade Show and Investors Exchange, Toronto, Ontario, March 3rd, 2014. Available on-line at https://cmic-footprints.ca/pdac-smc/2014

Yergeau, D., Mercier-Langevin, P., Malo, M., Dubé, B., Bernier, C., Savoie, A., Houle, N., et Simard, P., 2011. Géologie de la lentille de sulfures massifs polymétalliques aurifères Warrenmac, gisement Westwood, Abitibi, Québec, Dans: Résumés des conférences et des photoprésentations; Québec Exploration 2011, Ministère des Ressources naturelles et de la Faune du Québec, Québec, novembre 2011, DV 2011-03, p. 39.

Yergeau, D., Mercier-Langevin, P., et al., 2012. The Westwood deposit, southern Abitibi greenstone belt: a "hybrid" or "transitional" Archean gold deposit, *In:* Program with Abstracts; Geological Association of Canada – Mineralogical Association of Canada Annual Joint Meeting, Newfoundland, May 2012, v. 35, p. 154.

Yergeau, D., Mercier-Langevin, P., Dubé, B., Malo, M., Bernier, C., Savoie, A., and Simard, P., 2013. Synvolcanic Au-Cu±Ag-Zn-Pb massive sulphides, veins and disseminations of the Westwood deposit, Abitibi greenstone belt, Québec, *In:* Program with Abstracts; Geological Association of Canada – Mineralogical Association of Canada Annual Joint Meeting, Winnipeg, Manitoba, May 2013, v. 36, p. 201.

Yergeau, D., Mercier-Langevin, P., Dubé, B., Malo, M., Goutier, J. Bernier, C., Savoie, A., Houle, N. et Simard, P., 2013. Le gisement Westwood Abitibi, Québec: un sytème magmatique-hydrothermal aurifère archéen?, Dans: Résumés des conférences et des photoprésentations; Québec Mines 2012, Ministère des Ressources naturelles du Québec, Québec, novembre 2012, DV 2013-03, p. 51.